

Volume III

Midwestern Regional Carbon Sequestration Partnership  
(MRCSP) Phase III (Development Phase).



# Integrated Modeling Report for CO<sub>2</sub> Storage with Enhanced Oil Recovery in Northern Michigan

Prepared by:

Battelle  
505 King Avenue  
Columbus, Ohio 43201

Principal Investigator: Dr. Neeraj Gupta

Authors: Srikanta Mishra, Mark Kelley, Priya Ravi Ganesh, Autumn Haagsma, Samin Raziperchikolaei, Joel Main, Ashwin Pasumarti, Valerie Smith, Sanjay Mawalkar and Neeraj Gupta

Submitted to:

The U.S. Department of Energy, National Energy Technology Laboratory  
Program Manager: Andrea McNemar

DOE Project #DE-FC26-05NT42589

September 2020



## Notice

This report was prepared by Battelle as an account of work sponsored by an agency of the United States Government and other project sponsors, including Core Energy, LLC and The Ohio Development Services Agency. Neither the United States Government, nor any agency thereof, nor any of their employees, nor Battelle and other cosponsors, makes any warranty, express or implied, or assumes any liability or responsibility for the accuracy, completeness, or usefulness of any information, apparatus, product, or process disclosed, or represents that its use would not infringe privately owned rights. Reference herein to any specific commercial product, process, or service by trade name, trademark, manufacturer, or otherwise does not necessarily constitute or imply its endorsement, recommendations, or favoring by the United States Government or any agency thereof. The views and the opinions of authors expressed herein do not necessarily state or reflect those of the United States Government or any agency thereof.

Battelle does not engage in research for advertising, sales promotion, or endorsement of our clients' interests including raising investment capital or recommending investments decisions, or other publicity purposes, or for any use in litigation.

Battelle endeavors at all times to produce work of the highest quality, consistent with our contract commitments. However, because of the research and/or experimental nature of this work the client undertakes the sole responsibility for the consequence of any use or misuse of, or inability to use, any information, apparatus, process or result obtained from Battelle, and Battelle, its employees, officers, or Trustees have no legal liability for the accuracy, adequacy, or efficacy thereof.



## Acknowledgements

**Sponsorships** - This report is part of a series of reports prepared under the Midwestern Regional Carbon Sequestration Partnership (MRCSP) Phase III (Development Phase). These reports summarize and detail the findings of the work conducted under the Phase III project. The primary funding for the MRCSP program is from the US Department of Energy's National Energy Technology Laboratory (NETL) under DOE project number DE-FC26-05NT42589 with Ms. Andrea McNemar as the DOE project manager. The past DOE project managers for MRCSP include Dawn Deel, Lynn Brickett and Traci Rodosta. Many others in the DOE leadership supported, encouraged, and enabled the MRCSP work including but not limited to Kanwal Mahajan, John Litynski, Darin Damiani, and Sean Plasynski.

The Michigan Basin large-scale test received significant in-kind cost share from Core Energy, LLC, who also provided essential access to the field test site and related data. This contribution by Core Energy CEO Robert Mannes, VP Operations Rick Pardini, and Allan Modroo, VP Exploration, and the entire Core Energy staff is gratefully acknowledged. MRCSP work in Ohio has been supported by the Ohio Coal Development Office in the Ohio Development Services Agency under various grants (CDO D-10-7, CDO-D-13-22, CDO-D-13-24, and CDO-D-15-08) with Mr. Greg Payne as the OCDO project manager. Finally, several industry sponsors and numerous technical team members from State Geological Surveys, universities, field service providers have supported MRCSP through cash and in-kind contributions over the years as listed in the individual reports.

**Program Leadership** – During the MRCSP Phase III project period, several Battelle staff and external collaborators contributed to the successful completion of the program through their efforts in field work, geological data analysis and interpretation, and/or reporting. The primary project managers over the MRCSP performance period have included Rebecca Wessinger, Neeraj Gupta, Jared Walker, Rod Osborne, Darrell Paul, and David Ball. Additional project management support has been provided by Andrew Burchwell, Christa Duffy, Caitlin McNeil, and Jacqueline Gerst over the years.

**Principal Investigator:** Neeraj Gupta (614-424-3820/ [gupta@battelle.org](mailto:gupta@battelle.org))

**Report Authors and Principal Technical Contributors** – Srikanta Mishra, Mark Kelley, Priya Ravi Ganesh, Autumn Haagsma, Samin Raziperchikolaei, Joel Main, Ashwin Pasumarti, Valerie Smith, Sanjay Mawalkar and Neeraj Gupta

**Other Technical Contributors** – Rick Pardini, Allen Modroo, Bob Mannes, and Wayne Goodman



# Table of Contents

	Page
Acknowledgements .....	iii
Acronyms and Abbreviations .....	xxxiii
Executive Summary .....	xxxv
Preface .....	lxvii
1.0 Dover-33 Reef .....	1
1.1 Introduction .....	1
1.1.1 Reef Description .....	1
1.1.2 Modeling Objectives/Scope .....	3
1.2 Data Sources .....	4
1.2.1 Geologic Data .....	4
1.2.2 Primary Production .....	4
1.2.3 EOR/CO <sub>2</sub> Injection Rate and Pressure Data .....	6
1.3 Static Model .....	9
1.3.1 Framework .....	11
1.3.2 Property Modeling .....	21
1.4 Dynamic Model .....	34
1.4.1 Modeling Approach .....	34
1.4.2 Model Inputs .....	37
1.4.3 Primary Production History Match .....	41
1.4.4 EOR/CO <sub>2</sub> Injection History Match .....	43
1.4.5 Alternative Conceptualization Trials .....	46
1.4.6 Additional Model Variants and Insights .....	51
1.4.7 Exploring Time-Variant Property Changes .....	53
1.5 Geochemical Modeling .....	57
1.5.1 Modeling Approach .....	57
1.5.2 Geochemical Reactions in the Subsurface .....	59
1.5.3 Model Setup and Scenarios .....	59
1.5.4 Results .....	63
1.5.5 Summary .....	73
1.6 Conclusions .....	74
2.0 Bagley Reef .....	77
2.1 Modeling Objectives/Scope .....	77
2.2 Data Sources .....	78
2.2.1 Geologic and PVT Data .....	78
2.2.2 Primary Production and CO <sub>2</sub> Storage Phase .....	80
2.3 Static Model .....	82
2.3.1 Framework .....	82
2.3.2 Property Modeling .....	88
2.4 Dynamic Model .....	89
2.4.1 Modeling Approach and Input .....	89
2.4.2 Primary Production and CO <sub>2</sub> Injection Phase History Match .....	90
2.4.3 Model Forecast for the CO <sub>2</sub> -EOR Phase .....	93

2.5	Conclusions .....	96
3.0	Charlton 19 Reef .....	97
3.1	Introduction .....	97
3.1.1	Reef Description.....	97
3.1.2	Modeling Objectives/Scope .....	99
3.2	Data Sources .....	100
3.2.1	Geologic Data .....	100
3.2.2	Primary & Secondary Production.....	101
3.2.3	EOR/CO <sub>2</sub> Injection Rate and Pressure History.....	104
3.3	Static Model .....	105
3.3.1	Framework .....	105
3.3.2	Property Modeling.....	114
3.4	Dynamic Model .....	122
3.4.1	Modeling Approach .....	122
3.4.2	Model Inputs.....	123
3.4.3	Primary Production History Match .....	123
3.4.4	EOR/CO <sub>2</sub> Injection History Match.....	124
3.5	Conclusions .....	128
4.0	Chester 16 Reef .....	129
4.1	Introduction .....	129
4.1.1	Reef Description.....	129
4.1.2	Modeling Objectives/Scope .....	132
4.2	Data Sources .....	133
4.2.1	Geologic Data .....	133
4.2.2	Production and CO <sub>2</sub> Injection History .....	134
4.3	Static Model .....	139
4.3.1	Framework .....	140
4.3.2	Property Modeling.....	150
4.4	Dynamic Model .....	181
4.4.1	Modeling Approach .....	182
4.4.2	Model Inputs.....	186
4.4.3	Primary Production History Matching Process .....	190
4.4.4	EOR/CO <sub>2</sub> Injection History Matching Process .....	200
4.4.5	History Matching Results .....	205
4.4.6	History Matching with Alternative Conceptualization Using Seismic Data .....	213
4.4.7	Results of History Matching with Alternative Conceptualization.....	218
4.5	Forecasting Simulations .....	224
4.5.1	CO <sub>2</sub> -EOR Scenarios .....	224
4.5.2	Results and Discussion.....	232
4.6	Conclusions .....	238
5.0	Dover-33 Geomechanics .....	241
5.1	Introduction .....	241
5.2	System Description.....	243
5.3	Base Case Hydro-mechanical Response.....	244
5.4	Response Surface Model Fit and Independent Validation Results.....	249
5.4.1	Reservoir Top Vertical Displacement .....	249
5.4.2	Surface Uplift Prediction .....	256

## Table of Contents

5.4.3	I-stress (Horizontal Stress) Increment Prediction .....	260
5.4.4	K-stress (Vertical Stress) Increment Prediction .....	263
5.5	Validation of Results .....	266
5.6	Discussion .....	267
5.6.1	Importance of the Input Parameters .....	267
5.6.2	Optimization of Input Parameters Using Monte Carlo Simulation .....	268
5.7	Estimating Poroelastic Response of Injection using Experimental and Field Data .....	272
5.7.1	Experimental Description .....	272
5.7.2	Poroelastic Analytical Solution Results .....	276
5.7.3	Numerical Modeling Results of Multiphase Flow (CO <sub>2</sub> Injection) .....	280
5.8	Summary & Conclusions .....	283
6.0	References .....	285
Appendix A	Chester 16 Well-wise Oil and Gas Production History .....	A-1
Appendix B	Chester 16 Scenario 3 Simulation Results .....	B-1
Appendix C	Understanding Reservoir Mechanism Using History Matching: Dover 33 Field Carbon Dioxide EOR .....	C-1

## List of Tables

	Page
Table ES-1. Types of modeling applied to the reefs of interest .....	xxxvi
Table 1-1. Wells used to characterize the Dover-33 field with permit numbers and status .....	1
Table 1-2. Summary of available wireline log data for wells penetrating the Dover-33 reef field.....	4
Table 1-3. Horizon modeling in Petrel showing order of horizons and horizon type for the Dover-33 SEM.....	15
Table 1-4. Summary of the Dover-33 SEM zones, lithofacies, abbreviations, and descriptions.....	17
Table 1-5. Summary of grid parameters for the Dover-33 reef field. ....	19
Table 1-6. Summary of average porosity as computed in the fine-scale SEM for each zone and facies in the Dover-33 reef.....	24
Table 1-7. Summary of average permeability as computed in the fine-scale SEM for each zone and facies in the Dover-33 reef.....	26
Table 1-8. Summary of average water saturation as computed in the fine-scale SEM for each zone in the Dover-33 reef.....	27
Table 1-9. Volumetrics and HCPV for each reservoir reef facies. ....	29
Table 1-10. Summary of grid parameters for the Dover-33 reef field. ....	33
Table 1-11. Initial fluid composition used in the oil zone.....	40
Table 1-12. Initial conditions set up in the Level 3 Dover-33 dynamic model.....	40
Table 1-13. Petrophysical properties of the different zones in the modeled system of interest. ....	60
Table 1-14. Molecular weights of the pseudocomponents in the fluid modeled. ....	61
Table 1-15. Summary of brine geochemistry used to initialize the aqueous composition in the coupled GEM model.....	62
Table 1-16. Intra-aqueous chemical reactions considered for geochemistry in the coupled model .....	62
Table 1-17. Mineral dissolution/precipitation reactions considered in the coupled GEM model.....	62
Table 2-1. Wells in the Northern lobe.....	80
Table 2-2. Well logs in the Northern lobe.....	80
Table 2-3. Zones (intervals between two horizons) created for each formation in the Begley Reef.....	83
Table 2-4. Summary of grid parameters for the Bagley reef field .....	88
Table 2-5. Volumetrics and HCPV for Bagley reef.....	88
Table 3-1. Charlton 19 wells with permit number and status. ....	98
Table 3-2. Summary of wireline log data for the Charlton 19 reef; green shading indicates logs available by well. ....	100
Table 3-3. Field Summary information on reservoir conditions before and after primary production in Charlton 19 reef.....	101
Table 3-4. Zones (intervals between two horizons) created for each formation in the Charlton 19 SEM.....	109
Table 3-5. Summary of grid parameters for the Charlton-19 reef field. ....	113
Table 3-6. Summary of average porosity as computed in the SEM for each zone in the Charlton 19 reef. ....	117
Table 3-7. Method and values used to populate the permeability model. ....	119
Table 3-8. Summary of average permeability as computed in the SEM for each zone in the Charlton 19 reef. ....	120

Table 3-9.	Volumetrics and HCPV for each reservoir reef zone in the SEM. ....	121
Table 3-10.	Range of initial pressure ( $P_i$ ) estimates used as the input parameter and corresponding CRM results for Charlton 19. ....	126
Table 4-1.	Chester 16 wells with permit number and status (all wells are plugged). ....	129
Table 4-2.	Summary of available data for the wells in the Chester 16 reef field. ....	134
Table 4-3.	Summary of the various injection periods in the Chester 16, their associated target formations, and the quantities of $\text{CO}_2$ injected. ....	138
Table 4-4.	Summary of common lithofacies used in describing the reef and for model development. ....	143
Table 4-5.	Summary of grid parameters for the Chester 16 reef field. ....	146
Table 4-6.	Porosity property model input settings. ....	152
Table 4-7.	Summary of average porosity as computed in the fine-scale SEM for each zone in the Chester 16 reef. ....	152
Table 4-8.	Permeability property model input settings. ....	157
Table 4-9.	Summary of computed average permeability for each SEM zone. ....	158
Table 4-10.	Summary of average water saturation values for each zone in the Chester 16 SEM. ....	163
Table 4-11.	The three depositional facies of the Brown Niagaran do not conclusively map themselves onto three electro-facies. ....	168
Table 4-12.	Volumetrics and HCPV for each reef facies. ....	171
Table 4-13.	Volumetrics and HCPV for each reef facies. ....	179
Table 4-14.	Summary of computed average properties for the Brown Niagaran reef zone. ....	181
Table 4-15.	The various sources of data the model has integrated. ....	191
Table 4-16.	Shows the various permeability groups or "sub-facies," and the permeability bounds used to identify these regions within the Chester 16 model. The permeability multipliers or the permeability to each group is included. ....	194
Table 4-17.	Key uncertainties in the data and its impact on the dynamic modeling. ....	213
Table 4-18.	The ten scenarios evaluated by the forecasting simulations. ....	225
Table 4-19.	Cumulative amount of oil produced with each injector producer configuration, after 15 years of EOR. ....	234
Table 4-20.	Essential performance measures of each scenario relating to $\text{CO}_2$ , after 15 years of EOR. ....	234
Table 5-1.	Independent parameters distributions for the closed reservoir. ....	244
Table 5-2.	Model parameters for the base case. ....	245
Table 5-3.	Coefficient of quadratic polynomials and test of significance results for reservoir displacement (note: black color shows the excluded and red color shows the included terms). ....	250
Table 5-4.	Regression summary for full and reduced order polynomial model. ....	251
Table 5-5.	Coefficient of reduced order polynomial and test of significance results for reservoir displacement. ....	253
Table 5-6.	Regression summary for full and reduced order polynomial model. ....	258
Table 5-7.	Coefficient of reduced order polynomial and test of significance results for surface uplift. ....	258
Table 5-8.	Regression summary for full and reduced order polynomial model. ....	262
Table 5-9.	Coefficient of reduced order polynomial and test of significance results for I-stress increase. ....	262
Table 5-10.	Regression summary for full and reduced order polynomial model. ....	264
Table 5-11.	Coefficient of reduced order polynomial and test of significance results for K-stress increase. ....	264

## Table of Contents

Table 5-12.	Predictor values for the validation simulations.....	266
Table 5-13.	Simulation and model response prediction.....	267
Table 5-14.	Variable importance results of all responses in terms of R2 loss (red color shows high R2 loss). .....	267
Table 5-15.	Parameters to build the analytical model and geomechanical -multiphase flow model. ....	280
Table C-1	Summary of hierarchical history matching.....	C-7
Table C-2	Composition of the original fluid.....	C-11
Table C-3.	Comparison of experimental data with the calculated values from the history matched model for Case 1 .....	C-14
Table C-4.	Comparison of experimental data with the calculated values from the history matched model for Case 2.....	C-15
Table C-5.	Comparison of experimental data with the calculated values from the history matched model for Case 3.....	C-18
Table C-6.	Pore volume and fluid in place of the reservoir.....	C-20
Table C-7.	List of parameters to be considered for history matching .....	C-21

## List of Figures

	Page
Figure ES-1. Map showing location of reefs. ....	xxv
Figure ES-2. Simplified flow diagram of data integration into static and dynamic models.....	xxxvi
Figure ES-3. Cross section A-A' across the reef in the Dover -33 reef field showing changes in lithology and lithofacies from the southwest to the northeast. ....	xxxvii
Figure ES-4. Cross section of Charlton-19 Charlton-19's northern reef lobe showing thickness of formations and on-reef vs. off-reef Brown Niagaran (BN). ....	xxxviiii
Figure ES-5. Map view of Bagley reef showing multiple lobes and facies.....	xxxix
Figure ES-6. 2D cross section through the Chester-16 reef field showing the primary formations of interest (5x vertical exaggeration). Internal to the reef, the Brown Niagaran is further divided into three lithofacies: The Leeward, Reef Core, and Windward. ....	xli
Figure ES-7. Workflow for building static earth models. ....	xli
Figure ES-8. Cross section views of the porosity and permeability distributions in Dover-33 Depositional Lithofacies SEM. ....	xlivv
Figure ES-9. History-match results for: (a) oil production; (b) gas production; (c) water production; and (d) average reservoir pressure. The symbols represent field data and the lines show the model outputs.....	xlv
Figure ES-10. Modeled pressure response during the MRCSP Phase III CO <sub>2</sub> injection period. Here, the red circles represent observed bottom-hole pressure data, green circles represent simplified field CO <sub>2</sub> injection rate data, magenta lines are the modeled CO <sub>2</sub> injection rate, blue curve is the modeled injector bottom-hole pressure buildup and the brown and green curves are the modeled monitoring wells bottom-hole pressure buildup. ....	xlvi
Figure ES-11. Cross section views of the porosity and permeability distributions in Charlton-19 model. ....	xlviii
Figure ES-12. Filtered bottomhole pressure (left panel; psi units) and injection rate (right panel; rbbl/day units) data from the injection well during the CO <sub>2</sub> injection-only period being evaluated. ....	xlviii
Figure ES-13. Resulting coefficient of regression (R <sup>2</sup> ) and injectivity index (J) values for different initial pressure assumptions. The initial pressure value of 700 psi is seen to achieve the best fit or highest R <sup>2</sup> with a corresponding J value of 62 rbbl/day.psi.....	xlixix
Figure ES-14. The grid system for Bagley reef: The upper panel shows the top of A1-Carbonate. The lower panel shows the top of Brown Niagaran formation. ....	I
Figure ES-15. Predicted and measured average reservoir pressure.....	li
Figure ES-16. Injector Well (2-11) BHP comparison between field measurement and simulation.....	li
Figure ES-17. BHP and CO <sub>2</sub> injection rate for well 4-14 in Middle Lobe. The red box shows the time interval used for importing CRM model.....	lippi

Figure ES-18.	(A) Actual (field) CO <sub>2</sub> injection volume versus fitted data using simplified model (B) estimation of R <sup>2</sup> in different time interval.....	liii
Figure ES-19.	SEM upscaling results for the 79-layer model. A) Porosity model. B) Permeability model. ....	liv
Figure ES-20.	History-Match to the average pressure decline during the primary and secondary phase .....	lviii
Figure ES-21.	History match to the pressure response at the top of the Brown Niagaran, as measured at the 8-16 gauge.....	lviiii
Figure ES-22.	Comparison of all scenarios against each other in terms of oil recovery, CO <sub>2</sub> injection and CO <sub>2</sub> stored. Each performance metric is expressed as a percentage of the maximum observed across all 10 scenarios.....	lix
Figure ES-23.	Comparison of the average model pressure until the end of the post-injection period. The reference model with no geochemistry is shown as continuous curves while the geochemistry-coupled model for the CO <sub>2</sub> injection period is shown as dashed curves. The effect of these geochemical reactions can be seen by the divergence in the average pressures post 100-years of injection.....	lx
Figure ES-24.	Evolution of CO <sub>2</sub> , HCO <sub>3</sub> <sup>-</sup> and Cl <sup>-</sup> until the end of 1000 years in the coupled model. After the injection period, the moles of dissolved CO <sub>2</sub> increase as more CO <sub>2</sub> goes into solution with decreasing moles of CO <sub>2</sub> in the supercritical phase (orange dashed line). .....	lxii
Figure ES-25.	Surface uplift response surface based on reduced order model to estimate surface uplift.....	lxiii
Figure 1-1.	Plan view of the depositional model of the Dover- 33 reef field showing the subdivision into windward (purple), reef core (green), and leeward (blue) facies. ....	2
Figure 1-2.	Cross-section A-A' across the reef in the Dover -33 reef field showing changes in lithology and lithofacies from the southwest to the northeast. ....	2
Figure 1-3.	Simplified flow diagram of data integration into static and dynamic models.....	3
Figure 1-4.	Cumulative production in the Dover-33 reef field from 1974 through 2017 showing an increase in production rates after EOR operations began in 1996. ....	5
Figure 1-5.	Cumulative oil and gas production maps in the Dover-33 reef field showing the highest production in the middle of the reef in well 29565.....	6
Figure 1-6.	Historical monthly oil production and CO <sub>2</sub> injection rates, including primary and secondary recovery phases in Dover-33. ....	7
Figure 1-7.	Composite Plot of Bottomhole Pressure & Injection in Dover-33 .....	8
Figure 1-8.	Pressure buildup in injection and monitoring wells in Dover-33. IW1 refers to the injection well 1-33. MW1 and MW2 refer monitoring wells to 2-33 and 5-33 respectively. ....	9
Figure 1-9.	Comparison of Level 1 and Level 2 Dover-33 SEMs.....	10
Figure 1-10.	General workflow for the Michigan reef SEMs.....	11

Figure 1-11.	Side view of Dover-33 structural surfaces with wells used during SEM development.....	12
Figure 1-12.	Dover-33 structural surfaces. Elevation depth is from the mean sea level. A) Gray Niagaran, B) Brown Niagaran (reef), C) A1 Salt, D) A1 Carbonate, E) A2 Evaporite, and F) A2 Carbonate.....	13
Figure 1-13.	Isopach maps from the Dover-33 SEM. A) west to east trending cross-section a-a' through the SEM showing key formations. B) A2 Carbonate isopach. C) A2 Evaporite isopach. D) A1 Carbonate isopach. D) Brown Niagaran isopach.....	14
Figure 1-14.	Zoomed-in image of the SEM layers showing layers mimicking reef growth (blue, green, purple) and demonstrating deposition on top of the reef (orange, light gray, light blue).....	16
Figure 1-15.	Workflow depicting the delineation of lithofacies for the Brown Niagaran and A1 Salt in the Dover-33 reef. Polygons defining the reefal footprint and geometry were based on seismic interpretation along with formation tops. Polygons were prepared for generating surfaces that envelop reefal lithofacies.....	17
Figure 1-16.	Facies modeling of the A1 Carbonate to differentiate between reservoir (yellow) and non-reservoir flank (teal) by defining limits and orientation (A). B) illustrates the map view results of extent of the A1 Carbonate reservoir as oriented with paleo-wind direction and C) illustrates a 2D cross-section and results of facies modeling.....	18
Figure 1-17.	Cross-section through the Dover-33 SEM framework. Cross-section a-a' runs perpendicular to the reef structure, shown in panel (A) with the major reef zones and panel (B) with the reef facies. Cross-section b-b' runs parallel to the reef structure, shown in panel (C) with major reef zones and panel (D) with reef facies. The middle image shows the plan view of the x and y grid for the Dover-33 SEM with clipped boundary in red and full boundary in blue and locations of the two cross-section lines.....	20
Figure 1-18.	Core porosity-permeability transform plot for the A1 carbonate (yellow) and Brown Niagaran (brown).....	21
Figure 1-19.	Example of the scaled-up logs (right track) with the original logs overlying (red line) showing a close match at the SEMs grid resolution of 2-ft.....	23
Figure 1-20.	Porosity modeling results showing cross-section location (A), cross-section through SEM showing porosity (B), histogram comparing SEM porosity to wireline logs (C), and CDF of each porosity type (D).....	25
Figure 1-21.	Permeability modeling results showing cross-section location (A), and cross-section through SEM (B) with the histogram for the Brown Niagaran (C) and the A1 Carbonate Crest (D).....	26
Figure 1-22.	Results of the water saturation modeling in the Dover-33 SEM showing cross-section location (A), 3D side view of the oil water contact (B), and cross-section west to east colored by water saturation (C).....	28
Figure 1-23.	Cross-section through the SEM showing the computed HCPV by grid cell and location of OWC (blue plane).....	30

Figure 1-24.	Connect Up-grid results showing the design factor and step error for the Dover-33 SEM with the green dashed line highlighting the 64-layer case.....	31
Figure 1-25.	CDF comparison of wireline log porosity, fine-scale SEM porosity, and 64-layer SEM porosity.....	32
Figure 1-26.	Resulting porosity (A) and permeability (B) models for the 64-layer SEM showing preservation of reservoir property trends and heterogeneity.....	33
Figure 1-27.	Flowchart showing the different model versions that have been implemented for the Dover-33 reef.....	36
Figure 1-28.	Orthogonal cross-section views of the porosity and permeability distributions in the Level 3 Dover-33 model.....	38
Figure 1-29.	Phase envelope of tuned EOS with two sample laboratory calculations from historical fluid characterization effort.....	39
Figure 1-30.	Phase envelope (top panel) and oil viscosity comparison of tuned EOS with two sample laboratory calculations from historical fluid characterization effort.....	39
Figure 1-31.	Preliminary relative permeability curves for primary depletion period in Dover-33 Level 3 model.....	41
Figure 1-32.	Preliminary EOR and MRCSP period relative permeability curves in Dover-33 Level 3 model.....	41
Figure 1-33.	Example illustration of permeability scaling trial .....	42
Figure 1-34.	Final tuned relative permeability curves for primary depletion period in Dover-33 Level 3 model.....	42
Figure 1-35.	History match results for: (a) oil production; (b) gas production; (c) water production; and (d) average reservoir pressure during primary production until 1996. The symbols in the figures represent field data and the lines show model outputs.....	43
Figure 1-36.	Final tuned EOR and MRCSP period relative permeability curves in Dover-33 Level 3 model.....	43
Figure 1-37.	History match results for primary and CO <sub>2</sub> -EOR period: (a) oil production; (b) gas production; (c) water production; and (d) average reservoir pressure; the symbols in the figures represent field data and the lines show model outputs.....	44
Figure 1-38.	Simplified CO <sub>2</sub> injection rate schedule (green curve) imposed in the model for MRCSP Phase III CO <sub>2</sub> injection period. The blue lines show the daily injection rate data while the purple and red curves are the cumulative injection values for the modeled and daily rate data respectively. ....	45
Figure 1-39.	Modeled wells bottomhole pressure buildup response during the MRCSP Phase III CO <sub>2</sub> injection period in the latest Level 3 SEM conceptualization. Here, the red circles represent observed field data, magenta lines are the imposed CO <sub>2</sub> injection rate, blue curve is the modeled injector bottomhole pressure buildup and the brown and green curves are the modeled monitoring wells bottomhole pressure buildup.....	45

Figure 1-40.	Cross-section showing porosity and permeability distributions considered in the (1) simplified heterogeneity conceptualization with the equivalent homogeneous model, M0 and (2) simplified geometry with equivalent radial single-well model, M2 .....	46
Figure 1-41.	History match results for: (a) oil production; (b) gas production; (c) water production; and (d) average reservoir pressure. The symbols in the figures represent field data and the lines show M0 model outputs.....	47
Figure 1-42.	Modeled wells bottomhole pressure buildup response during the MRCSP Phase III CO <sub>2</sub> injection period in the equivalent homogeneous model conceptualization. Here, the red circles represent observed field pressure data, green circles represent simplified field CO <sub>2</sub> injection rate data, magenta lines are the modeled CO <sub>2</sub> injection rate, blue curve is the modeled injector bottomhole pressure buildup and the brown and green curves are the modeled monitoring wells bottomhole pressure buildup.....	48
Figure 1-43.	Cross-section of the porosity and permeability distribution in the equivalent homogeneous M1 model configuration.....	49
Figure 1-44.	Relative permeability curves for primary depletion period in the M1 model. ....	49
Figure 1-45.	EOR and MRCSP period relative permeability curves in the M1 model.....	49
Figure 1-46.	History match results for: (a) oil production; (b) gas production; (c) water production; and (d) average reservoir pressure. The symbols in the figures represent field data and the lines show M1 model outputs.....	50
Figure 1-47.	Modeled wells bottomhole pressure buildup response during the MRCSP Phase III CO <sub>2</sub> injection period in the equivalent homogeneous M1 model conceptualization. Here, the red circles represent observed field pressure data, green circles represent simplified field CO <sub>2</sub> injection rate data, magenta lines are the modeled CO <sub>2</sub> injection rate, the blue curve is the modeled injector bottomhole pressure buildup, and the brown and green curves are the modeled monitoring wells bottomhole pressure buildup.....	51
Figure 1-48.	Global mole fraction of CO <sub>2</sub> in a representative cross-section of the reef at different times during the Phase III injection and subsequent fall-off period. Difference maps in the bottom row indicate where CO <sub>2</sub> has moved to for the MRCSP injection period until October, 2014 and at the June, 2015 during the final fall-off period. Color scale represents presence versus absence (0.0) of CO <sub>2</sub> in any phase in the system. ....	52
Figure 1-49.	Possible explanations investigated to attribute the steeper pressure buildup near end of MRCSP injection.....	53
Figure 1-50.	Modeled pressure buildup during MRCSP injection period with increasing positive skin on injection well. While the trend of pressure buildup is steeper, the behavior of the injection well (blue model curves) deviates from the monitoring wells (overlying brown and green model curves), which is not in alignment with field observations. Reference M1 model does not have any well skin (i.e. skin = 0) modeled. Also, here the red circles represent observed field pressure data, green circles represent simplified field CO <sub>2</sub> injection rate data, and magenta lines are the modeled CO <sub>2</sub> injection rate.....	54

Figure 1-51.	Modeled injection well bottomhole pressure buildup response during the MRCSP Phase III CO <sub>2</sub> injection period in the equivalent radial M2 model conceptualization. Here, the black circles represent observed field pressure data while the green curve is the modeled injector bottomhole pressure buildup.....	55
Figure 1-52.	Comparison of simulated and observed pressures in the equivalent radial single-well model. ....	56
Figure 1-53.	Plot of pressure with total compressibility annotated for each CO <sub>2</sub> injection period. Total compressibility is calculated such that average reservoir pressure matches recorded field pressure data.....	56
Figure 1-54.	Schematic with considerations for the reactive and non-reactive processes considered during investigation of the dynamics of geologic carbon sequestration. The coupled model implemented in the current study thus included considerations for relevant hydrological and chemical processes indicated in Blue.....	58
Figure 1-55.	Radial model cross-section showing the porosity (left panel) and permeability (right panel) in the system.....	60
Figure 1-56.	Oil-water and gas-oil relative permeability curves used. ....	61
Figure 1-57.	Comparison of the pressure (injector bottomhole pressures in blue and average field pressure in cyan) response to CO <sub>2</sub> injection. Five injection- falloff periods feature in the injection schedule (injection rate in symbols and cumulative curves in brown) as shown. The reference model with no geochemistry is shown as continuous curves while the geochemistry-coupled model for the CO <sub>2</sub> injection period is shown as dashed curves.....	63
Figure 1-58.	Comparison of the gas saturation front and CO <sub>2</sub> presence at the end of the last injection period.....	64
Figure 1-59.	Comparison of the average model pressure until the end of the post-injection period. The reference model with no geochemistry is shown as continuous curves while the geochemistry-coupled model for the CO <sub>2</sub> injection period is shown as dashed curves. ....	65
Figure 1-60.	Difference maps of model cross-section to highlight comparison of the gas saturation front and CO <sub>2</sub> presence at the end of the 100 years and 1000 years after the injection period in the reference model.....	66
Figure 1-61.	Difference maps of model cross-section to highlight comparison of the gas saturation front and CO <sub>2</sub> presence at the end of the 100 years and 1000 years after the injection period in the coupled model. ....	67
Figure 1-62.	CO <sub>2</sub> distribution in the system at the end of injection .....	68
Figure 1-63.	CO <sub>2</sub> distribution in the system at the end of 100 years.....	68
Figure 1-64.	CO <sub>2</sub> distribution in the system at the end of 1000 years.....	68
Figure 1-65.	Evolution of CO <sub>2</sub> , HCO <sub>3</sub> <sup>-</sup> and Cl <sup>-</sup> until the end of 1000 years .....	69
Figure 1-66.	Evolution of calcite (red curves) and dolomite (blue curves) in the coupled GEM model .....	69

Figure 1-67.	Porosity change in coupled model at the end of 1000 years .....	70
Figure 1-68.	Comparison of the injector bottomhole pressure (blue curves) response to CO <sub>2</sub> injection between the reference coupled model and the high reservoir permeability coupled model. Five injection- falloff periods feature in the injection schedule (injection rate in symbols and cumulative curves in brown) as shown. The reference coupled model is shown as continuous curves while the high reservoir permeability coupled model is shown as dashed curves.....	71
Figure 1-69.	Comparison plots for the sensitivity to reservoir permeability (Top) Evolution of CO <sub>2</sub> , HCO <sub>3</sub> - and Cl <sup>-</sup> for 300 years (Bottom) Evolution of calcite (red curves) and dolomite (blue curves) in the coupled GEM models. ....	71
Figure 1-70.	Log 10 saturation indices for the dolomite (left column) and calcite (right column) minerals in the pH sensitivity trials. The top row corresponds to the reference pH coupled model while the bottom row corresponds to the higher pH coupled model scenario during the CO <sub>2</sub> injection period. ....	72
Figure 1-71.	Comparison plots for the sensitivity to formation brine pH (Top) Evolution of CO <sub>2</sub> , HCO <sub>3</sub> - and Cl <sup>-</sup> until the end of 300 years (bottom) Evolution of calcite (red curves) and dolomite (blue curves) in the coupled GEM models. ....	73
Figure 1-72.	Feedback to the latest geologic conceptual model using geologic know-how of the reef obtained from systematic dynamic modeling exercises for Dover-33 reef.....	75
Figure 2-1.	Cross-section of wells in northern pod.....	77
Figure 2-2.	Workflow of modeling approach for Bagley .....	78
Figure 2-3.	The estimated solution gas oil ratio using production data from Bagley oil field. ....	79
Figure 2-4.	The oil formation volume factor and solution gas-oil ratio versus pressure using standing correlation.....	79
Figure 2-5.	Primary production data for Bagley North lobe.....	81
Figure 2-6.	Bottomhole pressure and CO <sub>2</sub> injection rate for Bagley Northern lobe .....	82
Figure 2-7.	The surface map with depth contour of A1 carbonate (top) and Brown Niagaran formation (bottom).....	84
Figure 2-8.	The grid system for Bagley reef: The upper panel shows the top of A1-Carbonate. The lower panel shows the top of Brown Niagaran formation.....	85
Figure 2-9.	(Top) Map view of whole Bagley field (Bottom) Map view of study area: Northern lobe. ....	86
Figure 2-10.	(Top) Three-dimensional model for whole Bagley field (Bottom) Three-dimensional model for study area: Northern lobe .....	87
Figure 2-11.	Porosity distribution of Brown Niagaran Bagley Northern lobe based on log data.....	89
Figure 2-12.	Primary oil production data used as constraint in the model. ....	90
Figure 2-13.	Predicted and measured cumulative gas production (Top) Predicted and measured cumulative water production (Bottom). ....	91
Figure 2-14.	Predicted and measured average reservoir pressure.....	92
Figure 2-15.	Injector Well (2-11) BHP comparison between field measurement and simulation.....	92

Figure 2-16.	Oil-Water Relative permeability (top) Oil-Gas Relative permeability (bottom) used for history match process .....	93
Figure 2-17.	Predicted injector well BHP by injecting CO <sub>2</sub> (blue line). Note: The bottomhole pressure was not recorded during last phase of CO <sub>2</sub> injection (shown in red box).....	94
Figure 2-18.	(Top) oil and CO <sub>2</sub> production during a three months CO <sub>2</sub> -EOR forecast period (Bottom) effect of CO <sub>2</sub> -Oil mixing on oil recovery during CO <sub>2</sub> -EOR period .....	95
Figure 3-1.	Map of Charlton 19 reef field showing the two reef lobes and locations of wells used in the geologic analysis.....	97
Figure 3-2.	Cross-section of Charlton 19's northern reef lobe (as seen in Figure 3-1) showing thickness of formations and on-reef vs. off-reef Brown Niagaran (BN).....	99
Figure 3-3.	Simplified flow diagram of data integration into static and dynamic models.....	99
Figure 3-4.	Historical monthly production plot for 1-19. ....	102
Figure 3-5.	Historical monthly production plot for 2-18. ....	102
Figure 3-6.	Historical monthly production plot for 1-18. ....	103
Figure 3-7.	Charlton 19 cumulative production plot from 1988 through 2014.....	104
Figure 3-8.	Composite Plot of Bottomhole Pressure & Temperature in Charlton 19 during the MRCSP injection period from February 2015. ....	105
Figure 3-9.	Structural surfaces of the Charlton 19 model from the A2 Carbonate surface to the Model Base surface showing all wells that penetrate the reef structure.....	106
Figure 3-10.	Charlton structural surfaces. Elevation depth is from mean sea level. A) A2 Carbonate. B) A1 Carbonate. C) Brown Niagaran. D) Gray Niagaran. E) Oblique view of the A1 Carb Carbonate. F) Oblique view of the Brown Niagaran surface. Wells are labeled at the bottomhole location. ....	107
Figure 3-11.	Isopach maps from the Charlton 19 SEM. A) A2 Carbonate surface. B) A1 Carbonate surface. C) Brown Niagaran surface. D) Northeast-trending cross-section a-a' through the SEM showing these carbonate formations. ....	108
Figure 3-12.	Workflow depicting the delineation of lithofacies for the Brown Niagaran in the Charlton 19 reef. Polygons defining the reefal footprint and geometry were based on seismic interpretations. Along with formation tops, polygons were prepared for generating surfaces that envelop reefal lithofacies.....	109
Figure 3-13.	Horizon modeling in Petrel™ showing order of horizons and horizon type for the Charlton 19 SEM.....	110
Figure 3-14.	The map view right shows the Charlton 19 Brown Niagaran contours with the a-a' cross-section location. Only wells with logs are shown in the map view. The left shows Charlton 19 SEM layering schemes shown on Lithofacies cross-section. A) Preliminary SEM for developing and validating reefal architecture. B) Fine-scale, high-resolution model for petrophysical modeling. Note that the grid lines here are turned off; otherwise, the cross-section would appear black. ....	111
Figure 3-15.	Left: Plan view of the x and y grid for Charlton 19 SEM. SEM boundary in red. Left: Oblique view of the 357-layer SEM with cut-away revealing the northern and	

southern reef lobes. Black lines represent the BN reef elevation contours (SSTVD).....	112
Figure 3-16. Cross-section through the Charlton 19 SEM framework. SEM zones were partitioned by formation tops (surfaces). A) Partitioned zones in the northern reef structure and B) both reef structures. Lithofacies were distributed among the zones. The Brown Niagaran zone includes the reefal structure comprised of leeward, reef core, and windward lithofacies. NW-SE cross-section of the distribution of the reef facies in the C) northern reef structure and D) both reef structures. ....	114
Figure 3-17. Well log upscaling. Example of the tight match between well logs and well log upscaling at the SEM's grid resolution of 2-ft. Tracks left to right: gamma ray, facies, and average porosity. Top right: porosity histogram for the Elmac Hills 1-18A well comparing upscaled porosity log against original porosity (XPHIA) log. Bottom right: magnified view of the match between the well porosity log and its upscaled values.(colored blocks).....	116
Figure 3-18. A) Cross-section thought the porosity model. B) CDF comparison of average porosity for the A1 Carb. C) Map of the reef showing the orientation of cross-section a-a'. D) CDF comparison of average porosity for the Brown Niagaran reef. E) CDF comparison of average porosity for the entire SEM. ....	118
Figure 3-19. Dover-33 porosity-permeability cross-plots showing the power law transformations and associated equations used to populate permeability in the Charlton 19 model.....	119
Figure 3-20. A) Cross-section thought the permeability model. B) Histogram of permeability for the A1 Carb. C) Map of the reef showing the orientation of cross-section a-a'. D) Histogram of permeability for the Brown Niagaran reef. E) Histogram of permeability for the whole model. ....	120
Figure 3-21. Infographic highlighting the differences between the CRM and detailed numerical models used for reservoir simulation. ....	122
Figure 3-22. Oil Material Balance Calculations in May 2012. ....	124
Figure 3-23. Daily averaged bottomhole pressure (left panel; psi units) and bottomhole injection rate (right panel; rbbl/day units) data from the injection well during the CO <sub>2</sub> injection only period being evaluated. ....	125
Figure 3-24. Filtered bottomhole pressure (left panel; psi units) and injection rate (right panel; rbbl/day units) data from the injection well during the CO <sub>2</sub> injection only period being evaluated. ....	125
Figure 3-25. Resulting coefficient of regression (R <sup>2</sup> ) and injectivity index (J) values for different initial pressure assumptions. The initial pressure of 700 psi is seen to achieve the best fit or highest R <sup>2</sup> with a corresponding value of 62 rbbl/day.psi. ....	126
Figure 3-26. Snapshot of CRM interface showing the input and output fields. The calculations correspond to the initial pressure of 700 psi, which is seen to achieve the best fit or highest R <sup>2</sup> . ....	127

Figure 4-1.	Map of the Chester 16 reef field showing well locations and structure of the Brown Niagaran. The left panel shows a contour map depth-surface of the Chester 16. The right panel shows the two-pod structure of the Chester 16. ....	130
Figure 4-2.	Simplified stratigraphic column in the Chester 16 reef field highlighting key confining units and reservoirs. ....	131
Figure 4-3.	2D cross-section through the 3D SEM of the Chester 16 reef field showing resulting zones (5x vertical exaggeration). Internal to the reef, the Brown Niagaran is further divided into three lithofacies: the Leeward, Reef Core, and Windward. ....	132
Figure 4-4.	Simplified flow diagram of data integration into static and dynamic models.....	133
Figure 4-5.	The field-wide oil and gas production rates of the Chester 16 reef. ....	135
Figure 4-6.	Pie chart (above) and bubble chart (below) of total cumulative oil and gas production from the five wells of the Chester 16.....	136
Figure 4-7.	Cumulative barrels of water injected through the two injector wells, and the estimated total water production during the waterflood. Waterflooding occurred from 1984 to 1991.....	137
Figure 4-8.	Plot of the bottomhole pressure, injection rate, and cumulative injection quantities in the 6-16 well. ....	138
Figure 4-9.	Composite plot of the bottomhole pressures and temperature recorded at the 8-16 monitoring well, in response to the injection at the 6-16 well. ....	139
Figure 4-10.	General workflow for the Chester 16 reef SEM. ....	140
Figure 4-11.	Chester 16 structural surfaces shown with the seven wells used during SEM development.....	141
Figure 4-12.	Chester 16 structural surfaces. Elevation depth is from mean sea level. A) A2 Carbonate. B) A1 Carbonate. C) Brown Niagaran. D) Gray Niagaran. E) Oblique view of the A1 Carbonate. F) Oblique view of the Brown Niagaran surface.....	142
Figure 4-13.	Isopach maps from the Chester 16 SEM. A) Northeast trending cross-section a-a' through the SEM showing key carbonate formations. B) A2 Carbonate isopach. C) A1 Carbonate Crest isopach. D) Brown Niagaran isopach. E) Oblique view of SEM showing the A1 Carbonate Crest draped over the Brown Niagaran reef. ....	144
Figure 4-14.	Workflow depicting the delineation of lithofacies for the Brown Niagaran in the Chester 16 reef. Polygons defining the reefal footprint and geometry were based on seismic interpretations. Along with formation tops, polygons were prepared to generate surfaces that envelop reefal lithofacies. ....	145
Figure 4-15.	Horizon modeling in Petrel showing horizon order and type within the Chester 16 SEM. ....	146
Figure 4-16.	Top: Plan view of the x and y grid for Chester 16 SEM. SEM boundary in red. Bottom: Oblique view of the coarse-scale, 82-layer SEM with cut-away revealing two-pod Niagaran reefal structure.....	147
Figure 4-17.	Northeast trending cross-section through the Chester 16 SEM framework. A) SEM zones were partitioned by formation tops (horizons). B) Lithofacies were	

distributed among the zones. The Brown Niagaran zone includes the reefal structure comprised of leeward, reef core, and windward lithofacies. The A1 Carb Flank has been partitioned to include a saddle area that straddles the two pods.....	148
Figure 4-18. Chester 16 SEM layering schemes shown on lithofacies cross-section. A) Coarse-scale SEM for developing and validating reefal architecture. B) Fine-scale, high-resolution model for permeability prediction and petrophysical modeling. Note that the grid lines here are turned off; otherwise, the cross-section would appear black. C) Upscaled layering results originated from the fine-scale model. The layering scheme seeks to preserve heterogeneity and is for DRM use. ....	149
Figure 4-19. Well log upscaling. Example of the tight match between well logs and well log upscaling at the SEM's grid resolution of 0.5-ft. Tracks left to right: Gamma ray, facies, neutron porosity, synthesized permeability, and water saturation. Top right shows a zoomed-in view of the match between the well porosity log and its upscaled values (colored blocks). Bottom right: Porosity histogram for the A1 Carbonate Crest comparing upscaled porosity log against original neutron porosity (NPHI) log.....	151
Figure 4-20. A) Cross-section through the porosity model. B) CDF comparison of neutron porosity for the A1 Carbonate Crest. C) Map of the reef showing the orientation of cross-section a-a'. D) CDF comparison of neutron porosity for the Brown Niagaran reef (Leeward, Reef Core and Windward). E) CDF comparison of neutron porosity for the entire SEM. ....	153
Figure 4-21. Example core data cross plot of permeability versus porosity. Different trendlines or fits are shown and can be used to predict permeability. x= porosity, y=permeability.....	154
Figure 4-22. Permeability prediction workflow that adds simulated residuals (step 5) to the basic permeability transform (step 3). $K_{final}$ represents the final, synthesized permeability log. ....	155
Figure 4-23. A) Cross-section through the permeability model. B) CDF comparison of permeability for the A1 Carbonate Crest. C) Map of the reef showing the orientation of cross-section a-a'. D) CDF comparison of permeability for the Brown Niagaran reef (Leeward, Reef Core and Windward). E) CDF comparison of permeability for the A1 Carb Flank. ....	159
Figure 4-24. SEM upscaling optimization using CONNECT UpGrid™. A) Diagnostic plot showing upscaling design factor and step error as a function of SEM layer count. B) Zoomed-in to 400 layers; SE cycles show "over-homogenization." C) Zoomed-in to 200 layers, plot shows the selection of a 79-layer model with high DF and low SE. ....	160
Figure 4-25. SEM upscaling results. A) Oblique view of the 110,600 cell, 79-layer SEM. B) Cross-section through the SEM with varying layer thickness related to how layers had been grouped. ....	161
Figure 4-26. SEM upscaling results for the the 79-layer model. A) Porosity model. B) Permeability model.....	162

Figure 4-27.	The top panel shows flat OWC at the bottom of the Chester 16, while the bottom panel shows height from the OWC to the centroid of every cell in the Chester 16 reservoir model. ....	165
Figure 4-28.	Height vs water saturation for the A1 Carbonate.....	166
Figure 4-29.	J-function fit to the A1 Carbonate. ....	166
Figure 4-30.	Cluster dendrogram of the well logs in the Chester 16.....	168
Figure 4-31.	Height vs water saturation for the Brown Niagaran .....	169
Figure 4-32.	Height vs Water Saturation for the Brown Niagaran smoothed and split into "good" and "bad" quality rock.....	170
Figure 4-33.	Water saturation relationship for the Brown Niagaran .....	170
Figure 4-34.	A) Cross-section through the water saturation model. B) Water saturation histogram for the A1 Carbonate Crest. C) Water saturation histogram for the A1 Carb Flank which includes the saddle region. D) water saturation histogram for the Brown Niagaran reef consisting of the leeward, reef core, and windward lithofacies. ....	172
Figure 4-35.	Cross-section through the SEM showing the computed HCPV on the upscaled, 79-layer grid. ....	173
Figure 4-36.	Cross-sections through the seismic inversion results and property modeling. A) Acoustic impedance inversion volume in seismic domain. B) Porosity inversion volume in seismic domain. AI volume to porosity volume transform upper right. C) Sampled porosity inversion volume in SEM domain for the Brown Niagaran. D) Brown Niagaran porosity model in the SEM domain recalibrated to neutron porosity logs.....	174
Figure 4-37.	Porosity model with Brown Niagaran reef conditioned by seismic porosity inversion. A) Cross-section through the porosity model. B) CDF comparison of neutron porosity for the A1 Carbonate Crest. C) Map of the reef showing the orientation of cross-section a-a'. D) CDF comparison of neutron porosity for the Brown Niagaran reef (leeward, reef core and windward). E) CDF comparison of neutron porosity for the entire SEM. ....	176
Figure 4-38.	Permeability model with Brown Niagaran reef conditioned by seismic inversion. A) Cross-section through the permeability model. B) CDF comparison of permeability for the A1 Carbonate Crest. C) Map of the reef showing the orientation of cross-section a-a'. D) CDF comparison of permeability for the Brown Niagaran reef (leeward, reef core and windward). E) CDF comparison of permeability for the A1 Carb Flank. ....	178
Figure 4-39.	Water saturation model with Brown Niagaran reef affected by seismic inversion. A) Cross-section through the water saturation model. B) Water saturation histogram for the A1 Carbonate Crest. C) Water saturation histogram for the A1 Carb Flank that includes the saddle region. D) water saturation histogram for the Brown Niagaran reef consisting of the leeward, reef core, and windward lithofacies. ....	179
Figure 4-40.	Cross-section through the new SEM of the alternative conceptualization, showing the computed HCPV on the upscaled, 79-layer grid.....	180

Figure 4-41.	Cross-plots of Brown Niagaran model properties showing updated (with seismic inversion) versus original. A) Porosity models. B) Permeability models. C) Water saturation models.....	181
Figure 4-42.	An aerial view of the reservoir model showing the gridding and location of all wells of the Chester 16 (top panel) and a cross-section though the model showing the initial pressure gradient (bottom panel). .....	183
Figure 4-43.	The location of the perforated intervals for all wells (bottom) with respect to the formation is shown via a customized cross-section through all wells (top). .....	184
Figure 4-44.	Simple relative permeability curves (oil-water on the left, and liquid-gas on the right) were used in the model.....	186
Figure 4-45.	Ternary diagram displaying the oil relative permeability for 3-phase flow, as used in the model. The end points represent 100% saturations of water, oil and gas. Stone's second model as modified by Aziz and Settari was used to generate this diagram. ....	187
Figure 4-46.	Inflection point in pressure decline in the Chester 16 was around 1800 psi. ....	188
Figure 4-47.	Oil Formation Volume Factor of the Chester 16 oil.....	188
Figure 4-48.	Solution GOR of the Chester 16 oil.....	189
Figure 4-49.	Gas formation volume factor of the Chester 16 oil. ....	189
Figure 4-50.	oil viscosity of the Chester 16 oil.....	190
Figure 4-51.	Oil production from the preliminary runs does not match. ....	192
Figure 4-52.	Gas production from the preliminary run does not match.....	193
Figure 4-53.	The three sub-facies in the A1 Carbonate shown in blue, green and red. ....	195
Figure 4-54.	The distribution of the four sub-facies in the Upper Brown Niagaran, shown as blue (lowest permeability), light green, dark green and red (highest permeability). ....	196
Figure 4-55.	The four facies of the lower Brown Niagaran, shown in blue (lowest permeability), light green, dark green and red (highest permeability). ....	196
Figure 4-56.	Manual assignment of a 40md permeability around the 3-16 well in the Upper Brown Niagaran. ....	197
Figure 4-57.	Some flank layers, such as this, have been manually assigned permeability values. The light blue, green and red regions are 1 md, 3 md and 7 md respectively. The higher permeabilities reflect regions of higher porosity. The inner most dark blue region is the Saddle region, with a very low permeability (0.001 md). ....	197
Figure 4-58.	The higher permeability streak in the middle of the Brown Niagaran. The base of the A1 is a permeability baffle and has been assigned a low permeability of 0.01 md. ....	199
Figure 4-59.	Original permeability field in the Chester 16 before history matching. ....	199
Figure 4-60.	Permeability had to be scaled upward and the heterogeneity reduced significantly in order to obtain a history match.....	200

Figure 4-61.	The temperature response at the 6-16 injector well through the seven main injection periods from 2017 through 2018. ....	201
Figure 4-62.	A closer look at the injection and warm back period at the 6-16 well for injection period 4. ....	202
Figure 4-63.	Gauge pressure responses of the 8-16 well to the 7 seven injection periods. ....	203
Figure 4-64.	The temperature profile recorded at the 8-16 well. Data from the 2018, or the second year of injection is shown. ....	204
Figure 4-65.	The allocation of injection volumes to each perforation of the 6-16 well for all eight injection periods. ....	205
Figure 4-66.	History Match to the average pressure decline during the primary and secondary phase. ....	206
Figure 4-67.	History matched model produces the cumulative volume of oil as expected. ....	206
Figure 4-68.	The cumulative gas production of the history matched model vs field data ....	207
Figure 4-69.	The cumulative water production of the history matched model vs field data ....	207
Figure 4-70.	Lowering the relative permeability to water in the history matched model results in less water production from the waterflooding phase (left). However, this occurs at the expense of oil production (right). ....	208
Figure 4-71.	Lowered water production leads to a loss of the history match to the average reservoir pressure decline.....	208
Figure 4-72.	History match to the pressure response at the A1 carbonate, as measured at the 8-16 gauge.....	209
Figure 4-73.	History match to the pressure response at the top of the Brown Niagaran, as measured at the 8-16 gauge.....	210
Figure 4-74.	History match to the pressure response at middle of the Brown Niagaran, as measured at the 8-16 gauge.....	211
Figure 4-75.	History match to the pressure response at the bottom of the Brown Niagaran, as measured at the 8-16 gauge.....	211
Figure 4-76.	Shows the CO <sub>2</sub> saturation around the 8-16 monitoring well in April of 2018 (top) and the end of 2018 (bottom).....	212
Figure 4-77.	Cross-section of the Chester 16 showing its porosity distribution after integrating data from the seismic survey. ....	215
Figure 4-78.	The permeability field in the new model has been scaled to obtain the history match. ....	216
Figure 4-79.	The permeability in the Brown Niagaran in the new model integrating seismic data also had to be modified similarly to the earlier model. The heterogeneity was reduced, and the model permeability was scaled upward. ....	216
Figure 4-80.	Two cross-sections of the permeability field in the new Chester 16 model after history matching. ....	217
Figure 4-81.	Cross-section showing the initial water saturation in the new model. ....	218

Figure 4-82.	The average reservoir pressure decline in the alternative conceptualization.....	219
Figure 4-83.	All the oil production constraints are met in the new model.....	219
Figure 4-84.	The gas production history match with the alternative conceptualization.....	220
Figure 4-85.	The cumulative water production from the waterflood is more closely matched in the new model.....	220
Figure 4-86.	History match to the pressure response at the A1 carbonate, as measured at the 8-16 gauge, with the new model.....	221
Figure 4-87.	History match to the pressure response at the top of the Brown Niagaran, as measured at the 8-16 gauge, with the new model.....	222
Figure 4-88.	History match to the pressure response at the middle of the Brown Niagaran, as measured at the 8-16 gauge, with the new model.....	222
Figure 4-89.	History match to the pressure response at the bottom of the Brown Niagaran, as measured at the 8-16 gauge, with the new model.....	223
Figure 4-90.	The injector producer configurations of Scenario 1 are shown via various cross-sections through the Chester 16.....	227
Figure 4-91.	The injector producer configurations of Scenario 2 are shown via various cross-sections through the Chester 16.....	227
Figure 4-92.	The injector producer configurations of Scenario 3 are shown via various cross-sections through the Chester 16.....	228
Figure 4-93.	The injector producer configurations of Scenario 4 are shown via various cross-sections through the Chester 16.....	228
Figure 4-94.	The injector producer configurations of Scenario 5 are shown via various cross-sections through the Chester 16.....	229
Figure 4-95.	The injector producer configurations of Scenario 6 are shown via various cross-sections through the Chester 16.....	229
Figure 4-96.	The injector producer configurations of Scenario 7 are shown via various cross-sections through the Chester 16.....	230
Figure 4-97.	The injector producer configurations of Scenario 8 are shown via various cross-sections through the Chester 16.....	230
Figure 4-98.	The injector producer configurations of Scenario 9 are shown via various cross-sections through the Chester 16.....	231
Figure 4-99.	The injector producer configurations of Scenario 10 are shown via various cross-sections through the Chester 16.....	231
Figure 4-100.	Comparison of all scenarios against each other in terms of oil recovery, CO <sub>2</sub> injection and CO <sub>2</sub> stored. Each performance metric is expressed as a percentage of the maximum observed across all 10 scenarios.....	232
Figure 4-101.	A scatterplot of cumulative oil recovered, and net CO <sub>2</sub> stored in each scenario.....	233
Figure 4-102.	Cumulative oil recovery via CO <sub>2</sub> -EOR, from each scenario. ....	236
Figure 4-103.	Total field oil production rate during CO <sub>2</sub> -EOR, from each scenario. ....	236

Figure 4-104.	Producing CO <sub>2</sub> -oil ratio during CO <sub>2</sub> -EOR, from each scenario.....	237
Figure 5-1.	(A) Areal extend of pinnacle reefs in Northern Pinnacle Reef Trend of the Michigan Basin (B) Nomenclature and stratigraphy in Northern Pinnacle Reef Trend of the Michigan Basin. ....	243
Figure 5-2.	Reservoir cross-section .....	246
Figure 5-3.	Geomechanics cross-section with reservoir in the middle.....	247
Figure 5-4.	CO <sub>2</sub> saturation in the Reservoir cross-section at the end of 30 years injection period .....	247
Figure 5-5.	Vertical displacement in the geomechanics cross-section .....	248
Figure 5-6.	Surface uplift map in the geomechanics module .....	248
Figure 5-7.	(A) Actual (i.e., based on numerical model) versus predicted (i.e. based on reduced order model) reservoir displacement for quadratic model (B) Diagnostic plot for residual: residual versus predicted. ....	252
Figure 5-8.	(A) Actual (i.e., based on numerical model) versus predicted (i.e. based on reduced order model) reservoir displacement for reduced order model (B) Diagnostic plot for residual: residual versus predicted.....	254
Figure 5-9.	Reservoir Displacement Response Surface based on reduced order model.....	255
Figure 5-10.	(A) Actual (i.e., based on numerical model) versus predicted (i.e. based on reduced order model) surface uplift for reduced order model (B) Diagnostic plot for residual: residual versus predicted. ....	257
Figure 5-11.	Surface uplift response surface based on reduced order model.....	259
Figure 5-12.	(A) Actual (i.e., based on numerical model) versus predicted (i.e. based on reduced order model) I-stress increase for reduced order model (B) Diagnostic plot for residual: residual versus predicted .....	261
Figure 5-13.	I-stress increase response surface based on reduced order model.....	263
Figure 5-14.	(A) Actual (i.e., based on numerical model) versus predicted (i.e. based on reduced order model) reservoir displacement for reduced order model (B) Diagnostic plot for residual: residual versus predicted .....	265
Figure 5-15.	K-stress increase response surface based on reduced order model .....	266
Figure 5-16.	Input Parameters Distribution: (A) Young's modulus (B) Poisson's ratio (C) Depth.....	269
Figure 5-17.	Poroelastic response distribution: (A) I-stress distribution (B) K-stress distribution .....	270
Figure 5-18.	Poroelastic response distribution: (A) I-stress distribution (B) K-stress distribution (C) vertical displacement distribution (D) Surface uplift distribution .....	271
Figure 5-19.	(a) plot of volumetric strain versus confining stress, (b) Biot's Coefficient versus confining stress .....	274
Figure 5-20.	(c) Biot's Coefficient versus effective stress ( $\alpha = -8.965e-5\sigma' + 0.9$ ) (d) Predicted and measured Biot's Coefficient using multi-variate linear regression, $R^2$ of 0.98. ....	275

Figure 5-21.	(a) total stress increase versus pore pressure increase (b) effective stress decrease by pore pressure increase.....	278
Figure 5-22.	(c) trend of Biot's Coefficient as a function of pore pressure (d) surface uplift as a function of pore pressure increase.....	279
Figure 5-23.	Total stress increase versus pore pressure increase .....	281
Figure 5-24.	Effective stress decrease by pore pressure increase .....	282
Figure 5-25.	Uplift as a function of pore pressure increase. ....	282
Figure A-1.	Production history of the 1-16 well.....	A-2
Figure A-2.	Production history of the 2-16 well.....	A-2
Figure A-3.	Production history of the 3-16 well.....	A-3
Figure A-4.	Production history of the 4-21 well.....	A-3
Figure A-5.	Production history of the 5-21 well.....	A-4
Figure B-1.	CO <sub>2</sub> injection rate (left) and the cumulative CO <sub>2</sub> injected (right).....	B-2
Figure B-2.	Average reservoir pressure in the A1 Carbonate (top) and the Brown Niagaran (bottom) during CO <sub>2</sub> -EOR.....	B-2
Figure B-3.	Pressure distribution in the reservoir at the end of fill-up (top) and at the end of EOR (bottom).....	B-3
Figure B-4.	Field oil rate (top) and Cumulative oil production (bottom).....	B-3
Figure B-5.	Oil production contributions of individual producers. 8-16 Rev is shown on top and 6-16 is shown at the bottom.....	B-4
Figure B-6.	The bottomhole voidage replacement rate is kept as close to unity as possible for the duration of EOR .....	B-4
Figure B-7.	Oil saturation distribution initially (left) and after primary depletion (right).....	B-5
Figure B-8.	Oil saturation at the end of primary depletion (right) and at the end of waterflooding (right) .....	B-6
Figure B-9.	Oil Saturation at the end of waterflooding (left) and at the end of the fillup period (right).....	B-7
Figure B-10.	Oil saturation at the end of fill-up (left) to the end of EOR (right) .....	B-8
Figure B-11.	CO <sub>2</sub> saturation from the end of the fill-up period (left) to the end of CO <sub>2</sub> -EOR (right).....	B-9
Figure B-12.	Gross (left) and Net (right) utilization factors .....	B-10
Figure B-13.	Producing CO <sub>2</sub> -oil ratio (left) and the total CO <sub>2</sub> stored during EOR (right).....	B-10
Figure C-1.	Flowchart of hierarchical model calibration.....	C-4
Figure C-2.	Examples of phase behavior: Physically correct (left) and physically incorrect (right).....	C-6
Figure C-3.	Workflow of fluid model calibration .....	C-7
Figure C-4.	Three production periods in the Dover 33 field.....	C-8

Figure C-5.	Comparison of the bottomhole pressure of the injector during CO <sub>2</sub> injection only period .....	C-9
Figure C-6.	Basis functions using Grid Connectivity-based Transform (GCT) .....	C-9
Figure C-7.	Phase behavior of the original fluid.....	C-11
Figure C-8.	Volumetric properties of the original fluids.....	C-12
Figure C-9.	Three different oil formation volume factor cases .....	C-13
Figure C-10.	Results of Genetic Algorithm for Case 1.....	C-14
Figure C-11.	Oil formation volume factor of the history matched model for Case 1.....	C-14
Figure C-12.	Results of Genetic Algorithm for Case 2.....	C-15
Figure C-13.	Oil formation volume factor of the history matched model for Case 2.....	C-16
Figure C-14.	Results of Genetic Algorithm for Case 3.....	C-17
Figure C-15.	Oil formation volume factor of the history matched model for Case 3.....	C-17
Figure C-16.	Reservoir properties: porosity (left) and permeability (right).....	C-19
Figure C-17.	Initial pressure (left) and initial water saturation (right).....	C-19
Figure C-18.	Three phase relative permeability curves provided by the operator.....	C-20
Figure C-19.	Tornado chart for all objective functions .....	C-21
Figure C-20.	Performance of MOGA for primary depletion .....	C-22
Figure C-21.	Comparison of simulation responses of the history matched model with the observed data for primary depletion .....	C-23
Figure C-22.	Three different groups in optimal solutions depending on the importance of objective functions.....	C-24
Figure C-23.	Histogram of EOS models for each group .....	C-24
Figure C-24.	Comparison of phase behavior .....	C-25
Figure C-25.	Box plots of calibrated parameters for primary depletion for relative permeability.....	C-26
Figure C-26.	Box plots of calibrated parameters for primary depletion for permeability and pore volume.....	C-27
Figure C-27.	Comparison of simulation responses of the best updated model with the observed data .....	C-28
Figure C-28.	Comparison of relative permeability before and after history matching during primary depletion.....	C-28
Figure C-29.	Comparison of cumulative oil production with the updated model from primary depletion.....	C-29
Figure C-30.	Comparison of phase diagram for different oil and CO <sub>2</sub> mixtures .....	C-30
Figure C-31.	Determination of Minimum Miscibility Pressure (MMP) .....	C-30
Figure C-32.	Swelling factor of EOS 5 .....	C-31

Figure C-33.	Density of original fluid compared with oil and CO <sub>2</sub> mixture (CO <sub>2</sub> mole fraction of 50%) .....	C-31
Figure C-34.	Performance of MOGA for CO <sub>2</sub> EOR period.....	C-32
Figure C-35.	Comparison of simulation responses of the history matched model with the observed data for CO <sub>2</sub> EOR period.....	C-33
Figure C-36.	Box plots of parameters associated with relative permeability: endpoints (left) and exponents (right) .....	C-34
Figure C-37.	Comparison of relative permeability before and after history matching during CO <sub>2</sub> EOR period .....	C-34
Figure C-38.	Comparison of distribution for parameters associated with permeability between after primary depletion and after EOR period .....	C-35
Figure C-39.	Comparison of distribution for pore volume multipliers between after primary depletion and after EOR period .....	C-35
Figure C-40.	Comparison of simulation responses of the history matched model with the observed data (BHP: prediction).....	C-36
Figure C-41.	Difference in bottomhole pressure between simulation response and the measure data in comparison to the reduced gas injection rate .....	C-37
Figure C-42.	Performance of MOGA for CO <sub>2</sub> injection only period.....	C-38
Figure C-43.	Comparison of simulation responses of the history matched model with the observed data for CO <sub>2</sub> injection only period.....	C-38
Figure C-44.	Comparison of distribution for parameters associated with relative permeability between after EOR period and after CO <sub>2</sub> injection only period: endpoints (top) and exponents (bottom) .....	C-39
Figure C-45	Comparison of distribution for parameters associated with permeability between after EOR period and after CO <sub>2</sub> injection only period .....	C-40
Figure C-46.	Comparison of distribution for pore volume multipliers between after EOR period and after CO <sub>2</sub> injection only period .....	C-40
Figure C-47.	Results of Genetic Algorithm with a single objective function .....	C-41
Figure C-48.	Comparison of bottomhole pressure between updated models and history data .....	C-41
Figure C-49.	Location of monitoring wells.....	C-42
Figure C-50.	Comparison of the bottomhole pressure for two monitoring wells: the history matched model from MOGA .....	C-42
Figure C-51.	Comparison of the bottomhole pressure for two monitoring wells: the history matched model from GA .....	C-43
Figure C-52.	Comparison of distribution of pore volume multipliers between MOGA results and GA results .....	C-44
Figure C-53.	Comparison of the histograms of pore volume for the updated models .....	C-44
Figure C-54.	Comparison of the histograms of permeability for the updated models .....	C-45
Figure C-55.	Difference in permeability (CO <sub>2</sub> injection only period (GA) and CO <sub>2</sub> EOR period) .....	C-46

Table of Contents

Figure C-56.	Difference in permeability (CO2 injection only period (MOGA) and CO2 EOR period) .....	C-46
Figure C-57.	Permeability of CO2 injection only period after GA: (a) permeability distribution (b)and (c) with the high threshold (Perm > 50md) from two different perspectives .....	C-47
Figure C-58.	Permeability of CO2 injection only period after GA: (a) permeability distribution (b) and (c) with the low threshold (Perm < 0.005md) from two different perspective .....	C-47

**List of Equations**

	Page
Equation 1-1 .....	28
Equation 3-1 .....	121
Equation 3-2 .....	128
Equation 4-1 .....	164
Equation 4-2 .....	164
Equation 4-3 .....	164
Equation 4-4 .....	171
Equation 5-1 .....	249
Equation 5-2 .....	250
Equation 5-3 .....	256
Equation 5-4 .....	260
Equation 5-5 .....	263
Equation 5-6 .....	273
Equation 5-7 .....	273
Equation 5-8 .....	276
Equation 5-9 .....	277



## Acronyms and Abbreviations

AI	Acoustic Impedance
BBL	Barrel
Bbls	Cumulative Barrels
BHP	Bottomhole Pressure
CCS	Carbon Capture and Storage
CCUS	Carbon Capture, Utilization, and Storage
CDF	Cumulative Distribution Function
CRM	Capacitance-Resistive Model
CO <sub>2</sub> -EOR	Carbon Dioxide Enhanced Oil Recovery
DF	Design Factor
DOE	Department of Energy
DRM	Dynamic Reservoir Modeling
DTS	Distributed Temperature Sensing
EOR	Enhanced Oil Recovery
EOS	Equation of State
EPL	Error per Layer
GRFS	Gaussian Random Function Simulation
HCPV	Hydrocarbon Pore Volume
LAS	Log ASCII Standard
m	meter
mD	millidarcy
MICP	Mercury-Injection-Capillary Pressure
MMP	Minimum Miscibility Pressure
MRCSP	Midwest Regional Carbon Sequestration Partnership
MSCF	Million Standard Cubic Feet
MT	Metric tons
NETL	National Energy Technology Laboratory
NNPRT	Niagaran Pinnacle Reef Trend
NPHI	Neutron Porosity
OIP	Oil-in-place
OOIP	Original Oil-in-place
OWC	Oil Water Contact
PNC	Pulsed Neutron Capture
PVT	Pressure Volume Temperature
RVD	Reservoir Vertical Displacement
QA/QC	Quality Assurance/Quality Control
RMSE	Root Mean Squared Error
SE	Step Error
SEM	Static Earth Model
SPE	Society of Petroleum Engineers
STB	Stock Tank Barrell
STOOIP	Stock Tank Original Oil-in-Place
SU	Surface Uplift



# Executive Summary

## i. Introduction

The Midwest Regional Carbon Sequestration Partnership (MRCSP) has been investigating various reservoir characterization and modeling technologies related to Carbon Capture, Utilization, and Storage (CCUS) in conjunction with carbon dioxide enhanced oil recovery (CO<sub>2</sub>-EOR) operations in multiple Silurian-age (Niagaran), oil-bearing, carbonate pinnacle reefs in northern Michigan, USA. This report provides a comprehensive discussion of reservoir modeling studies that were conducted for tracking oil production, forecasting CO<sub>2</sub> plume migration, and estimating associated storage in a number of reefs that were at different stages of their CO<sub>2</sub>-EOR life cycle. Figure ES-1 shows the location of the various reefs of interest, such as (a) Dover-33, which has undergone primary production and CO<sub>2</sub>-EOR, (b) Charlton-19, and Bagley, where CO<sub>2</sub> injection has been followed by oil production, and (c) Chester-16, which is in the early stages of CO<sub>2</sub> injection prior to oil production.

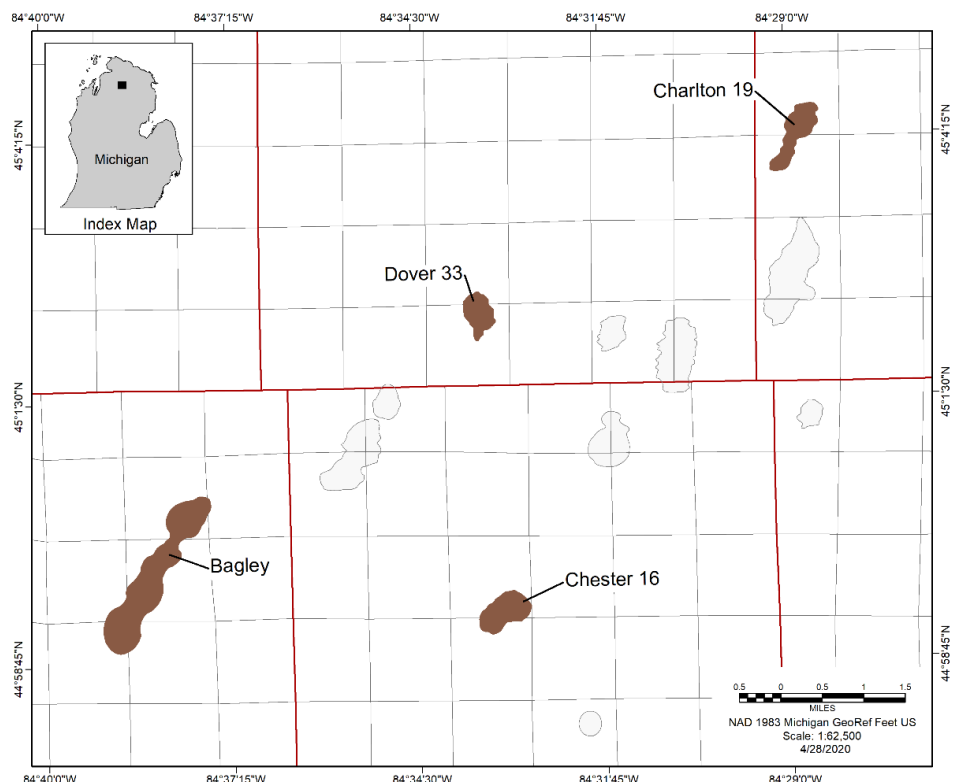


Figure ES-1. Map showing location of reefs.

The modeling process for simulating oil production, CO<sub>2</sub> injection, and associated storage in these reefs entails two phases. The first phase, geologic framework modeling, integrates all pertinent geological and geophysical data (from logs, cores and seismic surveys) about reservoir structure, geometry, rock types, and property distributions (porosity, permeability, water saturation) into a 3-D distributed grid-based static earth model (SEM). The second phase, dynamic reservoir modeling, uses the SEM as a platform to simulate the movement of oil, gas, water, and CO<sub>2</sub> within the reservoir during primary hydrocarbon production, as well as during subsequent phases such as CO<sub>2</sub>-injection assisted EOR, plume migration, and associated storage. In addition, an assessment of coupled process effects is also carried out,

where the impacts of geochemical and geo-mechanical processes induced by CO<sub>2</sub> injection are studied. Figure ES-2 shows the modeling workflow.

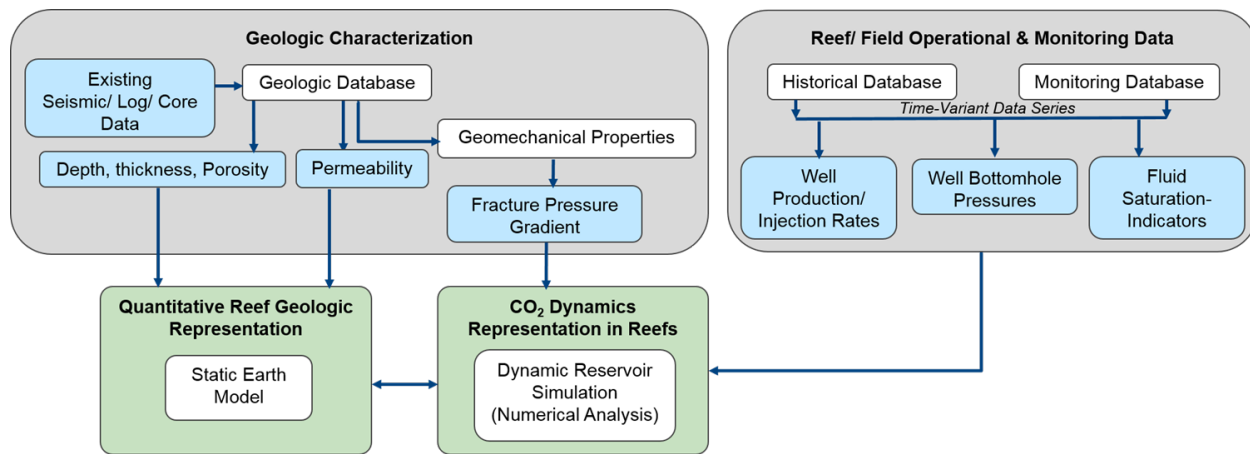


Figure ES-2. Simplified flow diagram of data integration into static and dynamic models.

These modeling studies support several goals:

- Geologic system representation – data integration (e.g., integration of all reservoir characterization data into a geologic framework)
- Scientific – coupled process understanding (e.g., how does CO<sub>2</sub> move through the formation and interact with rock/oil/brine)
- Calibration – history matching (e.g., update description of subsurface by comparing model predictions to observations)
- Engineering – system design (e.g., how many wells are needed to meet injection targets and optimize oil recovery and associated storage)

Table ES-1 shows the various types of modeling applied to the four reefs of interest.

Table ES-1. Types of modeling applied to the reefs of interest.

	Data Integration (SEM)	History Matching	System Design	Coupled Process Understanding
Dover-33	x	x	x	x
Charlton-19	x	x		
Bagley	x	x		

This Executive Summary is organized as follows: Section 2.0 describes the geology and production history of the reefs of interest. Section 3.0 briefly describes the approach used for static earth modeling and dynamic reservoir modeling tasks. Section 4.0 provides an overview of modeling results from each of the reefs. Section 5.0 presents results of the geochemical and geomechanical models. Finally, Section 6.0 summarizes the lessons learned from these modeling activities.

## ii. Reefs of Interest

### a. Dover-33

Dover-33 is an isolated reef with 3.2 million barrels original oil in place. From 1975 to 1996, primary production yielded 1.3 million barrels oil. Subsequently, 1.3 million metric tons (tonnes) CO<sub>2</sub> were injected for EOR from 1996 to 2007, which yielded an additional 0.5 million barrels of oil beyond the amount produced in primary production. Under the MRCSP Phase III project, from 2013 until 2019, an additional 570 thousand tonnes CO<sub>2</sub> were injected while all producing wells were shut in. The initial reservoir pressure and temperature for Dover-33 was 2894 psi and 108 deg F, respectively. The oil was measured at 43.6 API gravity. It was estimated the initial fluid saturation was 66.3 percent oil and 33.7 percent water.

Geophysical logs from wells in the Dover-33 reef were analyzed to develop a conceptual geologic framework. The primary formation of interest, the Brown Niagaran, was subdivided into three depositional lithofacies based on reservoir potential. Figure ES-3 shows an interpreted cross section across Dover-33 to illustrate the changes in lithology and the locations of the lithofacies. These are: 1) windward (purple) with high flow potential; 2) reef core (green) with moderate to high flow potential; 3) leeward (blue) with low to moderate flow potential; and 4) the flanks and off-reef Brown Niagaran with negligible flow potential. The overlying layer, A1 Carbonate, has moderate porosity with occasional salt plugged pore space. The underlying formation, Gray Niagaran, is water saturated with minimal porosity and permeability.

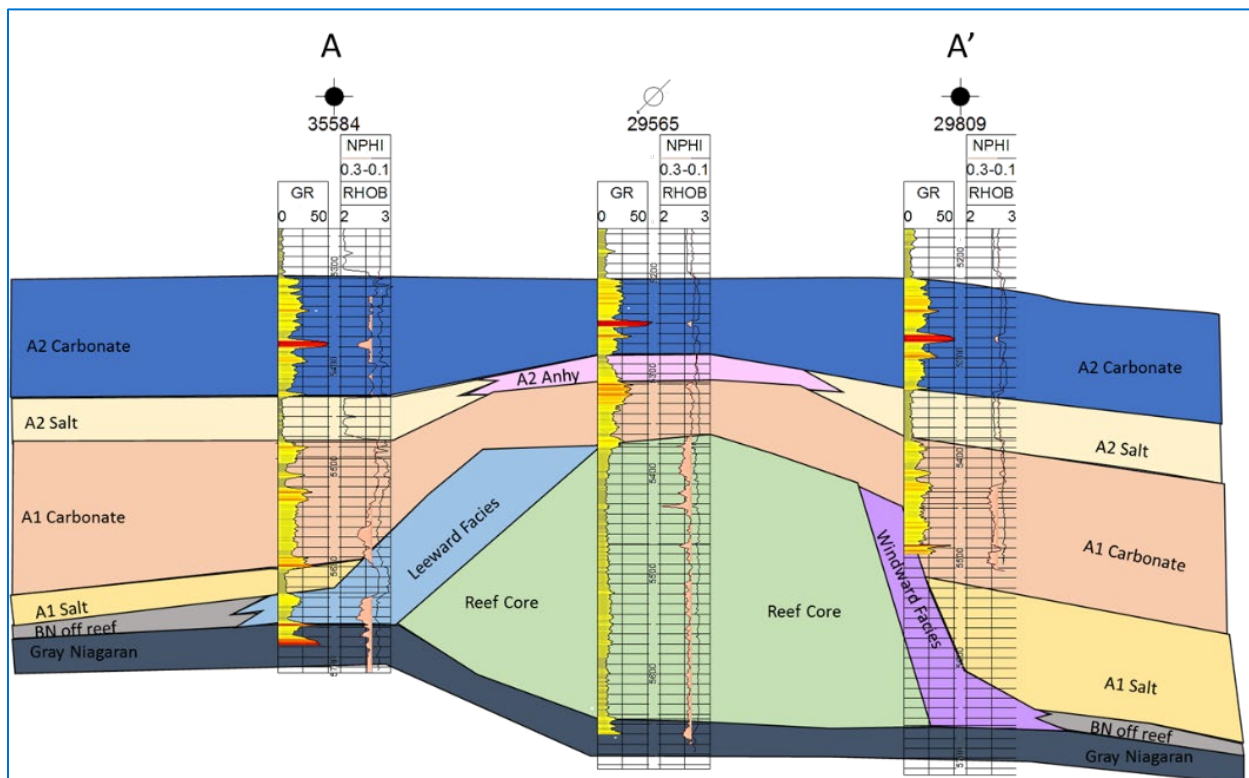


Figure ES-3. Cross section A-A' across the reef in the Dover -33 reef field showing changes in lithology and lithofacies from the southwest to the northeast.

Well-log data was available from 18 wells in the form of LAS and/or raster logs. All 18 wells have gamma ray, 15 have neutron porosity, six have bulk density, and eight have sonic logs. In addition, 12 wells have advanced logs, such as photoelectric index, pulsed neutron capture, and resistivity. Core was collected from a newly drilled well during 2016, Well 9-33, and analyzed for rock properties. All data were analyzed and integrated to develop a geologic framework and SEM.

## b. Charlton-19

The Charlton-19 reef is a dolomite reef in late stage production (i.e., has undergone primary production and currently is undergoing CO<sub>2</sub> EOR) with 2.6 million barrels oil in place. From 1988-2014, primary production yielded 1.1 million barrels oil. Subsequently, 145,000 tonnes of CO<sub>2</sub> were injected for EOR from 2014 to 2019, which yielded an additional 0.5 million barrels oil. The initial reservoir pressure and temperature for Charlton-19 was 2774 psi and 108 deg F, respectively. The oil was measured at 43.6 API gravity. It was estimated that the initial fluid saturation was 88.6 percent oil and 11.4 percent water.

3-D seismic suggests Charlton-19 includes two distinct reef lobes separated by a saddle with muted pressure communication between the two lobes. The reef complex contains both on-reef and off-reef (regional) Brown Niagaran facies. The off-reef facies is composed of a low porosity dolomite that surrounds the on-reef facies, which include three facies: windward, leeward, and reef core. Underlying the reef structure is the Gray Niagaran, which is a tight, water saturated carbonate that represents the lower boundary of the reef. These facies are the reservoir for the Charlton-19 reef and occur at two distinct isolated locations within the field, one in each the northern and southern lobes. Geometry of the northern reef lobe can be seen in Figure ES-4 (without the 3 reefal facies details for the Brown Niagaran).

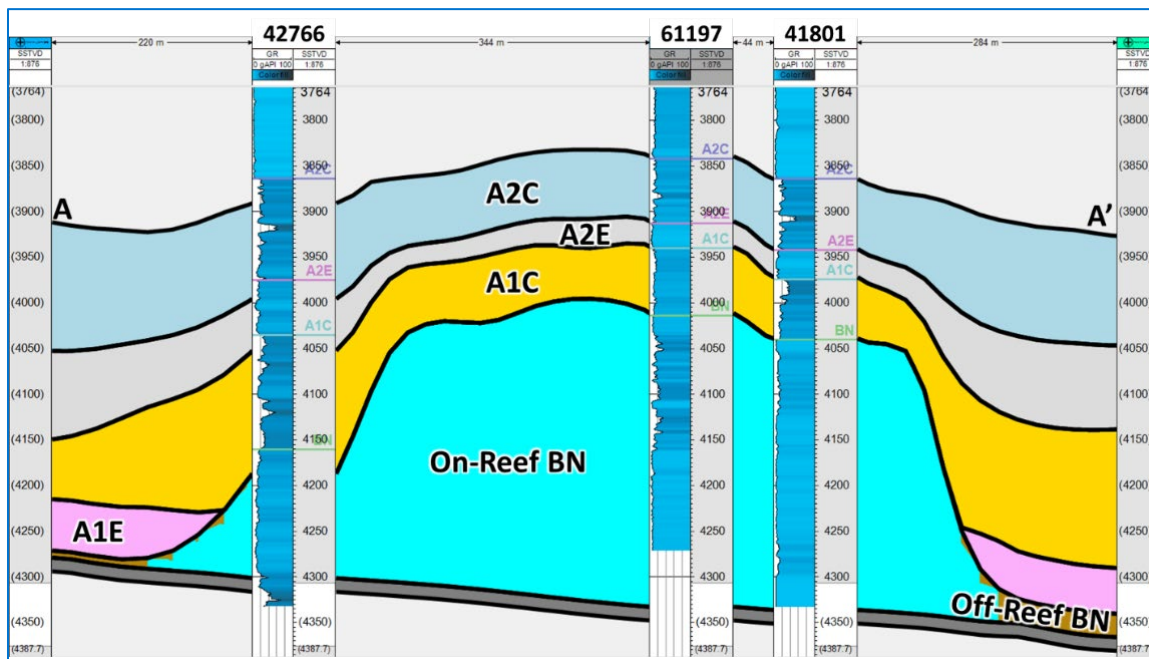


Figure ES-4. Cross section of Charlton-19 Charlton-19's northern reef lobe showing thickness of formations and on-reef vs. off-reef Brown Niagaran (BN).

Geophysical logs are available for five wells, including gamma ray, bulk density, and neutron porosity logs. In addition, selected wells also have various advanced logs, such as resistivity and photoelectric effect. All data were analyzed and integrated to develop a geologic framework and SEM.

### c. Bagley

Bagley reef is composed of three separated lobes (Northern, Middle, and Southern lobes), with the southern lobe possibly consisting of two distinct but interconnected lobes (Figure ES-5). The reef complex was estimated to originally contain 9 million barrels of oil in place. From 1985 to 2013, primary production yielded 2.9 million barrels of oil. Subsequently, 585 thousand tonnes of CO<sub>2</sub> have been injected since 2015 to fill up (pressurize) the reservoir for EOR prior to initiating oil production. The initial reservoir pressure and temperature for Bagley was 1900 psi and 115 deg F, respectively. The oil was measured at 43 API gravity. It was estimated that the initial fluid saturation was 80 percent oil and 20 percent water.

The producing formation is the Brown Niagaran, which is overlain by the A1 carbonate and underlain by the Grey Niagaran formations. Well log data (gamma ray and neutron porosity) are available from five wells in this reef, as well as 3D seismic data. The geologic interpretation and petrophysical analysis based on these data was used to develop surface maps for the three major formations of interest as noted above, as well as an SEM.

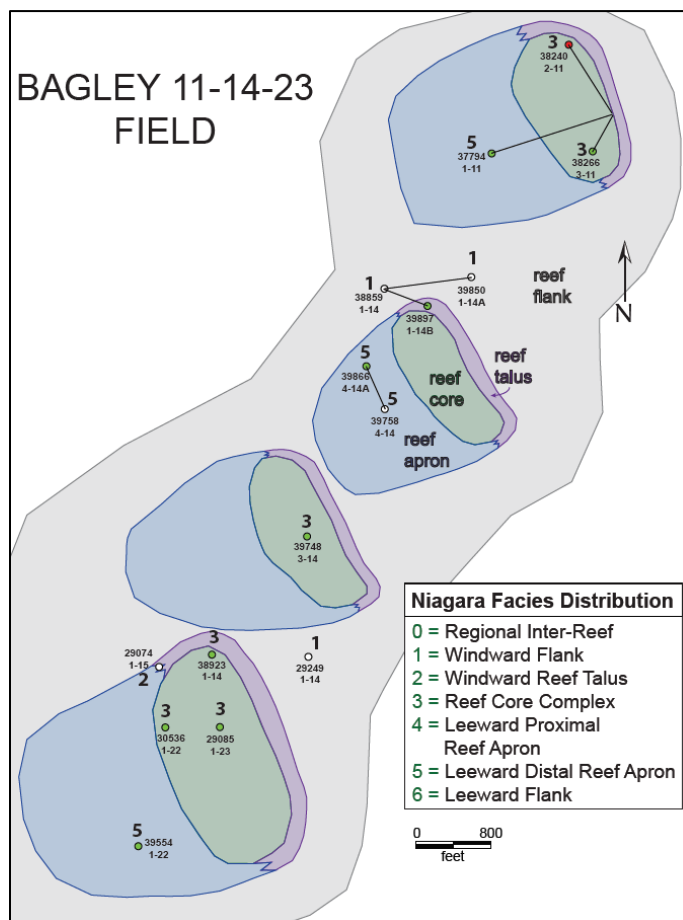


Figure ES-5. Map view of Bagley reef showing multiple lobes and facies.

#### d. Chester-16

The Chester-16 reef includes two main lobes with 6.9 million barrels original oil in place. From 1971 to 1990, primary production and secondary recovery (waterflooding) resulted in 2.4 million barrels of oil production. CO<sub>2</sub> injection to pressurize the reef for CO<sub>2</sub>-EOR commenced in February 2017 and is still ongoing as of this report (February 2020), with 155,000 tonnes being injected for pressurization. Oil production has not started. The initial reservoir pressure and temperature for Chester-16 was 3125 psi and 100 deg F, respectively. The oil was measured at 41 API gravity. It was estimated that the initial fluid saturation was ~70 percent oil and ~30 percent water.

Geometry of the reef field (based on 3D seismic) suggests two distinct but connected reef cores. There are two main reservoirs in this field—the Brown Niagaran and the A1 Carbonate. The Brown Niagaran tends to have low porosity due to lack of dolomitization with occasional fractures and/or dolomitic zones. The primary reservoir is the overlying A1 Carbonate, which has a distinct high porosity zone along the crest of the reef and is composed of porous dolomite. The porosity of the A1 Carbonate is lower along the flanks of the reef, suggesting a limited extent of the reservoir. The oil-water-contact (OWC) was documented to occur in the lower third of the Brown Niagaran, leaving the upper two-thirds of the reef viable for storage and production.

Confining units overlay the A1 Carbonate and include the A2 Evaporite and A2 Carbonate. Underlying the reef structure is the Gray Niagaran, which is a tight, water saturated carbonate and represents the lower boundary of the reef. A representative cross section for the Chester-16 reef is shown in Figure ES-6, which also depicts the division of Brown Niagaran into three lithofacies, the Leeward, Reef Core, and Windward.

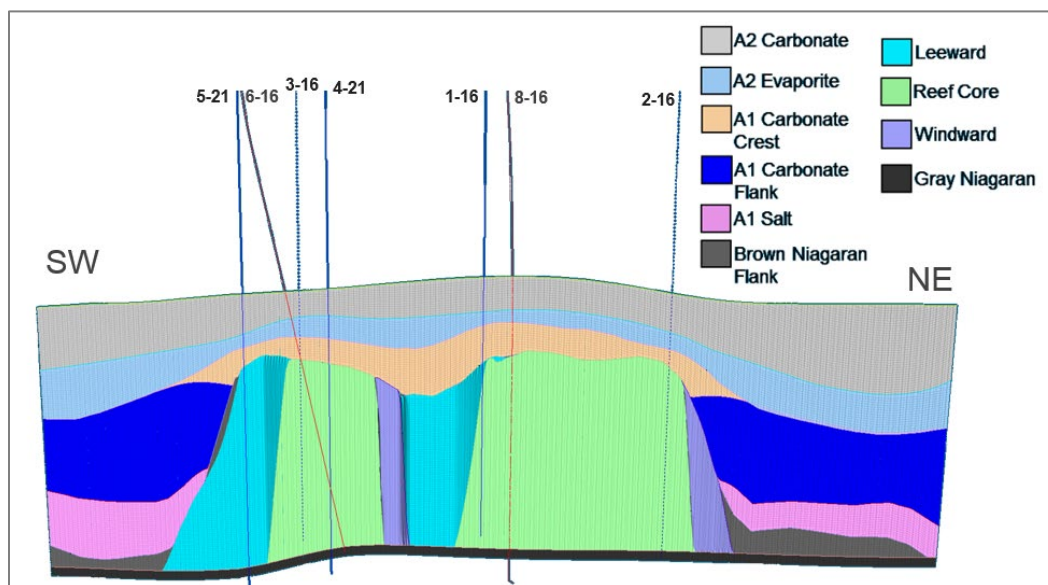


Figure ES-6. 2D cross section through the Chester-16 reef field showing the primary formations of interest (5x vertical exaggeration). Internal to the reef, the Brown Niagaran is further divided into three lithofacies: The Leeward, Reef Core, and Windward.

Subsurface data is sourced from wells in and near the Chester-16 field and includes seven existing wells plus two new wells. A 3D seismic survey was available and helped image the reef's areal extent. The geologic interpretation and petrophysical analysis based on the well log and seismic data were used to develop a conceptual geologic framework and an SEM.

### iii. Static and Dynamic Modeling Approach

The overall flow of the modeling work consisted of analyzing and integrating geologic data to define the extent, depth, thickness, porosity, permeability, and water saturation of the reservoir(s). In conjunction with geologic characterization, field operational and monitoring data were compiled to develop the production and injection history that was used in history matching the dynamic model. The geologic characterization work then was used to develop a static earth model that was upscaled into a dynamic model. Figure ES-7 illustrates the workflow for SEM development.

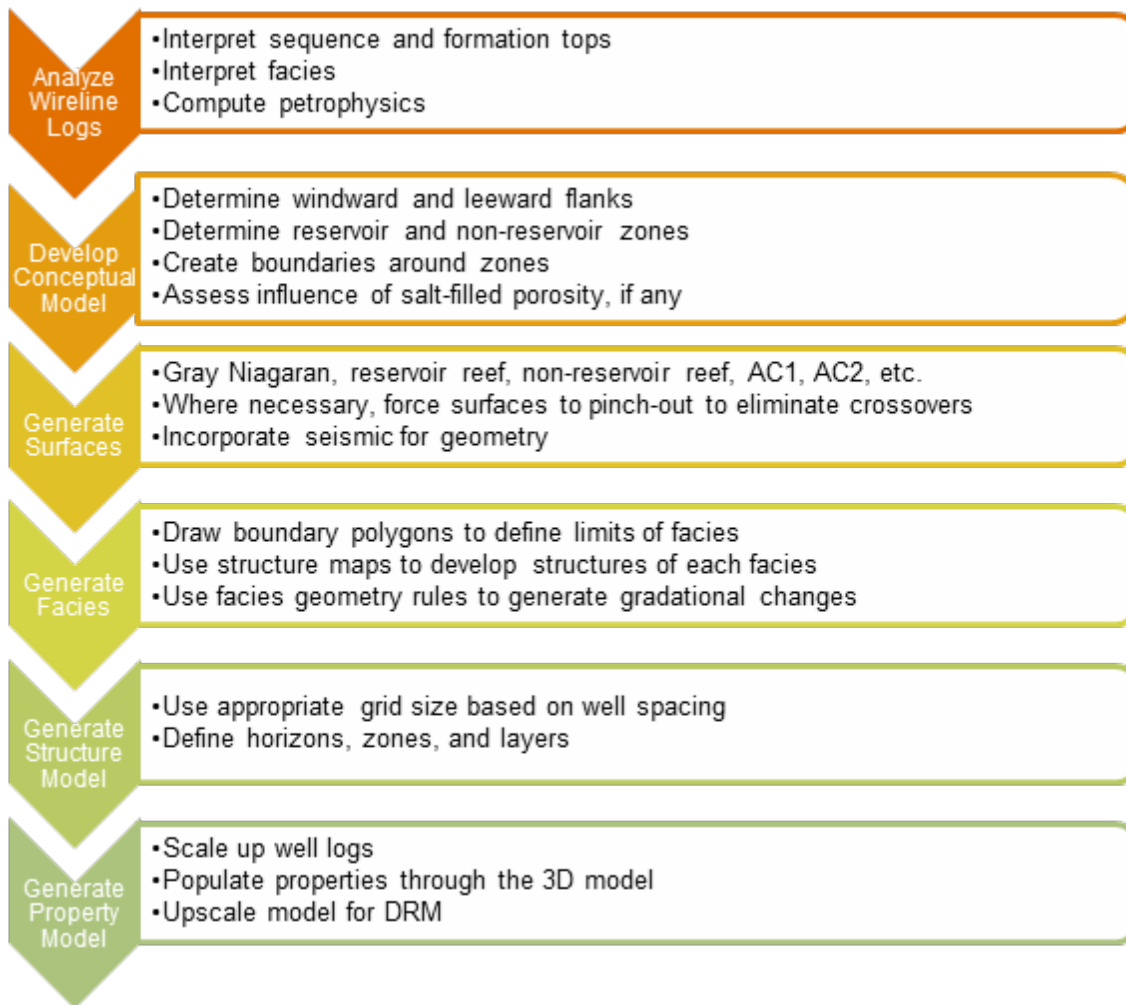


Figure ES-7. Workflow for building static earth models.

The objectives for the dynamic modeling activity include evaluating CO<sub>2</sub> injectivity and assessing fluid migration in the reefs. The dynamic modeling activity aims to validate the representativeness of the reef conceptual model (as implemented in the SEM) by history matching production (oil, water, gas) and pressure history during primary recovery period, and any secondary recovery (waterflooding, CO<sub>2</sub>-EOR) periods as appropriate. The model is then applied to match the pressure response for the MRCSP Phase III injection period. History matching would provide a validated representative model that captures the field observed response from primary production until the end of the Phase III CO<sub>2</sub> injection period. This representative reef model can then be useful to simulate CO<sub>2</sub>-injection assisted EOR, plume migration, and associated storage.

For dynamic modeling, three different approaches with varying data and computation needs were used. These include:

- *Fully compositional*: In this grid-based modeling approach, detailed interaction between various (pseudo) components in the crude oil, CO<sub>2</sub> and water are captured using a Peng-Robinson equation-of-state (EOS) based component mass balance. The appearance/disappearance of all components in all phases (oil, gas, water) is strictly tracked. The coupled formulations are highly non-linear, require additional data regarding crude oil composition/EOS representation, and are computation intensive.
- *Pseudo-miscible*: This grid-based modeling approach involves modifying the physical properties and the flowing characteristic of the solvent (CO<sub>2</sub>) and reservoir fluid in a three-phase black-oil simulator. Relative permeabilities and viscosity of different phases are also modified by solvent injection. A mixing parameter is used to determine the amount of mixing between the solvent and reservoir fluid within each grid block. This approach is popular in CO<sub>2</sub>-EOR projects for obtaining rapid but reasonably accurate solutions.
- *Capacitance-resistance model* (CRM): In this lumped-parameter modeling approach, the goal is to develop a simplified physics model for the control volume surrounding an injection or production well, where the rate-pressure relationship can be represented via two parameters, (a) compressibility-weighted pore volume, and (b) injectivity/productivity index. This lumped parameter representation is widely used in waterflooding projects and is computationally very fast. However, it cannot resolve fluid movement within the control volume.

Coupled fluid-flow/geochemical and fluid-flow/geomechanical process models were also undertaken to understand: (a) the impact of geochemical reactions following CO<sub>2</sub> injection into the subsurface, and (b) the geomechanical changes resulting from pressure increase following CO<sub>2</sub> injection, respectively. The approach used for these specialized modeling tasks (along with their results) is described in Section 5.0.

## iv. Static and Dynamic Modeling Results

### a. Dover-33

#### i) Modeling Objectives

The objectives of the Dover-33 modeling study were:

- Integrate all geologic and geophysical data into a SEM
- Build a dynamic model based on the SEM using a compositional simulation approach and history match it to the primary production data and the secondary CO<sub>2</sub> injection period for EOR
- Modify the model as needed to match the CO<sub>2</sub>-injection only period for the MRCSP Phase III injection

#### ii) Static Earth Models

The Dover-33 reef was initially interpreted and constructed into two models—Level 1 and Level 2. The Level 1 model contained two reef-associated layers (A1 carbonate and Brown Niagaran) based on lithostratigraphic formations. The Level 2 model used a sequence stratigraphic approach. With this approach, the individual sequence stratigraphic packages that make up the framework of the reef model were defined by geophysical log-data signatures that were correlated to regional sequence boundaries and interpreted lithofacies as defined in analog reef studies. Reservoir properties were distributed within

the sequences and conditioned to the individual lithofacies. Early versions of the reef dynamic model were built from both the Level 1 and Level 2 SEMs; however, it was not possible to successfully match the entire primary production, secondary production, and the MRCSP Phase III CO<sub>2</sub> injection data with either model. Therefore, a new SEM based on depositional lithofacies (geobodies) approach described below was developed to attempt to produce a dynamic reservoir model that could accurately reproduce the primary, secondary production data and the Phase III CO<sub>2</sub> injection pressure data.

First, the surfaces corresponding to A2 Carbonate, A2 Evaporite, A1 Carbonate, A1 Salt, Brown Niagaran, and Gray Niagaran were defined. These were then tied to horizons and layers within Petrel to create a structural framework. Next, interpreted lithofacies (as discussed earlier) were used to define zones within a formation to represent individual compartments or “geobodies.” The lithofacies were divided to represent groups of facies with similar porosity and permeability distributions. This creates a heterogeneous model with more control during property modeling. The gridded SEM covers an area 700 m x 950 m, with a maximum height of ~160 m. Grid cells in the x- and y-direction were kept at 25 m with variable thickness in the vertical (z) direction, resulting in ~590,000 cells in the fine-scale model.

For property modeling, neutron porosity data from 15 wells were used, along with core measured porosity-permeability data from core samples. The A1 Carbonate had a porosity range from 3.16 percent to 10.72 percent with a permeability range from 0 to 6.04 mD. The Brown Niagara had a porosity range from 1.51 percent to 7.14 percent with a permeability range from 0 to 204.28 mD. Power law transforms were fit to both sets of data. Kriging was applied to interpolate porosity values from upscaled neutron porosity logs for the Brown Niagaran and A1 Carbonate formations. All other zones were assigned an average value to represent the formation. The derived porosity to permeability transform was applied to the porosity model to predict permeability throughout the SEM for the Brown Niagaran and A1 Carbonate. Maximum and minimum permeability observed in whole core were used to constrain the model limits. All other zones were assigned an average value to represent the formation. Water saturation was calculated from resistivity log data in seven wells using Archie’s equation. Moving average was used to interpolate water saturation throughout the SEM for the Brown Niagaran, A1 Carbonate, and A2 Carbonate zones using only three wells that were near initial reservoir conditions. Volumetric calculations for this fine-scale model yielded a pore volume of 2.7E+7 ft<sup>3</sup>, corresponding to an original oil in place of 3.28 million STB.

To create a computationally tractable grid for the dynamic reservoir modeling, it was necessary to create an upscaled (i.e., coarser) model that could reproduce the behavior the fine-scale model with fewer cells. The Petrel plug-in CONNECT UpGrid™ was used to aid the upscaling process by optimizing the grouping of layers. This utility performs the optimum vertical upscaling design by minimizing the error on the pressure while combining vertical layers. The horizontal grid size remains unchanged. The 478-layer, fine-scale SEM served as input to the upscaling process, which resulted in a 64-layer model with ~68,000 cells (i.e., a reduction of more than 80 percent). A representative cross section with porosity and permeability distributions in the gridded upscaled model is shown in Figure ES-8.

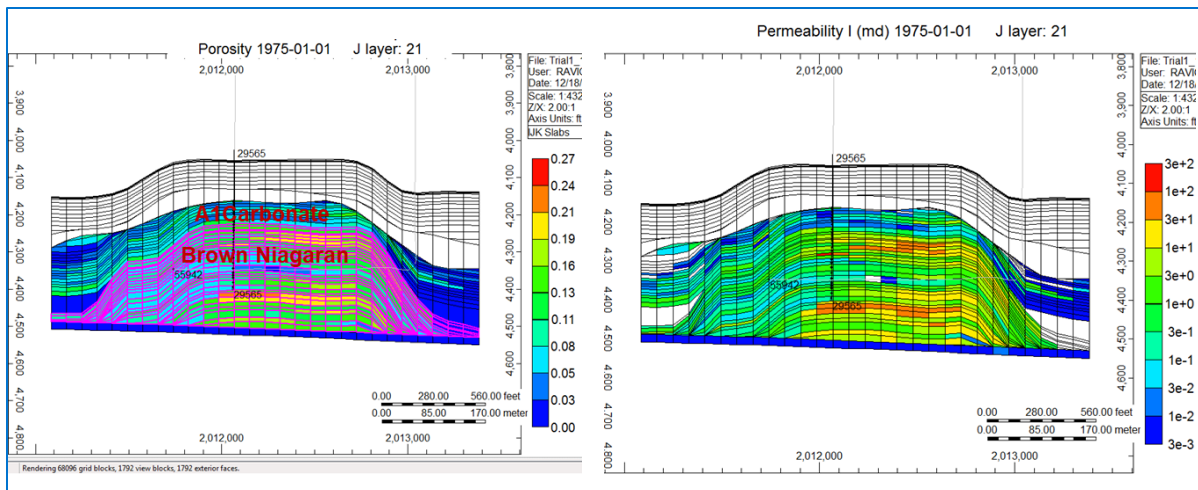


Figure ES-8. Cross section views of the porosity and permeability distributions in Dover-33 Depositional Lithofacies SEM.

### iii) Dynamic Reservoir Model – Compositional

A compositional simulation framework is used for modeling the primary production, CO<sub>2</sub> injection for EOR, and purely CO<sub>2</sub> injection periods. This requires first characterizing the reservoir fluid using multiple pseudo-components for equation-of-state based fluid mixing calculations. A total of seven pseudo-components were defined so that the estimated fluid properties such as density and viscosity matched that of the original fluid sample. These pseudo-components, their physical significance and the corresponding mole percentages are: F1 (C1, N2) – 40.9 percent, F2 (CO<sub>2</sub>) – 0.1 percent, F3 (C2-C4), 20.2 percent, F4 (C5-C9) – 17.4 percent, F5 (C10-C19) – 14.7 percent, F6 (C20-C24) – 2.8 percent, F6 (C25-C30+) – 3.9 percent.

The reservoir model was history matched to the primary production data and subsequent CO<sub>2</sub> injection for oil recovery and pressure changes during EOR periods. The goal was to manually adjust the permeability field and the relative permeability relationships to obtain a reasonable agreement between observed and model predicted values for cumulative fluid (oil, gas, water) production and average reservoir pressure. Figure ES-9 shows the history match that was obtained by adjusting the gas/oil relative permeability curves, and by modifying the permeability field to include: (1) a high-permeability streak in the core reservoir zone and (2) a vertical permeability baffle across this region and located ~2000 ft away from the injection well. The match with the cumulative oil and average pressure are quite good, while the errors in cumulative gas and cumulative water production appear to offset each other and preserve the overall reservoir voidage (as indicated by the good pressure match).

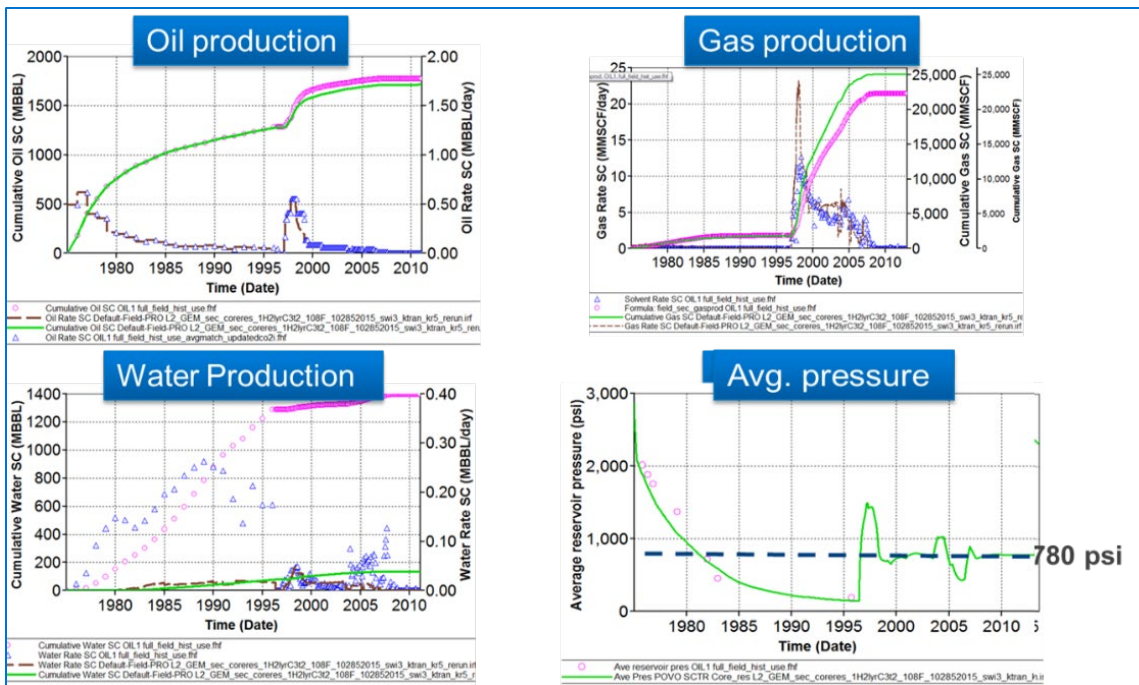


Figure ES-9. History-match results for: (a) oil production; (b) gas production; (c) water production; and (d) average reservoir pressure. The symbols represent field data and the lines show the model outputs.

This model was also applied in a blind prediction mode to compare predictions for the final CO<sub>2</sub> injection phase (without any oil production). Figure ES-10 shows that the overall amplitude of the pressure increases during the variable-rate injection periods, and the subsequent fall-off periods, are broadly captured. The trends in pressure change with time are not perfectly captured by the model. This could be due to subtle time-dependent (and hence pressure dependent behavior) potentially caused by geochemical reactions or geomechanical changes that have not been captured by the current model.

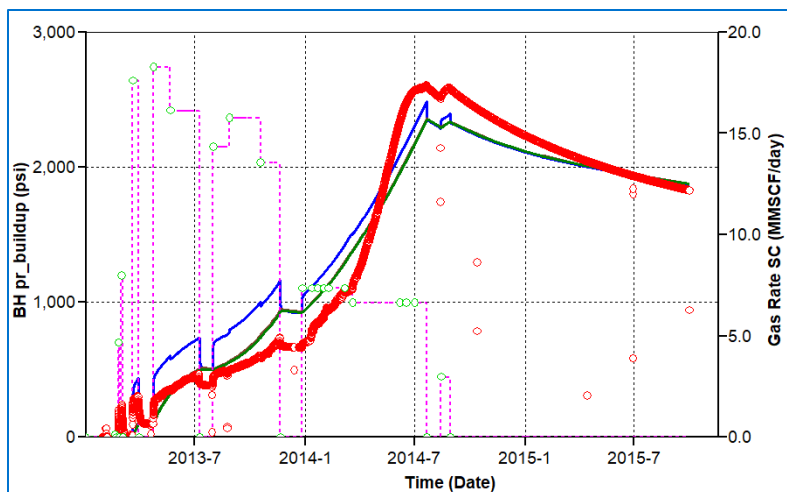


Figure ES-10. Modeled pressure response during the MRCSP Phase III CO<sub>2</sub> injection period. Here, the red circles represent observed bottom-hole pressure data, green circles represent simplified field CO<sub>2</sub> injection rate data, magenta lines are the modeled CO<sub>2</sub> injection rate, blue curve is the modeled injector bottom-hole pressure buildup and the brown and green curves are the modeled monitoring wells bottom-hole pressure buildup.

## b. Charlton-19

### v. Modeling Objectives

The objectives of the Charlton-19 modeling study were:

- Integrate all geologic and geophysical data into an SEM
- Using input data from the SEM, apply the simplified capacitance resistance model to determine the injectivity and compressible pore volume

### vi. Static Earth Model

All available geologic data, petrophysical analyses, and interpretations were used as input into the SEM. A 2D depositional model was used to guide the development of the model's structural framework. 3D seismic data was used to define the boundary and geometry of the reef. Surfaces for facies were created to subdivide the reservoirs into key zones. These zones were subsequently layered and followed by well log upscaling and property modeling.

The uppermost SEM zone for the Charlton-19 reef was the A2 Carbonate, which gently slopes off-reef. The A1 Carbonate follows the underlying Brown Niagaran Formation. Locally, the Brown Niagaran was comprised of two pinnacle reefs and a small reefal high in the saddle region between the two pods. The Gray Niagaran was relatively flat throughout the study area deepening to the southeast. These surfaces were defined from seismic data and well log-based formation top picks, and then tied to horizons and layers within Petrel to create a structural framework. Next, interpreted lithofacies (reef flank, windward, leeward, reef core) were used to define zones within the Brown Niagaran to represent individual compartments or “geobodies.” The lithofacies were divided to represent groups of facies with similar porosity and permeability distributions. This creates a heterogeneous model with more control during property modeling. The gridded SEM covers an area 1580 m x 680 m, with a maximum height of ~200 m.

Grid cells in the x- and y-direction were kept at 20 m with variable thickness in the vertical (z) direction, resulting in ~960,000 cells in the fine-scale model.

For property modeling, neutron porosity data from five wells were used, along with core measured porosity-permeability data from core samples in the Dover-33 reef due to lack of Charlton-19 samples. The Dover-33 reef was used as an analog because of its proximity and similar dolomitic reef lithology. Power law transforms were fit to the observed porosity-permeability relationships for the A1 carbonate and Brown Niagaran formations. The A1 Carbonate had an average porosity 5 percent and an average permeability of 0.35 mD. The Brown Niagaran had an average porosity of 7.9 percent with an average permeability of 3 mD. Gaussian Random Function Simulation method was applied to interpolate porosity values from upscaled neutron porosity logs for the Brown Niagaran and A1 Carbonate formations. The derived porosity to permeability transform was applied to the porosity model to predict permeability throughout the SEM for the Brown Niagaran and A1 Carbonate. Maximum and minimum permeability observed in whole core were used to constrain the model limits. Porosity and permeability values for all other zones were assigned a zone-specific average value. Figure ES-11 shows porosity and permeability distributions calculated for a representative cross section. An average initial water saturation of 11.35 percent was estimated from material balance calculations. Volumetric calculations for this 357-layer fine-scale model yielded a pore volume of 2.4E+7 ft<sup>3</sup>, corresponding to an original oil in place of 2.6 million STB.

There was no upscaling step applied to this fine-scale model as there was no detailed dynamic reservoir modeling done for the Charlton-19 reef.

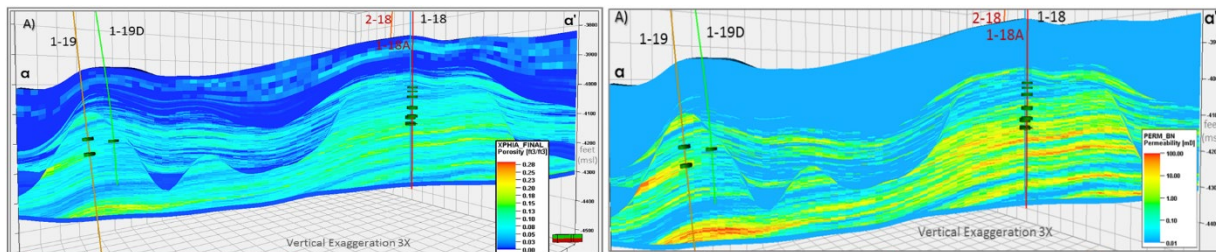


Figure ES-11. Cross section views of the porosity and permeability distributions in Charlton-19 model.

## vii. Capacitance Resistance Model (CRM)

The objectives for the dynamic modeling activity included evaluating CO<sub>2</sub> injectivity and assessing pore volume in this complex reef structure using the simplified CRM approach with available field data. Data were taken from the CO<sub>2</sub> injection-only period, from February 2015 through June 2017. This data was first filtered to eliminate point outlier values of injection rate. Figure ES-12 shows the filtered injection rate and bottomhole pressure data from the injection well during this period. This data was formatted and used as the input for the CRM.

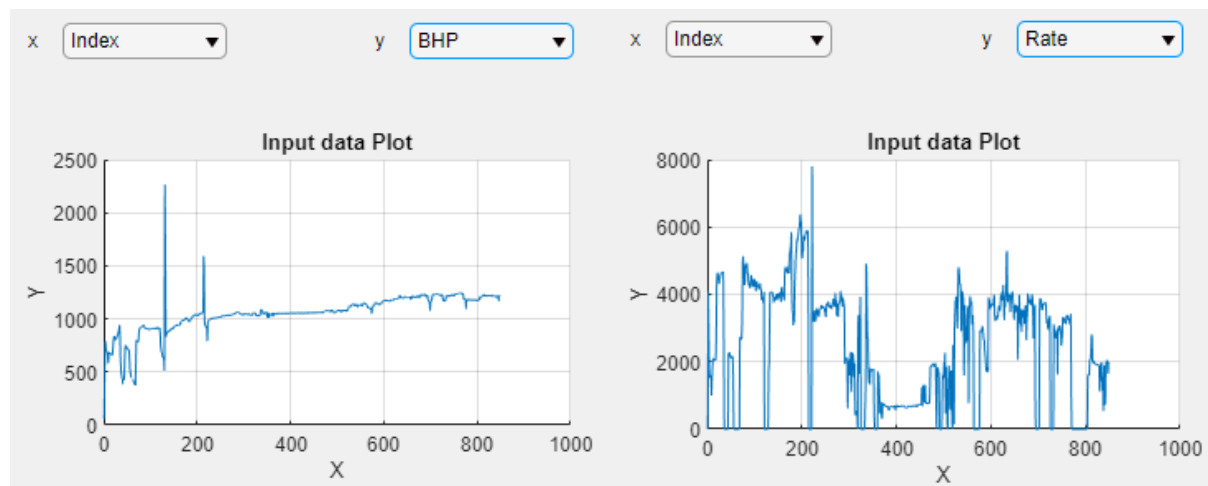


Figure ES-12. Filtered bottomhole pressure (left panel; psi units) and injection rate (right panel; rbbl/day units) data from the injection well during the CO<sub>2</sub> injection-only period being evaluated.

The CRM tool uses multi-variate regression analysis to minimize the difference between the predicted and field observed cumulative injected CO<sub>2</sub> volume to estimate two fitting parameters: (a) injectivity index, and (b) total compressible pore volume. The model is calibrated by assuming an initial pressure value based on the field history. Since this value was not known with certainty (following the end of primary production), a range of realistic initial pressure assumptions, bound by field data, is used to evaluate the performance of the CRM model. As shown in Figure ES-13, the optimal value for the initial pressure is found to be 700 psi, which corresponds to the best overall fit. The corresponding estimated model parameters are: compressible pore volume (c<sub>t</sub>.PV) = 3423 rbbl/psi, and injectivity index, J = 62 rbbl/day.psi.

For an average bottomhole CO<sub>2</sub> density of 48 lb/ft<sup>3</sup> corresponding to prevailing bottomhole pressure and temperature conditions during CO<sub>2</sub> injection, J is recalculated as 7.58 MT/day-psi. This compares very well with the previously determined injectivity index value of 2694 MT/yr.psi or 7.38 MT/day.psi using flowing material balance calculations. Also, given a hydrocarbon pore volume PV of 4.38E6 rbbl from material balance calculations, the total compressibility c<sub>t</sub> is calculated to be 7.8E-4 1/psi, which is consistent with the order of magnitude of total compressibility typical of oil and gas systems.

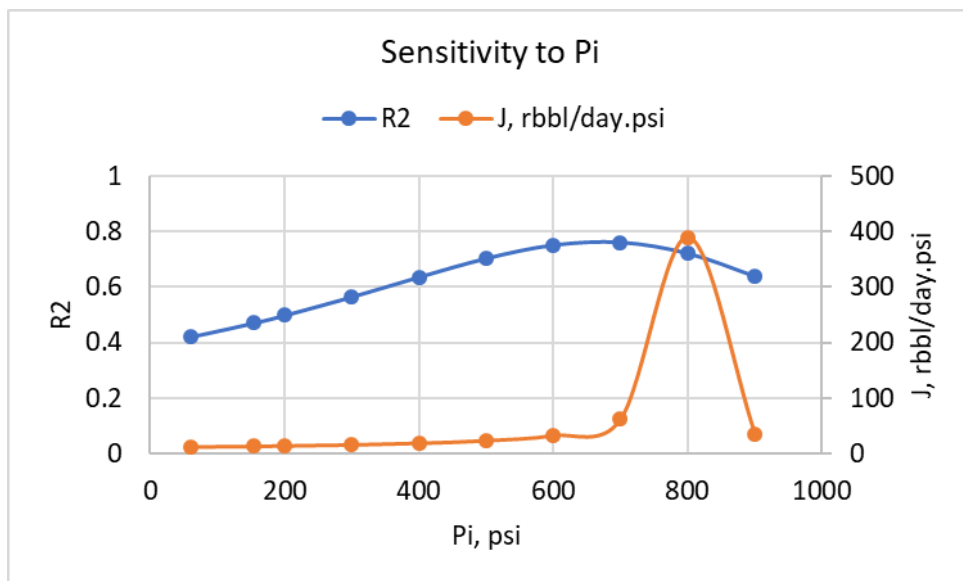


Figure ES-13. Resulting coefficient of regression ( $R^2$ ) and injectivity index ( $J$ ) values for different initial pressure assumptions. The initial pressure value of 700 psi is seen to achieve the best fit or highest  $R^2$  with a corresponding  $J$  value of 62 rbbl/day.psi.

### c. Bagley

#### viii. Modeling Objectives

The objectives of the Charlton-19 modeling study were:

- Integrate all geologic and geophysical data into an SEM
- Build a dynamic model based on the SEM using a pseudo-miscible approach and history match it to the primary production data and the CO<sub>2</sub> injection period for the fill up prior to onset of oil production for the EOR phase.
- Using input data from the SEM, apply the simplified capacitance resistance model to determine the injectivity and compressible pore volume

#### ix. Static Model

Geological parameters, including reservoir thickness and reservoir depth, were provided using geological contour maps for Brown Niagaran, Grey Niagaran, and A1 carbonate formations. These maps were then used to generate three-dimensional grids for each formation.

Unlike other reefs, extra surfaces were not prepared to delineate the distinct lithofacies within the Brown Niagaran because (1) the diagenesis is significant in carbonate reef that make presence of lithofacies meaningless, and (2) there is not enough evidence (such as seismic data) to support presence of lithofacies in Bagley reef. As a result, single zones (intervals between two horizons) were created for each formation in the Bagley reef. A 3-D model of the entire Bagley study area is shown in Figure ES-14.

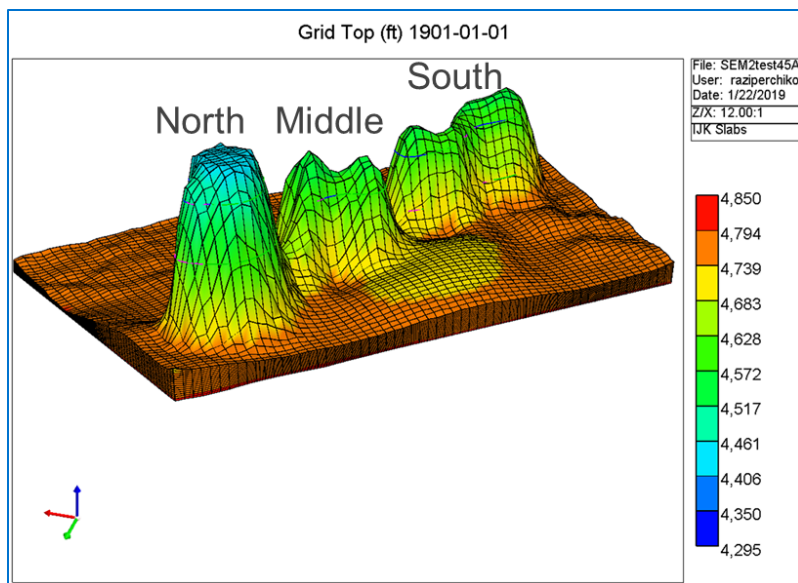


Figure ES-14. The grid system for Bagley reef: The upper panel shows the top of A1-Carbonate. The lower panel shows the top of Brown Niagaran formation.

For dynamic modeling, a sector model corresponding to the Northern lobe was extracted. This model used a  $60 \times 60 \times 30$  grid system and contained  $\sim 110,000$  cells. The property modeling included assigning porosity and water saturation values to the model. Because the Bagley task is divided into two subtasks, a single porosity model was used to develop the CRM and limited simplified history matched model. The histogram of neutron porosity from well-log data for the Bagley northern lobe has a range 0.05-0.20, with an average of 0.1034 which is used for the Brown Niagaran formation. A connate water saturation of 0.2 is used in the oil zone. Volumetric calculations for this yielded a pore volume of  $5.3E+9$  ft<sup>3</sup>, corresponding to an original oil in place of 9.6 million STB for the entire Bagley field.

## X. Dynamic Reservoir Model

Starting with the static model for the Northern lobe, different scenarios were used during the history match process to adjust the model parameters in order to match: (a) primary production response (i.e., oil and gas rates or equivalently, the corresponding cumulative production volumes), (b) average reservoir pressure during primary production, and (c) pressure buildup during the CO<sub>2</sub> injection period.

Model calibration involved adjusting both intrinsic permeability and relative permeability relationships. A constant permeability model is used for history match process. The cumulative oil production was used as the primary constraint for history match. Thus, the history match is primarily against the cumulative gas production, which is reasonably honored (Figure ES-15). The mismatch with the cumulative water production is greater, which results in a misfit against the average reservoir pressure. With a simplified permeability field, it was not possible to meet both water and oil production constraints.

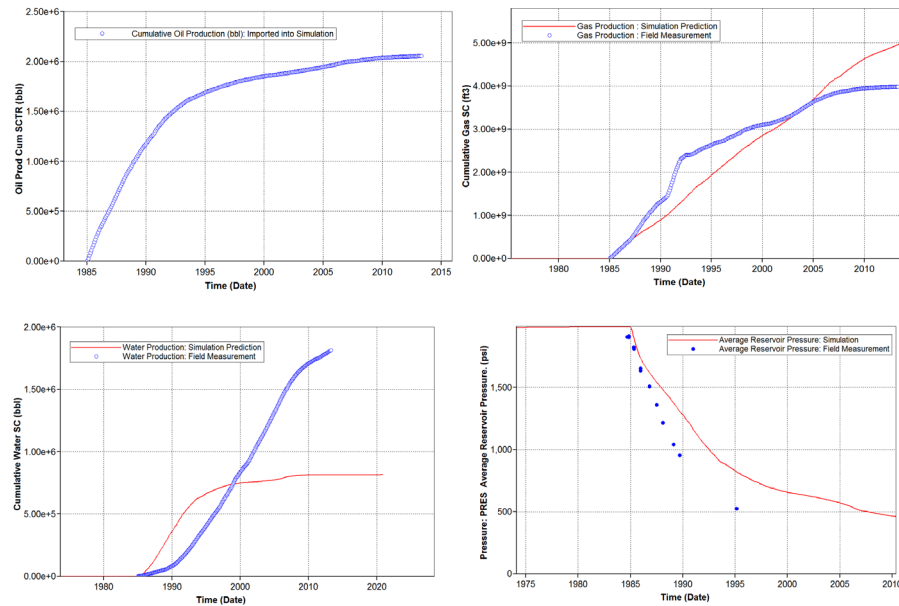


Figure ES-15. Predicted and measured average reservoir pressure.

Next, the CO<sub>2</sub> injection rate is used as a constraint for history match of CO<sub>2</sub> storage phase. The model was able to predict pressure response of injector (Figure ES-16) with good accuracy. This required using a skin factor of six for the injector well in order to achieve the pressure history match, suggesting some wellbore damage that has been corroborated from operational records. A reef permeability of 15 MD was used to history match primary production and CO<sub>2</sub> storage phase. Both the oil-water and gas-oil relative curves were also adjusted for the history match.

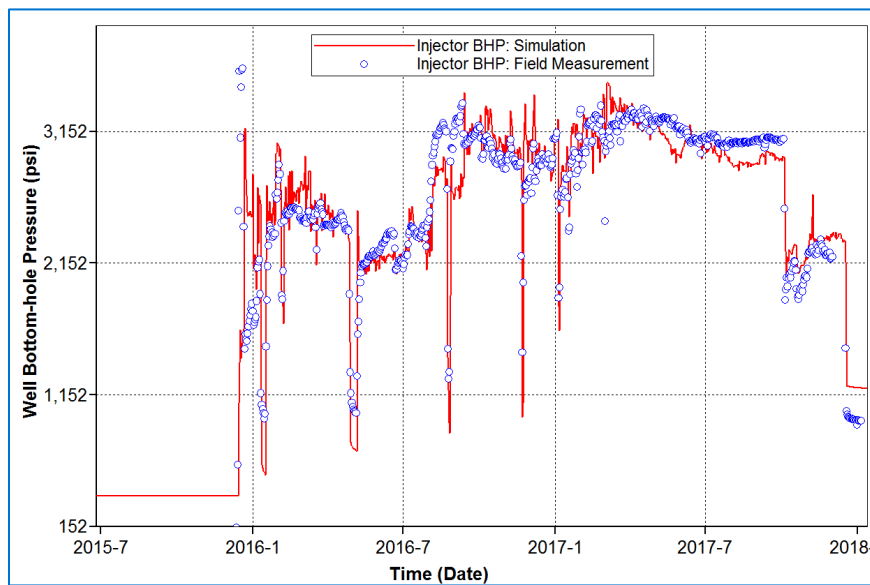


Figure ES-16. Injector Well (2-11) BHP comparison between field measurement and simulation.

## xii. Capacitance Resistance Model

The CRM model was applied to the injection data from the Northern, Middle and Southern Lobes of the Bagley reef. Cross plots of field versus cumulative CO<sub>2</sub> injection volume were used to evaluate the goodness of fit.

For the Middle Lobe, the R<sup>2</sup> for the CRM analysis is 0.89, which shows the simplified model is able to explain injection related data (Figure ES-17) and estimate fitted parameters (J and c<sub>t</sub>\*PV) with higher confidence (Figure ES-18). Initial pressure of 600 psi is used as an input for the model. The total compressibility times pore volume of the model is 2727 rbbl/psi, and estimated injectivity index is 4.89 rbbl/(day\*psi).

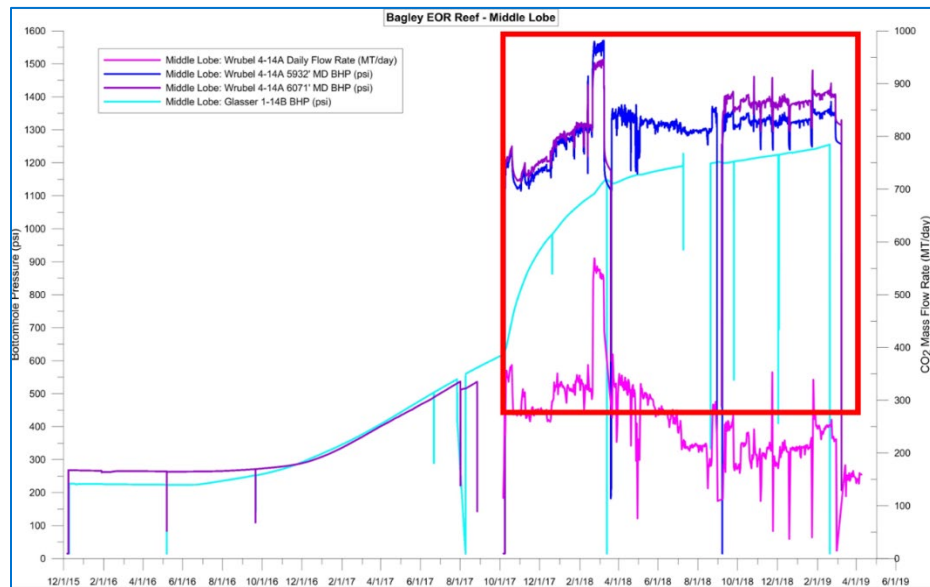


Figure ES-17. BHP and CO<sub>2</sub> injection rate for well 4-14 in Middle Lobe. The red box shows the time interval used for importing CRM model

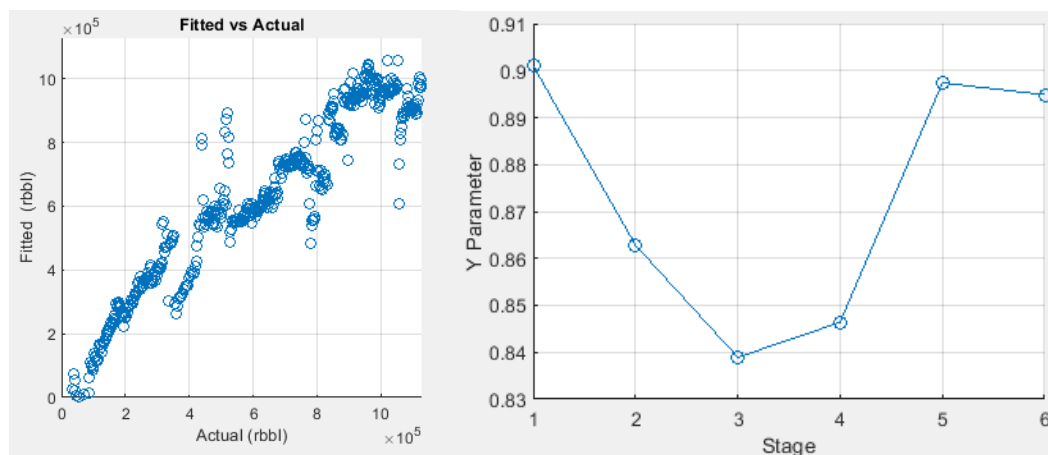


Figure ES-18. (A) Actual (field) CO<sub>2</sub> injection volume versus fitted data using simplified model (B) estimation of R<sup>2</sup> in different time interval.

However, for the Northern Lobe, the  $R^2$  for the CRM analysis was found to be only 0.37, which shows the simplified model is unable to explain injection related data and estimate fitted parameters ( $J$  and  $c_t \cdot PV$ ) accurately. Changing the initial pressure as a control parameter does not improve  $R^2$  of the model. The low  $R^2$  in this model could be because of additional wellbore effect (such as skin factor) in the injection well of North Lobe.

Although not shown here, the  $R^2$  for the CRM analysis of the Southern Lobe was found to be 0.76 showing the simplified model is able to explain injection related data and estimate fitted parameters ( $J$  and  $c_t \cdot PV$ ). Initial pressure of 500 psi is used as an input into the model. The total compressibility times pore volume of the model is 1310 rbbl/psi, and estimated injectivity index is 7.15 rbbl/(day\*psi).

#### **d. Chester-16**

##### **xii. Modeling Objectives**

- Integrate all geologic and geophysical data into an SEM
- Build a dynamic model based on the SEM using a pseudo-miscible approach, and history match it to the primary production data, waterflooding period, and the CO<sub>2</sub> injection period for the fill up prior to onset of oil production for the EOR phase.
- Use the history matched model to evaluate several production scenarios to examine tradeoff between incremental oil recovery and associated CO<sub>2</sub> storage.

##### **xiii. Static Model**

The Chester-16 static model construction follows a similar workflow to that of the other reefs. The geologic data and interpretations and petrophysical analyses were used as input into the SEM. A 2D depositional model interpretation was used to guide the development of the model's structural framework. 3D seismic data was used to define the boundary and geometry of the reef. The first step was to generate structural surfaces. The uppermost SEM zone for the Chester-16 reef was the A2 Carbonate, which has a higher elevation over the Northern Lobe and gently slopes off-reef. The A1 Carbonate follows the underlying Brown Niagaran Formation and is divided into three subunits: (a) Flank - which occupies the space adjacent to the reef and is relatively tight, (b) Crest – the oil-bearing portion that drapes over the reefal pods, and (c) Saddle – which occupies the saddle region between the two reef pod with poorly constrained properties. Locally, the Brown Niagaran was comprised of two pinnacle reefs, with the northeastern pod being the taller. The Gray Niagaran was relatively flat within the study area.

Next, surfaces for facies were created to subdivide the reservoirs into key zones. For this modeling effort, extra surfaces were prepared to delineate the distinct lithofacies within the Brown Niagaran, i.e., Flank, Windward, Leeward, and Reef Core. The gridded SEM covers an area around 3900 ft x 2300 ft, with a maximum height of ~590 ft. Grid cells in the x- and y-directions were kept at ~80 ft, with variable thickness in the vertical (z) direction, resulting in a fine-scale 2853-layer model containing ~4,000,000 cells.

For property modeling, neutron porosity logs from seven wells were used, along with core-measured porosity-permeability data from core samples. The A1 Carbonate had a porosity range from 3.16 percent to 10.72 percent with a permeability range from 0 to 6.04 mD. The Brown Niagaran had a porosity range from 1.51 percent to 7.14 percent with a permeability range from 0 to 204.28 mD. Power law transforms were fit to both sets of data. The fine-scale 2,853-layer geologic framework was used with scaled-up log properties to build porosity and permeability property models. During this exercise, both porosity and derived permeability logs were sampled to the grid resolution and subjected to variogram analysis to

characterize vertical heterogeneity in oil-bearing zones like the A1 Carbonate Crest and the Brown Niagaran. The variogram model, along with well logs, were then used in a conditional simulation algorithm to populate the 3D SEM with the key petrophysical rock properties. This process required interpolating the upscaled log porosity and permeability values across the entire 3D model grid. The GRFS method was used for these models. The GRFS is a stochastic method that honors the full range and variability of the input data. Each run creates one equiprobable distribution of a property throughout a model zone based on a model variogram and upscaled well logs.

The permeability modeling effort focused on GRFS for the oil-bearing zones, which include the A1 Carbonate Crest, A1 Carbonate Flank, and Brown Niagaran reef. Starting from the core-based porosity-permeability transform for these zones, a permeability log is computed from the neutron porosity log. This method characterizes the permeability residuals and then, through conditional simulation, adds the permeability residuals to the basic transform. The resulting transform is conducted along the cells penetrated by the well trajectory. Permeability values at the off-well grid cells were distributed via GRFS via collocated co-kriging with the porosity model. The permeability model was simplified for the non-oil-bearing zones by using average values from core measurements. These zones include the Gray Niagaran, A1 Salt, A2 Evaporite, and the A2 Carbonate. For modeling purposes, permeability for these zones are homogeneous.

Upscaling was then performed on the fine-scale model to create a tractable model for dynamic reservoir simulations using the Petrel plug-in called CONNECT UpGrid™. The optimal coarse-scale grid, which preserves an appropriate level of heterogeneity, was determined to be one with 79-layers containing 110,000 grid cells. Figure ES-19 shows a porosity and permeability distributions for a representative cross section in this upscaled model.

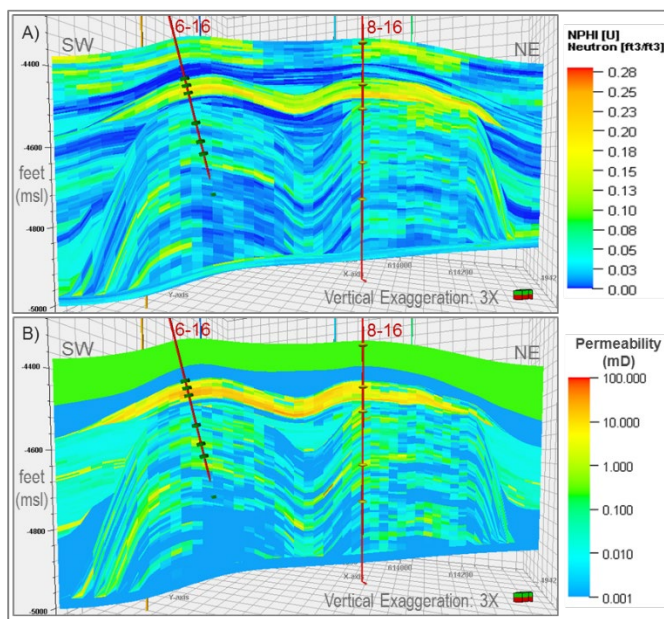


Figure ES-19. SEM upscaling results for the 79-layer model. A) Porosity model. B) Permeability model.

Water saturation was calculated from resistivity log data in seven wells using Archie's equation. The distribution of water saturation in the model was separated into three regions. The lower third of the reef structure was assumed to be water saturated. Formations outside the oil-bearing zones were also assigned a value of  $S_w = 1$ . The oil-bearing zones, A1 Carbonate Crest, the Brown Niagaran reef, and the A1 Carb Flank (saddle region) are recognized as oil-bearing. Water saturation versus height above

OWC was plotted individually for these zones. The Brown Niagaran employed a split on the basis of low (<3 percent) and high (>3 percent) porosity (or a pseudo rock-type), with the implication that the higher-porosity rock had a residual water saturation of around 0.15, while the lower porosity rock had an average residual water saturation of around 0.25. Most of the rock was of the low-porosity type and a curve fit of water saturation as a function of square-root of  $k/\phi$  was used to model saturations for this region. Volumetric calculations for this model yielded a pore volume of 5.2E7 ft<sup>3</sup>, corresponding to an oil in place of 9.2 MM STB.

#### **xiv. Dynamic Reservoir Model**

All simulations were done in CMG's IMEX module, which assumes black-oil and pseudo-miscibility of CO<sub>2</sub>. Performing simulations with this module is a computationally efficient alternative to full blown compositional simulation (CMG-GEM®), where the mass transport associated with each individual component of the reservoir fluid is calculated on the gridded domain. The black-oil option simplifies the numerical model by capturing the volumetric expansion of only oil, gas, and water in each grid block and calculates the mobility of these fluid at a given pressure.

Per the objectives of this project and the uncertainties inherent in the modelling, we are satisfied learning about the general movement or extent of the CO<sub>2</sub> plume, the average pressure response, associated oil production rates and gross CO<sub>2</sub>-storage capacity of Chester-16 with injection-production configuration. The data availability and computational-time constraints forced a trade-off where we chose general accuracy (pseudo-miscible mixing of CO<sub>2</sub> and oil via IMEX) over precision (fully compositional simulation via GEM) in this modelling effort.

Since laboratory measured fluid compositional data was unavailable, industry-standard correlations were used to generate black-oil properties (formation volume factors of oil and gas, solution gas-oil-ratio, oil and gas viscosity) as a function of pressure for the simulation. Inputs for applying these correlations are bubble-point pressure (~1800 psi), initial producing gas-oil-ratio (~650 scf/stb), stock-tank oil density (51.2 lb/ft<sup>3</sup>) and gas-gravity (0.83). In CMG-IMEX's pseudo-miscible module, CO<sub>2</sub> is assumed to be insoluble with formation water but assigned an omega (mixing) parameter of 0.7 at the miscibility pressure of 1,300 psi and above, and at 0 at sub-miscible pressures.

The objectives (performance indicators) of the history match were to: (1) honor all individual well oil production rates via the oil constraints, (2) honor individual water injection and CO<sub>2</sub> injection rates, (3) reproduce the pressure decline history recorded from the primary production period and at abandonment after waterflooding, (4) reproduce the pressure deflections recorded at the various depths (gauges) of the 8-16 monitoring well during CO<sub>2</sub> injection through the 6-16 injection well.

History matching of the Chester-16 reservoir model was a highly iterative process assessing model sensitivity to individual parameters via numerous forward simulations testing various parameter combinations in trial-and-error. Meeting objectives (1) to (3) involved revising the permeability field through the various layers. Significant uncertainty exists as to the allocation of the CO<sub>2</sub> injection rates between A1 Carbonate and the Brown Niagaran due to a malfunctioning seal inside the 6-16 well. As a result, meeting objective (4) required estimating the CO<sub>2</sub> injection volumetric split between the A1 and the Brown Niagaran that could reproduce the appropriate pressure deflections at various depths.

A significant component of the history matching workflow involved adjustment of permeability values. After extensive manual trial-and-error attempts, a total of 17 regions of permeability modification/enhancement were implemented. Three permeability groups were identified in the A1 carbonate from the SEM, generally representing permeability within two orders of magnitude. The Brown Niagaran on the other hand, is a generally more heterogeneous rock and thus had more permeability groups representing

a much wider range (four orders of magnitude). Well testing data also pointed toward a thin but contrastingly low-permeability region at the base of the A1 Carbonate (a baffle), in between the saddle region and the A1 carbonate. This layer was assigned a low permeability of 0.01 mD. Finally, the well-test also suggested that the saddle region itself had a very low overall permeability of 0.001 mD. All other rock layers – the Gray Niagaran and all the outermost flank layers to the Brown Niagaran — retained the very low permeabilities assumed in the original.

A uniform high permeability streak was introduced to the middle of the Brown Niagaran to meet oil production constraints with a model that retained the heterogeneity. While the porosity distribution in those layers was retained, the permeability heterogeneity in these layers was removed in favor of a uniform and layer-wide homogeneous permeability of 40md. Additionally, some gridblocks were manually assigned a permeability value, depending on their porosity value. The history matching process has (1) lowered the overall heterogeneity in the entire model, (2) consistently increased permeability in the entire model by at least one order of magnitude, and (3) introduced a horizontal permeability streak in the Brown Niagaran that is surrounded by a low background permeability.

Figure ES-20 shows that the history matched model adequately captures the average reservoir pressure decline even though continuous pressure decline data was unavailable. The model correctly predicts a post-waterflood, abandonment pressure of around 500 psi. With updated permeability field, the model was able to meet the oil production constraints for all five wells to match the field cumulative production. The model's prediction of gas production captures both the global trend in gas production as well as the overall cumulative produced volume. Water production data for the life of the field was unavailable. Although incremental water production data from after the waterflood was available, it is still a source of uncertainty. The current model overpredicts the water production from this period considerably. Attempts to match this level of water production by lowering water-oil relative permeability endpoint was not successful as it results in lower oil production and higher average pressure.

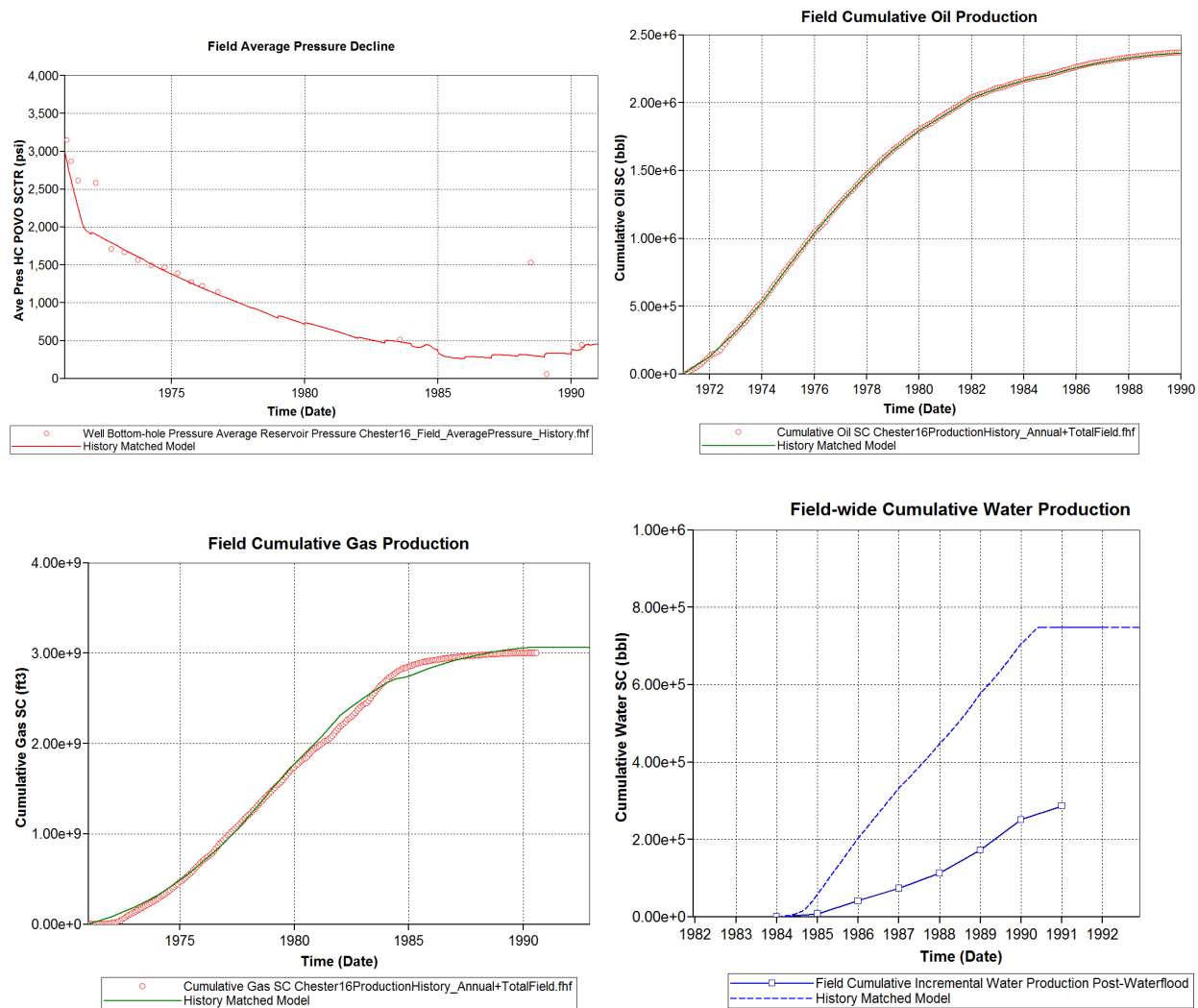
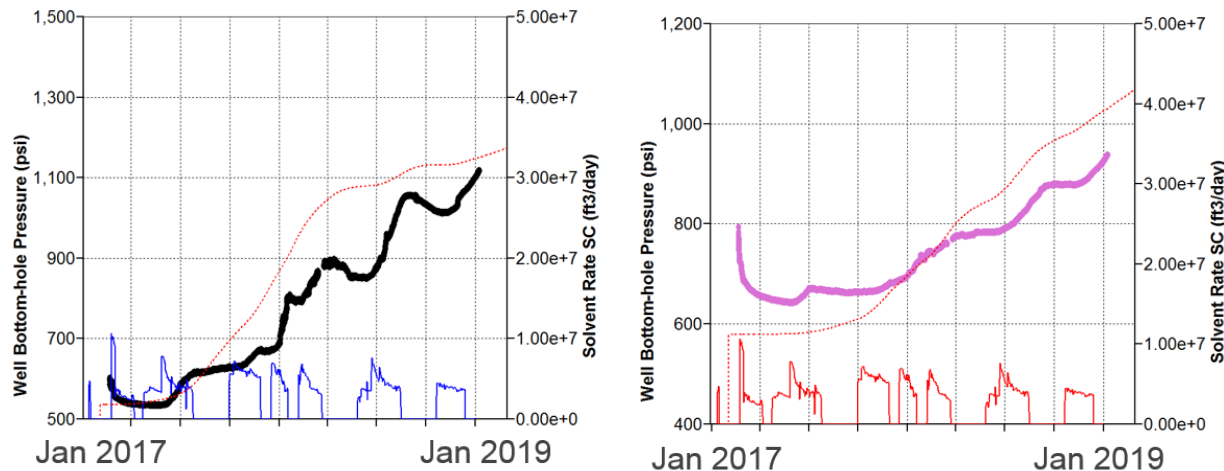


Figure ES-20. History-Match to the average pressure decline during the primary and secondary phase

The quality of the match during the CO<sub>2</sub> fill up phase is an indication of the reliability of the permeability field and the CO<sub>2</sub> injection rates allocated to the individual formations (and perforations). The match to the bottomhole pressure data at various depths in the location of the 8-16 well is the primary performance indicator. Several different rate allocations were attempted in trial-and-error, due to the non-uniqueness of the history matching problem.

Figure ES-21 (left) shows that the match to the pressure in the middle of the A1 Carbonate at the 8-16 well is good. The initial pressure prior to CO<sub>2</sub> injection has been matched nearly exactly. The model also captures the timing of the first arrival of the pressure pulse from the injection closely. The pressure at the end of injection has also been matched nearly exactly. However, the transition from the initial condition to the final has not been fully replicated. Figure ES-21 (right) also shows the match to the pressure in the middle of the Brown Niagaran at the 8-16 well. The initial pressure prior to CO<sub>2</sub> injection has been matched within 50 psi, although the pressure at the end of injection is off by around 150 psi. However, the transition from the initial condition to the final has not been replicated, nor has the pressure pulse arrival time. Because (1) the Brown Niagaran is over 300 ft thick and highly heterogeneous and the A1 Carbonate is relatively thin homogeneous rock in comparison, and (2) the simulator employs a less

rigorous pseudo-miscible black-oil model, the matches for the Brown Niagaran are not expected to be as good compared to the A1 Carbonate.



*Figure ES-21. History match to the pressure response at the top of the Brown Niagaran, as measured at the 8-16 gauge.*

Next, several “what-if” scenarios were investigated for the CO<sub>2</sub>-EOR period after the reef was pressurized beyond the minimum miscibility pressure target of 1300 psi. These 10 scenarios collectively investigated the use of vertical versus horizontal wells, production of the A1 Carbonate versus the Brown Niagaran, and location of injectors/producers. The forward simulation for each scenario used an injection rate constraint that was capped at 6 MMSCFD, and a maximum bottom-hole pressure of 4000 psi. Also, total fluid rates of the injected and produced volumes were to be kept approximately equal for pressure maintenance.

Figure ES-22 summarizes the performance of these scenarios, with each metric normalized to the highest quantity observed across all 10 scenarios. Scenarios 3, 8, 9, and 10 stand out for producing the most oil while accompanied with the lowest levels of CO<sub>2</sub> injection required. From these, Scenario 9 ranks best in terms of needing the lowest amount of CO<sub>2</sub> injected, and yet storing the most CO<sub>2</sub>. Scenario 9 thus appears to be optimal for both CCUS and CO<sub>2</sub>-EOR from this ranking analysis, followed by Scenario 3.

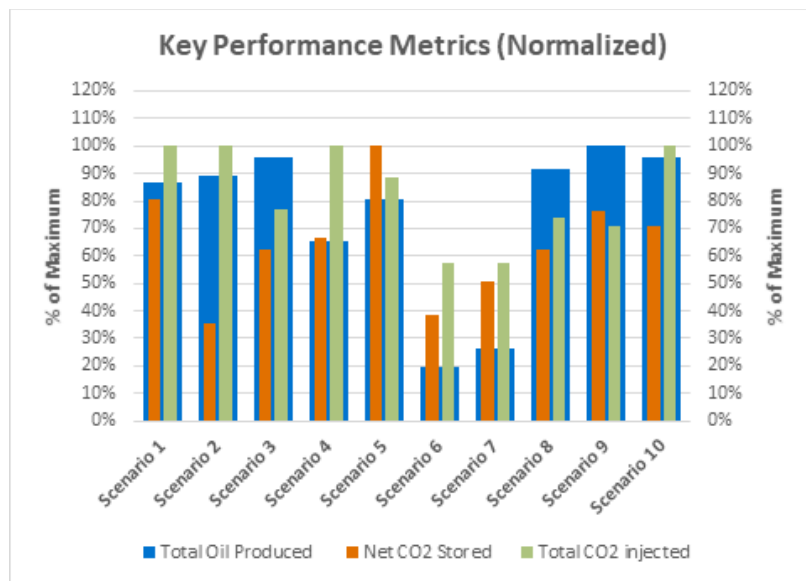


Figure ES-22. Comparison of all scenarios against each other in terms of oil recovery, CO<sub>2</sub> injection and CO<sub>2</sub> stored. Each performance metric is expressed as a percentage of the maximum observed across all 10 scenarios.

## xv. Coupled Process Modeling

### a. Geochemical Modeling

#### *Modeling Goals*

This task was performed as part of the dynamic modeling activities for the Dover-33 reef to demonstrate capability to model geochemical effects of CO<sub>2</sub> injection within a dynamic modeling framework. This task aimed to implement multicomponent flow simulation coupled with phase and chemical equilibrium and rate-dependent mineral dissolution/ precipitation to evaluate effects of geochemical processes on short-term observed pressure response during the injection period as well as longer-term behavior associated with CO<sub>2</sub> storage processes.

#### *Methodology/Approach*

The system of interest considered for the current study is a simplified equivalent coupled flow-geochemical model in CMG-GEM® consisting of a core reservoir region with an overlying low permeability zone and an underlying water column with logarithmically increased grid spacing in the radial direction to ensure more resolution closer to the well where most of the dynamic processes would be centered. This radial model was set up in a fully compositional setting to represent a depleted oil reservoir with one vertical CO<sub>2</sub> injection well to incorporate relevant field data. It was subject to an assumed CO<sub>2</sub> injection period to assess the impact of geochemical reactions on the observed pressure buildup during injection and the fate of the CO<sub>2</sub> through an extended 1000-year post-injection monitoring period. The methodology involved the following key steps:

- The reference simplified representative model involving CO<sub>2</sub> injection in a depleted oil reservoir without geochemistry was implemented in CMG-GEM®
- Required geochemistry-related input data such as mineralogy and fluid sampling data from the field, as well as previous equilibrium model considerations for the Dover-33 reef, were collected

- c. The geochemical module was included and set up in GEM for the CO<sub>2</sub> injection period and the simplified representative reef model was re-initialized
- d. Basic numerical sensitivity analyses were run to observe impact of geochemical reactions during and after the defined CO<sub>2</sub> injection period in the depleted oil reservoir and the coupled flow-geochemical model was compared with the reference model without geochemistry.

The geochemical modeling under CO<sub>2</sub> injection conditions considered the following important factors affecting CO<sub>2</sub> sequestration: (1) the kinetics of chemical interactions between the host rock minerals and the aqueous phase, (2) CO<sub>2</sub> solubility dependence on pressure, temperature, and salinity of the system, and (3) redox processes that could be important in deep subsurface environments.

## Results

For the given system, the pressure response and propagating CO<sub>2</sub> front showed minimal differences during the period of CO<sub>2</sub> injection between the reference and coupled models. During later times in the post-injection period however, there were noticeable differences in the results between the models with respect to the movement of the gas front and reservoir pressure. The effect of considering the aqueous and mineral reactions in the system of interest thus impacted the longer-term pressure response (Figure ES-23) and the plume progression during the 1000-year post- CO<sub>2</sub> injection period. The phase distribution of CO<sub>2</sub> in the system was studied as the system worked to retain a new equilibrium during the post-injection period with the CO<sub>2</sub> in the system slowly moving into more stable dissolved phases.

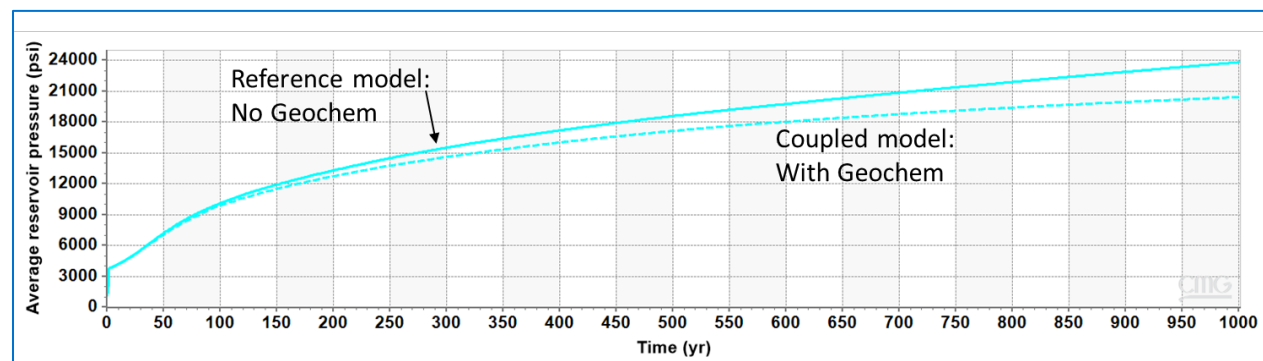


Figure ES-23. Comparison of the average model pressure until the end of the post-injection period. The reference model with no geochemistry is shown as continuous curves while the geochemistry-coupled model for the CO<sub>2</sub> injection period is shown as dashed curves. The effect of these geochemical reactions can be seen by the divergence in the average pressures post 100-years of injection.

Figure ES-24 shows the evolution of the total moles of HCO<sub>3</sub><sup>-</sup>, CO<sub>2</sub> in dense phase, and dissolved CO<sub>2</sub> in the system of interest. The presence of low pH brine with high Cl<sup>-</sup> in the assumed mineralogy resulted in a negative saturation index that drove the dissolution of dolomite and calcite present in the reservoir rock. However, the extent of this dissolution occurring in the chosen system of interest was not seen to significantly impact the porosity or hence the permeability of the rock. Basic sensitivity analyses to reservoir permeability and brine pH were performed to investigate the potential impact of basic reservoir and in-situ brine properties on the rate of aqueous and mineral reaction rates in the system of interest.

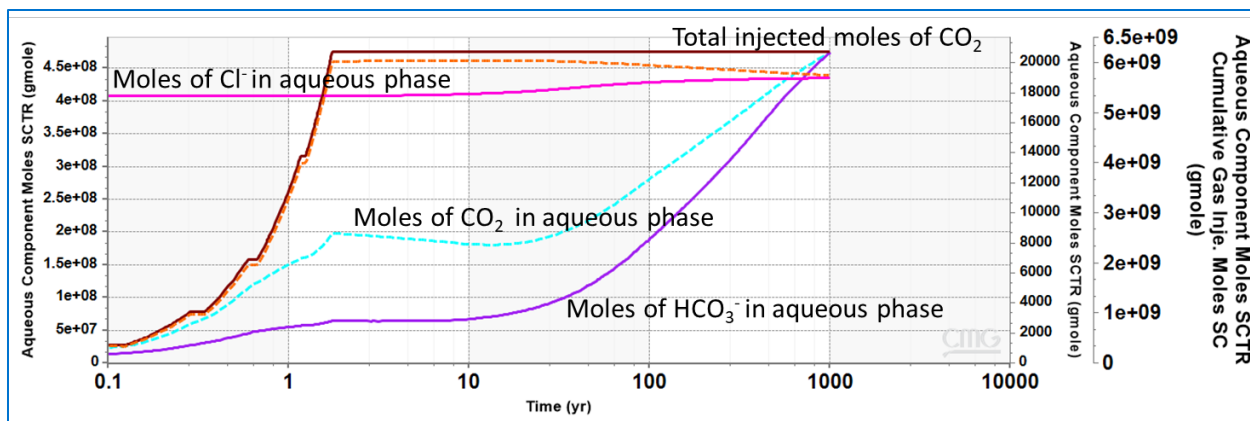


Figure ES-24. Evolution of  $\text{CO}_2$ ,  $\text{HCO}_3^-$  and  $\text{Cl}^-$  until the end of 1000 years in the coupled model. After the injection period, the moles of dissolved  $\text{CO}_2$  increase as more  $\text{CO}_2$  goes into solution with decreasing moles of  $\text{CO}_2$  in the supercritical phase (orange dashed line).

### Significance

Coupled reservoir models are useful to simulate many relevant subsurface processes as demonstrated in the reef modeling exercises, with the brine composition and mineralogy determining the longer-term system response. The input parameters, however, need to represent in situ field conditions and need validation through detailed site-specific field testing for these models to be as accurate and reliable as possible in practical applications.

## b. Geomechanical Modeling

### Geomechanical Modeling Goals

Understanding the geomechanical outcomes of  $\text{CO}_2$  storage into geological formations is necessary since it affects  $\text{CO}_2$  injectivity, reservoir mechanical integrity, and safety of the potential injection site. To ensure that the mechanical integrity of the reservoir caprock system is maintained during injection, in-situ stress changes caused by pore pressure changes (i.e., poroelastic effect of injection) should be investigated. Poroelastic effects of injection determine the final stress state in the reservoir as a precursor for evaluating tensile and shear failure potential. The final in-situ stress also limits practical injectivity of the reservoirs. Ground surface uplift and induced seismicity, which could have a detrimental effect on the safety of the injection site and its surrounding area, also depends on the poroelastic effect of injection. The main goal of the geomechanical modeling is to investigate the poroelastic response of  $\text{CO}_2$  injection into the Niagaran carbonate reef system. The poroelastic effects, investigated in this work, include stress changes, reservoir deformation, and surface uplift due to  $\text{CO}_2$  injection into the reservoir.

### Methodology/Approach

Statistical-based models were developed to provide a quick tool to evaluate the poroelastic effect of injection. A combination of experimental design for seven independent parameters (depth, caprock and reservoir Young's modulus, caprock and reservoir Poisson's ratio, pressure, and Biot's coefficient) and response surface modeling was used to develop statistical-based reduced-order models. We performed 147 numerical simulations to develop simplified models for the reefs. The poroelastic model responses were captured using a standard quadratic model with full interaction terms, as well as a reduced model with only statistically significant coefficients. Reduced-order models were then combined with a Monte Carlo simulation to perform poroelastic uncertainty analyses and better understand the poroelastic

performance of CO<sub>2</sub> storage in the closed carbonate system of the Michigan basin. Coupled hydromechanical simulations were used, as a second objective of the geomechanical modeling, to estimate stress changes and surface uplift due to injection into a depleted reef (i.e., Dover-33 reef).

## Results

Four poroelastic responses, evaluated using statistical based modeling, include: I-stress (horizontal stress) increment, K-stress (vertical stress) increment, reservoir vertical displacement, and surface uplift. Figure ES-25 shows the response surface plot for various combinations of reservoir block pressure and reservoir depth using statistical based models. When pressure increases, surface uplift increases. Decreasing depth causes surface uplift increase. The result of the statistical based modeling shows that each reservoir type has different control parameters for each performance metric. The pressure increase is the main parameter that controls stress increase, reservoir displacement, and surface uplift. While the reservoir depth is a significant parameter to predict surface uplift, Biot's coefficient is the main parameter to evaluate horizontal stress increase.

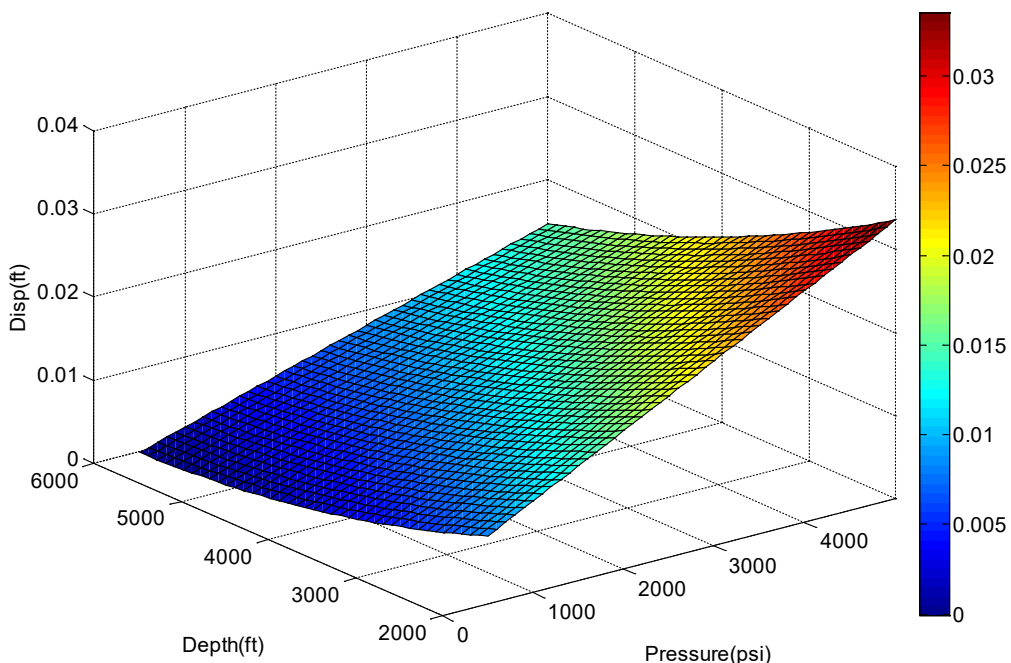


Figure ES-25. Surface uplift response surface based on reduced order model to estimate surface uplift

A stress independent constant Biot's Coefficient has typically been used to estimate poroelastic response of injection such as surface uplift modeling, reservoir stress path prediction, and fault activation. Numerical hydromechanical models were used to estimate the poroelastic response of injection by considering Biot's Coefficient dependency to the effective stress (as the second objective of geomechanical modeling). The modeling results demonstrated how the assumption of a constant Biot's Coefficient affect geomechanical responses of the subsurface injection. Modeling results showed that using a constant Biot's Coefficient would be inaccurate since effective stress changes cause Biot's Coefficient increase.

## **Significance**

Coupled hydromechanical modeling is typically used to evaluate the poroelastic effect of injection as well as the resulting geomechanical outcomes. Solving several equations over many grid blocks numerically can be computationally expensive. As a result, statistical-based models were developed to provide a quick tool to evaluate the poroelastic effect of injection. Using the simple statistical based mechanical model, the screening process to select the best site for CO<sub>2</sub> sequestration, in terms of mechanical integrity, could be more efficient.

## **xvi. Summary and Lessons Learned**

### **a. Static Model Development**

A standard static earth model (SEM) workflow common in the oil and gas industry has been used in these studies using the Petrel software. The geologic framework was first established from seismic and geophysical log analysis. Property modeling for porosity and permeability involved geostatistical simulations using porosity-permeability transforms. Several lithofacies were identified from geological considerations, but the geometry and properties of some of the lithofacies can be highly uncertain because of limited sampling via wells and/or cores. Water saturation data were derived from geophysical logs or modeled using capillary pressure and Leverett J-function concepts. Volumetric calculations for original oil in place were cross-checked against material balance analysis results to verify the property modeling. Another key feature was SEM upscaling (coarsening of the geocellular grid) using CONNECT UpGrid™, a Petrel plug-in. This application, which scales the grid-based on the vertical distribution of porosity, is an enhancement over arbitrarily changing a model's layer count through the standard proportional layering method independent of the variation in rock properties. Model cell counts can be reduced by ~80 percent while preserving the key patterns of geologic heterogeneity. In the Chester 16 reef, a porosity cube inferred from seismic inversion was used to update and condition property models. In general, it was possible to repeat the workflow across multiple reefs, subject to the availability of well log data, core data, and seismic inversions (when available) that spanned each of the reefs (and the lithofacies therein) in a representative manner.

- **What we did:** developed static earth models using standard oil and gas workflows including geophysical log and seismic data integration and rock property modeling
- **What was new and improved:** geostatistical porosity-permeability modeling; grid upscaling to reduce cell size, porosity cube from seismic inversion
- **What were remaining uncertainties:** geometry and location of lithofacies, constraints on inter-well property estimates from seismic inversion

### **b. Dynamic Reservoir Modeling**

Two types of grid-based dynamic simulations were carried out: (a) compositional simulations (Dover 33), and (b) pseudo-miscible black-oil calculations (Bagley, Chester 16). Computation intensive compositional simulations require detailed oil sample characterization and experimental data on fluid properties as well as equation of -state based fluid property modeling. The pseudo-miscible option is computationally efficient, requires only a few adjustable parameters, and is reasonably accurate. History matching of the primary production and subsequent CO<sub>2</sub> injection history with both modeling options generally involves significant adjustment to the initial permeability field (often derived from porosity to permeability transform functions derived from laboratory porosity and permeability data). This suggests that the small-scale core-derived porosity-permeability transforms may not be a good representation of field-scale permeability

distribution, especially in a carbonate reservoir setting. Nonetheless, the history matching process was able to suggest large-scale permeability trends in Dover 33 and Chester 16 that appear to be geologically reasonable (albeit unsampled because of limited number of wells).

Data availability can also impact the quality of history matching because of issues such as: (a) limited static bottomhole pressure data from the historical primary production period, (b) questionable water production data that have an impact on reservoir voidage calculations, and (c) uncertain apportionment of injection volume between multiple permeable zones. In addition, pressure volume temperature (PVT) data from each reef was not always available, and data from the best analog reef was used as a proxy. This is also another source of uncertainty. Finally, oil-water and oil-gas relative permeability relationships are generally not available and have to be assumed. Even a limited number of laboratory experiments would be useful in constraining end point saturations, end point relative permeabilities and the curvature of the relationships.

The application of the history matched model for forecasting CO<sub>2</sub> Enhanced Oil Recovery (EOR) and associated scenarios in Chester 16 was helpful in elucidating the relative efficacy of vertical versus horizontal wells, location of producers versus injectors, and incremental recovery versus associated CO<sub>2</sub> storage.

In Bagley, a simple homogenous model is used to history match the primary production data, as opposed to having an unnecessarily complex heterogeneous complex static geological model. The simple model can also match the CO<sub>2</sub> injection pressure history. This suggests that production and pressure response can be represented using a simple reservoir model. The uncertainty for the modeling comes from the lack of input data like seismic data.

In order to conduct a rapid, simplified analysis of the reservoir injectivity and capacity, the lumped parameter Capacitance-Resistive Model (CRM) was successfully applied for the CO<sub>2</sub>-injection only period of the MRCSP injection in the reef. CO<sub>2</sub> injectivity in closed, depleted oil reservoirs is affected by the phase changes and interactions with the existing fluid phases as well as with the rock itself. The average representative injectivity index (stabilized flow rate normalized by pressure buildup) from the CRM was found to concur with an independent injectivity analysis done for the reef. The model also addressed uncertainty in the initial pressure estimate for the reef with the resulting compressible pore volume found to be consistent with total system compressibility representative of typical oil and gas systems. In addition, the resulting fitted model has the potential to serve as a rapid forecasting tool for a quick prediction of the pressure buildup or rate for a desired target injection scenario in the future.

- **What we did:** dynamic grid-based simulations using compositional and pseudo-miscible modeling approaches based on the SEMs developed in this project and lumped parameter capacitance-resistance modeling to match pressure-production/injection data
- **What we learned:** manual history matching can be tedious and non-unique, initial permeability fields (generated from core porosity-permeability transforms) may need to be significantly adjusted, calibrated models can be useful for evaluating EOR related well-placement options, and CRM models can be useful forecasting tools with limited data
- **What were remaining uncertainties:** availability of pressure data during primary production, quality of water production data, lack of experimental PVT data, and relative permeability information.

### c. Coupled Process Modeling

The coupled flow-geochemical modeling task successfully utilized a simplified 2-D radial model using relevant rock and fluid data from the field to generate synthetic pressure responses following CO<sub>2</sub> injection into a depleted oil reservoir. The brine composition and mineralogy determine the tendency and rate of mineral dissolution/ precipitation. The effect of considering the aqueous and mineral reactions in the system of interest impacted the longer-term (post 100-years of injection) pressure response and the plume progression during the 1000-year post- CO<sub>2</sub> injection period. The CO<sub>2</sub> injected in the system slowly moved into more stable dissolved phases in the post-injected period to attain a new system equilibrium. The accuracy of such coupled models depends upon input parameters representative of in situ conditions and need validation through detailed site-specific field testing to provide practical and relevant results.

Geomechanical processes associated with CO<sub>2</sub> sequestration should be investigated to ensure long-term safe storage of CO<sub>2</sub>. To that end, impacts such as surface uplift, reservoir expansion, and in situ stress changes have been studied using statistical based reduced order models (developed from coupled flow and geomechanics model results). This approach provides a tool to evaluate the poroelastic response of injection whenever practical limitations (budget and time) require a quick response. A key insight from these studies was that fracture pressure increases during injection due to poroelastic effects. In fact, the main reason that hydraulic fracture test shows such a low fracture pressure is that minifrac test was performed when the reef was depleted from primary oil production to low pore pressure (~500 psi). Data limitations are a major challenge for geomechanical studies. Therefore, additional field and laboratory data should be collected on geomechanical properties of the overburden and the formation.

- **What we did:** coupled fluid flow and geochemical modeling to understand chemical reactions after CO<sub>2</sub> injection, developed statistical proxy models based on coupled fluid flow and geomechanical modeling to predict surface uplift, reservoir expansion, and in situ stress changes from CO<sub>2</sub> injection
- **What we learned:** aqueous and mineral reactions are slow but can impact pressure response in ~100 year time frame and plume progression in the ~1000 year time, fracture pressure increases during injection due to poroelastic effects, proxy models can capture the behavior of full-physics geomechanical models with good accuracy
- **What were remaining uncertainties:** reactive transport parameters representative of in situ conditions, availability of in situ field testing for modeling model validation, field and laboratory data collection to provide formation geomechanical properties



## Preface

The Midwest Regional Carbon Sequestration Partnership (MRCSP) has been investigating various reservoir characterization and modeling technologies related to CCUS in conjunction with CO<sub>2</sub>-EOR operations in multiple Silurian-age (Niagaran), oil-bearing, carbonate pinnacle reefs in northern Michigan, USA. This report provides a comprehensive discussion of reservoir modeling studies that were conducted for tracking oil production, forecasting CO<sub>2</sub> plume migration and estimating associated storage in a number of reefs that were at different stages of their CO<sub>2</sub>-EOR life cycle. These include: (a) Dover-33 which has undergone primary production followed by CO<sub>2</sub>-EOR, (b) Charlton-19 and Bagley where CO<sub>2</sub> injection has been followed by initial EOR related oil production, and (c) Chester-16 which is in the early stages of CO<sub>2</sub> injection prior to oil production.

The modeling process for simulating oil production, CO<sub>2</sub> injection and associated storage in these reefs entails two phases. The first phase, geologic framework modeling, integrates all pertinent geological and geophysical data (from logs, cores and seismic surveys) about reservoir structure, geometry, rock types and property distributions (porosity, permeability, water saturation) into a 3-D distributed grid-based SEM. The second phase, dynamic reservoir modeling, uses the SEM as a platform to simulate the movement of oil, gas, water and CO<sub>2</sub> within the reservoir during primary hydrocarbon production as well as during subsequent phases such as CO<sub>2</sub>-injection assisted EOR, plume migration, and associated storage. In addition, an assessment of coupled process effects is also carried out, where the impacts of geochemical and geo-mechanical processes induced by CO<sub>2</sub> injection are studied.

The SEM process uses a standard oil and gas workflow for building static earth models for all the reefs. The dynamic reservoir modeling part is carried out using a detailed compositional approach (i.e., for Dover-33) that considers mass transfer between different components (i.e., crude oil, water, CO<sub>2</sub>) using an Equation-of-state based representation, or a pseudo-miscible approach (i.e., for Bagley and Chester-16) that is computationally efficient and reasonably (if not fully) accurate. A lumped parameter methodology called Capacitance Resistance Model is also used (i.e., for Charlton-19 and Bagley) to determine injectivity and compressible pore volume as a coarse tank-type model representation.

These modeling studies support several goals, i.e.,

- Geologic System representation – data integration (e.g., integration of all reservoir characterization data into a geologic framework) – performed for all reefs
- Scientific – coupled process understanding (e.g., how does CO<sub>2</sub> move through the formation and interact with rock/oil/brine) – performed for Dover-33
- Calibration – history matching (e.g., update description of subsurface by comparing model predictions to observations) – performed for all reefs
- Engineering – system design (e.g., how many wells are needed to meet injection targets and optimize oil recovery and associated storage) – performed for Chester-16

This report is organized into multiple chapters as follows. Chapters 1 through 4 cover static and dynamic reservoir modeling for Dover-33, Charlton-19, Bagley and Chester-16 reefs, respectively. The Dover-33 chapter also includes a discussion of coupled geochemical process modeling. A discussion of generic coupled geomechanical process modeling is presented in Chapter 5. The conclusions from each of the chapters has been collated into a Summary and Lessons Learned section that was presented earlier as part of the Executive Summary.



# 1.0 Dover-33 Reef

## 1.1 Introduction

MRCSP has been conducting large-scale CO<sub>2</sub> injection in the Dover-33 oil field in northern Michigan in cooperation with site host Core Energy LLC. This field is one of the several hundred pinnacle reef structures in the Michigan basin. Dover-33 is a late-stage reef that has undergone extensive primary and secondary recovery phases. Through the Carbon Dioxide Enhanced Oil Recovery (CO<sub>2</sub>-EOR) and the two-year Phase III injection period beginning in March 2013, about 0.5 million tonnes of CO<sub>2</sub> have been stored in this reef. This reef is a good example of a full CO<sub>2</sub>-EOR lifecycle and ultimately demonstrates the capacity and safe storage of CO<sub>2</sub>. The reef has also been used for multiple static earth model (SEM) approaches to determine how best to represent the geology and heterogeneity of a complex reef reservoir. The results of the early models, Level 1 and Level 2, are presented in Miller et al., 2014. The previous models struggled to represent the geology and had several challenges in history matching the dynamic models.

### 1.1.1 Reef Description

Dover-33 is an isolated reef structure in the northern Niagaran pinnacle reef trend that is approximately 270 ft thick at a depth of about 5400 ft (top of reef). The reservoir is in the late-stage of recovery, having undergone extensive primary and secondary oil recovery with CO<sub>2</sub>.

Wireline logs for 13 wells were analyzed for the Dover-33 field. A new well, Lawnichak 9-33, was drilled in 2016 as part of the characterization efforts (Table 1-1). The reef core, reef apron, and bioherm were composed of mixed limestone and dolomite with moderate to high porosity. The A1 carbonate showed moderate porosity with occasional salt plugs. Moderate porosity/storage potential was observed along the flanks of the reef in the distal reef apron and rubble where there was vugular dolomite.

**Table 1-1. Wells used to characterize the Dover-33 field with permit numbers and status.**

Well Name	Permit Number	Status	Position
Lawnichak & Myszkier 1-33	29565	Active	Leeward
Lawnichak & Myszkier 3-33	29781	Plugged	Leeward
Koblinksi & Fisher 1-28	29809	Plugged	Windward
Kirt House 2-28	29840	Plugged	Off-reef
Winter 2-33	30392	Plugged	Off-reef
Amejka 2-34	31108	Plugged	Off-reef
Boughner State Dover 4-28	32298	Plugged	Off-reef
Lawnichak & Myszkier 5-33	33830	Plugged	Leeward
Lawnichak & Myszkier 5-33A	33937	Plugged	Leeward
Winter 1-33	35159	Plugged	Windward
Lawnichak & Morey 1-33	35584	Plugged	Off-reef
Lawnichak & Myszkier 2-33	50985	Plugged	Windward
Lawnichak & Myszkier 2-33 HD1	51601	Plugged	Reef Core
Lawnichak & Myszkier 5-33 HD1	51603	Shut-in	Leeward
Lawnichak and Myszkier 2-33 HD2	55479	Plugged	Off-reef
Lawnichak & Myszkier 2-33 HD3	55845	Plugged	Leeward
Lawnichak & Myszkier 2-33 HD4	55942	Shut-in	Leeward
Lawnichak 9-33	61209	Active	Leeward

The interpretations of the log data were used to subdivide the reef into zones based on reservoir potential. Figure 1-1 illustrates the subdivisions of the interpreted lithofacies in map view. Four lithofacies were defined: 1) windward (purple) with high flow potential; 2) reef core, (green) which includes the reef core facies with moderate to high flow potential; 3) leeward, (blue) which includes the leeward facies with low to moderate flow potential; and 4) includes the flanks and off-reef Brown Niagaran with no-flow potential.

An interpreted cross-section was constructed across the reef (A-A') to illustrate the changes in lithology and the locations of the lithofacies. Cross-section A-A' (Figure 1-2) illustrates the thicker salts and carbonates off-reef and the thinning of the A1 and A2 formations on the crest of the reef. Internally, the leeward facies are to the southwest, the reef core is central, and the windward facies are to the northeast.

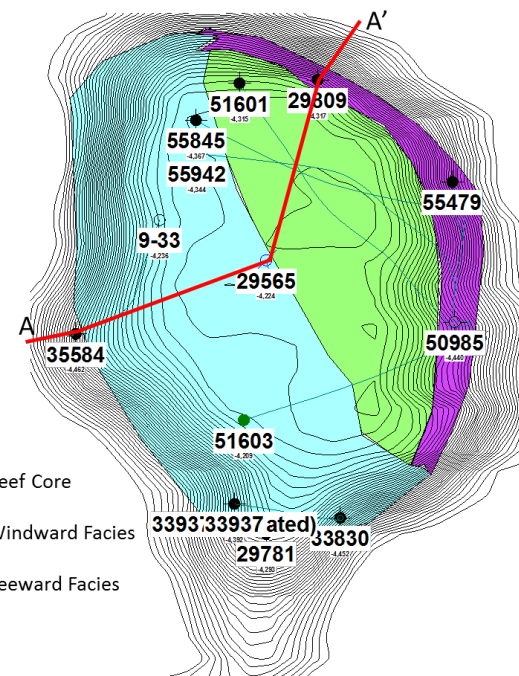


Figure 1-1. Plan view of the depositional model of the Dover-33 reef field showing the subdivision into windward (purple), reef core (green), and leeward (blue) facies.

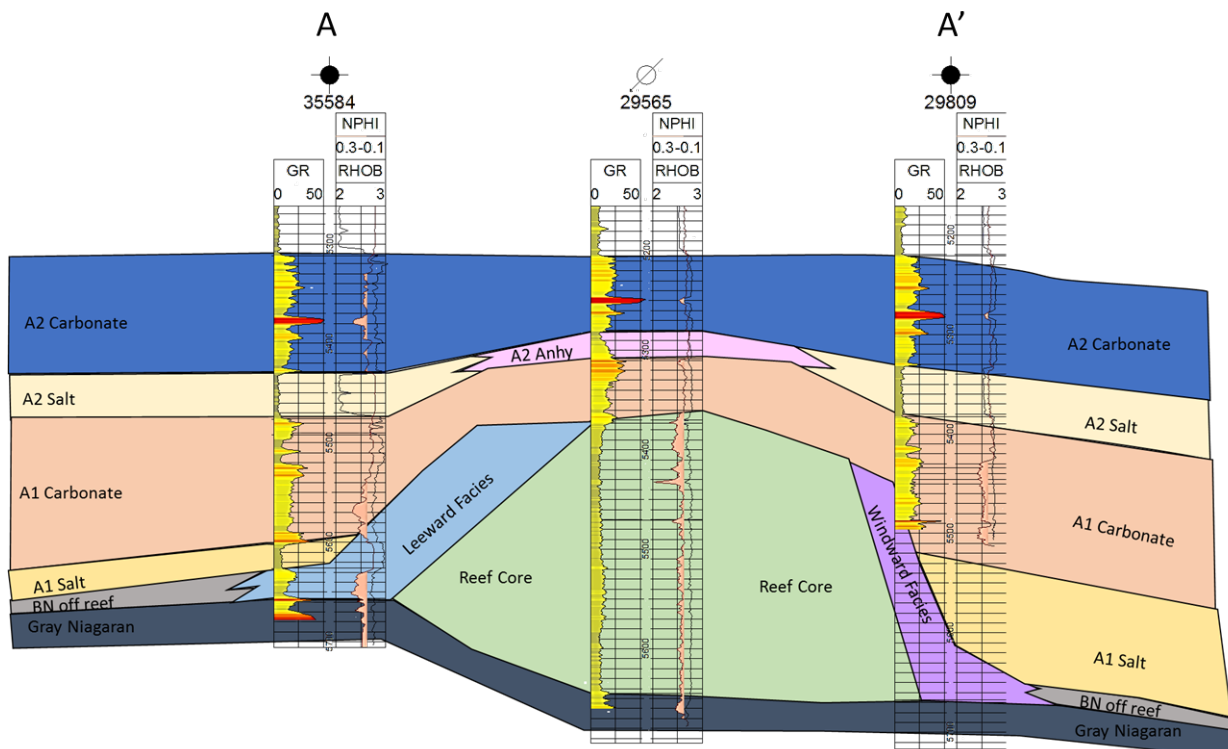


Figure 1-2. Cross-section A-A' across the reef in the Dover-33 reef field showing changes in lithology and lithofacies from the southwest to the northeast.

### 1.1.2 Modeling Objectives/Scope

The overall flow of the modeling work consisted of analyzing and integrating geologic data to define the extent, depth, thickness, porosity, permeability, and water saturation of the reservoir(s). In conjunction with geologic characterization, field operational and monitoring data was compiled to develop the reef history that was used in history matching the dynamic model. The geologic characterization work then was used to develop a SEM that was upscaled into a dynamic model. Figure 1-3 illustrates the flow and connections between analysis and data types to develop final static and dynamic models.

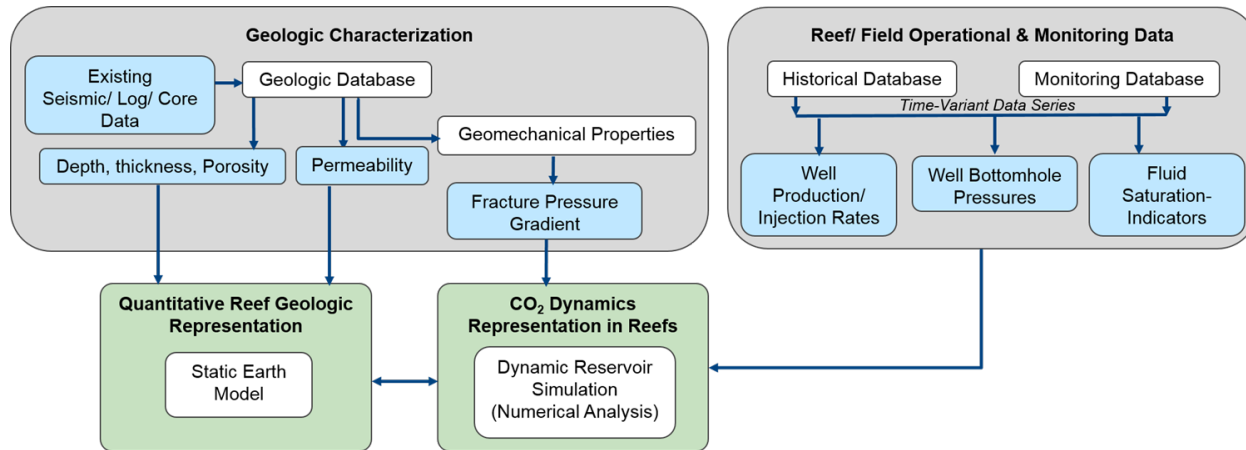


Figure 1-3. Simplified flow diagram of data integration into static and dynamic models.

By implementing the lessons learned from previous modeling experiences with the Dover- 33 reef and integrating new geologic understanding from latest geologic characterization activities in the field, a new conceptual model (Level 3) was developed with the following objectives:

1. Simplify geologic lithofacies while maintaining reservoir heterogeneity,
2. Represent key reservoir properties (porosity, permeability, water saturation), and
3. Integrate multiple data types.

The objectives for the dynamic modeling activity include evaluating CO<sub>2</sub> injectivity and assessing fluid migration in this complex reef structure. The dynamic modeling activity aims to validate the representativeness of the reef conceptual model by history matching production and pressure history during primary and CO<sub>2</sub>-EOR periods and subsequently match the pressure response in the history matched reef model during the Phase III CO<sub>2</sub> injection period. History matching would provide a validated representative model that captures the field observed response from primary production until the end of the Phase III CO<sub>2</sub> injection period. This representative reef model can then be useful for predictive simulations as needed in the project. We evaluate different conceptual geologic models of the reef, namely, to understand the level of detail required to honor observed reservoir response without compromising computational efficiency. Dynamic reservoir modeling has been carried out using the industry-standard fully compositional full-physics simulator CMG-GEM®. Appendix C presents a statistical and automated history-matching approach using the fully heterogeneous Level 3 model version of the Dover 33 reef.

## 1.2 Data Sources

The Dover-33 field had a range of vintages and sources for data. Many wireline logs were provided by Core Energy, LLC and ranged in vendor and age. Battelle worked with Core Energy to collect new data in the injection well along with the drilling of a new characterization well. 3D seismic was also provided to aid in the geometry definition.

### 1.2.1 Geologic Data

There are 20 wells that penetrate the Dover-33 reef system. Of these 20 wells, 18 have multiple Log ASCII files (LAS) and/or raster logs available. All 18 have gamma ray, 15 have neutron porosity, and six have bulk density. Additionally, eight wells have sonic logs; in cases where bulk density logs were not present, the sonic logs were used to calculate bulk density. In addition, 12 wells have advanced logs available, such as photoelectric index, pulsed neutron capture (PNC), and resistivity. Table 1-2 summarizes the wireline log data available for the 20 wells in the Dover-33 reef field; Figure 1-4 illustrates the well locations.

Additionally, whole core was collected from the Dover 9-33 well, which included photographs, descriptions, porosity, permeability, CT scans, Mercury-Injection-Capillary Pressure (MICP), and geomechanical properties. All data were integrated and analyzed as described in the *Geologic Characterization for CO<sub>2</sub> Storage with Enhanced Oil Recovery in Northern Michigan* [Haagsma et al., 2020] technical report to provide a geologic interpretation and data preparation for SEM work.

**Table 1-2. Summary of available wireline log data for wells penetrating the Dover-33 reef field.**

	Permit Number	29565	29781	29809	29840	30392	31108	31228	31303	32298	33830	33937	35195	35584	50985	51601	51603	55479	55845	55942	61209
CAL	Caliper																				
DT	Sonic																				
GR	Gamma Ray																				
LLD	Latero-Log Deep (Resistivity)																				
LLS	Latero-Log Shallow (Resistivity)																				
NPHI	Neutron Porosity																				
RES	Resistivity																				
PNC	Pulsed Neutron Capture	2													3		3				
RHOB	Bulk Density																				
SNP	Sidewall Neutron Porosity																				
XMAC	Acoustic log																				
BHP	Bottom Hole Pressure Monitoring																				

Note: Green shading indicates logs available by well and number indicated repeat collection.

### 1.2.2 Primary Production

The primary production period occurred at Dover-33 between 1974 and 1996. It was estimated to have an original oil-in-place of 3,200,000 barrels. The oil was measured at 43.6 API gravity with initial reservoir pressure of 2,894 psi and initial reservoir temperature of 108°F. It was estimated the initial fluid saturation was 66.25 percent oil and 33.75 percent water. Initial gas saturations were recorded at zero, as gas was produced as it came out of solution during the production of oil. Well 29565 had the highest cumulative oil and gas production of any other well in the reef field (Figure 1-5).

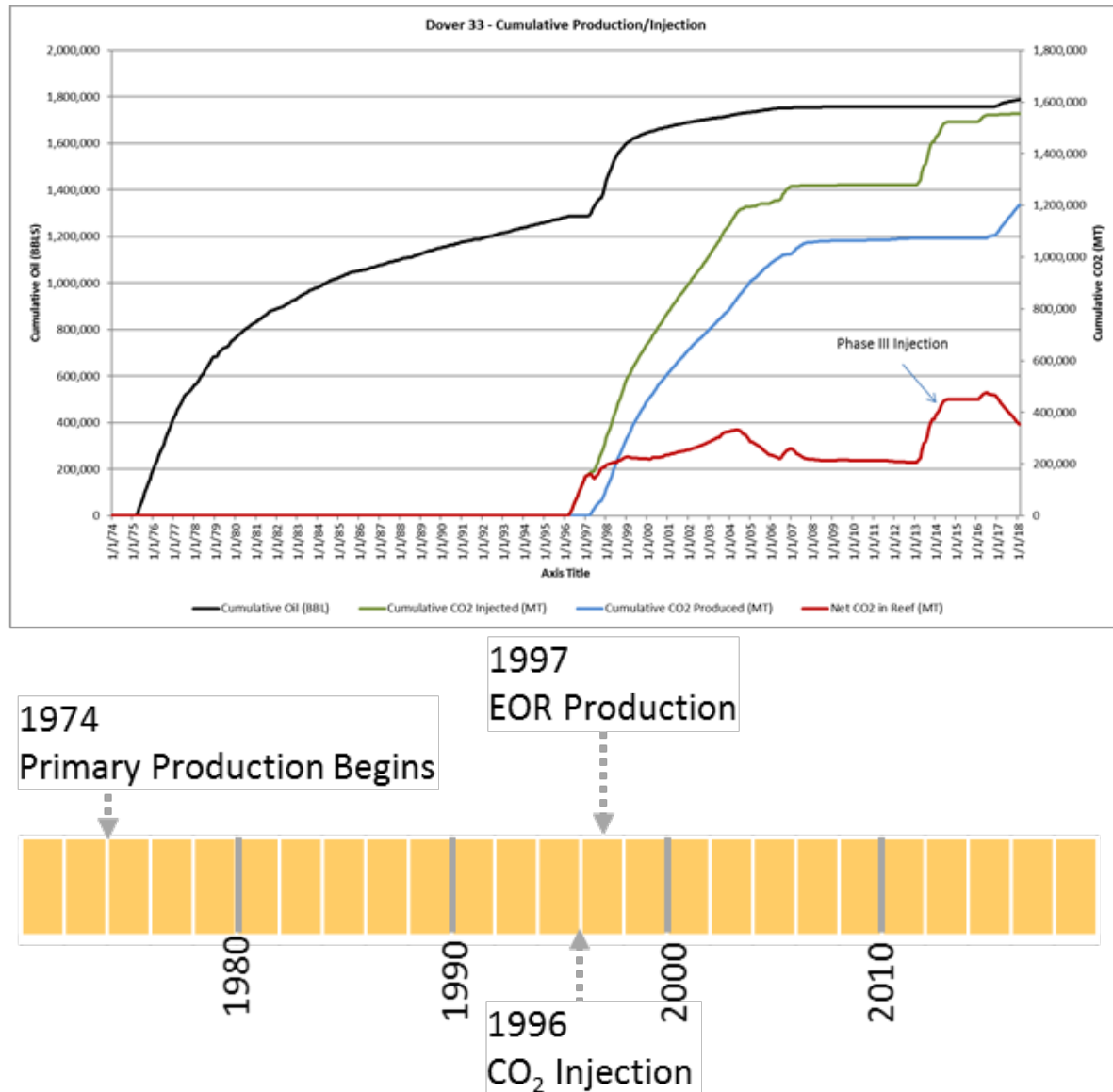


Figure 1-4. Cumulative production in the Dover-33 reef field from 1974 through 2017 showing an increase in production rates after EOR operations began in 1996.

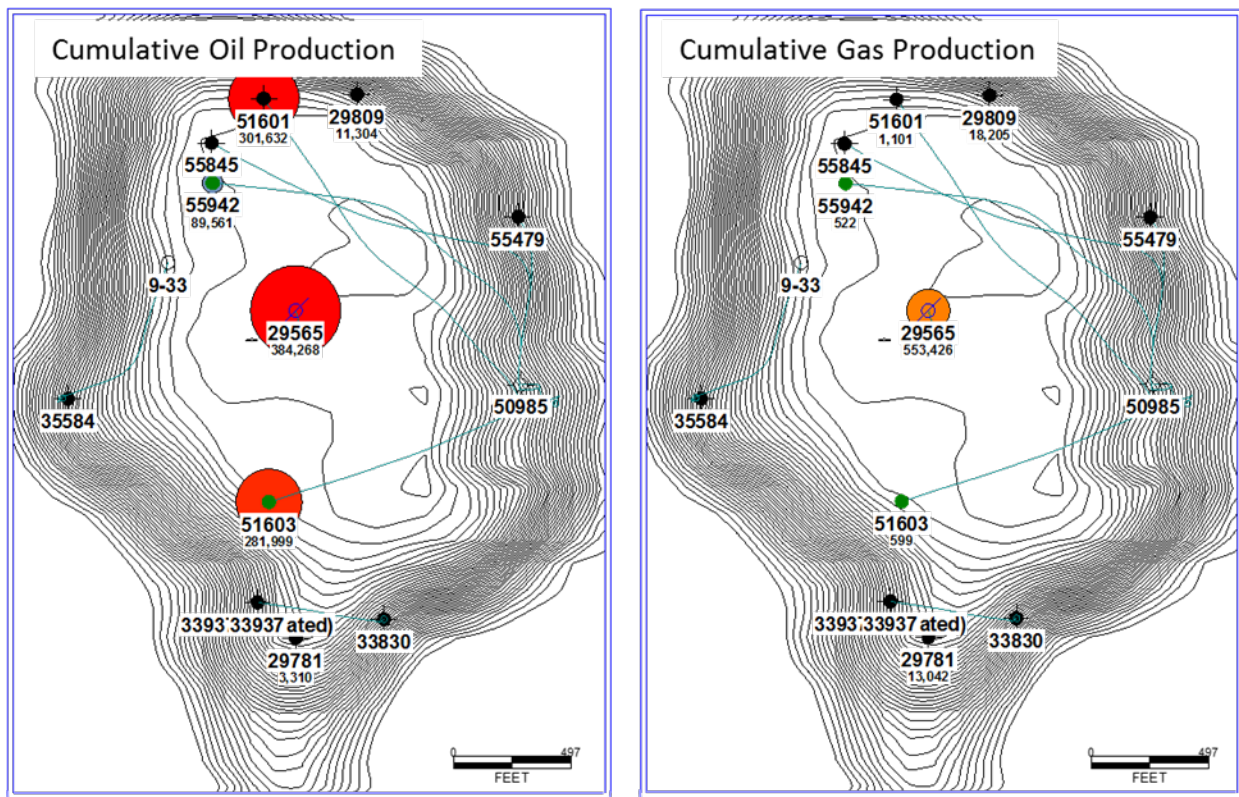
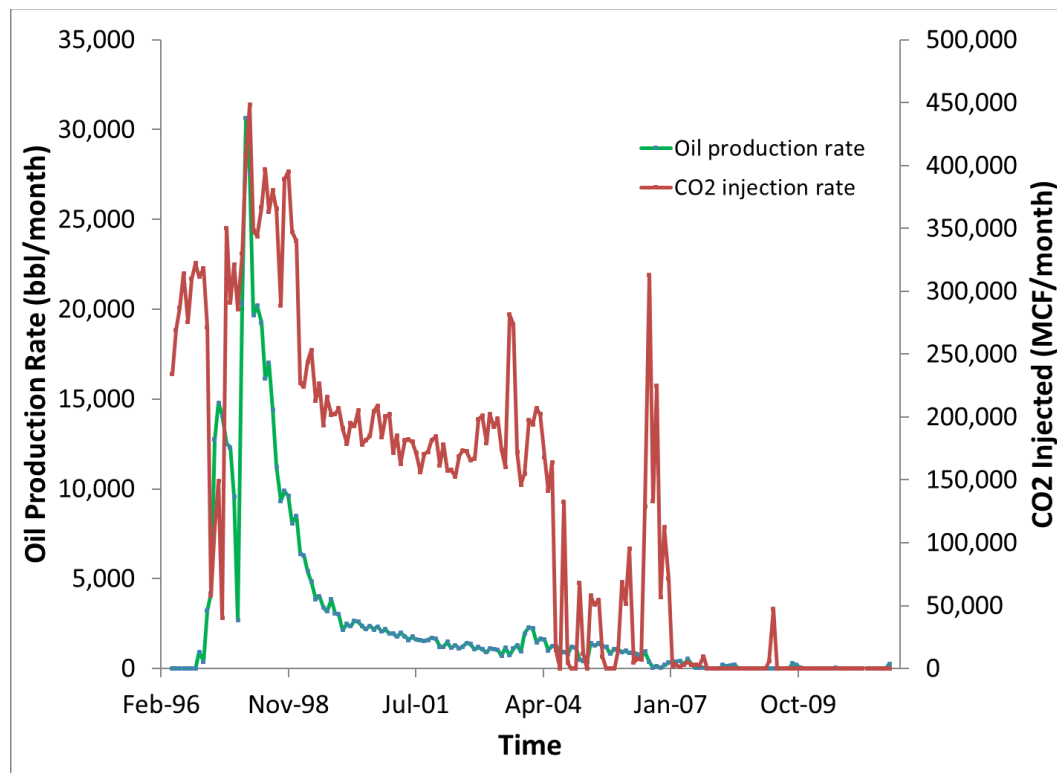


Figure 1-5. Cumulative oil and gas production maps in the Dover-33 reef field showing the highest production in the middle of the reef in well 29565.

### 1.2.3 EOR/CO<sub>2</sub> Injection Rate and Pressure Data

While Dover-33 underwent primary production from 1975 to 1996 to yield 1,286,033 cumulative barrels (bbls) of oil, an additional 492 MBBL oil was recovered through CO<sub>2</sub> flooding for secondary recovery, which was implemented from 1996 to 2007 (Figure 1-6). CO<sub>2</sub> injection and EOR began in 1996. CO<sub>2</sub> injection was halted in 2007 and resumed in 2013. MRCSP has been injecting CO<sub>2</sub> into Dover-33 at a maximum of 1000 tonnes per day (based on availability of CO<sub>2</sub>) since March 2013. Since MRCSP monitoring began in February 2013, a cumulative total of 91,187 metric tons (MT) of net CO<sub>2</sub> has been injected into the late-stage Dover-33 reef. During the large-scale injection tests carried out between February 2013 and July 2016, 271,144 MT of CO<sub>2</sub> was injected in Dover 1-33 injection well. After this time, the reef was returned to Core Energy for EOR production purposes. As of December 31, 2017, about 1,788,000 bbls of oil have been produced and 1,555,400 MT of CO<sub>2</sub> have been injected into the Dover-33 field (Figure 1-7).



*Figure 1-6. Historical monthly oil production and CO<sub>2</sub> injection rates, including primary and secondary recovery phases in Dover-33.*

During the MRCSP CO<sub>2</sub> injection only period, Dover-33 consisted of the one CO<sub>2</sub> injector well, 1-33, with the two producers, 2-33 and 5-33, converted into monitoring wells. Figure 1-5 shows the location of these three wells within the reef. 1-33 is a vertical well that injects CO<sub>2</sub> into the Brown Niagaran and A1 carbonate formations primarily placed at 5410' MD below the surface. The monitoring well 2-33 is a deviated well and 5-33 is an open hole well. Bottomhole pressure memory gauges and surface pressure, flow and temperature gauges were installed at all three wells to track the reservoir response to CO<sub>2</sub> injection during the Phase III CO<sub>2</sub> injection test period in the Dover-33 reservoir. Figure 1-7 shows the composite plot of available bottomhole pressure data in the three wells in Dover-33 during the Phase III CO<sub>2</sub> injection test period. The Phase III CO<sub>2</sub> injection period consisted of seven discrete injection events until 2016, with late-stage production since 2016. Figure 1-7 shows bottomhole pressure, CO<sub>2</sub> injection rate, produced recycle gas, and the cumulative injected quantities during the MRCSP monitoring period.

## 1.0 Dover-33 Reef

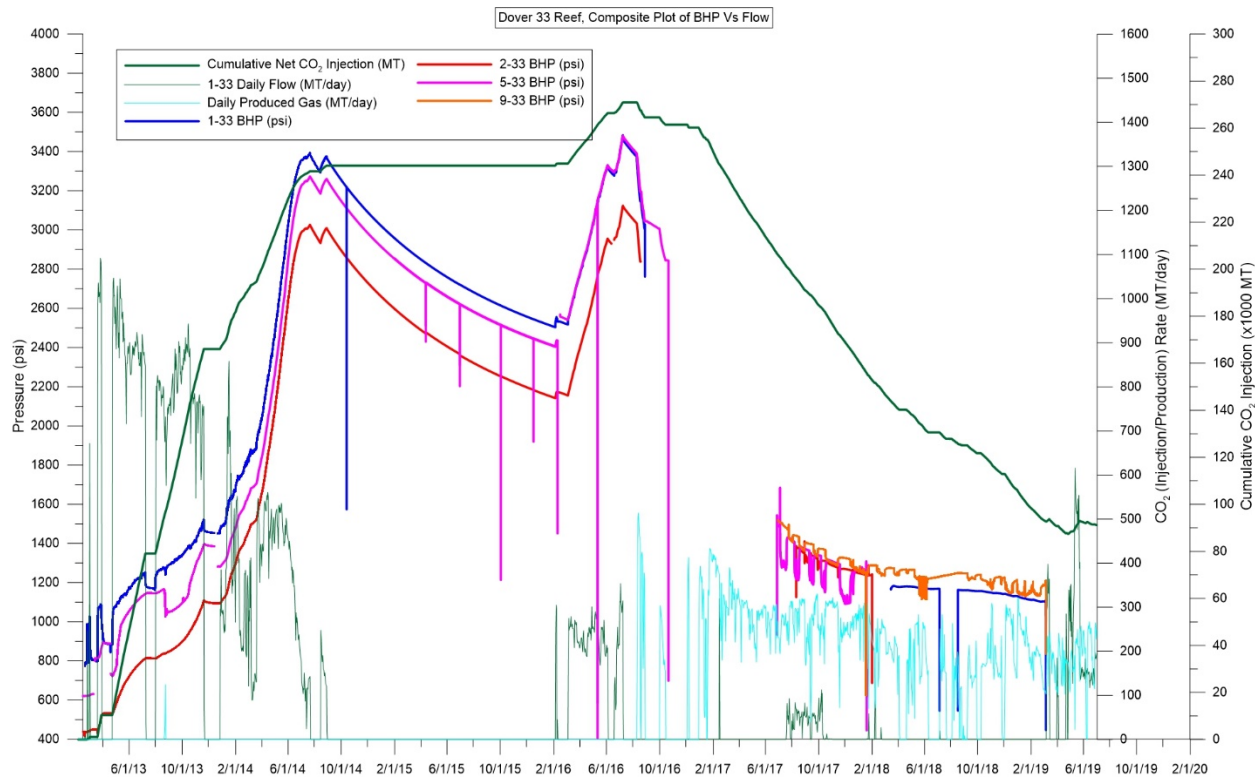


Figure 1-7. Composite Plot of Bottomhole Pressure & Injection in Dover-33

Figure 1-8 shows the pressure buildup in the three wells during the Phase III CO<sub>2</sub> injection only period in the reef. The observed Phase III pressure response in the field shows the following notable behaviors:

- All three wells in pressure communication
- Sharp pressure rise around January 2014 despite rate reductions (shown in Figure 1-8)

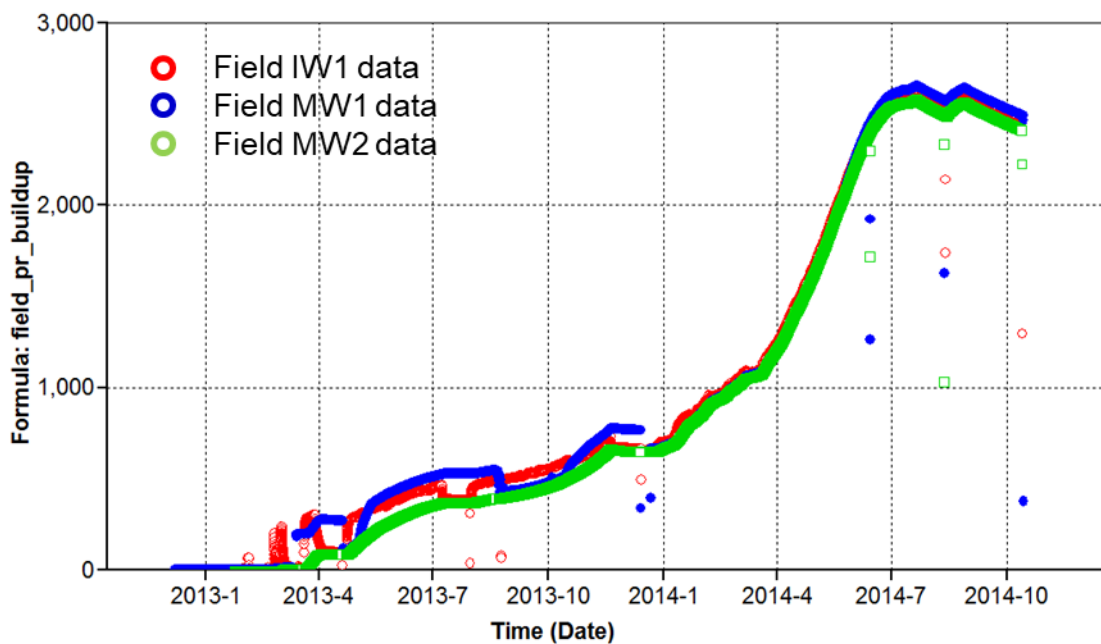


Figure 1-8. Pressure buildup in injection and monitoring wells in Dover-33. IW1 refers to the injection well 1-33. MW1 and MW2 refer monitoring wells to 2-33 and 5-33 respectively.

### 1.3 Static Model

The Dover-33 reef was previously interpreted and constructed into two models—Level 1 and Level 2. The Level 1 model contained two reef-associated layers based on lithostratigraphic formations. The Level 2 model used a sequence stratigraphic approach where the framework of the reef model was defined by wireline signatures that were correlated to regional sequence boundaries, and interpreted lithofacies as defined in analog reef studies. Reservoir properties were distributed within the sequences and conditioned to the individual lithofacies. A high-level comparison of the two models is shown in Figure 1-9. The Level 2 model approach provided more opportunity to analyze 3D spatial details within the reef but is more time and labor intense than the Level 1 model. Neither model successfully matched the production and injection history during dynamic simulations, so the new lithofacies/geobody approach described below was applied following more recent reef interpretations. For more details on the Level 1 and Level 2 models, refer to Miller et al., 2014.

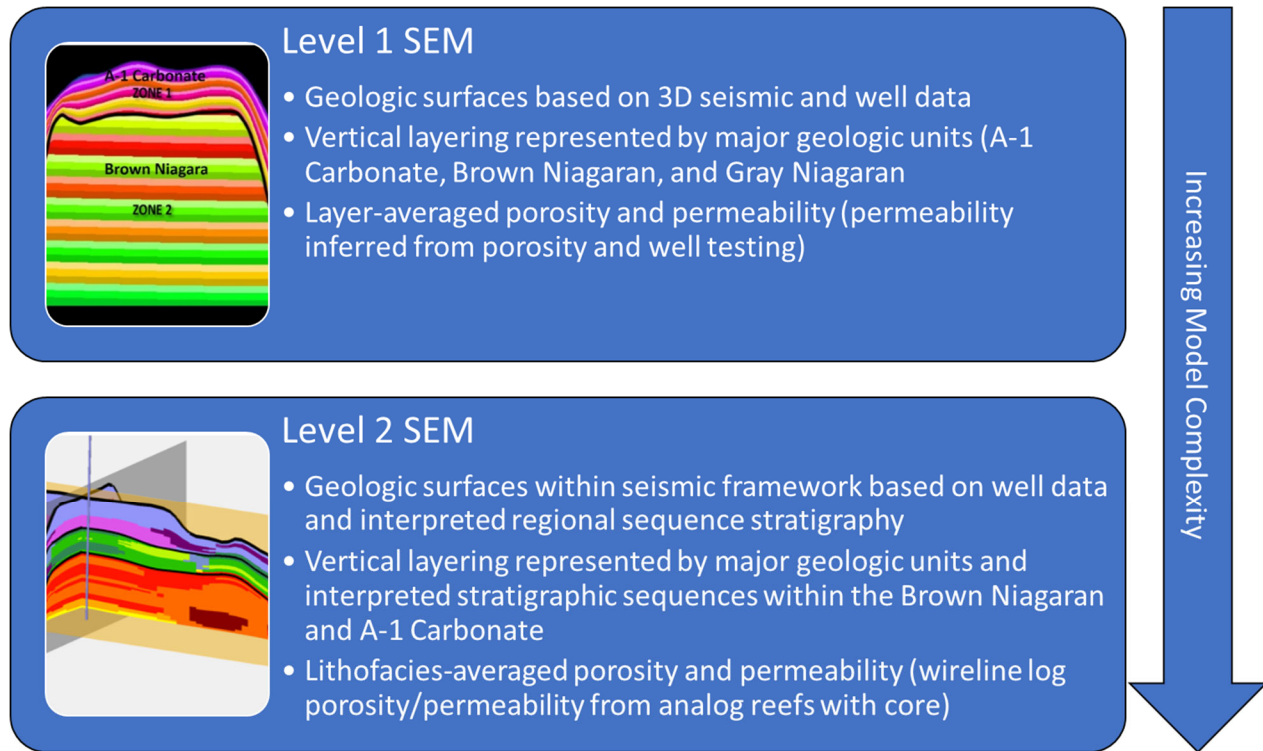


Figure 1-9. Comparison of Level 1 and Level 2 Dover-33 SEMs

The geologic data and interpretations described in the *Geologic Characterization for CO<sub>2</sub> Storage with Enhanced Oil Recovery in Northern Michigan* [Haagsma et al., 2020] were used to construct a geologic SEM and is outlined using the workflow illustrated in Figure 1-10. The petrophysical analyses and interpretations were used as input into the SEM. A 2D depositional model interpretation was used to guide the development of the model's structural framework. 3D seismic data was used to define the boundary and geometry of the reef. The SEM was built using Petrel™ software and began with generating structural surfaces. Next, surfaces for facies were created to subdivide the reservoirs into key zones. These zones were subsequently layered, followed by well log upscaling and property modeling. A water saturation model was prepared for estimating hydrocarbon pore volume. This workflow concluded with model upscaling for the fine-scale model SEM to a coarser version suitable for dynamic reservoir modeling (DRM).

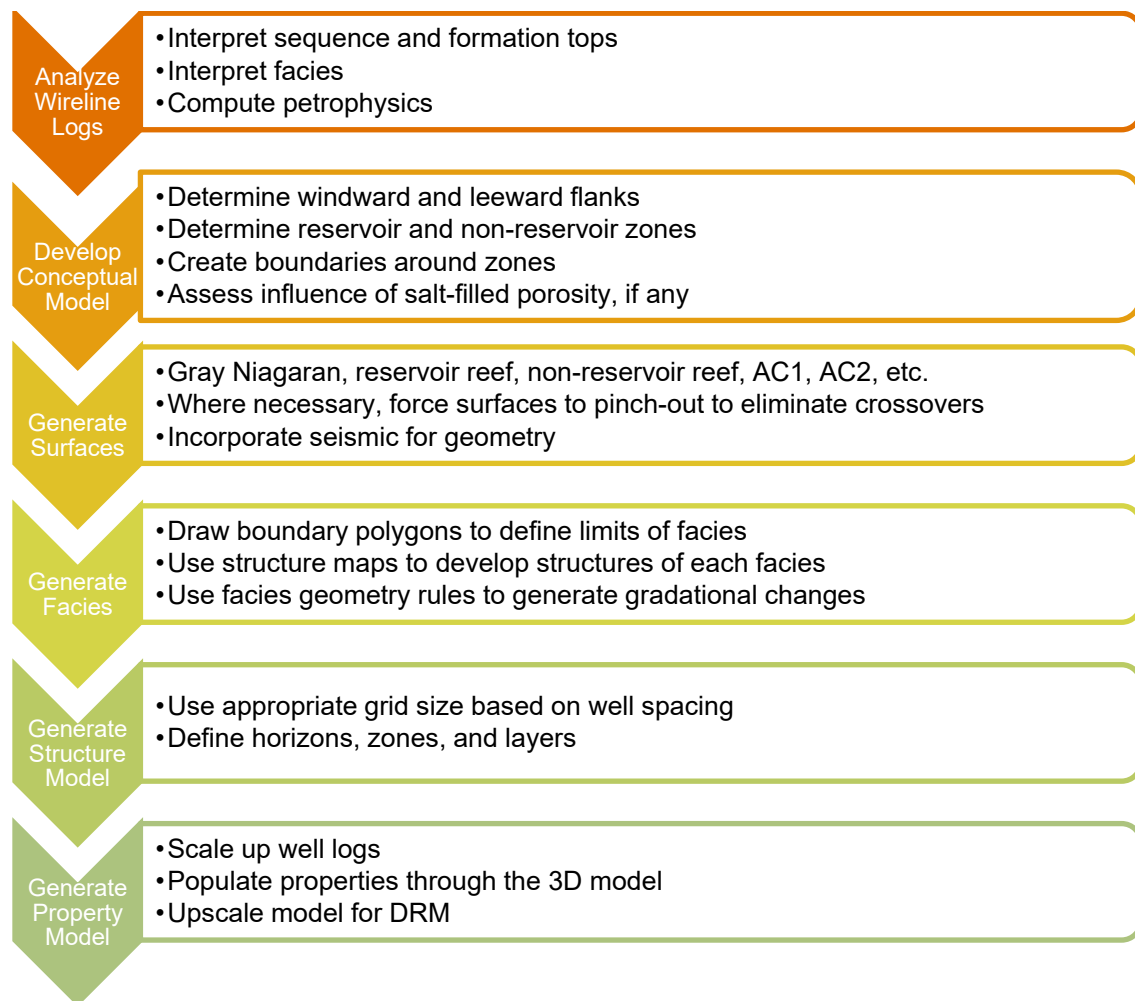


Figure 1-10. General workflow for the Michigan reef SEMs.

### 1.3.1 Framework

#### Structural Surfaces and Isochore Maps

A structural surface map was generated to designate a horizon, or a 2D representation of a formations surface. A structural surface map is a 2D (plan view) figure of the elevation of the horizon within the model area. The structural surfaces form the structural framework, so the surfaces were thoroughly quality checked by looking for crossovers between surfaces and viewing surfaces in cross-section. Each surface was plotted over seismic horizon surfaces to quality check the geometry of the surface. Each structural surface was generated by gridding the sparse formation top data corresponding to the surface, using the convergent interpolation algorithm in Petrel, to create a dense grid of data (i.e., the gridding process calculates a surface elevation value for each cell in the model grid).

It was important to establish an off-reef trend in order to guide and represent the geology around the boundaries of the reef structure. The regional surfaces generated using 946 wells over 659 km<sup>2</sup> (7.08x10<sup>9</sup> ft<sup>2</sup>) area encompassing Otsego County were used to guide the surfaces off-reef, along with geologic knowledge of off-reef behavior. The surfaces were hand-edited until the regional trend was matched. Isochore maps were generated by taking the difference between adjacent structural surfaces. The same gridding and interpolation methods were applied to all isochore maps from the structure maps

The structural framework included the A2 Carbonate, A2 Evaporite, A1 Carbonate, A1 Salt, Brown Niagaran, Gray Niagaran, and model base (Figure 1-11). The A2 Carbonate had a higher elevation over the northernmost lobe with gentle slopes around. The A1 Carbonate followed the underlying Brown Niagaran. The Brown Niagaran had two distinct reefs with the northern reef much larger than the southern. The Gray Niagaran stayed consistently flat throughout the study area. Figure 1-12 and Figure 1-13 are the structural surfaces and isochore maps for the A2 Carbonate, A1 Carbonate, Brown Niagaran, and Gray Niagaran.

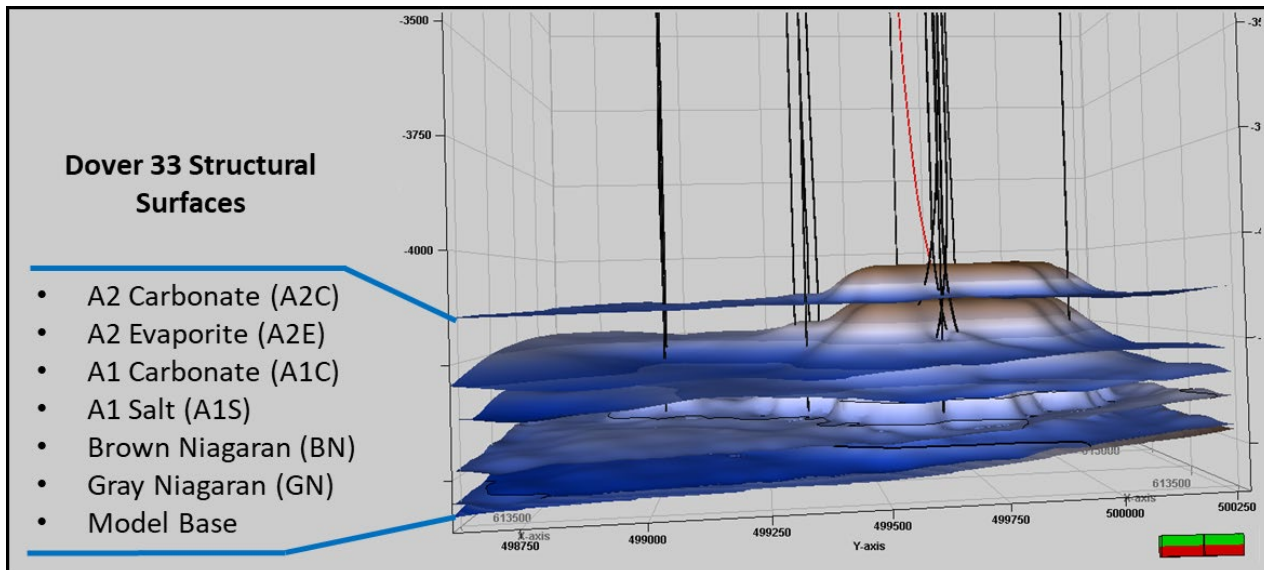


Figure 1-11. Side view of Dover-33 structural surfaces with wells used during SEM development.

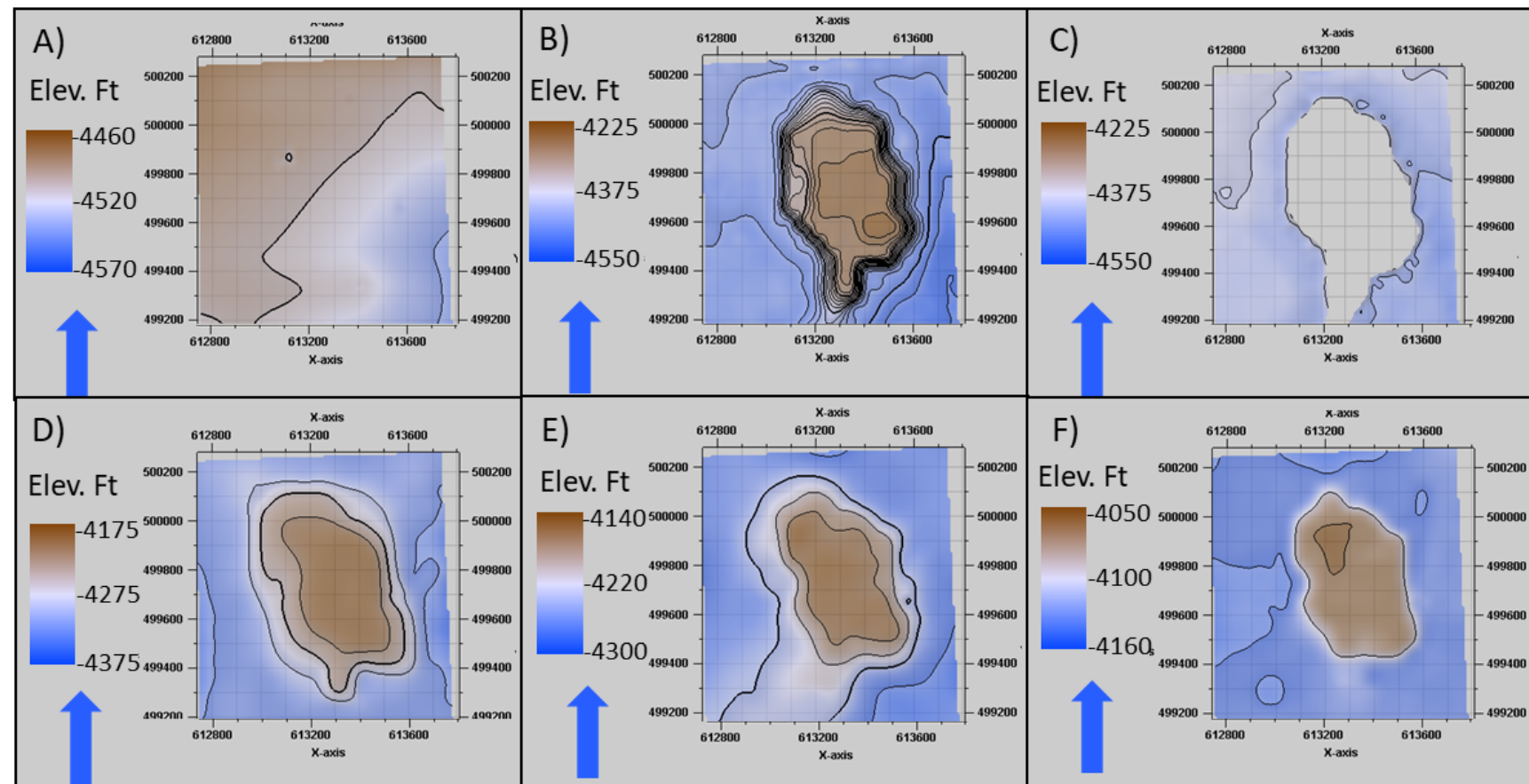


Figure 1-12. Dover-33 structural surfaces. Elevation depth is from the mean sea level. A) Gray Niagaran, B) Brown Niagaran (reef), C) A1 Salt, D) A1 Carbonate, E) A2 Evaporite, and F) A2 Carbonate.

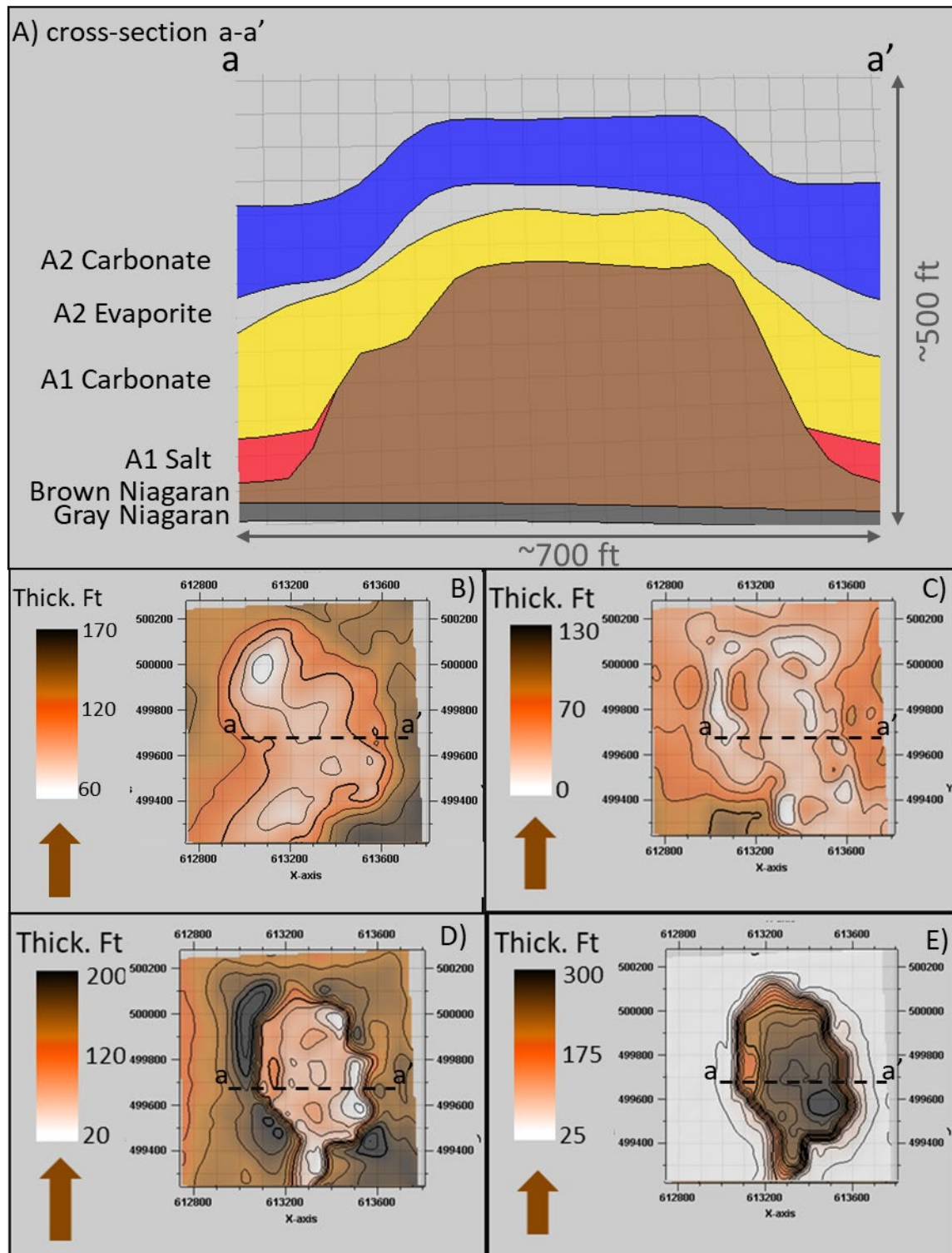


Figure 1-13. Isopach maps from the Dover-33 SEM. A) west to east trending cross-section a-a' through the SEM showing key formations. B) A2 Carbonate isopach. C) A2 Evaporite isopach. D) A1 Carbonate isopach. D) Brown Niagaran isopach.

### 1.3.1.1 Horizon Modeling

The structural surfaces were incorporated into the structural framework through a process called horizon modeling. In this process, geologic rules defining the conformability of surfaces were applied to each formation to guide the SEM's horizons. These rules prevent the modeled horizons from crossing over one another and allow them to be discontinuous in areas where they pinch out.

The rules are implemented via Petrel's horizon type definitions:

- Conformable: All horizons belong to the same group and build conformable to each other.
- Erosional: Erosions belong to the group above; the group below erosion is numbered differently than the group above.
- Discontinuous: Discontinuities do not belong to groups above or below; they correspond to a separate group that is collapsed into a single surface.
- Base: Horizons above will truncate into a base.

Horizon modeling was an essential tool to control horizons and build zones. The A2 Carbonate, A2 Evaporite (salt and anhydrite) and A1 Carbonate Crest were all set to conformable. The A1 Carbonate was split to represent flank (off-reef) and crest. The A1 Salt was incorporated off-reef and conformed to the Brown Niagaran. The Brown Niagaran surface was used as a control to conform the reef core, windward, and leeward zones. The Gray Niagaran was set to be the model's lowermost formation. Table 1-3 summarizes the horizon scheme used in the SEM.

**Table 1-3. Horizon modeling in Petrel showing order of horizons and horizon type for the Dover-33 SEM.**

Index	Horizon name	Color	Calculate	Horizon type	Conform to another horizon		Status	Smooth iterations	Use horizon-fault lines	Well tops	Input #1
1	A2C	Blue	<input checked="" type="checkbox"/> Yes	Conformable	No	1	✓ Done	0	<input checked="" type="checkbox"/> Yes		 dover 33_A
2	A2E	Gray	<input checked="" type="checkbox"/> Yes	Conformable	No	1	✓ Done	0	<input checked="" type="checkbox"/> Yes		 dover 33_A
3	A1C	Yellow	<input checked="" type="checkbox"/> Yes	Conformable	No	4	✓ Done	0	<input checked="" type="checkbox"/> Yes		 dover 33_A
4	A1 Salt	Red	<input checked="" type="checkbox"/> Yes	Conformable	No	1	✓ Done	0	<input checked="" type="checkbox"/> Yes		 Copy of A1
5	Brown Niag	Gray	<input checked="" type="checkbox"/> Yes	Base	No	1	✓ Done	0	<input checked="" type="checkbox"/> Yes		 Dover 33_E
6	gray	Dark Gray	<input checked="" type="checkbox"/> Yes	Discontinuous	No	1	✓ Done	0	<input checked="" type="checkbox"/> Yes		 Dover 33_g
7	base	Black	<input checked="" type="checkbox"/> Yes	Base	No	1	✓ Done	0	<input checked="" type="checkbox"/> Yes		 Dover 33_g

### 1.3.1.2 Zones and Layers

The horizons create a base framework, and the next step was to fill in a volume between horizons. The zones are subdivided into layers based on the desired vertical resolution and the thickness of each zone. A layer thickness of 20 ft was initially used for the A2 Carbonate and A1 Carbonate. The A2 Evaporite, A1 Salt, and Brown Niagaran were initially set at 10 ft thick. A minimum grid cell size of 5 ft was used to prevent infinitely small grid cells.

Different methodologies are available for building the layers within a zone. This sets the directionality of each zone and controls how properties are distributed within a zone (following base, following top, proportional, etc.). The Brown Niagaran was set to follow the top of the surface to represent reef grown on top of the Gray Niagaran. The A1 Carbonate and A2 Carbonate were set to follow the base to represent the deposition of these units on top of the Brown Niagaran. Figure 1-14 illustrates the resulting layers and the direction they were built. The layering scheme resulted in a total of 478 layers for the Dover-33 SEM.

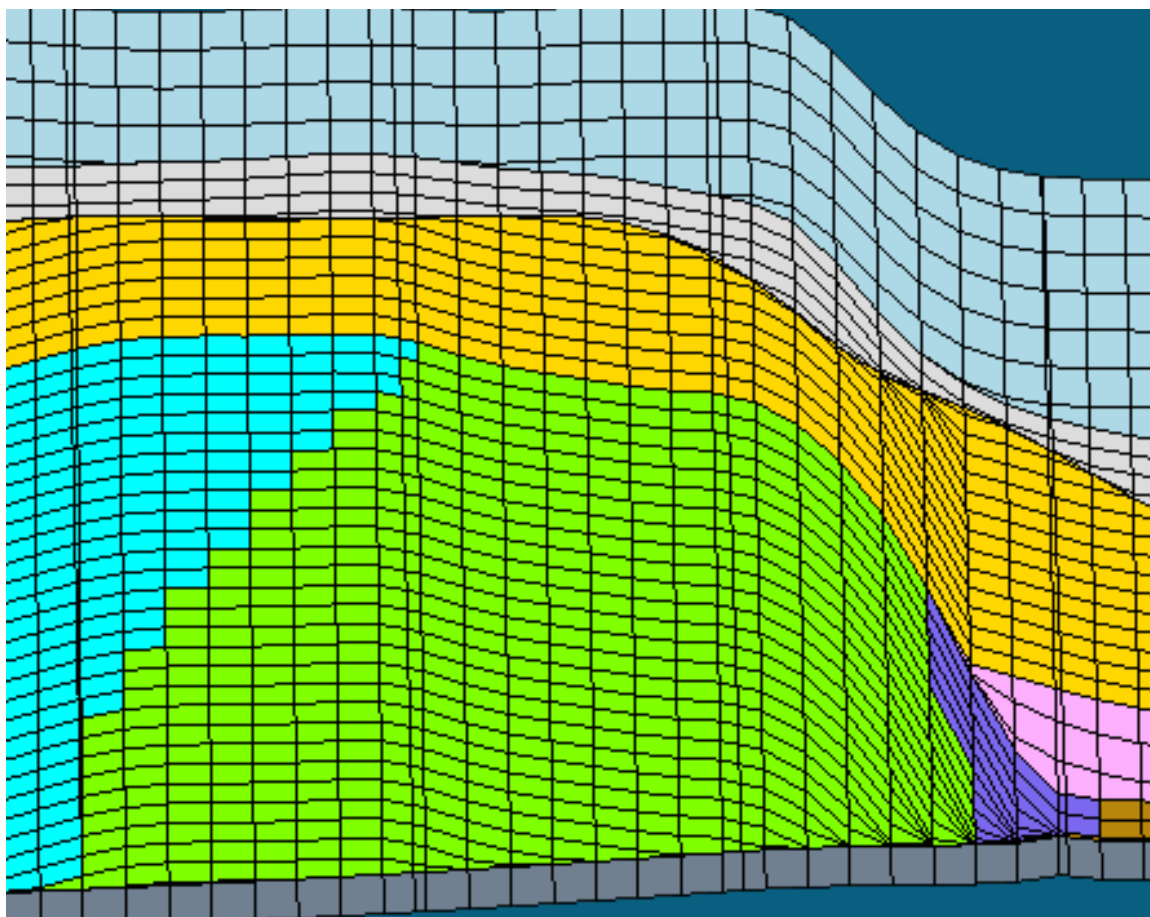


Figure 1-14. Zoomed-in image of the SEM layers showing layers mimicking reef growth (blue, green, purple) and demonstrating deposition on top of the reef (orange, light gray, light blue).

### 1.3.1.3 Lithofacies

Interpreted lithofacies were used to define zones within a formation to represent individual compartments or “geobodies.” The lithofacies were divided to represent groups of facies with similar porosity and permeability distributions. This creates a heterogeneous model with more control during property modeling. Table 1-4 lists the zones (intervals between two horizons) created for each formation in the Dover-33 SEM.

Polygons were created first to outline the boundary top and base of each facies and to clip structure surfaces used to generate the lithofacies surfaces. The tops of the zones were then combined with the base of the model to contain the compartment. This resulted in each zone having a defined 3D volume. Figure 1-15 illustrates the layering of the lithofacies created for the lithofacies of the Brown Niagaran and A1 Salt.

**Table 1-4. Summary of the Dover-33 SEM zones, lithofacies, abbreviations, and descriptions.**

SEM Zone	Lithofacies	Abbr.	Comment
A2 Carbonate	A2 Carbonate	A2C	Continuous unit over the reef
A2 Evaporite	A2 Evaporite	A2E	Seal, continuous unit over the reef
A1 Carbonate	A1 Carbonate Crest	A1C	Reservoir unit over the reef
	A1 Carbonate Flank		Seal along flank of the reef
A1 Salt, Flank	A1 Salt (Flank)		Seal
Brown Niagaran	Brown Niagaran (Flank)	BN	Flanks the reef
	Brown Niagaran (Leeward)	LW	A portion of reef body
	Brown Niagaran (Reef Core)	RC	A portion of reef body
	Brown Niagaran (Windward)	WW	A portion of reef body
Gray Niagaran	Gray Niagaran	GN	Rock unit underlying the reef

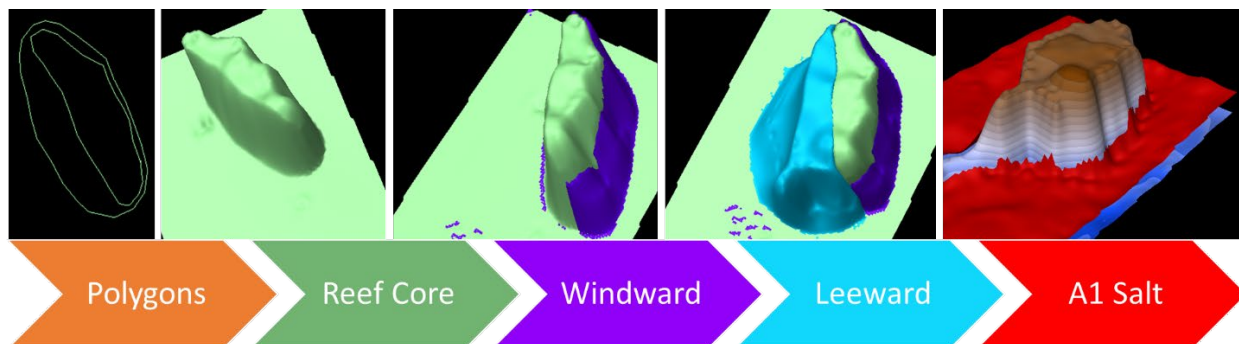


*Figure 1-15. Workflow depicting the delineation of lithofacies for the Brown Niagaran and A1 Salt in the Dover-33 reef. Polygons defining the reefal footprint and geometry were based on seismic interpretation along with formation tops. Polygons were prepared for generating surfaces that envelop reefal lithofacies.*

The A1 Carbonate does not have a strict boundary between reservoir and non-reservoir lithofacies. Petrel's facies modeling tools were used to define the geometry and orientation of a gradational change in the A1 Carbonate. Based on wireline log data, core data, and regional expertise, the reservoir facies of the A1 Carbonate occurs on top of the main reef structure extending further in the leeward direction than windward. It also occurs at the top of the formation and rather than the lower parts of the formation. Figure 1-16 illustrates the final facies geometry A) and B) with a west to east cross-section and C) showing the asymmetrical distribution of reservoir facies.

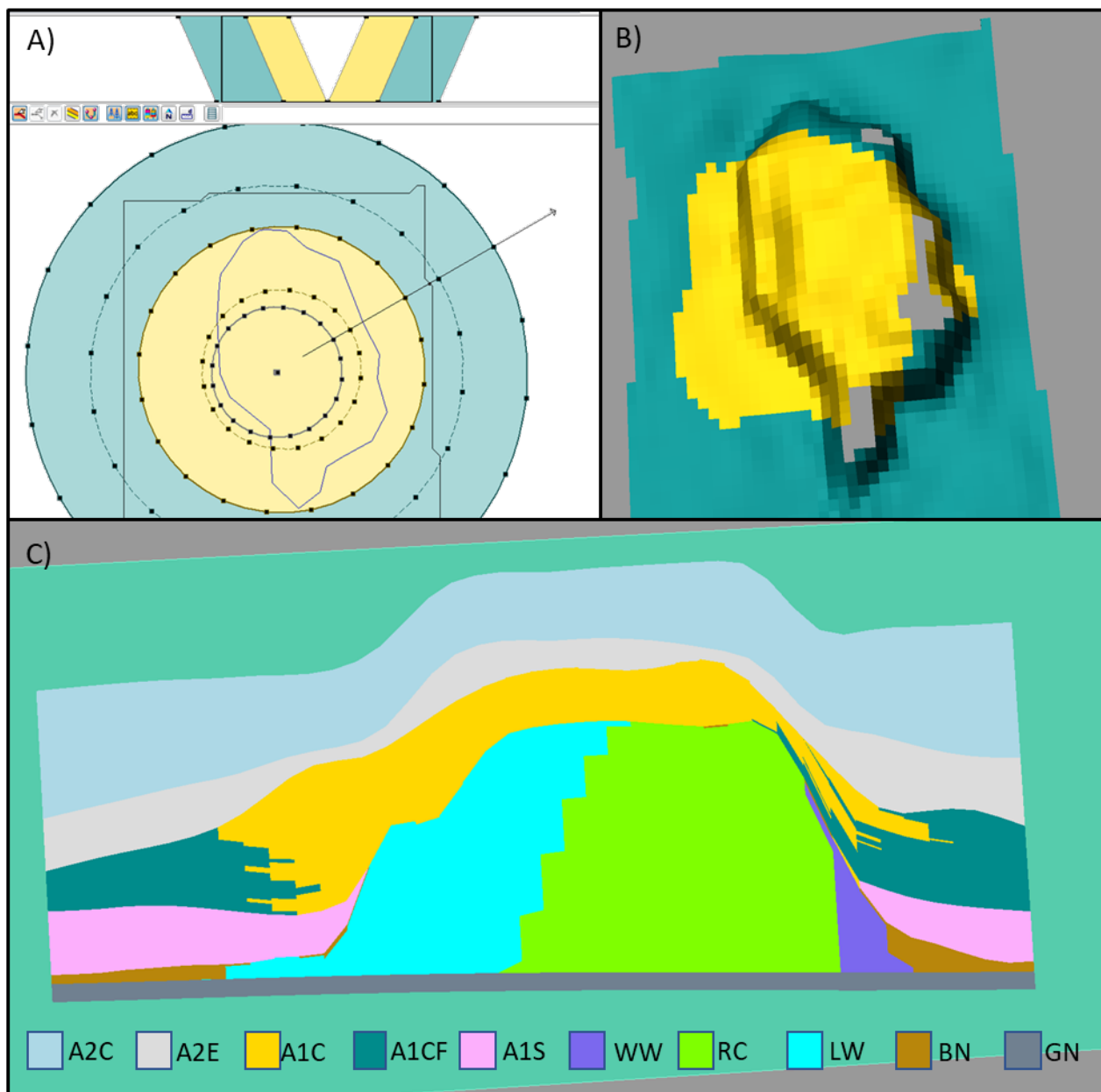


Figure 1-16. Facies modeling of the A1 Carbonate to differentiate between reservoir (yellow) and non-reservoir flank (teal) by defining limits and orientation (A). B) illustrates the map view results of extent of the A1 Carbonate reservoir as oriented with paleo-wind direction and C) illustrates a 2D cross-section and results of facies modeling.

#### 1.3.1.4 Geometry and Model Grid Definition

The boundary used for the SEM's structural framework is shown as a blue outline in Figure 1-17, which covers enough area to reduce boundary effects when building structural surfaces. The red outline represents the final clipped boundary and covers 622,547 m<sup>2</sup> or 153.8 acres. This area was selected to capture the reef's geometry and formations that flank the reef while also matching previous SEM work. The SEM was comprised of cells, with grid cell size in the x-y directions of 82 ft. This size permitted enough resolution between wells while generally limiting cell count for DRM work. A list of the grid parameters for the SEM is provided in Table 1-5. The SEM's top is represented by the A2 Carbonate at an approximate depth of 5,379 feet below ground level. The SEM's overall thickness is approximately 522 ft.

The resulting SEM for the Dover-33 field followed the geologic interpretation developed through wireline log analyses. The crest of the A1 Carbonate followed the zone of high porosity identified on top of the reef structure while the flank of the A1 Carbonate represented a lower porosity carbonate. The A1 Salt also developed along the flanks of the reef and coincided with the identification of salt in flank wells. The Brown Niagaran was composed of two distinct reef cores with no overlap in between, as is represented by the off-reef Brown Niagaran in between. The leeward lithofacies has gentler slopes and the windward lithofacies has steeper slopes, as is consistent with paleo-wind direction, waves, and their related effect on the reef. Overall, the SEM's structure is consistent with interpretations and therefore considered representative of the geology of the reef system. The final SEM was clipped to the Northern lobe only (Figure 1-17) to be consistent with the original Level 1 and Level 2 SEMs.

**Table 1-5. Summary of grid parameters for the Dover-33 reef field.**

Grid Parameter	Dover-33	Comments
SEM size (x by y)	700 m by 950 m (2,296.6 ft x 3,116.8 ft)	Model Area: 622,547 m <sup>2</sup> or 153.8 acres
SEM height (z direction)	159.1 m (522 ft)	Average SEM thickness
Cell grid size in x and y direction	25 m (82 ft)	Cell heights vary
Minimum well spacing	~2.3 m (7.5 ft)	Several kick-offs
Layers / Number of grid cells	478 / 508,592	Fine-scale SEM

Note: m = meter

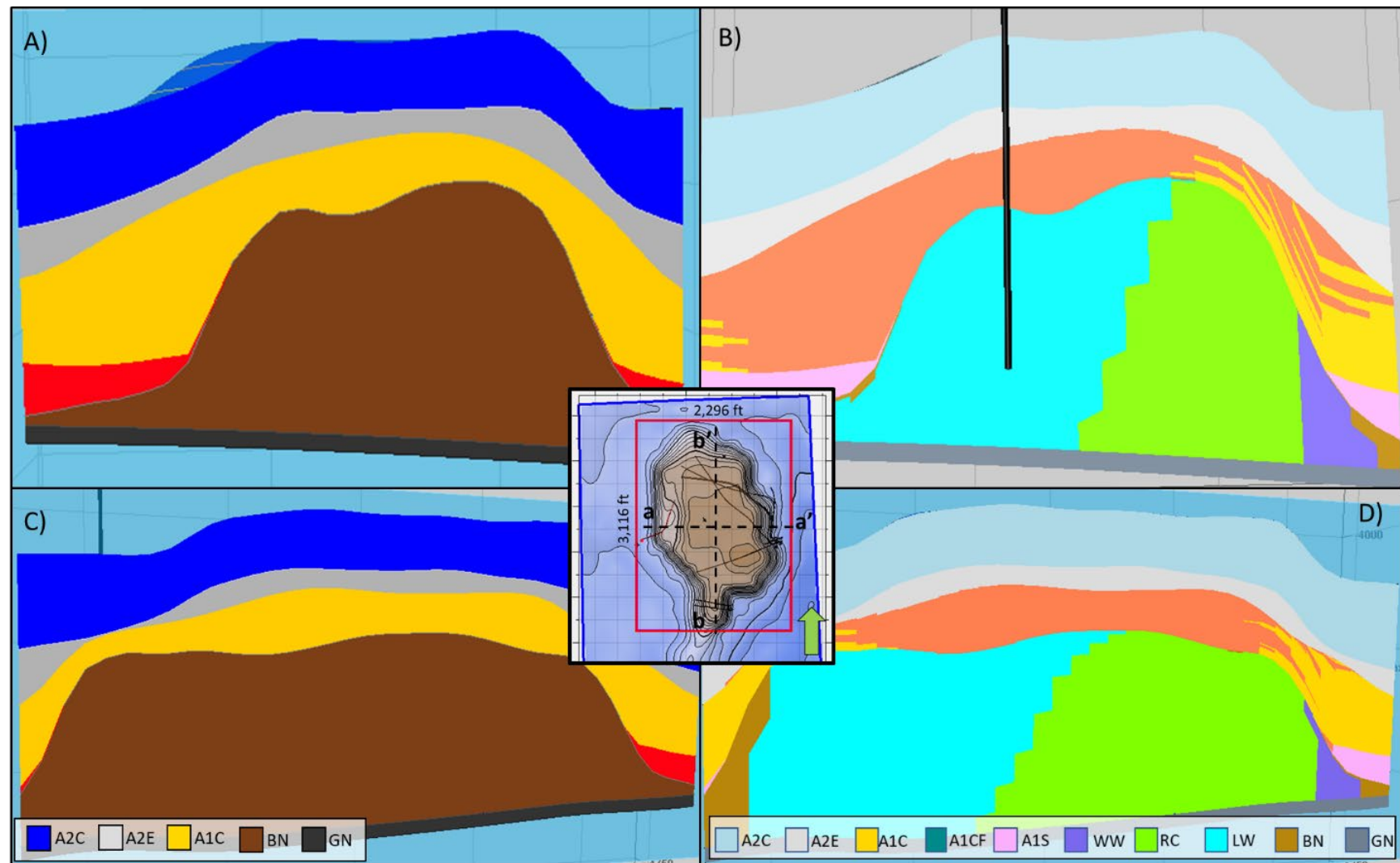


Figure 1-17. Cross-section through the Dover-33 SEM framework. Cross-section a-a' runs perpendicular to the reef structure, shown in panel (A) with the major reef zones and panel (B) with the reef facies. Cross-section b-b' runs parallel to the reef structure, shown in panel (C) with major reef zones and panel (D) with reef facies. The middle image shows the plan view of the x and y grid for the Dover-33 SEM with clipped boundary in red and full boundary in blue and locations of the two cross-section lines.

### 1.3.2 Property Modeling

Property modeling was based on the following data sources:

- Porosity: Neutron porosity logs from 15 wells were used. As the reef is largely comprised of carbonates, the neutron logs were calibrated per their respective lithologies, either limestone or dolomite. The carbonates were considered relatively clean and so the neutron logs were representative of effective porosity.
- Permeability: For Dover-33, there was poor agreement between porosity measured on core samples and neutron porosity logs due to depth calibration issues; however, there was a strong correlation between core measured porosity and permeability. Permeability logs were derived through a log-based porosity-permeability transform using a power-law fit applied to neutron porosity logs.
  - The A1 Carbonate had a porosity range from 3.16 percent to 10.72 percent with a permeability range from 0.00 to 6.04 mD. The Brown Niagara had a porosity range from 1.51 percent to 7.14 percent with a permeability range from .00 to 204.28 mD. This data has been plotted in Figure 1-18 with respective transforms between porosity and permeability.
- Water saturation: Based on seven wells, the water saturation logs were computed via Archie's equation using resistivity and neutron porosity logs. Standard Archie's constants of a, m, and n were used (1,2,2 respectively).

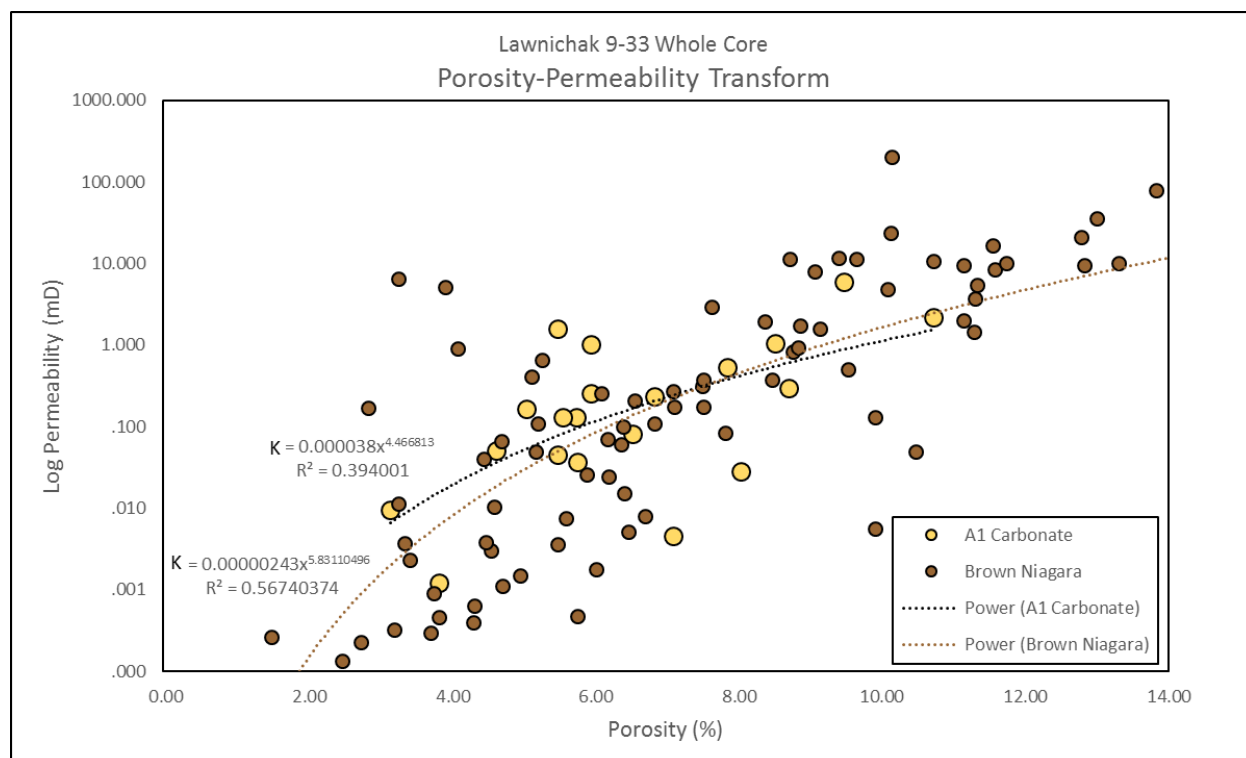


Figure 1-18. Core porosity-permeability transform plot for the A1 carbonate (yellow) and Brown Niagara (brown).

The geologic framework was used with scaled-up log properties to build porosity and permeability property models. Both porosity and derived permeability logs were sampled to the grid resolution and subjected to vertical variogram analysis to characterize vertical heterogeneity in oil-bearing zones like the

A1 Carbonate Crest and the Brown Niagaran. A variogram characterizes the spatial continuity or variability of a dataset and begins with an *experimental variogram* calculated from the data. One can select from several mathematical functions to fit the *experimental variogram*; these are called *variogram models*. When a fit is achieved, the variogram model describes the spatial relationships inherent in the dataset. Model variogram parameters include sill, nugget, and range. The variogram model, along with well logs, are then used in a conditional simulation algorithm to populate the 3D SEM with the key petrophysical rock properties. This process required interpolating the upscaled log porosity and permeability values across the entire 3D model grid. The sequential gaussian simulation method was used for these models. Each run creates one equiprobable distribution of a property throughout a model zone based on a model variogram and upscaled well logs. Results were compared to original log values and the scaled-up values using cumulative distribution curves (CDFs) to ensure the algorithm was representative of the data.

### 1.3.2.1 *Upscaling of Wireline Logs*

Neutron porosity log data was available for 15 wells in the Dover-33 field and represented a good estimate of porosity for the carbonate units. When needed, the log data was corrected to a dolomite matrix, as the Dover-33 reef was mostly dolomitic. The log measurements were collected every half foot, except for the newest well (9-33), where porosity was recorded at every .25-foot increment.

The well logs were upscaled or sampled along the well trajectories to the SEM grid's vertical resolution of 2-ft. Permeability logs were computed using the derived porosity to permeability relationship. Like porosity, both the permeability log and water saturation log were sampled into the SEM along the well trajectories at the grid's 2-ft vertical resolution. The scaled-up logs were viewed in cross-section for each well to quality check the process. The scaled-up logs match the original well logs and formation tops, honoring the variations in porosity, water saturation, and permeability. Figure 1-19 shows an example of the scaled-up neutron porosity (colored bars) that matches very closely with the original porosity log. This close match is expected as the SEM's resolution is very close to the resolution of the well logs. Figure 1-19 also shows the scaled-up logs for permeability and water saturation.

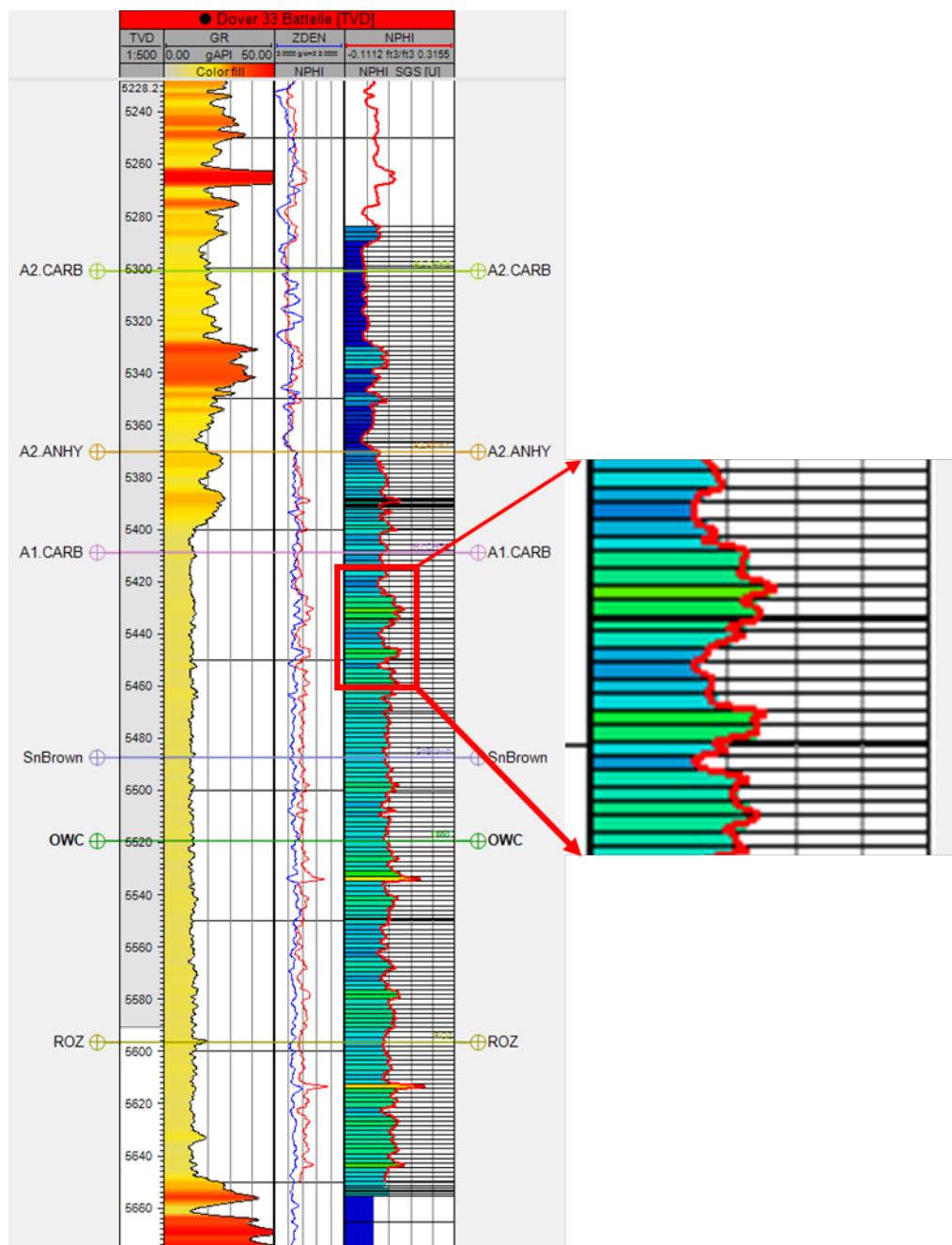


Figure 1-19. Example of the scaled-up logs (right track) with the original logs overlying (red line) showing a close match at the SEMs grid resolution of 2-ft.

### 1.3.2.2 Porosity

Kriging was applied to interpolate porosity values from upscaled neutron porosity logs for the Brown Niagaran and A1 Carbonate formations. All other zones were assigned an average value to represent the formation. The porosity model is consistent with the scaled-up logs and original well logs, as shown in the histogram in Figure 1-20C and in the cumulative distribution function (CDF) in Figure 1-20D. The porosity in the A1 Carbonate was highest along the crest of the reef and decreased gradationally towards the flanks. The Brown Niagaran showed higher porosity at the top, near the contact with the A1 Carbonate. The Brown Niagaran porosity was less on the leeward direction (left section of the reef) than on the windward side (right) as illustrated in Figure 1-20B. Table 1-6 summarizes the average porosity and ranges for each zone and facies.

**Table 1-6. Summary of average porosity as computed in the fine-scale SEM for each zone and facies in the Dover-33 reef**

Zone	Average SEM Porosity (decimal)	Standard Deviation (decimal)
<b>A2 Carbonate</b>	0.03	.03
<b>A2 Evaporite</b>	0.0	0.0
<b>A1 Carbonate</b>	0.03	0.03
A1 Carbonate Crest	0.05	0.03
A1 Carbonate Flank	0.01	0.0
<b>A1 Salt</b>	0.0	0.0
<b>Brown Niagaran</b>	0.09	0.04
Brown Niagaran Flank	0.01	0.0
Brown Niagaran Leeward	0.09	0.03
Brown Niagaran Windward	0.09	0.04
Brown Niagaran Reef Core	0.11	0.04
<b>Gray Niagaran</b>	0.031	0.024

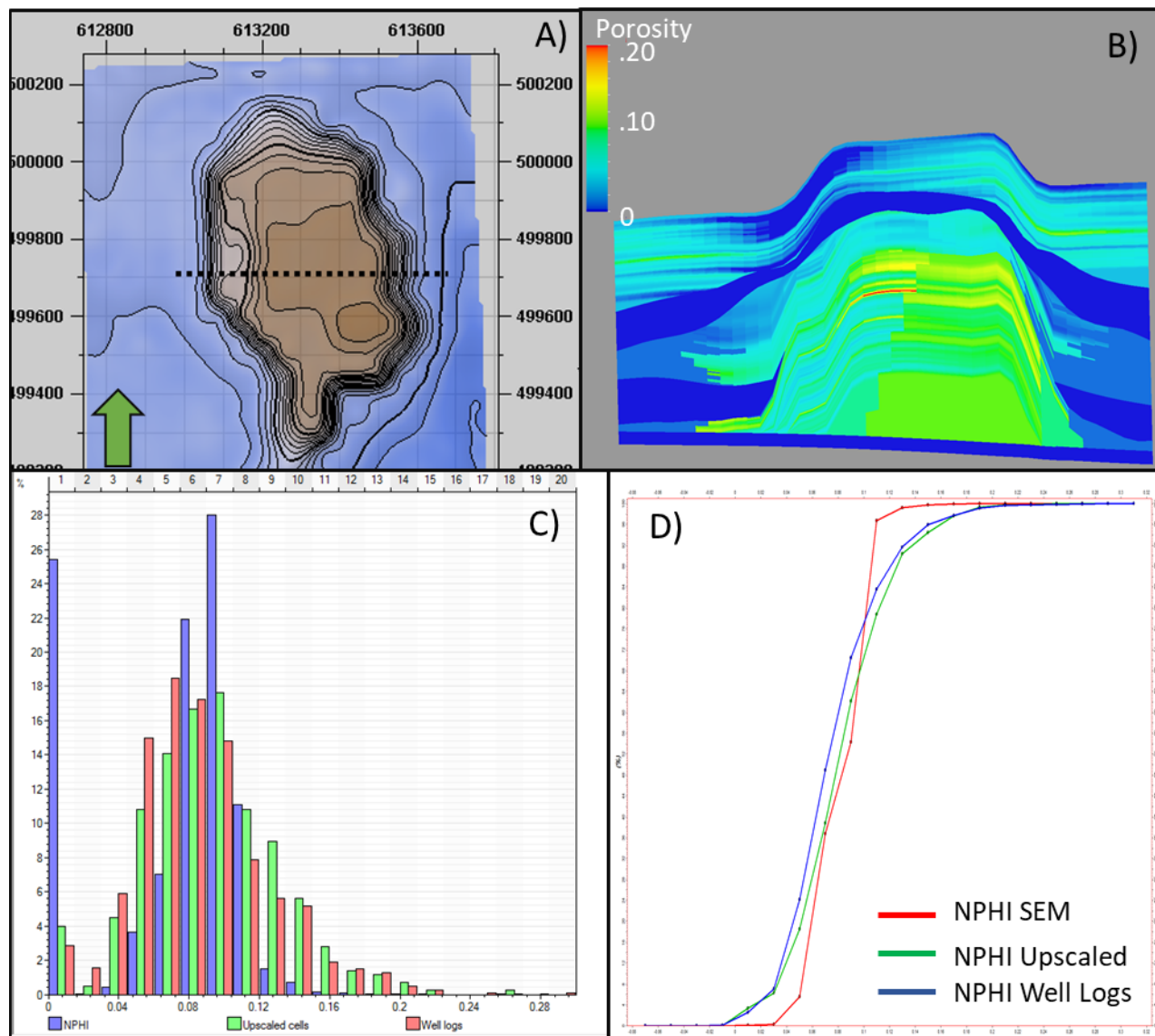


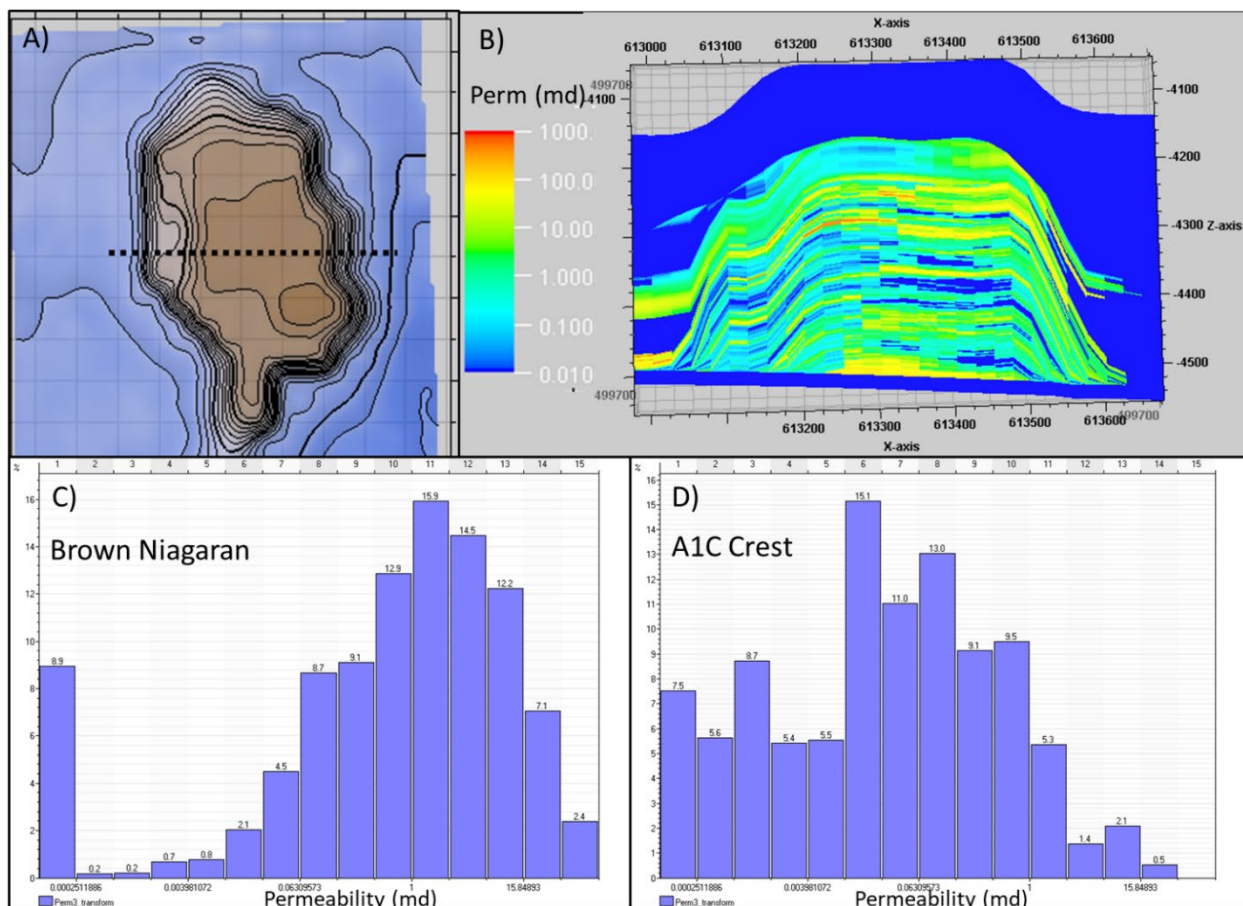
Figure 1-20. Porosity modeling results showing cross-section location (A), cross-section through SEM showing porosity (B), histogram comparing SEM porosity to wireline logs (C), and CDF of each porosity type (D).

### 1.3.2.3 Permeability

The derived porosity to permeability transform was applied to the porosity model to predict permeability throughout the SEM for the Brown Niagaran and A1 Carbonate. Maximum and minimum permeability observed in whole core were used to constrain the model limits. All other zones were assigned an average value to represent the formation. The permeability in the A1 Carbonate was highest along the crest of the reef and decreased gradually towards the flanks. The Brown Niagaran showed higher permeability at the top, near the contact with the A1 Carbonate. The Brown Niagaran permeability was less on the leeward direction (left section of the reef) than on the windward side (right), as illustrated in Figure 1-21. Table 1-7 summarizes the average permeability and ranges for each zone and facies.

**Table 1-7. Summary of average permeability as computed in the fine-scale SEM for each zone and facies in the Dover-33 reef**

Zone	Average SEM Permeability (mD)	Standard Deviation (mD)
<b>A2 Carbonate</b>	0.01	0.0
<b>A2 Evaporite</b>	0.0	0.0
<b>A1 Carbonate</b>	0.24	1.45
A1 Carbonate Crest	0.45	2.01
A1 Carbonate Flank	0.0	0.0
<b>A1 Salt</b>	0.0	0.0
<b>Brown Niagaran</b>		
Brown Niagaran Flank	0.0	0.0
Brown Niagaran Leeward	3.37	15.18
Brown Niagaran Windward	2.76	2.25
Brown Niagaran Reef Core	10.23	16.65
<b>Gray Niagaran</b>	0.0	0.0

**Figure 1-21. Permeability modeling results showing cross-section location (A), and cross-section through SEM (B) with the histogram for the Brown Niagaran (C) and the A1 Carbonate Crest (D).**

#### 1.3.2.4 Water Saturation

Moving average was used to interpolate water saturation throughout the SEM for the Brown Niagaran, A1 Carbonate, and A2 Carbonate zones using only three wells that were near initial reservoir conditions. The data collected at the other wells was after production began and not representative of initial conditions. All other zones were set to 100 percent saturated to represent non-reservoir rocks along the flanks and base. The oil-water contact was comparably high in the reef, leaving the upper third as the hydrocarbon or storage interval as shown in Figure 1-22B. The water saturation was low at the top of the A1 Carbonate and gradually increased towards 15 percent near the contact with the Brown Niagaran. The Brown Niagaran water saturation was low and spiked up to 60+ percent at the oil water contact (Figure 1-22C). Table 1-8 summarizes the average water saturation and ranges for each zone and facies.

**Table 1-8. Summary of average water saturation as computed in the fine-scale SEM for each zone in the Dover-33 reef**

Zone	Average SEM Water Saturation (decimal)	Standard Deviation (decimal)
A2 Carbonate	0.27	0.10
A2 Evaporite	1.00	0.0
A1 Carbonate	0.13	0.10
A1 Salt	1.00	0.0
Brown Niagaran	0.52	0.21
Gray Niagaran	1.00	0.0

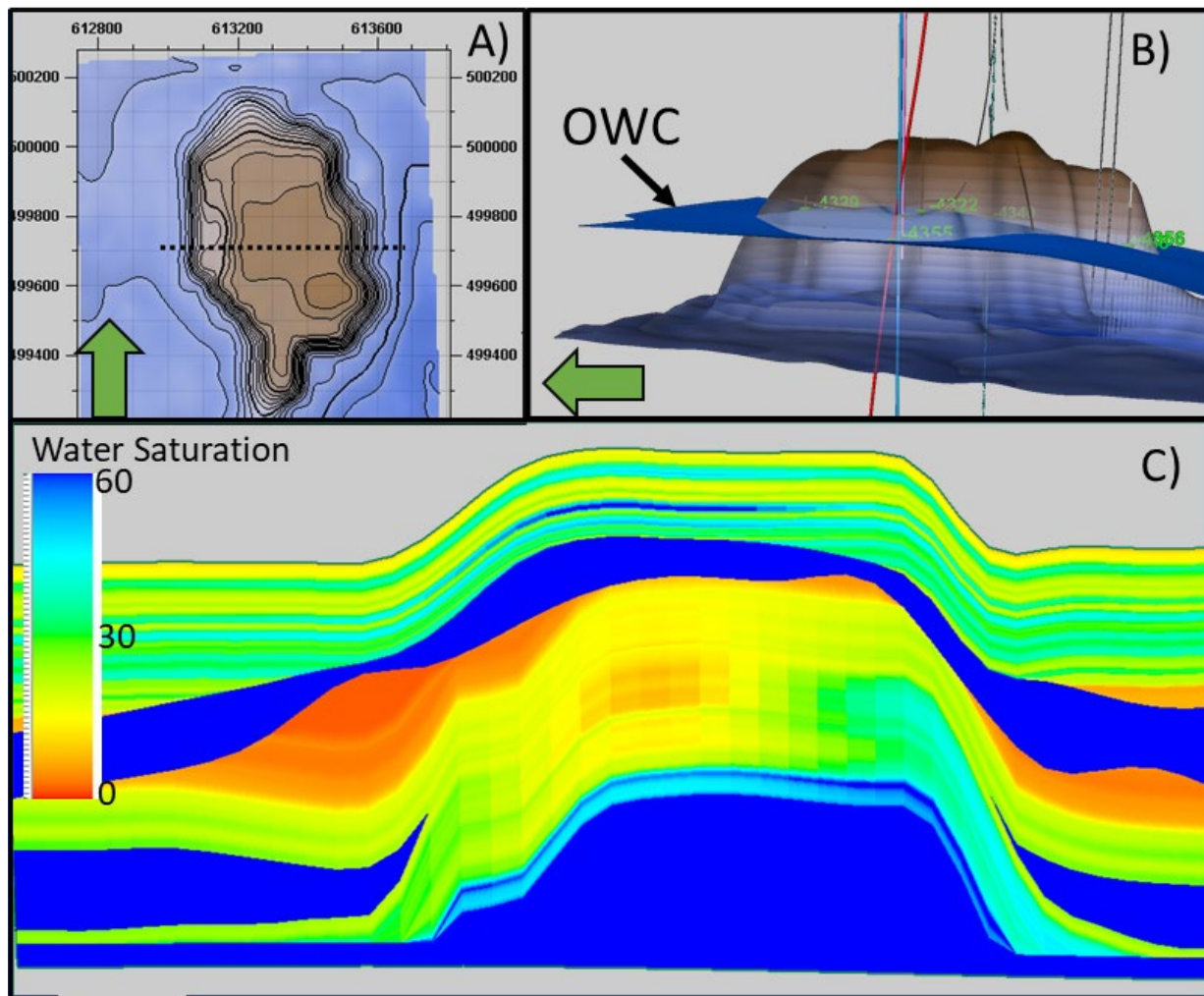


Figure 1-22. Results of the water saturation modeling in the Dover-33 SEM showing cross-section location (A), 3D side view of the oil water contact (B), and cross-section west to east colored by water saturation (C).

### 1.3.2.5 Volumetrics

The hydrocarbon pore volume (HCPV) for the SEM was computed for the reef. The general equation for this calculation is:

$$HCPV = GRV * N/G * \phi * S_{hc}$$

**Equation 1-1**

where:

GRV: Gross rock volume in the trap above the hydrocarbon-water contact.

N/G: Average Net Reservoir/ Gross rock

$\phi$ : Average Porosity

$S_{hc}$ : Average hydrocarbon saturation =  $(1-S_w)$ .

While the general equation may use average values, the calculations here are based on individual cells and represent a more accurate estimate of the HCPV. The cross-section in Figure 1-23 reveals where HCPV is likely to occur based on the oil water contact (OWC), model porosity, and water saturation. Note that cell color is also related to individual cell volume. The dominant lithology for oil-bearing units were clean carbonate rocks, so the N/G value was set to 1 as a simplification to the model.

The resulting HCPV of oil for the reef model used for dynamic modeling was computed at ~2.743E+7 ft<sup>3</sup>. Table 1-9 summarizes the volume and hydrocarbon (oil) estimates for all SEM zones and reflects volume of oil at reservoir (in situ) conditions; the Formation Volume Factor (Bo) was set to 1.44 (bbl/STB [Stock Tank Barrel]) (ratio of the volume of oil at reservoir conditions to standard conditions). The Dover-33 reef is reported to have an estimated original stock tank oil-in-place of 3.28 Million STB. The Static Earth Modeling was followed by Dynamic Earth Modeling where a more rigorous treatment of volume estimates and history matching was conducted.

**Table 1-9. Volumetrics and HCPV for each reservoir reef facies.**

Case	Bulk Volume [ft <sup>3</sup> ]	Net Volume [ft <sup>3</sup> ]	Pore Volume [ft <sup>3</sup> ]	HCPV Oil [bbl]
<b>A1 Carbonate</b>	292,702,738	292,702,738	2,466,576	2,142,209
Crest	292,702,738	292,702,738	2,466,576	2,142,209
Flank	0	0	0	0
<b>Brown Niagaran</b>	211,516,098	211,516,098	3,749,800	2,271,791
Leeward	113,036,201	113,036,201	1,814,059	1,228,916
Windward	1,111,046	1,111,046	20,393	13,203
Reef Core	92,788,140	92,788,140	1,906,330	1,023,040
Flank	4,580,711	4,580,711	9,018	6,632
<b>Total</b>	<b>504,218,836</b>	<b>504,218,836</b>	<b>6,216,376</b>	<b>4,414,000</b>

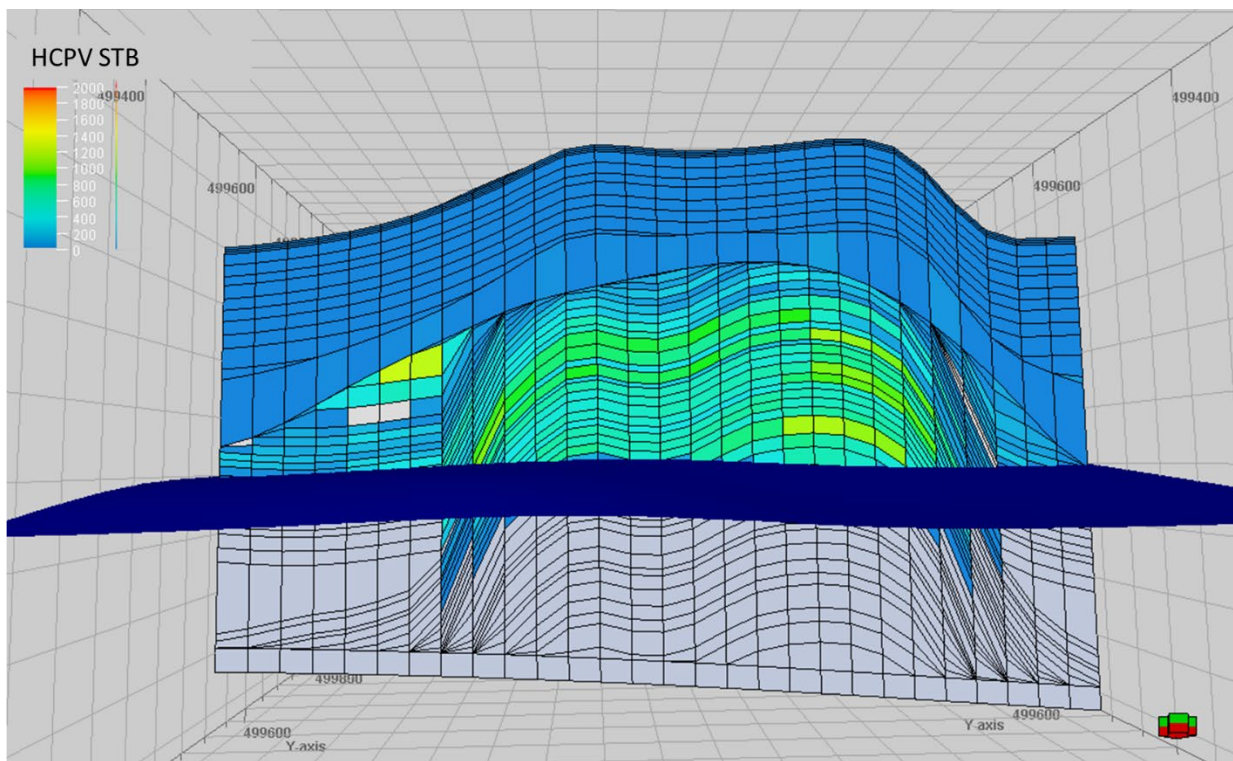


Figure 1-23. Cross-section through the SEM showing the computed HCPV by grid cell and location of OWC (blue plane).

#### 1.3.2.6 Upscaling of the Grid for Dynamic Modeling

The petrophysical SEM consisted of 508,592 cells. The reduction of model cell count was necessary for facilitating the time-intensive DRM work that would follow.

Upscaling can cause the loss of the SEM's heterogeneity. One goal in SEM upscaling is to maintain flow units by pairing certain layers together. The Petrel plug-in CONNECT UpGrid™ was used to aid the upscaling process by optimizing the grouping of layers. This utility performs the optimum vertical upscaling design by minimizing the error on the pressure while combining vertical layers. The horizontal grid size remains unchanged. Layers having similar pressure distributions are combined first, and the layers with distinct pressure profiles are isolated. By preserving the dynamic behavior, the upscaled model can reproduce the behavior of the fine-scale model with fewer cells. The 478-layer, fine-scale SEM served as input to the upscaling process which reduces the number of layers.

Working with CONNECT UpGrid™, the selection of an optimum vertical layer design should consider both the Design Factor (DF) and the Step Error (SE) as shown in Figure 1-24. These two parameters are plotted as a function of SEM layer design. A higher DF indicates an effective upscaling design for separating distinct layers. A lower DF indicates no effect on the layering design and is closer to Petrel's standard, proportional layering method. Whenever the Error per Layer (EPL) trend starts to pick up, it means that "over-homogenizing" has occurred for the reservoir. The preference is to select the optimum number of layers with a high value of DF, but before the EPL trend starts to pick up. Therefore, the criterion to select the optimum design is to select the points with maximum DF and at the same time provide the minimum SE change per layer. The optimum combination of DF and SE was selected at 64 layers. Figure 1-25 compares the resulting distributions of porosity between the fine scale and upscaled models with the original wireline logs.

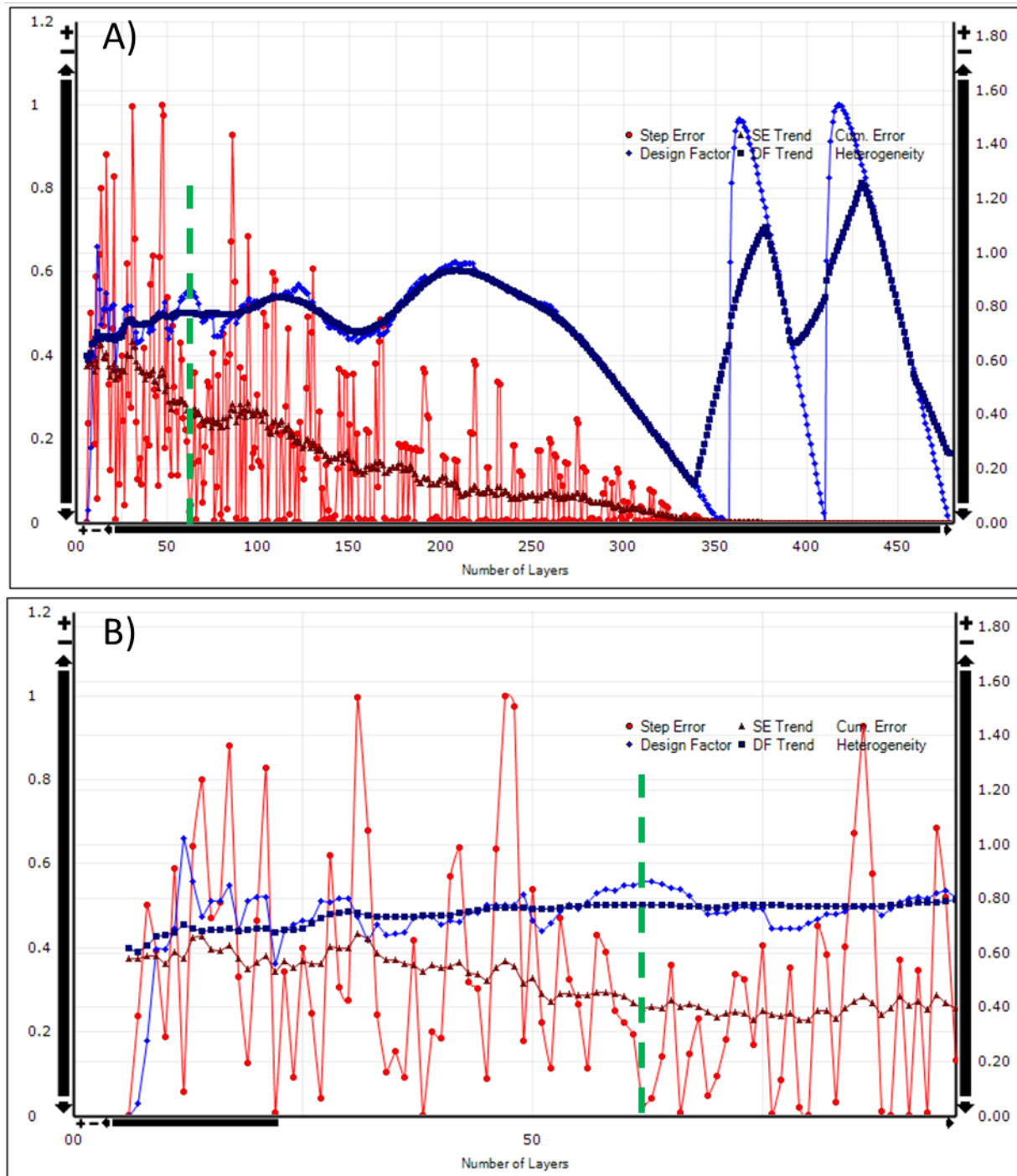


Figure 1-24. Connect Up-grid results showing the design factor and step error for the Dover-33 SEM with the green dashed line highlighting the 64-layer case.

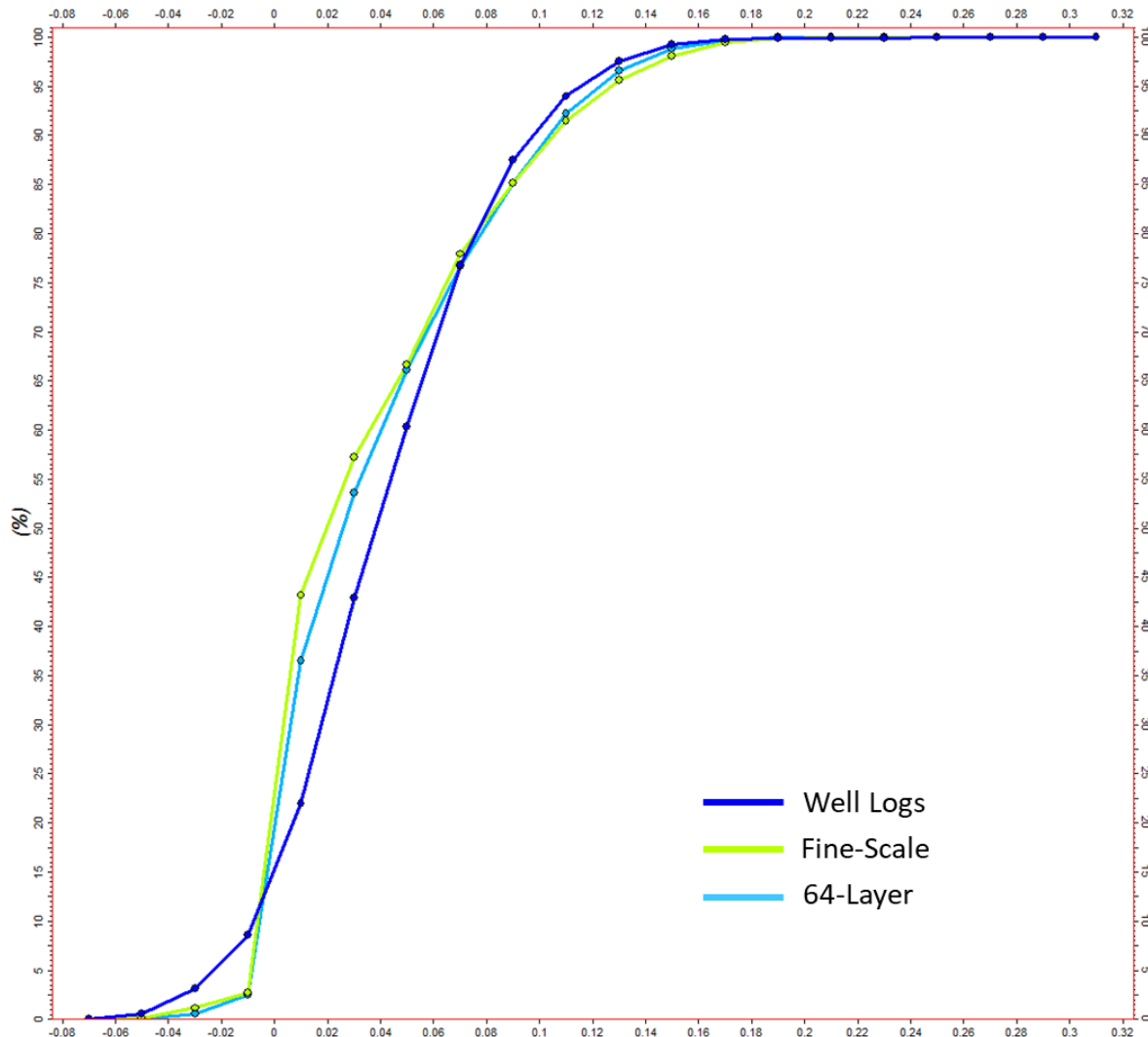


Figure 1-25. CDF comparison of wireline log porosity, fine-scale SEM porosity, and 64-layer SEM porosity.

CONNECT UpGrid™ provided the layering scheme for the 64-layer model. The layering for the upscaled SEM appears to vary depending on which original layers were grouped and preserves model zones. The resulting upscaled SEM has 68,096 cells, which makes it more suitable for DRM work than the original fine-scale model (summarized in Table 1-10).

**Table 1-10. Summary of grid parameters for the Dover-33 reef field.**

Grid Parameter	Dover-33 Upscaled	Comments
SEM size (x by y)	700 m by 950 m (2,296.6 ft x 3,116.8 ft)	Model Area: 622,547 m <sup>2</sup> or 153.8 acres
SEM height (z direction)	159.1 m (522 ft)	Average SEM thickness
Cell grid size in x and y direction	25 m (82 ft)	Cell heights vary
Minimum well spacing	~2.3 m (7.5 ft)	Several kick-offs
Layers / Number of grid cells	64 / 68,096	Fine-scale SEM

Working with the new upscaled framework, the fine-scale porosity model was upscaled into the new grid using the arithmetic averaging method. For permeability, the harmonic averaging method was selected. The upscaled SEM appears to preserve both high porosity and permeability trends for the A1 Carbonate and the Brown Niagaran (Figure 1-26).

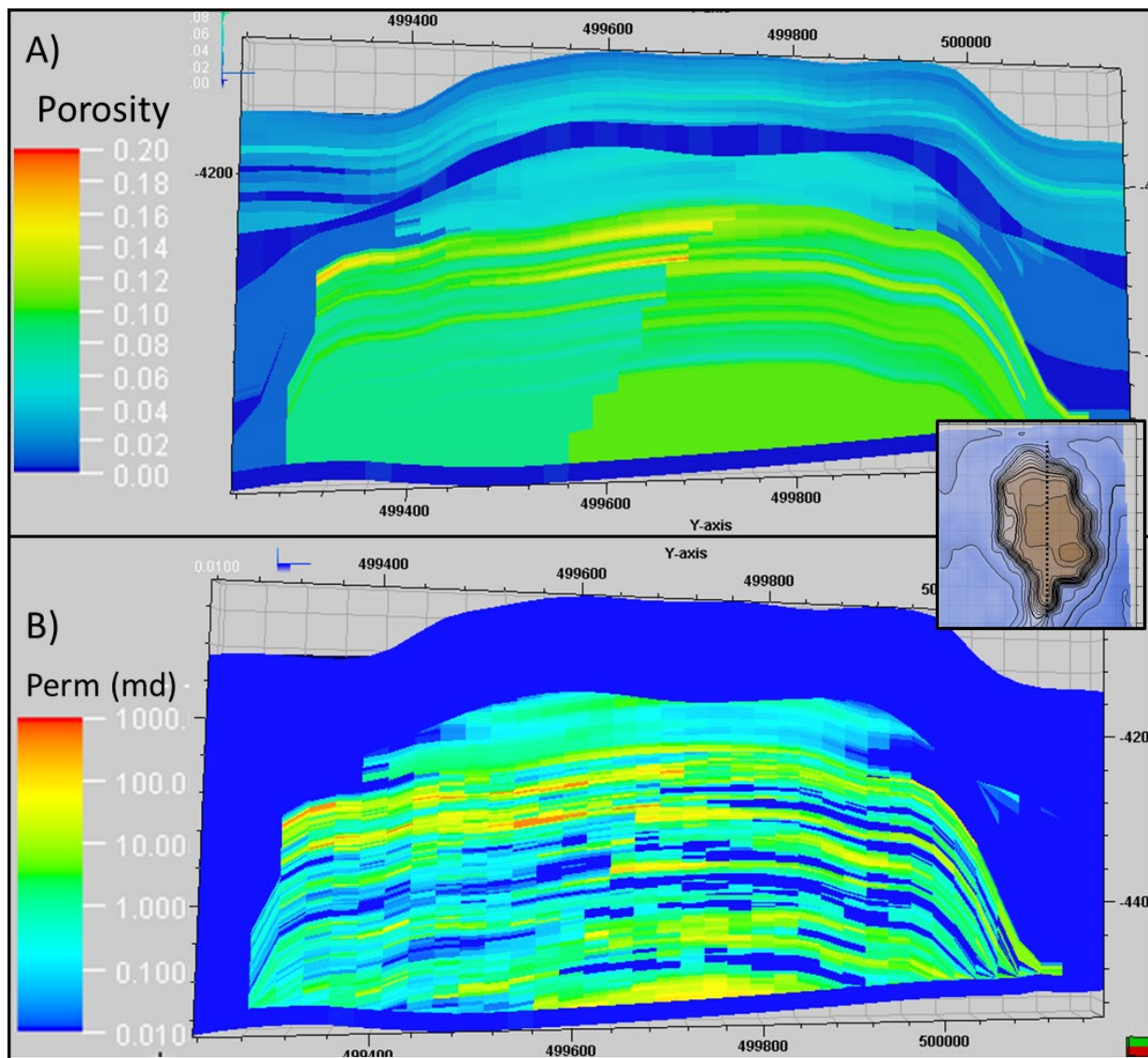


*Figure 1-26. Resulting porosity (A) and permeability (B) models for the 64-layer SEM showing preservation of reservoir property trends and heterogeneity.*

### 1.3.2.7 Alternative Conceptualizations

Alternative conceptualizations were previously designed, known as Level 1 and Level 2, which failed to match production history. An overview of these models can be found in Miller et al., 2014.

Alternative conceptualization models were also considered for numerical efficiency during dynamic simulations by implementing varying degrees of simplification of the heterogeneity resolution in the reef. Simplifications implemented included the rock property distribution in 3-dimensions as well as the reef geometry. The alternative conceptualizations in dynamic modeling are discussed in detail in Section 1.4.5.

## 1.4 Dynamic Model

The objectives for the dynamic modeling activity include evaluating CO<sub>2</sub> injectivity and assessing fluid migration in this complex reef structure. This section describes numerical simulations for capacity and injectivity calculations performed to characterize and history match the dynamic reservoir behavior during primary production and secondary recovery to date. The history matching process enables verification of the available pore volume, as well as provide insights into representative petrophysical rock and fluid property distributions such as permeability in the system of interest. Pressure response during the MRCSP CO<sub>2</sub> injection phase is used to validate and fine-tune this history matched model for better conceptual understanding of CO<sub>2</sub> dynamics in the closed reef system.

### 1.4.1 Modeling Approach

Additional site characterization data was used to build a revised SEM that incorporates all available and acquired geologic and geophysical data, core analysis and implement a new lithofacies-based geologic conceptual model for reef architecture. This latest Level 3 SEM, described in Section 1.3, implemented facies-based reef architecture to quantitatively characterize the revised understanding of porosity, permeability, and water saturation distribution in the Dover-33 reef.

For a given SEM, the dynamic modeling approach seeks to explain historical primary production and secondary recovery data, as well as observed field pressure response to MRCSP CO<sub>2</sub> injection, and monitoring data. This report describes numerical simulations for capacity and injectivity calculations performed to characterize and history match the dynamic reservoir behavior during primary production and secondary recovery to date. The fully compositional dynamic model is built in CMG-GEM® to adjust preliminary static model parameters as needed to replicate the observed field response using a two-stage hierarchical history matching process. The first stage of the history matching process adjusts model input parameters such as permeability, permeability anisotropy, and relative permeability curves to match observed primary production from the reef and the subsequent stage matches the CO<sub>2</sub> injection, and incremental oil production data by adjusting the relative permeability curves for the EOR period.

The initial oil-in-place from our model was determined to be 3.2 MMSTB, which was consistent with material balance calculations using field production data. This method uses the general principle of conservation of mass to determine the original fluids in place by effectively relating fluid withdrawal, i.e. the phase production volumes and static pressure data.

The compositional simulator CMG-GEM® was used for the dynamic modeling of this oil reservoir.

- **Target variables:** Time histories of reservoir pressure, cumulative oil, gas and water production, and cumulative CO<sub>2</sub> injected were used as the basis for matching field performance.
- **Tuning parameters:** History matching of the reservoir model for the primary and secondary recovery phases requires a trial-and-error procedure of adjusting various uncertain reservoir parameters such as the absolute permeability field, permeability anisotropy and the relative permeability curves for oil, water, and gas.

The reported water production values were determined to be less reliable and the baseline pressure recorded for the wells in the reef before the start of Phase III injection had the least uncertainty. Hence the target variable of importance in the CO<sub>2</sub> EOR period was the “golden” final average reservoir pressure value of 780 psi determined before the start of the MRCSP CO<sub>2</sub> injection only period. The calibrated or history matched model performance was finally compared with the field well bottomhole pressures during the MRCSP CO<sub>2</sub> injection period and the tuning stages were repeated until an acceptable match was obtained.

For Dover-33, the key dynamic model versions follow the different SEM versions in order to investigate and improve our understanding of the subsurface system for a representative depiction of the dynamic field response during the Phase III injection period. Figure 1-27 shows the different model versions that have been implemented for the Dover-33 reef. The most extensively investigated version is the Level 2 sequence stratigraphic version, while the latest version is the Level 3 lithofacies model version. As each of the SEM versions build upon increasing resolution of the subsurface, the dynamic modeling process evaluated these high-resolution models, as well as their numerically simplified versions as needed for an overall efficient history matching process. While numerous trials were performed as part of the history matching process for all model versions considered, only the closest results of model performance to field observations is discussed in detail in the current report. A highlight of this process was that the observations of dynamic model performance from each of the previous model versions helped validate and provide insights into the updated geologic conceptualizations for the consequent SEM version.

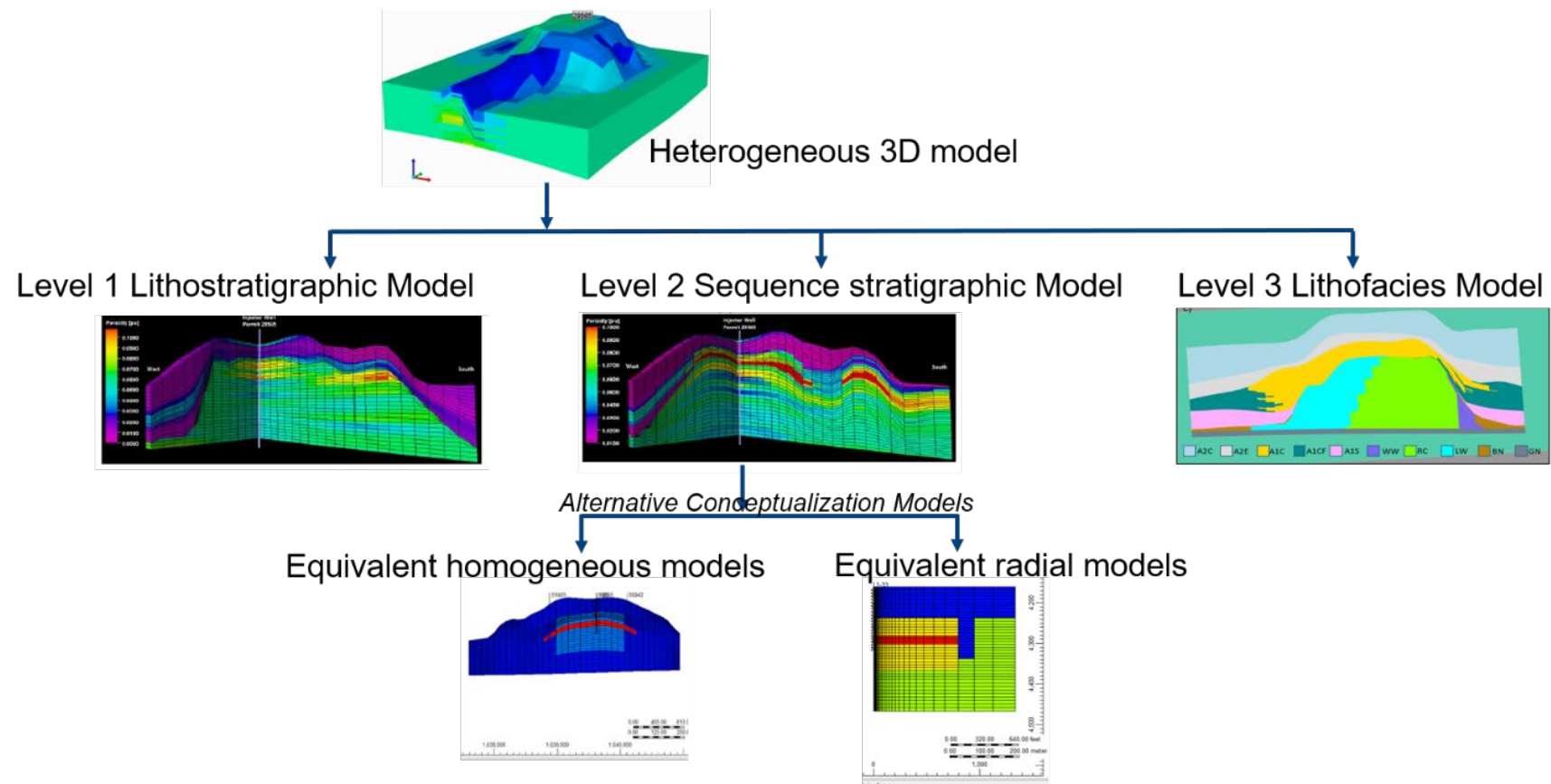


Figure 1-27. Flowchart showing the different model versions that have been implemented for the Dover-33 reef.

## 1.4.2 Model Inputs

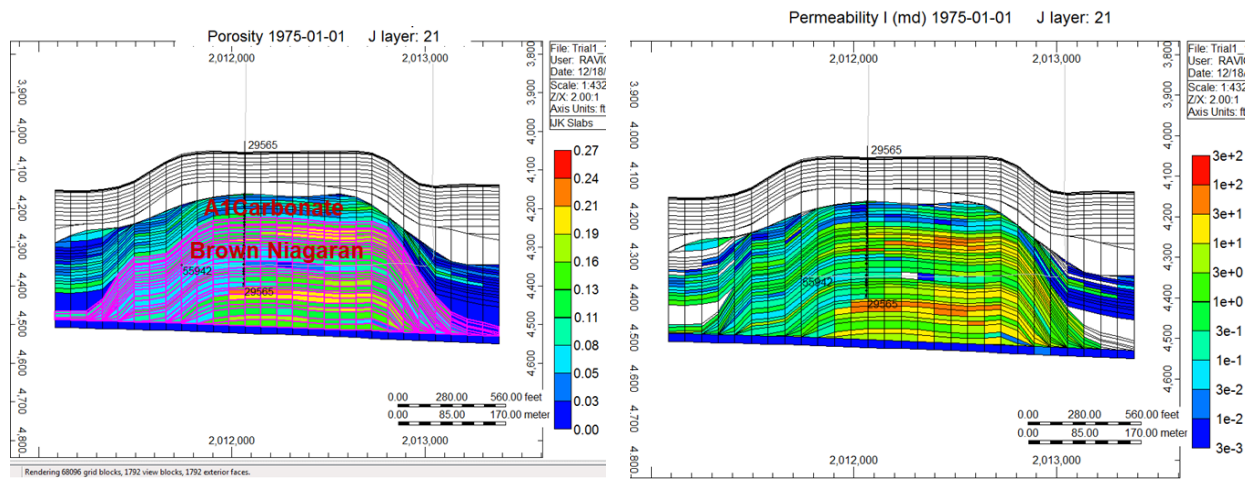
The starting point for dynamic modeling is a geologic framework model for the reef implemented in Petrel. The upscaled Level 3 model consisted of 68096 grid blocks with  $28 (I) \times 38 (J) \times 64 (K)$  blocks in the respectively mentioned dimensions. The model permeability field has been calculated from the input porosity field using a porosity-permeability transform obtained from cores in neighboring reefs for lack of better data. The upscaled lithofacies model was imported into CMG-GEM® and subject to a data validation exercise to ensure its overall consistency with our current insights into the reef geology conceptualization from prior dynamic modeling exercises.

### 1.4.2.1 Rock Properties

This reef is separated from other units by salt and anhydrite layers. The reservoir has two main producing zones – A1 carbonate and Brown Niagaran with a pore volume weighted average porosity of 12.5 percent in the Brown Niagaran.

The latest reef model version and its upscaling is described in the preceding geologic (SEM) section. Figure 1-28 shows the upscaled model porosity and base permeability cross-sections imported into CMG-GEM® for history matching.

## I-K cross-section view:



## J-K cross-section view:

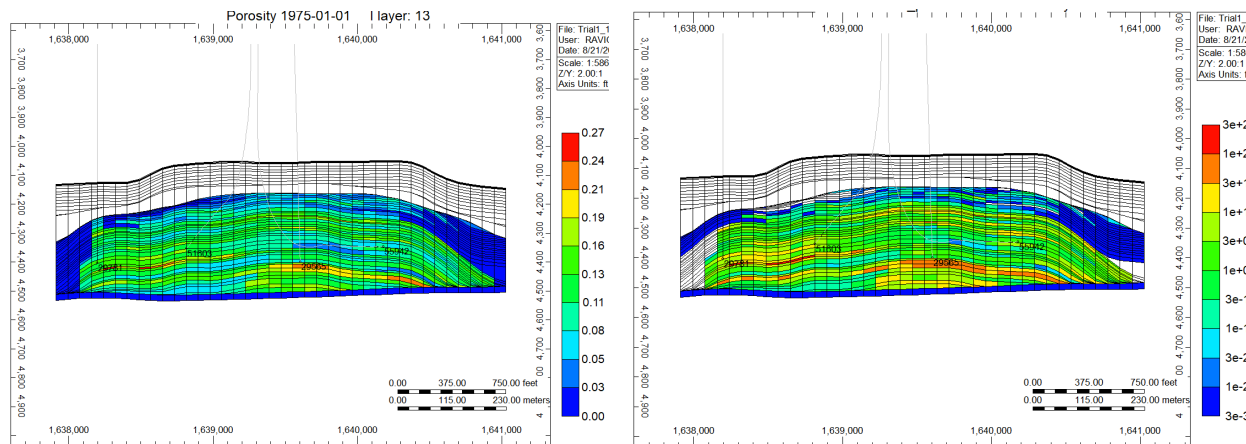


Figure 1-28. Orthogonal cross-section views of the porosity and permeability distributions in the Level 3 Dover-33 model.

#### 1.4.2.2 Fluid Properties

No original fluid samples were taken from wells in the Dover-33 field to represent true initial reservoir conditions. A fluid sample was collected during the end of the primary recovery period that helped approximate the original fluid composition in the reservoir utilizing the equation of state (EOS). The PVT model used was the modified Peng-Robinson EOS. The fluid property was modeled by utilizing seven pseudocomponents lumped to represent the 34 different hydrocarbon components determined as part of the fluid characterization. The lumping was accomplished by grouping hydrocarbon compounds of nearby molecular weights and determining the EOS and physical constants of the mixtures representing the pseudocomponents. The EOS parameters, such as volume shift parameters, interaction coefficients of F1:F7 and F2:F7, were considered as regression variables for tuning in order to match the laboratory/experimental results for fluid properties such as oil viscosity from CO<sub>2</sub> swelling tests. Figure 1-30 shows the comparison of oil viscosity with sample laboratory results obtained after regression of EOS parameters of the pseudocomponents to tune the fluid property model. The match using the tuned EOS was reasonable representation of the fluid parameters determined for the Dover-33 reef and used for dynamic modeling exercises of all Dover-33 geologic model versions.

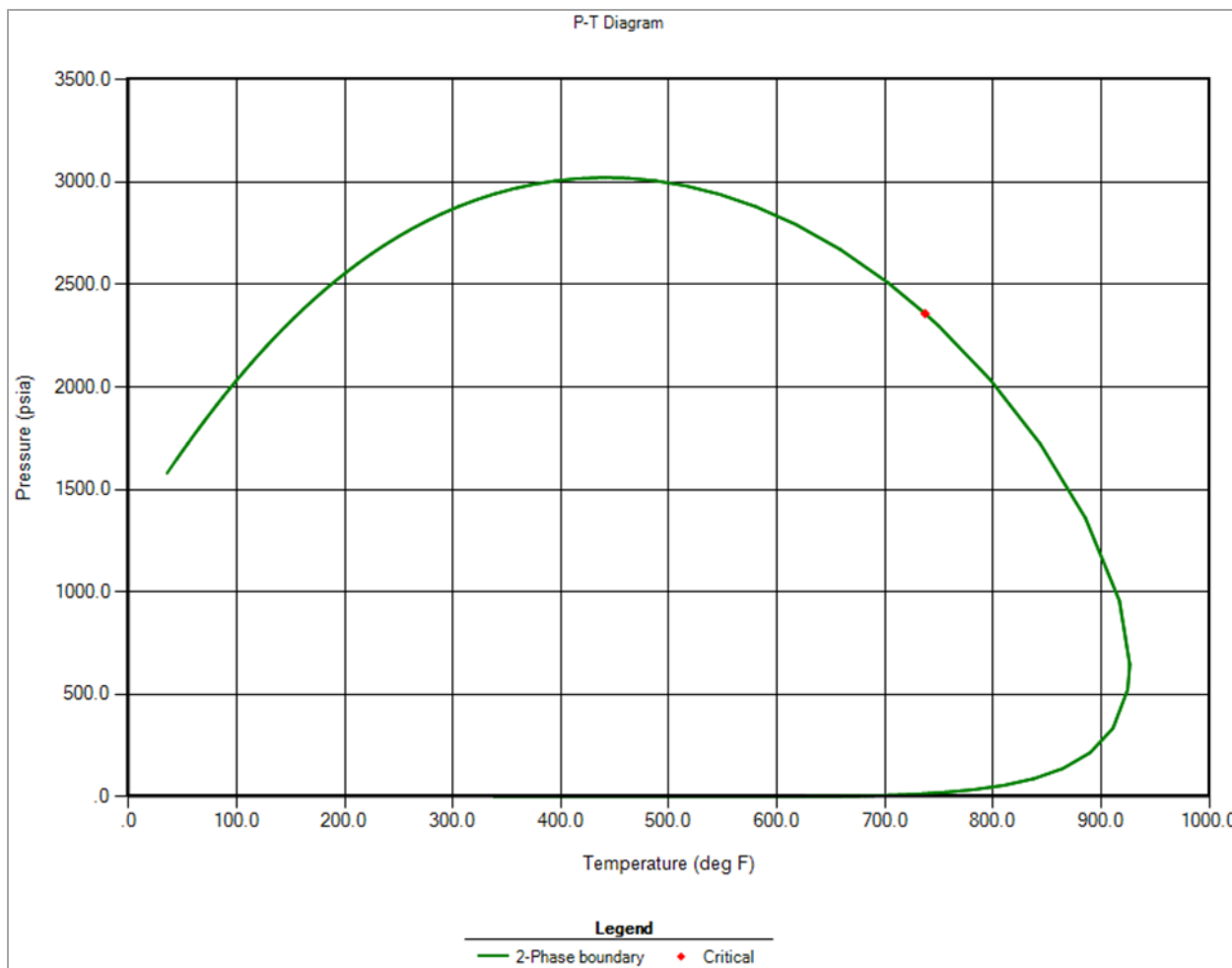


Figure 1-29. Phase envelope of tuned EOS with two sample laboratory calculations from historical fluid characterization effort

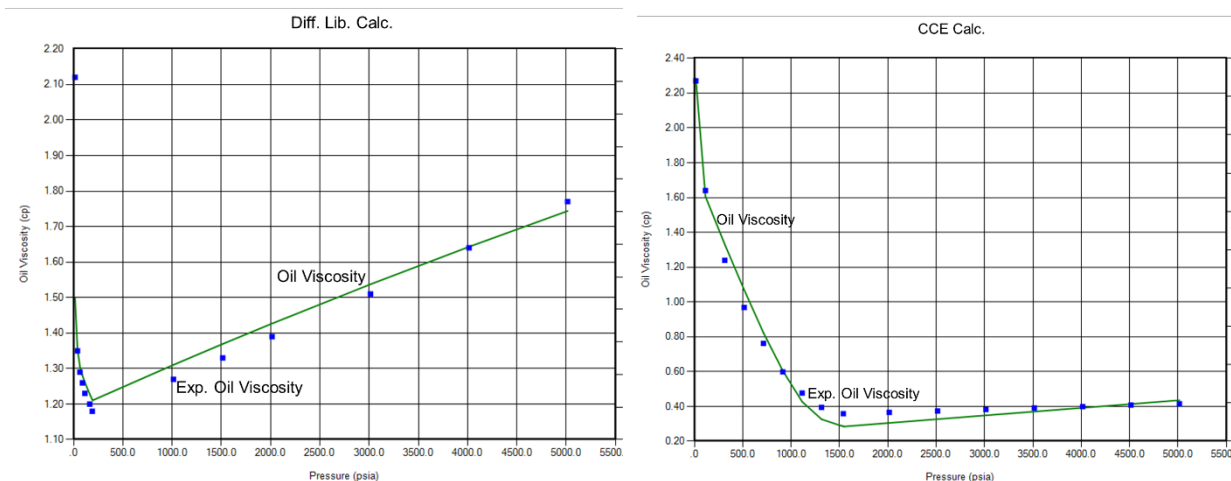


Figure 1-30. Phase envelope (top panel) and oil viscosity comparison of tuned EOS with two sample laboratory calculations from historical fluid characterization effort

Table 1-11 shows the initial fluid composition defined in the model oil zone. Original oil-in-place was estimated using material balance methods and the reservoir was initialized to be consistent with these values. The model reservoir is thus initialized to be in equilibrium with no gas cap and an initial oil-in-place of ~3.2 MMSTB before primary production began. The initial oil-in-place from our model was kept consistent with material balance calculations using field production data. Table 1-12 shows the initial set up in the Level 3 model.

**Table 1-11. Initial fluid composition used in the oil zone**

Pseudocomponent	Mole %
F1: C1, N <sub>2</sub>	40.9117
F2: CO <sub>2</sub>	0.1019
F3: C <sub>2</sub> , C <sub>3</sub> , IC <sub>4</sub> , C <sub>4</sub>	20.2348
F4: IC <sub>5</sub> , C <sub>5</sub> – C <sub>9</sub>	17.3894
F5: C <sub>10</sub> – C <sub>19</sub>	14.7254
F6: C <sub>20</sub> – C <sub>24</sub>	2.75139
F7, C <sub>25</sub> – C <sub>30+</sub>	3.88549

**Table 1-12. Initial conditions set up in the Level 3 Dover-33 dynamic model**

Initial Condition Model Parameter	Value
Pore volume (MM res ft <sup>3</sup> )	118.754
Reservoir volume of oil (MM STB)	3.279
Reservoir volume of water (MM STB)	16.392
Reservoir volume of gas (MMM SCF)	3.121
Initial reservoir pressure (psi)	2900
Initial reservoir temperature (deg F)	108
Depth of Oil-Water contact (ft)	4330

#### 1.4.2.3 Relative Permeability Model

Relative permeability curves for the oil-gas-water phases were assumed for the primary depletion period and then tuned in the second stage of the hierarchical history match process once CO<sub>2</sub> was introduced as the injected 'solvent' into this three-phase system. The relative permeability curves were one of the key tuning parameters in the history matching process owing to the uncertainty associated with their characterization in the field. Figure 1-31 and Figure 1-32 show the preliminary relative permeability curves used for the Level 3 Lithofacies model.

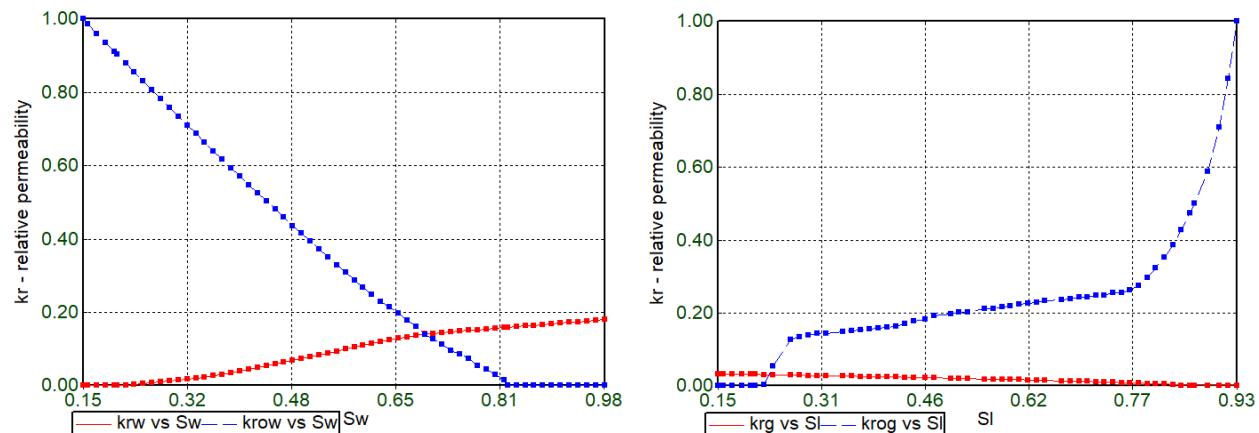


Figure 1-31. Preliminary relative permeability curves for primary depletion period in Dover-33 Level 3 model

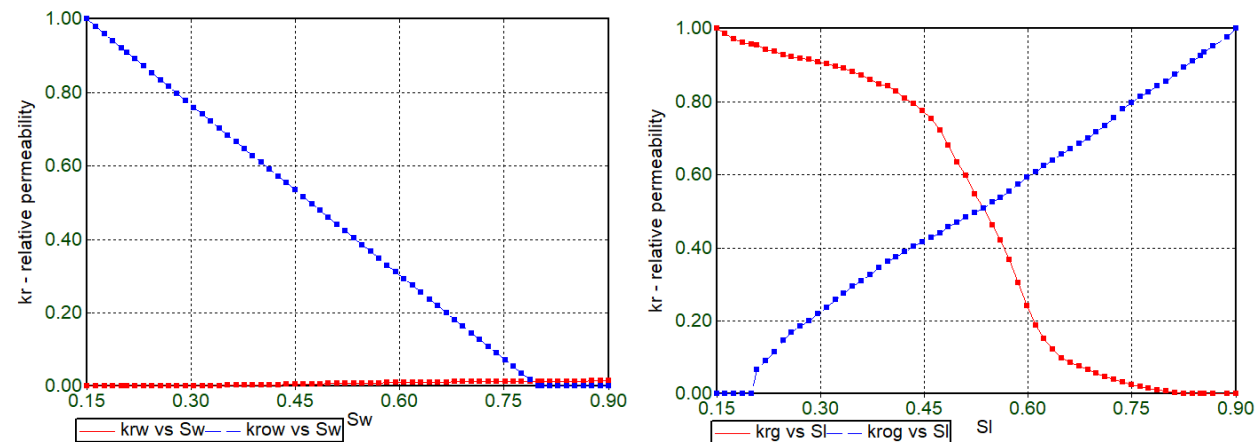


Figure 1-32. Preliminary EOR and MRCSP period relative permeability curves in Dover-33 Level 3 model

#### 1.4.3 Primary Production History Match

The absolute permeability is one of the key parameters with significant uncertainty in the characterization process and is used as a tuning parameter during the history match process.

Figure 1-33 shows a scenario in which local permeability scaling was considered to obtain a good history match for the primary recovery and CO<sub>2</sub>-EOR periods.

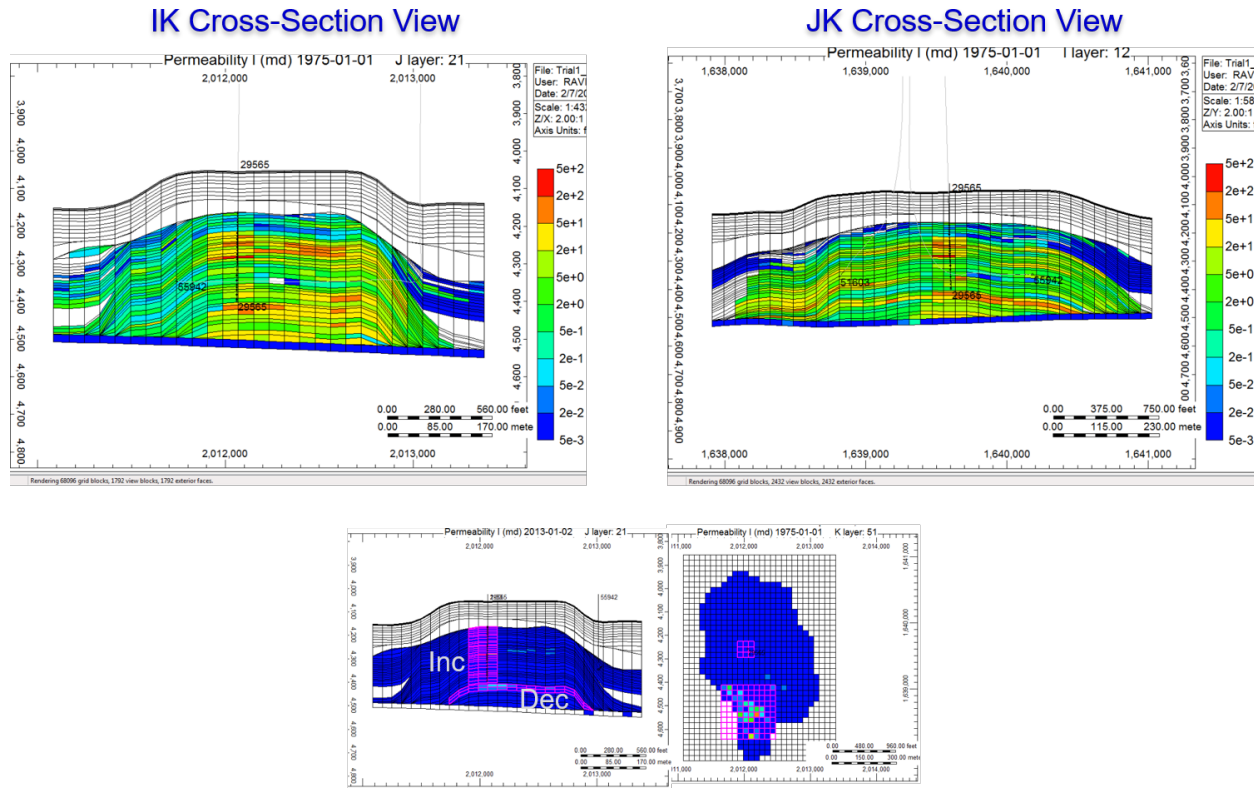


Figure 1-33. Example illustration of permeability scaling trial

The permeability near the injection well is increased while the connection of the reservoir core to the water column is decreased using permeability multipliers.

Figure 1-34 shows the tuned relative permeability curves used for a history match of the primary recovery period in this Level 3 model. The history matched model results to produce the three fluid phases (oil, hydrocarbon gas and water) from the reservoir are shown in Figure 1-35 for the primary recovery period. The model results show a good match for the cumulative oil and gas production. However, the model produces significantly less water during this primary depletion period and results in a slightly higher average reservoir pressure compared to the field observations, as shown in Figure 1-35.

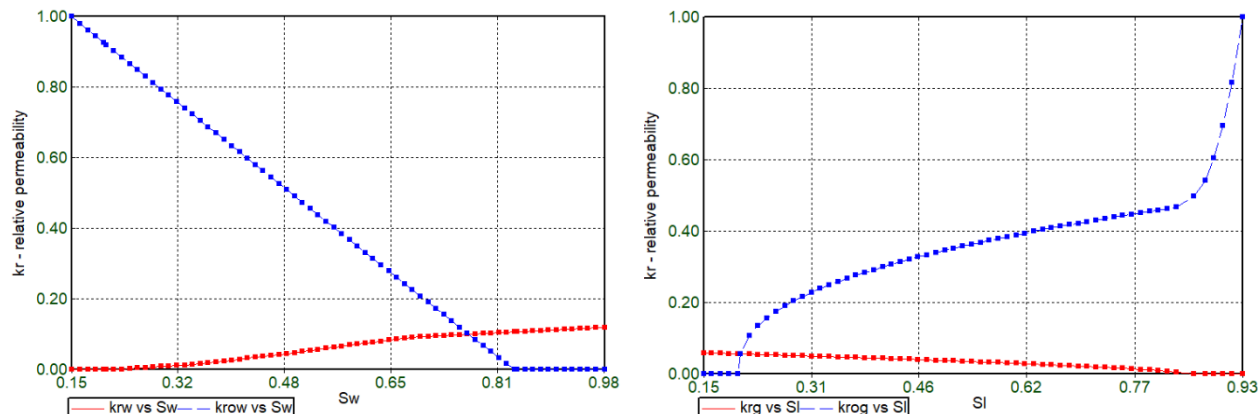


Figure 1-34. Final tuned relative permeability curves for primary depletion period in Dover-33 Level 3 model

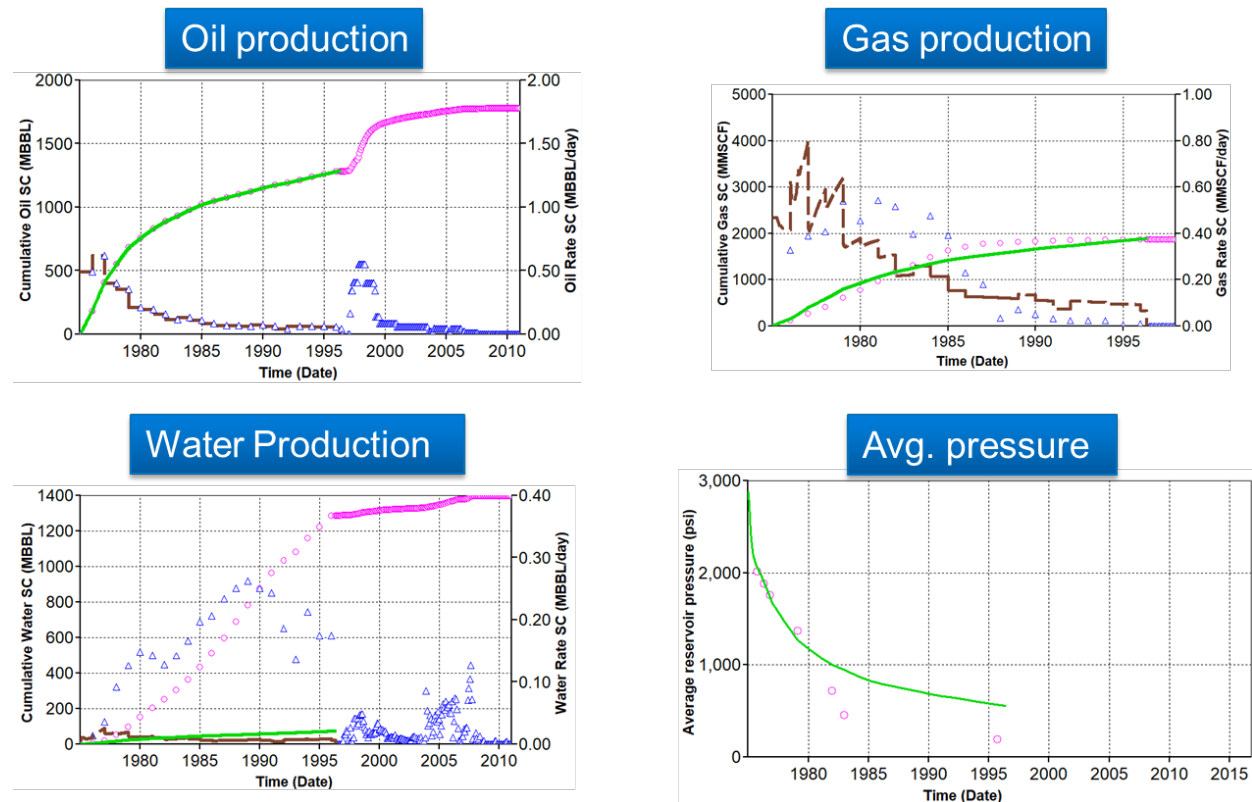


Figure 1-35. History match results for: (a) oil production; (b) gas production; (c) water production; and (d) average reservoir pressure during primary production until 1996. The symbols in the figures represent field data and the lines show model outputs.

#### 1.4.4 EOR/CO<sub>2</sub> Injection History Match

The relative permeability curves were further tuned for the EOR and CO<sub>2</sub> injection period history match of the Level 3 model scenario discussed in Section 1.4.3. Figure 1-36 shows the tuned relative permeability curves used to obtain a history match for the secondary recovery period.

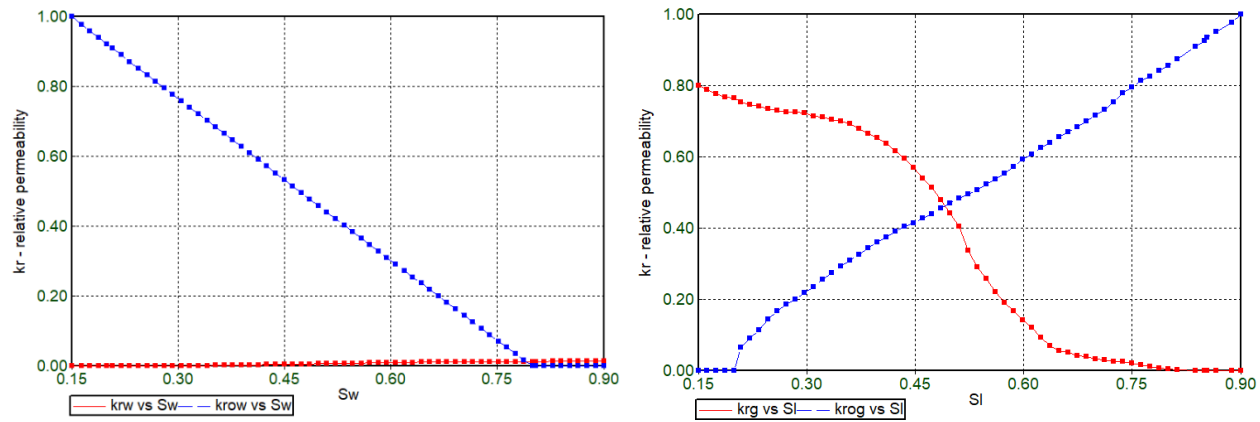


Figure 1-36. Final tuned EOR and MRCSP period relative permeability curves in Dover-33 Level 3 model.

The injection rates were used as the input data while the average reservoir pressures were successfully compared to the observed field values. This ensures the robustness of the simulation model to be used for predicting the reservoir behavior under future constraints. Results of the model performance until the end of the secondary recovery period is shown in Figure 1-37. The model is unable to meet the oil production constraints during the early CO<sub>2</sub>-EOR period and hence results in lower oil production in comparison to the field data. Conversely, the higher relative permeability to gas in this period results in a much higher cumulative gas production to inject the required target amount of CO<sub>2</sub> while achieving the target average pressure of 780 psi at the end of the CO<sub>2</sub>-EOR period.

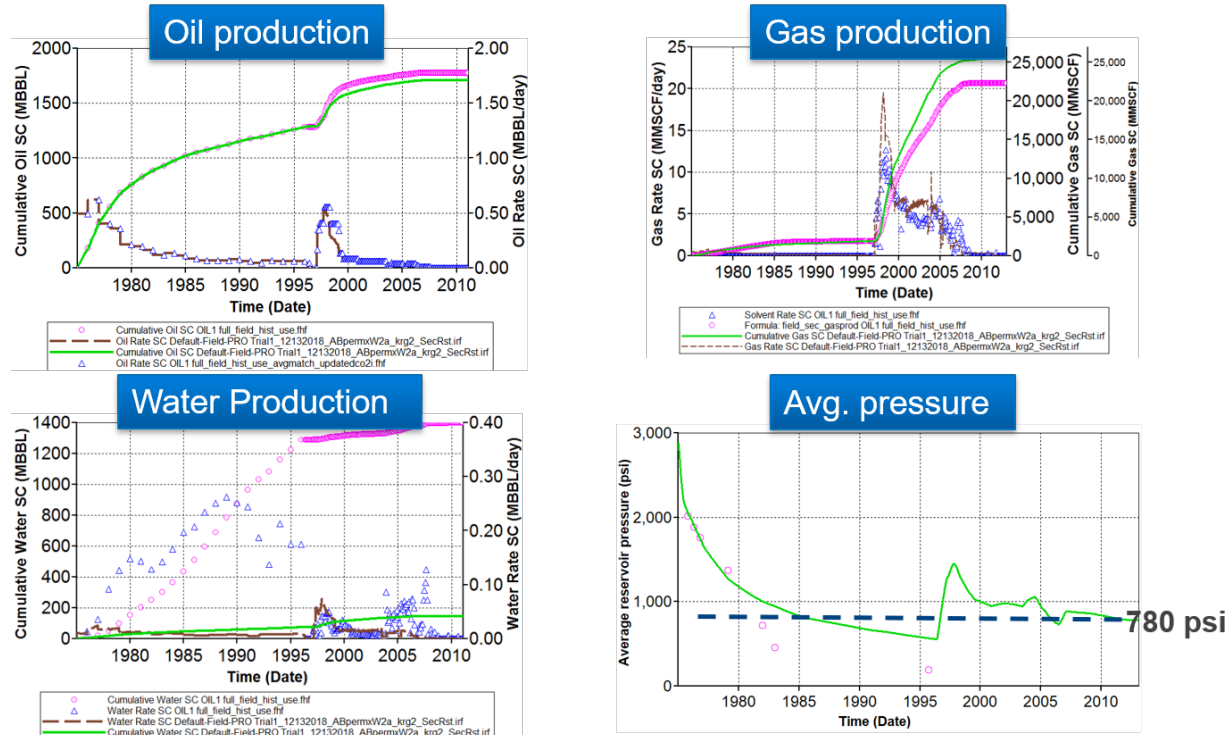


Figure 1-37. History match results for primary and CO<sub>2</sub>-EOR period: (a) oil production; (b) gas production; (c) water production; and (d) average reservoir pressure; the symbols in the figures represent field data and the lines show model outputs.

This CMG-GEM® model was then validated with field pressure response from the CO<sub>2</sub> injection period. Figure 1-38 shows the MRCSP Phase III CO<sub>2</sub> injection history modeled in Dover-33. The rate simplification was done by grouping and averaging the high frequency (daily) gauge data for purposes of dynamic simulation while ensuring the cumulative injection amount remained unaffected. The CO<sub>2</sub> injection rate was used as the input data while the bottomhole pressure buildup in the injection and monitoring wells were compared to the observed field values. Figure 1-39 shows the model performance compared to the field observed bottomhole pressure response. This validation is expected to ensure the robustness of the simulation model to be used for predicting the reservoir behavior under future constraints.

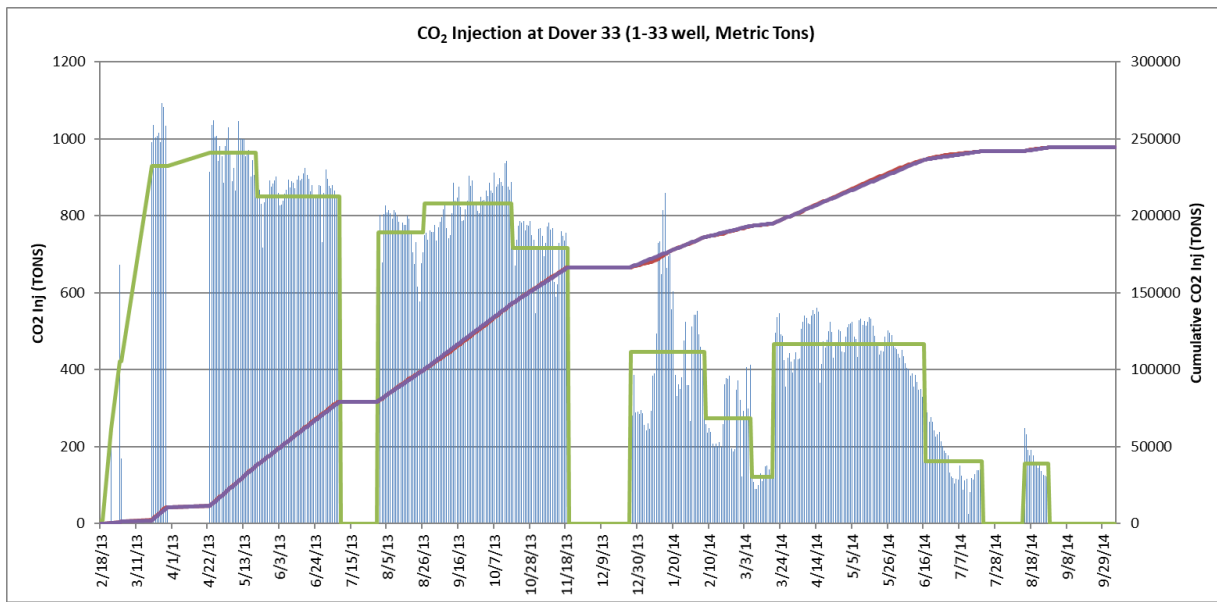


Figure 1-38. Simplified CO<sub>2</sub> injection rate schedule (green curve) imposed in the model for MRCSP Phase III CO<sub>2</sub> injection period. The blue lines show the daily injection rate data while the purple and red curves are the cumulative injection values for the modeled and daily rate data respectively.

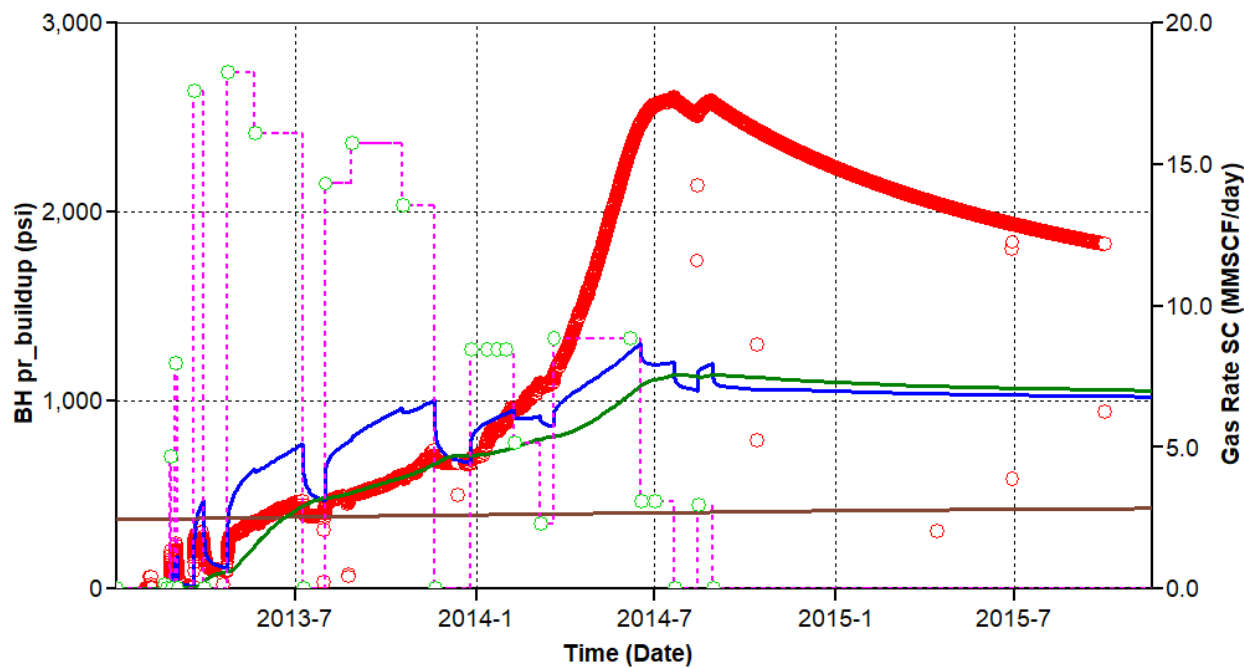


Figure 1-39. Modeled wells bottomhole pressure buildup response during the MRCSP Phase III CO<sub>2</sub> injection period in the latest Level 3 SEM conceptualization. Here, the red circles represent observed field data, magenta lines are the imposed CO<sub>2</sub> injection rate, blue curve is the modeled injector bottomhole pressure buildup and the brown and green curves are the modeled monitoring wells bottomhole pressure buildup.

Figure 1-39 clearly shows the model not capturing the steep pressure buildup during end of Phase III CO<sub>2</sub> injection period from January 2014. In addition, the divergence in the modeled bottomhole pressure response of the three wells suggests that the geologic conditions modeled do not completely represent reservoir conditions. Therefore, sensitivity of reservoir response observed in the field was evaluated using equivalent simplified model conceptualizations of the reef. Equivalent homogeneous reef models produced by simplified zone considerations extracted from key insights using the heterogeneous model are used to help understand the level of detail required to honor observed reservoir response without compromising computational efficiency. Alternative conceptualization models were therefore explored with simplified heterogeneity and geometry based on the lithostratigraphic model for ease of computational convenience.

#### 1.4.5 Alternative Conceptualization Trials

Two types of trials were done as part of the design matrix to better capture the model response to the Phase III CO<sub>2</sub> injection period: (1) simplified heterogeneity conceptualization with the equivalent homogeneous model and (2) simplified geometry with equivalent radial single-(injection) well model. The models (shown in Figure 1-40) have been initialized using the properties and results from the Level 2 lithostratigraphic model (Figure 1-27).

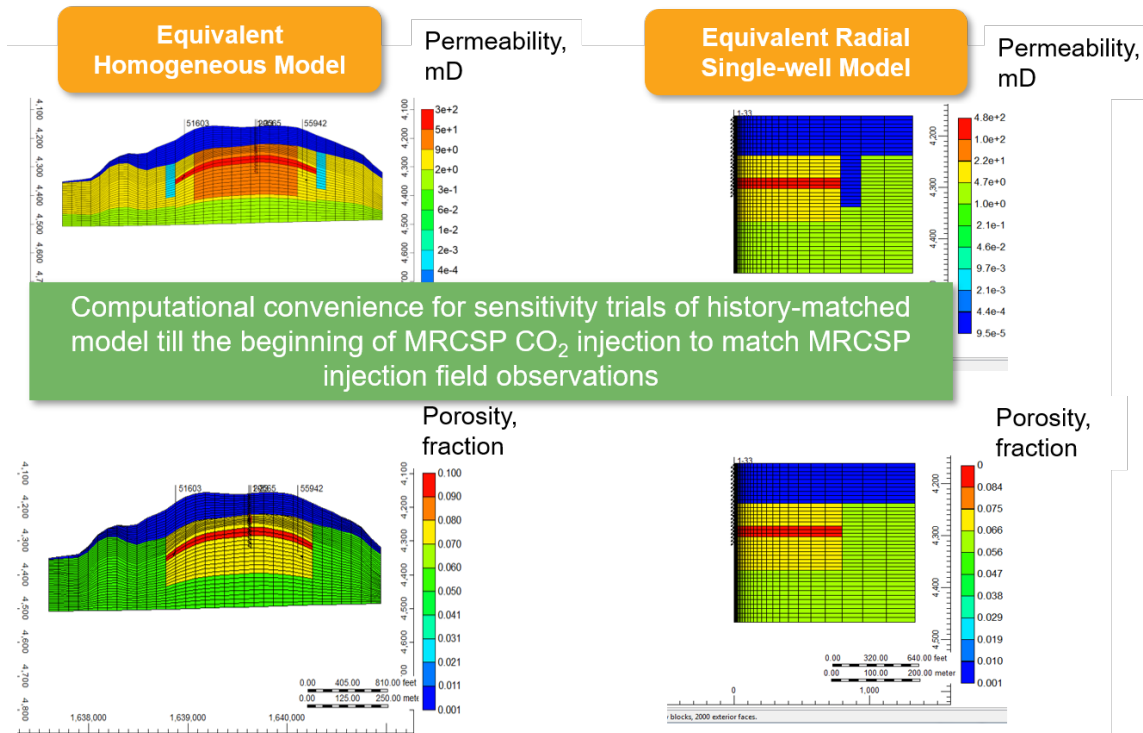


Figure 1-40. Cross-section showing porosity and permeability distributions considered in the (1) simplified heterogeneity conceptualization with the equivalent homogeneous model, M0 and (2) simplified geometry with equivalent radial single-well model, M2.

### Equivalent Homogeneous Model

Equivalent homogeneous zones such as the core reservoir, reservoir flanks, water column and A1 Carbonate are delineated within the reef based on the current understanding of geology affecting the pressure response. The reef geometry is maintained in the first set of conceptualization trials with the equivalent homogeneous model while ensuring the original oil-in-place and reservoir conditions are honored. History match for primary and EOR using equivalent homogeneous model, M0 (left column) is shown in Figure 1-41. The M0 model is unable to meet the oil production during the early CO<sub>2</sub>-EOR period and results in lower oil production in comparison to the field data. Conversely, the higher relative permeability to gas in this period results in a much higher cumulative gas production to inject the required target amount of CO<sub>2</sub> while achieving the target average pressure of 780 psi at the end of the CO<sub>2</sub>-EOR period. The comparable model performance for the primary and secondary recovery periods to the level 3 dynamic model (Figure 1-37) is considered acceptable quality for the simplified heterogeneity conceptualizations implemented in this section.

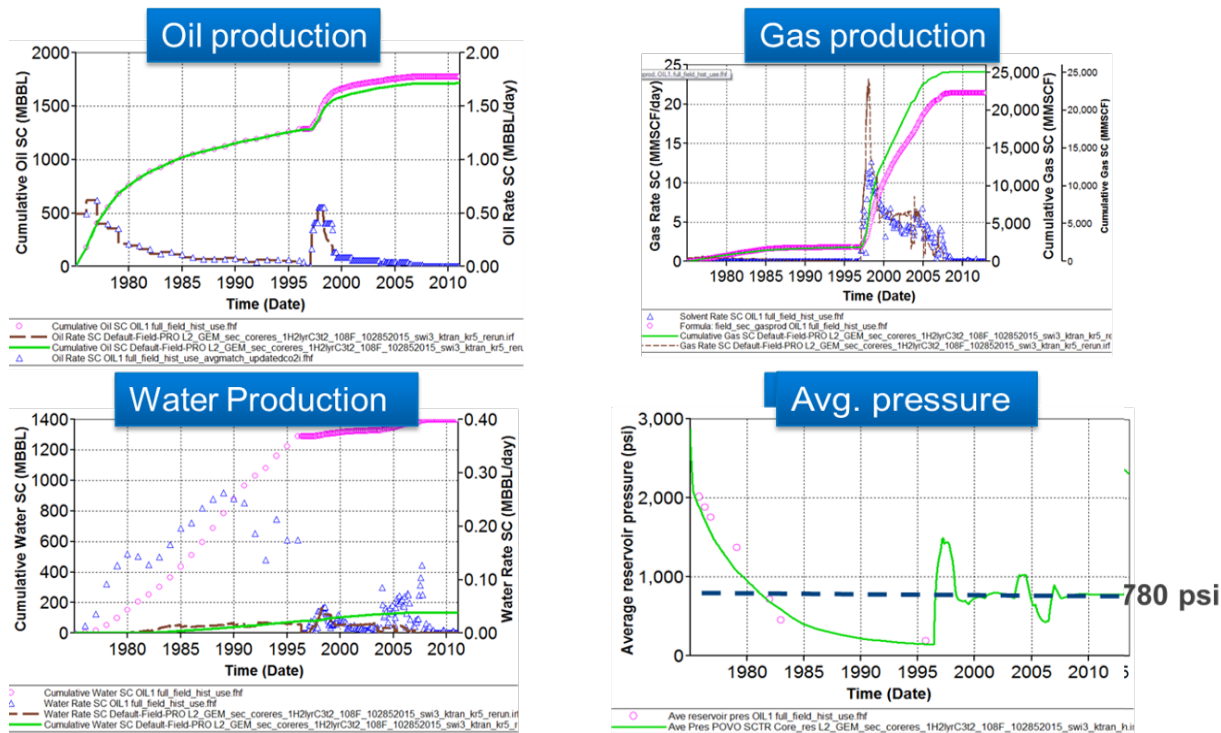


Figure 1-41. History match results for: (a) oil production; (b) gas production; (c) water production; and (d) average reservoir pressure. The symbols in the figures represent field data and the lines show M0 model outputs.

This history matched alternative conceptualization GEM ® model was then validated with CO<sub>2</sub> injection data from the field. Figure 1-42 shows the M0 MRCSP phase III CO<sub>2</sub> injection history in Dover-33.

1-33 L2\_GEM\_sec\_632019\_ktran2\_3krg.irf

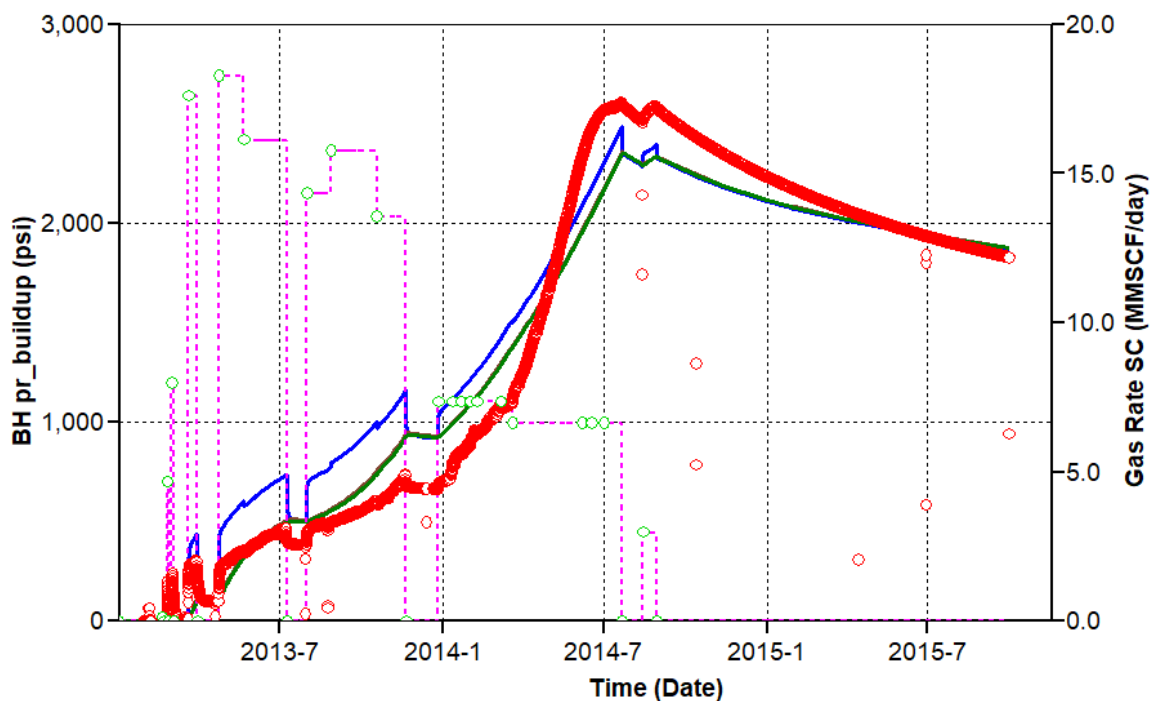


Figure 1-42. Modeled wells bottomhole pressure buildup response during the MRCSP Phase III CO<sub>2</sub> injection period in the equivalent homogeneous model conceptualization. Here, the red circles represent observed field pressure data, green circles represent simplified field CO<sub>2</sub> injection rate data, magenta lines are the modeled CO<sub>2</sub> injection rate, blue curve is the modeled injector bottomhole pressure buildup and the brown and green curves are the modeled monitoring wells bottomhole pressure buildup.

The injection rates were used as the input data while the average reservoir pressures were successfully compared to the observed field values. This ensures the robustness of our simulation model to be used for predicting the reservoir behavior under future constraints.

While the match for the Phase III period was acceptable, there was a material balance error of 4 percent observed in this M0 model. This material balance error was possibly because the three-phase relative permeability using the default STONE2 model shows non-zero oil relative permeability at zero oil saturation for this case. This problem was addressed by changing the oil phase relative permeability calculation method and redoing the history match to avoid non-zero oil relative permeability at zero oil saturation and as a result would not show the high material balance error seen in the M0 model.

The resulting equivalent homogeneous M1 model configuration honors material balance (material balance error ~9E-02 percent) with an acceptable match for the Phase III injection period and provides more resolution to the permeability heterogeneity. This assumes that the permeability transitions stepwise as we move from the core of the reservoir with the injection and monitoring wells (shown in orange in the right panel of Figure 1-43) to the flanks of the reservoir (shown in green in the right panel of Figure 1-43). Figure 1-43 also shows the porosity and permeability distribution considered in the M1 model.

## 1.0 Dover-33 Reef

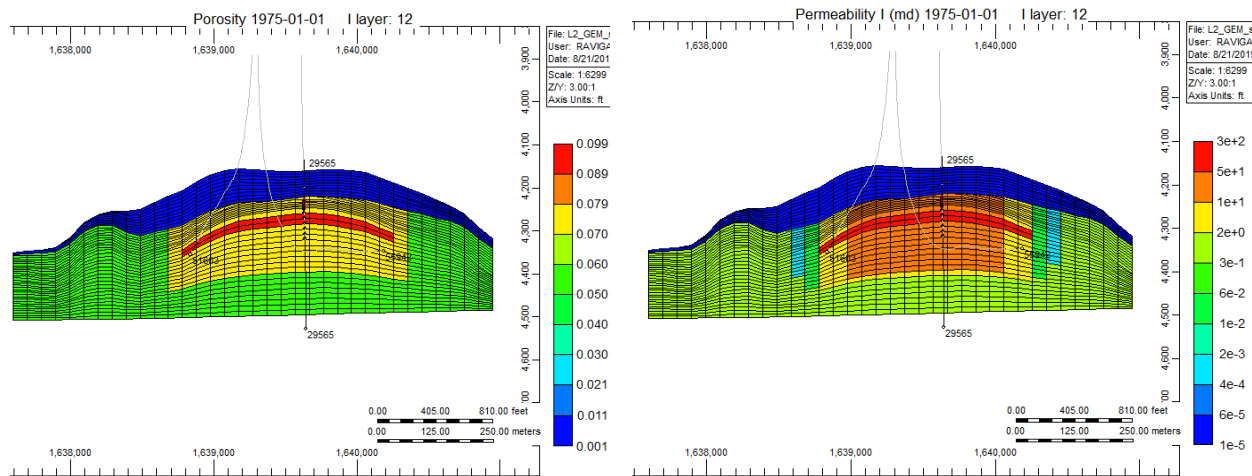


Figure 1-43. Cross-section of the porosity and permeability distribution in the equivalent homogeneous M1 model configuration.

The tuned three-phase relative permeability curves for the primary and secondary periods in the GEM model are shown in Figure 1-44 and Figure 1-45.

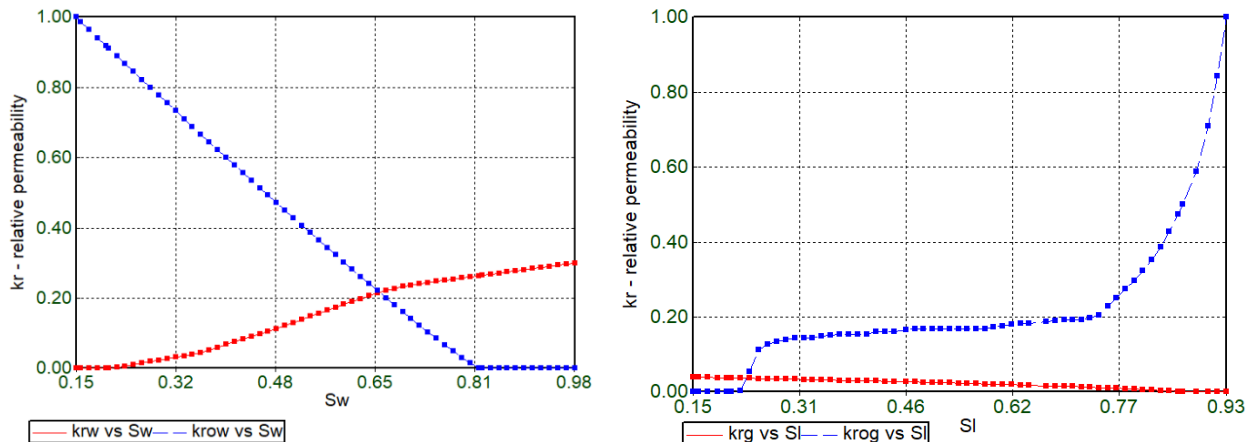


Figure 1-44. Relative permeability curves for primary depletion period in the M1 model.

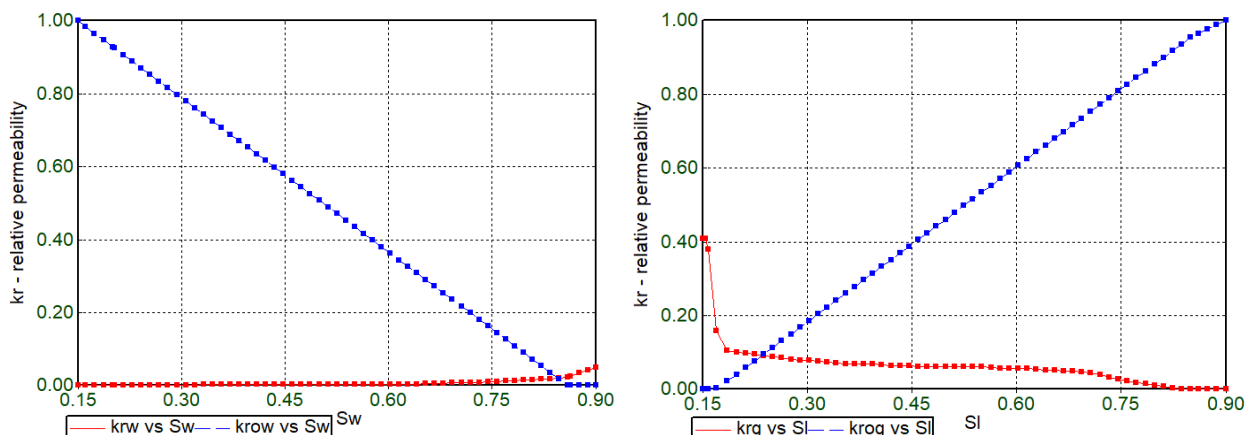


Figure 1-45. EOR and MRCSP period relative permeability curves in the M1 model.

The history match for primary and EOR periods using equivalent homogeneous M1 model configuration is shown in Figure 1-46. Like the M0 model, the M1 model is unable to meet the oil production during the early CO<sub>2</sub>-EOR period, resulting in lower oil production compared to the field data. Conversely, the cumulative gas production is higher than the field observed data to inject the required target amount of CO<sub>2</sub> while achieving the target average pressure of 780 psi at the end of the CO<sub>2</sub>-EOR period, similar to the earlier M0 model.

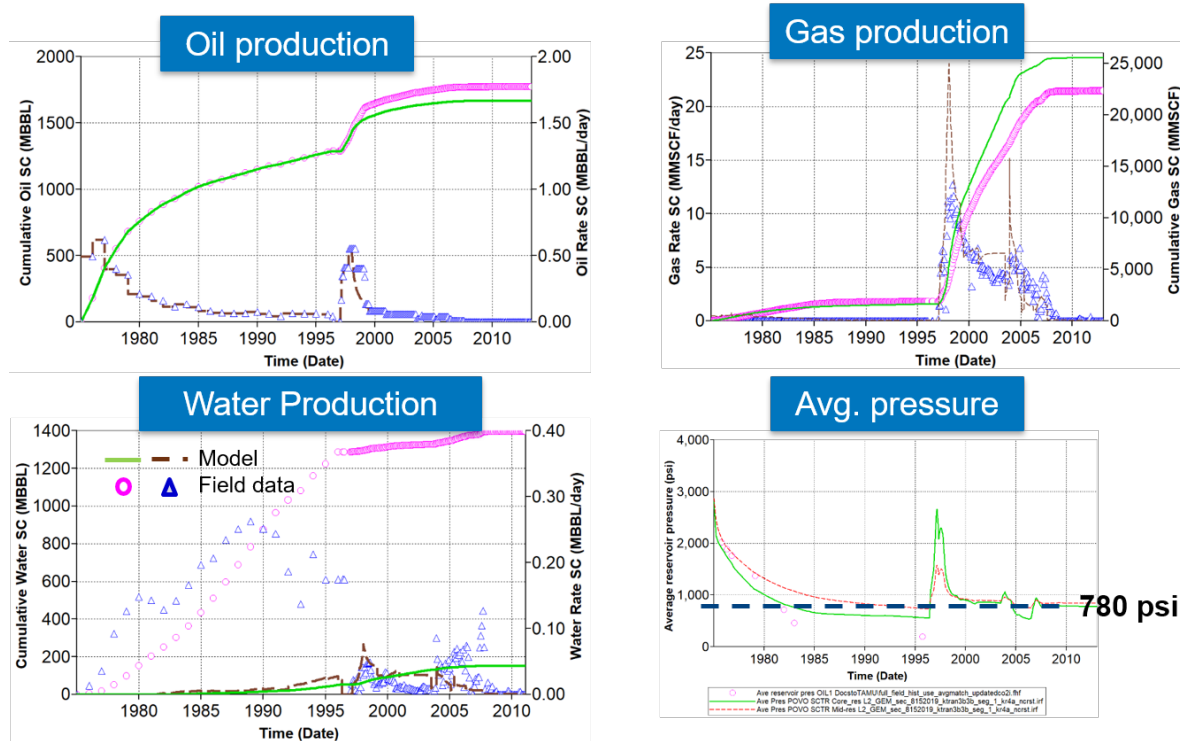


Figure 1-46. History match results for: (a) oil production; (b) gas production; (c) water production; and (d) average reservoir pressure. The symbols in the figures represent field data and the lines show M1 model outputs.

This history matched alternative conceptualization GEM ® model was then validated with CO<sub>2</sub> injection data from the field. Figure 1-47 shows the M1 model MRCSP Phase III CO<sub>2</sub> injection response in Dover-33.

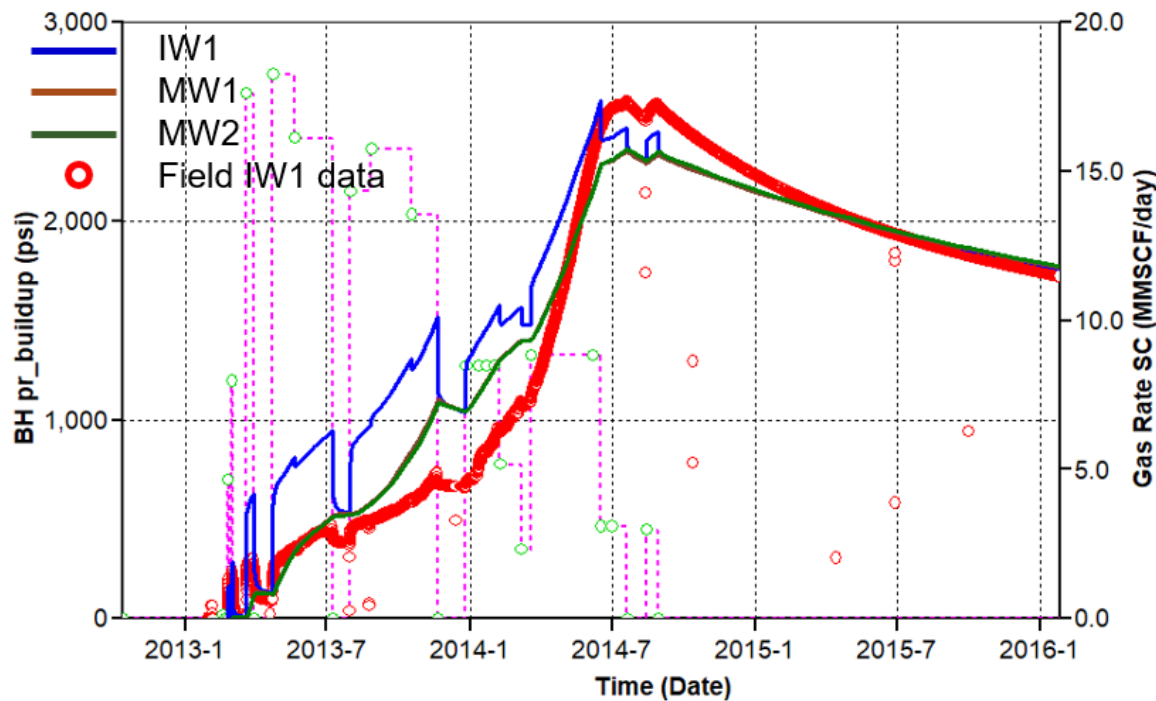


Figure 1-47. Modeled wells bottomhole pressure buildup response during the MRCSP Phase III CO<sub>2</sub> injection period in the equivalent homogeneous M1 model conceptualization. Here, the red circles represent observed field pressure data, green circles represent simplified field CO<sub>2</sub> injection rate data, magenta lines are the modeled CO<sub>2</sub> injection rate, the blue curve is the modeled injector bottomhole pressure buildup, and the brown and green curves are the modeled monitoring wells bottomhole pressure buildup.

The injection rates were used as the input data and the well bottomhole pressures were successfully compared to the observed field values. The steep increasing trend in the pressure buildup and linear decline during the final fall-off along with the peak and endpoint pressures are well captured in the equivalent homogeneous model. However, model trends vary slightly compared to the field observed trends for the CO<sub>2</sub> injection-fall-off cycles between late 2013 and early 2014 with the current simplified reservoir property distributions considered. Possible explanations to improve the representativeness of the model include:

- The homogenization and injection schedule simplification for numerical efficiency and that adding more heterogeneity could help capture the nuances in the field observations for pressure buildup at the wells.
- Subtle time dependent (and hence pressure dependent behavior) that have not been captured in these models, such as geochemical reactions or geomechanical changes that would be captured in the coupled modeling exercises.

#### 1.4.6 Additional Model Variants and Insights

*Understanding subsurface dynamics: Discussion on tracking CO<sub>2</sub> distribution within the reef using alternative conceptualization model*

The existence of a core reservoir region around the three wells in Dover-33 is established from the validated alternative conceptualization model versions. This region transitions to lower permeability

flanks that are overlain by a very low permeability region (average permeability of the order of 1E-5 mD). In both models, the core reservoir region has a high permeability region (layer) that is also substantiated by the SEM permeability distribution. The Level 3 SEM also corroborates the conceptualization of a water column with reasonable permeability that enables with the dissolution of CO<sub>2</sub> over time.

The equivalent homogeneous model also gives insights into the late-stage subsurface dynamics as the CO<sub>2</sub> distribution is tracked in the system through the EOR, Phase III injection and fall-off periods. Figure 1-48 shows difference maps that indicate where CO<sub>2</sub> has moved for the MRCSP injection period until October 2014 and at the February 2016 during the final fall-off period in the M1 model. Key observations include:

- CO<sub>2</sub> moves outward from the injection well during MRCSP injection.
- Production activity and dynamics mostly in the upper and upper-middle reservoir regions of the closed late-stage reef.
- Simulated CO<sub>2</sub> distribution shows CO<sub>2</sub> migrating outward into the reef flanks and dissolving in the formation brine over time.
- While most of the CO<sub>2</sub> continues dissolving in the formation brine, CO<sub>2</sub> also moves outward laterally to the flanks and towards the top of the perforations during MRCSP fall-off.

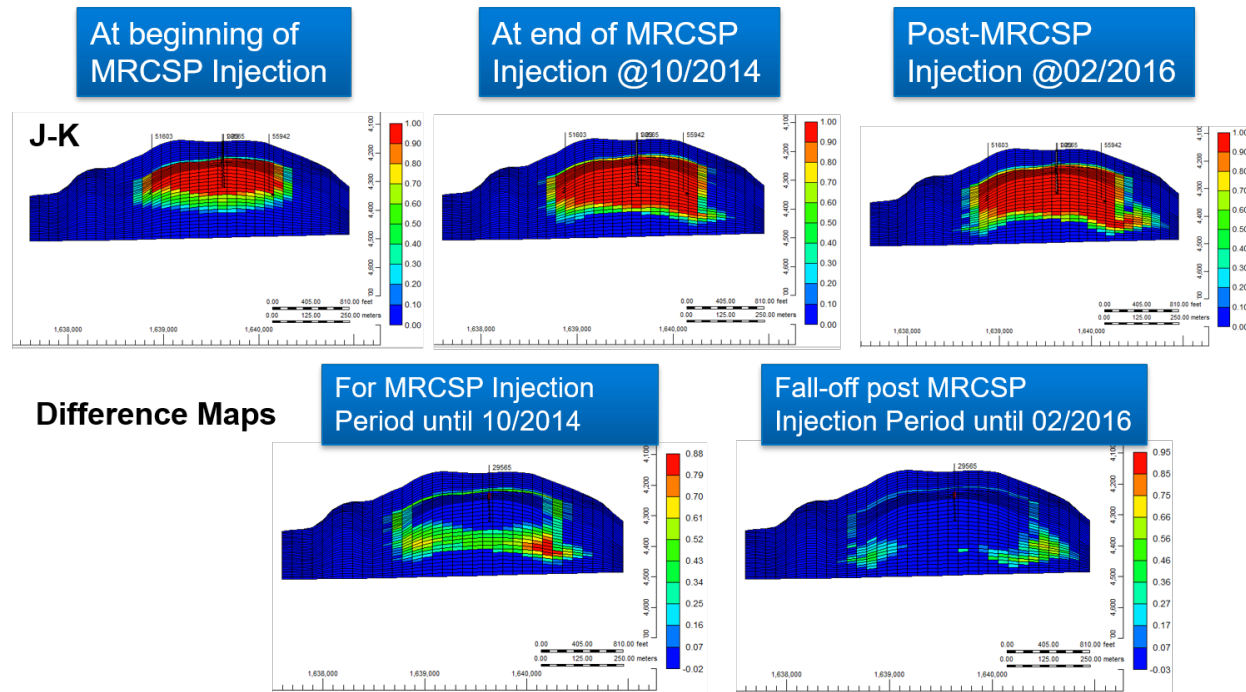


Figure 1-48. Global mole fraction of CO<sub>2</sub> in a representative cross-section of the reef at different times during the Phase III injection and subsequent fall-off period. Difference maps in the bottom row indicate where CO<sub>2</sub> has moved to for the MRCSP injection period until October, 2014 and at the June, 2015 during the final fall-off period. Color scale represents presence versus absence (0.0) of CO<sub>2</sub> in any phase in the system.

Observations gave valuable feedback and validated geologic conceptualization updates during Level 3 model building process.

### 1.4.7 Exploring Time-Variant Property Changes

*Understanding subsurface dynamics: Discussion on possible explanation for pressure buildup behavior observed in the field*

A time independent, heterogeneity-related tuning for improved history match and a time dependent component not captured in these modeling exercises are two possible explanations for a closer match to the pressure buildup behavior that was observed in the field, as shown in Figure 1-49. Both explanations represent constrained pore space conditions available for the injected CO<sub>2</sub>. While part of the first explanation is explored in the consequent section using a simpler geometric configuration simulating the Phase III CO<sub>2</sub> injection period, the second explanation is explored briefly in this section to validate the explanations for future investigation.

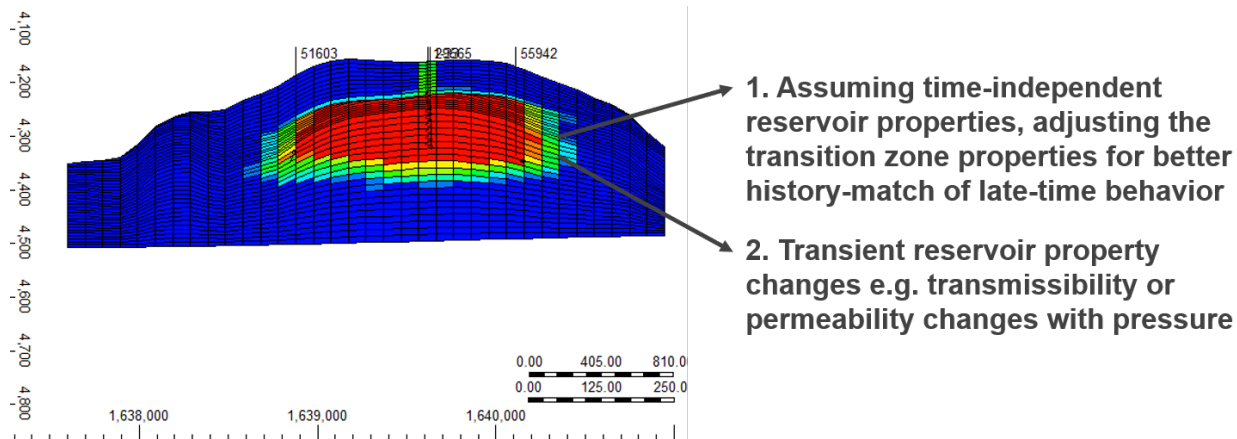


Figure 1-49. Possible explanations investigated to attribute the steeper pressure buildup near end of MRCSP injection.

The investigation of the preliminary effect of time-variant properties, such as well skin changes and permeability changes with increasing CO<sub>2</sub> in the near-well region in the conceptual model M1, is not in the desired direction—the concurrence of the response from all the three wells with field observations is not honored with localized phenomena. Figure 1-50 shows the comparison of pressure response at the injection and monitoring wells for a sample set of trials with increasing positive skin (+4 and +8) at the injection well during the early 2014 period. This reinforces the criticality of reservoir heterogeneity characterization in the current conceptual model and the assumption that incremental tuning to represent the same would result in a more rigorous history match if needed.

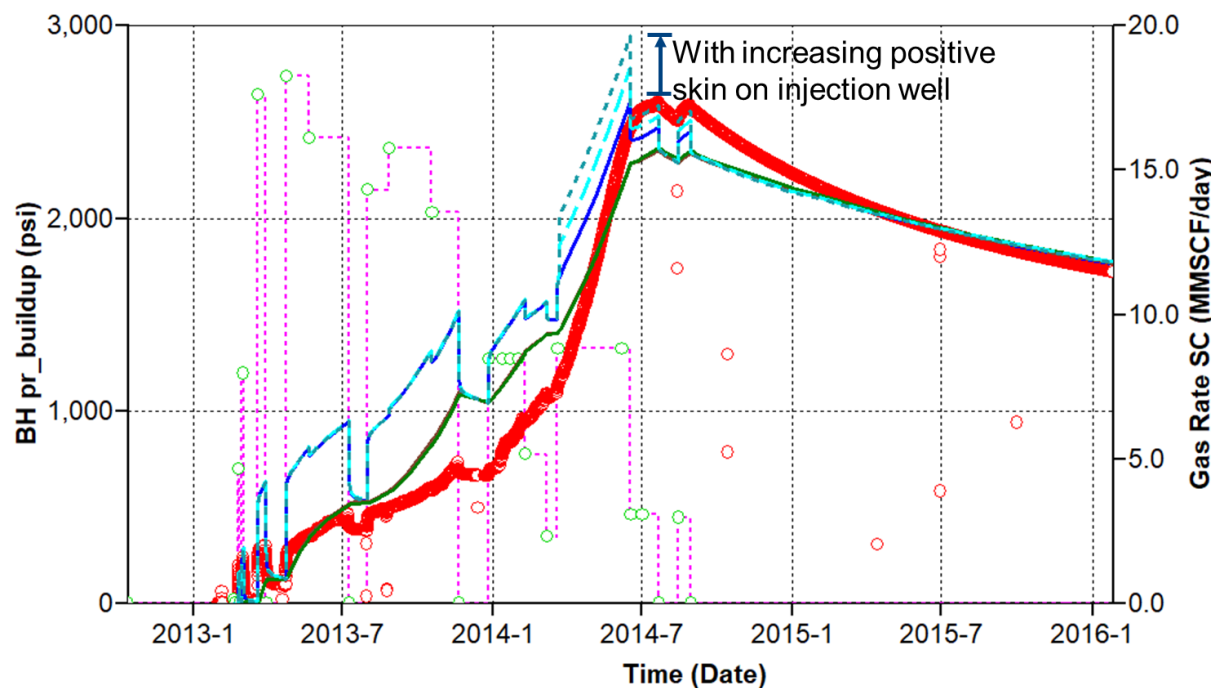


Figure 1-50. Modeled pressure buildup during MRCSP injection period with increasing positive skin on injection well. While the trend of pressure buildup is steeper, the behavior of the injection well (blue model curves) deviates from the monitoring wells (overlying brown and green model curves), which is not in alignment with field observations. Reference M1 model does not have any well skin (i.e. skin = 0) modeled. Also, here the red circles represent observed field pressure data, green circles represent simplified field CO<sub>2</sub> injection rate data, and magenta lines are the modeled CO<sub>2</sub> injection rate.

#### Radial Configuration for MRCSP CO<sub>2</sub> Injection Period

Equivalent homogeneous zones are created within the reef based on understanding of geology affecting the pressure response while ensuring the original oil-in-place and reservoir conditions are honored. The reef geometry is simplified to a radial configuration in this set of trials that considers only the Phase III CO<sub>2</sub> injection period with the equivalent radial single-well model. The model (right column of panels in Figure 1-40) is assumed to be symmetric with the injection well located at the center of the model. Since the equivalent homogeneous radial CMG-GEM® model realizations used in this analysis were initialized with the fluid distribution and reservoir conditions corresponding to the end of secondary recovery/beginning of MRCSP Phase III injection, there is no history matching exercise for the historic reef production-injection operations.

Figure 1-51 shows the injection well pressure buildup during Phase III injection period. With this conceptualization, the modeled injection wells' bottomhole pressure follows the steep increasing trend of the field pressure response very closely but model shifted from peak field observed values by ~250-275psi with the current reservoir property distributions considered. The decline trend is very well captured in this configuration. A simpler representation of the reef heterogeneity thus captured the final decline trend well but missed the extent of pressure buildup seen during the final injection period while simulating Phase III CO<sub>2</sub> injection. Further tuning of the rock properties for history matching was not conducted as the learnings from this model were applied to develop and set up the Level 3 lithofacies model that included new additional characterization data from the reef.

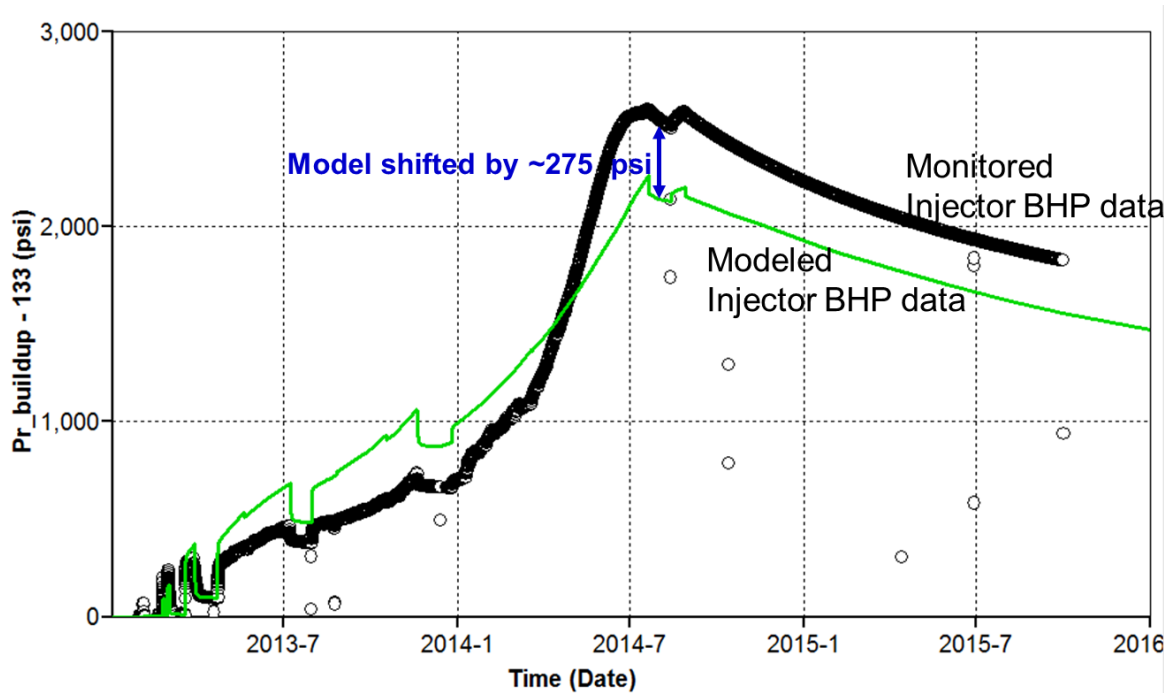


Figure 1-51. Modeled injection well bottomhole pressure buildup response during the MRCSP Phase III CO<sub>2</sub> injection period in the equivalent radial M2 model conceptualization. Here, the black circles represent observed field pressure data while the green curve is the modeled injector bottomhole pressure buildup.

### Simulated Pressure History for Mini-injection Test

A mini- injection test was carried out in the reef that involved injecting 883 tonnes of CO<sub>2</sub> from February 4-8, 2016. The CO<sub>2</sub> injector pressure response predictions from equivalent radial single-well model were tested successfully with response predictions for this mini- injection test during February 2016. As shown in Figure 1-52, there was only a minor discrepancy of ~52 psi between the scaled model bottomhole pressure response and the observed field bottomhole pressure response in Dover-33.

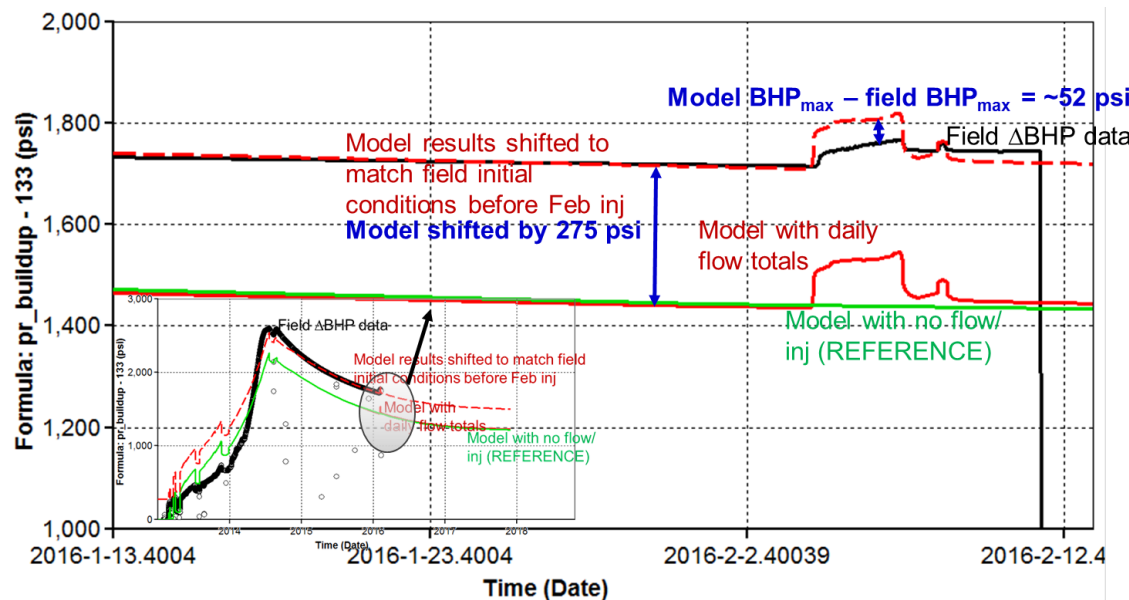


Figure 1-52. Comparison of simulated and observed pressures in the equivalent radial single-well model.

### Total Compressibility Calculations for Injectivity Analysis

Another independent evaluation of the injectivity was performed by calculating the effective total compressibility of the system using field pressure build-up test values during CO<sub>2</sub> injection. Figure 1-53 shows the resulting total compressibility values for each injection period.

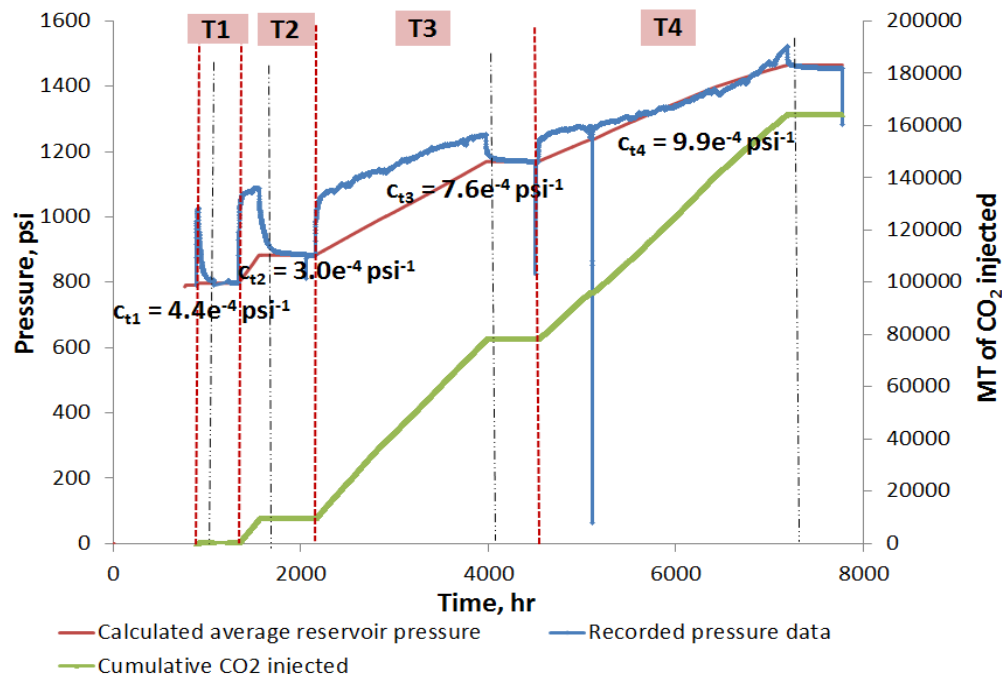


Figure 1-53. Plot of pressure with total compressibility annotated for each CO<sub>2</sub> injection period. Total compressibility is calculated such that average reservoir pressure matches recorded field pressure data.

The obtained values for injection periods T1 through T4 lie in the range of values consistent with the presence of dominant gaseous phase in typical oil and gas systems. In subsequent injection periods, as supercritical CO<sub>2</sub> phase dominates the reservoir pore volume with additional CO<sub>2</sub> injected, increasing reservoir pressures could result from the decreasing total compressibility of this dynamic system. Lessons learned from this basic exercise can be drawn upon for possible use in injectivity evaluation of other reefs in the region.

The total compressibility from the T4 injection period can potentially be reliably used to predict the pressure build-up for target injection rates or injection rates possible for target pressure differentials planned for operation (assuming reservoir conditions remain unchanged once CO<sub>2</sub> is in supercritical phase). This total compressibility can also be reliably used to predict the pressure build-up for target injection rates or injection rates possible for target pressure differentials planned for operation.

## 1.5 Geochemical Modeling

Multiple processes can affect the fate and transport of CO<sub>2</sub> in the subsurface, including advection, dispersion, and mixing/dilution among other hydrodynamic processes, as well as chemical processes such as water/rock interactions, partitioning into aqueous and non-aqueous phases (e.g., oil), and dissolution/precipitation of in situ carbonate minerals (Hitchon, 1996). Characterizing the relevant processes affecting CO<sub>2</sub> transport for a given subsurface environment is essential to determine the fate of the injected CO<sub>2</sub> and to estimate the storage characteristics of that reservoir.

This task is performed as part of the dynamic modeling activities for the Dover-33 reef in order to demonstrate capability to model geochemical effects of CO<sub>2</sub> injection within a dynamic modeling framework. This task aims to implement multicomponent flow simulation coupled with phase and chemical equilibrium and rate-dependent mineral dissolution/ precipitation to evaluate effects of geochemical processes on short-term observed pressure response during the injection period. It also demonstrates longer-term behavior associated with CO<sub>2</sub> storage processes. Relevant field data collected as part of the geochemical monitoring program under MRCSP for the analysis of general geochemical parameters of fluids and gases sampled and analysis of core samples to determine geochemical processes occurring in the Niagaran reef structure, especially in Dover-33, because of CO<sub>2</sub> injection (Welch et al., 2019) were utilized where applicable in the coupled dynamic models.

### 1.5.1 Modeling Approach

The task incorporates interacting geochemistry with subsurface flow dynamics involving all three fluid phases and injected CO<sub>2</sub> to better understand the role of various processes in our system of interest. The system of interest considered for the current study is a simplified equivalent coupled flow-geochemical model in CMG-GEM® similar to the synthetic radial model, described in Mishra et al., 2017. This radial model was subject to an assumed CO<sub>2</sub> injection period to assess the impact of geochemical reactions on the observed pressure buildup during injection and the fate of the CO<sub>2</sub> through an extended 1000-year post-injection monitoring period. The methodology involved the following key steps:

- a. The reference simplified representative model involving CO<sub>2</sub> injection in a depleted oil reservoir without geochemistry was implemented in CMG-GEM®
- b. Required geochemistry-related input data such as mineralogy and fluid sampling data from the field, as well as previous equilibrium model considerations for the Dover-33 reef, were collected
- c. The geochemical module was included and set up in GEM for the CO<sub>2</sub> injection period and the simplified representative reef model was re-initialized

d. Basic numerical sensitivity analyses were run to observe impact of geochemical reactions during and after the defined CO<sub>2</sub> injection period in the depleted oil reservoir and the coupled flow-geochemical model was compared with the reference model without geochemistry.

The geochemical modeling under CO<sub>2</sub> injection conditions considered the following important factors affecting CO<sub>2</sub> sequestration: (1) the kinetics of chemical interactions between the host rock minerals and the aqueous phase, (2) CO<sub>2</sub> solubility dependence on pressure, temperature and salinity of the system, and (3) redox processes that could be important in deep subsurface environments. Figure 1-54 shows a schematic of the basic considerations for reactive transport modeling of geologic carbon sequestration. For a constant CO<sub>2</sub> injection rate constraint imposed on the injection well, the effect of including geochemical reactions on the pressure buildup response in the closed reservoir was compared. The CO<sub>2</sub> sequestration capacity of both aqueous and mineral phases was evaluated. Potential changes in the porosity and consequently permeability due to mineral dissolution or precipitation were also monitored.

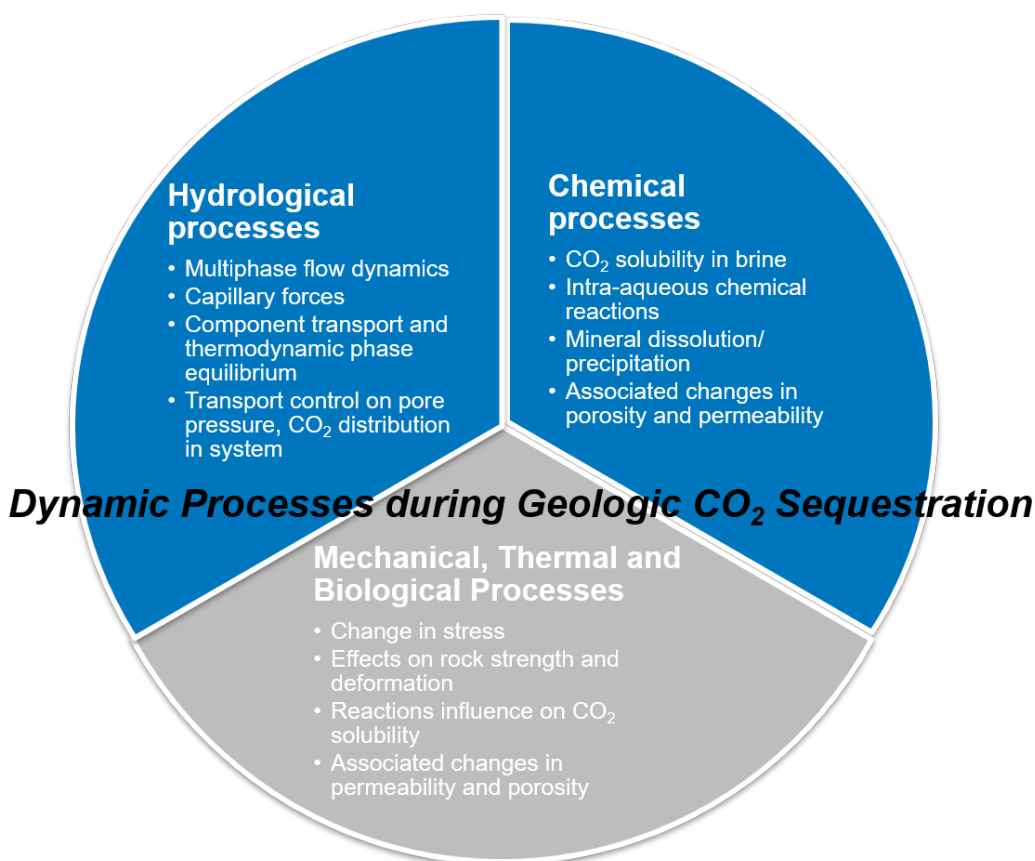


*Figure 1-54. Schematic with considerations for the reactive and non-reactive processes considered during investigation of the dynamics of geologic carbon sequestration. The coupled model implemented in the current study thus included considerations for relevant hydrological and chemical processes indicated in Blue.*

### 1.5.2 Geochemical Reactions in the Subsurface

There are four main ways by which carbon dioxide is retained in geologic formations. The most common and important trapping mechanism is hydrodynamic or structural trapping, in which CO<sub>2</sub> can be trapped as a gas or supercritical fluid under a low permeability caprock. A longer-term trapping mechanism involves the reaction of CO<sub>2</sub> directly or indirectly with the in-situ brine and minerals such as calcite and dolomite in the geologic formation. Depending on the mineralogy of the formation, these reactions can induce the precipitation of secondary carbonate minerals that essentially corresponds to the conversion of CO<sub>2</sub> into minerals. This so-called 'mineral trapping' (Bachu et al., 1994), is potentially attractive because it could essentially immobilize CO<sub>2</sub> for very long periods of time. The dissolution of alkaline aluminosilicate minerals by CO<sub>2</sub> will also increase the concentration of soluble carbonates and bicarbonates in solution, thereby enhancing "solubility trapping."

Ortoleva et al. (1998) describe the chemical reactions induced by CO<sub>2</sub> injection. Basic geochemical processes include CO<sub>2</sub> dissolution into the formation water and decomposing into HCO<sub>3</sub><sup>-</sup> and H<sup>+</sup> (the latter acidizes the water), and mineralization. CO<sub>2</sub> mineralization is the result of chemical reactions between HCO<sub>3</sub><sup>-</sup> and other ions with the minerals in place to form new carbonate minerals. The ratio (Q<sub>β</sub>/K<sub>eq,β</sub>) is called the saturation index of the reaction where K<sub>eq,β</sub> is the chemical equilibrium constant for mineral reaction β and Q<sub>β</sub> is the activity product of mineral reaction β. If (Q<sub>β</sub>/K<sub>eq,β</sub>) > 1, mineral dissolution occurs and if (Q<sub>β</sub>/K<sub>eq,β</sub>) < 1, mineral precipitation occurs. Actual sequestration capacity depends on the geochemical and physical conditions.

Chemical reactions occur between components in the aqueous phase and between minerals and aqueous components. The components in the aqueous phase comprise gaseous components that are soluble in the aqueous phase (CO<sub>2</sub>), as well as components that exist only in the aqueous phase (NaCl). Typically, reactions between components in the aqueous phase are fast relative to mineral dissolution/precipitation reactions (Nghiem et al., 2009). Therefore, intra-aqueous reactions are represented as chemical equilibrium reactions, whereas mineral dissolutions/precipitations are represented as rate-dependent reactions in GEM.

### 1.5.3 Model Setup and Scenarios

The model considered for this task has a radial configuration representing an oil reservoir with one vertical production well at the center that is later converted into a CO<sub>2</sub> injection well following primary depletion. The model, consisting of a core reservoir region with an overlying low permeability zone and an underlying water column, has with logarithmically increased grid spacing in the radial direction to ensure more resolution closer to the well where most of the dynamic processes would be centered. Modeled rock and fluid properties are similar to the synthetic radial model described in earlier work, as referenced in Section 1.6. The porosity and permeability of the 131 ft reservoir zone were 7 percent and 23 mD, respectively. The porosities of the overlying 79 ft of low permeability rock and underlying 102 ft of water column were 0.1 percent and 6 percent respectively, while their permeabilities were defined to be 1E- mD and 2 mD, respectively. Figure 1-55 shows the model porosity and permeability, while Table 1-13 summarizes the rock properties modeled in the system of interest.

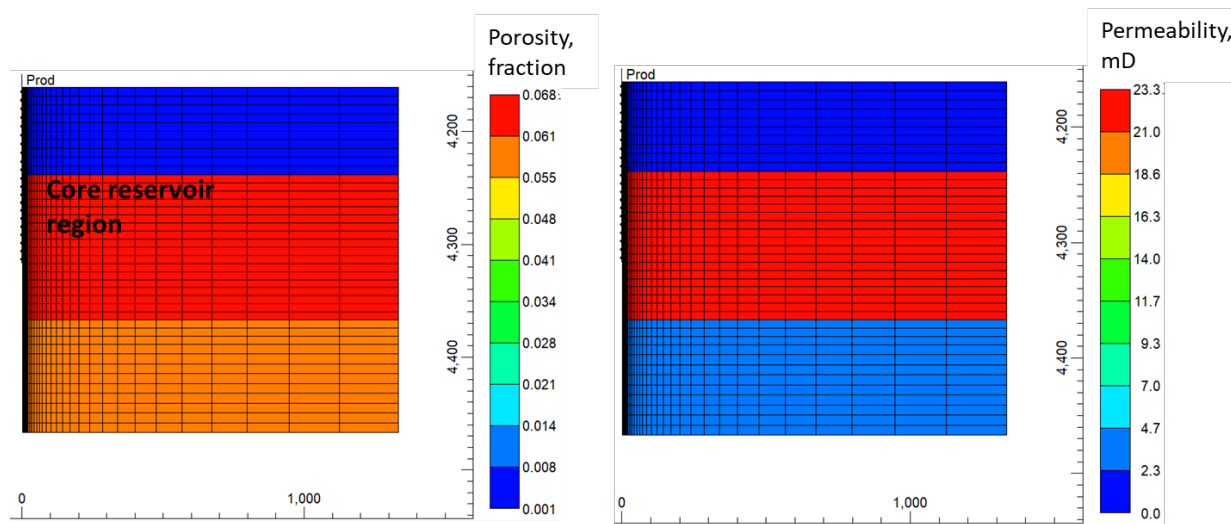


Figure 1-55. Radial model cross-section showing the porosity (left panel) and permeability (right panel) in the system.

Table 1-13. Petrophysical properties of the different zones in the modeled system of interest.

Petrophysical Property	Overlying Low Permeability Zone	Core/ Middle Reservoir Zone	Underlying Water Column Zone
Thickness, m (ft)	24 (79)	40 (131)	31 (102)
Porosity, %	0.1	7	6
Permeability, mD	1E-4	23	2

The model was initialized at a pressure of ~2900 psi at a reference depth of ~4400 ft with no initial gas cap present. Table 1-14 lists the composition and molecular weights of the pseudocomponents in the in situ hydrocarbon fluid phase modeled. The PVT model used was the modified Peng-Robinson EOS (Peng and Robinson, 1976). The fluid property was modeled by utilizing seven pseudocomponents to represent different hydrocarbon components similar to the Dover-33 fluid characterization to be used for the numerical evaluation exercises in the current study. It was produced for a period of 10 years at a constant bottom-hole pressure of ~100 psi, during which 1.1 MMSTB or approximately 48 percent of the original oil-in-place was produced. Thereafter, CO<sub>2</sub> was injected at a constant rate of 500 MT per day using a gradual ramp-up schedule, i.e., (1) one month injection and two week shut-in, (2) two month injection and three week shut-in, (3) three-month injection and four week shut-in, and (4)-(5) two additional periods of six month injection and four week shut-in. A total of 273,592 tonnes of CO<sub>2</sub> was thus injected but no production phase following primary recovery. Figure 1-56 shows the three-phase relative permeability curves implemented in the model.

**Table 1-14. Molecular weights of the pseudocomponents in the fluid modeled.**

Component	Mol. Weight	Initial Mole Fraction
F1	16.116	0.409
CO <sub>2</sub>	44.010	0.001
F3	44.207	0.202
F4	95.459	0.174
F5	179.68	0.147
F6	297.181	0.028
F7	530.093	0.039

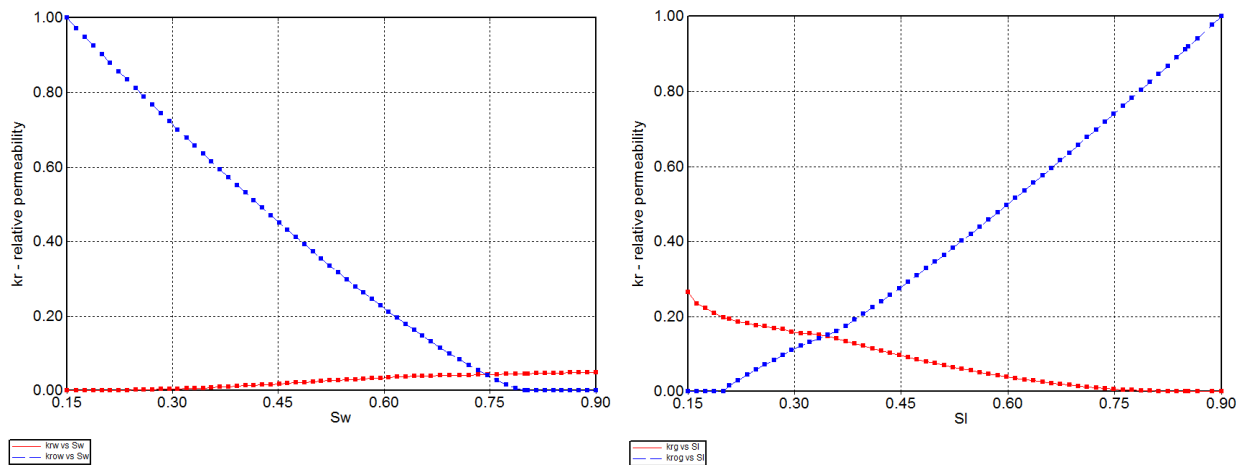


*Figure 1-56. Oil-water and gas-oil relative permeability curves used.*

The gas density is calculated with the Peng-Robinson EOS. The gas viscosity is estimated from the Jossi, Stiel and Thodos correlation (Reid et al., 1977). The aqueous phase density and viscosity are calculated respectively from the Rowe and Chou (1970) correlation and the Kestin et al. (1981) correlation.

Geochemical coupled modeling was implemented only during the CO<sub>2</sub> injection period in the model to gain insights into the effect of introducing CO<sub>2</sub> solvent in the system of interest. For the coupled modeling trials, to model geochemical reactions within the simulator, the following reactive minerals and associated ions were specified based on geochemical studies performed in Dover-33:

- Thirteen (13) relevant aqueous components were 'OH<sup>-</sup>', 'H<sup>+</sup>' (water speciation), 'HCO<sub>3</sub><sup>-</sup>', 'CO<sub>3</sub><sup>2-</sup>' (CO<sub>2</sub> speciation), 'Na<sup>+</sup>', 'K<sup>+</sup>', 'Cl<sup>-</sup>', 'Ca<sup>2+</sup>', 'Mg<sup>2+</sup>', 'CaCl<sup>+</sup>', 'MgCl<sup>+</sup>', 'NaCl' and 'KCl' (for ionic strength calculation and carbonate dissolution)
- Two (2) selected predominant reactive minerals were calcite and dolomite

Table 1-15 shows the sample water composition from the *Geochemical Changes in Response to CO<sub>2</sub> Injection in a CO<sub>2</sub>-EOR Complex in Northern Michigan report* [Place et al., 2020] used to initialize the GEM model for the primary aqueous components. The brine sample considered displays very high salinity and a low pH.

**Table 1-15. Summary of brine geochemistry used to initialize the aqueous composition in the coupled GEM model**

Constituent	Molality, Moles/kg Water
Ca <sup>2+</sup>	1.84
Mg <sup>2+</sup>	0.36
Na <sup>+</sup>	0.64
K <sup>+</sup>	0.37
Sr <sup>2+</sup>	0.031
Cl <sup>-</sup>	5.85
SO <sub>4</sub> <sup>2-</sup>	0.0011
HCO <sub>3</sub> <sup>-</sup>	0.00352
Br	--
Fe <sup>2+/3+</sup>	0.0034
SiO <sub>2</sub>	6.50e-07
pH	4.1
Alkalinity (mg/L as HCO <sub>3</sub> <sup>-</sup> )	357
Salinity (g/kg)	380

Chemical equilibrium reactions considered in the coupled CMG-GEM® model based on the dominant chemical species in the aqueous phase are shown in Table 1-16.

**Table 1-16. Intra-aqueous chemical reactions considered for geochemistry in the coupled model**

Reaction	Chemical Equilibrium Constant (log)
'CO <sub>2</sub> ' + 'H <sub>2</sub> O' = 'H <sup>+</sup> ' + 'HCO <sub>3</sub> <sup>-</sup> '	-6.332E+00
'CaCl <sup>++</sup> ' = 'Ca <sup>++</sup> ' + 'Cl <sup>-</sup> '	-5.880E-01
'MgCl <sup>++</sup> ' = 'Mg <sup>++</sup> ' + 'Cl <sup>-</sup> '	-7.995E-02
'OH <sup>-</sup> ' + 'H <sup>+</sup> ' = 'H <sub>2</sub> O'	1.347E+01
'CO <sub>3</sub> <sup>2-</sup> ' + 'H <sup>+</sup> ' = 'HCO <sub>3</sub> <sup>-</sup> '	1.026E+01
'NaCl' = 'Na <sup>+</sup> ' + 'Cl <sup>-</sup> '	1.443E+00
'KCl' = 'K <sup>+</sup> ' + 'Cl <sup>-</sup> '	1.485E+00

Calcite and dolomite are assumed to be the two reactive minerals in the system of interest for the current numerical analyses. Mineral reactions considered are shown in below Table 1-17 (Thibeau and Nghiem, 2007; Xu et al., 2004; Kharaka et al, 1989; Delany and Lundeen, 1990).

**Table 1-17. Mineral dissolution/precipitation reactions considered in the coupled GEM model**

Reactions	log $K_{eq}^m$ (50 °C)	log $k_\beta$ [mol/(m <sup>2</sup> s)] at 25 °C	$\hat{A}_\beta$ [m <sup>2</sup> /m <sup>3</sup> ]	$E_{a\beta}$ [J/mol]
Calcite + H <sup>+</sup> = Ca <sup>++</sup> + HCO <sub>3</sub> <sup>-</sup>	1.3560	-8.79588	88	41,870
Dolomite + 2H <sup>+</sup> = Ca <sup>++</sup> + Mg <sup>++</sup> + HCO <sub>3</sub> <sup>-</sup>	1.6727	-9.2218	88	41,870

A damping factor was defined for all aqueous reactions using the keyword CRDAMP-ALL. This causes the aqueous reactions in the model to achieve equilibrium in a rate-based manner rather than instantaneously. This is typically the case when using field-scale block sizes when the instantaneous equilibrium assumption may not be valid. Using a damping factor value equal to 0.1 molal/day, equilibrium is reached within a short period of time and works well for nearly all cases. With this option, the model can converge better, and the number of time-step cuts is reduced drastically.

#### 1.5.4 Results

The task illustrates the impact of mineralogy and aqueous components on the CO<sub>2</sub> storage processes. The key identified metrics mentioned in this section are extracted and analyzed to improve our understanding of the role of different subsurface processes in both the reference and coupled models.

##### *During CO<sub>2</sub> Injection*

Output metrics of interest are (a) pressure response and (b) global mole fraction of CO<sub>2</sub>. The average system pressure at the end of depletion and prior to start of the CO<sub>2</sub> injection phase was 1082 psi. Figure 1-57 shows the comparable pressure response to CO<sub>2</sub> injection in the depleted radial model with and without geochemical coupling for the different injection periods. The average reservoir pressure is seen to rise by 2215 psi for the models at the end of the five injection periods.

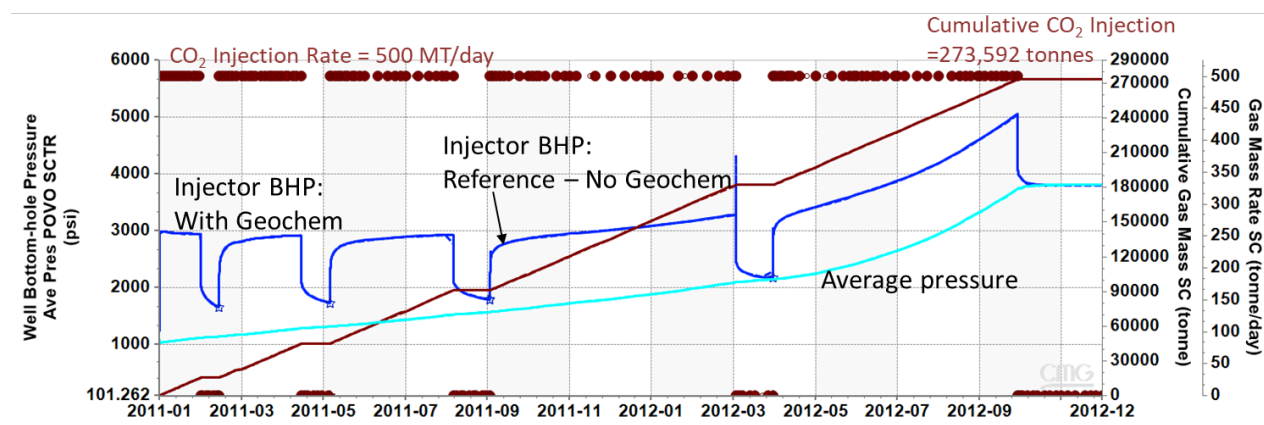


Figure 1-57. Comparison of the pressure (injector bottomhole pressures in blue and average field pressure in cyan) response to CO<sub>2</sub> injection. Five injection-falloff periods feature in the injection schedule (injection rate in symbols and cumulative curves in brown) as shown. The reference model with no geochemistry is shown as continuous curves while the geochemistry-coupled model for the CO<sub>2</sub> injection period is shown as dashed curves.

In addition to pressure response, the CO<sub>2</sub> front progression is also comparable between the models at the end of the last CO<sub>2</sub> injection period. Figure 1-58 shows the global mole fraction of CO<sub>2</sub> in interface Layer 11 and the cross-section of gas saturation at the end of the last CO<sub>2</sub> injection period in the two models.

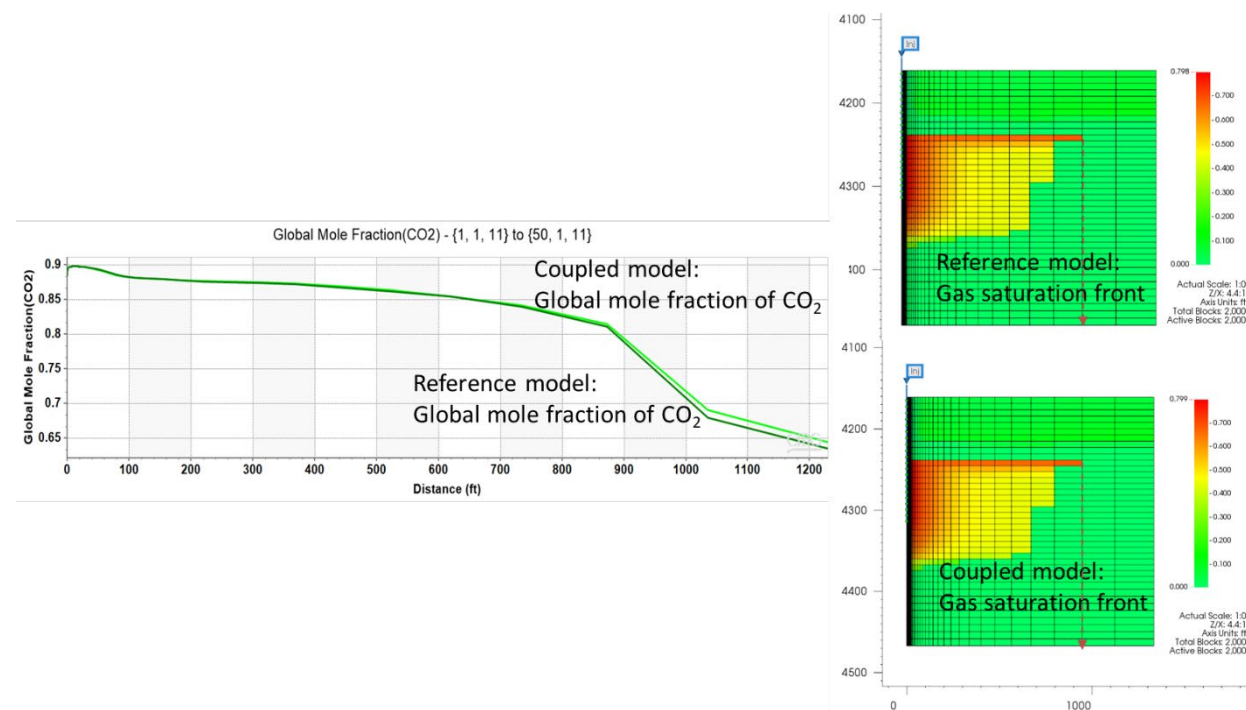


Figure 1-58. Comparison of the gas saturation front and CO<sub>2</sub> presence at the end of the last injection period.

### Post-injection Behavior

Output metrics of interest track the a) pressure and CO<sub>2</sub> saturation front, b) phase state of CO<sub>2</sub> and c) mineralization progress in the system of interest. Variables such as the mole fraction of CO<sub>2</sub> in the gas, oil and aqueous phases, as well as the moles of other ionic aqueous components such as HCO<sub>3</sub><sup>-</sup> help track the phase state of CO<sub>2</sub> and chemical equilibrium reactions taking place over time. Mineralization progress can be tracked using variables such as the number of moles of the different minerals present in the system over time.

#### a) Pressure and CO<sub>2</sub> saturation front

For the given system, the pressure response and propagating CO<sub>2</sub> front show minimal differences during the period of CO<sub>2</sub> injection. During later times in the post-injection period however, there are noticeable differences in the results between the coupled and the reference models with respect to the movement of the gas front and reservoir pressure.

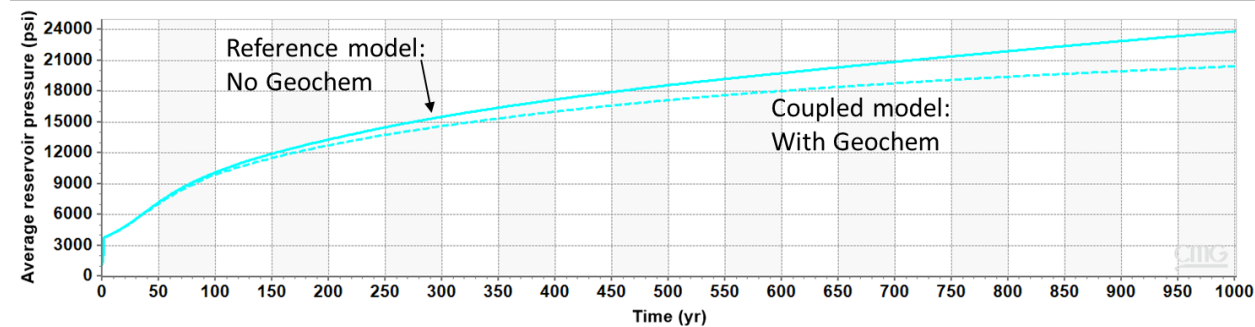


Figure 1-59 shows the comparison of the average reservoir pressure between the two cases. Mineral reactions occurring during the post-injection period are seen to drive lower pressure buildup in the coupled model in comparison to the reference case without geochemical reactions. The effect of these geochemical reactions are validated to be more long-term, as can be seen in the figure by the divergence in the average pressures only post 100-years of the injection.

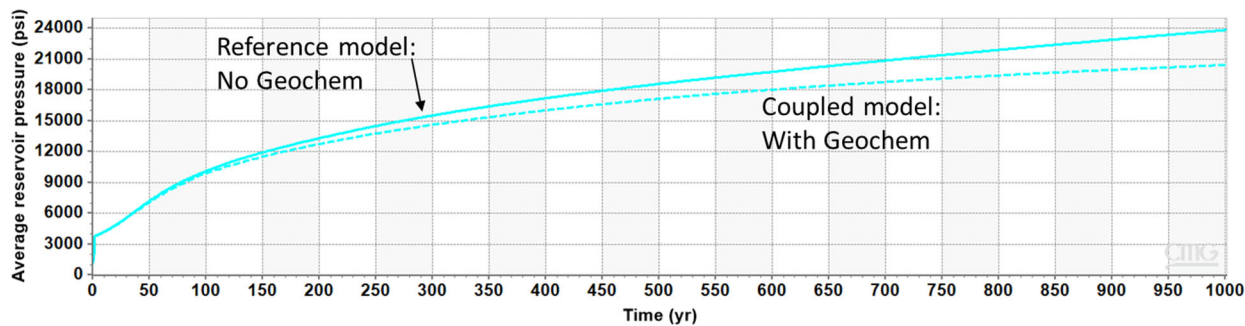


Figure 1-59. Comparison of the average model pressure until the end of the post-injection period. The reference model with no geochemistry is shown as continuous curves while the geochemistry-coupled model for the CO<sub>2</sub> injection period is shown as dashed curves.

Figure 1-60 and Figure 1-61 are difference maps of the model cross-section showing the change in gas saturation and CO<sub>2</sub> presence in the system at the end of 100 years of post-injection and end of simulation (1000 years of post-injection). The injected gas tends to migrate to the top of the core reservoir or high permeability region because of the larger density of the formation water that is displaced. This causes the injected gas to go further into the reservoir near the top, as shown in the figures. The longer-term impact of geochemical reactions is also noted from the larger changes in the difference maps for the 1000-year post-injection period.

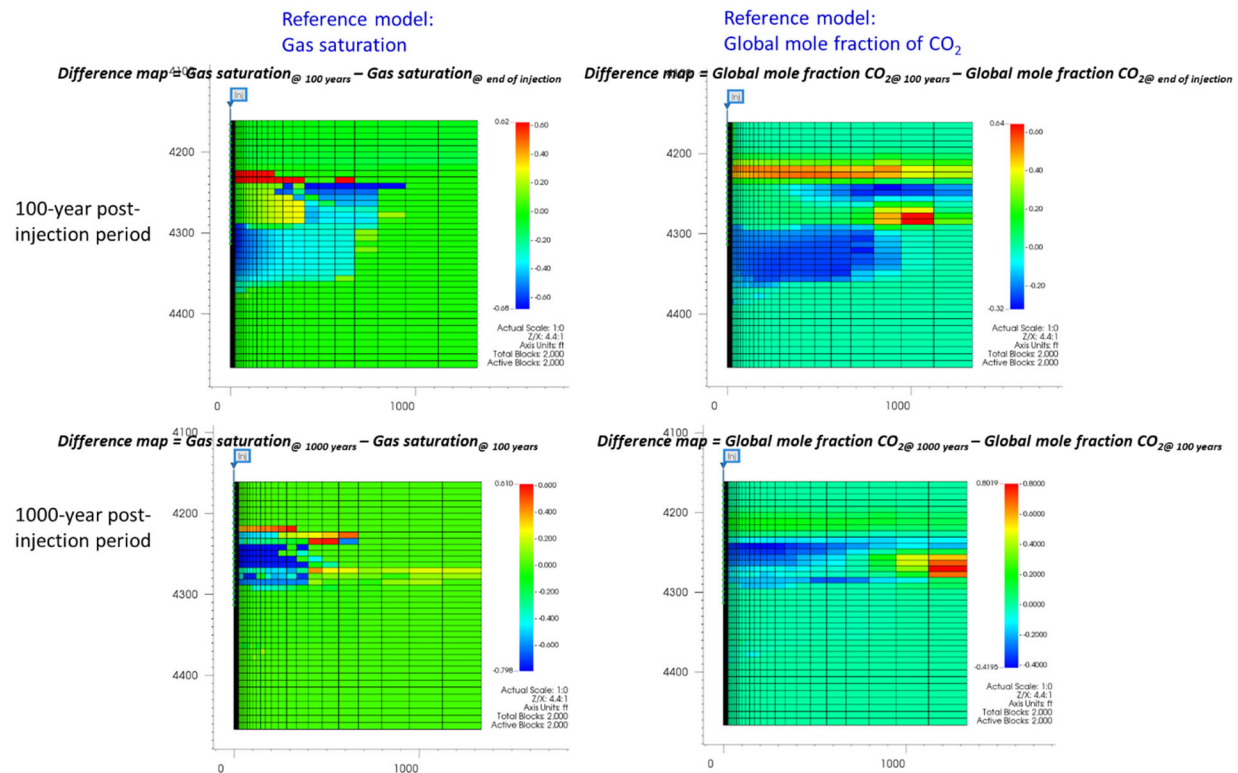


Figure 1-60. Difference maps of model cross-section to highlight comparison of the gas saturation front and CO<sub>2</sub> presence at the end of the 100 years and 1000 years after the injection period in the reference model.

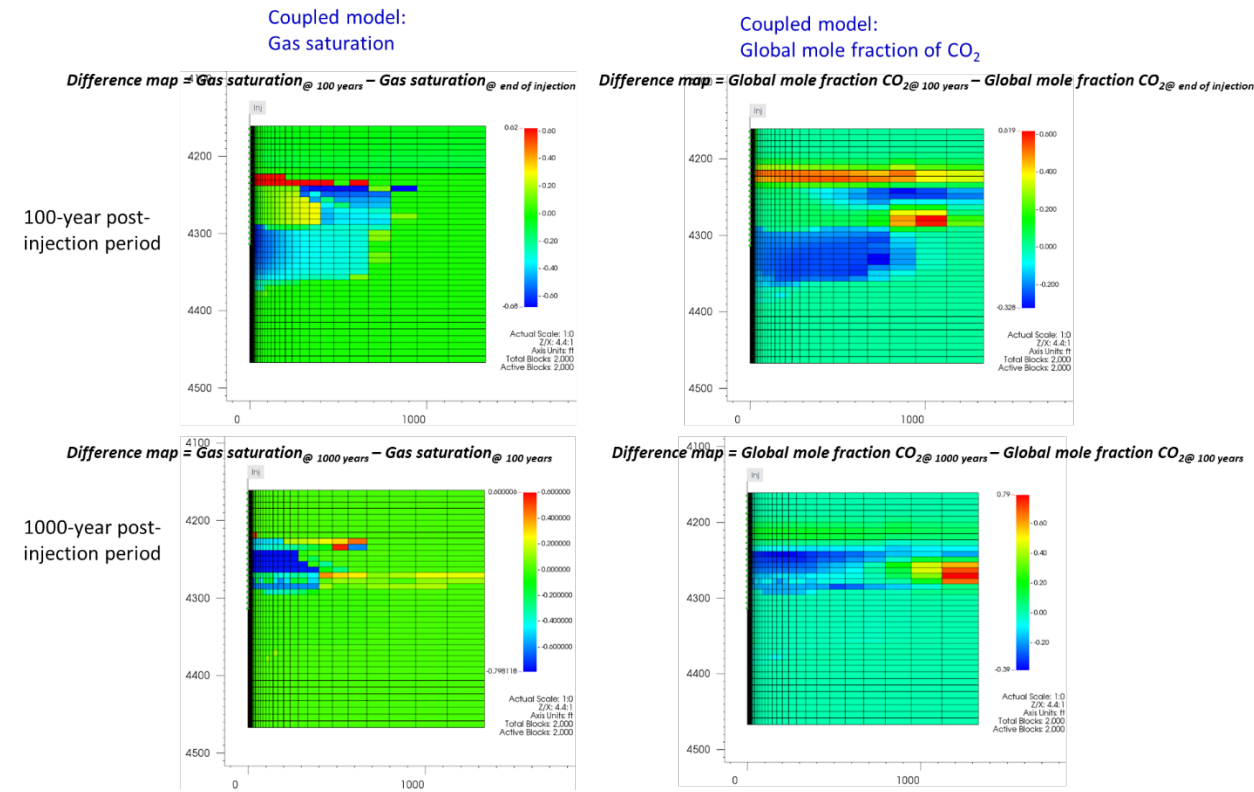


Figure 1-61. Difference maps of model cross-section to highlight comparison of the gas saturation front and CO<sub>2</sub> presence at the end of the 100 years and 1000 years after the injection period in the coupled model.

### b) Phase state of CO<sub>2</sub>

At the end of the injection period in both the reference and coupled models, it is seen that of the 273,592 tonnes or 6.22E+09 moles of CO<sub>2</sub> injected into the system, 97 percent is present in the supercritical phase. Of that, 3 percent was dissolved in the formation brine. Figure 1-62 shows the CO<sub>2</sub> distribution in the different phases at the end of the injection period. As the system works to retain equilibrium, the CO<sub>2</sub> phase distribution changes during the post-injection period. This distribution in the coupled model decreases in the supercritical phase to 96 percent at the end of 100 years and 92 percent at the end of 1000 years, as shown in Figure 1-63 and Figure 1-64. This occurs as more CO<sub>2</sub> moves from a free, dense phase into more stable dissolved phases. The moles of CO<sub>2</sub> in the aqueous phase increase to 5 percent at the end of 100 years and 8 percent at the end of 1000 years in the coupled model, as shown in Figure 1-63 and Figure 1-64. In the reference model, there is slightly more CO<sub>2</sub> in the aqueous phase than in the coupled model during the post-injection period. Additionally, 5 percent of the CO<sub>2</sub> in the system in the aqueous phase at the end of 100 years increases to 9.5 percent at the end of 1000 years as the system attempts to regain equilibrium conditions.

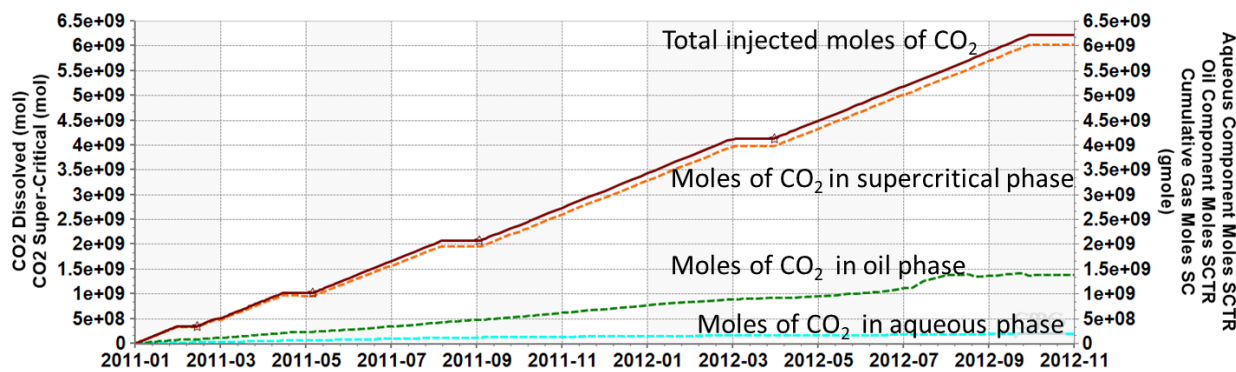
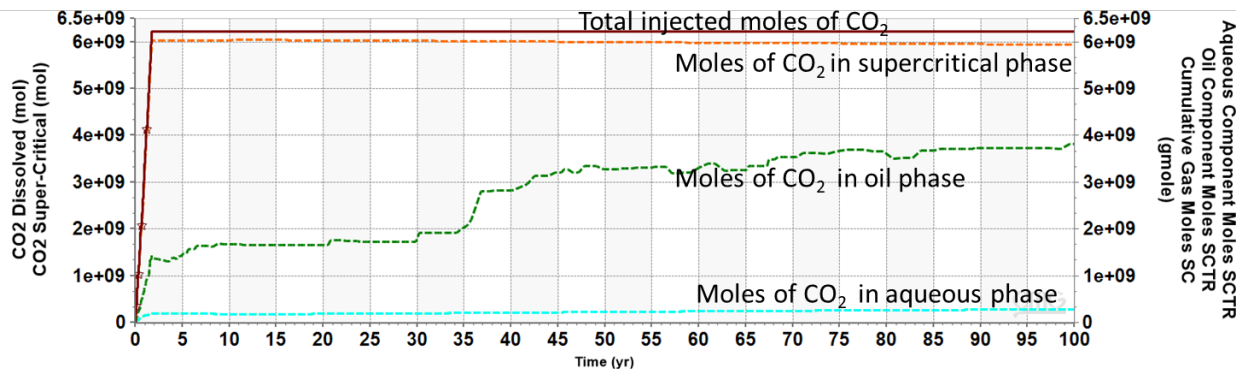
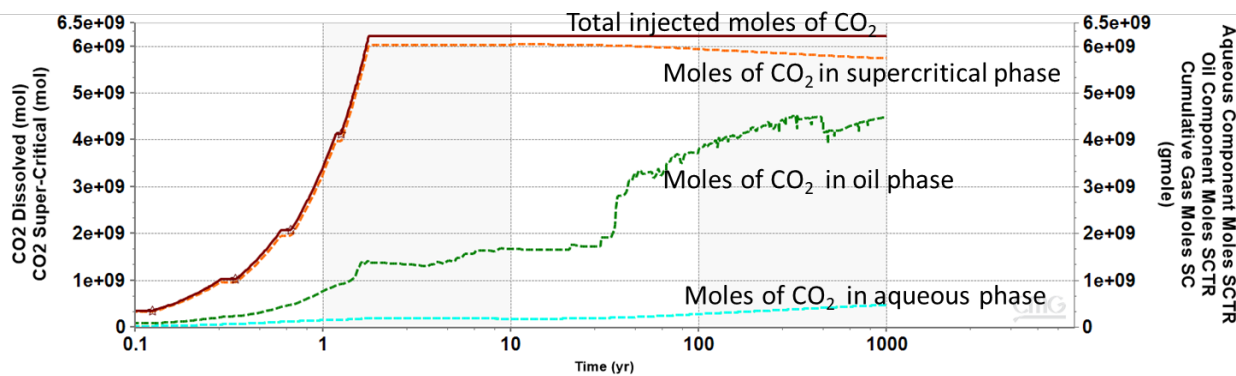
Figure 1-62.  $\text{CO}_2$  distribution in the system at the end of injectionFigure 1-63.  $\text{CO}_2$  distribution in the system at the end of 100 yearsFigure 1-64.  $\text{CO}_2$  distribution in the system at the end of 1000 years

Figure 1-65 shows the evolution of the total moles of  $\text{HCO}_3^-$ ,  $\text{CO}_2$  in dense phase and dissolved  $\text{CO}_2$  in the system of interest. After the injection period, the moles of dissolved  $\text{CO}_2$  increase as more  $\text{CO}_2$  goes into solution in the aqueous phase (brine) and oil phase. The aqueous ions  $\text{H}^+$  and  $\text{HCO}_3^-$  that result from the dissociation of  $\text{CO}_2$  (aq), according to reactions shown in Table 1-17, react with the calcite and dolomite minerals in place.

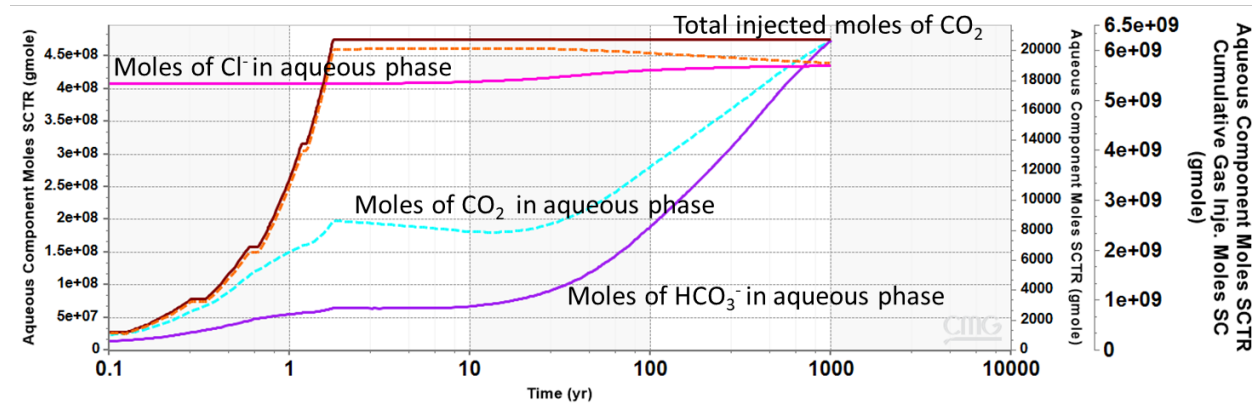


Figure 1-65. Evolution of  $\text{CO}_2$ ,  $\text{HCO}_3^-$  and  $\text{Cl}^-$  until the end of 1000 years

### c) Mineralization progress

The presence of low pH brine with high  $\text{Cl}^-$  in this dolomite-dominant mineralogy triggers the dissolution of dolomite present in the reservoir rock. Bicarbonates ( $\text{HCO}_3^-$ ) are added to the formation water as a result of this dissolution, which results in a negative net mineralization of  $\text{CO}_2$ . Figure 1-66 shows the total amounts of dissolution of these minerals. The saturation index is seen to be negative for both the minerals in the system of interest, which drives their dissolution over time. For the coupled model, the dissolution of calcite and dolomite are small compared to the initial quantity of the minerals, which is at least two orders of magnitude larger. After 1000 years, approximately 0.03 percent of dolomite and 0.5 percent of calcite are dissolved.

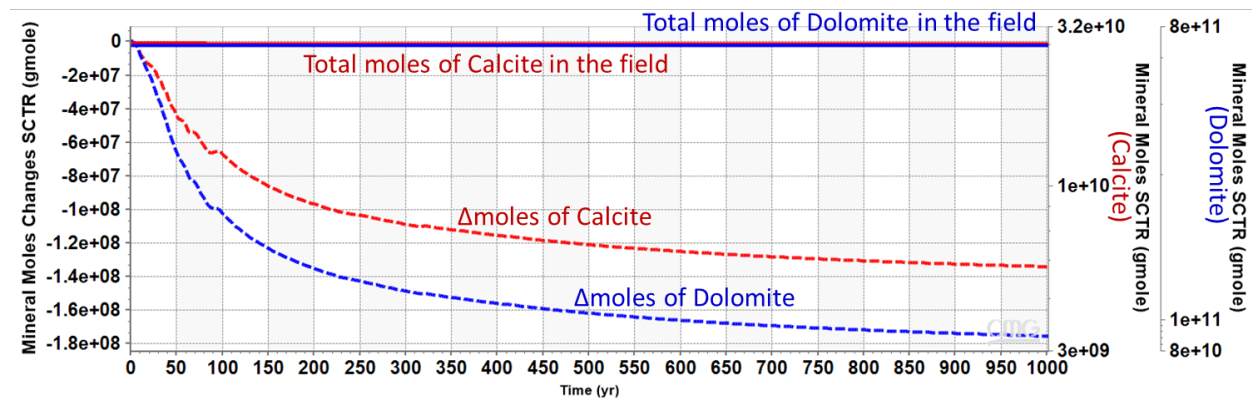


Figure 1-66. Evolution of calcite (red curves) and dolomite (blue curves) in the coupled GEM model

Figure 1-67 shows changes in porosity in the system of interest due to the mineral reactions. As seen, the change in porosity is minor and positive as affected by the extent of dissolution of the in situ reactive minerals considered.

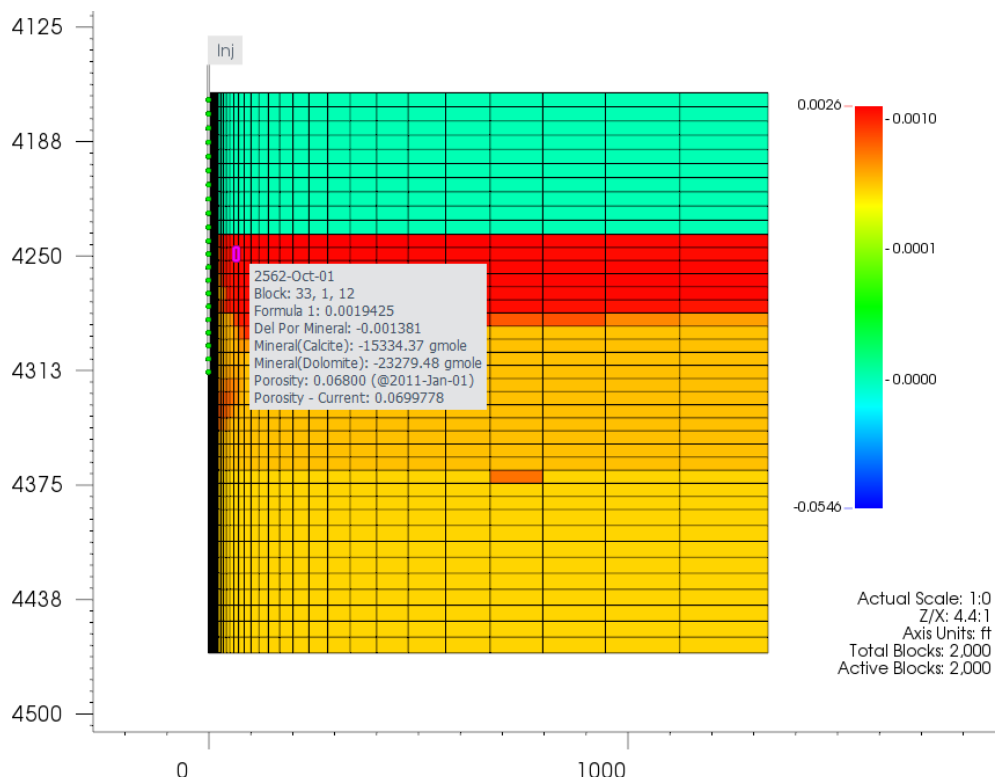


Figure 1-67. Porosity change in coupled model at the end of 1000 years

### Sensitivity Trials

Basic sensitivity analyses were performed to investigate the potential impact of basic reservoir and in situ brine properties on the rate of aqueous and mineral reaction rates in the system of interest. The properties considered for sensitivity analyses were:

- a. effect of reservoir permeability
- b. effect of brine composition i.e. pH

The two scenarios have all other parameters the same as the reference coupled model with only the parameter of interest in each scenario being varied. Insights from the sensitivity analysis scenarios are discussed below.

#### a) Effect of reservoir permeability

Since most of the changes in the system are observed to occur in the core reservoir zone, a sensitivity to the impact of increased reservoir permeability in this zone was investigated. The reference coupled model reservoir permeability of 23.3 mD was compared with a scenario where the reservoir permeability was doubled to 46.6 mD. Figure 1-68 shows the expected lower pressure buildup for a higher permeability reservoir compared to the reference coupled model case for the same amount of injected CO<sub>2</sub> in the system.

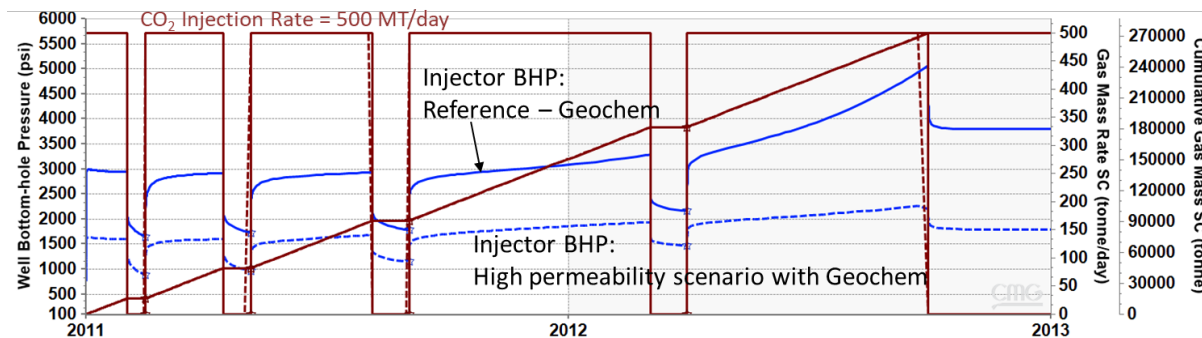


Figure 1-68. Comparison of the injector bottomhole pressure (blue curves) response to  $\text{CO}_2$  injection between the reference coupled model and the high reservoir permeability coupled model. Five injection-falloff periods feature in the injection schedule (injection rate in symbols and cumulative curves in brown) as shown. The reference coupled model is shown as continuous curves while the high reservoir permeability coupled model is shown as dashed curves.

The top panel in Figure 1-69 shows the evolution of the total moles of  $\text{HCO}_3^-$ ,  $\text{CO}_2$  in dense phase and dissolved  $\text{CO}_2$  in the system of interest. For the same mineralogy, reservoir permeability is observed to be inversely related to the mineral reaction rates. Resistance to fluid flow is lower in higher permeability media that resulting in lesser contact that is crucial to drive mineral reactions in the system. There is decreased rate of mineral reactions in the higher permeability reservoir scenario, which leads to lesser  $\text{HCO}_3^-$  in the system (Table 1-17). The bottom panel in Figure 1-69 shows the total amounts of dissolution of these minerals.

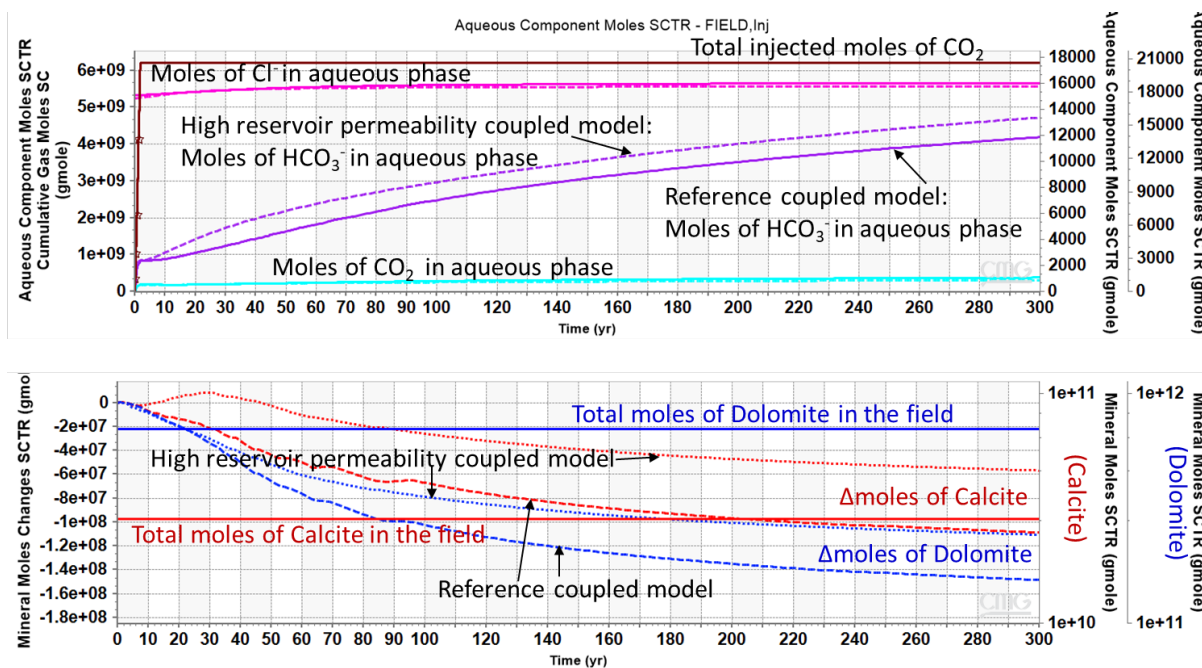


Figure 1-69. Comparison plots for the sensitivity to reservoir permeability (Top) Evolution of  $\text{CO}_2$ ,  $\text{HCO}_3^-$  and  $\text{Cl}^-$  for 300 years (Bottom) Evolution of calcite (red curves) and dolomite (blue curves) in the coupled GEM models.

### b) Effect of brine composition

Formation brine composition affects properties like salinity and pH that are crucial to the dynamics of CO<sub>2</sub> behavior in the system of interest. It is expected that higher brine salinity would result in a denser brine, which would result in a higher bottomhole pressure response at the CO<sub>2</sub> injection well for a given amount of CO<sub>2</sub> being injected into the system. The scenario for the current sensitivity analysis focused on the effect of pH. The reference coupled model pH of 4.1 was compared with a scenario where the brine pH was increased to 7.5. Despite a positive saturation index as shown in Figure 1-70 for a higher formation brine pH, the high salinity brine is still seen to trigger mineral dissolution with a higher reaction rate.

The top panel in Figure 1-71 shows the evolution of the total moles of HCO<sub>3</sub><sup>-</sup>, CO<sub>2</sub> in dense phase and dissolved CO<sub>2</sub> in the system of interest. The alkaline scenario has predominantly more CO<sub>2</sub> as aqueous ions like HCO<sub>3</sub><sup>-</sup> in the system compared to the more neutral reference brine scenario. The bottom panel in Figure 1-71 shows the total amounts of dissolution of these minerals.

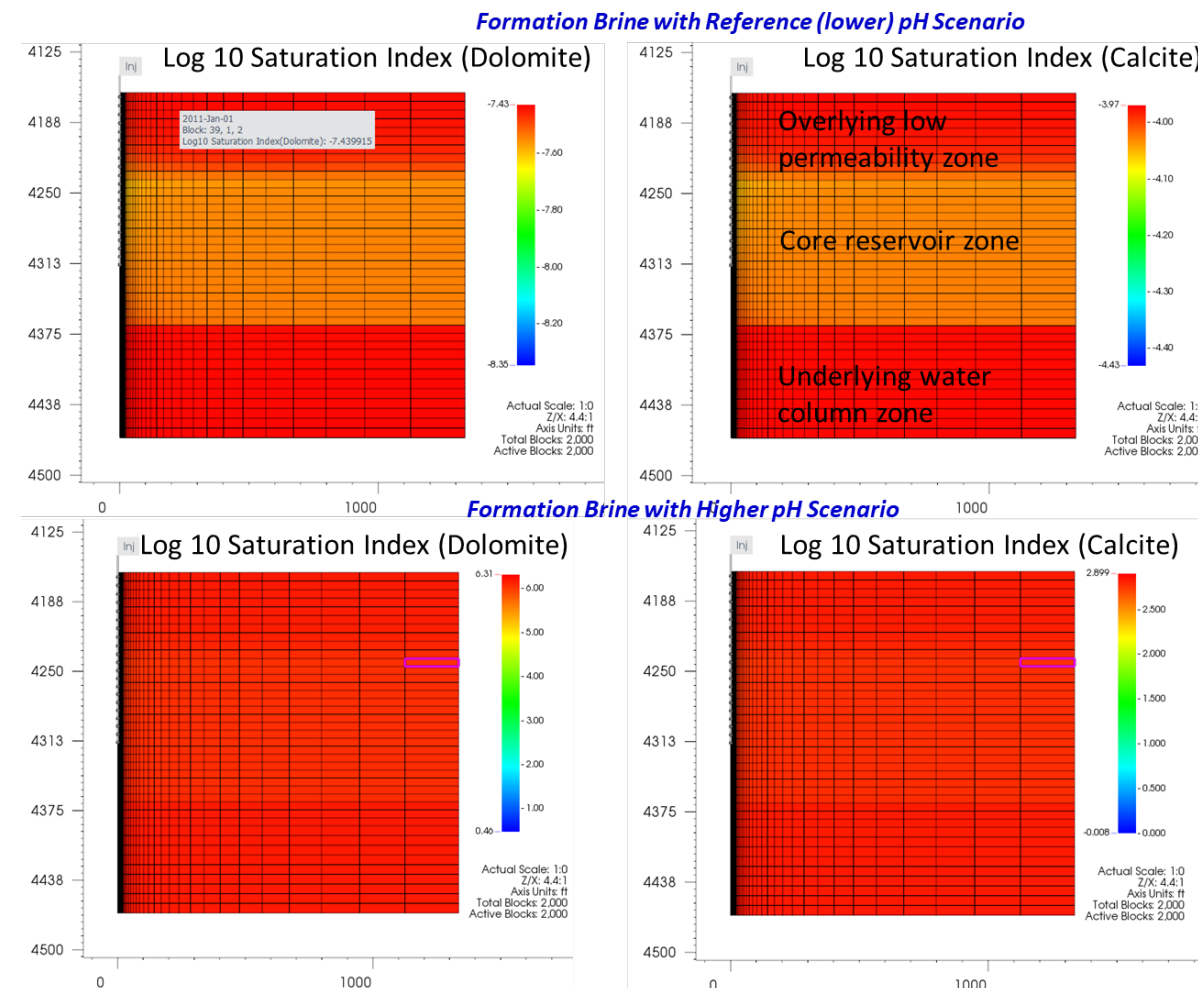


Figure 1-70. Log 10 saturation indices for the dolomite (left column) and calcite (right column) minerals in the pH sensitivity trials. The top row corresponds to the reference pH coupled model while the bottom row corresponds to the higher pH coupled model scenario during the CO<sub>2</sub> injection period.

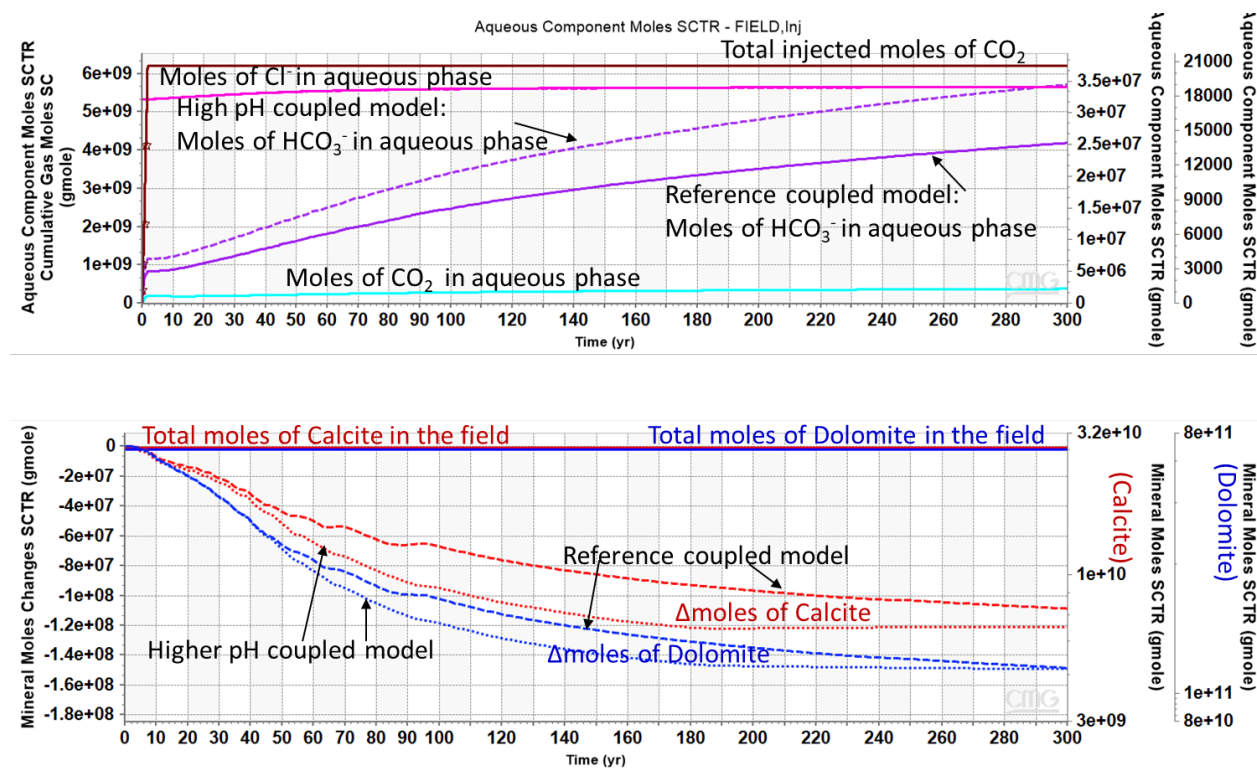


Figure 1-71. Comparison plots for the sensitivity to formation brine pH (Top) Evolution of  $\text{CO}_2$ ,  $\text{HCO}_3^-$  and  $\text{Cl}^-$  until the end of 300 years (bottom) Evolution of calcite (red curves) and dolomite (blue curves) in the coupled GEM models.

### 1.5.5 Summary

Numerical modeling is essential to improve understanding of subsurface dynamics in both short-term and long-term and relevant drivers affecting transport of injected  $\text{CO}_2$  that cannot always be conveniently simulated in the laboratory or the field. Several studies such as Gaus et al., 2005; Audigane et al., 2007; Andre et al., 2007 and Dalkhaa et al., 2013 investigate the effect of geochemical reactions on aspects of containment and storage integrity in saline aquifer systems. On the other hand, few  $\text{CO}_2$  reactive transport modeling studies have been successfully evaluated with considerably fewer insights for geochemical reactions in oil reservoir systems. The geochemical monitoring program under MRCSP provided valuable field data and systematic analyses on the geochemistry of the brines in the Niagaran reefs, especially Dover-33, using brine and gas samples collected to determine changes occurring between reefs prior to and following  $\text{CO}_2$  injection. The general chemical analyses and basic chemical equilibrium models indicated that the reef brines are supersaturated with respect to many carbonate minerals (calcite, aragonite, dolomite, huntite, and magnesite) prior to  $\text{CO}_2$  injection. While the injection of  $\text{CO}_2$  appears to drive the brine to greater saturation levels, the observed precipitates could not be directly tied to the injection of  $\text{CO}_2$  through the isotopic analyses. The coupled flow-geochemical modeling task successfully utilized a simplified 2-D radial model using this relevant field data to generate synthetic pressure responses following  $\text{CO}_2$  injection into a similar depleted oil reservoir system. Basic sensitivity analyses to reservoir rock and formation brine properties were conducted in order to obtain a better understanding of the drivers of the aqueous chemical equilibrium reactions, as well as the mineral reactions in the system of interest. The effect of considering the aqueous and mineral reactions in the system of interest impacted the longer-term pressure response and the plume progression during the 1000-year post-  $\text{CO}_2$  injection period. The phase distribution of  $\text{CO}_2$  in the system was studied as the

system worked to re-attain a new equilibrium during the post-injection period as the CO<sub>2</sub> in the system slowly moved into more stable dissolved phases. The presence of low pH brine with high Cl- in the assumed mineralogy results in a negative saturation index that drives the dissolution of dolomite and calcite present in the reservoir rock. However, the extent of this dissolution occurring in the chosen system of interest was not seen to significantly impact the porosity or permeability of the rock. Other potential key parameter sensitivities include reservoir heterogeneity (spatially variant permeability) and formation brine salinity. While reservoir heterogeneity is expected to impact localized mineral reactions, simplified representations that honor the average rock properties are likely to honor overall system response to CO<sub>2</sub> injection. Formation brine salinity affects the initial density of the brine that directly impacts pressure response and drives propagation of the injected fluid in the system of interest. While coupled reservoir models are useful and can be designed to simulate many relevant subsurface processes, as demonstrated in the reef modeling exercises, the accuracy of these models depends upon input parameters that represent in situ conditions and need validation through detailed site-specific field testing to provide practical and relevant results.

## 1.6 Conclusions

Dover-33 is a late-stage reef that has undergone extensive primary and secondary recovery phases. During the large-scale injection tests carried out between February 2013 and July 2016, 271,144 MT of CO<sub>2</sub> was injected in Dover 1-33 injection well. The reef has also been characterized with SEM approaches to determine how best to represent the geology and heterogeneity of a complex reef reservoir.

The objectives of the Dover-33 modeling were successfully met, providing an improved understanding of the subsurface system of interest. The latest heterogeneous 3D SEM (Level 3 model) was built based on current geologic conceptual model by integrating available characterization data. This was validated by the current level of understanding of the reef from different stages of the dynamic modeling activity. Figure 1-72 shows the feedback from dynamic modeling stages that helped in the validation of the latest Level 3 SEM conceptualization.

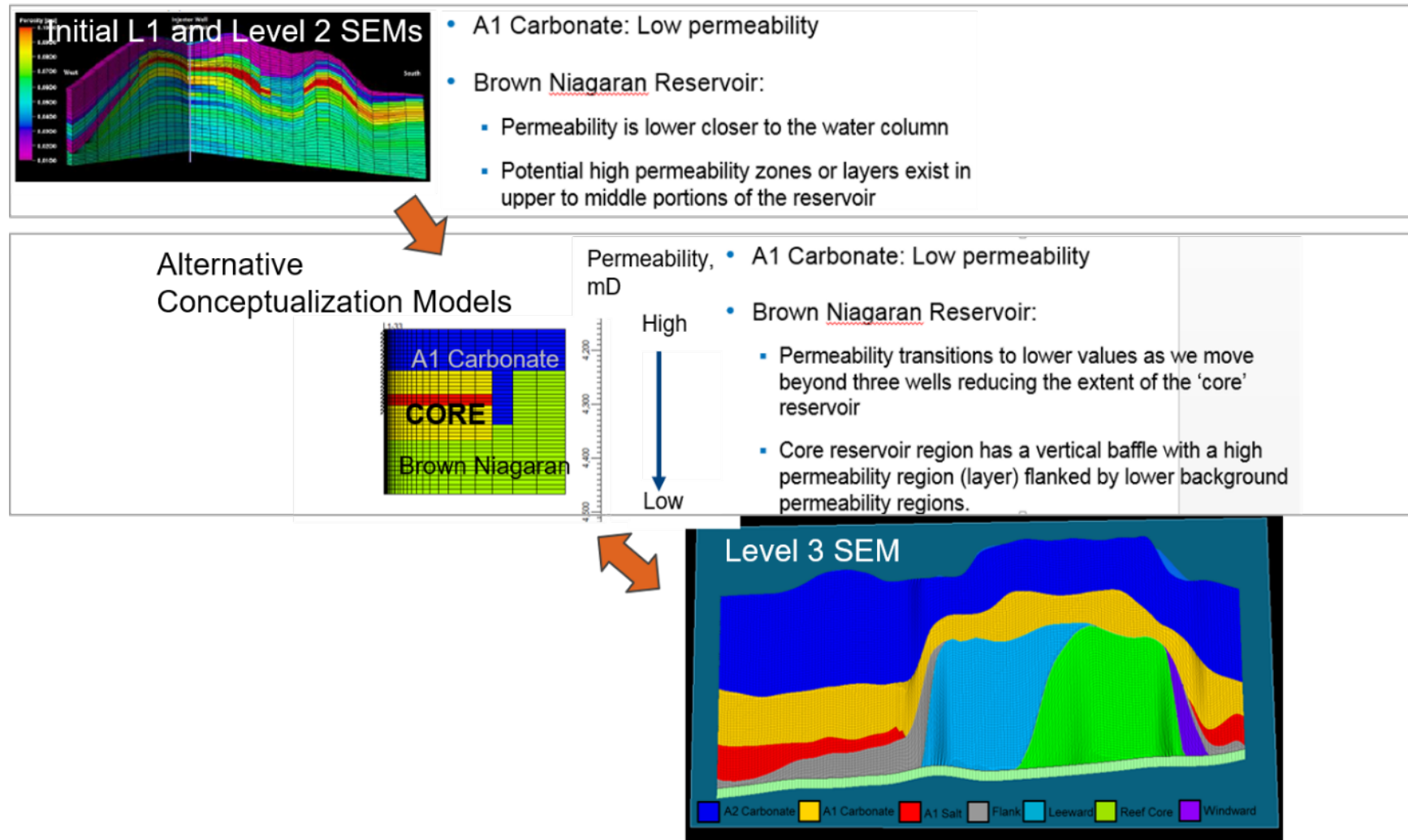


Figure 1-72. Feedback to the latest geologic conceptual model using geologic know-how of the reef obtained from systematic dynamic modeling exercises for Dover-33 reef.

The current level of understanding of the reef consists of the following key characteristics about the two producing formations:

- The overlying A1 Carbonate is of lower permeability compared to the Brown Niagaran formation.
- Within the Brown Niagaran formation in the reservoir:
  - Permeability transitions from good quality (i.e. permeable) rock in the center of the reservoir to lower values as we move beyond the three wells (injection and monitoring wells) reducing the extent of the 'core reservoir' region.
  - Core reservoir region has a vertical baffle separating the core and the flank regions, with the core containing high permeability layer(s) flanked by lower background permeability regions.

Production activity and dynamics are seen to occur mostly in the upper and upper-middle reservoir regions of the closed late-stage reef. Insights into late-stage subsurface dynamics from modeling include:

- Simulated CO<sub>2</sub> distribution shows CO<sub>2</sub> migrating outward into the reef flanks and dissolving in the formation brine over time.
- While most of the CO<sub>2</sub> continues dissolving in the formation brine, CO<sub>2</sub> also moves outward laterally to the flanks and towards the top of the perforations during MRCSP falloff.

The dynamic modeling was extremely beneficial in increasing the understanding of the reef with respect to CO<sub>2</sub> injectivity and capacity and to corroborate the quantitative representation obtained from the SEM using dynamic field data, as shown in Figure 1-72. Appendix C presents a statistical and automated history-matching approach using the Level 3 model. These two end members are used to compare the insights derived for the system of interest and understand the level of detail required to honor observed reservoir response without compromising computational efficiency. Since there are only three wells providing a sense of the reservoir properties, lack of intense characterization of the reef heterogeneity made the detailed geologic models not very useful during the history matching process of MRCSP injection in the reef. Trials to investigate drivers of the anomalous pressure buildup behavior were complicated and numerically intensive using the detailed geologic models. However, the equivalent simplified models were extremely convenient, more manageable, and numerically efficient to handle the investigation of the sensitivity of different reservoir properties to explain the observed pressure buildup in the reef during the MRCSP CO<sub>2</sub> injection phase. Refining the heterogeneity in the transition region of the reservoir zone was effective in improving the history match obtained in the simplified model conceptualizations. The validated models are also extremely useful for potential predictive modeling for considering operational optimization and evaluating subsequent production scenarios relevant to the reef.

The history matched M1 model was successfully used for coupled modeling activities with the inclusion of geomechanical module and geochemical considerations independently in order to understand their role in capturing the subsurface dynamics observed in the field. Geochemical parameters added to the fluid flow model helped evaluate effects of geochemical processes on observed pressure response while geomechanical parameters added to the fluid flow model helped evaluate effects of re-pressurization during the Phase III injection following depletion at the end of EOR in Dover-33.

## 2.0 Bagley Reef

The Bagley reef is composed of three separated lobes (Northern, Middle, and Southern lobes) and is one of the reefs located in the completely dolomitized zone. Cross-section of wells in the Northern lobe is shown in Figure 2-1. The Bagley northern lobe has been gone through primary production since 1985 and CO<sub>2</sub> storage after that since 2015.

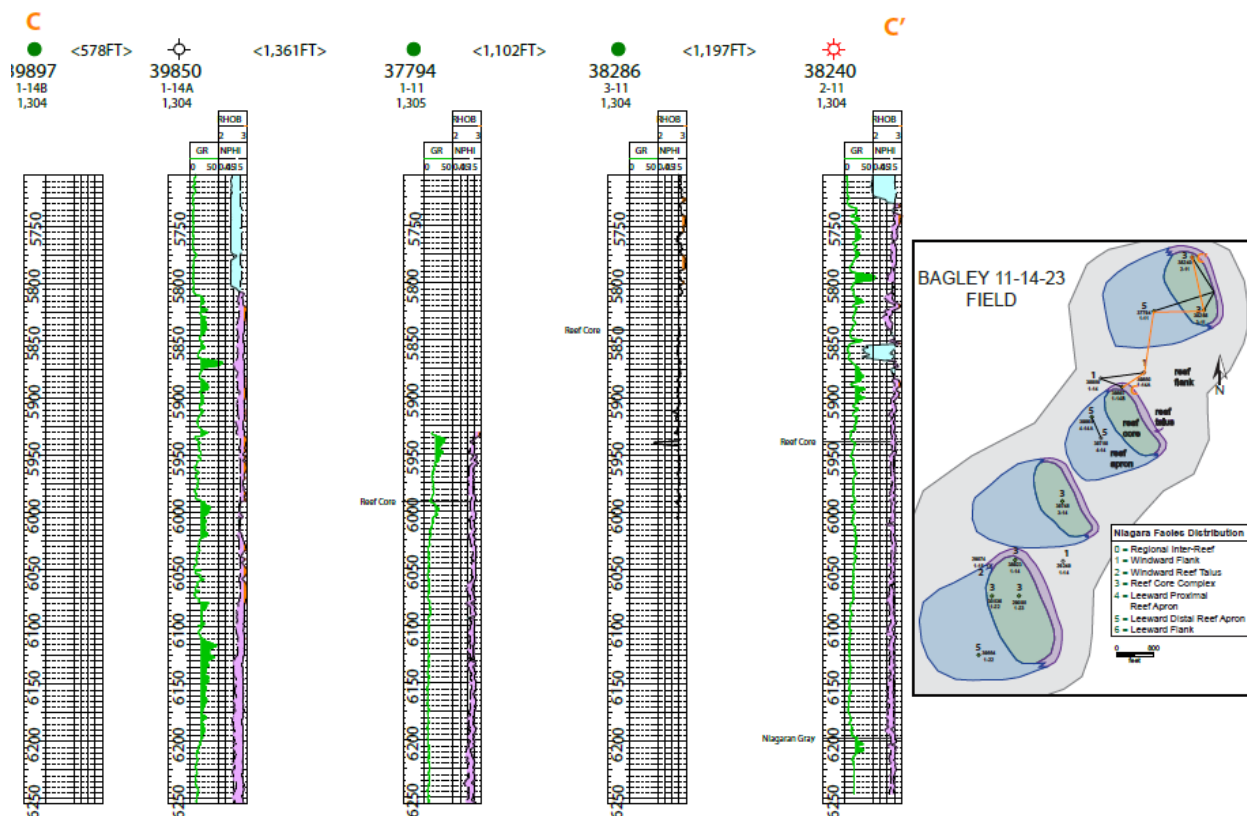


Figure 2-1. Cross-section of wells in northern pod

### 2.1 Modeling Objectives/Scope

The objective of geological model (SEM) is to provide a framework for dynamic fluid flow modeling. The main purpose of modeling was to history match the primary production and CO<sub>2</sub> storage phase, MRCSP phase, for Bagley Northern lobe. The DRM evaluates the behavior of the Bagley oil reservoirs, specifically the Northern lobe, during primary production and CO<sub>2</sub> storage phase. The workflow of modeling is shown in Figure 2-2. In order to address the modeling objective, a numerical model was constructed using a black-oil reservoir simulator to replicate the performance of the oil reservoir during primary production and CO<sub>2</sub> storage phase. Key features of the numerical models include: (1) a corner point grid system to model the reservoir with varying grid size in vertical and areal directions (2) sealing the reservoir at the top of the formations, (3) production and injection well located in the model using well path information, (4) rock properties do not vary in the lateral and horizontal direction, and (5) multi-phase fluid flow modeling is performed. A numerical model was then developed and calibrated to both the historical production data, as well as the pressure data obtained during the CO<sub>2</sub> injection. Model calibration involved adjusting both intrinsic permeability (a property of the rock) and relative permeability (which is affected by rock-fluid interaction) to match primary production and CO<sub>2</sub> storage phase.

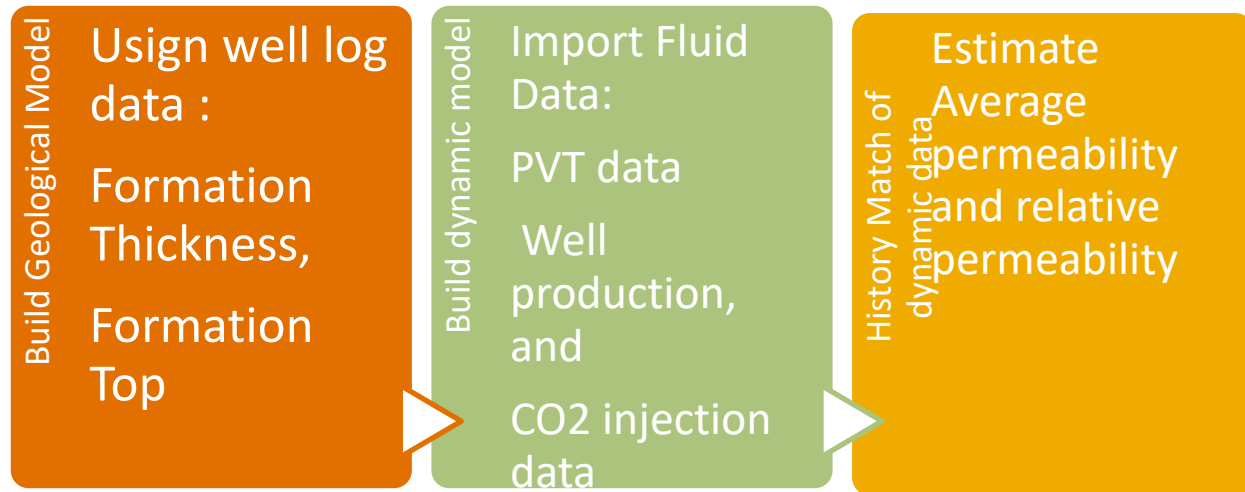


Figure 2-2. Workflow of modeling approach for Bagley

## 2.2 Data Sources

### 2.2.1 Geologic and PVT Data

During primary production and CO<sub>2</sub> injection, various data should be incorporated to build a fluid flow model and simulate the behavior of reservoirs. In this work, the reservoir model is based on available data in depleted Bagley oil reservoir. The producing formation is mainly Brown Niagaran for Bagley reef. Geological parameters, including reservoir thickness and reservoir depth, were provided using geological contour maps (Zmaps format surfaces) for Brown Niagaran, Gray Niagaran, and A1 carbonate formations. Well data for Bagley Northern lobe was imported (Table 2-1). Neutron porosity log was used to estimate average porosity, as shown in Table 2-2.

Oil samples were collected from the Bagley Oil Field. Core Energy provided the oil formation factor of 1.47, the solution gas oil ratio of 911 SCF/STB at Bubble point pressure of 1951 psi, and oil gravity of 43 API. To investigate the solution gas ratio of Bagley, the initial gas production and oil production were recorded, and solution gas oil ratio was then calculated by dividing producing gas to the producing oil. Figure 2-3 shows the estimated solution gas oil ratio using production data from Bagley oil field, which is in good agreement with the provided solution gas oil ratio of 911 SCF/STB. Standing correlation was used to generate oil formation volume factor and solution gas ratio data as a function of pressure using data provided from Core Energy. Figure 2-4 represents the oil formation volume factor and solution gas-oil ratio versus pressure using standing correlation.

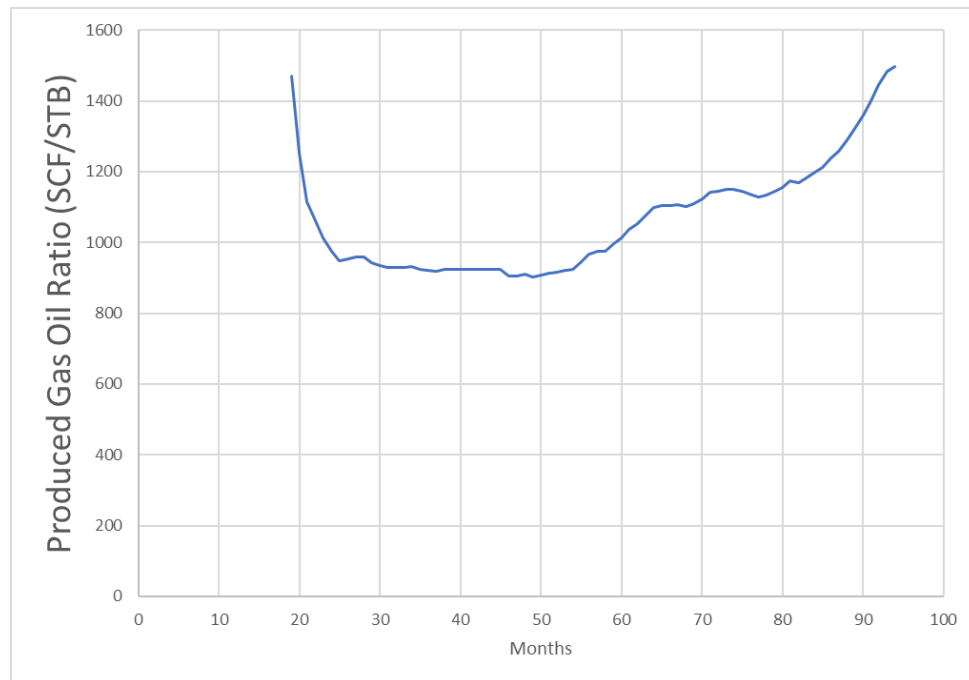


Figure 2-3. The estimated solution gas oil ratio using production data from Bagley oil field.

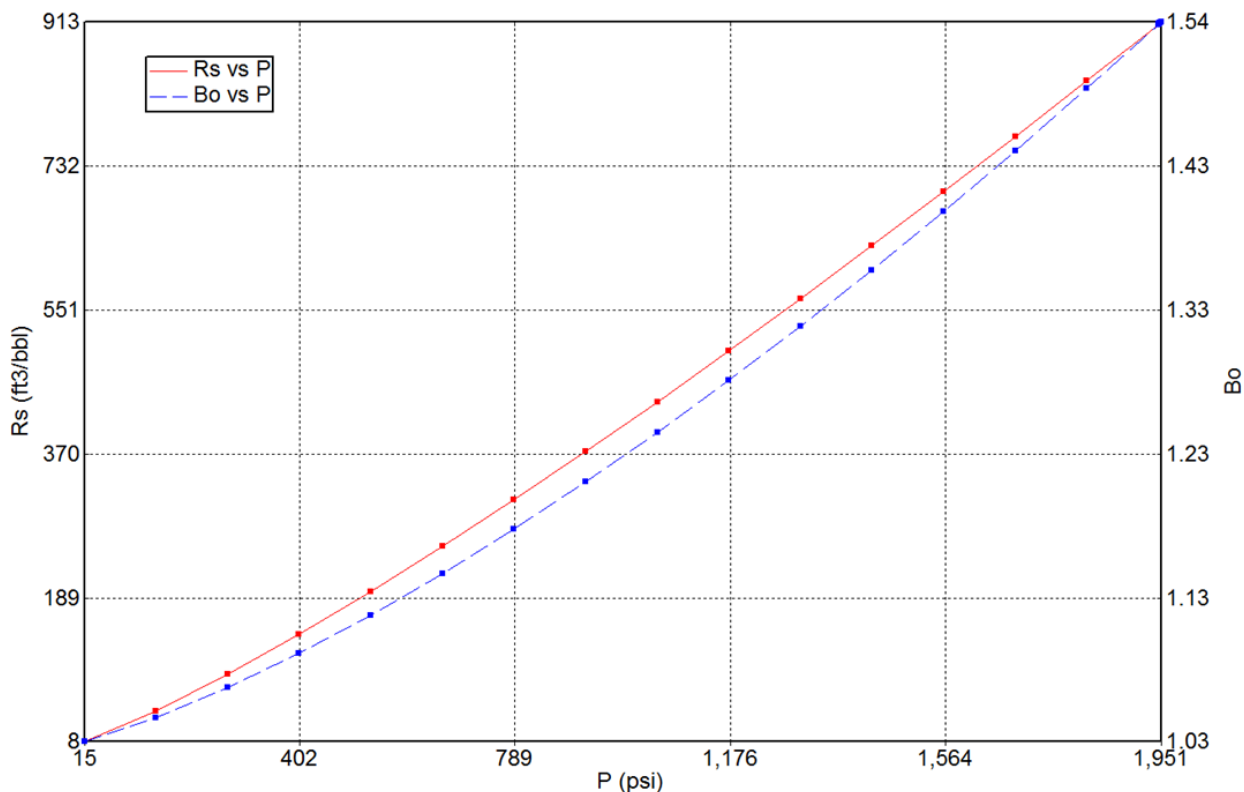


Figure 2-4. The oil formation volume factor and solution gas-oil ratio versus pressure using standing correlation

## 2.2.2 Primary Production and CO<sub>2</sub> Storage Phase

Bagley reef is made of three lobes, Northern lobe comprising of one injection and two production wells, Middle Lobe with one injection and one production well, and Southern Lobe, also with one injection and one production well. The wells in the Northern Lobe are listed in Table 2-1 and the logs in Table 2-2, since the primary objective of this work focuses on history matching of Northern lobe primary production and injection. Primary production in the Northern Lobe started in 1985 and continued until start of CO<sub>2</sub> storage phase in 2015. Primary production data is shown in Figure 2-5.

**Table 2-1. Wells in the Northern lobe**

Lobe	Well Name	Short Name	Permit #	Drill Depth MD (ft)
Northern lobe	Daughters of Friel 2-11	DF 2-11	38240	6250
Northern lobe	Janik Mackowiac 1-11	JM 1-11	37794	6326
Northern lobe	Janik Stevens 3-11	JS 3-11	38286	6045

**Table 2-2. Well logs in the Northern lobe**

Lobe	Well Name	Short Name	Well Log Used
Northern lobe	Daughters of Friel 2-11	DF 2-11	Neutron Porosity Log
Northern lobe	Janik Mackowiac 1-11	JM 1-11	Neutron Porosity Log
Northern lobe	Janik Stevens 3-11	JS 3-11	Neutron Porosity Log

CO<sub>2</sub> injection flood began in Bagley reef during the MRCSP monitoring period, starting with DF 2-11 injection well in the Northern lobe on Dec. 14, 2015. Figure 2-6 shows the plot of available pressure data since Battelle started monitoring injection in December 2015 for the Northern Lobe. These plots show bottomhole pressure (BHP), injection rate, and the cumulative injected quantities during the MRCSP period.

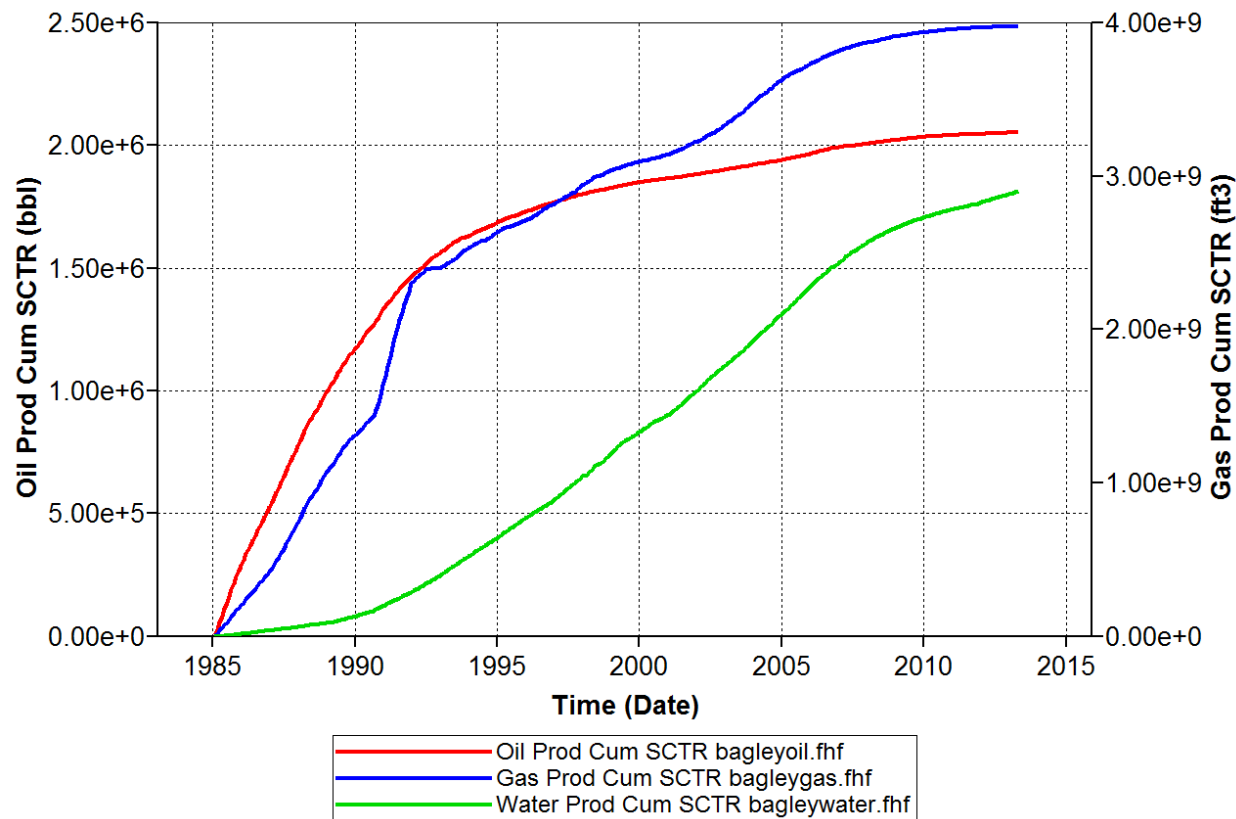


Figure 2-5. Primary production data for Bagley North lobe.

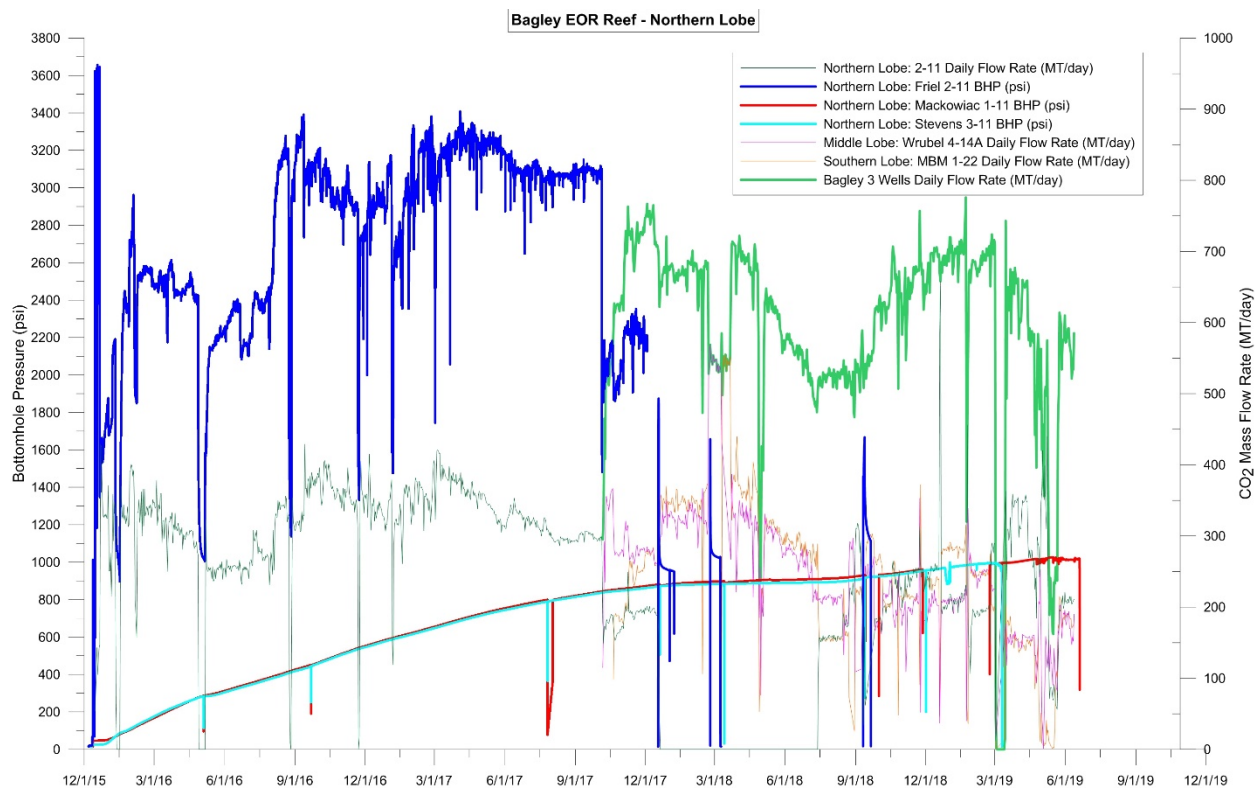


Figure 2-6. Bottomhole pressure and CO<sub>2</sub> injection rate for Bagley Northern lobe

## 2.3 Static Model

### 2.3.1 Framework

#### 2.3.1.1 Structural Surfaces

Geological parameters, including reservoir thickness and reservoir depth, were provided using geological contour maps for Brown Niagaran, Gray Niagaran, and A1 Carbonate formations. These maps were then used to generate three-dimensional grids for each formation. Figure 2-7 shows the surface map with depth contour of A1 carbonate and Brown Niagaran formations. A three-dimensional grid system was generated using the depth contour map of adjacent formations. The grid system for Bagley reef is shown in Figure 2-8.

#### 2.3.1.2 Lithofacies – Surfaces

For this modeling, extra surfaces were not prepared to delineate the distinct lithofacies within the Brown Niagaran because (1) the diagenesis is significant in carbonate reef that make presence of lithofacies meaningless. (2) There is not enough evidence (such as seismic data) to support presence of lithofacies in Bagley reef.

#### 2.3.1.3 Zones – Layers

Table 2-3 itemizes the zones (intervals between two horizons) created for each formation in the Bagley reef.

**Table 2-3. Zones (intervals between two horizons) created for each formation in the Begley Reef**

Zone	Formations	Comment
A1 Carbonate	A1 Carbonate	Impermeable unit over the reef
Brown Niagaran	Brown Niagaran	Main reservoir
Gray Niagaran	Gray Niagaran	Impermeable unit underlying the reef

#### 2.3.1.4 Geometry and Model Grid

. The primary focus was to perform history match of primary production and CO<sub>2</sub> injection phase for the Northern lobe. Figure 2-9 shows the top view (map view) of the whole Bagley grid system and selected study area, which only includes Bagley Northern lobe. Figure 2-10 shows a three-dimensional model of whole Bagley grid system and selected study area, which only includes Bagley Northern lobe and excludes Bagley Middle and Southern lobe from the system. Table 2-4 lists the number of grids used to build the model.

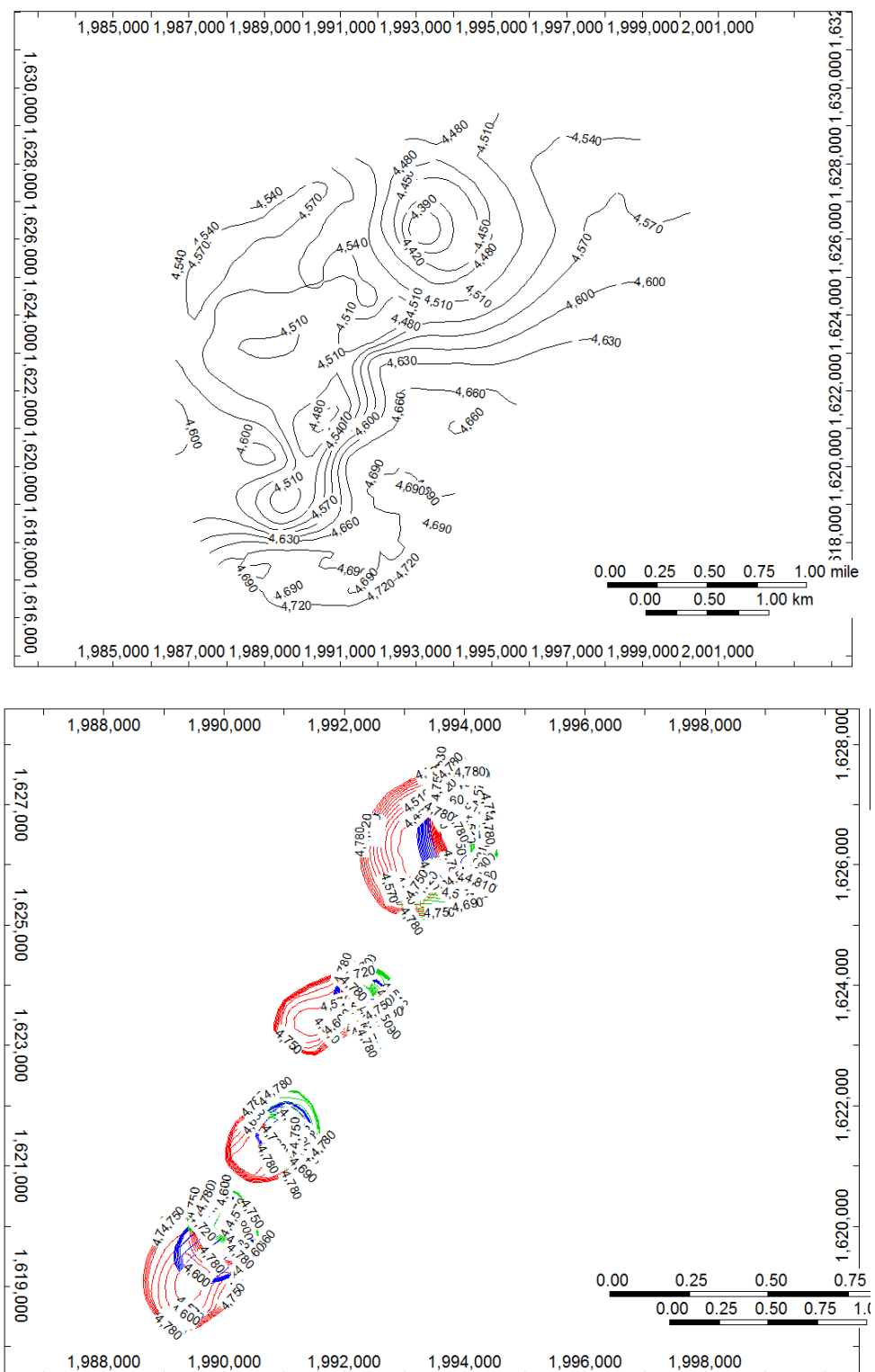


Figure 2-7. The surface map with depth contour of A1 carbonate (top) and Brown Niagaran formation (bottom).

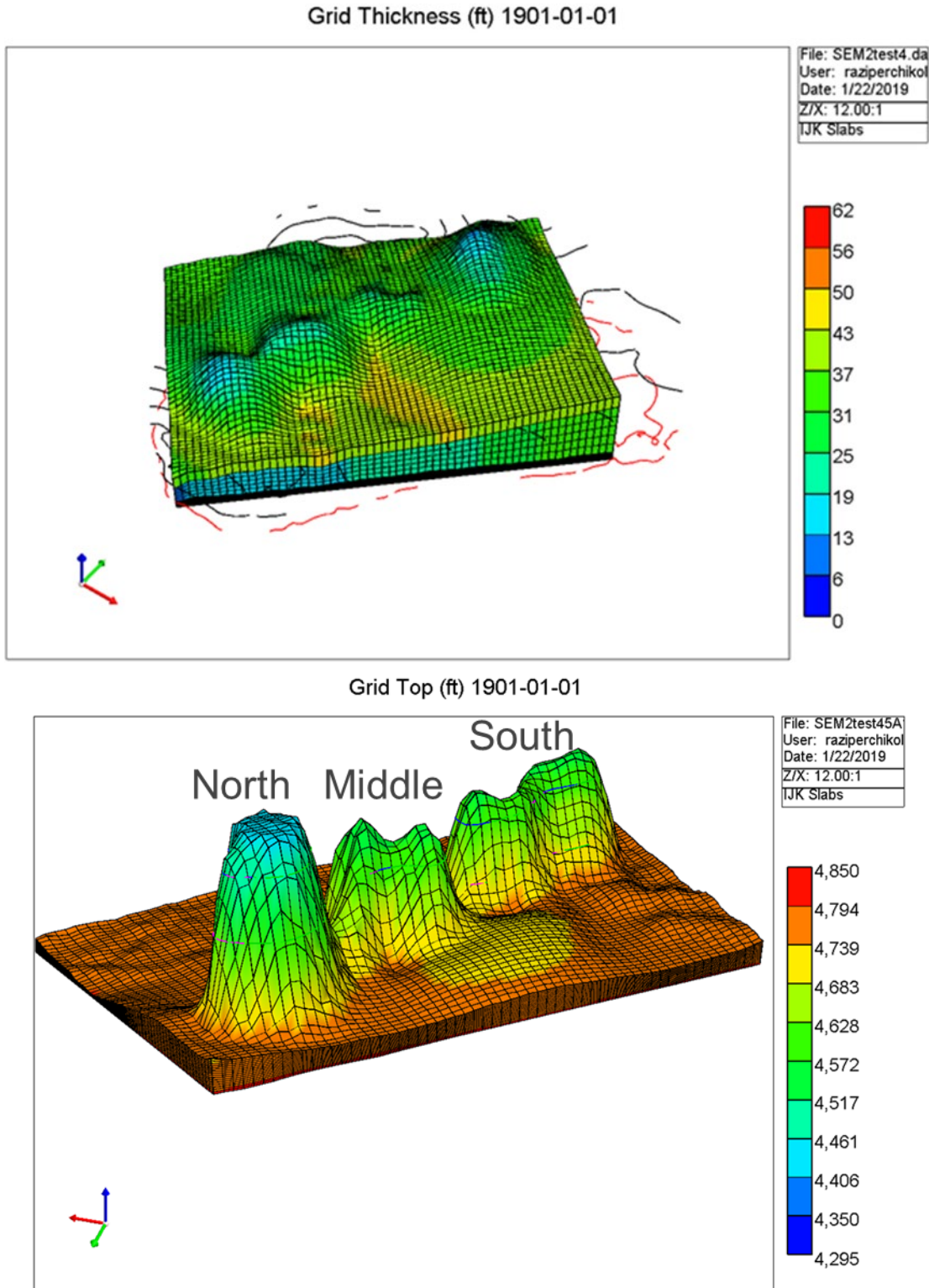


Figure 2-8. The grid system for Bagley reef: The upper panel shows the top of A1-Carbonate. The lower panel shows the top of Brown Niagaran formation.

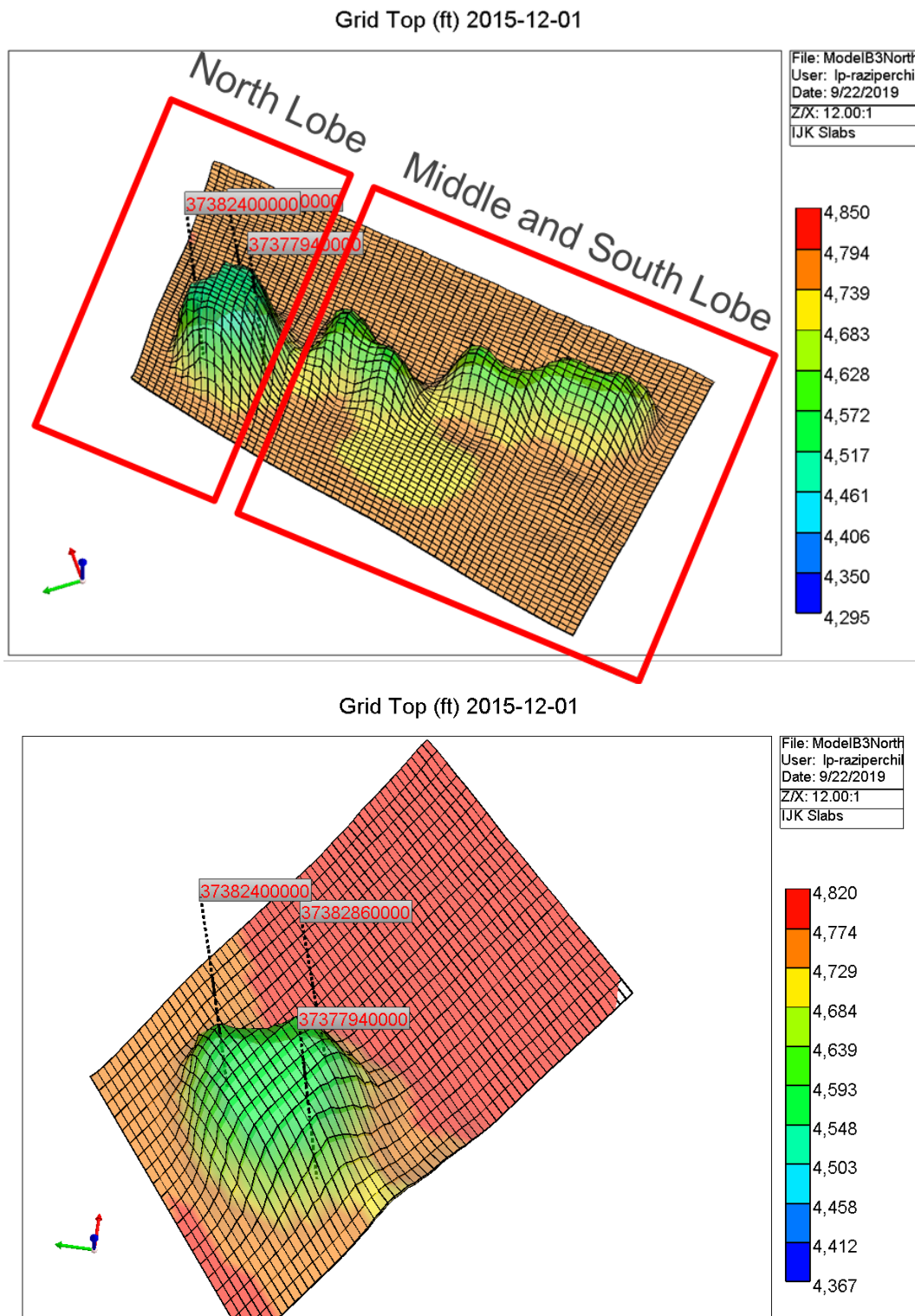


Figure 2-9. (Top) Map view of whole Bagley field (Bottom) Map view of study area: Northern lobe.

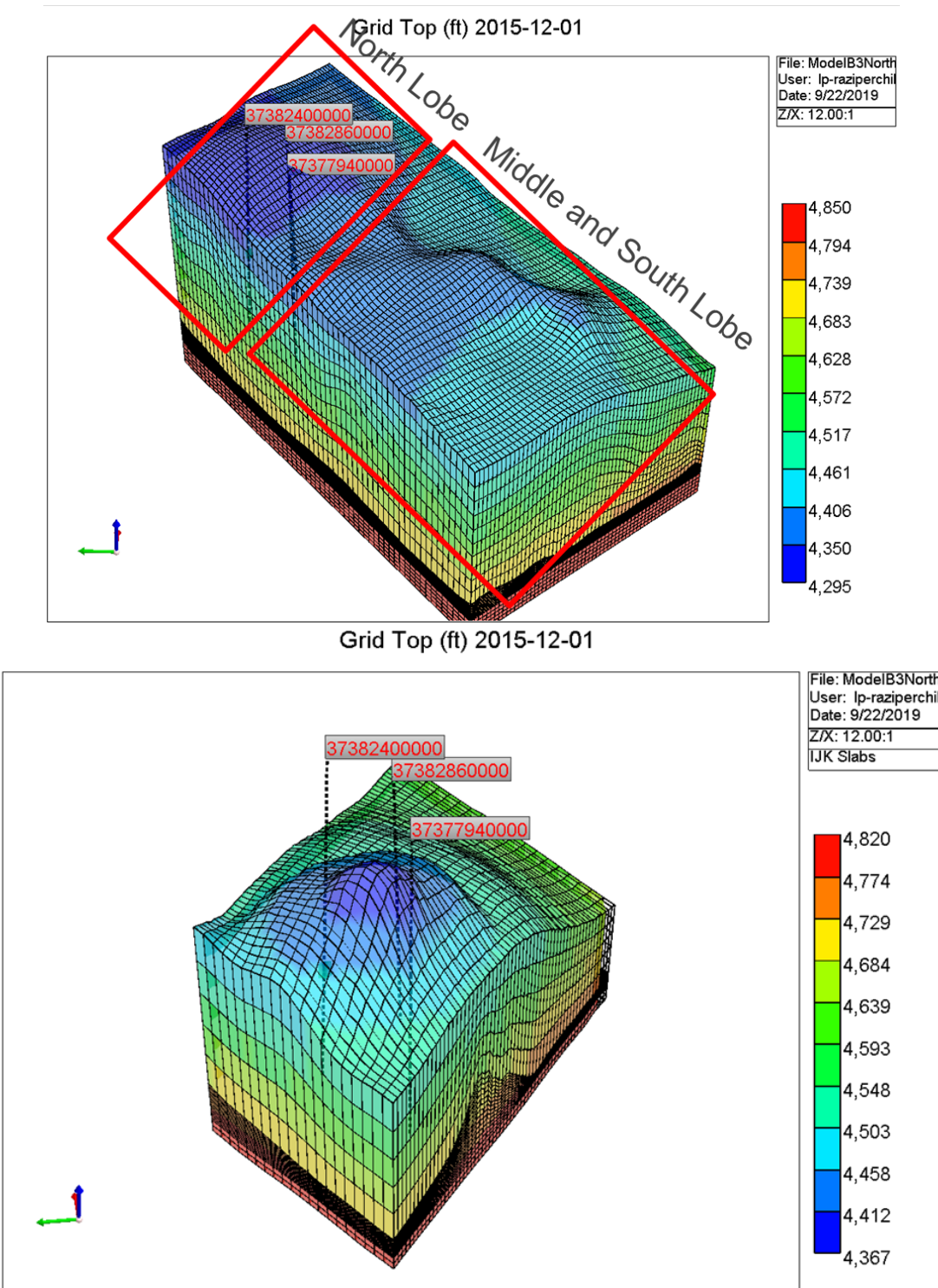


Figure 2-10. (Top) Three-dimensional model for whole Bagley field (Bottom) Three-dimensional model for study area: Northern lobe

**Table 2-4. Summary of grid parameters for the Bagley reef field**

Grid Parameter	Bagley
Total Number of Grids	108390
Grid Numbers	60 *60 *30
Number of Active Blocks	26786
Number of Null Blocks	81600

### 2.3.2 Property Modeling

The property modeling includes assigning porosity and water saturation values to the model. In this work, a single porosity value is assigned for Bagley Northern lobe model. Because the Bagley task is divided into two subtasks, a single porosity model is used to develop the CRM and limited simplified history matched model. The histogram of porosity distribution using well log data for Bagley Northern lobe (neutron porosity data) is shown in Figure 2-11. The mean of porosity data (10.34 percent) is then used for Bagley Northern lobe. The well production data for the wells in Bagley Northern lobe shows the initial water oil contact of 6060 ft. The connate water saturation of 0.2 is used in the oil zone. Lower water saturation leads to a lower water production and higher water saturation means the oil production constraint was not met. The estimated original oil-in-place in the modeled reservoir is 9.6 million STB (Table 2-5), which agrees with provided original oil-in-place of 9 million STB using material balance method by Core Energy. Model calibration involved adjusting both intrinsic permeability (which is a property of the rock) and relative permeability (which is affected by rock-fluid interaction) to match primary production and CO<sub>2</sub> storage phase.

**Table 2-5. Volumetrics and HCPV for Bagley reef**

Zone	Bulk Volume [ft <sup>3</sup> ]	Pore Volume [m <sup>3</sup> rbbi]	HCPV Oil [m <sup>3</sup> rbbi]	STOIP [mSTB]
Brown Niagaran	5.33531e+009	33016	14519	9663

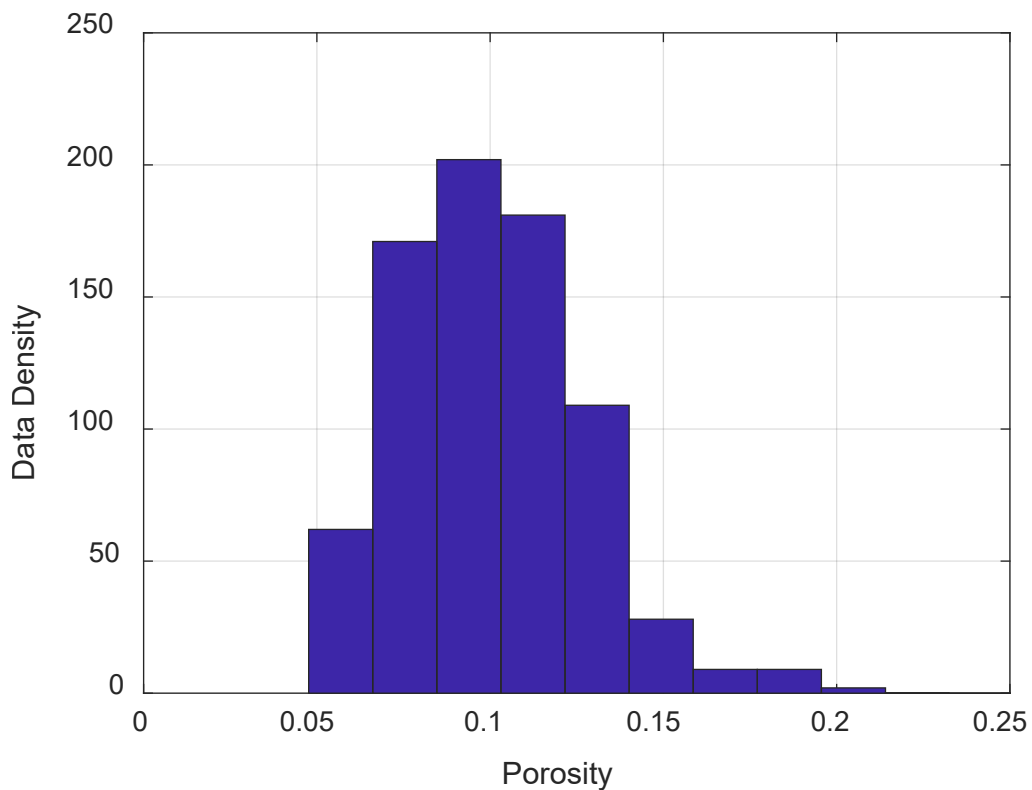


Figure 2-11. Porosity distribution of Brown Niagaran Bagley Northern lobe based on log data

## 2.4 Dynamic Model

### 2.4.1 Modeling Approach and Input

A numerical model was developed and calibrated to both the historical production data and the pressure data obtained during the CO<sub>2</sub> injection period. A black-oil simulator, CMG-IMEX, was used to achieve the objectives. The CMG-IMEX simulator models primary production and CO<sub>2</sub> behavior in an oil reservoir using four-component (oil-water-gas-solvent) mode. (Cmg, 2017) A pseudo-miscible approach in black-oil formulation has been effectively used to simulate CO<sub>2</sub> injection into oil reservoirs.(Aziz, Ramesh, & Woo, 1987; Killough & Kossack, 1987) The technique involves modifying the physical properties and the flowing characteristic of the solvent and reservoir fluid in a three-phase black-oil simulator. The mass conservation equations for solvent also consider immiscible displacement if there is a loss of miscibility. Relative permeabilities and viscosity of different phases are also modified by solvent injection. A mixing parameter is used to determine the amount of mixing between the solvent and reservoir fluid within a grid block. Previous studies have attempted to estimate an optimal value for the mixing parameter by history matching field pilot tests. This matched mixing parameter is then used judiciously to predict full-scale performance. When no better data are available, the limited work to date suggests a value in the range of 0.4 to 0.6 as a first approximation.(Bilhartz, Charlson, Stalkup, & Miller, 1978; Youngren, 1980) The model is isothermal. The geochemical interaction of CO<sub>2</sub> and oil is not considered in this model.

## 2.4.2 Primary Production and CO<sub>2</sub> Injection Phase History Match

Field geological and well log data were used to constrain reservoir thickness, boundary, average porosity, and water saturation. Different scenarios were used during the history match process to adjust the model parameters in order to match: (a) primary production response (i.e., oil and gas rates or equivalently, the corresponding cumulative production volumes), (b) average reservoir pressure during primary production, and (c) pressure buildup during the CO<sub>2</sub> injection period.

Model calibration involved adjusting both intrinsic permeability (which is a property of the rock) and relative permeability (which is affected by rock-fluid interaction). A constant permeability model is used for history match process. The cumulative oil production was used as constraint for history match of primary production (Figure 2-12). Thus, the history match is primarily against the cumulative gas production. The calibrated model was able to reasonably predict primary production response (gas and water cumulative production) (Figure 2-13) as well as average reservoir pressure (Figure 2-14) during primary production phase. A better agreement between measured and predicted values was observed for gas production than water production. If the water production increases, the constraint for oil production cannot be made. As a result, the trial-and- error process was stopped to meet the oil production constraint. Then, the CO<sub>2</sub> injection rate is used as a constraint for history match of CO<sub>2</sub> storage phase. The model was able to predict pressure response of injector (Figure 2-15) with good accuracy. Additionally, a skin factor of six is used for injector well in order to achieve the pressure history match. Core Energy said that the well-test results also confirm the high skin factor for this well (verbal communication with Rock Pardini)

A reef permeability of 15 mD was used to achieve history match for primary production and CO<sub>2</sub> storage phase. Figure 2-16 shows the water -oil and gas-oil relative permeability curves applied for history matched model.

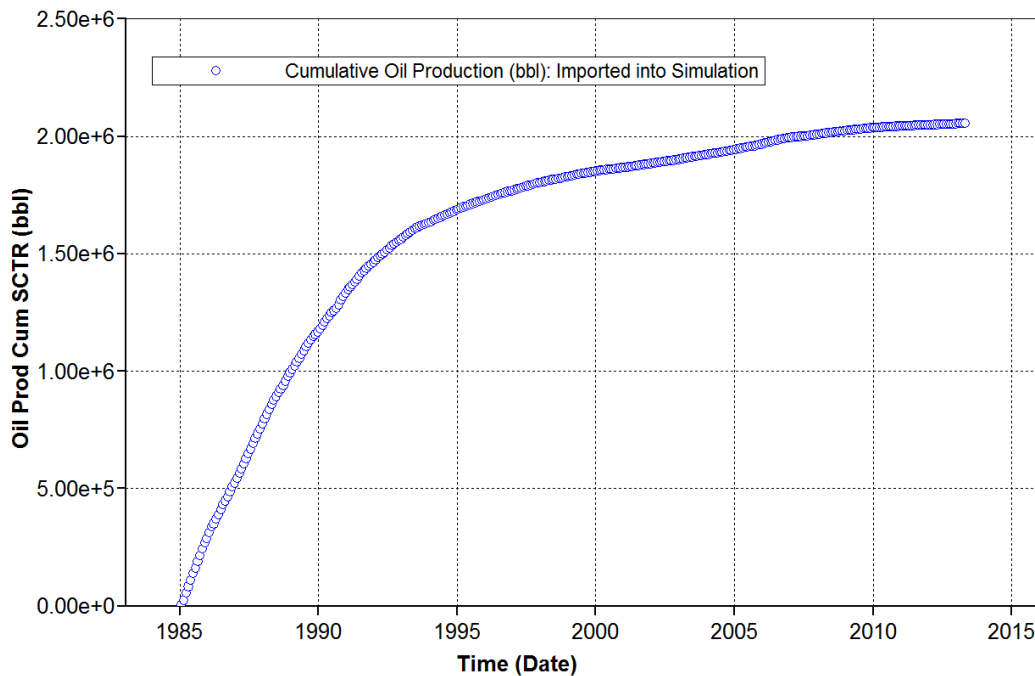


Figure 2-12. Primary oil production data used as constraint in the model.

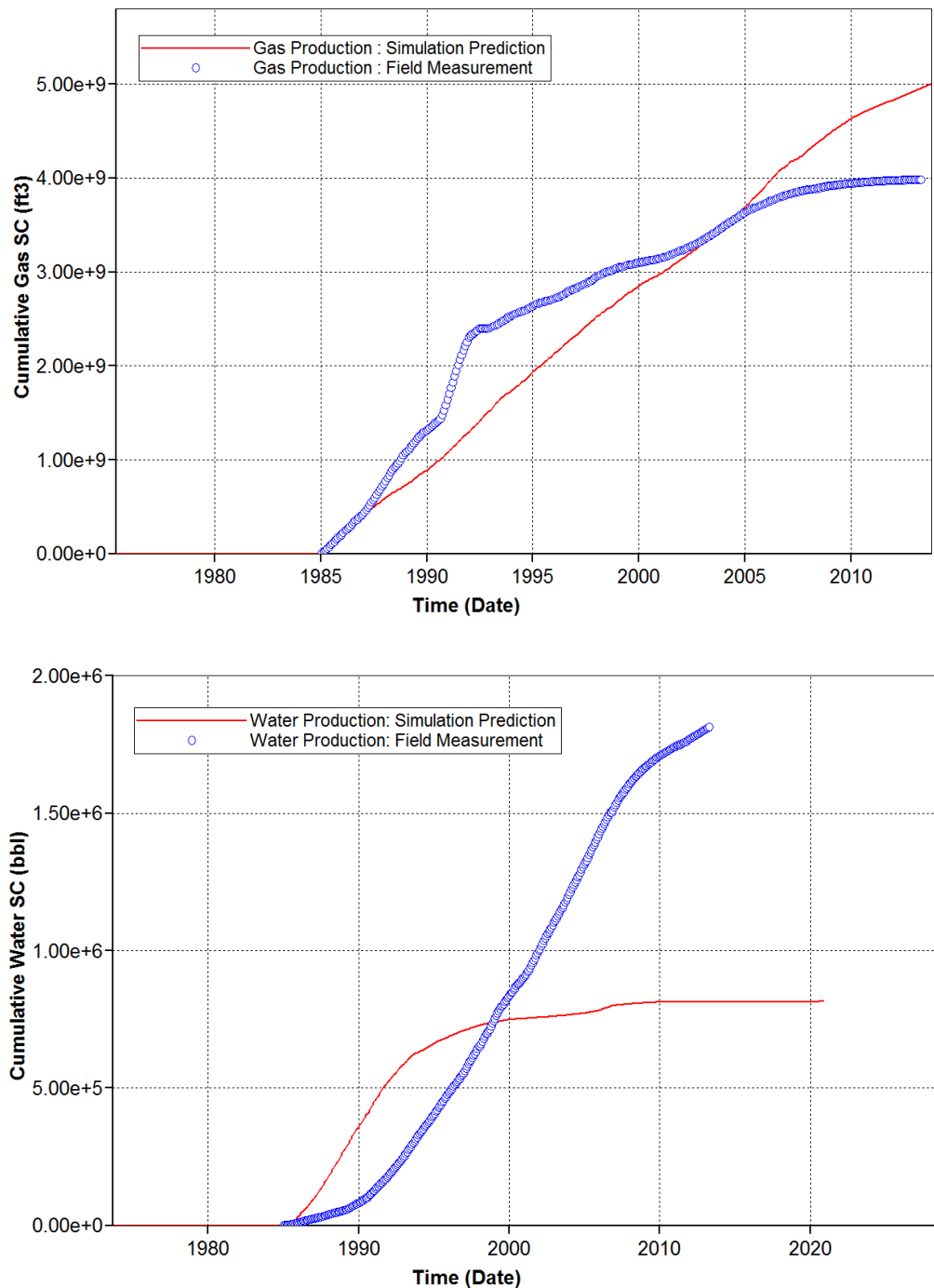


Figure 2-13. Predicted and measured cumulative gas production (Top) Predicted and measured cumulative water production (Bottom).

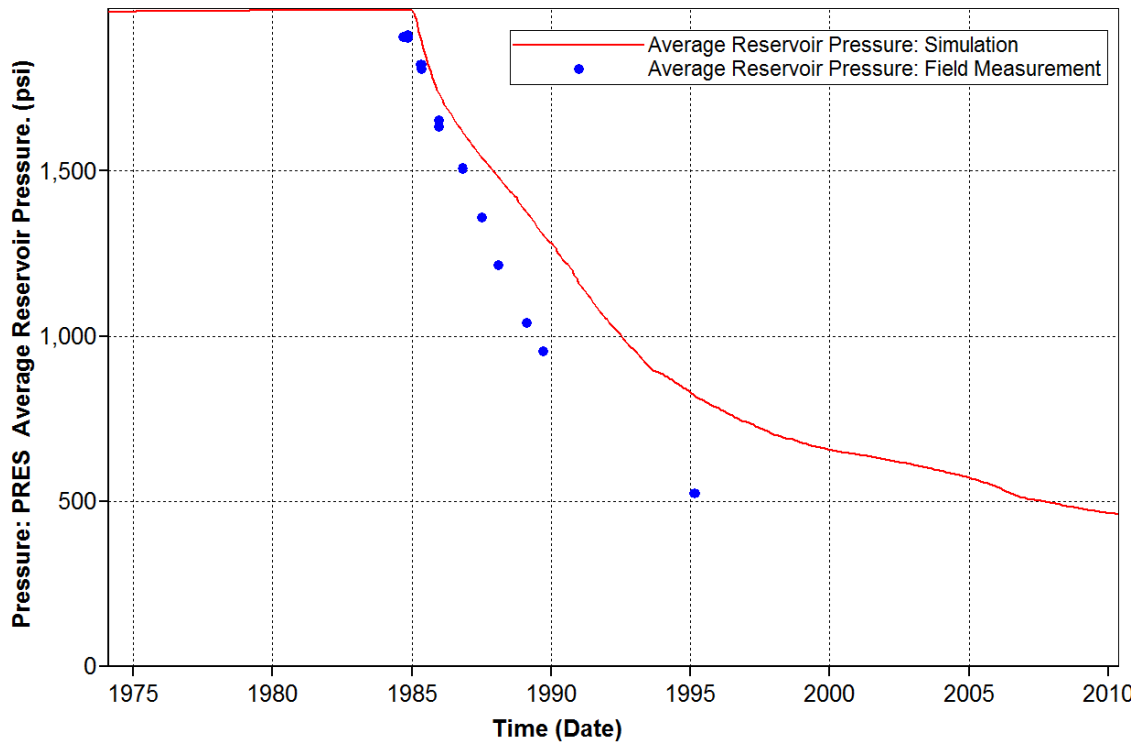


Figure 2-14. Predicted and measured average reservoir pressure.

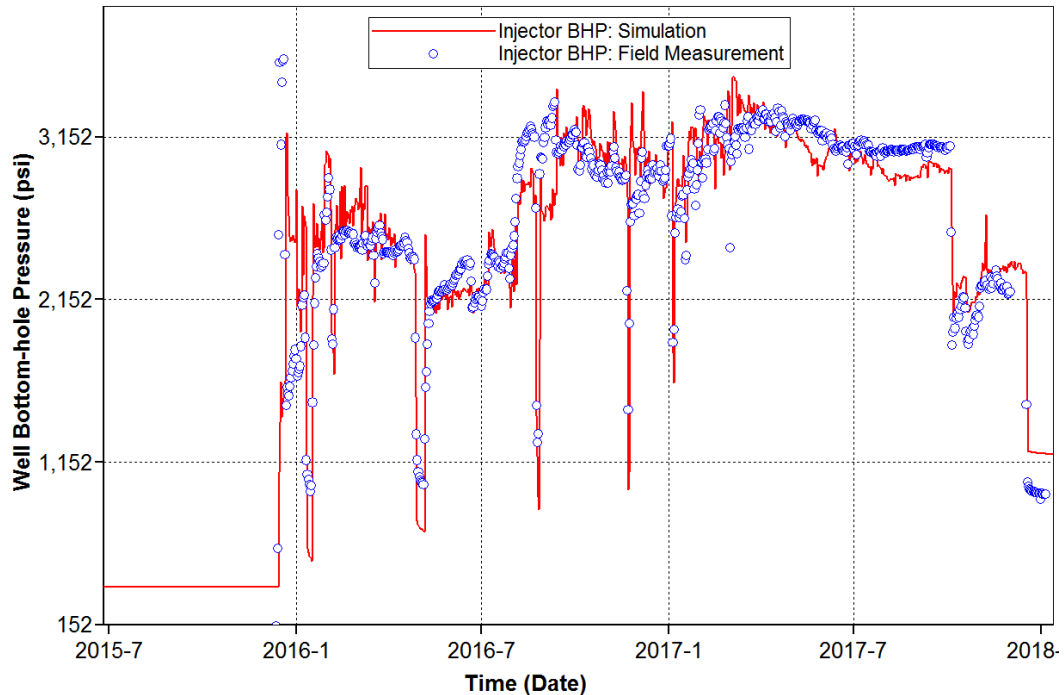


Figure 2-15. Injector Well (2-11) BHP comparison between field measurement and simulation.

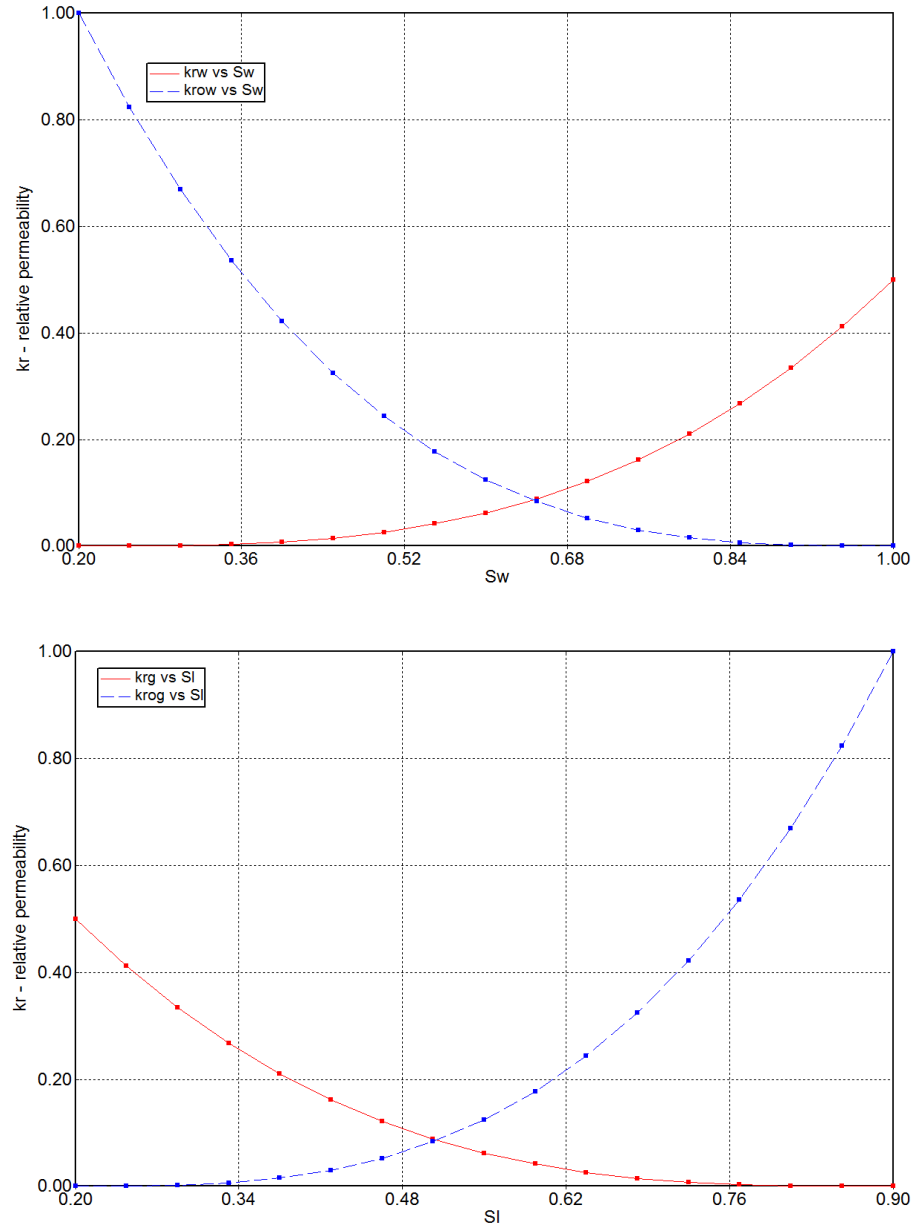


Figure 2-16. Oil-Water Relative permeability (top) Oil-Gas Relative permeability (bottom) used for history match process

#### 2.4.3 Model Forecast for the CO<sub>2</sub>-EOR Phase

A limited number of simulations were then performed to forecast the oil recovery during the CO<sub>2</sub>-EOR phase. First, additional CO<sub>2</sub> injection rate during CO<sub>2</sub> phase was imported to the simulator as a constraint. Figure 2-17 shows the predicted bottomhole pressure during last phase of injection and CO<sub>2</sub>-EOR period. The bottomhole pressure was not recorded during the last phase of CO<sub>2</sub> injection in injector. An average bottomhole pressure of 1020 psi was used for producer to forecast oil recovery. The pressure is provided using bottomhole pressure gauge in the producer well. Figure 2-18 shows the oil production and CO<sub>2</sub> production forecast during a three-month period. Figure 2-18 also shows the effect of CO<sub>2</sub>-oil mixing on rate of oil production. A mixing value of 0.5 between CO<sub>2</sub> and oil for the base case model was used. By

decreasing the mixing between CO<sub>2</sub> and oil (from 0.5 to 0.2), the rate of oil production is significantly reduced.

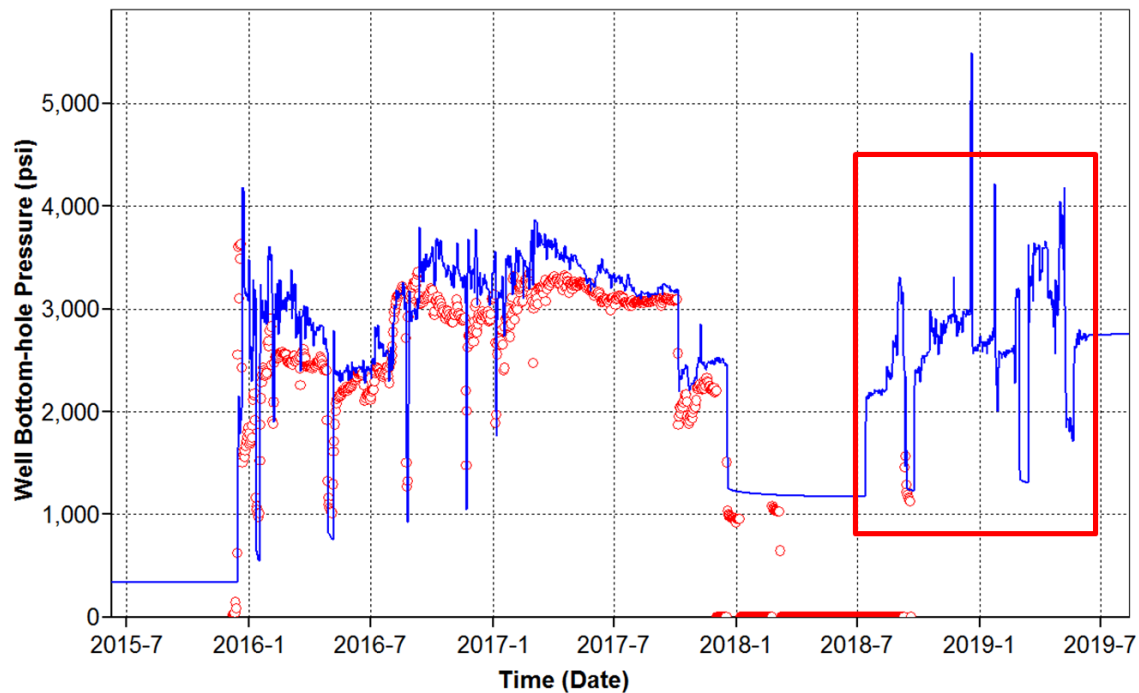


Figure 2-17. Predicted injector well BHP by injecting CO<sub>2</sub> (blue line). Note: The bottomhole pressure was not recorded during last phase of CO<sub>2</sub> injection (shown in red box)

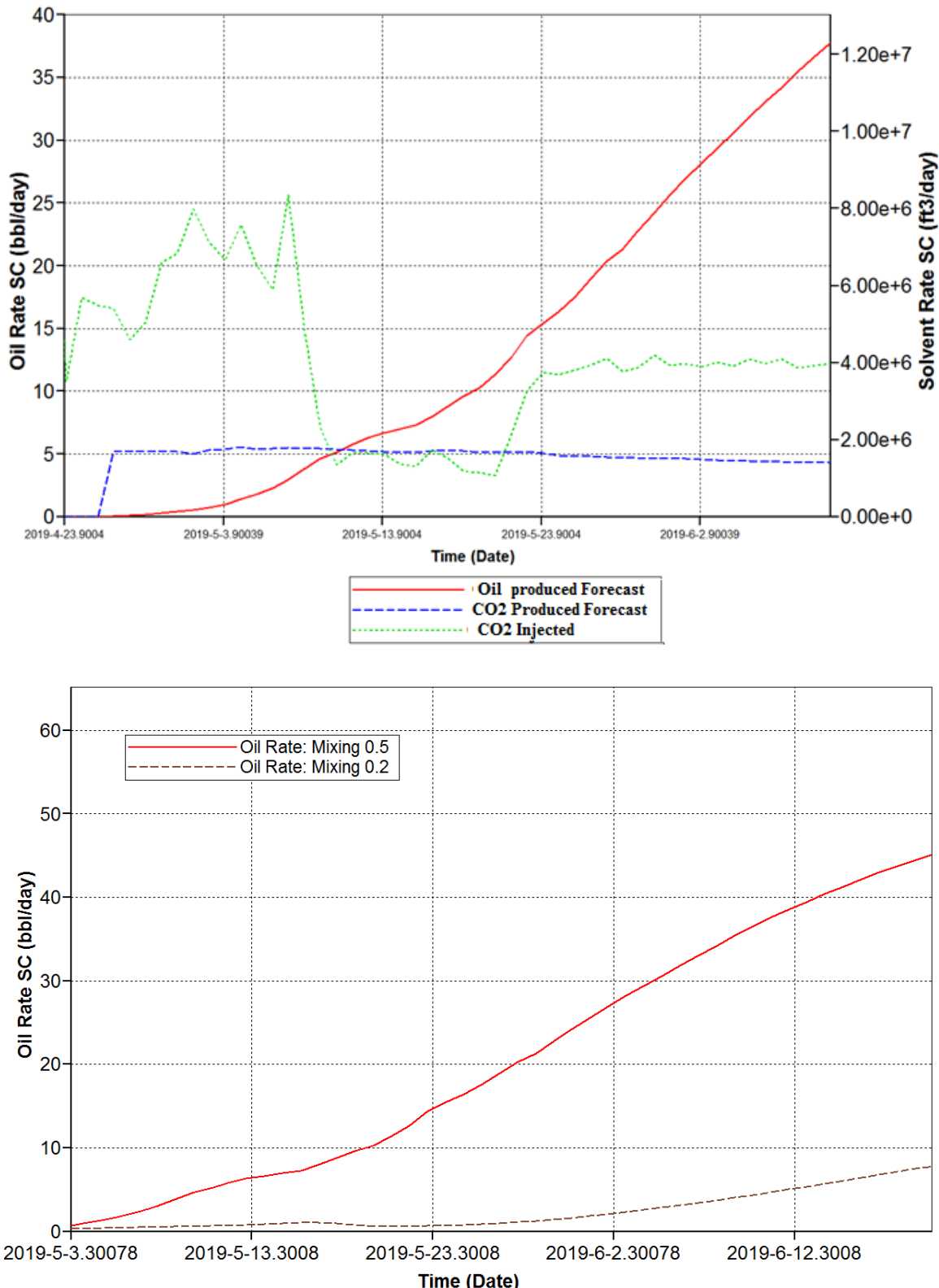


Figure 2-18. (Top) oil and CO<sub>2</sub> production during a three months CO<sub>2</sub>-EOR forecast period (Bottom) effect of CO<sub>2</sub>-Oil mixing on oil recovery during CO<sub>2</sub>-EOR period

## 2.5 Conclusions

Black-oil simulations with a pseudo-miscible option were used to match both primary production and CO<sub>2</sub> injection period pressure and fluid production data, as well as forecast the response of CO<sub>2</sub>-EOR. PVT data and knowledge of part of geological parameters (e.g. reservoir thickness, reservoir porosity) enabled us to reduce part of the uncertainty involved in the numerical simulations leading a history match with acceptable agreement between measured and modeled data. A constant permeability of 15 mD was used to achieve the history match. A limited number of simulations were also performed to forecast the oil recovery during a three- month CO<sub>2</sub>-EOR phase. The simulation results show that CO<sub>2</sub>-oil mixing can significantly affect the rate of oil production. The results of this exercise show instead of having an unnecessarily complex heterogenous complex static geological mode, a simple homogenous model can be used for dynamic model (history match). The uncertainty for the modeling comes from the lack of input data, like seismic data.

## 3.0 Charlton 19 Reef

### 3.1 Introduction

The Charlton 19 reef is a dolomite reef in late-stage production (undergone primary production and currently undergoing EOR). In late 2014, Core Energy and MRCSP started CO<sub>2</sub> injection in the Northern lobe of Charlton 19. The results of the early models are presented in earlier work as an attachment to the *Geologic Characterization for CO<sub>2</sub> Storage with Enhanced Oil Recovery in Northern Michigan* technical report [Haagsma et al., 2020].

The data available for this reef include: 3D seismic, formation well tops, well logs, and production data. The 3D seismic was interpreted by the operator of the reef and surfaces and points were output for key horizons of the reef. These surfaces and point sets were then used in conjunction with the formation well tops to create a 3D geocellular structure that was populated with porosity using well porosity logs. Charlton 19 is a dolomite reef similar to the Dover-33 reef. Since no core data exists in the Charlton 19 reef, Dover-33 core permeability-porosity transforms were used to populate permeability in the static model.

#### 3.1.1 Reef Description

The Charlton 19 field consists of two reef lobes, one north and one south, that underwent primary production starting early 1988 and ending late 2014 (Figure 3-1). The reef underwent primary recovery but was not flooded with CO<sub>2</sub> prior to 2014. A total of eight wells were drilled in Charlton 19, which had three active wells during the time of modeling (Table 3-1). A brief well history is included in the primary and secondary history section below.

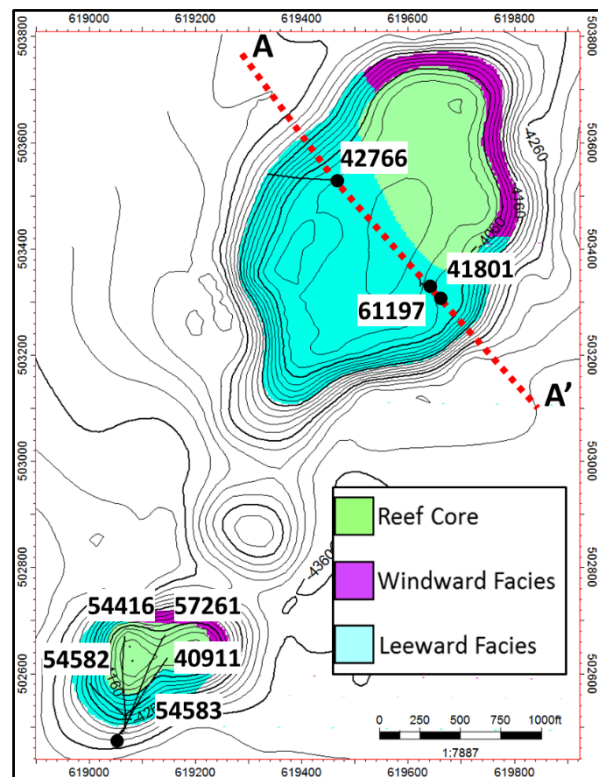


Figure 3-1. Map of Charlton 19 reef field showing the two reef lobes and locations of wells used in the geologic analysis.

**Table 3-1. Charlton 19 wells with permit number and status.**

Well Name	Well Number	Permit Number	Status	Reef Lobe
ELMAC HILLS	1-19	40911	Plugged	South
ELMAC HILLS	1-19A	54416	Plugged	South
ELMAC HILLS	1-19B	54582	Plugged	South
ELMAC HILLS	1-19C	54583	Plugged	South
ELMAC HILLS	1-19D	57261	Active	South
ELMAC HILLS	1-18	41801	Abandoned	North
ELMAC HILLS	1-18A	61197	Active	North
ELMAC HILLS #4	2-18	42766	Active	North

### 3.1.1.1 Geology Overview of Charlton 19

Charlton 19 is a dolomite reef located in the Northern Niagaran Pinnacle Reef Trend (NNPRT). Geometry of the reef, indicated by 3D seismic, suggests two distinct reef lobes separated by a saddle (Figure 3-1). The two reef lobes show little communication between each other as indicated by bottomhole pressure/temperature gauges. Charlton 19 contains on-reef and off-reef (regional) Brown Niagaran facies. The off-reef facies is composed of a low porous dolomite that surrounds the on-reef facies. The on-reef Brown Niagaran is composed of three facies: windward, leeward, and reef core. These facies are the reservoir for the Charlton 19 reef and occur at two distinct isolated locations within the field, one in each the northern and southern lobes. Geometry of the northern reef lobe can be seen in Figure 3-2. The Brown Niagaran contains moderate porosities due to dolomitization. The overlying A1 Carbonate is mostly tight, except the lower portion of the formation directly overlying the Brown Niagaran. The original OWC was documented in the lower half of each reef structure, with the Northern lobe containing an OWC tens of feet higher in elevation than the southern lobe.

The confining units overlay the A1 Carbonate and include the A2 Evaporite and A2 Carbonate. The ultimate confining units include the Salina G through the Salina B-Salt. Underlying the reef structure is the Gray Niagaran which is a tight, water saturated carbonate and represents the lower boundary of the reef. Interior to the reef, the Brown Niagaran is divided into three lithofacies, the Leeward, Reef Core, and Windward. These represent a geologic simplification that was used in SEM development and were described in the *Task 5: Baseline Geologic Characterization Report* technical report [Haagsma et al., 2017].

Wireline logs for five wells were analyzed for the Charlton 19 field. The reef core, reef apron, and bioherm were composed of mixed limestone and dolomite with moderate to high porosity. The A1 carbonate is composed of limestone and dolomite in relatively equal portions within intervals of anhydrite in the upper 10-20 feet of the formation. The best porosity observed occurred in the lower section of the formation at the contact between the A1 Carbonate and Brown Niagaran with up to 13.8 percent neutron porosity. Zones of lost circulation occurred in the Brown Niagaran, indicating highly permeable rock.

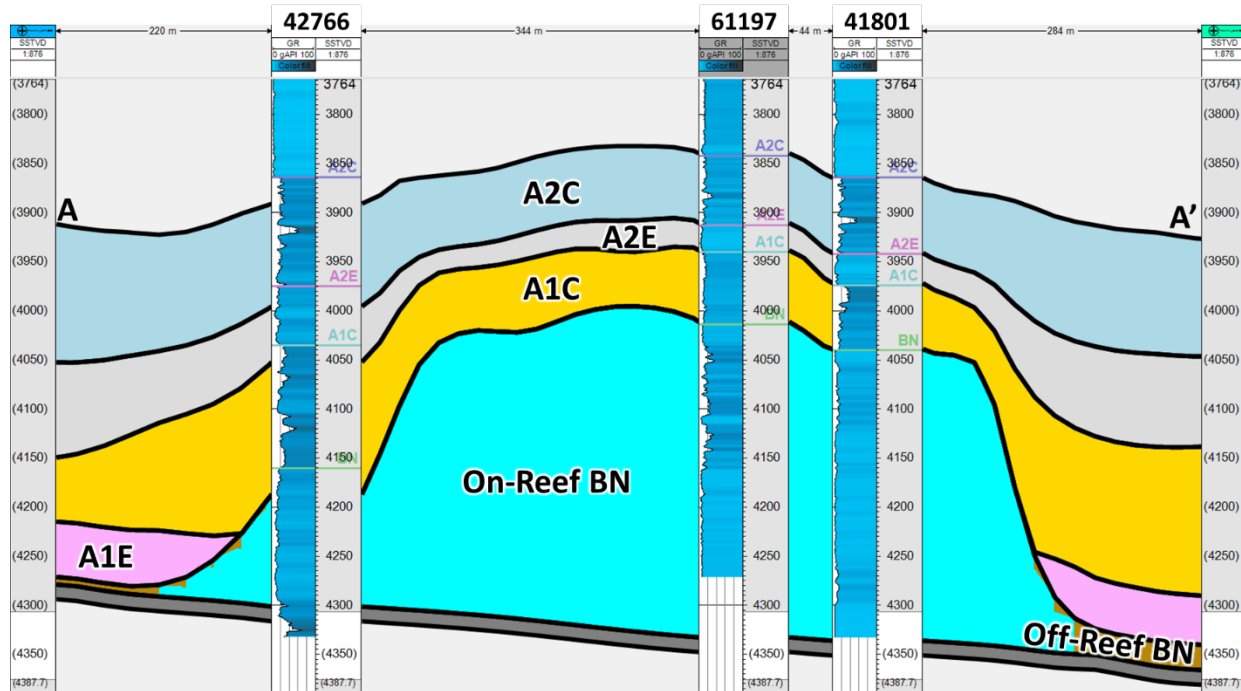


Figure 3-2. Cross-section of Charlton 19's northern reef lobe (as seen in Figure 3-1) showing thickness of formations and on-reef vs. off-reef Brown Niagaran (BN).

### 3.1.2 Modeling Objectives/Scope

The overall flow of the modeling work consisted of analyzing and integrating geologic data to define the extent, depth, thickness, porosity, permeability, and water saturation of the reservoir (s). In conjunction with geologic characterization, field operational and monitoring data was compiled to develop the reef history typically to be used in history matching the dynamic model. The geologic characterization work then was used to develop a SEM. Figure 3-3 illustrates the typical flow and connections between analysis and data types to develop final static and dynamic models. Note that Charlton 19 was not chosen for dynamic analysis but instead underwent analytical modeling for evaluation of pore volume and injectivity index. The modeling was carried out using the Capacitance Resistive Model (CRM) (Nguyen et al., 2011) and is discussed in other sections.

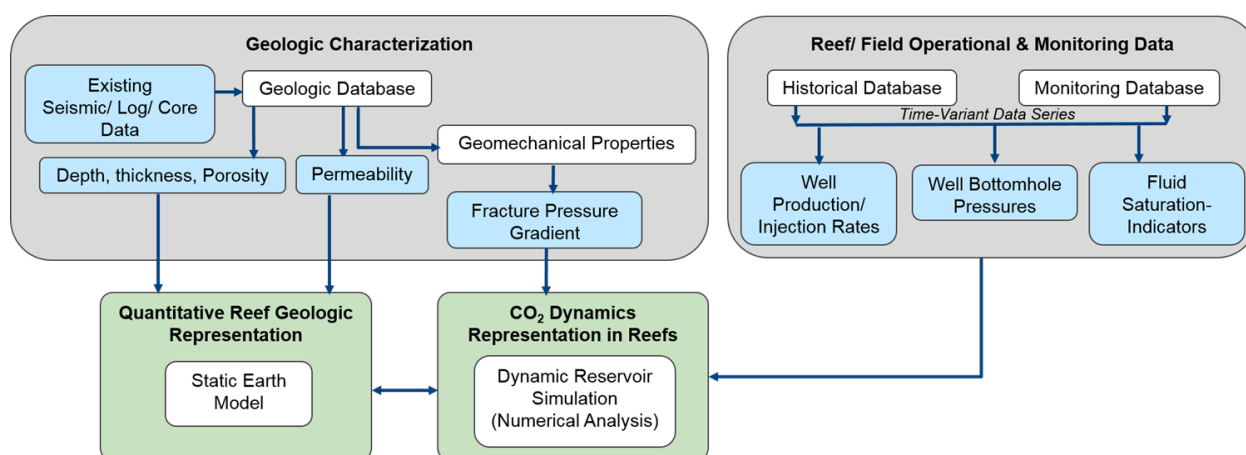


Figure 3-3. Simplified flow diagram of data integration into static and dynamic models.

The objectives of the Charlton 19 models are to:

1. Simplify geologic lithofacies while maintaining reservoir heterogeneity,
2. Create a representative quantitative model of the reef that includes key petrophysical properties (porosity, permeability, water saturation),
3. Integrate multiple data types,
4. Verify the reported fluids in place in the reef, and
5. Validate modeled reservoir properties using field data during the CO<sub>2</sub>-injection period.

## 3.2 Data Sources

The Charlton 19 field had a range of vintages and sources for data. Many wireline logs were provided by Core Energy, LLC and ranged in vendor and age. Battelle worked with Core Energy to collect new data in the injection well along with the drilling of a new characterization well. 3D seismic was also provided to aid in the geometry definition.

### 3.2.1 Geologic Data

There are eight wells that penetrate the Charlton 19 reef in Michigan. Of these wells, five have digitized logs, and none have raster logs available. All five wells have gamma ray, bulk density, and neutron porosity logs available (Table 3-2). These wells also have various advanced logs, such as resistivity and photoelectric effect. These wells also have formation tops identified from the Glacial Drift Base to the Gray Niagaran. The three wells that do not have log data available are directional kickoffs from well 21137409110000 (Figure 3-2).

**Table 3-2. Summary of wireline log data for the Charlton 19 reef; green shading indicates logs available by well.**

		Permit #							
		40911	54416	54582	54583	57261	61197	41801	42766
CAL	Caliper								
DT	Sonic								
GR	Gamma Ray								
LLD	Latero-Log Deep (Resistivity)								
LLS	Latero-Log Shallow (Resistivity)								
NPHI	Neutron Porosity								
PNC	Pulsed Neutron Capture					2	1		1
RHOB	Bulk Density								
BHP	Bottom Hole Pressure Monitoring								
Common Name		El Mac Hills 1-19	El Mac Hills 1-19 A	El Mac Hills 1-19 B	El Mac Hills 1-19 C	El Mac 1-19D	El Mac Hills 1-18A	El Mac Hills 1-18	El Mac 2-18

### 3.2.2 Primary & Secondary Production

Charlton 19 underwent primary production from 1988 through 2014 and did not see CO<sub>2</sub> in the system before MRCSP injection. About 14500 MT CO<sub>2</sub> have been injected into this reef since January 2015. The Charlton 19 reef was discovered in late 1980s with an initial BHP of about 2,774 psi and produced 1,065 MBO (40.4 percent of Original Oil-in-place [OOIP]) and 2,291 MMCF (sales) through 5/2012. Table 3-3 summarizes field fluids in place and different phase saturation values at initial and end of primary production conditions in the reef.

**Table 3-3. Field Summary information on reservoir conditions before and after primary production in Charlton 19 reef.**

Reservoir Conditions	Initial Conditions	Current Conditions (as of 05/2012)
Oil-in-place, MBO	2,634	1,569
Gas In Place, MMCF	2,545	251
Oil Saturation	88.65%	37.51%
Gas Saturation	0.00%	51.14%
Water Saturation	11.35%	11.35%
BHP, psi (estimated)	2,774	155
% OOIP Recovery	0.00%	40.4%
% OGIP Recovery	0.00%	90.1%

#### **Well Details:**

Charlton 19 had three production wells during primary production phase, one of which was later redrilled due to a wellbore failure. The primary producers are El Mac Hills #1-19, El Mac Hills #1-18 and El Mac Hills #4 2-18, respectively. The oldest well is EMH 1-19. EMH 1-18 was first brought in line for production during March 1989, while EMH 2-18 was first brought in line for production during March 1990. EMH 1-19 is a deviated well that is currently converted into a monitoring well. EMH 1-18 was a vertical production well that is currently plugged. EMH 2-18 is the CO<sub>2</sub> injection well currently.

### Available Well-wise Primary Production History of Charlton 19

Figure 3-4 through Figure 3-7 show the monthly three-phase production of individual producers and the overall field for the primary recovery period in Charlton 19. EMH 1-19 produced 400,940 STB oil and 829,138 MSCF gas.

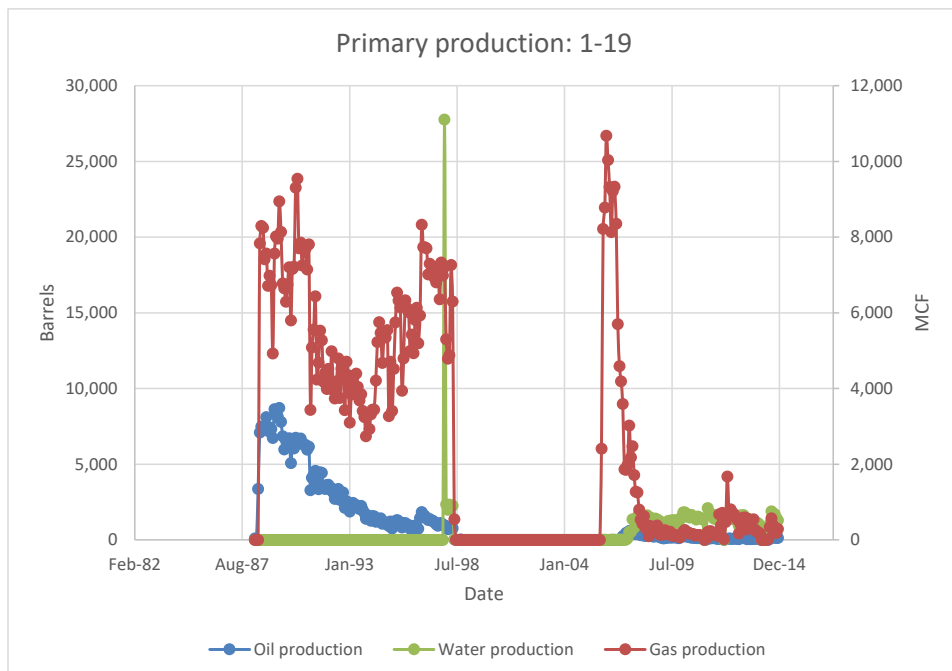


Figure 3-4. Historical monthly production plot for 1-19.

EMH 2-18 produced 172,131 STB oil and 319,356 MSCF sales gas.

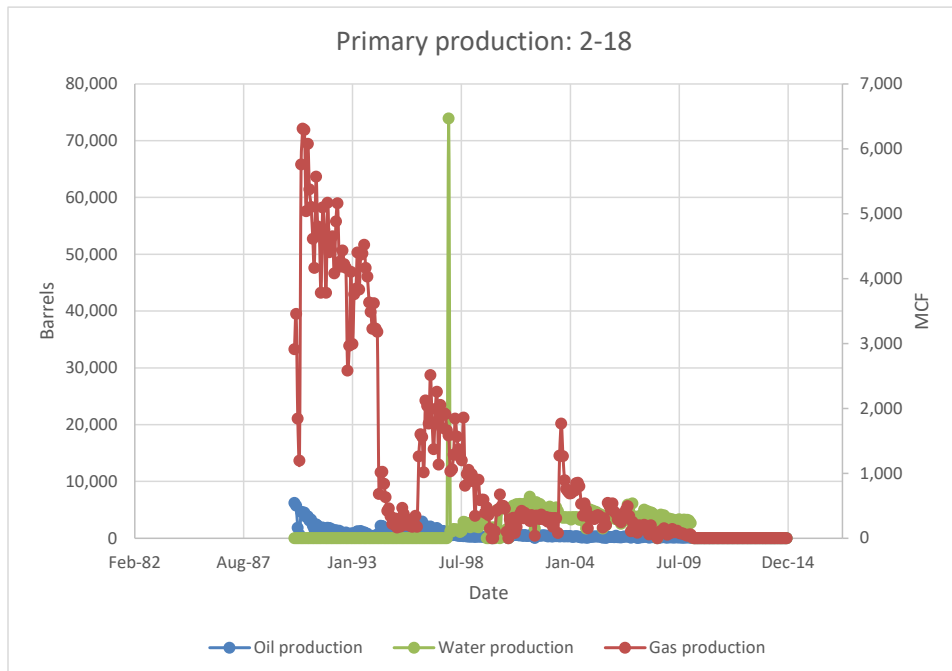


Figure 3-5. Historical monthly production plot for 2-18.

EMH 1-18 produced 500,749 STB oil and 1,154,248 MSCF sales gas.

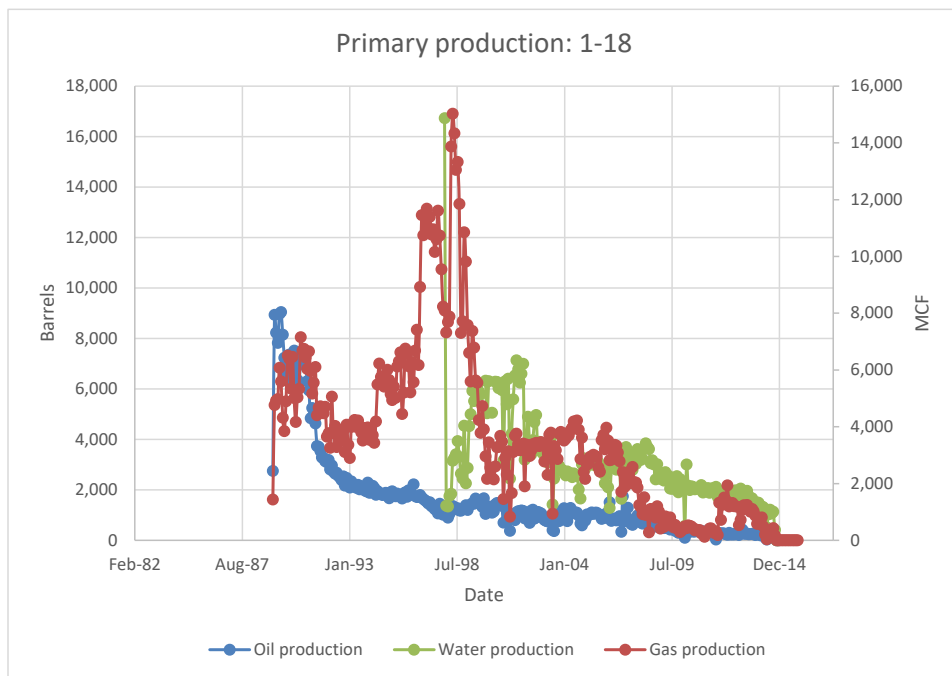


Figure 3-6. Historical monthly production plot for 1-18.

Overall, Charlton 19 has produced 1,073,820 STB oil (40.7 percent of OOIP recovered) and 2,302,742 MSCF gas through 2014.

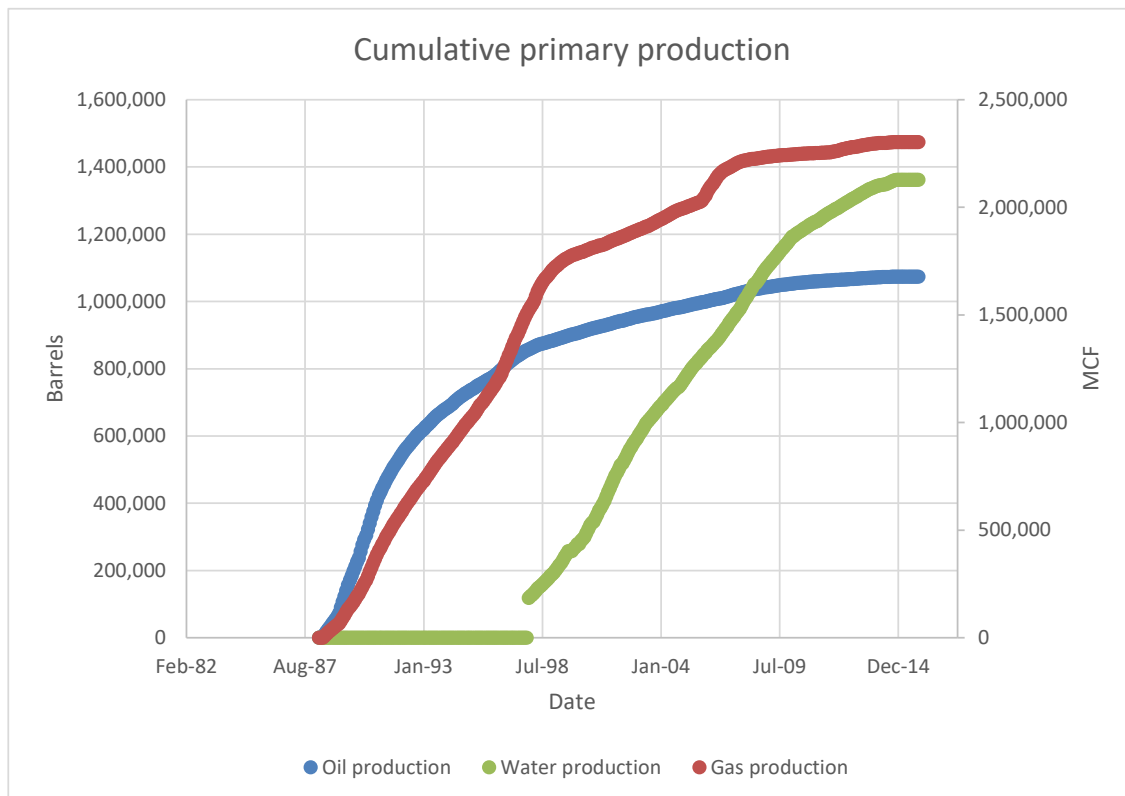


Figure 3-7. Charlton 19 cumulative production plot from 1988 through 2014.

While the initial/discovery pressure was 2774 psi, the estimated BHP at the end of primary production is 155 psi per material balance calculations by Core Energy.

### 3.2.3 EOR/CO<sub>2</sub> Injection Rate and Pressure History

During the MRCSP monitoring period, a cumulative total of 293,160 MT of net CO<sub>2</sub> was injected into the Charlton 19 reef. The Charlton 19 reef began its initial CO<sub>2</sub> flood during the MRCSP monitoring period, on March 1, 2015. The miscible CO<sub>2</sub> flood lasted until June 26, 2017, during which the Charlton 19 reef received 233,300 MT of CO<sub>2</sub>. After that time, the EMH 1-18A production well began to produce oil.

Figure 3-8 below shows the composite plot of available pressure data since Battelle started monitoring injection in February 2015. This plot shows bottomhole pressure, temperature, injection rate, produced recycle gas, and the cumulative injected quantities in the injection and production wells during the MRCSP monitoring period for the significant injection events and the fall-off periods in the reef.

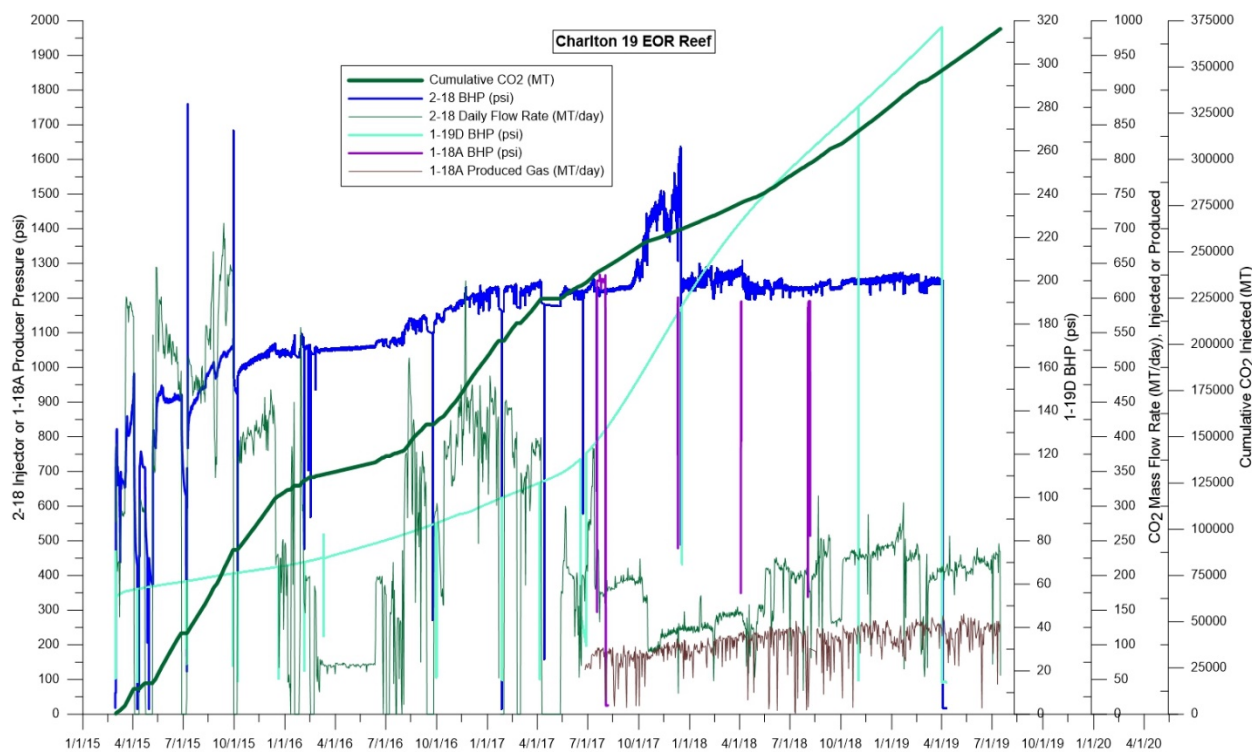


Figure 3-8. Composite Plot of Bottomhole Pressure & Temperature in Charlton 19 during the MRCSP injection period from February 2015.

### 3.3 Static Model

The geologic data and interpretations described in the *Task 5: Baseline Geologic Characterization Report* technical report [Haagsma et al., 2017] were used to construct a geologic SEM. The petrophysical analyses and interpretations were used as input into the SEM. A 2D depositional model interpretation was used to guide the development of the model's structural framework. 3D seismic data was used to define the boundary and geometry of the reef. The SEM was built using Petrel software and began with the generation of structural surfaces. Next, surfaces for facies were created to subdivide the reservoirs into key zones. These zones were subsequently layered and followed by well log upscaling and property modeling.

#### 3.3.1 Framework

##### 3.3.1.1 Structural Surfaces and Isochore Maps

Earlier work produced regional surfaces using 946 wells over a 659 km<sup>2</sup> (7.08x10<sup>9</sup> ft<sup>2</sup>) area encompassing Otsego County. These, along with local geologic knowledge of off-reef behavior, were used to establish off-reef trends and the geology around the perimeter of the reef structure. Where necessary, flanking surfaces were hand-edited until the regional trend was matched.

Field-scale contoured structural surface maps were generated for formation tops, Figure 3-9. A structural surface map is a 2D (plan view) figure of a formation's elevation within the model area. Each structural surface was generated by gridding the sparse formation top data and reefal polygons using the convergent interpolation algorithm in Petrel to create a three-dimensional surface consistent with reefal geometry. These structural surfaces form the SEM's structural framework and were quality checked to

ensure that all surfaces were geologically conformable without anomalous, geometric cross-overs. Interpreted seismic horizons were used to validate the geometry of the modeled reef surfaces.

The uppermost SEM zone for the Charlton 19 reef was the A2 Carbonate, which gently slopes off-reef. The A1 Carbonate follows the underlying Brown Niagaran Formation. Locally, the Brown Niagaran was comprised of two pinnacle reefs and a small reefal high in the saddle region between the two pods. The southwestern pod is the thicker of the two but contains less rock volume than the northeastern pod. The saddle region reefal high is likely attributed to either a slumped part of one of the lobes or a thick saddle region between the lobes without enough seismic resolution to accurately map the saddle region. The Gray Niagaran was relatively flat throughout the study area deepening to the southeast. Figure 3-10 shows the structural surfaces for the reef's carbonate units and includes the A2 Carbonate, A1 Carbonate, Brown Niagaran, and Gray Niagaran.

Isochore maps were generated by computing the difference between adjacent structural surfaces. An isochore is a contour line that connects points of equal vertical thickness.

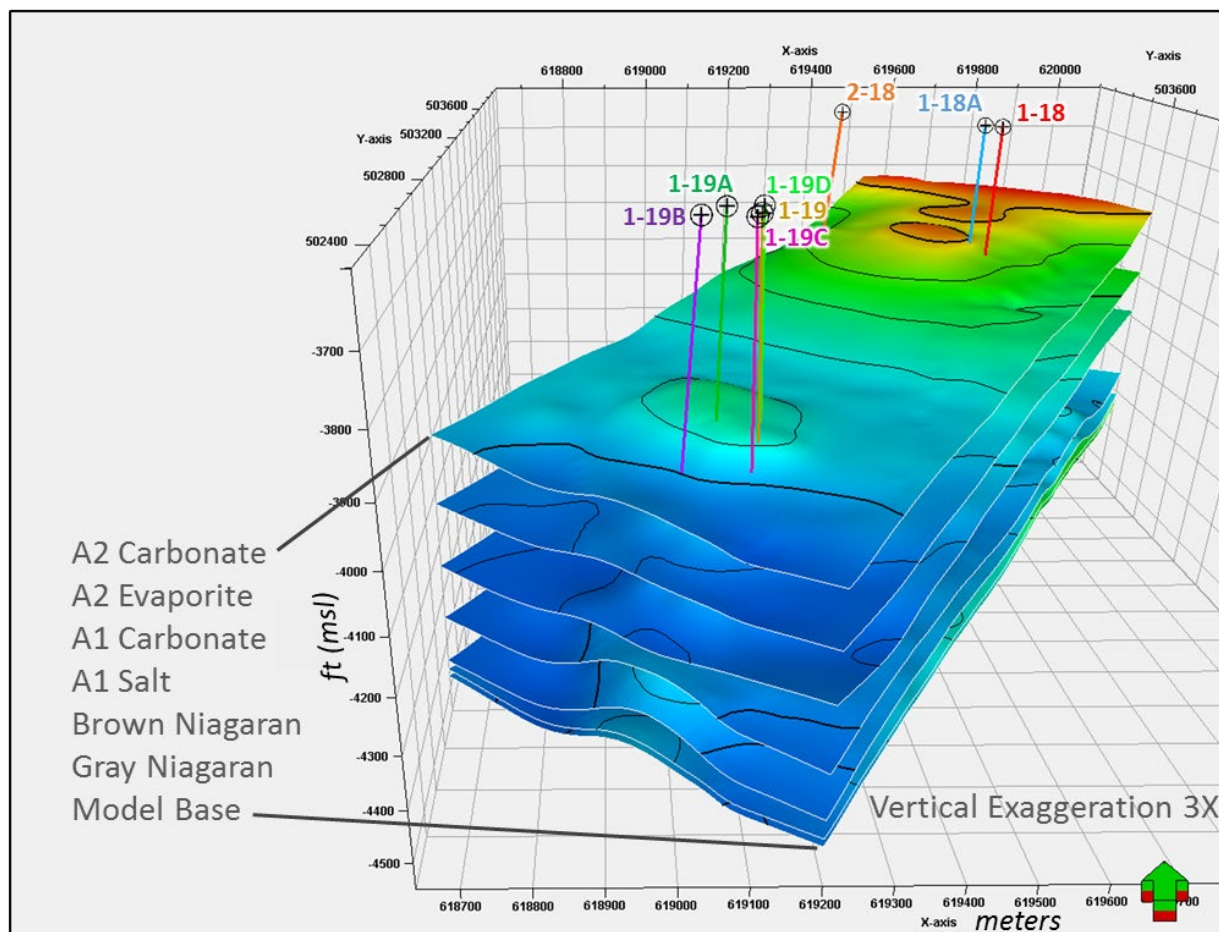


Figure 3-9. Structural surfaces of the Charlton 19 model from the A2 Carbonate surface to the Model Base surface showing all wells that penetrate the reef structure.

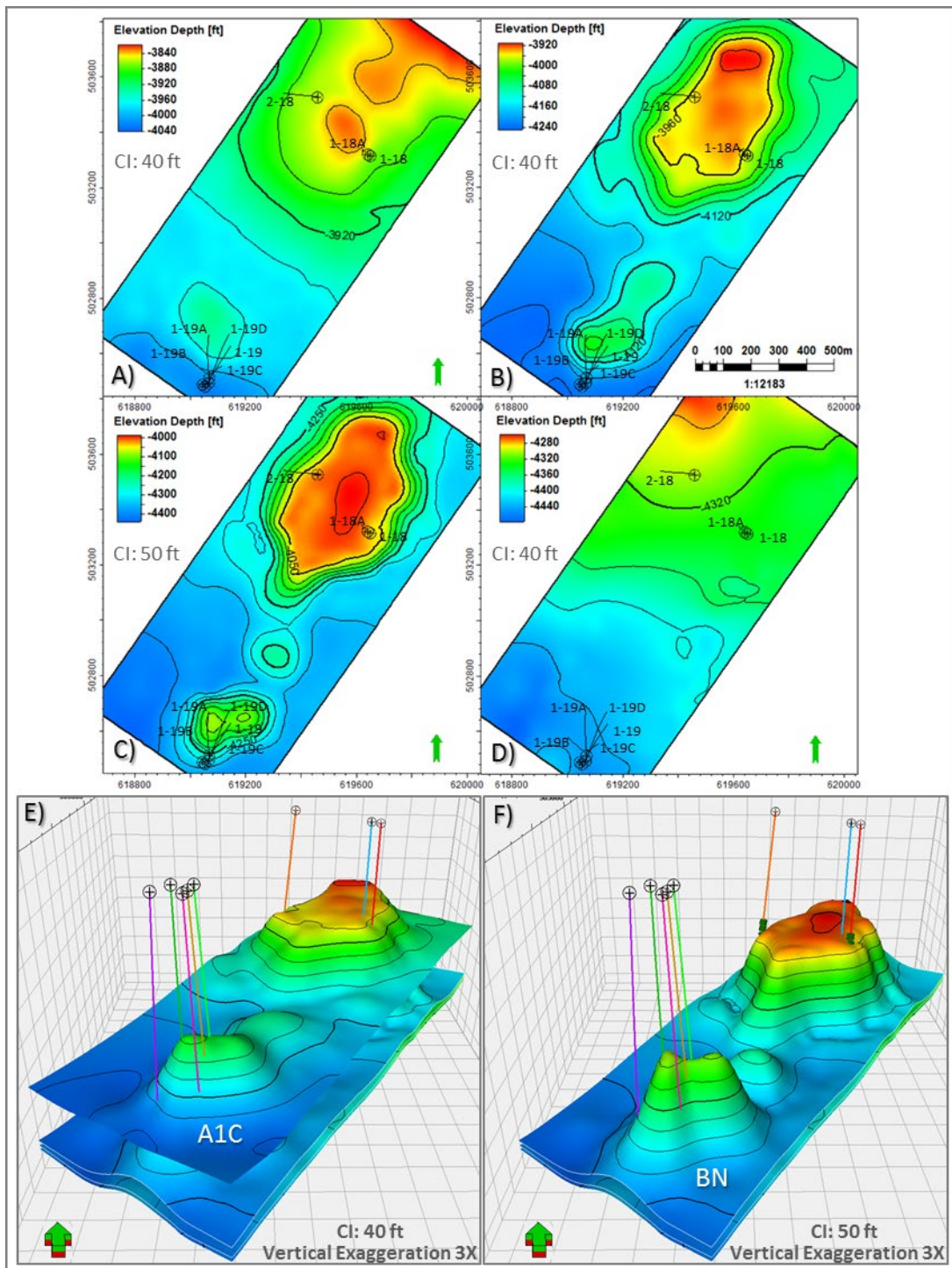


Figure 3-10. Charlton structural surfaces. Elevation depth is from mean sea level. A) A2 Carbonate. B) A1 Carbonate. C) Brown Niagaran. D) Gray Niagaran. E) Oblique view of the A1 Carb Carbonate. F) Oblique view of the Brown Niagaran surface. Wells are labeled at the bottomhole location.

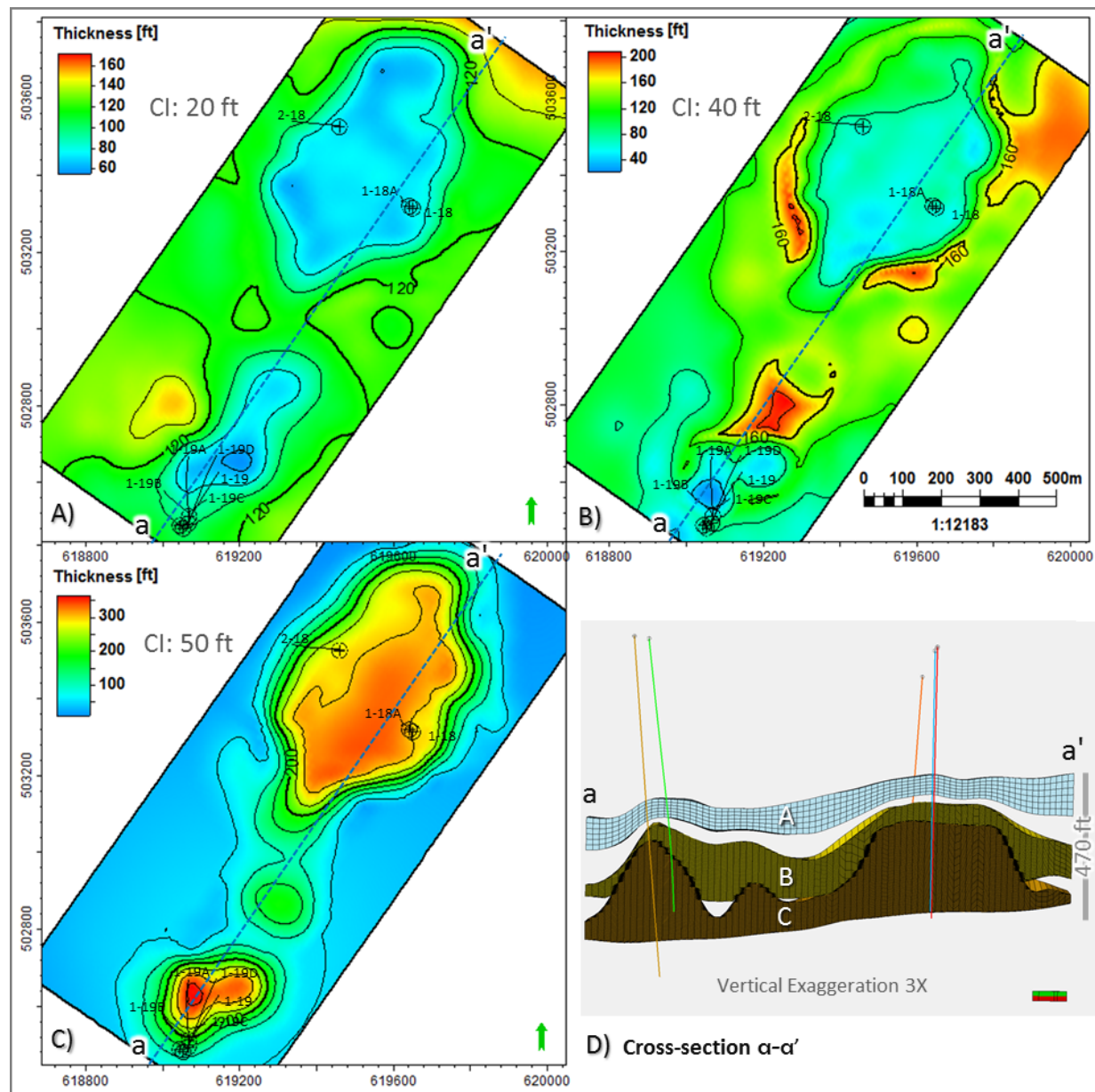


Figure 3-11. Isopach maps from the Charlton 19 SEM. A) A2 Carbonate surface. B) A1 Carbonate surface. C) Brown Niagaran surface. D) Northeast-trending cross-section a-a' through the SEM showing these carbonate formations.

Figure 3-11 shows the isochore maps for the A2 Carbonate, A1 Carbonate, and Brown Niagaran; a cross-section through these units is shown in Figure 3-11D.

### 3.3.1.2 Lithofacies – Surfaces

Commonly, the lithofacies modeling exercise occurs further in the workflow under facies modeling. However, for this modeling effort, extra surfaces were prepared to delineate the distinct lithofacies within the Brown Niagaran. For this model, the interpreted lithofacies were used to define regions within a formation to represent individual compartments or “geobodies.” The lithofacies represent rock with similar composition, porosity and permeability distributions. Implementing these lithofacies enables greater

flexibility and control for both property modeling and DRM work. Table 3-4 itemizes the zones (intervals between two horizons) created for each formation in the Charlton 19 SEM. Each zone is comprised of one or more lithofacies.

**Table 3-4. Zones (intervals between two horizons) created for each formation in the Charlton 19 SEM**

Zone	Lithofacies	Comment
A2 Carbonate	A2 Carbonate	Continuous unit over the reef
A2 Evaporite	A2 Evaporite	Seal, continuous over the reef
A1 Carbonate	A1 Carbonate	Porous unit over the reef
A1 Salt (Flank)	A1 Salt (Flank)	Seal
	Brown Niagaran (Flank)	A portion of the reef body
	Brown Niagaran (Leeward)	A portion of the reef body
	Brown Niagaran (Reef Core)	A portion of the reef body
	Brown Niagaran (Windward)	A portion of the reef body
Gray Niagaran	Gray Niagaran	Rock unit underlying the reef

The Brown Niagaran is a good example where polygons were created to outline the top and base boundaries of each lithofacies, and to clip structural surfaces used to generate the lithofacies surfaces. The polygons serve as data-input to the surface contouring algorithm. The top and base polygons are combined as input to define, constrain, and delineate the reefal zones. The resulting surfaces ensure that each reefal zone has a defined 3D volume. Figure 3-12 illustrates this process and the zones created for the lithofacies of the Brown Niagaran.

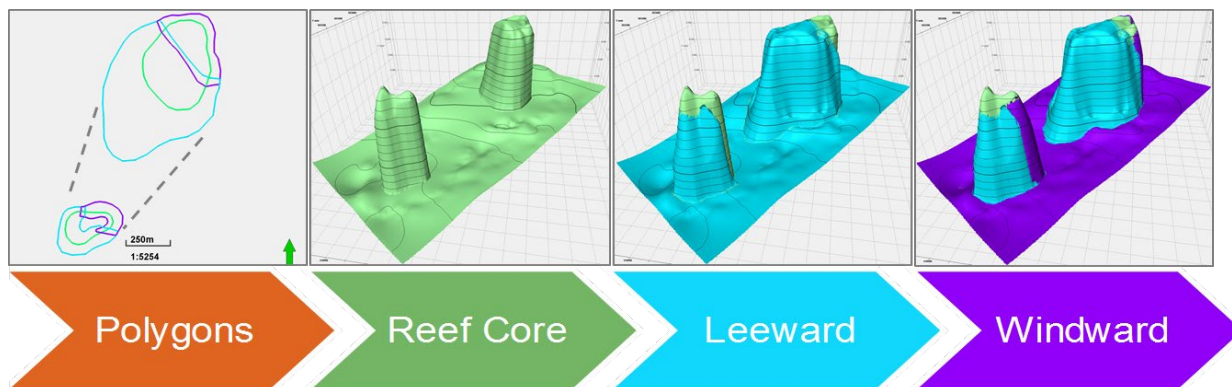


*Figure 3-12. Workflow depicting the delineation of lithofacies for the Brown Niagaran in the Charlton 19 reef. Polygons defining the reefal footprint and geometry were based on seismic interpretations. Along with formation tops, polygons were prepared for generating surfaces that envelop reefal lithofacies.*

### **Horizon Modeling**

The structural surfaces were incorporated into the structural framework through the process called horizon modeling. In this process, geologic rules were applied to each formation to guide the SEM's horizons. The geologic rules prevent the modeled horizons from crossing over one another and allow them to be discontinuous in areas where they pinch out.

Petrel's definitions of horizon types are:

- Conformable: All horizons belong to the same group and build conformable to each other.
- Erosional: Erosions belong to the group above, the group below erosion is numbered differently than the group above.
- Discontinuous: Discontinuities do not belong to groups above or below; they correspond to a separate group that is collapsed into a single surface.
- Base: Horizons above will truncate into a base.

Horizon modeling was an essential tool to control horizons and build zones. The A2 Carbonate, A2 Evaporite (salt and anhydrite), A1 Carbonate, A1 Salt, and Gray Niagaran were all set to conformable. The Brown Niagaran surface was used as a control to conform the reef core, windward, and leeward zones and set as a base horizon. This allowed the A1 Salt to truncate into the Brown Niagaran appropriately. The “Final Base,” the base surface of the model, was created 20 feet below the Gray Niagaran and set as a base horizon. Figure 3-13 illustrates the horizon scheme used in the SEM.

Index	Horizon name	Color	Calculate	Horizon type	Conform to another horizon		Status	Smooth iterations	Use horizon-fault lines	Well tops	Input #1			
1	FINAL_A2C		<input type="button" value="▼"/>	<input checked="" type="checkbox"/> Yes	Conformable	<input type="button" value="▼"/>	No	<input type="button" value="▼"/>	1	<input checked="" type="checkbox"/> Done	0	<input checked="" type="checkbox"/> Yes		FINAL_A2C
2	FINAL_A2E		<input type="button" value="▼"/>	<input checked="" type="checkbox"/> Yes	Conformable	<input type="button" value="▼"/>	No	<input type="button" value="▼"/>	1	<input checked="" type="checkbox"/> Done	0	<input checked="" type="checkbox"/> Yes		FINAL_A2E
3	FINAL_A1C		<input type="button" value="▼"/>	<input checked="" type="checkbox"/> Yes	Conformable	<input type="button" value="▼"/>	No	<input type="button" value="▼"/>	1	<input checked="" type="checkbox"/> Done	0	<input checked="" type="checkbox"/> Yes		FINAL_A1C
4	FINAL_A1E		<input type="button" value="▼"/>	<input checked="" type="checkbox"/> Yes	Conformable	<input type="button" value="▼"/>	No	<input type="button" value="▼"/>	1	<input checked="" type="checkbox"/> Done	0	<input checked="" type="checkbox"/> Yes		FINAL_A1E
5	FINAL_BN		<input type="button" value="▼"/>	<input checked="" type="checkbox"/> Yes	Base	<input type="button" value="▼"/>	No	<input type="button" value="▼"/>	1	<input checked="" type="checkbox"/> Done	0	<input checked="" type="checkbox"/> Yes		FINAL_BN
6	FINAL_GN		<input type="button" value="▼"/>	<input checked="" type="checkbox"/> Yes	Conformable	<input type="button" value="▼"/>	No	<input type="button" value="▼"/>	1	<input checked="" type="checkbox"/> Done	0	<input checked="" type="checkbox"/> Yes		FINAL_GN
7	FINAL_BASE		<input type="button" value="▼"/>	<input checked="" type="checkbox"/> Yes	Base	<input type="button" value="▼"/>	No	<input type="button" value="▼"/>	1	<input checked="" type="checkbox"/> Done	0	<input checked="" type="checkbox"/> Yes		FINAL_BASE

Figure 3-13. Horizon modeling in Petrel™ showing order of horizons and horizon type for the Charlton 19 SEM.

### 3.3.1.3 Zones and Layers

Horizons define the SEM's base framework consisting of stratigraphic zones. SEM zones are then subdivided into layers to capture the desired vertical resolution and thickness of each zone. The vertical layering resolution seeks to capture the variability observed in well logs. At this stage, the SEM's layering scheme may be sufficient to support computing pore volume and HCPV estimates. SEMs are used to capture high-resolution geologic heterogeneity and often contain higher cell counts than a flow simulation software platform can handle. In this case the SEM may require upscaling to reduce overall cell count. Though, for Charlton 19, there was no need for upscaling since no dynamic simulations were to be run.

There were two SEM layering schemes used during the modeling exercise. These are described below and are illustrated in Figure 3-14.

- A) Preliminary model: Employed proportional layering, with vertical thickness targeting 5-ft for formations with hydrocarbon production like the A1 Carb Crest and Brown Niagaran (LW, RC, WW). Fewer layers were proved for evaporites and otherwise tight formations.
- B) Petrophysical model: A 2-ft layer model was used to perform property modeling for porosity and permeability. No sidewall core or core data was available and therefore a 2-foot layer was implemented to capture the 2-foot resolution of the wireline logs. For all the model zones except the Brown Niagaran, layers “followed top” (formation top). The Brown Niagaran layers followed a trend surface created by averaging the Brown Niagaran with the Gray Niagaran surface. This allowed for the layers to truncate into the Brown Niagaran, giving a more geologic representation of the internal

reef geometry typically seen in Michigan Reefs (Barnes et. al, 2013). Given the density of layers (2853 layers), the grid lines are turned off in B.

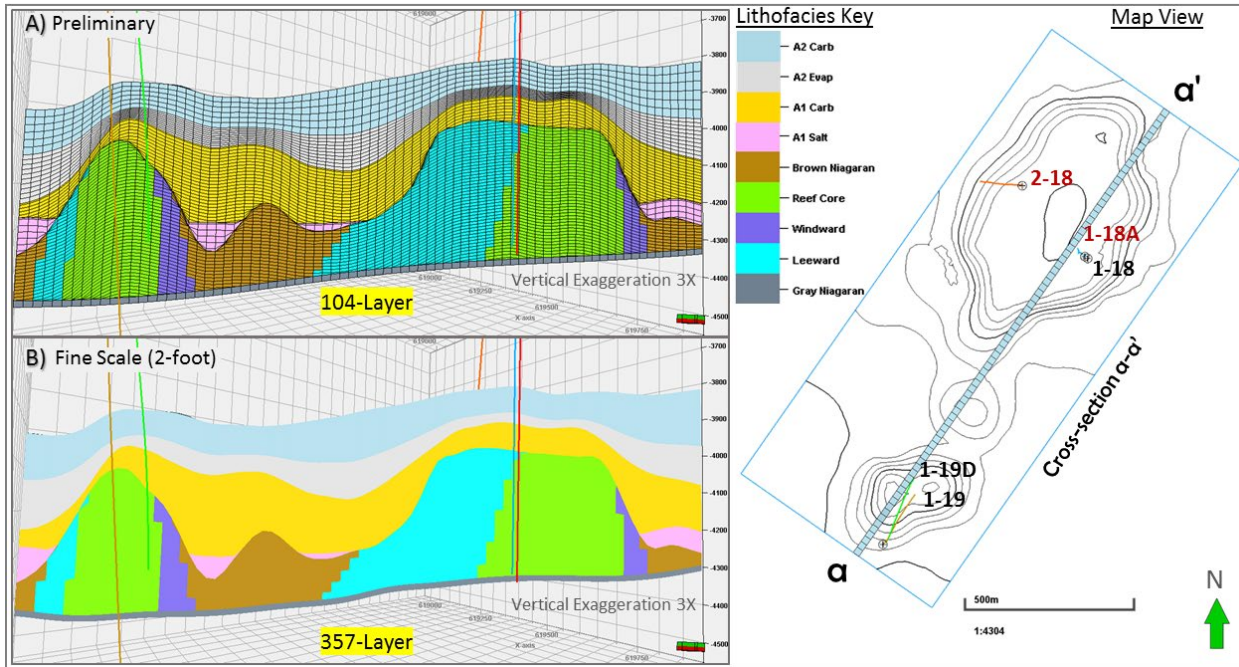


Figure 3-14. The map view right shows the Charlton 19 Brown Niagaran contours with the a-a' cross-section location. Only wells with logs are shown in the map view. The left shows Charlton 19 SEM layering schemes shown on Lithofacies cross-section. A) Preliminary SEM for developing and validating reefal architecture. B) Fine-scale, high-resolution model for petrophysical modeling. Note that the grid lines here are turned off; otherwise, the cross-section would appear black.

### 3.3.1.4 Geometry and Model Grid Definition

The boundary used for the SEM's structural framework is shown as a red outline in Figure 3-15 and covers 1,074,400 m<sup>2</sup> or 265.5 acres. This area was selected to capture the reef's geometry and formations that flank the reef. The SEM was comprised of cells, with grid cell size in the x-y directions of 20 meters. This size permitted enough resolution between wells while generally limiting cell count. A list of the grid parameters for the SEM is provided in Table 3-5. Figure 3-15 shows an oblique cut-away view of the SEM and reveals the two reefal pods at the Charlton 19 field. The SEM's top is represented by the A2 Carbonate at an approximate depth of 4,903 feet below ground level. The SEM's overall thickness is approximately 675 ft.

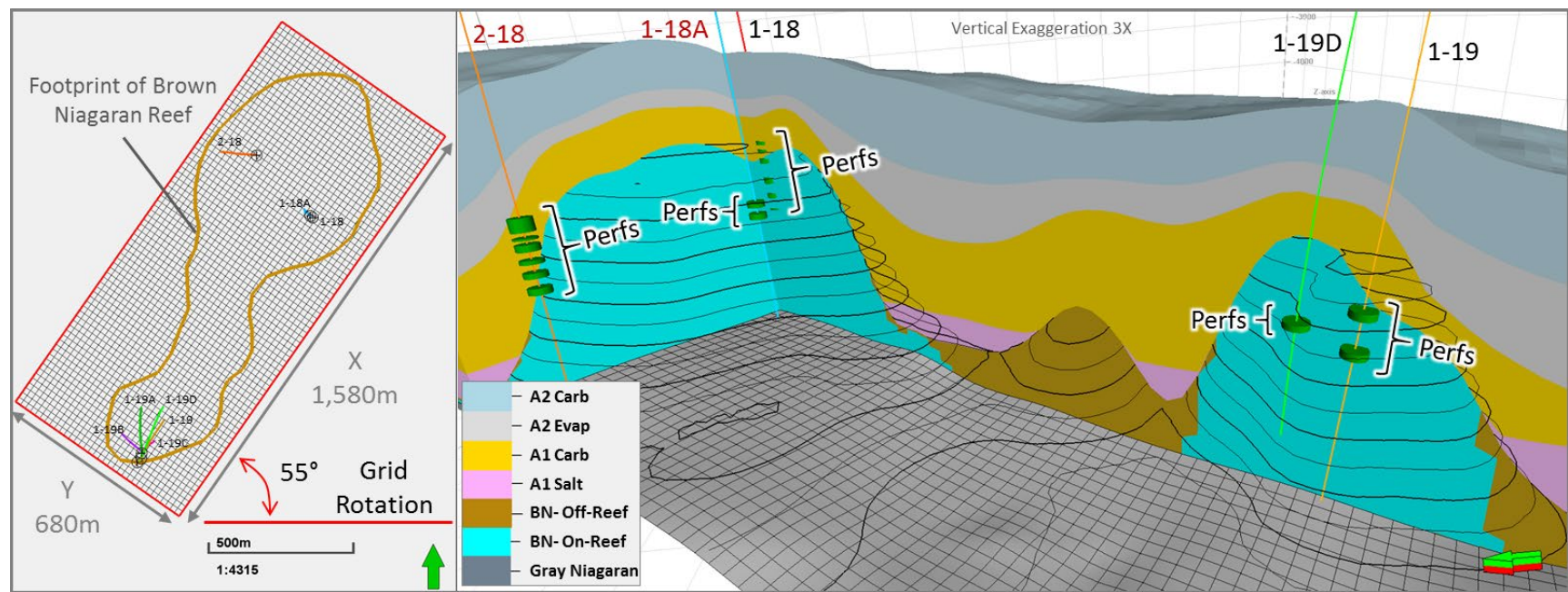


Figure 3-15. Left: Plan view of the x and y grid for Charlton 19 SEM. SEM boundary in red. Left: Oblique view of the 357-layer SEM with cut-away revealing the northern and southern reef lobes. Black lines represent the BN reef elevation contours (SSTVD).

The resulting SEM for the Charlton 19 field followed the geologic interpretation developed through wireline log analyses for this reef and the Dover-33 reef. The Brown Niagaran was composed of two distinct sets reef lithofacies (reef core, windward, leeward) separated by the flank facies in the saddle region of the reef. The leeward lithofacies has gentler slopes and the windward lithofacies has steeper slopes as is consistent with paleowind direction, waves, and their related effect on the reef. Overall, the SEM's structure is consistent with interpretations and hence considered representative of the geology of the reef system. Figure 3-16 shows a cross-section through the SEM framework and the resulting zones/lithofacies.

**Table 3-5. Summary of grid parameters for the Charlton-19 reef field.**

Grid Parameter	Charlton 19	Comments
SEM dimension in x direction	1,580 meters	-
SEM dimension in y direction	680 meters	-
SEM dimension in z direction	675 ft	-
Cell grid size in x and y direction	20 meters	-
Cell grid size in y direction	20 meters	-
Model area	1,074,400 meters <sup>2</sup> (265.5 acres)	-
Minimum well spacing	~44 meters	Spacing between wells at reservoir depth.
Layers / Number of grid cells	104 / 279,344	Preliminary Model: <i>Charlton19_Clipped_Lithofacies</i>
Layers / Number of grid cells	357 / 958,902	Petrophysical modeling: <i>Charlton19_Clipped_Petrophysical_2ft</i>

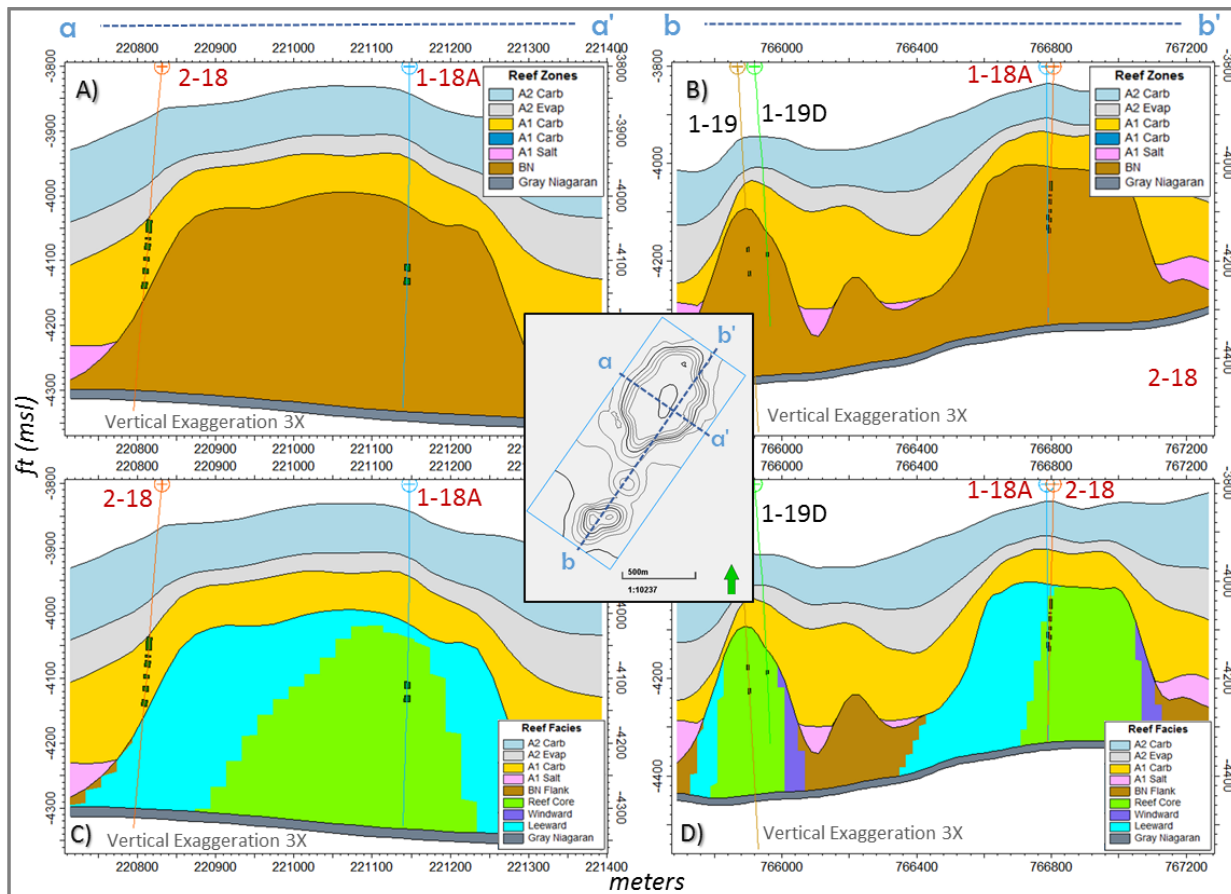


Figure 3-16. Cross-section through the Charlton 19 SEM framework. SEM zones were partitioned by formation tops (surfaces). A) Partitioned zones in the northern reef structure and B) both reef structures. Lithofacies were distributed among the zones. The Brown Niagaran zone includes the reefal structure comprised of leeward, reef core, and windward lithofacies. NW-SE cross-section of the distribution of the reef facies in the C) northern reef structure and D) both reef structures.

### 3.3.2 Property Modeling

The geologic framework was used with scaled-up log properties to build porosity and permeability property models. A preliminary property model was built for porosity and permeability. The process began with the upscaling of wireline logs at the scale of the SEM's vertical resolution consisting of 104 layers. The purpose of this model was to refine the SEM framework and develop an understanding of reservoir character.

The preliminary model was superseded by a higher vertical resolution model containing 2-foot layering and resulted in an SEM with 357 layers. During this exercise, average porosity logs (average of neutron and density porosities) were scaled-up to the grid resolution and subjected to vertical variogram analysis to characterize vertical heterogeneity in oil-bearing zones like the Brown Niagaran. Variogram statistics from these well logs were used in a conditional simulation algorithm to populate the 3D SEM with the key petrophysical rock properties. This process required interpolating the upscaled log porosity values across the entire 3D model grid. The Gaussian Random Function Simulation (GRFS) method was used for these models. The GRFS is a stochastic method that honors the full range and variability of the input data. Each run creates one equiprobable distribution of a property throughout a model zone based on a model

variogram. Results were compared to original log values and the scaled-up values using cumulative distribution curves (CDFs) to ensure the algorithm was representative of the data.

Permeability was populated in the static model using Dover-33's core porosity-permeability transform equations. Dover-33's core data was used because of its proximity to Charlton 19 and similar dolomitic reef lithology. These equations were applied directly to the porosity model. The following sections will focus on the higher resolution, 357-layer model.

### ***3.3.2.1 Upscale of Wireline Logs***

Average neutron-density porosity log data was available for five wells at Charlton 19 and represents a good estimate of porosity for the dolomite units. These log measurements were collected every half foot, typically with a two-foot resolution. These well logs were upscaled or sampled along the well trajectories to the SEM grid's vertical resolution of 2 ft. These "scaled-up" logs were viewed in cross-section for each well to quality check the process. The scaled-up logs match the original well logs and formation tops, honoring the variations in porosity. Figure 3-17 shows an example of the scaled-up average neutron-density porosity (colored bars) that matches closely with the original porosity log. This close match is expected as the SEM's resolution is very close to the resolution of the well logs.

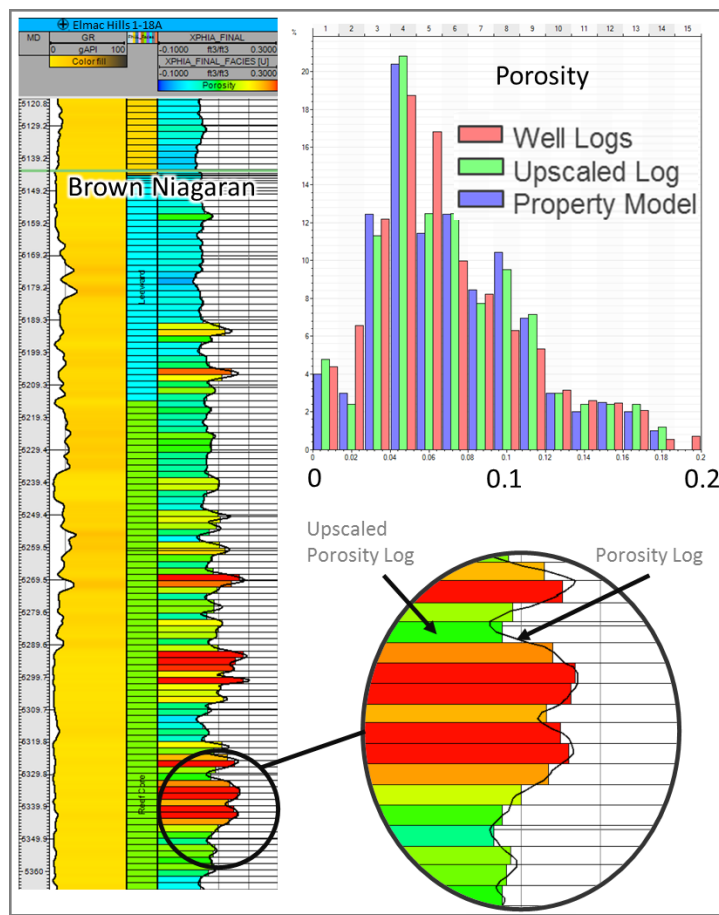


Figure 3-17. Well log upscaling. Example of the tight match between well logs and well log upscaling at the SEM's grid resolution of 2-ft. Tracks left to right: gamma ray, facies, and average porosity. Top right: porosity histogram for the Elmac Hills 1-18A well comparing upscaled porosity log against original porosity (XPHIA) log. Bottom right: magnified view of the match between the well porosity log and its upscaled values.(colored blocks).

### 3.3.2.2 Porosity

The resulting porosity model followed the scaled-up and original well logs closely as shown in the CDFs in Figure 3-18. The A1 Carbonate contained the second highest average porosity value at 5 percent (Table 3-6). The northern reef lobe contained high moderate porosity values over the reef structure and along the upper flanks of the reef. This trend is shown in the Elmac Hills 2-18 porosity log and is likely where the A1 Carbonate and Brown Niagaran communicate. The Brown Niagaran had the highest average porosity of 7.9 percent. In the Northern lobe, the top of the reef contained moderate porosity, mid-reef contained the highest porosity, and the lower portion of the reef contained streaks of high and low porosity. The southern reef lobe shows high porosity streaks at the top of the reef, mid- reef on the leeward side, and at the base of the reef. This is consistent with what is seen in the log data and could be attributed to vuggy dolomite intervals. It should be noted that the wells with logs only penetrated the core and leeward reef facies. This will likely skew the porosity model to porosities that represent those facies, in this case toward the lower value end. The two wells that penetrated the Gray Niagaran contained erroneous log data and were omitted from the model. The Gray Niagaran was assigned a constant value of 0.5 percent porosity to represent a low porosity low permeability zone. Figure 3-18 shows histograms

and CDF plots for the oil-bearing units (A1 Carb and Brown Niagaran Reef) and for the entire SEM which includes all zones.

**Table 3-6. Summary of average porosity as computed in the SEM for each zone in the Charlton 19 reef.**

Zone	Average SEM Porosity	Standard Deviation
A2 Carbonate	0.011	0.013
A2 Evaporite	0.002	0.006
A1 Carbonate	0.050	0.034
A1 Salt	0.003	0.001
Brown Niagaran	0.079	0.034
Gray Niagaran	0.005	NA
All SEM zones together	0.056	0.04

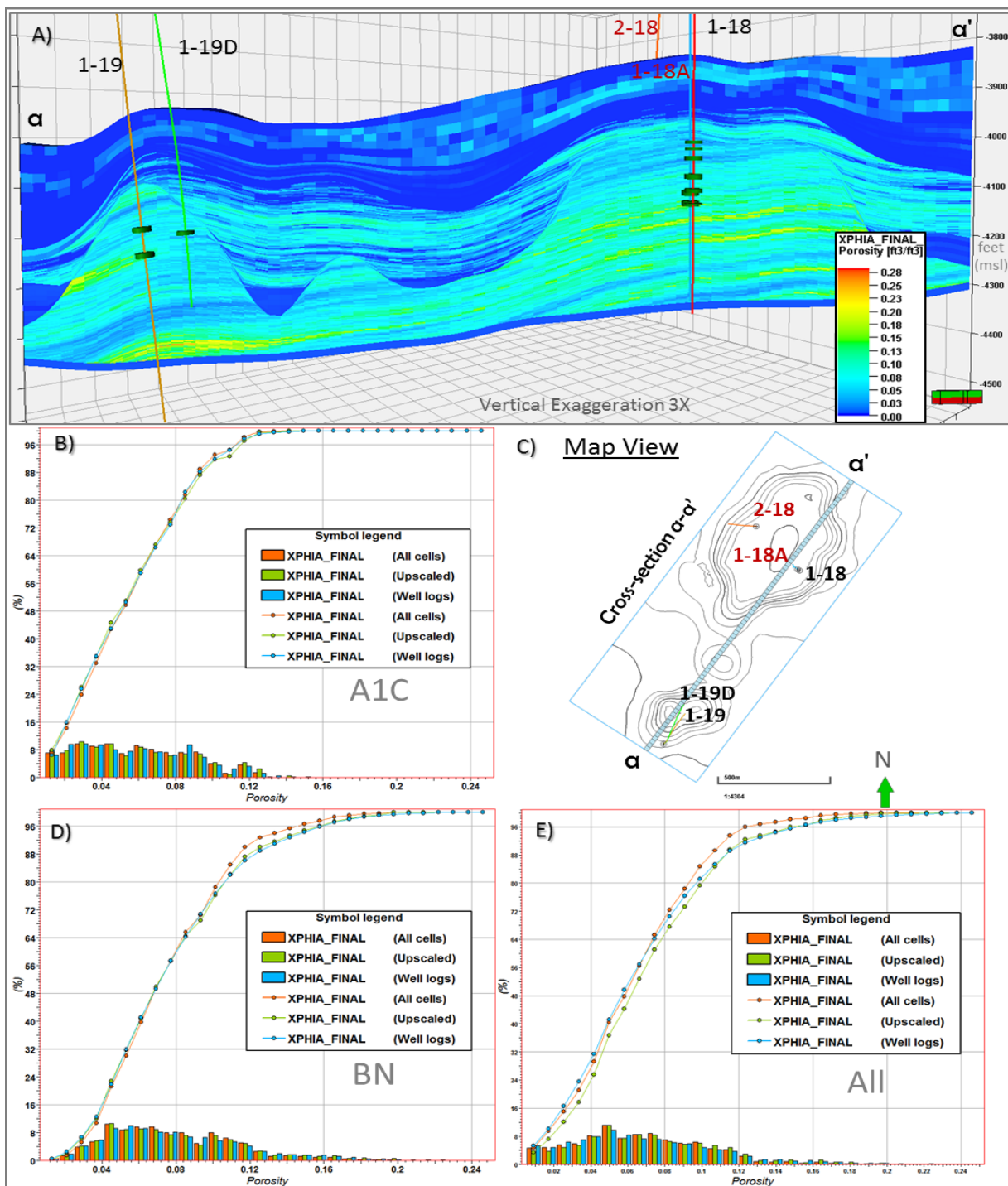


Figure 3-18. A) Cross-section thought the porosity model. B) CDF comparison of average porosity for the A1 Carb. C) Map of the reef showing the orientation of cross-section a-a'. D) CDF comparison of average porosity for the Brown Niagaran reef. E) CDF comparison of average porosity for the entire SEM.

### 3.3.2.3 Permeability

The permeability modeling effort used Dover-33 core porosity-permeability transform equations to populate the model for the oil-bearing zones. Figure 3-19 shows Dover-33 core porosity-permeability cross plot and associated power-law transformations for the Brown Niagaran and A1 Carbonate.

Table 3-7 shows the method and values used to populate the permeability model.

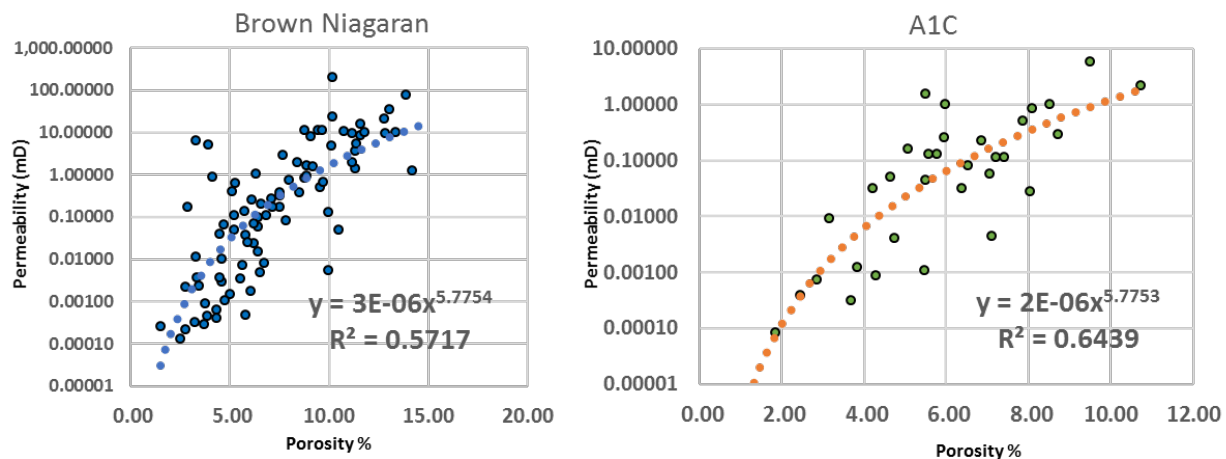


Figure 3-19. Dover-33 porosity-permeability cross-plots showing the power law transformations and associated equations used to populate permeability in the Charlton 19 model.

**Table 3-7. Method and values used to populate the permeability model.**

Zone	Distribution	Constant	Transform
A2 Carbonate	Constant	0.01	N/A
A2 Evaporite	Constant	0.01	N/A
A1 Carbonate	Transform	N/A	$2E-06x^{5.7753}$
A1 Salt	Constant	0.01	N/A
Brown Niagaran	Transform	N/A	$3E-06x^{5.7754}$
Gray Niagaran	Constant	0.01	N/A

The permeability model was simplified for the non-oil-bearing zones by using constant low porosity values to indicate low porosity - low permeable zones. These zones include the Gray Niagaran, A1 Salt, A2 Evap, and the A2 Carbonate.

Figure 3-20 shows a cross-section through the permeability model. The average permeability for each zone is given in Table 3-8.

**Table 3-8. Summary of average permeability as computed in the SEM for each zone in the Charlton 19 reef.**

Zone	Average SEM Permeability (mD)	Standard Deviation (mD)	Zone
A2 Carbonate	0.01	-	A2 Carbonate
A2 Evaporite	0.01	-	A2 Evaporite
A1 Carbonate	0.35	7.501	A1 Carbonate
A1 Salt	0.01	-	A1 Salt
Brown Niagaran	3	11.863	Brown Niagaran
Gray Niagaran	0.01	-	Gray Niagaran

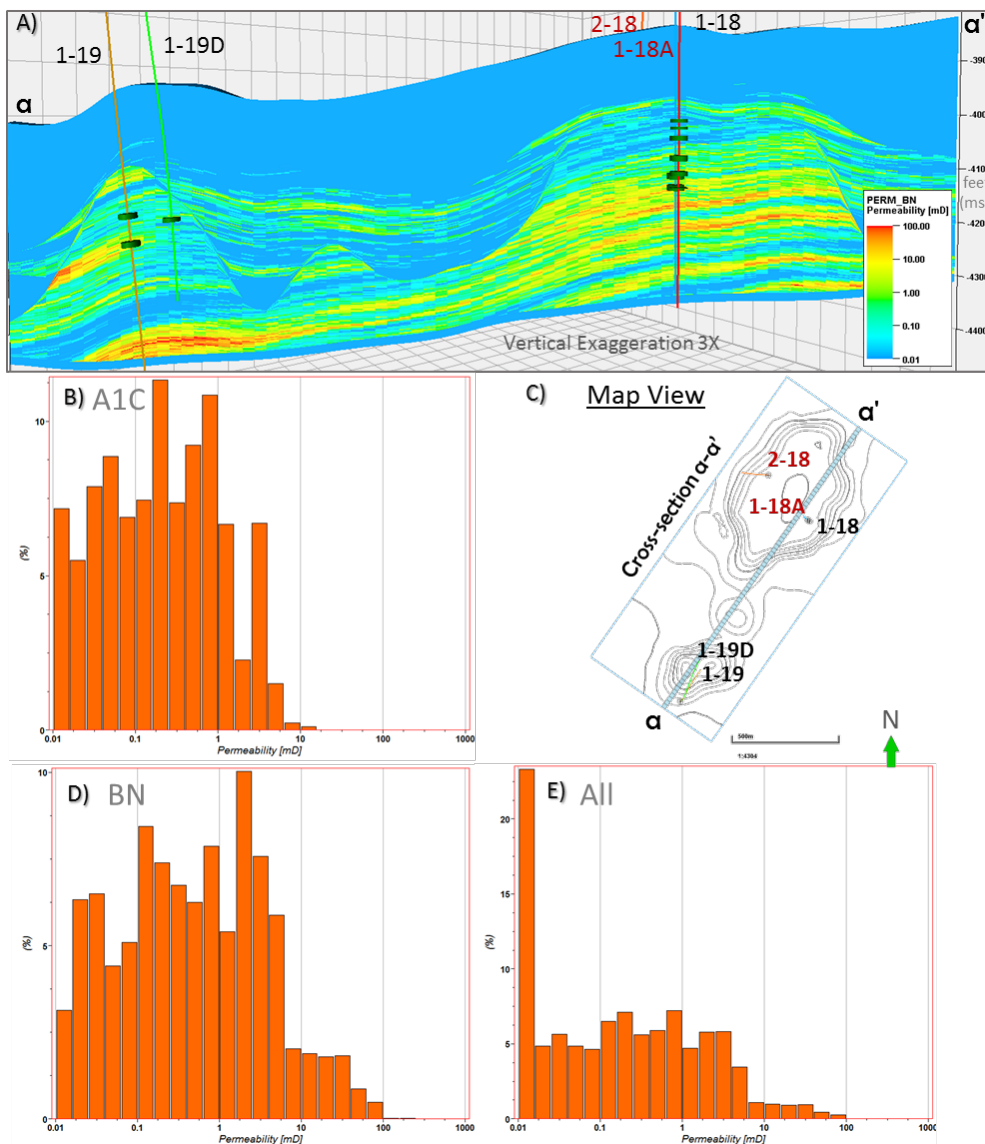


**Figure 3-20. A) Cross-section thought the permeability model. B) Histogram of permeability for the A1 Carb. C) Map of the reef showing the orientation of cross-section a-a'. D) Histogram of permeability for the Brown Niagaran reef. E) Histogram of permeability for the whole model.**

### 3.3.2.4 Water Saturation

A detailed 3D distribution of the initial water saturation in the reef was not calculated as there were no detailed dynamic modeling exercises planned. An average value of initial water saturation of 11.35 percent (Table 3-3) was considered above the OWC defined, from material balance calculations, in order to validate the hydrocarbon pore volume and hence initial oil-in-place obtained from the Charlton 19 reef SEM.

### 3.3.2.5 Volumetrics

The HCPV for the SEM was computed for the reef. The general equation for this calculation is:

$$\text{HCPV} = \text{GRV} * \text{N/G} * \phi * S_{hc}$$

**Equation 3-1**

where:

GRV: Gross rock volume in the trap above the hydrocarbon-water contact.

N/G: Average Net Reservoir/ Gross rock

$\phi$ : Average Porosity

$S_{hc}$ : Average hydrocarbon saturation =  $(1 - S_w)$ .

While the general equation may use average values, the calculations here are based on the porosity of individual cells. Since the initial water saturation distribution was not calculated as mentioned in Section 3.3.2.3, an average water saturation of 11.35 percent (Table 3-3) was used throughout the reef in line with material balance considerations. The dominant lithology for oil-bearing units were clean carbonate rocks, so the N/G value was set to 1 as a simplification to the model.

The resulting HCPV of oil for the reef was computed at ~1.3 million reservoir barrels. Petrel computes the HCPV by taking the pore volume of each cell multiplied by the oil saturation of each cell above the OWC. The oil saturation is assumed to be 90 percent above the OWC. Table 3-9 summarizes the volume and hydrocarbon (oil) estimates for all SEM zones and reflects volume of oil at reservoir (in situ) conditions; the Formation Volume Factor (Bo) was set to 1.4746 bbl/STB. The Charlton 19 reef is reported to have an estimated original stock tank oil-in-place (OOIP) of 2.6 MMSTB. The key producing formation expected to contain the oil in the reef is the Brown Niagaran formation which has the initial oil-in-place in line with the reported reef OOIP of 2.6 MMSTB. The SEM however is found to overestimate the oil-in-place due to limited characterization data for the flank, off-reef regions and the saddle connecting the reef pods which are interpolated in the SEM with connectivity assumptions that are found to be overly optimistic.

**Table 3-9. Volumetrics and HCPV for each reservoir reef zone in the SEM.**

Zone	Bulk Volume [ft <sup>3</sup> ]	Pore Volume [ft <sup>3</sup> ]	HCPV Oil [bbl]	STOIP [STB]
A2 Carbonate	1,255,901,447	2,355,520	2,088,168	1,416,091
Final A2E – Final A1C	876,614,755	395,456	350,571	237,740
Final A1C – Final A1E	737,076,472	6,870,551	6,090,744	4,130,438
Final A1E – Final Brown Niagaran	127,536	72	64	44
Final Brown Niagaran – Final Gray Niagaran	347,121,866	4,811,625	4,265,506	2,892,653
Final Gray Niagaran – Final Base	0	0	0	0
<b>Total</b>	<b>3,216,842,076</b>	<b>144,33,225</b>	<b>12,795,054</b>	<b>8,676,966</b>

### 3.3.2.6 *Upscaling*

The detailed high-resolution Charlton 19 SEM was not subjected to upscaling to coarsen the grid for dynamic modeling as there were no detailed dynamic modeling exercises planned for the reef.

### 3.3.2.7 *Alternative Conceptualizations*

No alternative geologic conceptualizations were considered for the Charlton 19 reef.

## 3.4 Dynamic Model

The objectives for the dynamic modeling activity include evaluating CO<sub>2</sub> injectivity and assessment of pore volume in this complex reef structure using a simplified approach with available field data. This section describes simplified analytical approach to model the compressible pore volume and injectivity index for the CO<sub>2</sub> injection only period of the MRCSP Phase III injection in the reef. The CRM method is implemented for this purpose.

### 3.4.1 Modeling Approach

There are various reservoir simulation tools used for modeling and history matching reservoir performance, ranging from detailed full-physics finite difference simulators to the simple analytical techniques, which include material balance equations and fractional flow curve methods. Figure 3-21 highlights the differences between CRM and detailed numerical models typically used for reservoir simulation. Finite difference models constitute the ‘traditional’ or ‘conventional’ simulation tools that enable the representation of the subsurface system of interest at desired resolution by accounting for the dynamics between hydrogeological, geomechanical, geochemical, and thermodynamic processes. Analytical methods, on the other hand, were developed to be computational inexpensive and less-data intensive alternatives to conventional simulation tools. Analytical methods are thus typically numerically fast and sufficiently reliable for screening or preliminary evaluation of a given system of interest. For Charlton 19, the CRM is applied to aid our understanding of the reef properties by using minimal field data from CO<sub>2</sub> injection operations. The resulting fitted model has the potential to rapidly predict the pressure buildup or rate for a desired target injection scenario.

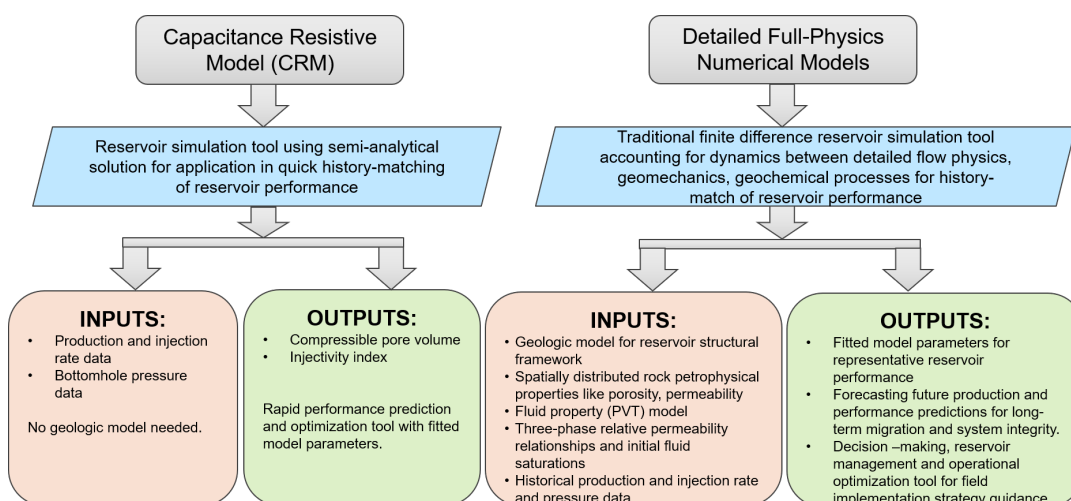


Figure 3-21. Infographic highlighting the differences between the CRM and detailed numerical models used for reservoir simulation.

Distributed reservoir model in 3D was not utilized for dynamic modeling for the Charlton 19 reef. A semi-analytical model was applied for the MRCSP CO<sub>2</sub> injection only period to estimate reef properties such as pore volume, reservoir pressure and well injectivity index using available field data. The CRM approach is to analytically integrate the simplified continuity material balance equation using nonlinear multivariate regression on the rate, bottomhole pressure and initial pressure data from the reef (Nguyen et al., 2011). This code has been implemented in-house in MATLAB and used for the Charlton 19 reef evaluation. Thus, the injection rate and injector bottomhole pressure history from the field during the MRCSP CO<sub>2</sub> injection phase is used to tune the CRM to obtain a representative average CO<sub>2</sub> injectivity index and the compressible pore volume or the 'capacitance' of the reef system. No geologic conceptualization is required for this modeling exercise; however, a comparison of the results is performed with our understanding and relevant independent evaluations of the reservoir for validation of the CRM.

The CRM code was applied to the Charlton 19 reef data that included the input of an initial pressure estimate. Since this parameter had considerable uncertainty for the reef, the modeling approach considered a reasonable range of initial pressure values to run the trials for the given injection and pressure history. The model fit was evaluated throughout the range of initial pressure assumptions to determine the 'optimal' resulting representative injectivity index and compressible pore volume for the reef. The resulting injectivity index was compared with independent injectivity analyses done for the reef while the compressibility calculated from the resulting pore volume was validated by consistency check with typical oil and gas systems. Thus, using basic available field data, the obtained knowledge of representative CO<sub>2</sub> injection performance has valuable potential for performing potential operational optimization related predictive analyses such as the pressure buildup or rate for a desired target injection scenario in the reef.

### 3.4.2 Model Inputs

The required inputs for the CRM include field data such as the injection rate and injector bottomhole pressure history from the field during the MRCSP CO<sub>2</sub> injection phase. The Charlton 19 SEM was not upscaled for detailed numerical evaluation of the reef or history matching purposes. Thus, there were no steps performed for characterization and import of pertinent rock and fluid properties applicable to the reef.

#### 3.4.2.1 Rock Properties

Distribution of key rock properties such as porosity and permeability have been determined as part of the SEM development as described earlier. CRM does not require the determined rock properties from the geologic conceptual model.

#### 3.4.2.2 Fluid Properties

Fluid model is not a required input for the CRM and is hence not applicable for the consequent discussion.

### 3.4.3 Primary Production History Match

No dynamic modeling of the primary production was performed as part of the history match process.

Material balance calculations were performed in order to verify the fluid (oil) saturation in place at a known time in 2012. Using the original oil-in-place calculated from material balance by Core Energy, the oil saturation (fraction) in May, 2012 was successfully independently estimated from oil balance as 0.38 as shown in Figure 3-22.

Parameter	Value	Unit	Comment
Cumulative oil Production, $N_p$	1065000	STB	
Cumulative Gas Production, $G_p$	2.27E+09	SCF	
Cumulative Water Production, $W_p$	1284000	STB	
Rock Compressibility, $C_{rock}$	3.00E-06	1/psi	Assumption
Initial Oil Formation Volume Factor, $B_{oi}$	1.4746	rb/stb	
Final Oil Formation Volume Factor, $B_{of}$	1.0473	rb/stb	
Initial Water Saturation, $Sw_i$	0.1135	fraction	
Porosity, phi	0.085	fraction	
Original Oil in Place, $N$	2634000	STB	Provided by Core Energy
Reservoir Pore Volume, $V_{p1}$ = (Area. Thickness)phi	4381383.418	rb	Calculated using $(N.B_{oi}) / (1-Sw_i)$
	24597086.51	ft <sup>3</sup>	
Initial Pressure, $P_i$	2774	psi	
Final Pressure @ 05/2012, $P_f$	155	psi	
$\Delta P = P_i - P_f$	2619	psi	Oil initial - Oil produced = Oil remaining in reservoir
<b>OIL Material Balance Calculation</b>			
$N - N_p = V_{p2} \cdot S_{o2} / B_{of}$			
Where,			
$V_{p2} = V_{p1} (1 + \text{crock} \cdot \Delta P)$			Accounting for PV change
$V_{p2}$	4.42E+06	rb	0.7796 %decrease
	24790345.82	ft <sup>3</sup>	
<b>Neglecting Minor Pore Volume Change due to Oil Production, Oil saturation is calculated from <math>(N - N_p = V_{p1} \cdot S_{o2} / B_{of})</math></b>			
Oil Saturation @ 05/2012, $S_{o2}$	0.3750		
Reported $S_{o2}$	0.3751		
% error	0.014799297		

Figure 3-22. Oil Material Balance Calculations in May 2012.

### 3.4.4 EOR/CO<sub>2</sub> Injection History Match

Analytical modeling was considered for a simplified evaluation of the pore volume and injectivity index by using the basic available pressure and rate information from the reef operations (Figure 3-9). The CRM (Nguyen et al., 2011) was used to model the injectivity index and pore volume by evaluating the injection only period in Charlton19, from February 2015 through June 2017. Figure 3-23 shows the daily averaged bottomhole rate and pressure data from the injection well during this period.

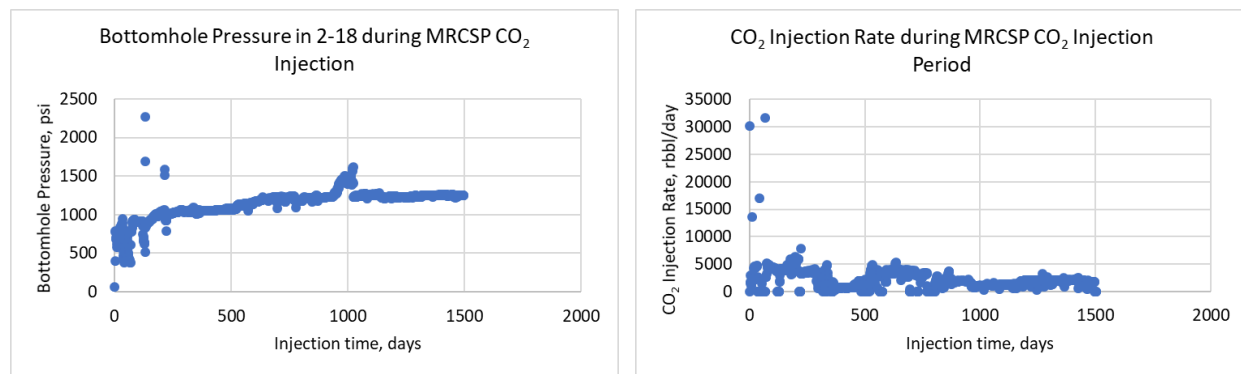


Figure 3-23. Daily averaged bottomhole pressure (left panel; psi units) and bottomhole injection rate (right panel; rbbl/day units) data from the injection well during the CO<sub>2</sub> injection only period being evaluated.

This data was filtered to eliminate point outlier values of injection rate. Figure 3-24 shows the filtered rate and bottomhole pressure data from the injection well during this period. This data was formatted and used as the input for the CRM.

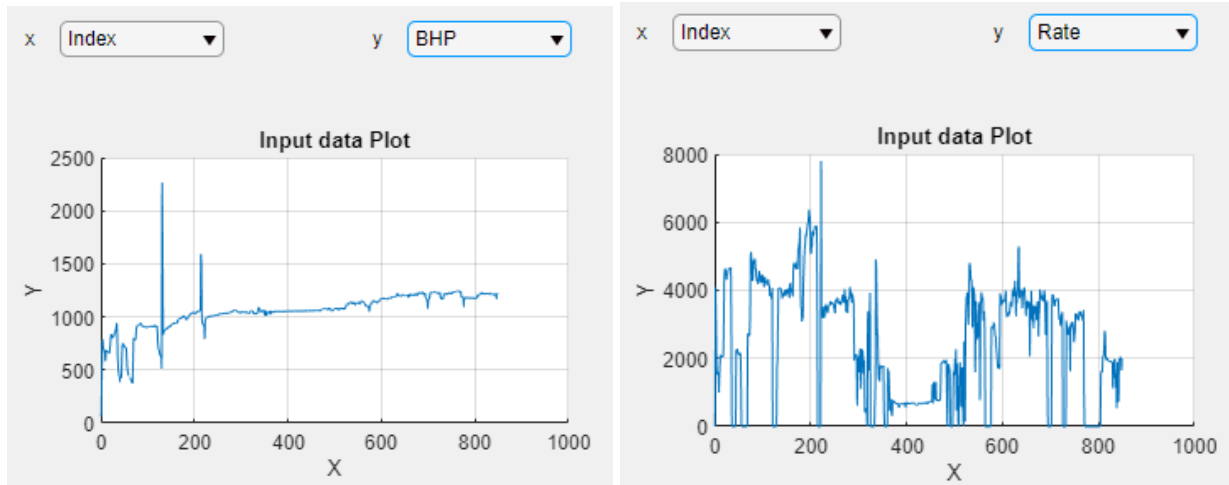


Figure 3-24. Filtered bottomhole pressure (left panel; psi units) and injection rate (right panel; rbbl/day units) data from the injection well during the CO<sub>2</sub> injection only period being evaluated.

The inputs to the model include the injection well field data such as injection rate, bottomhole pressure and the cumulative CO<sub>2</sub> injected during this period. The multi-variate regression model estimates the fitting parameters including injectivity index and total compressible pore volume to minimize the difference between the predicted and true field stored cumulative injected CO<sub>2</sub> volume. The model is calibrated by assuming an initial pressure value based on the field history. To address uncertainty in the initial pressure parameter input for the Charlton 19 reef, a range of realistic initial pressure assumptions, bound by field data, is used to evaluate the performance of the CRM model. Table 3-10 gives the range of initial pressure estimates, in 100 psi increments, used as the input parameter for Charlton 19 along with the CRM results for the co-efficient of regression, injectivity index and pore volume. The resulting coefficient of regression (R<sup>2</sup>) and injectivity index (J) values are plotted below in Figure 3-25.

**Table 3-10. Range of initial pressure ( $P_i$ ) estimates used as the input parameter and corresponding CRM results for Charlton 19.**

$P_i$ , psi	$R^2$	J, rbbl/day.psi	CtPv, rbbl/psi	Comment
60	0.4201	11.74	1492	Previous day gauge reading at injection and monitoring wells at start of MRCSP CO <sub>2</sub> injection in reef
155	0.4704	12.94	1646	Predicted pressure value at 2012 in preliminary material balance calculations by Core Energy
200	0.4976	13.63	1731	
300	0.5638	15.59	1950	
400	0.6349	18.44	2220	
500	0.7022	23.09	2554	
600	0.7502	32.38	2960	
700	0.76	62.01	3423	Best fit in CRM
800	0.7204	389.5	3845	
900	0.6382	34.8	3940	

Figure 3-26 shows the behavior of the goodness of fit ( $R^2$ ) as well as the injectivity index (J) with the range of initial pressures ( $P_i$ ) considered. Both the  $R^2$  and J tend to increase with increasing  $P_i$  until the “best fit” point. Beyond this “best fit” point, seen at 700 psi in Figure 3-25, the  $R^2$  begin to decrease. At this 700 psi initial pressure estimate, the calculated (Ct.PV) is 3423 rbbl/psi and the J is 62 rbbl/day.psi. Figure 3-26 shows a snapshot of the CRM interface with the calculations for the initial pressure input value of 700 psi.

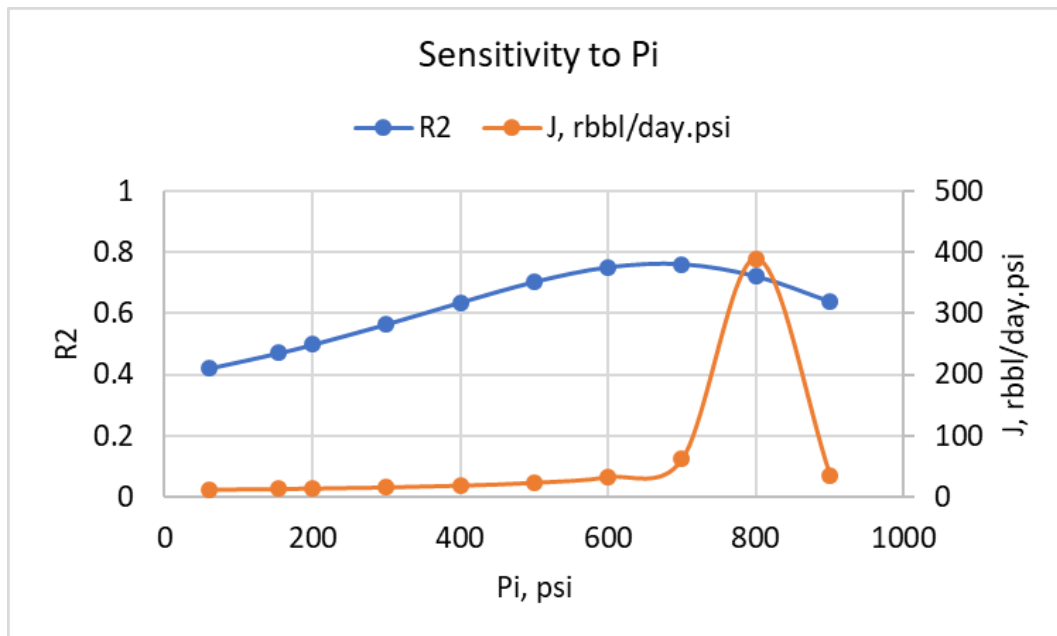


*Figure 3-25. Resulting coefficient of regression ( $R^2$ ) and injectivity index (J) values for different initial pressure assumptions. The initial pressure of 700 psi is seen to achieve the best fit or highest  $R^2$  with a corresponding value of 62 rbbl/day.psi.*

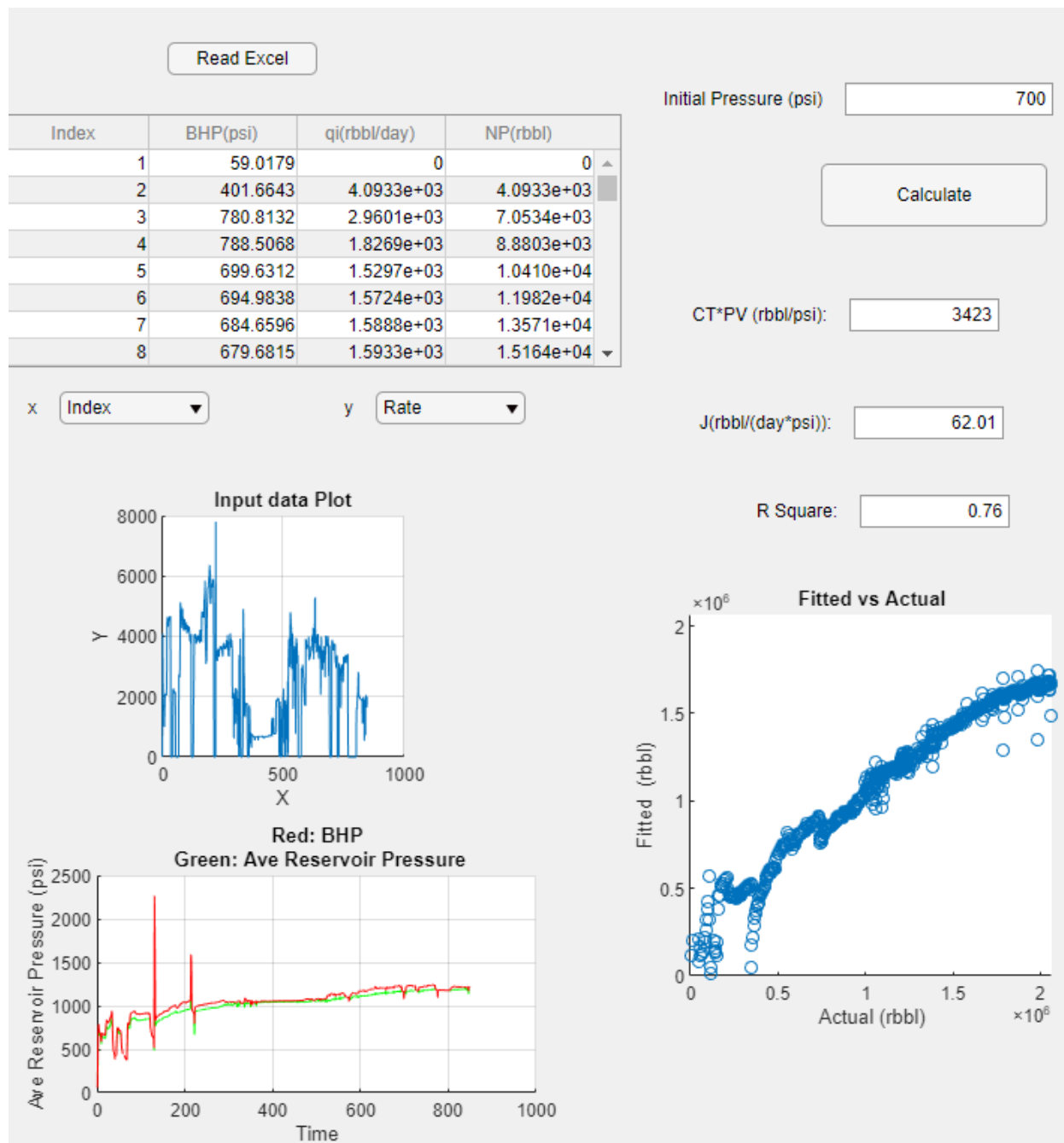


Figure 3-26. Snapshot of CRM interface showing the input and output fields. The calculations correspond to the initial pressure of 700 psi, which is seen to achieve the best fit or highest  $R^2$ .

The determined “best fit” value of  $J$  is compared with the earlier determined injectivity index of 2694 MT/yr.psi or 7.38 MT/day.psi for the reef using flowing material balance calculations. Using the average bottomhole CO<sub>2</sub> density of 48 lb/ft<sup>3</sup> corresponding to bottomhole pressure and temperature conditions during the MRCSP CO<sub>2</sub> period under consideration, the units of  $J$  are converted from reservoir volumetric conditions to be 7.58 MT/day.psi. This agrees very well with the estimated average injectivity index from flowing material balance calculations and thus helps in the validation of the CRM results for the Charlton 19 reef.

At the optimal determined 700 psi initial pressure, the calculated (Ct. PV) is 3423 rbbl/psi. This is used with the pore volume, Vp1, determined from material balance calculations (Figure 3-22) to evaluate the total compressibility. The total compressibility is thus calculated to be:

$$C_t = \frac{(Ct. PV)_{CRM}}{(PV)_{Material\ Balance}} = \frac{3423}{4381383.418} = 7.8e-4 \text{ psi}^{-1}$$

**Equation 3-2**

which is consistent with the order of magnitude of total compressibility typical of oil and gas systems.

### 3.5 Conclusions

The Charlton 19 reef is a dolomite reef that has undergone primary production and has been undergoing CO<sub>2</sub> EOR, with CO<sub>2</sub> injection in the Northern lobe of Charlton 19 since late 2014. The objectives of the Charlton 19 modeling were successfully met, providing an improved understanding of the subsurface system of interest. Preliminary heterogeneous 3D SEM was built based on current geologic conceptual model by integrating available characterization data.

In order to conduct a rapid, simplified analysis of the reservoir injectivity and capacity, the analytical CRM was successfully applied for the CO<sub>2</sub>-injection only period of the MRCSP injection in the reef. CO<sub>2</sub> injectivity in closed, depleted oil reservoirs is affected by the phase changes and interactions with the existing fluid phases as well as with the rock itself. The average representative injectivity index from the CRM of 7.58 MT/day.psi concurred with independent injectivity analysis evaluation done for the reef. The model also addressed uncertainty in the initial pressure estimate for the reef with the resulting compressible pore volume of 7.8e-04 psi<sup>-1</sup> that was consistent with total system compressibilities representative of typical oil and gas systems. In addition, the resulting fitted model has the potential to be a rapid forecasting tool for a quick prediction of the pressure buildup or rate for a desired target injection scenario in the future. Successful application suggests potential to rapidly evaluate injection performance in similar reservoir systems such as carbonate reef systems present in the Michigan basin.

Lessons learned from the oil-in-place validation for the SEM indicate the need to reevaluate the assumptions/considerations for the data-limited regions of the reef in order to avoid overestimating the rock properties modeled in the SEM.

## 4.0 Chester 16 Reef

### 4.1 Introduction

The Chester 16 reef is a Category 3 reef (newly targeted reef) and was part of Task 5, which aimed to characterize, monitor, and model a mid-stage reef. The Chester 16 reef has undergone primary production but not CO<sub>2</sub>-EOR prior to the MRCSP work. It is a good example of a full CO<sub>2</sub>-EOR lifecycle and ultimately demonstrates the capacity and safe storage of CO<sub>2</sub>. The reef has also been used for multiple SEM approaches to determine how best to represent the geology and heterogeneity of a complex reef reservoir. The results of a previous modeling effort are documented in the Task 5: Baseline Geologic Characterization Report technical report [Haagsma et al., 2017].

#### 4.1.1 Reef Description

The Chester 16 field was drilled and completed in the early 1970s and produced through the 1980s and 1990s. The reef has undergone primary recovery and waterflooding but has not been flooded with CO<sub>2</sub>. All the existing wells in the reef were plugged and abandoned. Therefore, new infrastructure was needed for CO<sub>2</sub>-EOR operations by Core Energy, including one injection well to be used for CO<sub>2</sub> injection and one monitoring well, which will be converted to a production well following monitoring during the pressurization period.

There were seven existing wellbores in and near the Chester 16 field that penetrated the Brown Niagaran (Table 4-1). Two new wells, Chester 6-16 and 8-16, were drilled in 2016 and 2017 on the reef to support reservoir characterization and subsequent injection and production strategies.

**Table 4-1. Chester 16 wells with permit number and status (all wells are plugged).**

Well Name	Permit Number	Status	Position
Gaylord Mortgage #1	28159	Plugged	Reef
Gaylord Mortgage 2-16	28511	Plugged	Flank
Gaylord Mortgage 3-16	28796	Plugged	Flank
Veraghen 4-21	28433	Plugged	Reef
Veraghen-Rypkowski 5-21	28743	Plugged	Reef
Veraghen Drefts 6-21	28918	Plugged	Off-reef
Drefts, Frank 4-16	28798	Plugged	Off-reef
Chester 6-16 <sup>a</sup>	60950	Active	Reef
Chester 8-16 <sup>a</sup>	61186	Active	Reef

a. Drilled in collaboration with MRCSP.

The Chester 16 reef is part of the NNPRT. Figure 4-1 shows a map view and three-dimensional (3D) view of the Chester 16 reef with two currently operative wells. The CO<sub>2</sub> injection well #6-16 penetrates the reef complex at a high flank position in the southern reef core area and the monitoring well #8-16 penetrates the reef complex at a crestal position in the northern reef core area. The primary reservoir is the overlying A1 Carbonate (highly dolomitized high porosity zone along the crest of the reef). The A1 Carbonate is low porosity and low permeability along the flanks of the reef, as is often the case and bounds the reservoir on all sides. The Brown Niagaran is a lower porosity reservoir with occasional fractures and/or dolomitic zones. These two formations are overlain by ~1,500 ft. MD of confining rock units comprised of

interbedded salt, shale, and low porosity carbonate. The original OWC occurs in the lower third of the reef structure, leaving two-thirds of the reef viable for EOR production.

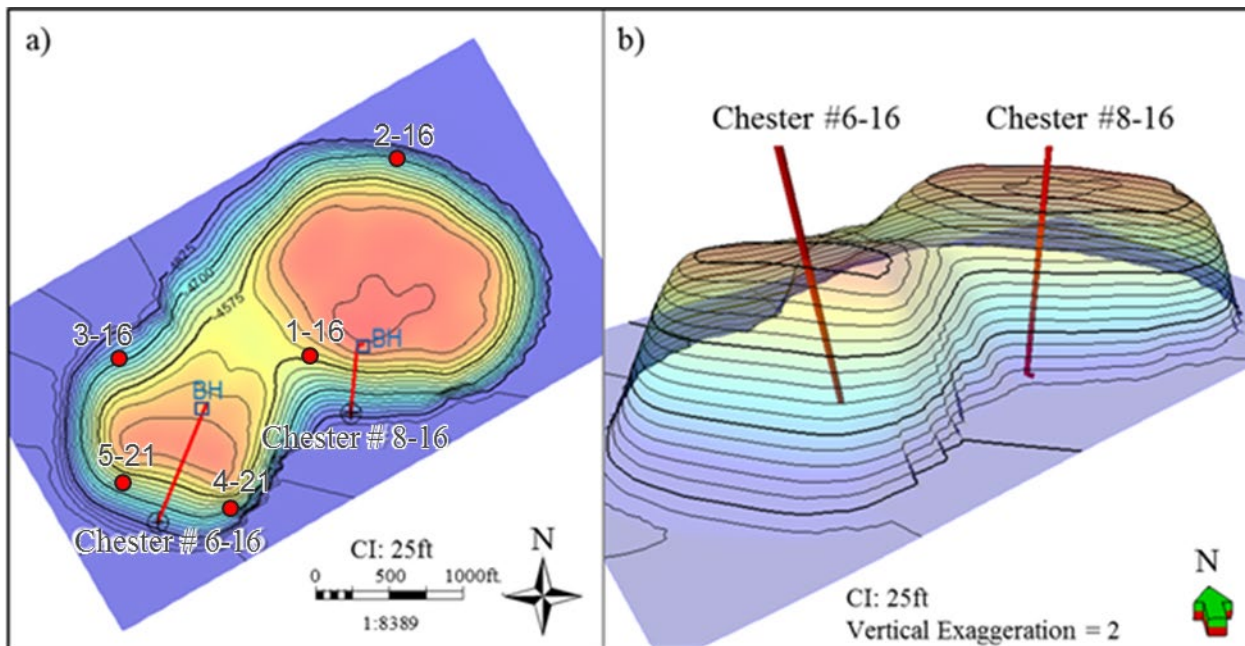


Figure 4-1. Map of the Chester 16 reef field showing well locations and structure of the Brown Niagaran. The left panel shows a contour map depth-surface of the Chester 16. The right panel shows the two-pod structure of the Chester 16.

The Chester 16 reef field is located along the limestone trend in the northern pinnacle reef trend. Geometry of the reef field (based on 3D seismic) suggests two distinct reef cores in close enough proximity to one another to be connected. There are two main reservoirs in this field—the Brown Niagaran and the A1 Carbonate (Figure 4-2). The Brown Niagaran tends to have low porosity due to lack of dolomitization with occasional fractures and/or dolomitic zones. The primary reservoir is the overlying A1 Carbonate, which has a distinct high porosity zone along the crest of the reef and was composed of porous dolomite. The A1 Carbonate is tight along the flanks of the reef, suggesting a limited extent of the reservoir. Salt plugging is also common in the Brown Niagaran in the limestone reefs, limiting the available pore space. The OWC was documented in the lower third of the reef structure, leaving the upper two-thirds of the reef viable for storage and production.

The confining units overlay the A1 Carbonate and include the A2 Evaporite and A2 Carbonate. The ultimate confining units include the Salina G through the Salina B-Salt. Underlying the reef structure is the Gray Niagaran which is a tight, water saturated carbonate that represents the lower boundary of the reef. The stratigraphic layout for the Chester 16 reef is shown in Figure 4-3. Interior to the reef, the Brown Niagaran is divided into three lithofacies, the Leeward, Reef Core, and Windward (Figure 4-3). These represent a geologic simplification that was used in to develop SEM and were described in the Task 5: Baseline Geologic Characterization Report technical report (Haagsma et al., 2017).

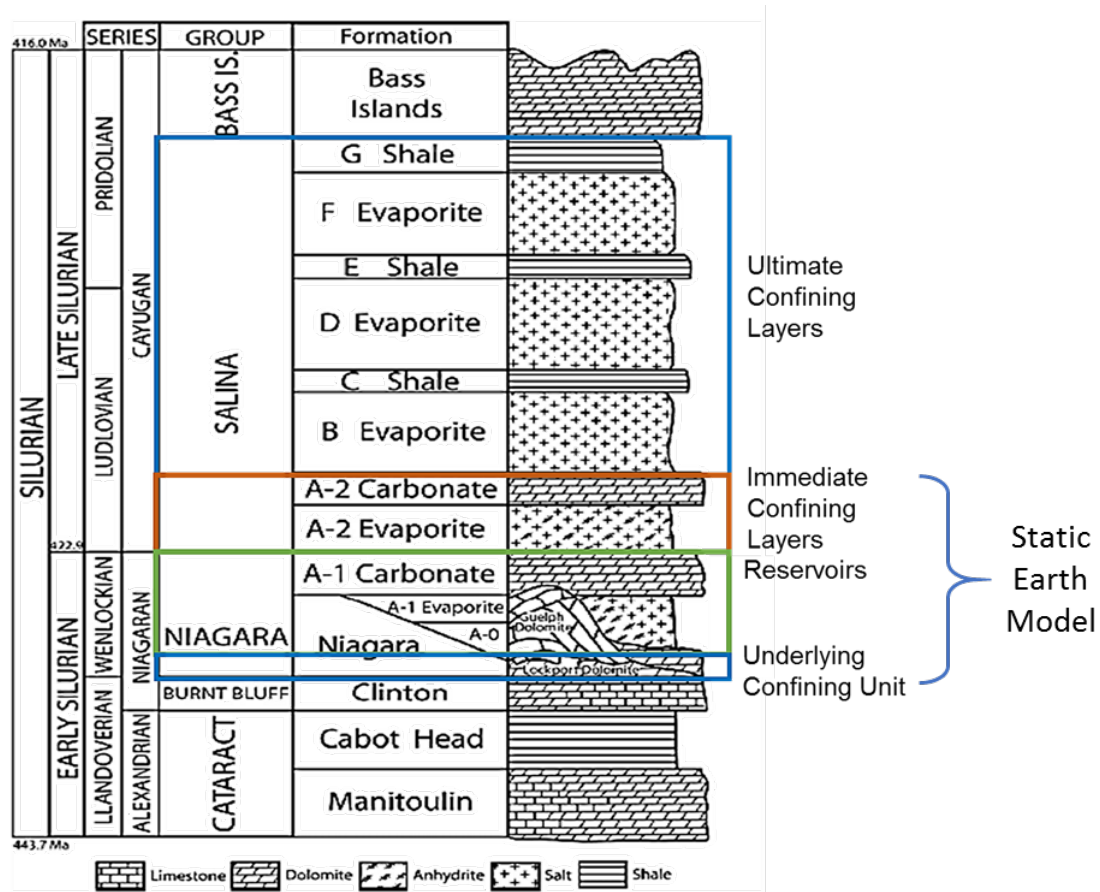


Figure 4-2. Simplified stratigraphic column in the Chester 16 reef field highlighting key confining units and reservoirs.

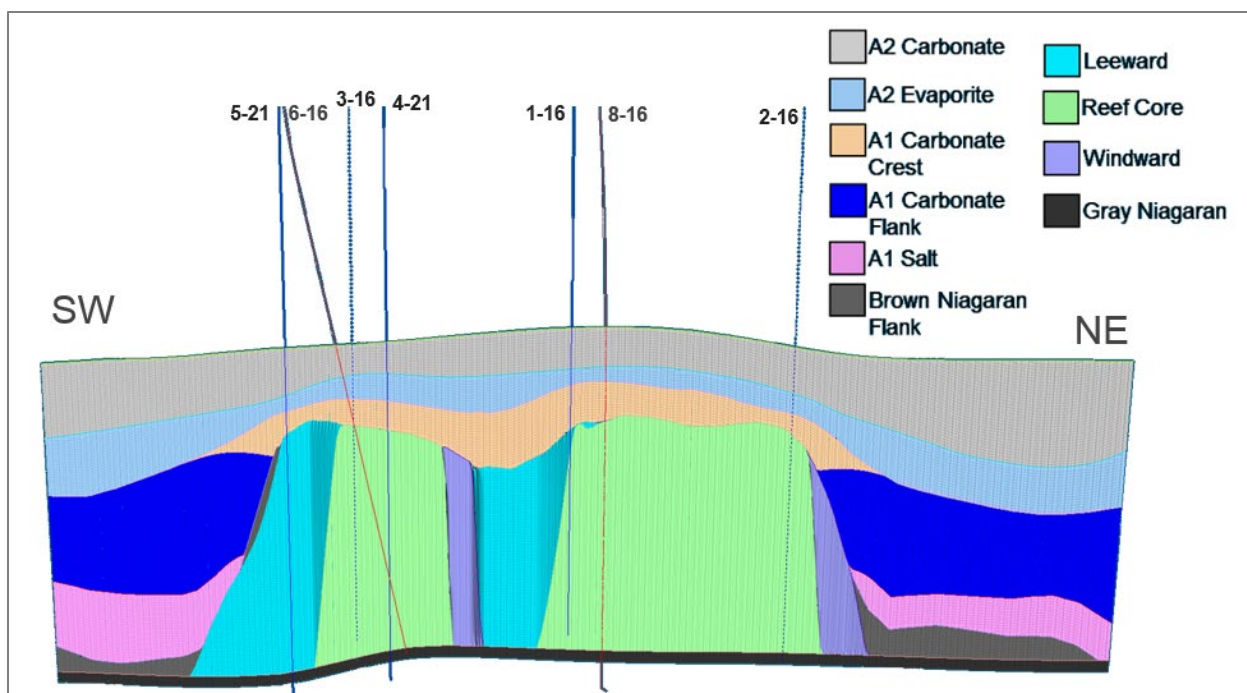


Figure 4-3. 2D cross-section through the 3D SEM of the Chester 16 reef field showing resulting zones (5x vertical exaggeration). Internal to the reef, the Brown Niagaran is further divided into three lithofacies: the Leeward, Reef Core, and Windward.

#### 4.1.2 Modeling Objectives/Scope

The objectives of the latest Chester 16 models are to:

1. Simplify geologic lithofacies while maintaining reservoir heterogeneity,
2. Represent key reservoir properties (porosity, permeability, water saturation),
3. Integrate multiple data types,
4. Match production and pressure history of primary production, and
5. Match production and pressure history of CO<sub>2</sub>-EOR.

The overall flow of the modeling work consisted of analyzing and integrating geologic data to define the extent, depth, thickness, porosity, permeability, and water saturation of the reservoir (s). In conjunction with geologic characterization, field operational and monitoring data was compiled to develop the reef history to be used in history matching the dynamic model. The geologic characterization work then was used to develop a SEM that was upscaled into a dynamic model. Figure 4-4 illustrates the flow and connections between analysis and data types to develop final static and dynamic models.

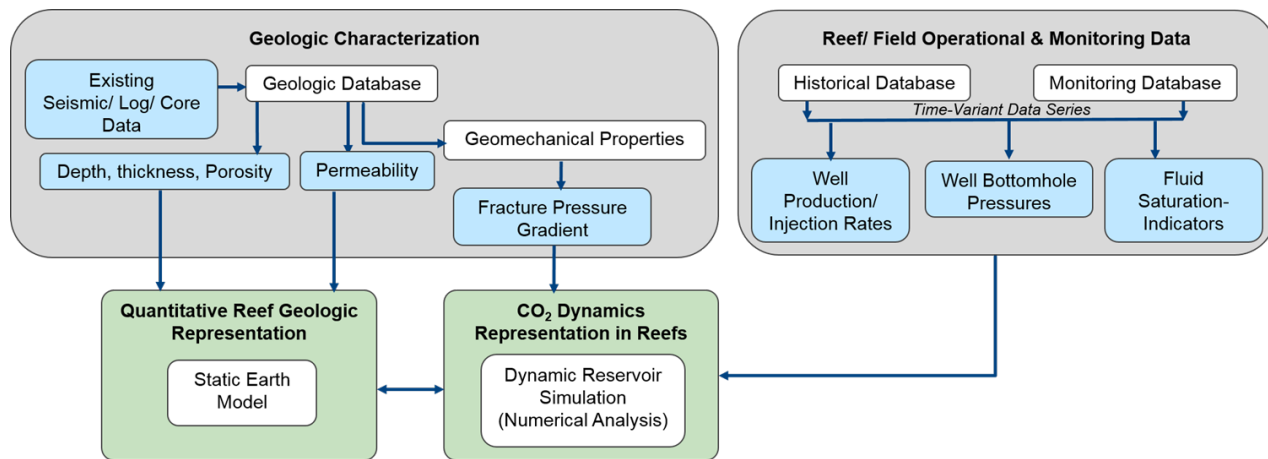


Figure 4-4. Simplified flow diagram of data integration into static and dynamic models

## 4.2 Data Sources

Subsurface data is sourced from wells in and near the Chester 16 field and includes seven existing wells plus two new wells (6-16 and 8-16). The modeling effort was complemented by a 3D seismic survey that permitted the imaging of the reef's footprint. The seismic survey was subsequently inverted to produce an acoustic impedance volume and a porosity inversion. These were used in the property modeling process to delineate trends within the Brown Niagaran reef.

### 4.2.1 Geologic Data

Of the nine wells used in this model update, two wells are located off-reef and provide guidance on geologic changes outside the reef. Two wells are located along the flanks of the reef and the remaining five wells penetrate the reef structure. All wells have gamma ray, neutron porosity, and resistivity logs. Bulk density was available for three wells and sonic logs were used to compute bulk density where it was missing. Advanced data was collected on the new wells, Chester 6-16 and 8-16. The advanced data included image logs, elemental spectroscopy, PNC data, sonic and geomechanics data, and well testing data. The wireline log data collectively ranged in acquisition time from 1971 to 2017. All data was thoroughly vetted using quality assurance/quality control (QA/QC) checks, then raster logs were digitized to fill data gaps. Whole core and sidewall cores were available from three existing wells and supplemented with new core from the 6-16 and 8-16 wells. Data availability is summarized in Table 4-2. Note that the 6-16 and 8-16 wells have been equipped with fiber optic cables that provide distributed temperature sensing (DTS) across the length of the well. Since the injected CO<sub>2</sub> is expected to be at a cooler than the formation, and CO<sub>2</sub> delays the rock from regaining its former (warmer) temperature, the DTS provides a vertical temperature profile that can help qualitatively identify the presence and migration of CO<sub>2</sub>.

**Table 4-2. Summary of available data for the wells in the Chester 16 reef field.**

Data Type	Well Name							
	1-16	4-21	2-16	5-21	3-16	28798	28918	6-16
Bulk Density	■						■	■
Neutron Porosity	■	■	■	■	■	■	■	■
Gamma Ray	■	■	■	■	■	■	■	■
Sonic		■			■		■	■
Resistivity	■	■	■	■	■	■	■	■
Photoelectric Index							■	■
Image							■	■
Elemental Spectroscopy								■
Mud Log	■						■	■
Advanced Geomechanics							■	■
Well Tests							■	■
Whole/sidewall Core	■	■	■				■	■

## 4.2.2 Production and CO<sub>2</sub> Injection History

Chester 16 is an oil-bearing carbonate reservoir that has an approximately 20-year history of production from two component formations, the A1 Carbonate overlying the Brown Niagaran. Production occurred via five wells targeting the A1 carbonate and Brown Niagaran, both from primary and secondary recovery (waterflooding), recovering ~2.4 MMSTB of oil and 3.0 BCF of gas. After a 26-year period of abandonment, Core Energy has begun CO<sub>2</sub> injection into the reservoir, with the intent of re-pressurizing the reservoir to ~1500 psi – pressure greater than the minimum miscibility pressure of the oil to CO<sub>2</sub> – before attempting CO<sub>2</sub>-EOR for optimal tertiary recovery.

Compared to the Brown Niagaran, the A1 carbonate is much thinner and generally a more homogeneous and higher quality (permeability) rock layer. The A1 Carbonate and the Brown Niagaran are thought to be in hydraulic communication and share the same OWC. The two formations, however, are separated by a very tight and thin layer of rock at the bottom of the A1 Carbonate “crest,” and by a saddle region above the Brown Niagaran (between the two reefs) that is thought to be highly vertically stratified and generally of low permeability.

Figure 4-5 shows the field-wide oil and gas production from the Chester 16 reef. The field reached a peak production around 800 bbl/month, sustaining it for ~3 years before a protracted ~15-year decline to abandonment. Figure 4-6 shows the cumulative oil and gas production from each of the five wells. Of the five producing wells, two wells (2-16 and 3-16) are relatively marginal wells flanking the main producing units within the Chester 16. The other three (1-16, 4-21, and 5-21) produce from within the reservoir. The 1-16 well drilled through the very center of the reef is the flagship well for this field, accounting for almost half of the entire hydrocarbon production. The non-flank wells producing through A1 carbonate and Brown Niagaran collectively account for 90 percent of the total hydrocarbon production. Appendix A contains well-wise production information.

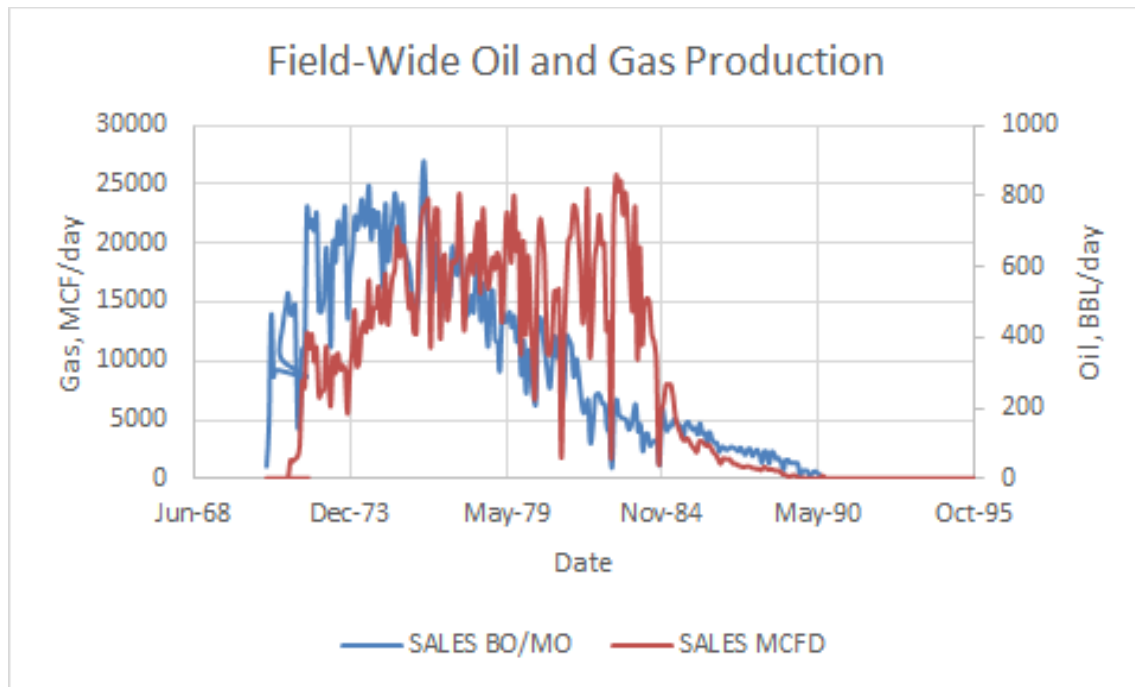


Figure 4-5. The field-wide oil and gas production rates of the Chester 16 reef.

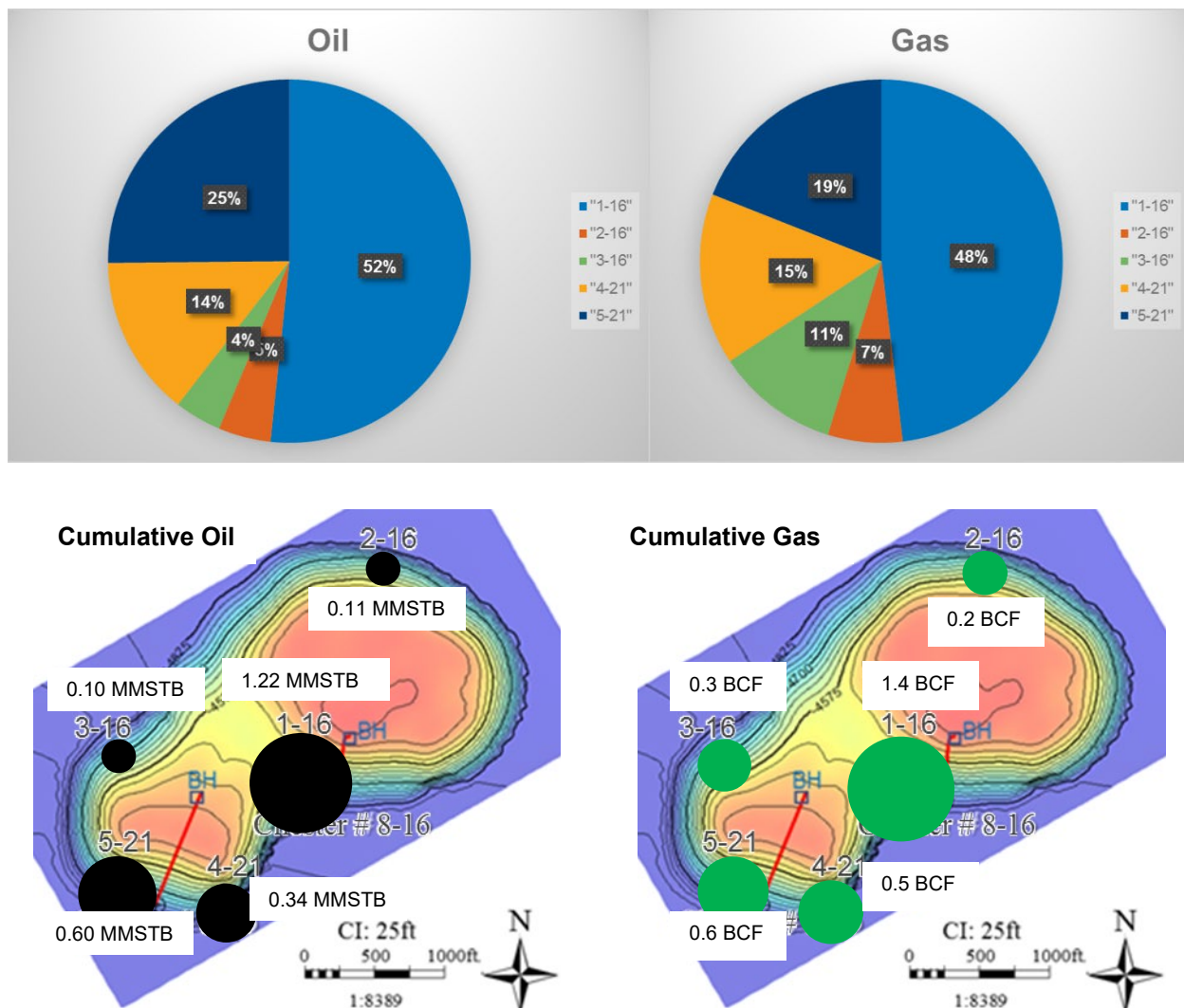


Figure 4-6. Pie chart (above) and bubble chart (below) of total cumulative oil and gas production from the five wells of the Chester 16.

Starting in 1984, waterflooding effort took place for around eight years to revive faltering production (Figure 4-7). Water injection originally occurred through both the 5-21 and the flank 2-16 well. However, the 2-16 well was shut-in after around four years, leaving the 5-21 well to be the lone injector. Oil production during this period occurred through the 4-21 and 1-16 wells. Water production data from this period, though available, is not considered very reliable and is thought to have been considerably higher. Around 2.5 million barrel (BBL) of water was injected, of which at least 0.3 million BBL was produced back along with the oil.

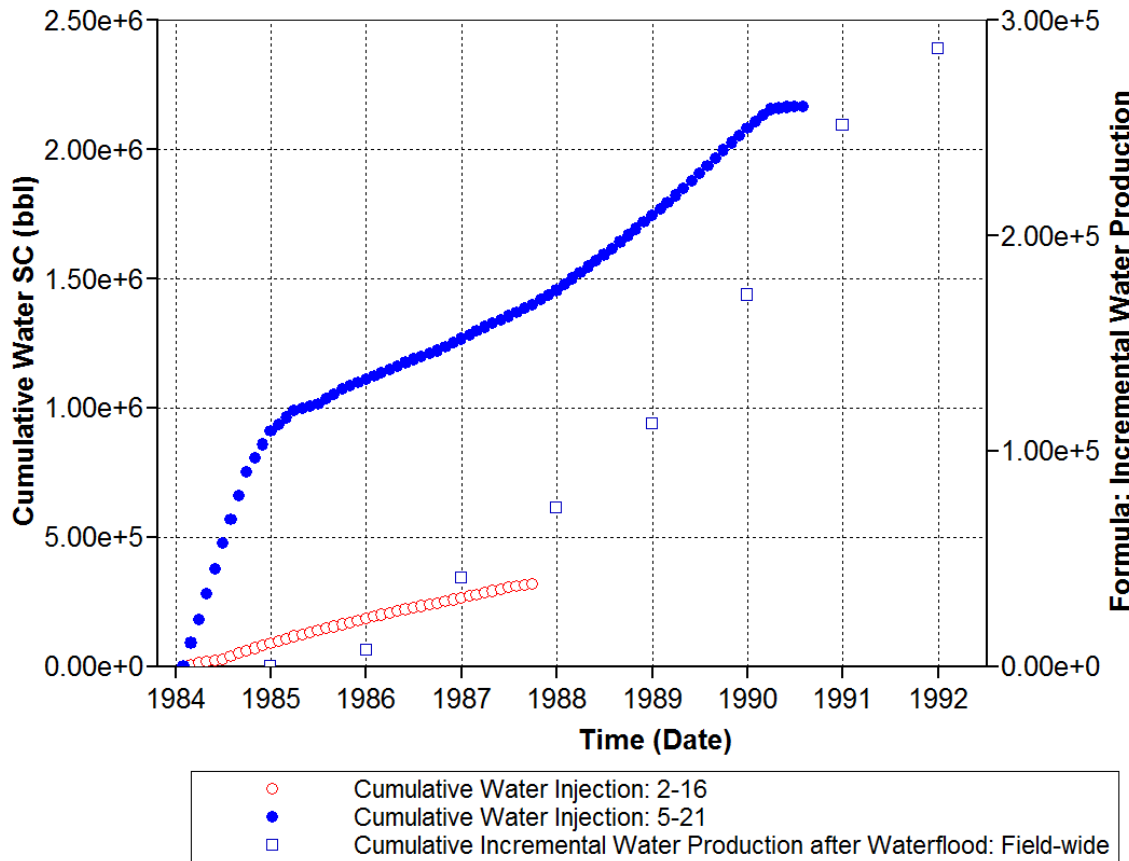


Figure 4-7. Cumulative barrels of water injected through the two injector wells, and the estimated total water production during the waterflood. Waterflooding occurred from 1984 to 1991.

Two new wells have been introduced during the CO<sub>2</sub> fill-up phase in anticipation of an injection-production pair in the future during CO<sub>2</sub>-EOR. Both the 6-16 and 8-16 wells penetrate the A1 Carbonate and the Brown Niagaran are spaced around 1000 ft apart. The 6-16 well is currently injecting CO<sub>2</sub> and the 8-16 well is being used for pressure/temperature monitoring purposes. The data collected from this period is generally richer and more reliable, containing daily injection rates, bottomhole pressures at the injector and monitoring well, and temperature deflections in the injector and monitoring well (used to indicate the presence of CO<sub>2</sub>).

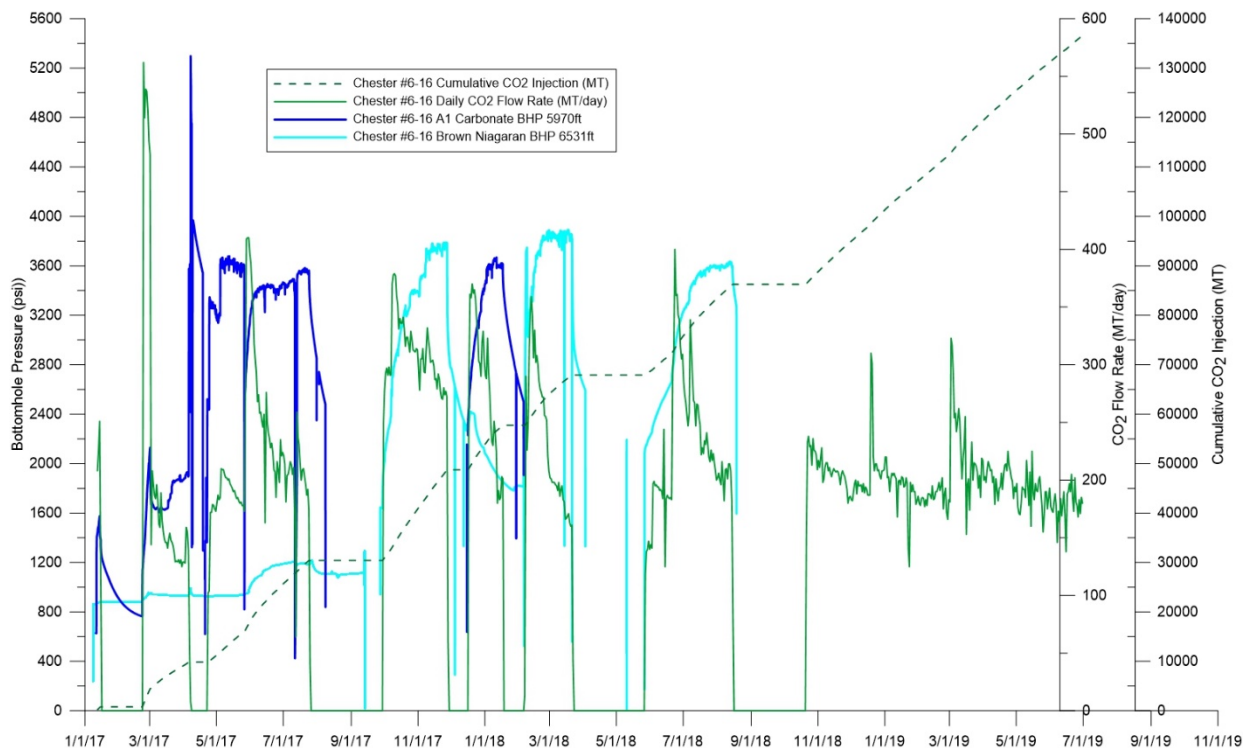
Since January 2017, Chester 16 has been undergoing re-pressurization via CO<sub>2</sub> injection. The target is to inject around 5.5 BCF before commencing CO<sub>2</sub>-EOR. The goal is to finish re-pressurizing the reservoir before mid-2020. As of July 2019, ~2.6 BCF of CO<sub>2</sub> have already been injected into Chester 16. This injection has been over eight injection periods, with the most recent injection period being the longest and currently underway. CO<sub>2</sub> injection is currently ongoing at a rate of ~3.7 MMSCFD. Table 4-3 lists further details of each individual injection period (eight in total). Note that injection period 1 was conducted as a preliminary test. Injection periods 2 – 5 represent attempts to isolate injection into a single formation. Due to operational circumstances, this was not feasible, and all subsequent injections were commingled.

Figure 4-8 and Figure 4-9 are composite plots that show the pressure and temperature data obtained at the 6-16 injection well and 8-16 monitoring well, respectively, in response to the CO<sub>2</sub> injection periods. The shape of the pressure curve at the 6-16 well suggests that each rate is associated with a peak (and stable) pressure characteristic of the injectivity (a function of near wellbore permeability and fluid compressibility) associated with the target interval. The similarity of the bottomhole pressure trend in both

formations during injection period 4 suggests some interval communication. Note that the pressure response in the 8-16 well represents a field-scale pressure change and is first felt midway in the second injection period. Note also that the A1 Carbonate, despite being the shallower of the two formations, is pressurized far beyond Brown Niagaran, suggesting that the process of hydrostatic equilibration in the Chester 16 is slow.

**Table 4-3. Summary of the various injection periods in the Chester 16, their associated target formations, and the quantities of CO<sub>2</sub> injected.**

Injection Period	Date Range	Days Injected	Target Formation	CO <sub>2</sub> Injected (MT)
1	1/11/17 - 1/14/17	3	A1 Carbonate	804
2	2/22/2017 - 4/6/2017	43	A1 Carbonate	9,039
3	4/22/2017 - 7/24/2017	93	A1 Carbonate	20,585
4	9/29/2017 - 11/27/2017	59	Brown Niagaran	18,314
5	12/16/2017 - 1/16/2018	31	A1 Carbonate	9,010
6	2/5/2018 - 3/21/2018	44	A1 Carbonate and Brown Niagaran	10,178
7	5/26/2018 - 8/14/2018	80	A1 Carbonate and Brown Niagaran	18,320
8	10/20/2018 - 7/29/2019	Continuing	A1 Carbonate and Brown Niagaran	55,390



**Figure 4-8. Plot of the bottomhole pressure, injection rate, and cumulative injection quantities in the 6-16 well.**

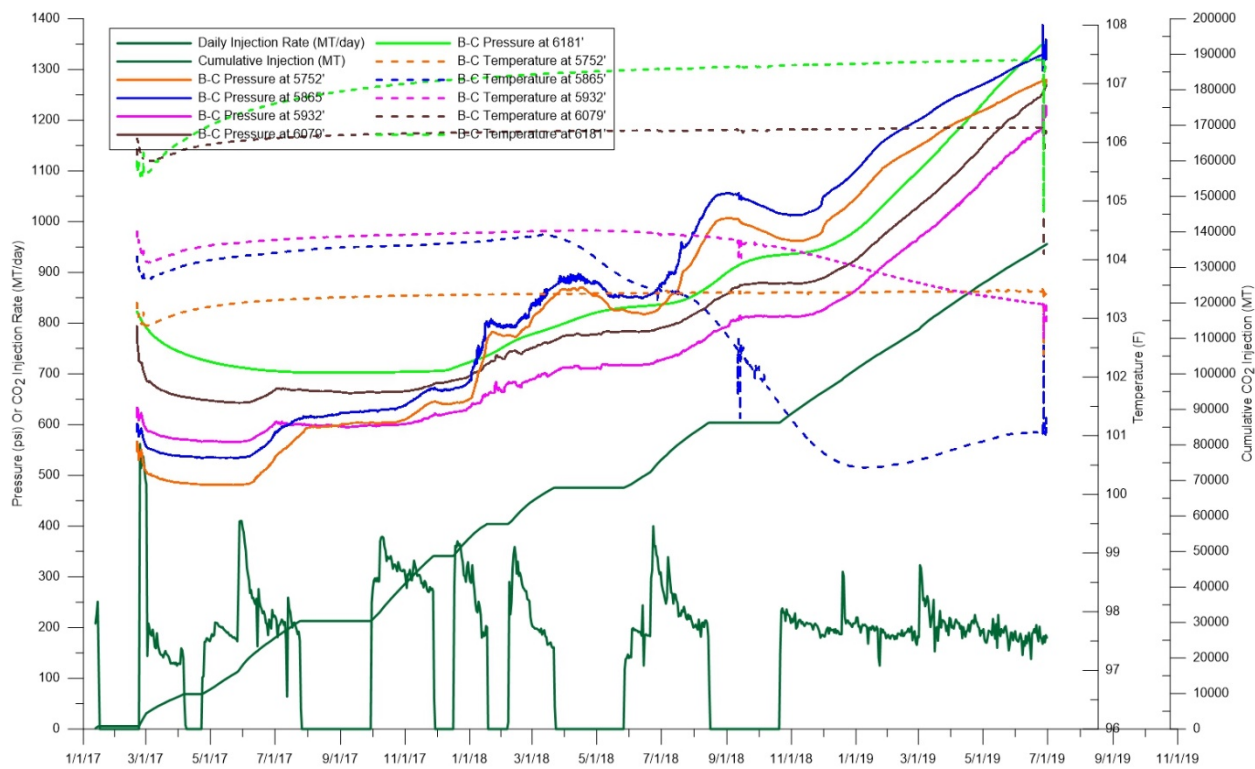


Figure 4-9. Composite plot of the bottomhole pressures and temperature recorded at the 8-16 monitoring well, in response to the injection at the 6-16 well.

### 4.3 Static Model

The geologic data and interpretations described in the *Task 5: Baseline Geologic Characterization Report* technical report (Haagsma et al., 2017) were used to construct a geologic SEM and is outlined using the workflow illustrated in Figure 4-10. The petrophysical analyses and interpretations were used as input into the SEM. A 2D depositional model interpretation was used to guide the development of the model's structural framework. 3D seismic data was used to define the boundary and geometry of the reef. The SEM was built using Petrel software and began by generating structural surfaces. Next, surfaces for facies were created to subdivide the reservoirs into key zones. These zones were subsequently layered and followed by well log upscaling and property modeling. A water saturation model was prepared for estimating hydrocarbon pore volume. This workflow concluded with upscaling of the fine-scale SEM to a coarser version suitable for DRM. This workflow was repeated for a second upscaled version whereby the Brown Niagaran reef zone was conditioned by porosity trends seen in 3D seismic inversion.

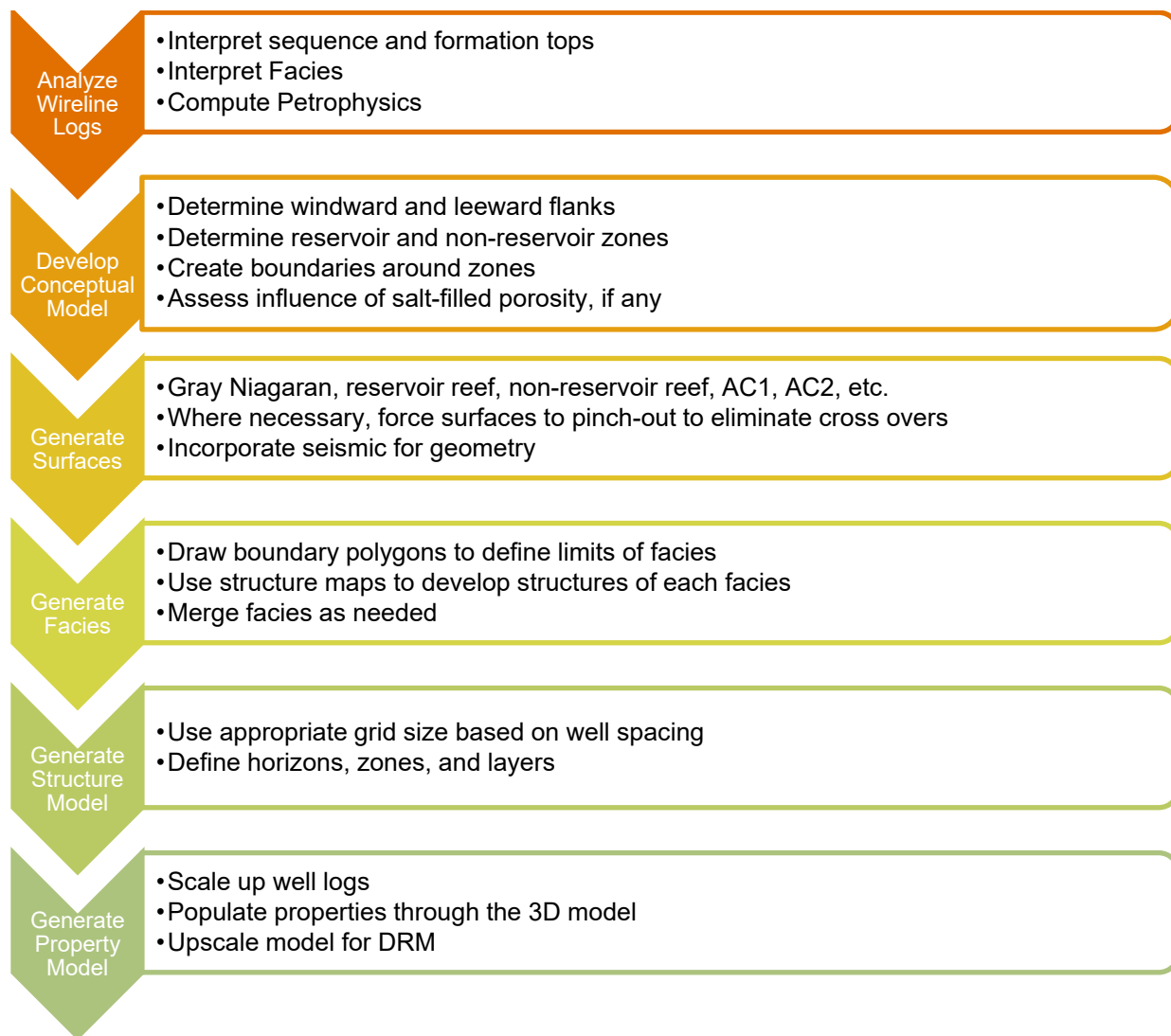


Figure 4-10. General workflow for the Chester 16 reef SEM.

### 4.3.1 Framework

Earlier work produced regional surfaces using 946 wells over a  $659 \text{ km}^2$  ( $7.08 \times 10^9 \text{ ft}^2$ ) area encompassing Otsego County, (Geologic Characterization for  $\text{CO}_2$  Storage with Enhanced Oil Recovery in Northern Michigan [Haagsma e al., 2020]). These, along with local geologic knowledge of off-reef behavior, were used to establish off-reef trends and the geology around the perimeter of the reef structure. Where necessary, flanking surfaces were hand-edited until the regional trend was matched.

#### 4.3.1.1 Structural Surfaces

Field-scale contoured structural surface maps were generated for formation tops. A structural surface map is a 2D (plan view) figure of a formation's elevation within the model area. Each structural surface was generated by gridding the sparse formation top data and reefal polygons using the convergent interpolation algorithm in Petrel to create a three-dimensional surface consistent with reefal geometry. These structural surfaces form the SEM's structural framework (Figure 4-11) and were quality checked to ensure that all surfaces were geologically conformable without anomalous, geometric crossovers.

Interpreted seismic horizons (Geologic Characterization for CO<sub>2</sub> Storage with Enhanced Oil Recovery in Northern Michigan [Haagsma et al., 2020]) were used to validate the geometry of the modeled reef surfaces.

The uppermost SEM zone for the Chester 16 reef was the A2 Carbonate, which has a higher elevation over the Northern lobe and gently slopes off-reef. The A1 Carbonate follows the underlying Brown Niagaran Formation. Locally, the Brown Niagaran was comprised of two pinnacle reefs, with the northeastern pod being the taller. The Gray Niagaran was relatively flat throughout the study area. Figure 4-12 shows the structural surfaces for the reef's carbonate units and includes the A2 Carbonate, A1 Carbonate, Brown Niagaran, and Gray Niagaran.

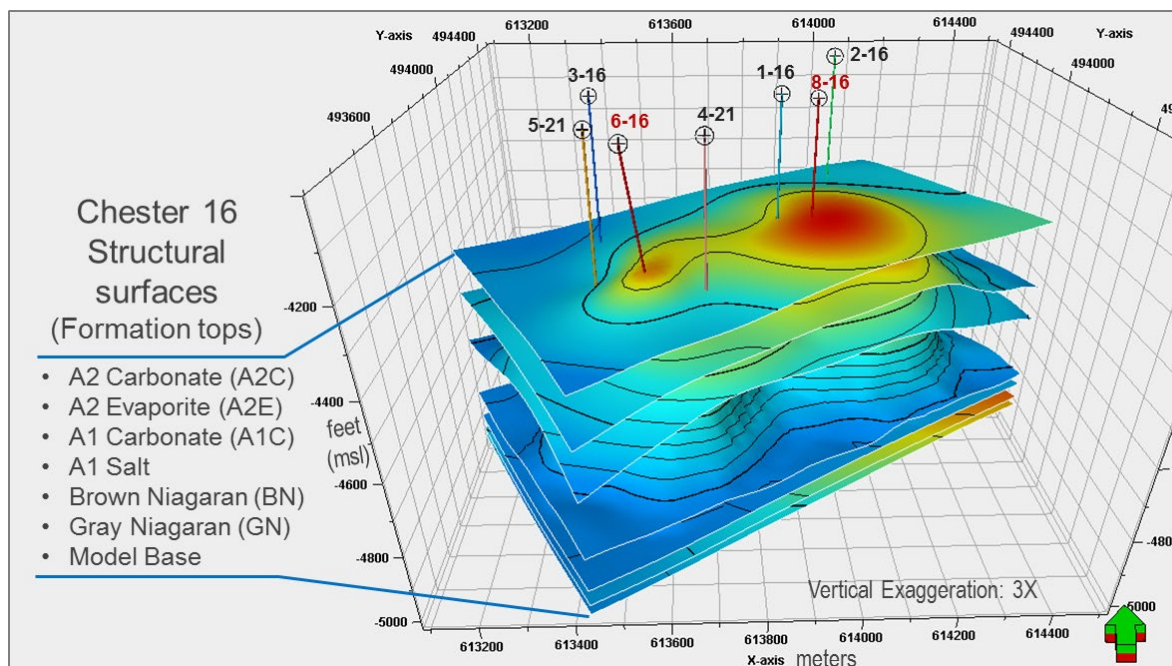


Figure 4-11. Chester 16 structural surfaces shown with the seven wells used during SEM development.

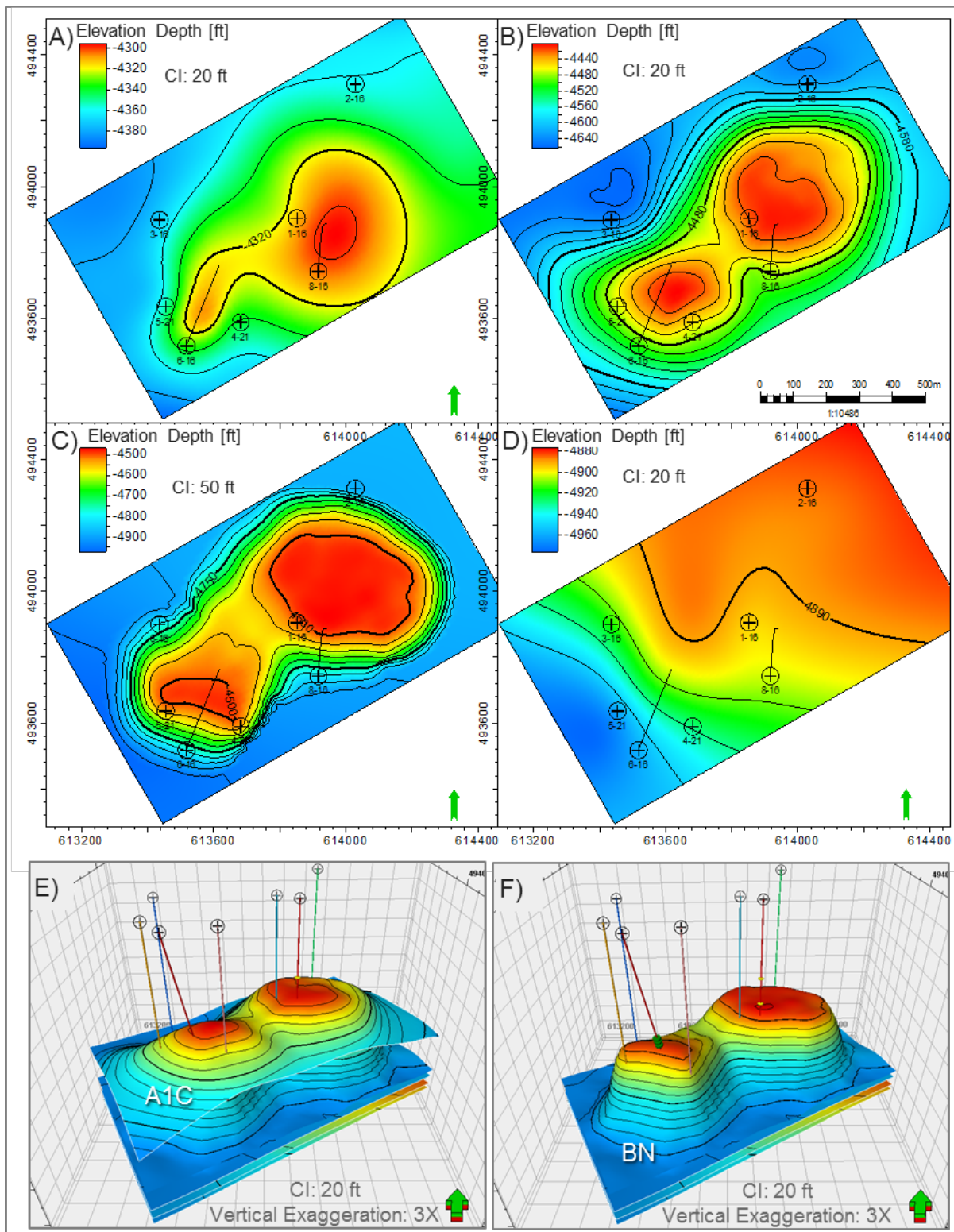


Figure 4-12. Chester 16 structural surfaces. Elevation depth is from mean sea level. A) A2 Carbonate. B) A1 Carbonate. C) Brown Niagaran. D) Gray Niagaran. E) Oblique view of the A1 Carbonate. F) Oblique view of the Brown Niagaran surface.

The A1 Carbonate is a thick unit that flanks and drapes the reefal structure. In the interest of hydrocarbon production, reserve estimates, and production history matching, the A1 Carbonate was divided into three subunits. These subunits have been represented in the SEM and are described below and appear in Figure 4-13A:

- A1 Carbonate Flank is the largest portion that occupies the space adjacent to the reef and is considered relatively tight. A1 Carbonate Crest is the portion that drapes over the reefal pods.
- A1 Carbonate Crest is the portion that drapes over the reefal pods. This unit is oil-bearing and has some of the most favorable reservoir quality for this oilfield.
- A1 Carbonate Saddle occupies the saddle region between the reefal pods. Currently unpenetrated by wells, its petrophysical properties are poorly constrained.

Isochore maps were generated by computing the difference between adjacent structural surfaces. An isochore is a contour line that connects points of equal vertical thickness. Figure 4-13A shows a cross-section through reef followed by isochore maps for the A2 Carbonate, A1 Carbonate Crest, and Brown Niagaran (Figure 4-13B, C, and D respectively). Figure 4-13E shows an oblique view of the A1 Carbonate Crest (A1C Crest) draped over the Brown Niagaran reef.

#### 4.3.1.2 *Lithofacies - Surfaces*

Commonly, the lithofacies modeling exercise occurs further in the workflow under facies modeling. However, for this modeling effort, extra surfaces were prepared to delineate the distinct lithofacies within the Brown Niagaran. For this model, the interpreted lithofacies were used to define regions within a formation to represent individual compartments or “geobodies.” The lithofacies represent regions with similar composition, porosity and permeability distributions. Implementing these lithofacies enables greater flexibility and control for both property modeling and (Dynamic Reservoir Model) DRM work. Table 4-4 itemizes the zones (intervals between two horizons) created for each formation in the Chester 16 SEM. Each zone is comprised of one or more lithofacies.

**Table 4-4. Summary of common lithofacies used in describing the reef and for model development.**

SEM Zone	Lithofacies	Abbr.	Comment
A2 Carbonate	A2 Carbonate	A2C	Continuous unit over the reef
A2 Evaporite	A2 Evaporite	A2E	Seal, continuous unit over the reef
A1 Carbonate (Crest)	A1 Carbonate (Crest)	A1C	Reservoir unit over the reef
A1 Carbonate (Flank)	A1 Carbonate (Saddle)		Potential reservoir, the straddle area between reef pods
	A1 Carbonate (Flank)		Flanks the reef
A1 Salt, Flank	A1 Salt (Flank)		Seal
Brown Niagaran	Brown Niagaran (Flank)	BN	Flanks the reef
	Brown Niagaran (Leeward)	LW	A portion of reef body
	Brown Niagaran (Reef Core)	RC	A portion of reef body
	Brown Niagaran (Windward)	WW	A portion of reef body
Gray Niagaran	Gray Niagaran	GN	Rock unit underlying the reef

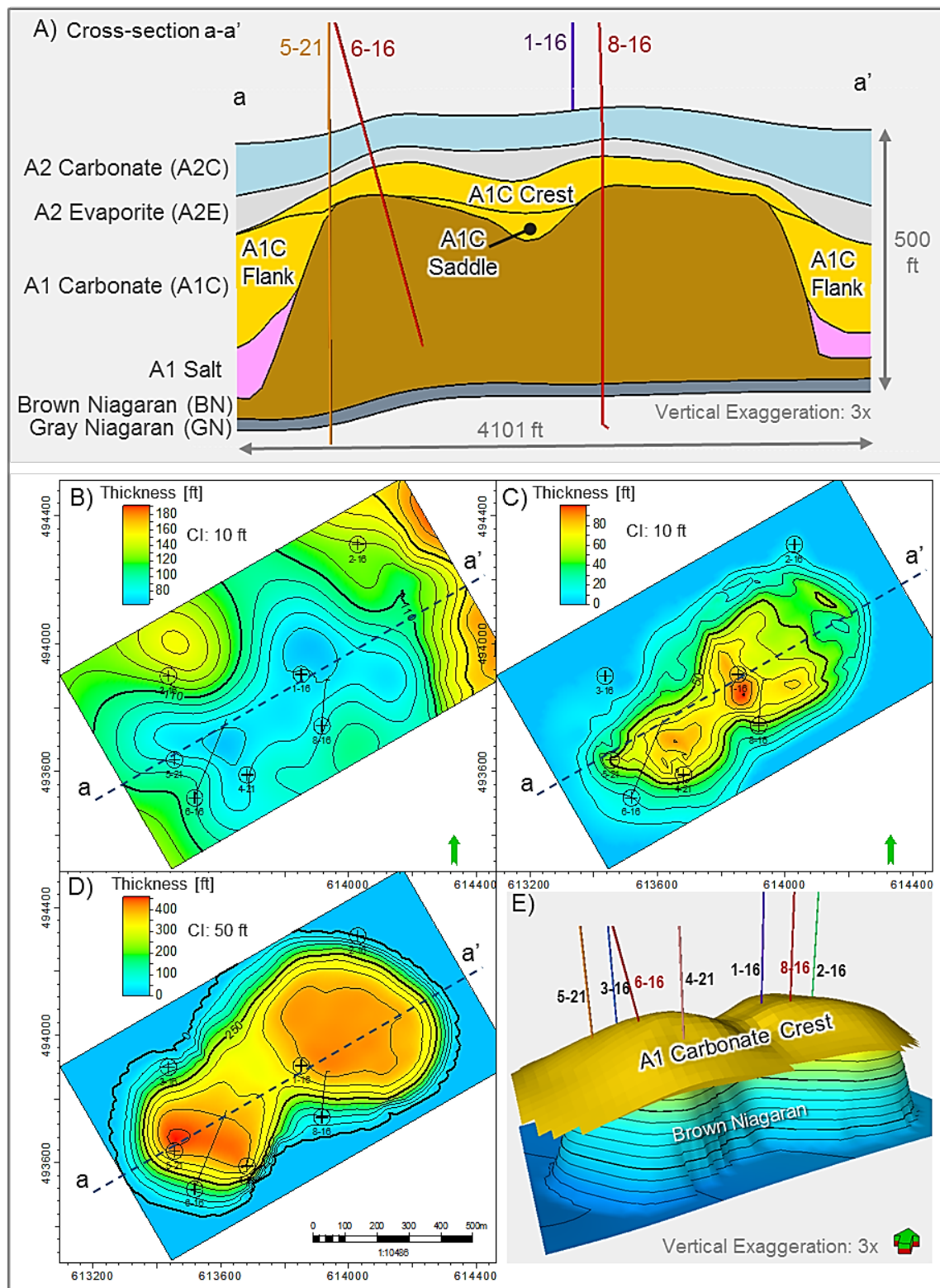


Figure 4-13. Isopach maps from the Chester 16 SEM. A) Northeast trending cross-section a-a' through the SEM showing key carbonate formations. B) A2 Carbonate isopach. C) A1 Carbonate Crest isopach. D) Brown Niagaran isopach. E) Oblique view of SEM showing the A1 Carbonate Crest draped over the Brown Niagaran reef.

The Brown Niagaran is a good example where polygons were created to outline the top and base boundaries of each lithofacies, and to clip structural surfaces used in the generation of the lithofacies surfaces. The polygons serve as data-input to the surface contouring algorithm. The top and base polygons are combined as input to define, constrain, and delineate the reefal zones. The resulting surfaces ensure that each reefal zone has a defined 3D volume. Figure 4-14 illustrates this process and the zones created for the lithofacies of the Brown Niagaran.

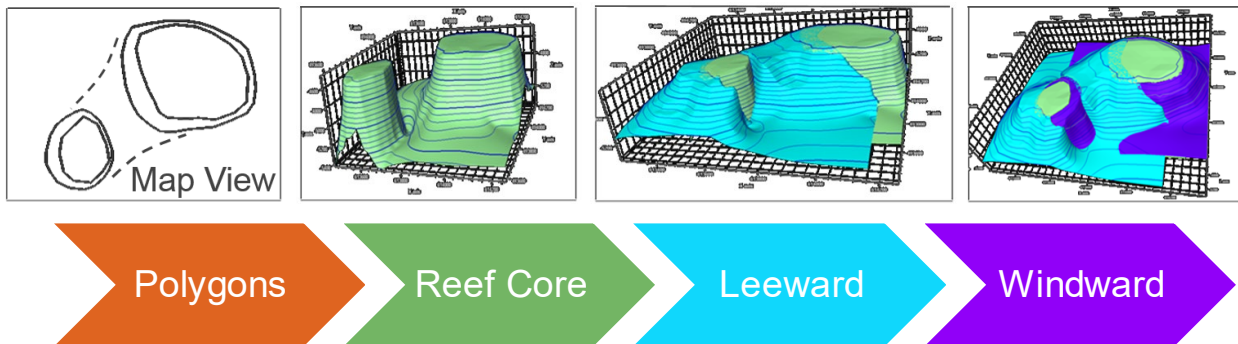


Figure 4-14. Workflow depicting the delineation of lithofacies for the Brown Niagaran in the Chester 16 reef. Polygons defining the reefal footprint and geometry were based on seismic interpretations. Along with formation tops, polygons were prepared to generate surfaces that envelop reefal lithofacies.

#### 4.3.1.3 Horizon Modeling

The structural surfaces were incorporated into the structural framework through the process called horizon modeling. In this process, geologic rules defining the conformability of surfaces were applied to each formation to guide the SEM's horizons. For example, these rules prevent the modeled horizons from crossing over one another and allows them to be discontinuous in areas where they pinch out.

The rules are implemented via Petrel's horizon type definitions:

- Conformable: All horizons belong to the same group and build conformable to each other.
- Erosional: Erosions belong to the group above, the group below erosion is numbered differently than the group above.
- Discontinuous: Discontinuities do not belong to groups above or below; they correspond to a separate group that is collapsed into a single surface.
- Base: Horizons above will truncate into a base.

Horizon modeling was an essential tool to control horizons and build zones. The A2 Carbonate A2 Evaporite (salt and anhydrite) and A1 Carbonate Crest were all set to conformable. The A1 Carbonate was split to represent flank (off-reef) and crest. The A1 Salt was incorporated off-reef and conformed to the Brown Niagaran. The Brown Niagaran surface was used as a control to conform the reef core, windward, and leeward zones. The Gray Niagaran was set to be the model's lowermost formation. Figure 4-15 summarizes the horizon scheme used in the SEM.

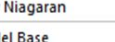
Index	Horizon name	Color	Calculate	Horizon type	Conform to another horizon	Status	Smooth iterations	Use horizon-fault lines	Well tops	Input #1
1	A2 Carb	Green	<input checked="" type="checkbox"/> Yes	Conformable	No ▾ 1	✓ Done	0	<input checked="" type="checkbox"/> Yes		
2	A2Evap	Cyan	<input checked="" type="checkbox"/> Yes	Conformable	No ▾ 1	✓ Done	0	<input checked="" type="checkbox"/> Yes		
3	A1C	Pink	<input checked="" type="checkbox"/> Yes	Conformable	No ▾ 1	✓ Done	0	<input checked="" type="checkbox"/> Yes		
4	A1C_flank	Magenta	<input checked="" type="checkbox"/> Yes	Conformable	Yes ▾ 5	✓ Done	0	<input checked="" type="checkbox"/> Yes		
5	A1Salt	Red	<input checked="" type="checkbox"/> Yes	Conformable	Yes ▾ 6	✓ Done	0	<input checked="" type="checkbox"/> Yes		
6	BN	Blue	<input checked="" type="checkbox"/> Yes	Conformable	Yes ▾ 7	✓ Done	0	<input checked="" type="checkbox"/> Yes		
7	Reef	Yellow	<input checked="" type="checkbox"/> Yes	Base	Yes ▾ 8	✓ Done	0	<input checked="" type="checkbox"/> Yes		
8	Gray Niagaran	Light Red	<input checked="" type="checkbox"/> Yes	Discontinuous	No ▾ 1	✓ Done	0	<input checked="" type="checkbox"/> Yes		
9	Base of model	Black	<input checked="" type="checkbox"/> Yes	Conformable	No ▾ 1	✓ Done	0	<input checked="" type="checkbox"/> Yes		

Figure 4-15. Horizon modeling in Petrel showing horizon order and type within the Chester 16 SEM.

#### 4.3.1.4 Geometry and Model Grid Definition

The boundary used for the SEM's structural framework is shown as a red outline in Figure 4-16 (top) and covers 875,000 m<sup>2</sup> or 216.2 acres. This area was selected to capture the reef's geometry and formations that flank the reef. Figure 4-16 (bottom) shows an oblique cut-away view of the SEM and reveals the two reefal pods at the Chester 16 field. The SEM's top is represented by the A2 Carbonate at an approximate depth of 5,625 feet below ground level. The SEM's overall thickness is approximately 589 ft. The SEM was comprised of cells, with grid cell size in the x-y directions of 25 meters. This size permitted enough resolution between wells while generally limiting cell count for DRM work. A list of the grid parameters for the SEM is provided in Table 4-5.

The resulting SEM for the Chester 16 field followed the geologic interpretation developed through wireline log analyses. The crest of the A1 Carbonate followed the zone of high porosity identified on top of the reef structure while the flank of the A1 Carbonate represented a lower porosity carbonate (Figure 4-17). The A1 Salt also developed along the flanks of the reef and coincided with the identification of salt in flank wells. The Brown Niagaran was composed of two distinct reef cores with significant overlap in between, as is represented by the leeward and windward contacts. The leeward lithofacies has gentler slopes and the windward lithofacies has steeper slopes as is consistent with paleowind direction, waves, and their related effect on the reef. Overall, the SEM's structure is consistent with interpretations and hence considered representative of the geology of the reef system.

Table 4-5. Summary of grid parameters for the Chester 16 reef field.

Grid Parameter	Chester 16 Dimension	Comments
SEM size (x by y)	1,250 m by 700 m (4,101 ft x 2,296.5 ft)	Model Area: 875,000 m <sup>2</sup> or 216.2 acres
SEM height (z direction)	179.5 m (589 ft)	Average SEM thickness
Cell grid size in x and y direction	25 m (82 ft)	Cell heights vary
Minimum well spacing	~82 m (269 ft)	
Layers / Number of grid cells	82 / 114,800	Course-scale SEM
Layers / Number of grid cells	2853 / 3,994,200	Fine-scale SEM
Layers / Number of grid cells	79 / 110,600	Upscaled SEM

Note: m = meter

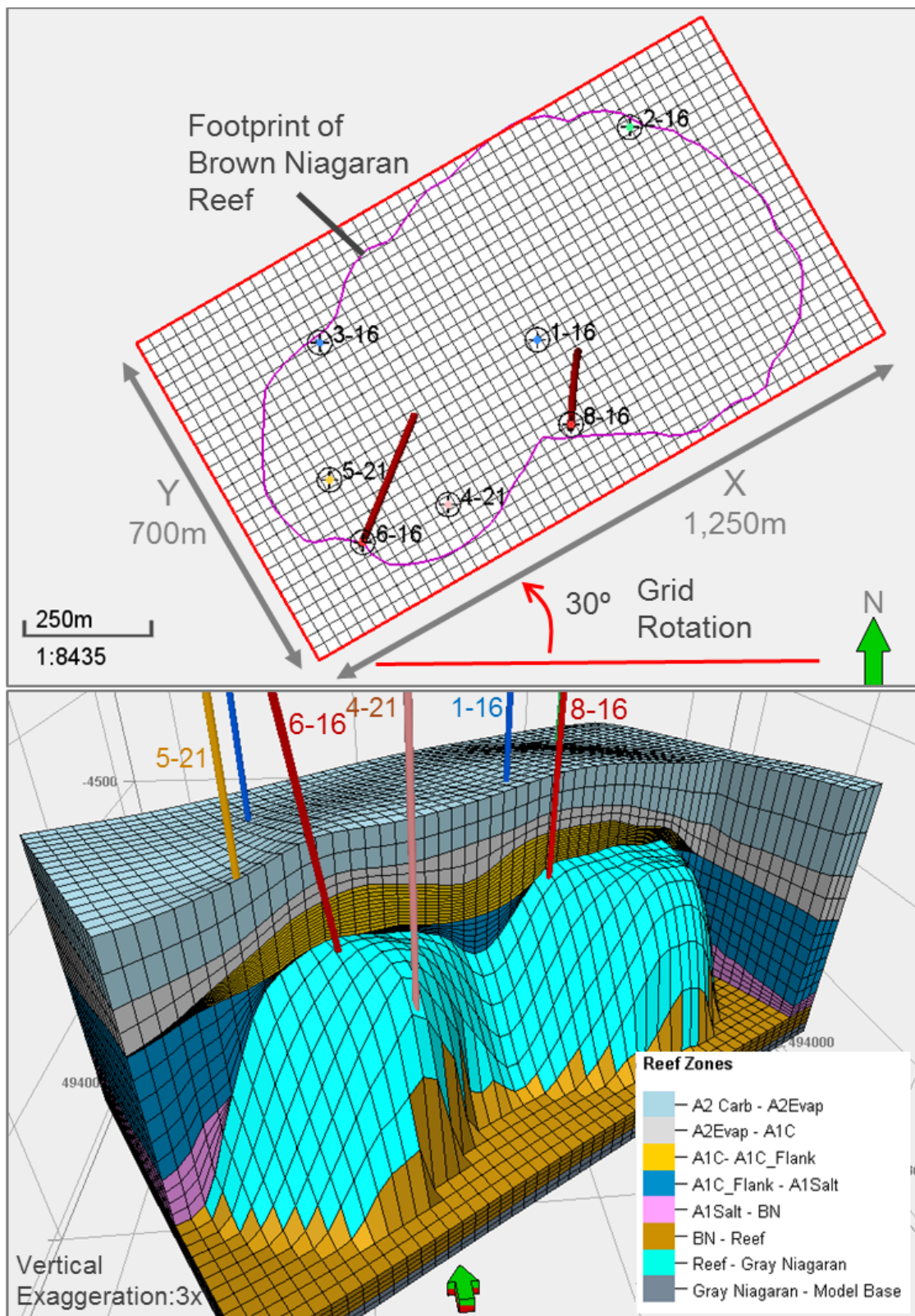


Figure 4-16. Top: Plan view of the x and y grid for Chester 16 SEM. SEM boundary in red. Bottom: Oblique view of the coarse-scale, 82-layer SEM with cut-away revealing two-pod Niagaran reefal structure.

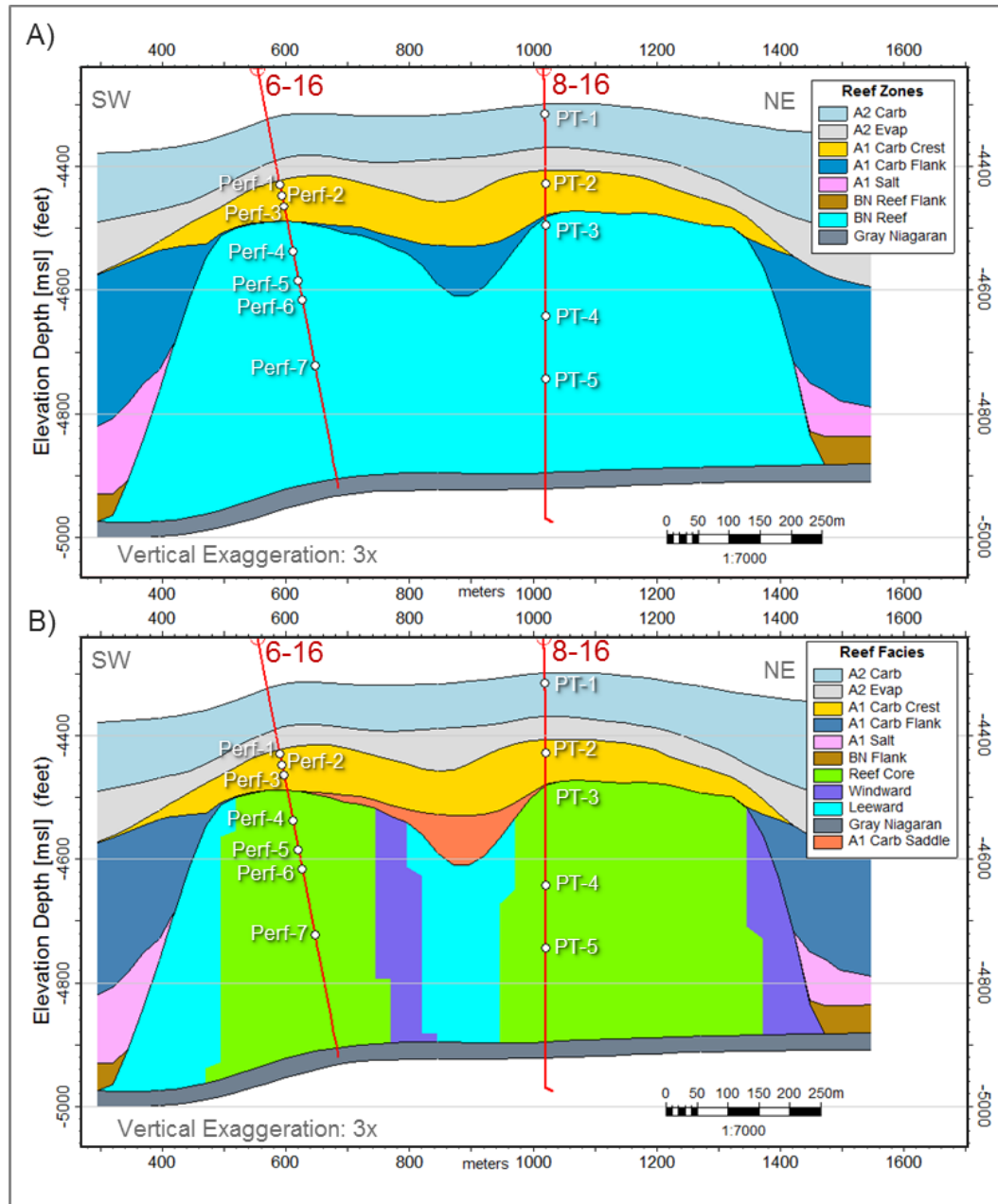


Figure 4-17. Northeast trending cross-section through the Chester 16 SEM framework. A) SEM zones were partitioned by formation tops (horizons). B) Lithofacies were distributed among the zones. The Brown Niagaran zone includes the reefal structure comprised of leeward, reef core, and windward lithofacies. The A1 Carb Flank has been partitioned to include a saddle area that straddles the two pods.

#### 4.3.1.5 Zones and Layers

Horizons define the SEM's base framework consisting of stratigraphic zones. SEM zones are then subdivided into layers to capture the desired vertical resolution and thickness of each zone. The vertical layering resolution seeks to capture the variability observed in well logs. Often the end-purpose of SEMs is to conduct flow simulations via a DRM. In this case the SEM may require the process of upscaling to reduce overall cell count.

There were three SEM layering schemes used during development of the SEM. These are described below and are illustrated in Figure 4-18.

C) Course-Scale Model: The purpose of the course-scale model was to facilitate the development of the SEM's framework and ensure that the horizon contacts and zone geometries were being accurately represented (Figure 4-18A). The model employed proportional layering, with vertical thickness targeting 5-ft for formations with hydrocarbon production like the A1 Carb Crest and Brown Niagaran (comprising the reef core, windward, and leeward lithofacies). Fewer layers were proved for evaporites and formations considered tight.

D) Fine-Scale Model: This model used a 0.5-ft layering scheme. For each model zone, layers followed formation tops. Given the density of layers (2,853 layers), the grid lines are turned off in Figure 4-18B. The purpose of the this fine-scale model was to synthesize permeability logs based on laboratory measured porosity and permeability derived from sidewall core and coupled with neutron porosity logs. This process was called "permeability prediction" and is described in Section 4.3.2.5. The fine-scale model was then used to perform property modeling for porosity, permeability, and water saturation as described in the next section.

E) Upscaled Model: This model was prepared for conducting DRM work. It originates from the 0.5-ft layer, fine-scale model that was upscaled using CONNECT UpGrid™ resulting in a model with fewer layers and fewer cells. The upscaling resulted in a proportional layering scheme (Figure 4-18C). Closer inspection shows that individual layers vary in thickness. Details on the upscaling work are provided in the Model Upscaling section below.

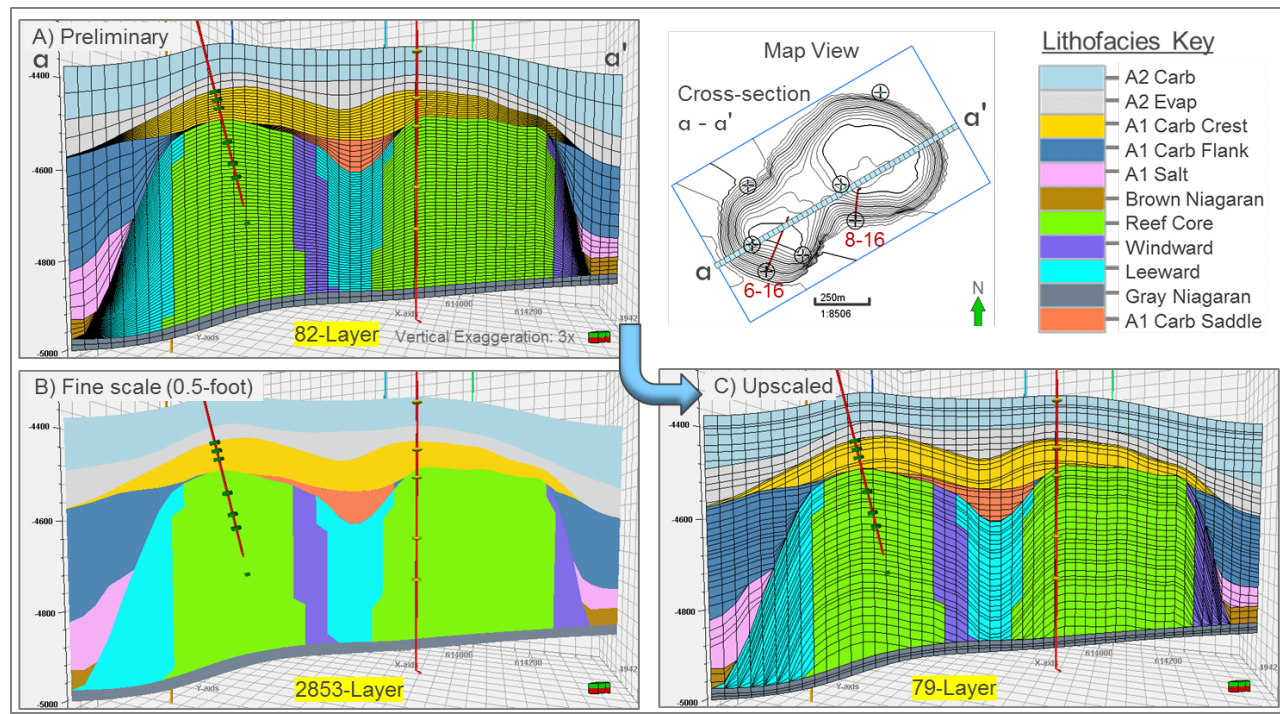


Figure 4-18. Chester 16 SEM layering schemes shown on lithofacies cross-section. A) Coarse-scale SEM for developing and validating reefal architecture. B) Fine-scale, high-resolution model for permeability prediction and petrophysical modeling. Note that the grid lines here are turned off; otherwise, the cross-section would appear black. C) Upscaled layering results originated from the fine-scale model. The layering scheme seeks to preserve heterogeneity and is for DRM use.

## 4.3.2 Property Modeling

### 4.3.2.1 Data Sources

Property modeling was based on the following data sources:

- Porosity: Neutron porosity logs from seven wells were used. As the reef is largely comprised of carbonates, the neutron logs were calibrated per their respective lithologies, either limestone or dolomite. The carbonates were considered relatively clean and so the neutron logs were representative of effective porosity. The neutron logs showed a close match when validated against laboratory measured core results for porosity.
- Permeability: For Chester 16, there was good agreement between porosity measured on core samples and neutron porosity logs. Permeability logs were derived through a log-based porosity-permeability transform. Essentially, working with core data, a power-law fit between porosity and permeability was established. Then, this transform was used to calculate permeability logs based on the neutron porosity logs. Further details on this permeability log process is found in Section 4.3.2.5.
- Water saturation: Based on seven wells, the water saturation logs were computed via Archie's equation using resistivity and neutron porosity logs. Standard Archie's constants of  $a=1$ ,  $m=1$ , and  $n=2$  were used.

### 4.3.2.2 Methodology Overview

The fine-scale 2,853-layer geologic framework was used with scaled-up log properties to build porosity and permeability property models. During this exercise, both porosity and derived permeability logs were sampled to the grid resolution and subjected to vertical variogram analysis to characterize vertical heterogeneity in oil-bearing zones like the A1 Carbonate Crest and the Brown Niagaran. A variogram characterizes the spatial continuity or variability of a dataset and begins with an *experimental variogram* calculated from the data. One can select from several mathematical functions to fit the *experimental variogram*; these are called *variogram models*. When a fit is achieved, the variogram model describes the spatial relationships inherent in the dataset. Model variogram parameters include sill, nugget, and range. The variogram model, along with well logs, are then used in a conditional simulation algorithm to populate the 3D SEM with the key petrophysical rock properties. This process required interpolating the upscaled log porosity and permeability values across the entire 3D model grid. The GRFS method was used for these models. The GRFS is a stochastic method that honors the full range and variability of the input data. Each run creates one equiprobable distribution of a property throughout a model zone based on a model variogram and upscaled well logs. Results were compared to original log values and the scaled-up values using CDFs to ensure the algorithm was representative of the data.

Petrophysical properties along with water saturation were used to estimate hydrocarbon pore volume (HCPV). The following sections will focus on the high-resolution, 2,853-layer model and conclude with 79-layer upscaled model.

### 4.3.2.3 Upscaling of Wireline Logs

Neutron porosity log data was available for seven wells at Chester 16 and represented a good estimate of porosity for the limestone units; logs were corrected for dolomite units where required. These log measurements were collected every half foot, except for the two newer wells (6-16 and 8-16) where porosity was recorded at quarter-foot increments.

For the fine-scale SEM, these well logs were upscaled or sampled along the well trajectories to the SEM grid's vertical resolution of 0.5-ft. Core samples yielding porosity and permeability data were also sampled into the SEM as part of the workflow to develop a porosity-permeability transform resulting in a synthesized permeability log (Section 4.3.2.5). Like porosity, both the permeability log and water saturation log were sampled into the SEM along the well trajectories at the grid's 0.5-ft vertical resolution. These "scaled-up" logs were viewed in cross-section for each well to quality check the process. The scaled-up logs match the original well logs and formation tops, honoring the variations in porosity, water saturation, and permeability. Figure 4-19 shows an example of the scaled-up neutron porosity (colored bars) that matches very closely with the original porosity log. This close match is expected as the SEM's resolution is very close to the resolution of the well logs. Figure 4-19 also shows the scaled-up logs for permeability and water saturation.

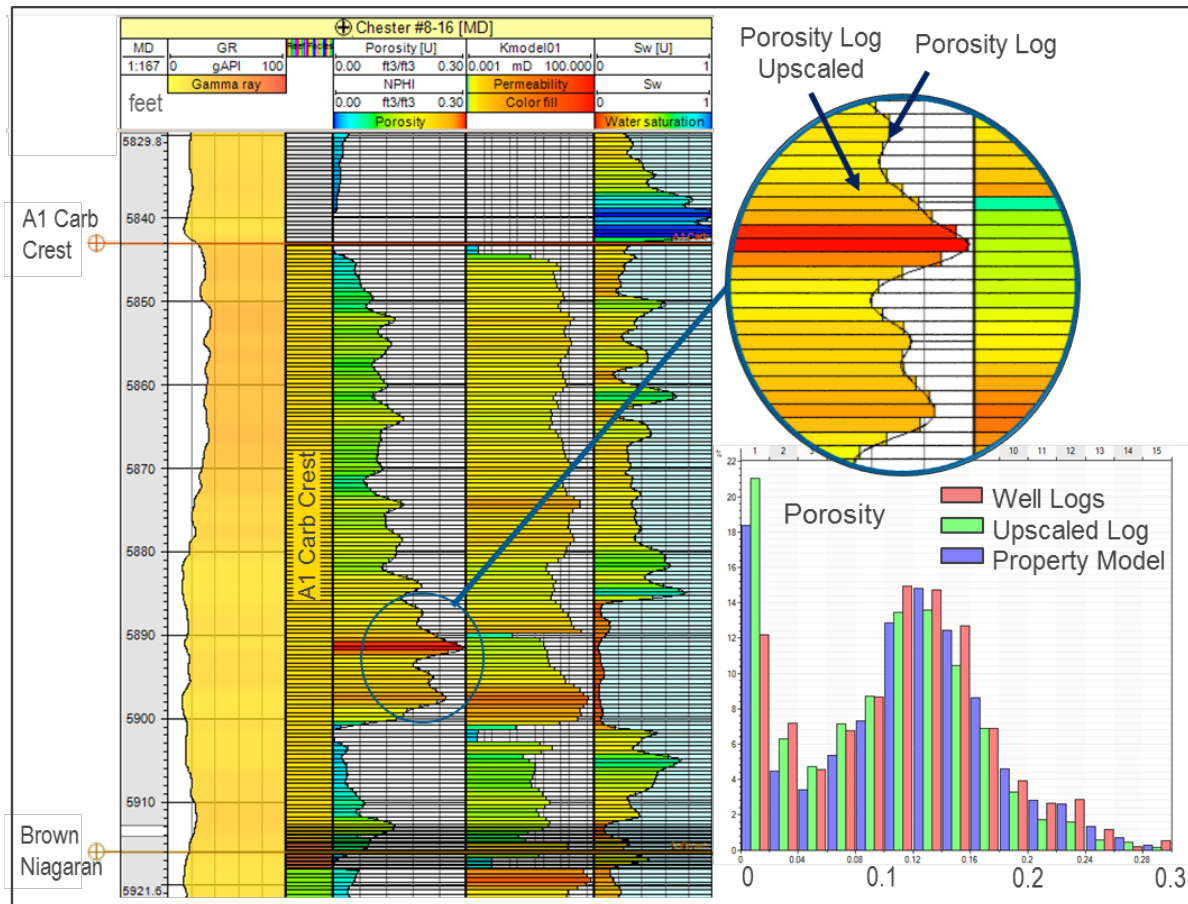


Figure 4-19. Well log upscaling. Example of the tight match between well logs and well log upscaling at the SEM's grid resolution of 0.5-ft. Tracks left to right: Gamma ray, facies, neutron porosity, synthesized permeability, and water saturation. Top right shows a zoomed-in view of the match between the well porosity log and its upscaled values (colored blocks). Bottom right: Porosity histogram for the A1 Carbonate Crest comparing upscaled porosity log against original neutron porosity (NPHI) log.

#### 4.3.2.4 Porosity Model

The porosity modeling effort employed the GRFS for the oil-bearing zones, which include the A1 Carbonate Crest, A1 Carbonate Flank (A1C Flank), and Brown Niagaran reef. The A1C Flank was included as this zone contains the A1 Carbonate Saddle, which may potentially be oil-bearing. The porosity model input parameters are summarized by model zone in Table 4-6. Figure 4-20 shows a cross-section through the porosity model histograms along with CDF plots for the oil-bearing units (A1 Carbonate Crest and Brown Niagaran) and for the entire SEM, which includes all zones.

The porosity model is consistent with the scaled-up logs and original well logs as shown in the CDFs in Figure 4-20. The porosity model had a strong porosity trend in the A1 Carbonate Crest that overlies the Brown Niagaran reef. The A1 Carbonate Crest had the highest average porosity of 11 percent. Thin streaks of porosity were noted in the Brown Niagaran reef (Figure 4-20A), which is consistent with porosity spikes on wireline logs. These could be attributed to dolomitic intervals or possible fractures. Moderate porosity was observed at the top of the reef, which could provide some connectivity to the overlying A1 Carbonate, and porosity decreased toward the base of the reef. The Brown Niagaran reef lithofacies had porosity near 3.4 percent. The A2 Carbonate had an average of 5.1 percent porosity. This porosity was influenced by a layer of mudstone/shale with micro-porosity and some leaching of evaporates. Formations with high concentrations of salt (e.g. A2 Evaporite, A2 Salt) had porosities near 2 percent. Table 4-7 summarizes these average values by SEM zone.

**Table 4-6. Porosity property model input settings.**

POROSITY	Zone	A2 Carbonate	A2 Evaporite	A1 Carb Crest	A1 Carb Flank	A1 Salt	BN - Flank	BN Reef	Gray Niagaran
	Algorithm	GRFS*	GRFS*	GRFS*	GRFS*	GRFS*	GRFS*	GRFS*	GRFS*
	Constant, Porosity (%)	N/A	N/A	N/A	N/A	N/A	N/A	N/A	N/A
Variogram Values	Nugget	0.0001	0.0001	0.0332	0.0277	0.0001	0.0587	0.0435	0.0001
	Type	Spherical	Spherical	Exponential	Spherical	Spherical	Spherical	Exponential	Exponential
	Major	130	130	950	300	150	50	85	500
	Minor	130	130	950	300	150	50	85	500
	Vertical	10.801	3.651	21.449	17	10.518	10	25	8.21
	Sill	0.7743	0.268	1	1	1	1	0.8263	0.745

\* With Petrel, used Data Analysis Transforms and Variograms along with Gaussian Random Function Simulation

**Table 4-7. Summary of average porosity as computed in the fine-scale SEM for each zone in the Chester 16 reef.**

Zone	Average SEM Porosity (decimal)	Standard Deviation (decimal)
A2 Carbonate	0.051	0.047
A2 Evaporite	0.027	0.017
A1 Carbonate Crest	0.109	0.067
A1 Carbonate Flank	0.024	0.022
A1 Salt	0.018	0.018
Brown Niagaran Flank	0.081	0.033
Brown Niagaran Reef	0.034	0.032
Gray Niagaran	0.031	0.024
All SEM zones together	0.037	0.038

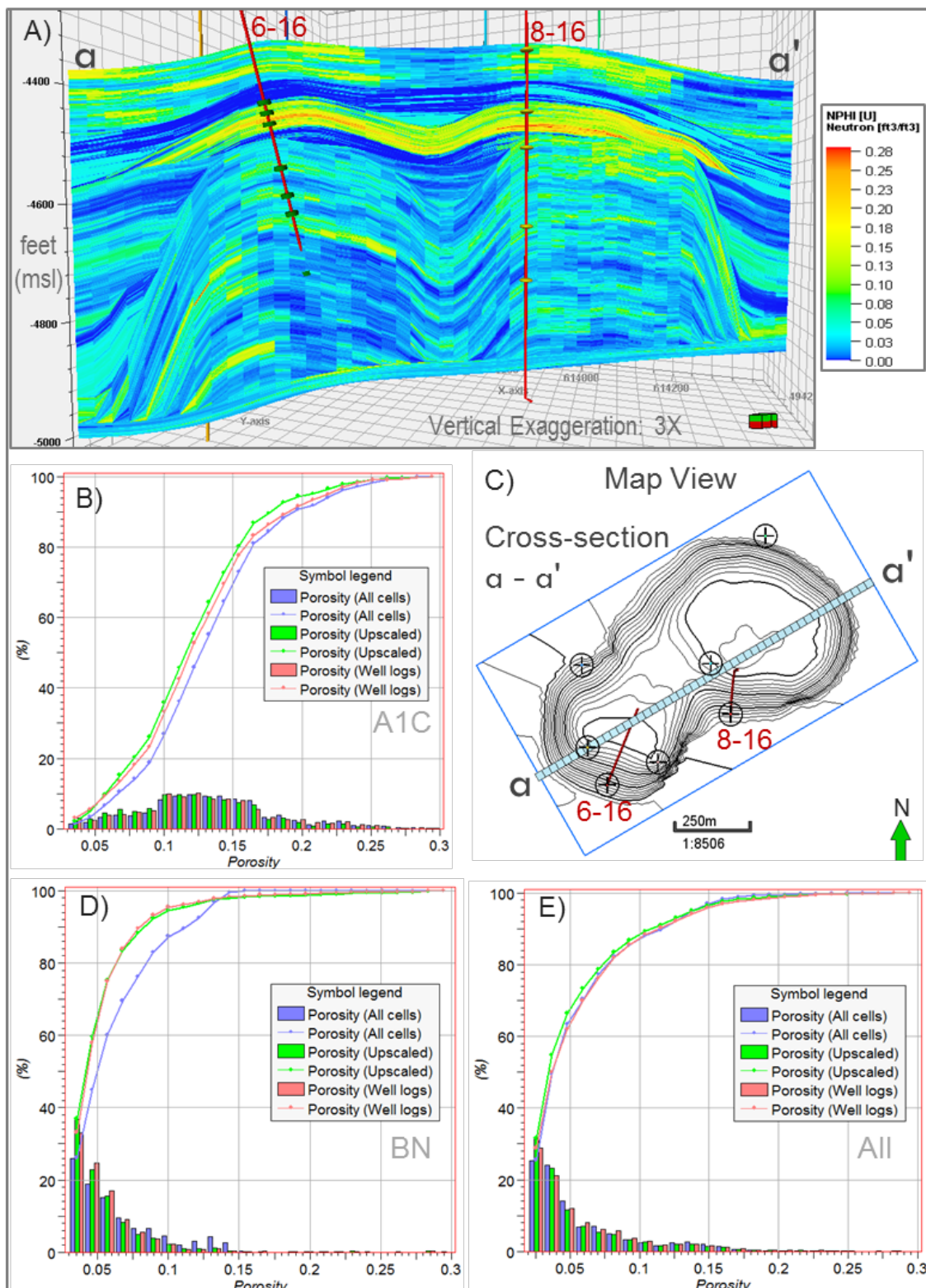


Figure 4-20. A) Cross-section through the porosity model. B) CDF comparison of neutron porosity for the A1 Carbonate Crest. C) Map of the reef showing the orientation of cross-section a-a'. D) CDF comparison of neutron porosity for the Brown Niagaran reef (Leeward, Reef Core and Windward). E) CDF comparison of neutron porosity for the entire SEM.

#### 4.3.2.5 Permeability Prediction Workflow

This section describes the basic porosity-permeability transform commonly used to prepare a permeability well log. This is followed by an advanced treatment whereby permeability residuals (representing the scatter off the basic trend) are used to synthesize a residual well log. Together, the basic trend, plus the residual well log, are used to produce a final permeability well log.

Several key well logs in addition to porosity are often available to enable SEM development. However, permeability logs are generally computed based on a relationship with porosity. While there are exceptions, for most lithologies as porosity increases, so does permeability. Working with core data, the common solution to predicting permeability is to cross plot permeability as a function of porosity and fit the data to produce a porosity-permeability (poro-perm) equation or transform. Example poro-perm transforms are shown in Figure 4-21. Exponential and power-law equations typically provide the best fit based on their  $R^2$  values. Still, there is generally a lot of scatter in the data, which results in poor correlation coefficients. Selecting one of these transforms can be difficult while others may be ruled out. For example, a poor choice would be the exponential fit in Figure 4-21, where porosity values above 20 percent would predict permeability values greater than 200 mD in a formation known to be relatively tight. The power-law fit was selected for the modeling and represented more reasonable permeabilities for higher porosity rock than the exponential fit.

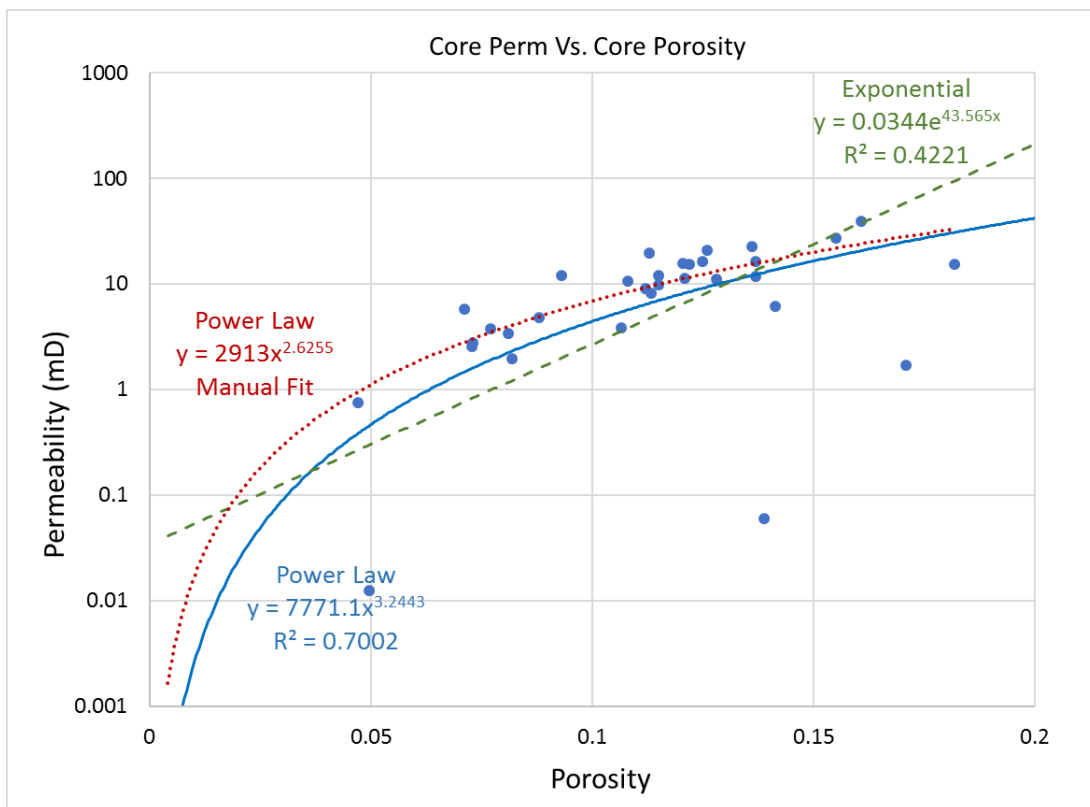


Figure 4-21. Example core data cross plot of permeability versus porosity. Different trendlines or fits are shown and can be used to predict permeability.  $x$ = porosity,  $y$ =permeability.

Once a poro-perm transform is selected, one can compute a permeability log based on porosity wireline log data. There are three assumptions regarding the use of this transform:

- There is confidence in the accuracy of the porosity log.
- The porosity log agrees with core porosity or has otherwise been calibrated to core.
- The transform represents a good fit with a high degree of correlation between porosity and permeability.

For this research, the accuracy of the porosity logs (NPHI) are trusted as they are on clean carbonates and have been adjusted for dolomite where present. These porosity logs have also shown very good agreement with core measurements. For assumption number three, we have noted a fair amount of scatter in the poro-perm data and this observation is common for carbonate rock.

In general practice, a transform would be selected, permeability logs would be computed, and SEM work would proceed with log upscaling and petrophysical modeling.

In this study, the manual fit power-law transform was selected, and the scatter seen in Figure 4-21 can be considered as residuals when the transform is implemented. These residuals can be statistically quantified, their variation simulated, and can be added to the original predicted permeability trend. Figure 4-22 illustrates this predicted permeability workflow, described in the following six steps.

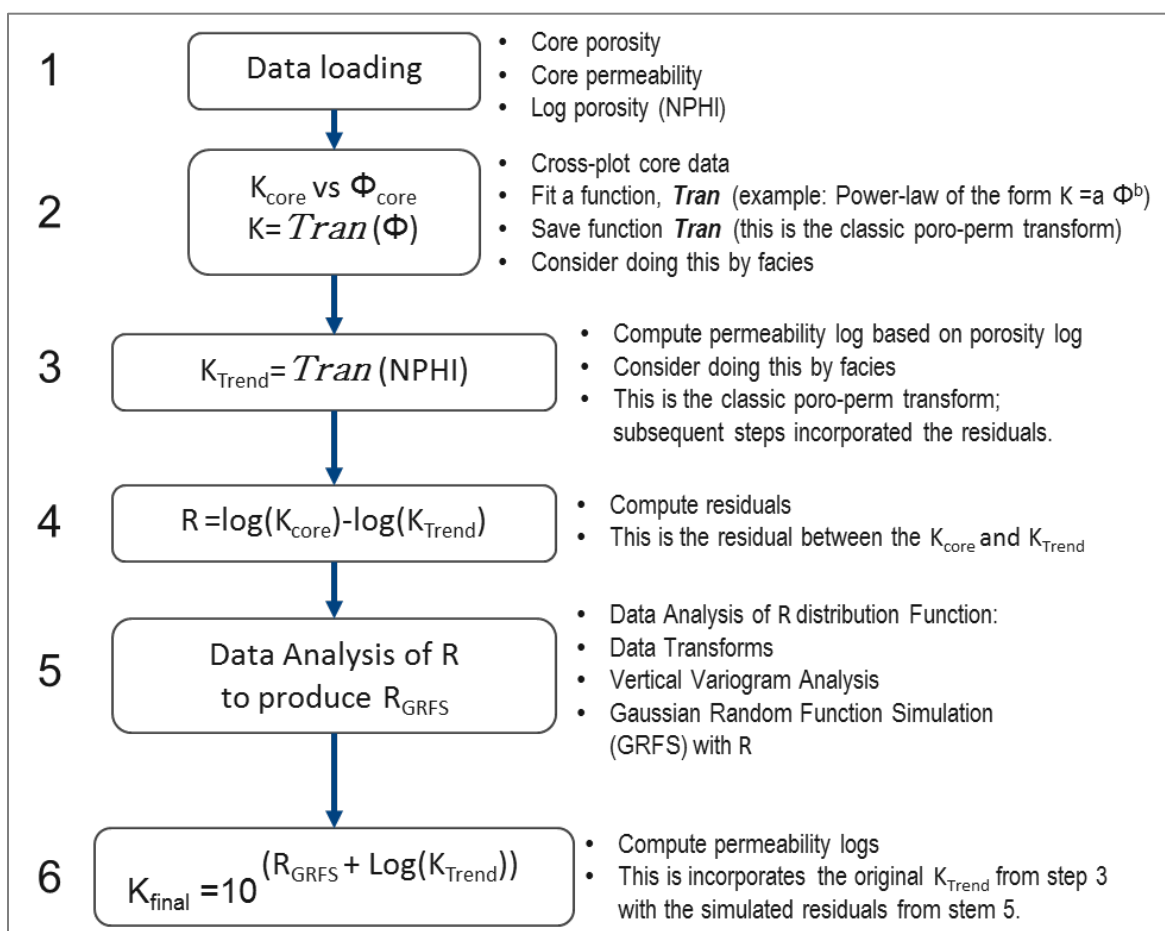


Figure 4-22. Permeability prediction workflow that adds simulated residuals (step 5) to the basic permeability transform (step 3).  $K_{final}$  represents the final, synthesized permeability log.

## 1. Data Loading

Laboratory measured core data for porosity and permeability are loaded into software that provides several curve fitting options. Log porosity, for example NPHI, is loaded into software that permits log editing calculating new logs.

## 2. Cross-plotting and curve fitting

Cross-plots of core permeability as a function of core porosity are prepared. Various trendlines are fit to this data. The most satisfactory fit will be recorded; this is considered the porosity-permeability transform,  $K_{Trend} = Tran(\Phi)$ , Figure 4-12. Depending on rock types, it may be necessary to subdivide the dataset by facies if it means developing a better fit.

## 3. Compute permeability log

Using the transform from step 2, the permeability log is calculated from the porosity log. This basic transform represents a basic or classic fit for predicting permeability from porosity.

## 4. Compute residuals

Residuals are computed using the equation  $R = \log(K_{core}) - \log(K_{Trend})$ . These residuals represent the difference between the predicted permeability ( $K_{Trend}$ ) and the original core permeability ( $K_{core}$ ). This calculation occurs at their representative depths, i.e. the depths that the core samples were taken.

## 5. Data Analysis of R distribution

This step involves the geostatistical treatment of the residuals, which requires several steps:

- a. Data Transforms: a histogram of the residual data is prepared and is paired with a gaussian distribution to enable the simulation that follows in step 5c.
- b. Variogram Analysis: A variogram analysis is performed along the well trajectories for this residual dataset. This means that the residuals have a spatial component and by performing a variogram analysis, we can quantify the residual's continuity and variability in depth along the well trajectories. This analysis produces a variogram model that is described by parameters such as sill, nugget, and range. This model is used in step 5c.
- c. Simulate Residuals  $R_{[GRFS]}$ : Run a GRFS on the residuals. The GRFS is a stochastic method that honors the full range and variability of the input data. Each run creates one equiprobable distribution of a property throughout the defined spatial volume (well trajectory) based on the model variogram (step b) and the existing residuals. The GRFS algorithm does this based on a normalized Gaussian distribution and thus the recommendation to include step (a) above to back-transform the simulated residuals to their original domain. This procedure will fill in simulated residual values between existing residuals for each point along the well trajectory, essentially producing a residuals log.

## 6. Compute the final permeability log

With the basic permeability trend from step 3 and the simulated residual log from step 5, compute the final permeability log using:  $K_{final} = 10^{(R_{[GRFS]} + Log(K_{Trend}))}$ . This final log should honor the original permeability trends from step 3 while incorporating the variability in step 5 attributed to the simulated residual log.

#### 4.3.2.6 Permeability

The permeability modeling effort focused on GRFS for the oil-bearing zones, which include the A1 Carbonate Crest, A1 Carb Flank, and Brown Niagaran reef. The permeability prediction workflow (Section 4.3.2.5) was based on core data to prepare permeability logs for these zones. The workflow essentially creates a core-based porosity-permeability transform for these zones; then, computes a permeability log based on the transform using the neutron porosity log. This method characterizes the permeability residuals and then, through conditional simulation, adds the permeability residuals to the basic transform. The resulting transform is conducted along the cells penetrated by the well trajectory. Note that upscaled logs equal well logs because the permeability logs were prepared or synthesized within the SEM's fine, 0.5-foot-layered grid. A vertical variogram analysis for the permeability logs was conducted for oil-bearing zones.

For permeability modeling, the permeability was distributed via GRFS while doing collocation, co-kriging with the porosity model. Table 4-8 summarizes the algorithm and constants used for each of the model zones. The permeability model was simplified for the non-oil-bearing zones by using average values from core measurements. These zones include the Gray Niagaran, A1 Salt, A2 Evaporite, and the A2 Carbonate. For modeling purposes, permeability for these zones are homogeneous.

**Table 4-8. Permeability property model input settings.**

PERMEABILITY	Zone	A2 Carbonate	A2 Evaporite	A1 Carb Crest	A1 Carb Flank	A1 Salt	BN - Flank	BN Reef	Gray Niagaran
	Algorithm	Constant	Constant	GRFS*	GRFS*	Constant	Constant	GRFS*	Constant
	Constant (mD)	0.235	0.001	-	-	0.001	0.001	-	0.001
Variogram Values	Nugget			0.0079	0.01			0.05	
	Type			Exponential	Exponential			Exponential	
	Major			527.42	500			120	
	Minor			385.812	500			120	
	Vertical			20.52	3.767			22.186	
	Sill			1	0.8746			0.4835	
Collocation Co-kriging with Porosity	with Volume			A1C porosity**	A1C porosity**			BN porosity***	
	Correlation coeff.			0.73	0.51			0.48	
	Sec. prop. transform			Normal score	Normal score			Normal score	
* With Petrel, used Data Analysis Transforms and Variograms along with Gaussian Random Function Simulation									
** NPHI Anisotropic for the A1 Carbonate									
*** NPHI Anisotropic for the Brown Niagaran Reef									

The average permeability for each zone was computed and is summarized in Table 4-9. Model zones where the standard deviation is zero were assigned average permeability values from core measurements.

**Table 4-9. Summary of computed average permeability for each SEM zone.**

Zone	Average SEM Permeability (mD)*	Standard Deviation (mD)
A2 Carbonate	0.235	0
A2 Evaporite	0.001	0
A1 Carbonate Crest	6.132	7.501
A1 Carbonate Flank	2.053	7.009
A1 Salt	0.004	0.506
Brown Niagaran Flank	0.002	0.05
Brown Niagaran Reef	0.649	10.813
Gray Niagaran	0.001	0
All SEM zones together	0.916	7.044

\* These computed averages are arithmetic averages, not harmonic averages.

Results for the permeability model are shown in Figure 4-23, which includes a cross-section through the model with permeability histograms and CDF plots. A histogram of the permeability for the A1 Carbonate Crest shows a good match among original logs and final model as shown in Figure 4-23B; the CDF plot also shows good agreement. The Brown Niagaran also shows reasonable agreement (Figure 4-23D), but there is a little divergence in CDF plots, possibly attributed to the reef's limbs. Finally, the A1 Carbonate Flank (Figure 4-23E) shows a great match going from original well logs to full property model. Although the A1 Carbonate Flank is generally considered tight, it is believed that the saddle region between the reef's two pods may have favorable conditions for some oil.

#### 4.3.2.7 Grid Upscaling

The petrophysical SEM consisted of nearly 4 million cells. The reduction of model cell count was necessary to facilitate the time-intensive DRM work that would follow.

Upscaling was performed and came at the expense of losing some of the SEM's heterogeneity. One goal in SEM upscaling is to maintain flow units by pairing certain layers together. The Petrel plug-in CONNECT UpGrid™ was used to aid the upscaling process by optimizing the grouping of layers. This utility performs the optimum vertical upscaling design by minimizing the error on the pressure while combining vertical layers. The horizontal grid size remains unchanged. Layers having similar pressure distributions are combined first, and the layers with distinct pressure profiles are isolated. By preserving the dynamic behavior, the upscaled model can reproduce the behavior of the fine-scale model with fewer cells. The 2853-layer, fine-scale SEM served as input to the upscaling process, which reduces the number of layers.

Working with CONNECT UpGrid™, the selection of an optimum vertical layer design should consider both the DF and the SE as shown in Figure 4-24A. These two parameters are plotted as a function of SEM layer design. A higher DF indicates an effective upscaling design for separating distinct layers. A lower DF indicates no effect on the layering design and is closer to Petrel's standard, proportional layering method. Whenever the Error per Layer (EPL) trend starts to pick up, it means that "over-homogenizing" has occurred for the reservoir, as shown in Figure 4-24B. The preference is to select the optimum number of layers with a high value of DF but before the EPL trend starts to pick up. Therefore, the criterion to select the optimum design is to select the points with maximum DF and at the same time provide the

minimum SE change per layer. Figure 4-24C shows the DF and SE combination that was selected, which resulted in a 79-layer upscaled SEM.

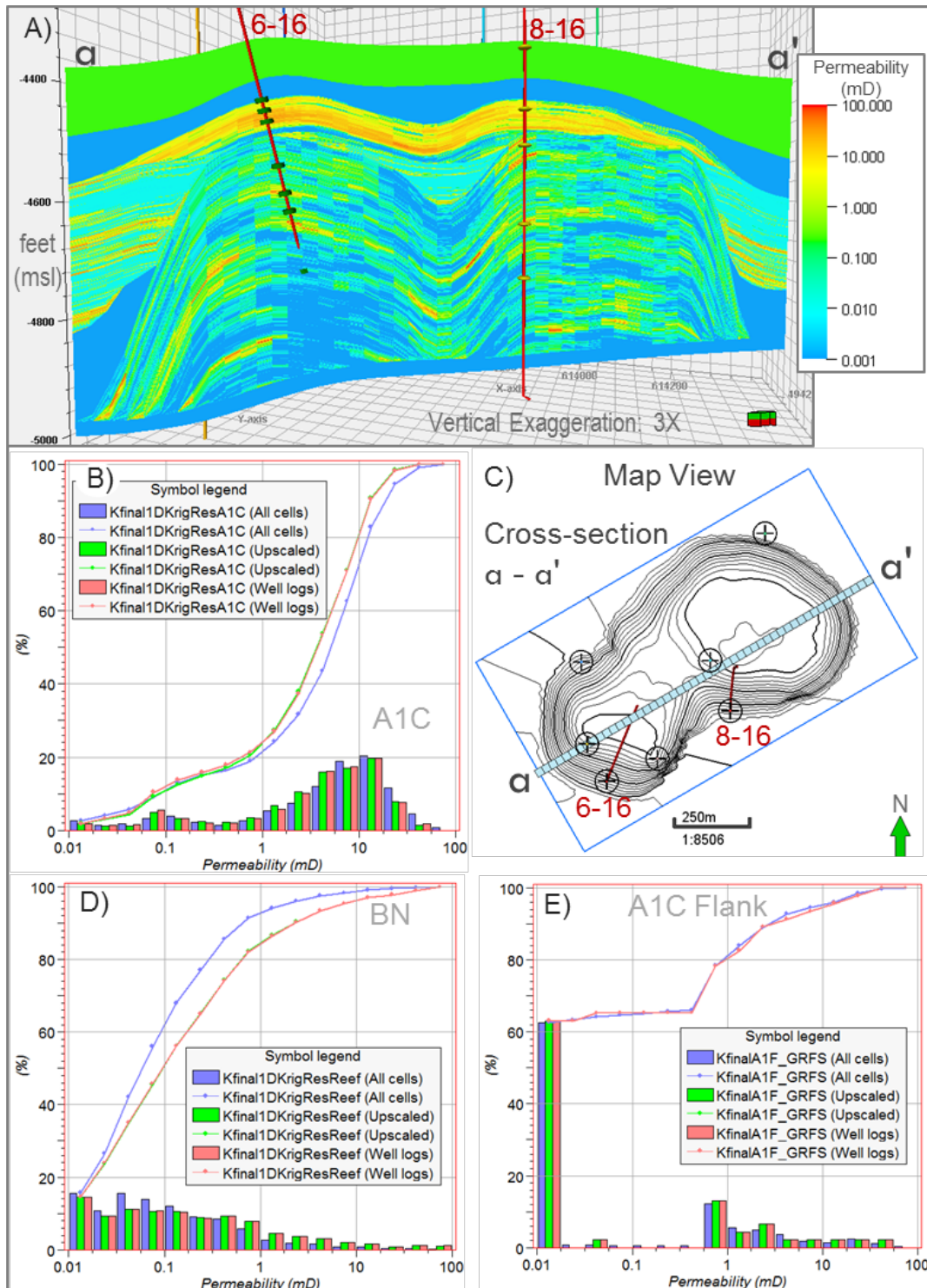


Figure 4-23. A) Cross-section through the permeability model. B) CDF comparison of permeability for the A1 Carbonate Crest. C) Map of the reef showing the orientation of cross-section a-a'. D) CDF comparison of permeability for the Brown Niagaran reef (Leeward, Reef Core and Windward). E) CDF comparison of permeability for the A1 Carb Flank.

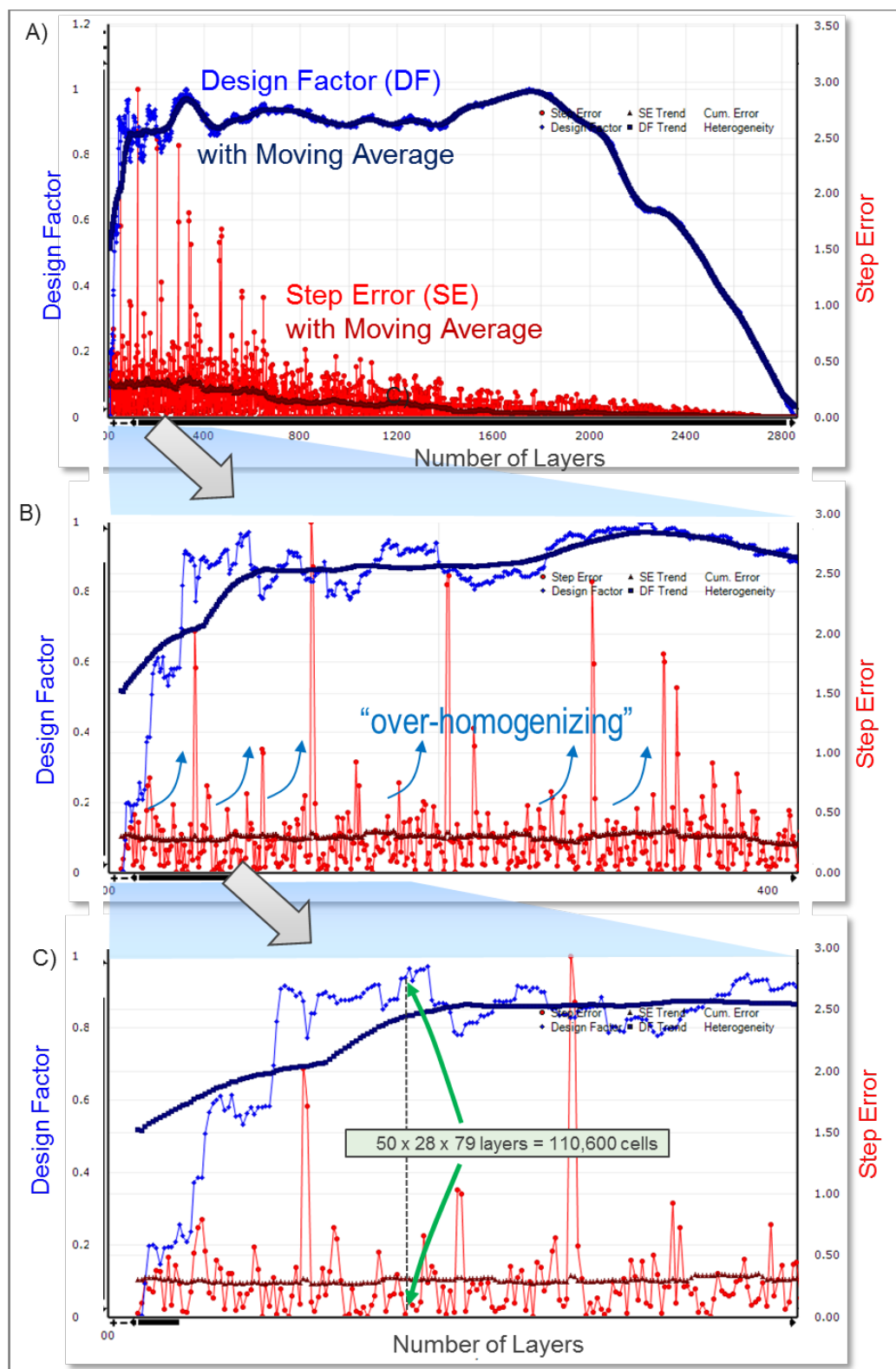


Figure 4-24. SEM upscaling optimization using CONNECT UpGrid™. A) Diagnostic plot showing upscaling design factor and step error as a function of SEM layer count. B) Zoomed-in to 400 layers; SE cycles show “over-homogenization.” C) Zoomed-in to 200 layers, plot shows the selection of a 79-layer model with high DF and low SE.

CONNECT UpGrid™ provided the layering scheme for the 79-layer model, as shown in Figure 4-25. The layering for the upscaled SEM appears to vary depending on which original layers were grouped and preserves model zones. The resulting upscaled SEM has 110,600 cells, which makes it more suitable for DRM work than the original fine-scale model.

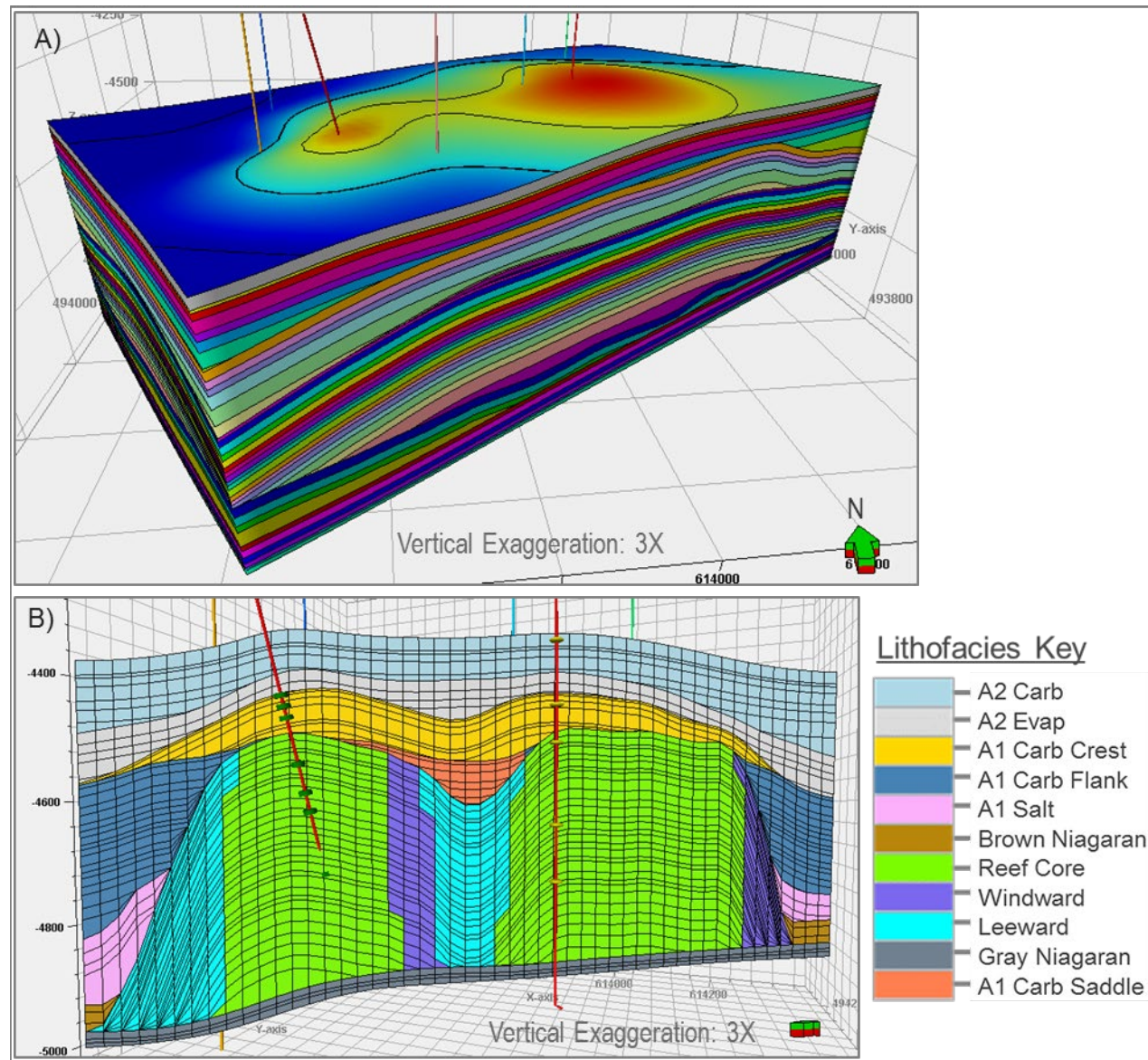


Figure 4-25. SEM upscaling results. A) Oblique view of the 110,600 cell, 79-layer SEM. B) Cross-section through the SEM with varying layer thickness related to how layers had been grouped.

Working with the new upscaled framework, the fine-scale porosity model was upscaled into the new grid using the arithmetic averaging method. For permeability, the harmonic averaging method was selected, and the results are shown in Figure 4-26. The upscaled SEM appears to preserve both high porosity and permeability trends for the A1 Carb Crest and the Brown Niagaran when compared to Figure 4-20 and Figure 4-23.

This final upscaled SEM consisted of 110,600 cells and was used for DRM work.

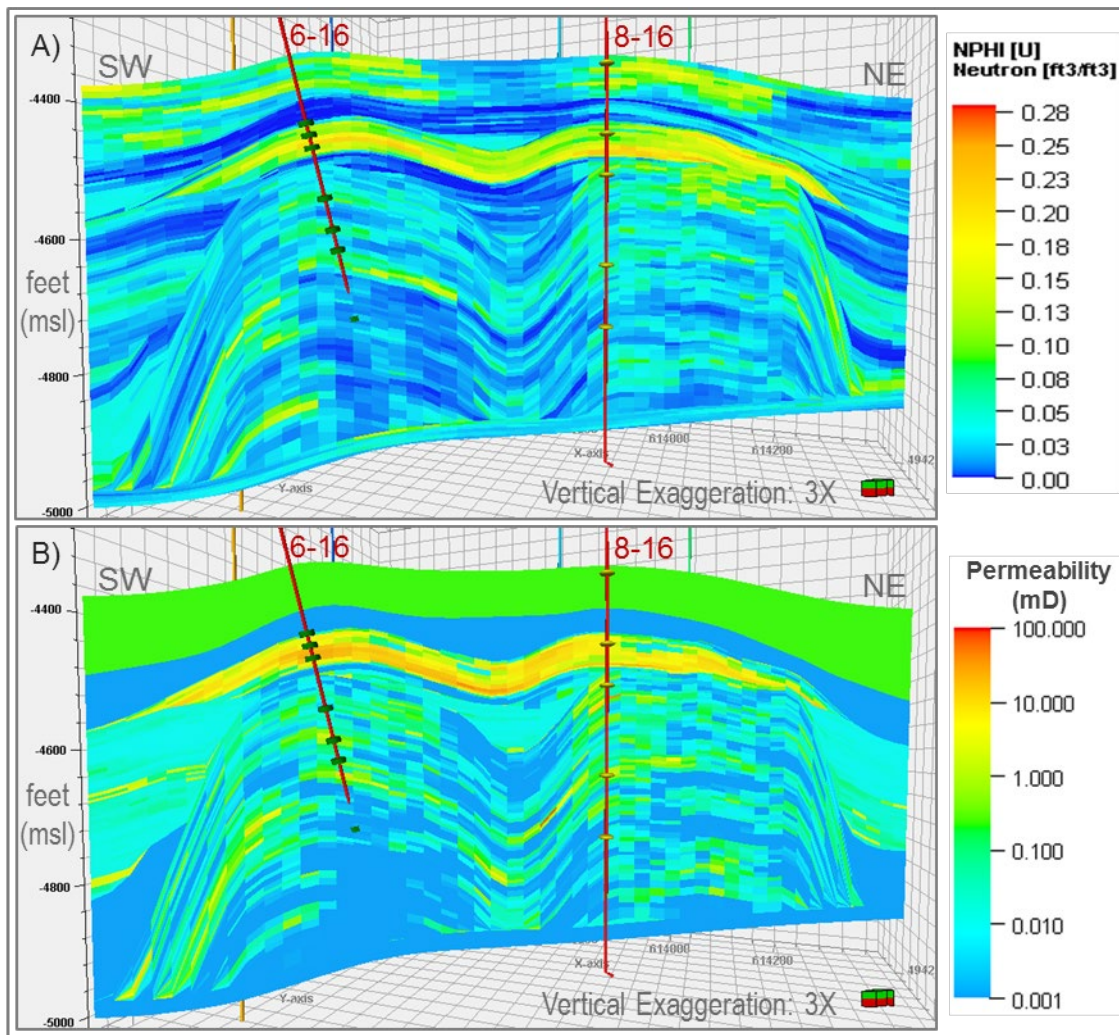


Figure 4-26. SEM upscaling results for the 79-layer model. A) Porosity model. B) Permeability model.

#### 4.3.2.8 Water Saturation

For the purposes of dynamic simulation in the Chester 16, the uncertainty in the distribution of porosity is not considered to be as significant as compared to permeability and can be very reasonably constrained via available log /core measurements. The Chester 16 reservoir (and generally any carbonate reef) is known to be highly heterogeneous permeability-wise, with the permeability distribution thought to be the most sensitive parameter controlling the output of the model. As a result, it is the primary subject of the model calibration process and a lot of latitude is permitted in the distribution of permeability before history matching, since it will invariably be modified.

The average initial water saturation distribution on the other hand, is a parameter that is tightly constrained as a result of “a-priori” knowledge of the total volume of oil in the reservoir (around 7 MM STB in Chester 16). This information is generally considered to be very reliable as it is obtained from an independently performed material balance study that associates the rate of the overall field-scale production to the size of the field while considering pressure dependent black-oil fluid properties. Aside from a means of integrating OOIP information into the model, it is also important to capture the geologic distribution of the initial water saturation initially, since this distribution is further morphed during production and injection activities. The water saturation distribution controls the relative permeability to

the various fluids throughout the reservoir, and hence is an important parameter that indirectly controls the pressure-depletion and buildup within the reservoir. Finally, from a practical standpoint, poor initialization of water saturation distribution (e.g. without hydrostatic equilibrium in the reservoir) can also lead to numerical/convergence issues in the simulation in the later stages of the modeling.

Distributing water saturation via geostatistical methods like those used for porosity and permeability is generally not recommended. While highly sophisticated methods that involve a rigorous rock-typing workflow are desirable, the lack of detailed MICP measurements for all the cores limited their application. Chester 16 utilized the equilibrium method or a Leverett J-Function-type evaluation for the region above the OWC. Details of the methodology are provided later in the section.

The distribution of water saturation in the model was separated into three regions as described below.

1. The lower third of the reef structure was water saturated. The OWC for the reef was identified from well logs. An OWC surface was created at -4,808 feet elevation depth. SEM cells below this surface were assigned a value of 1 corresponding to 100 percent water saturation.
2. Formations outside the oil-bearing zones were also assigned a value of  $Sw = 1$ . This simplification is consistent with wireline logs. For example, the A2 Evaporite has high water saturations overlying the reef and on the flanks. This is due to the presence of evaporites and the influence they have on resistivity curves. For modeling purposes, the  $Sw$  assignment of 1 ensures that estimates for hydrocarbon pore volume in these zones are zero or negligible.
3. The A1 Carb Crest, the Brown Niagaran reef, and the A1 Carb Flank (saddle region) are recognized as oil-bearing. Water saturation versus height above OWC was plotted individually for these zones. The Brown Niagaran employed a split on the basis of low (<3 percent) and high (>3 percent) porosity (or a pseudo rock-type), with the implication that the higher porosity rock had a residual water saturation of around 0.15, while the lower porosity rock had an average residual water saturation of around 0.25. Most of the rock was of the low porosity type and a curve fit of water saturation as a function of square-root of  $k/\phi$  ( $Sw = \text{SQRT}(k/\phi)$ ) was used to model saturations for this region.

Table 4-10 summarizes the water saturation values for each SEM zone.

**Table 4-10. Summary of average water saturation values for each zone in the Chester 16 SEM.**

Zone	Water Saturation (fraction)	Standard Deviation
A2 Carbonate	1	0
A2 Evaporite	1	0
A1 Carbonate Crest	0.43	0.23
A1 Carbonate Flank	0.81*	0.14
A1 Salt	1	0
Brown Niagaran Flank	1	0
Brown Niagaran Reef	0.49	0.36
Gray Niagaran	1	0
All SEM zones together	0.77	0.31

\* Includes the A1 Carbonate Flank Saddle area that has been set to 70%.

#### 4.3.2.8.1 Methodology: Equilibrium Method

The equilibrium method is a more flexible version of the J-function method when a rigorous rock-type categorization is either not available (Brown Niagaran) or not necessary (A1 Carbonate). This method has four steps:

1. Mercury-Injection- Capillary Pressure (MICP) data is transformed into a graph of lab-measured capillary pressure vs water saturation. Alternatively, a J-function that uses the cores porosity and permeability can be calculated to smooth the capillary pressure data.

$$J = \frac{0.218 P_c}{\sigma \cos \theta} \sqrt{\frac{k}{\phi}}$$

**Equation 4-1**

2. This plot is corrected into a plot of reservoir-measured capillary pressure through a scalar multiplier.

$$P_{c,res} = P_{c,lab} \frac{(2\sigma \cos \theta)_{res}}{(2\sigma \cos \theta)_{lab}}$$

**Equation 4-2**

3. This graph is then further morphed into height in the reservoir vs water saturation graph, by applying a new scalar multiplier that relates the capillary pressure to the density difference between oil and water.

$$P_c = \frac{h(\rho_1 - \rho_2)}{144}$$

**Equation 4-3**

4. The function fit to the height in the reservoir vs water saturation graph is fed into the geocellular model, where each cell is a known height above the OWC. This results in each cell being associated with a water saturation.

The next sub-section discusses the details of the water saturation population for both the Brown Niagaran and the A1 Carbonate.

#### 4.3.2.8.2 Water Saturation in the A1 Carbonate

In the Chester 16, the A1 and Brown Niagaran (BN) are thought to be in hydraulic communication sharing the same OWC, which is a flat surface at the bottom of the BN (Figure 4-27).

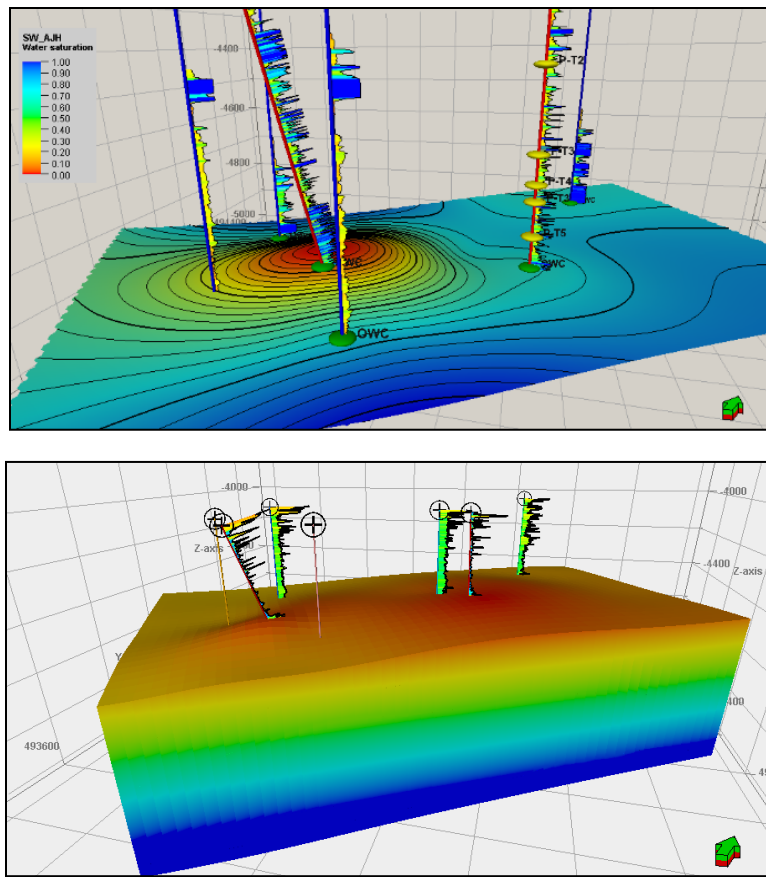


Figure 4-27. The top panel shows flat OWC at the bottom of the Chester 16, while the bottom panel shows height from the OWC to the centroid of every cell in the Chester 16 reservoir model.

Figure 4-28, which is a plot of the height above the OWC vs the log-derived water saturation, suggests that the A1 Carbonate does in fact conform to a single rock-type (black curved line), with a very small connate water saturation. This reflects the formation's good porosity and general homogeneity. A J-function was comfortably fit to the MICP data gathered from the A1 carbonate and this function was input into the geocellular model to distribute water saturation within only the A1 crest. Figure 4-29 shows the J-function fit based upon the capillary pressure and core-based water saturation data for the A1 Carbonate. The dots in yellow highlight the goodness of -fit for the A1 Crest alone (eliminating the data from A1 flanks) in particular.

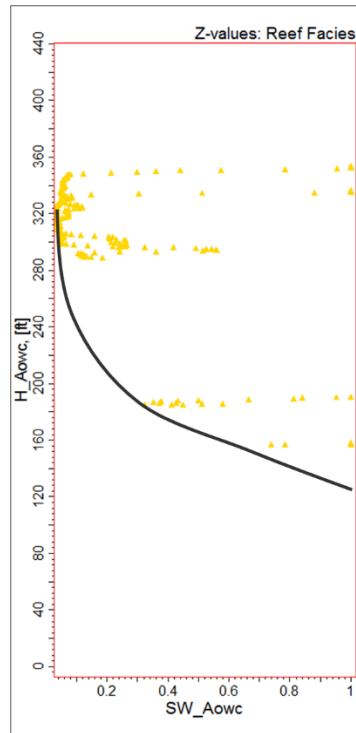


Figure 4-28. Height vs water saturation for the A1 Carbonate.

J vs Sw in A1C from all 5 wells (with 1-16)

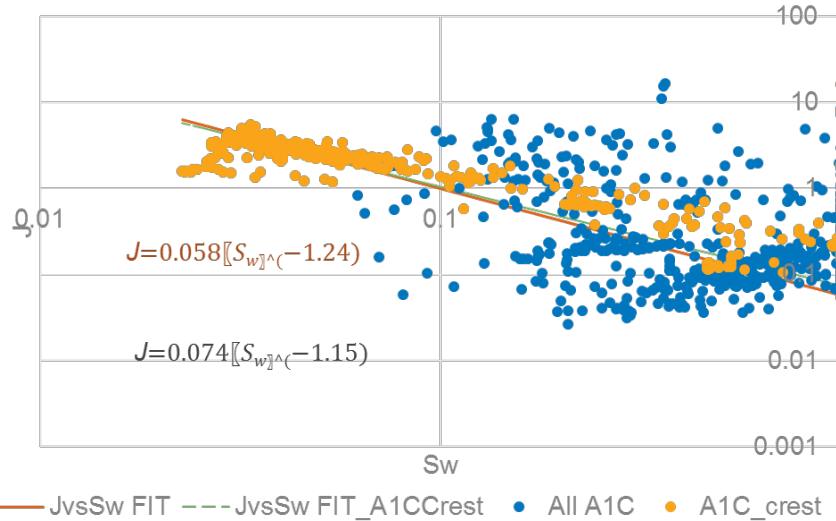


Figure 4-29. J-function fit to the A1 Carbonate.

#### 4.3.2.8.3 Water Saturation in the Brown Niagaran

While a detailed description of the rock-type identification process with a complete data set is beyond the scope of this report, a pseudo-rock-typing process was customized for the Chester 16. Electro-facies can be defined in this analysis as the distinct groups of correlated log properties from all the wells sampling the region, taken as a proxy for lab-measured core properties. An analysis to determine the number of electro-facies determined that the depositional facies had undergone significant diagenesis as to alter the rock-typing. The dendrogram in Figure 4-29 shows the result of the clustering analysis using all three well logs from all the wells in Chester 16. One interpretation of a dendrogram is to equate nodes to rock types (clusters) and equate the height (x-axis) as proportional to the amount of information *lost*. While using a dendrogram to determine the exact number of clusters is not recommended, the dendrogram still enables a simplistic evaluation of *whether the pre-determined or assumed number of clusters leads is adequate*. The number of clusters should also minimize the height of the dendrogram. Figure 4-30 suggests that grouping the data into three clusters (highlighted as blue dots) may be adequate, although more conservative interpretation of the dendrogram would imply that there are at least five rock types in the model.

If the assumption that there are three rock types is correct, Table 4-11 would show that each electro-facies cluster predominantly (>75 percent) maps itself back onto one of the depositional facies (windward, leeward and reef core). The reef core is an approximately cylindrical region in the center of each pod and flanked by the windward and leeward facies on either side. A diagonal along Table 4-11 would strongly suggest that depositional facies provide enough resolution to describe the Brown Niagaran. The fact that this does not happen suggests that the diagenesis has significantly changed each rock-type and that this classification does not work for the purpose of water saturation modeling. In addition, the plot of log-derived water saturation with the height above the OWC (Figure 4-31) differs significantly from that made for the A1 (not a smooth curve with a clearly defined asymptote). This further confirms that some level of rock-typing does exist in the reservoir that needs reflection in the rock description.

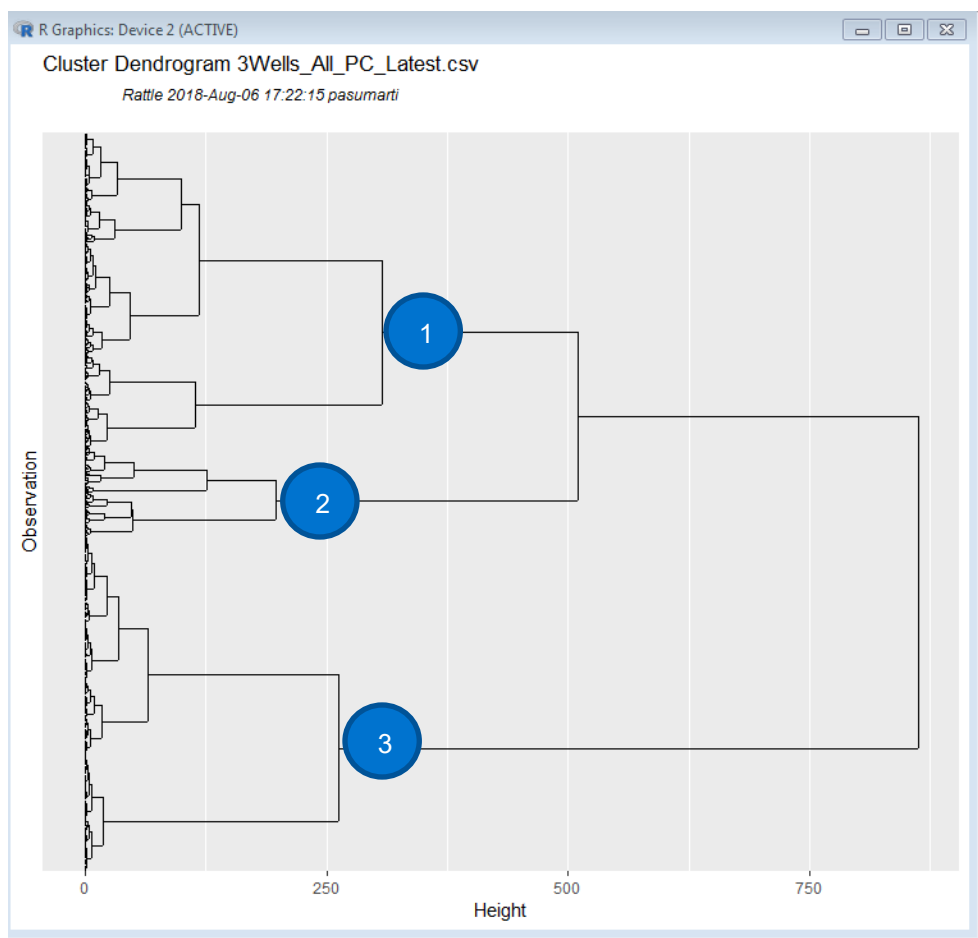


Figure 4-30. Cluster dendrogram of the well logs in the Chester 16.

**Table 4-11.** The three depositional facies of the Brown Niagaran do not conclusively map themselves onto three electro-facies.

Depositional Facies	(Diagenetic) Electro-Facies – Number Labelled			Total # of Points
	# of "1"s	# of "2"s	# of "3"s	
Windward	66%	14%	20%	865
Leeward	27%	22%	51%	635
Reef Core	27%	24%	49%	2400

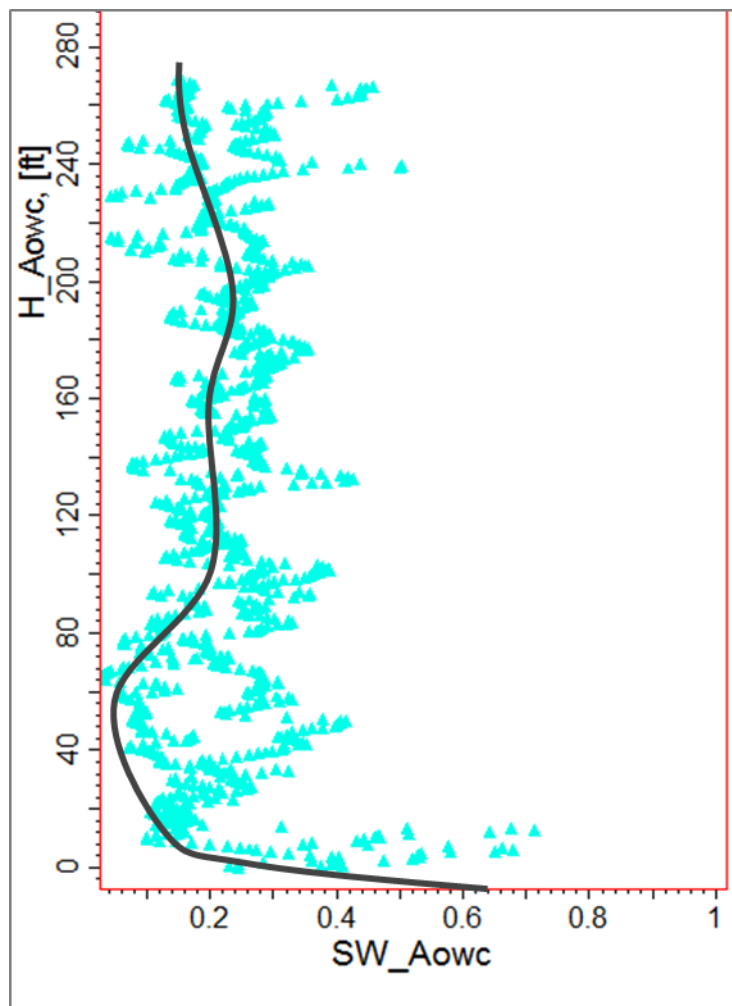


Figure 4-31. Height vs water saturation for the Brown Niagaran

To address this issue, the height above the OWC vs water saturation curve in the Brown Niagaran was split based on low (<3 percent) and high (>3 percent) porosity or a pseudo rock-type and was then smoothed (Figure 4-32). This allowed for the inference that the “good” or high porosity rock had a residual water saturation of around 0.15, while the “bad” or low porosity rock had a residual water saturation of around 0.25. Considering that low porosity rock occupied 70 percent of the rock volume in the Brown Niagaran, a saturation function was desirable only to this volume of rock, and the constant value was deemed adequate for all the rock with high porosity. Within this low porosity-rock, instead of directly using the equilibrium function, a simpler function was extracted based on the correlation between the well log-derived water saturation and a “pseudo-J-function”. This pseudo-J-function assumes a uniform thickness and uses the corresponding porosity and permeability values in the cores (Figure 4-33). This function was fit back into the geo-cellular volume, where every cell already had a porosity/permeability value from the property model (discussed in the previous chapter).

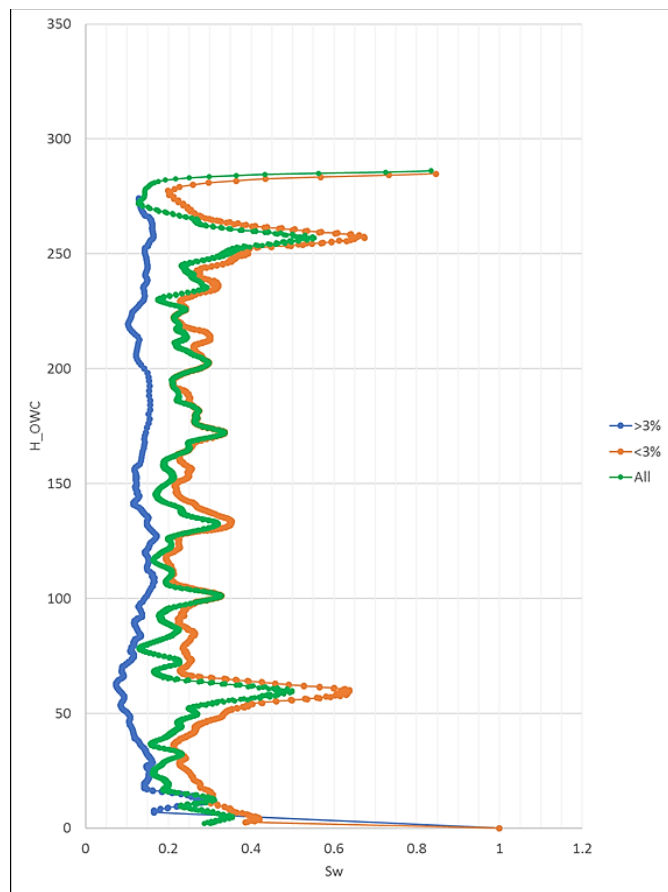


Figure 4-32. Height vs Water Saturation for the Brown Niagaran smoothed and split into "good" and "bad" quality rock.

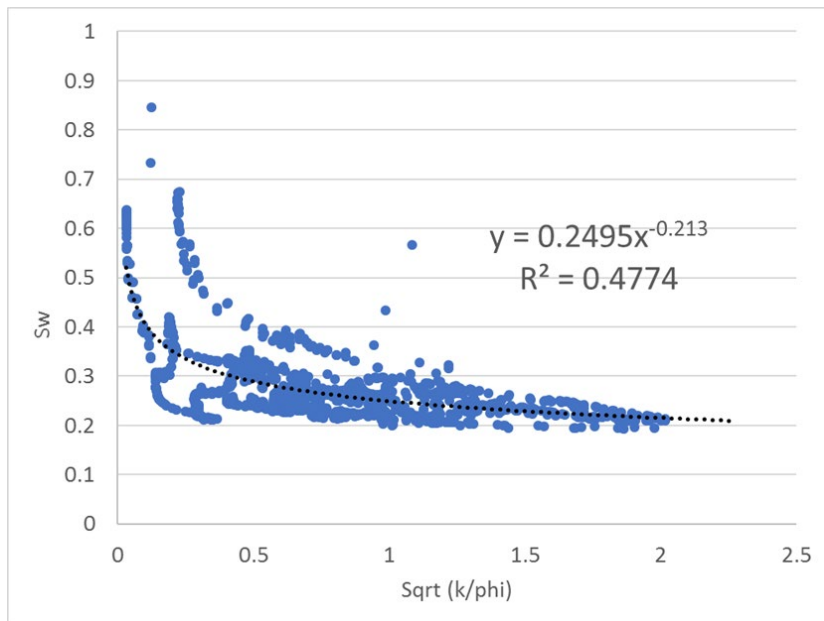


Figure 4-33. Water saturation relationship for the Brown Niagaran

#### 4.3.2.9 Initial Water Saturation Distribution and Volumetrics

The hydrocarbon pore volume (HCPV) for the SEM was computed for the reef. The general equation for this calculation is:

$$\text{HCPV} = \text{GRV} * \text{N/G} * \phi * S_{hc}$$

**Equation 4-4**

where:

GRV: Gross rock volume in the trap above the hydrocarbon-water contact.

N/G: Average Net Reservoir/ Gross rock

$\phi$ : Average Porosity

$S_{hc}$ : Average hydrocarbon saturation =  $(1-S_w)$ .

While the general equation may use average values, the calculations here are based on individual cells and represent a more accurate estimate of the HCPV. The cross-section in Figure 4-34 and Figure 4-35 reveals where HCPV is likely to occur based on the OWC, model porosity, and water saturation. Note that cell color is also related to individual cell volume. The dominant lithology for oil-bearing units were clean carbonate rocks limestone and dolomite, so the N/G value was set to one as a simplification to the model. The resulting HCPV of oil for the reef was computed at ~9.2 million barrels. Table 4-12 summarizes the volume and hydrocarbon (oil) estimates for all SEM zones and reflects volume of oil at reservoir (in situ) conditions.

**Table 4-12. Volumetrics and HCPV for each reef facies.**

Case	Bulk volume [ft <sup>3</sup> ]	Net volume [ft <sup>3</sup> ]	Pore volume [ft <sup>3</sup> ]	HCPV oil [ft <sup>3</sup> ]**	HCPV oil [bbl]**
Totals	4,376,396,221	4,376,396,221	165,415,285	51,685,520	9,205,584
A2 Carbonate	1,013,195,065	1,013,195,065	51,341,938	-	-
A2 Evaporite	752,151,400	752,151,400	20,407,290	896	160
A1 Carbonate	224,747,445	224,747,445	24,400,276	14,547,948	2,591,100
A1 Carb Flank	734,876,664	734,876,664	18,318,407	2,519,977	448,827
A1 Salt	116,188,990	116,188,990	1,108,212	1,189	212
Brown Niagaran*	854,387	854,387	58,579	-	-
Reef Core	677,223,927	677,223,927	23,288,653	18,528,862	3,300,131
Windward	171,473,779	171,473,779	7,602,956	5,898,332	1,050,538
Leeward	285,837,699	285,837,699	9,728,578	7,440,399	1,325,192
Gray Niagaran	-	-	-	-	-
A1 Carb Saddle	399,846,866	399,846,866	9,160,396	2,747,918	489,425

\* Brown Niagaran here is referring to the perimeter region that flanks the reef.

\*\* Volume of oil at reservoir (in situ) conditions. Formation Volume Factor (Bo) = 1.

Since the reservoir pressure was above the bubble point pressure in the beginning, Chester 16 was initially an undersaturated reservoir containing only oil and water. The OOIP in the reservoir was obtained from the initialization of the dynamic model. A summation of oil contained in each cell in the geo-cellular model – each cell was assigned its own formation volume factor (cell-average of approximately 1.33) since a vertical pressure gradient was employed to bring the initial average reservoir pressure to 3,150 psi – produced an estimate of 6.9 MM STB. This corroborates with the volumetric estimate obtained from an independently undertaken material balance analysis of the Chester 16 (7 MM STB) and

thus validates the water saturation mapping exercise. Figure 4-34 shows a cross-section through the Chester 16 representing water saturation distribution in the first model. Water saturated zones show up as blue ( $Sw=1$ ). The OWC is present in the lower portion of the Brown Niagaran. The saddle region of the A1 Carbonate Flank was assigned a value of 0.7 as revealed in the histogram, Figure 4-34C. The water saturation histogram for the Brown Niagaran reef reveals two spikes: one is at 1 (100 percent) full water saturation below the OWC, the other at ~15 percent corresponding to higher porosity streaks within the reef. A cross-section of the reservoir showing the distribution of oil in the model is shown in Figure 4-35.

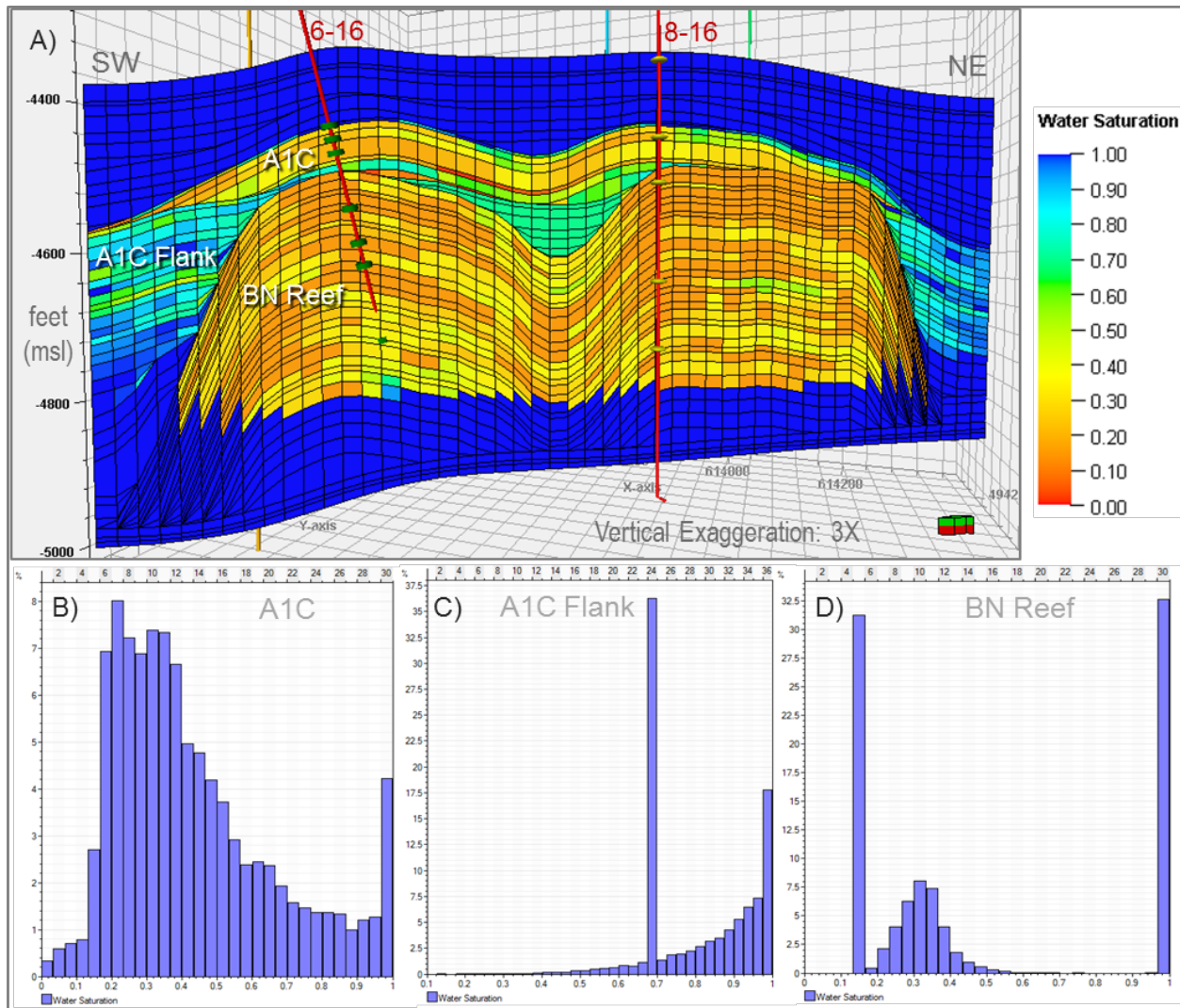


Figure 4-34. A) Cross-section through the water saturation model. B) Water saturation histogram for the A1 Carbonate Crest. C) Water saturation histogram for the A1 Carb Flank which includes the saddle region. D) water saturation histogram for the Brown Niagaran reef consisting of the leeward, reef core, and windward lithofacies.

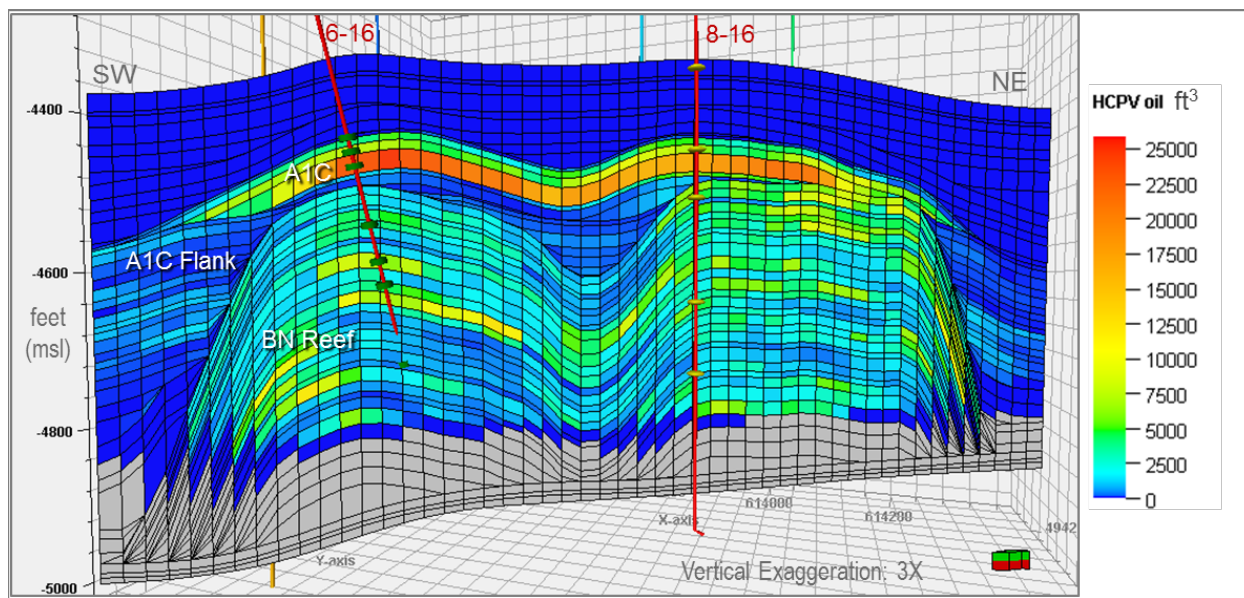


Figure 4-35. Cross-section through the SEM showing the computed HCPV on the upscaled, 79-layer grid.

#### 4.3.2.10 Alternative Conceptualization (Seismic Inversion and Property Modeling)

The Chester 16 3D seismic survey was processed for inversion in 2019. The inversion products included an Acoustic Impedance (AI) volume and a Porosity volume, Figure 4-36A and Figure 4-36B. The porosity volume was derived using a univariate transform based on AI and porosity (NPHI) logs to convert the AI volume to porosity. The transform was fit to a population that had low gamma ray values, which correspond to clean limestone prevalent within the Brown Niagaran reef. These two inversions were depth converted. The inverted porosity volume was then sampled from the seismic domain into a 3D geocellular domain representing Chester 16's SEM framework, Figure 4-36C. Because the seismic inversion is geospatially consistent with the Chester 16 reef, this porosity inversion information was used to inform the porosity model (Figure 4-36D) and is described further below.

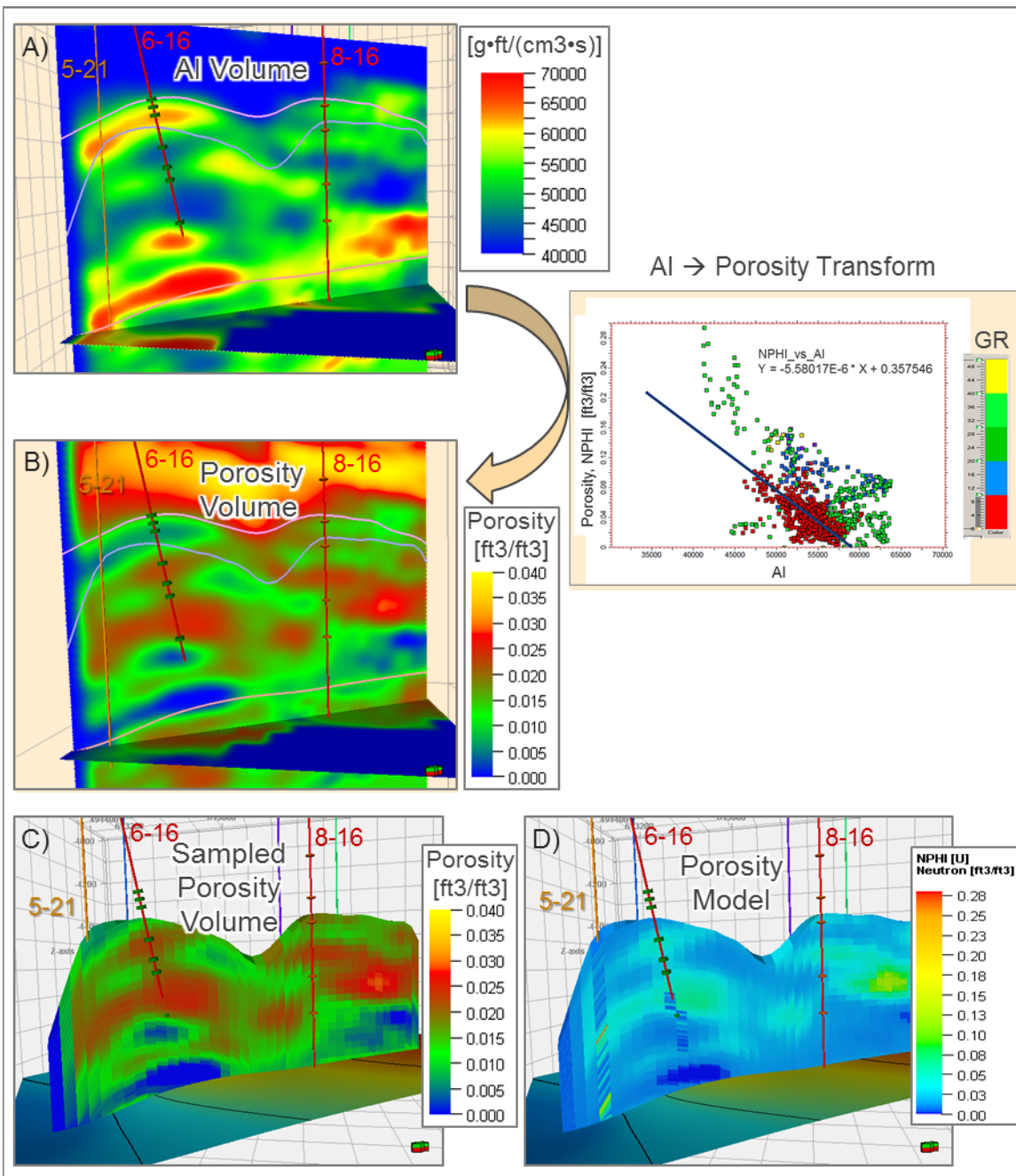


Figure 4-36. Cross-sections through the seismic inversion results and property modeling. A) Acoustic impedance inversion volume in seismic domain. B) Porosity inversion volume in seismic domain. AI volume to porosity volume transform upper right. C) Sampled porosity inversion volume in SEM domain for the Brown Niagaran. D) Brown Niagaran porosity model in the SEM domain recalibrated to neutron porosity logs.

#### 4.3.2.11 Porosity Model (Based on Seismic Inversion)

An alternative conceptualization (resulting in a second SEM) was developed that integrated seismic data. This resulted in updates to the porosity and permeability distribution – hence an alternative water saturation distribution. The seismic porosity inversion comes with certain limitations and shouldn't be used as the final porosity model because it lacks the vertical resolution available from the well logs and

can potentially yield a range of values that may deviate or shift from the porosity log's histogram. The real value of the porosity inversion volume is to provide porosity trend information away from wells and between wells. This is accomplished through property modeling where the porosity logs (NPHI) are co-kriged with the inverted porosity volume. This was performed within the 3D grid and combines the best of both data types. The porosity model reflects the true range of porosity log values and preserves the trend information from the seismic inversion while introducing some heterogeneity that would naturally occur within a reservoir.

The porosity modeling effort employed the GRFS for the oil-bearing zones, which include the A1 Carbonate Crest, A1 Carbonate Flank (A1C Flank), and Brown Niagaran reef. The A1C Flank was included, as this zone contains the A1 Carbonate Saddle, which may potentially be oil-bearing. The Brown Niagaran reef employed the GRFS method using porosity logs (NPHI) that were co-kriged with the inverted porosity volume and was the only zone to receive this treatment.

The porosity model input parameters are summarized by model zone in Table 4-7. Figure 4-37 shows a cross-section through the updated porosity model histograms along with CDF plots for the oil-bearing units (A1 Carbonate Crest and Brown Niagaran) and for the entire SEM which includes all zones.

The porosity model is consistent with the scaled-up logs and original well logs as shown in the CDFs in Figure 4-37. The porosity model had a strong porosity trend in the A1 Carbonate Crest that overlies the Brown Niagaran reef. The A1 Carbonate Crest had the highest average porosity of 11 percent. Porosity for the Brown Niagaran reef appears more smoothed and reflects preservation of porosity trends observed in the seismic inversion (Figure 4-36D). Porosity trends could be attributed to dolomitic intervals or possible fractures. Moderate porosity was observed at the top of the reef, which could provide some connectivity to the overlying A1 Carbonate, and porosity decreased toward the base of the reef. The Brown Niagaran reef lithofacies had porosity near 3.4 percent. The A2 Carbonate had an average of 5.1 percent porosity. This porosity was influenced by a layer of mudstone/shale with micro-porosity and some leaching of evaporates. Formations with high concentrations of salt (e.g. A2 Evaporite, A2 Salt) had porosities near 2 percent. Table 4-9 summarizes these average values by SEM zone. As a result of this update, the Brown Niagaran reef's average porosity changed from 3.4 percent to 3.0 percent and its standard deviation changed from 3.2 percent to 2.8 percent.

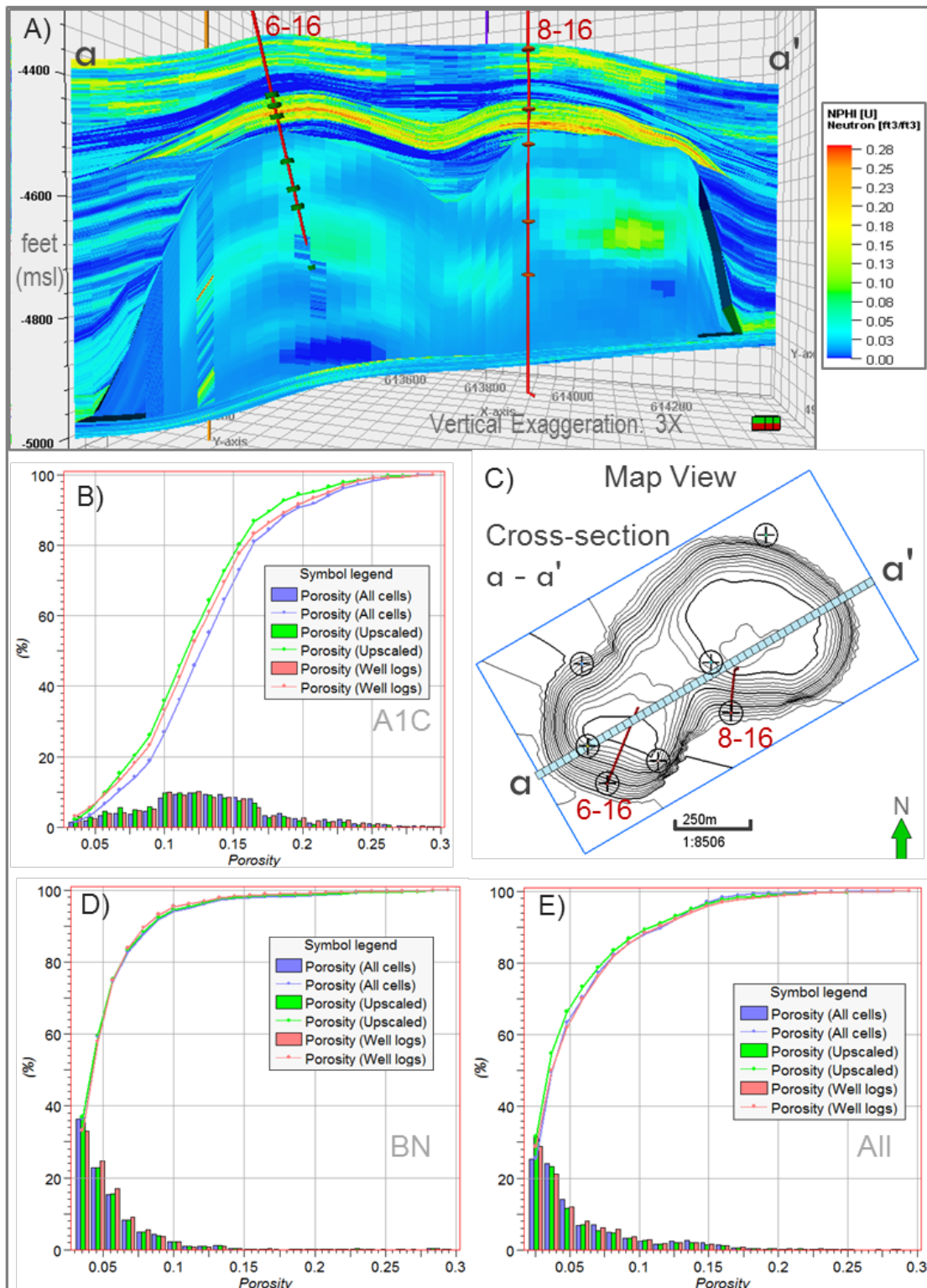


Figure 4-37. Porosity model with Brown Niagaran reef conditioned by seismic porosity inversion. A) Cross-section through the porosity model. B) CDF comparison of neutron porosity for the A1 Carbonate Crest. C) Map of the reef showing the orientation of cross-section a-a'. D) CDF comparison of neutron porosity for the Brown Niagaran reef (leeward, reef core and windward). E) CDF comparison of neutron porosity for the entire SEM.

#### 4.3.2.12 Permeability Model (Based on Seismic Inversion)

For the oil-bearing zones, which include the A1 Carbonate Crest, A1 Carb Flank, and Brown Niagaran reef, the permeability modeling used permeability logs and the GRFS method paired with collocated cokriging with the porosity model. Because permeability is generally related to porosity, this method helps ensure that the porosity and permeability models are spatially related. The permeability model was simplified for the non-oil-bearing zones by using average values from core measurements. These zones include the Gray Niagaran, A1 Salt, A2 Evaporite, and the A2 Carbonate. For modeling purposes, permeability for these zones are homogeneous. Table 4-9 summarizes the algorithm and constants used for each of the model zones.

In this updated model, the Brown Niagaran's permeability has been indirectly conditioned by seismic inversion via the collocated co-kriging with the porosity model and preserves trends observed in the seismic porosity inversion, Figure 4-38. As a result of this update, the Brown Niagaran reef's average permeability changed from 0.649 mD to 1.618 mD and its standard deviation changed from 10.813 mD to 12.025 mD. The computed permeability average is an arithmetic average, not harmonic average.

#### 4.3.2.13 Initial Water Saturation Distribution and Volumetrics (Based on Seismic Inversion)

The workflow for the water saturation model is described in Section 4.3.2.8 and includes the following adaptation for the Brown Niagaran reef. Water saturation for the Brown Niagaran was split based on low (<3 percent) and high (>3 percent) porosity (or pseudo rock-type).

- For porosity > 0.03,  $Sw = 0.15$
- For porosity < 0.03,  $Sw = 0.2495 * (\text{SQRT}[Permeability/\text{Porosity}])^{-0.213}$ .

This made it possible to infer that the Brown Niagaran reef's higher porosity rock had a residual water saturation of 0.15, while the lower porosity rock had an average residual water saturation of around 0.31, above the OWC.

Figure 4-38 shows a cross-section through the water saturation model. Water saturated zones show up as blue ( $Sw=1$ ). The OWC is present in the lower portion of the Brown Niagaran. The saddle region of the A1 Carb Flank was assigned a value of 0.7 as revealed in the histogram, Figure 4-38C. The water saturation histogram for the Brown Niagaran reef reveals two spikes: One is at 1 (100 percent) full water saturation below the OWC, the other at ~15 percent corresponding to higher porosity trends within the reef.

Figure 4-39 reveals where HCPV is likely to occur based on the OWC, model porosity, and water saturation. Note that cell color is also related to individual cell volume. The dominant lithology for oil-bearing units were clean carbonate rocks limestone and dolomite, so the N/G value was set to 1 as a simplification to the model. The resulting HCPV of oil for the reef was computed at ~9 million barrels. Table 4-13 repeats the information of Table 4-12, but for the new model. It summarizes the volume and hydrocarbon (oil) estimates for all SEM zones and reflects volume of oil at reservoir (in situ) conditions. Essentially, both models have near identical HCPVs, but distributed differently inside the Brown Niagaran.

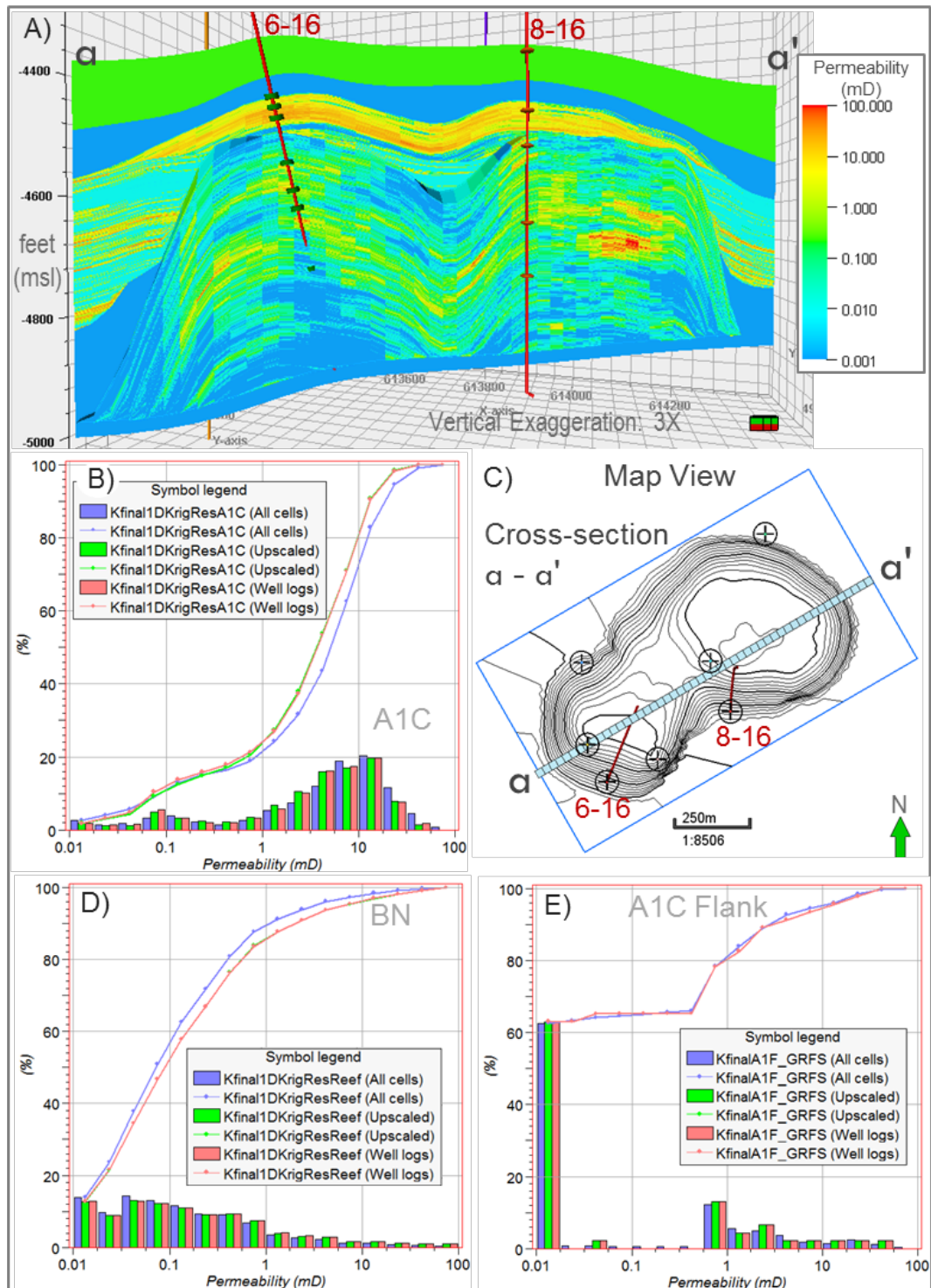


Figure 4-38. Permeability model with Brown Niagaran reef conditioned by seismic inversion. A) Cross-section through the permeability model. B) CDF comparison of permeability for the A1 Carbonate Crest. C) Map of the reef showing the orientation of cross-section a-a'. D) CDF comparison of permeability for the Brown Niagaran reef (leeward, reef core and windward). E) CDF comparison of permeability for the A1 Carb Flank.

**Table 4-13. Volumetrics and HCPV for each reef facies.**

Case	Bulk Volume [ft <sup>3</sup> ]	Net Volume [ft <sup>3</sup> ]	Pore Volume [ft <sup>3</sup> ]	HCPV Oil [ft <sup>3</sup> ] <sup>**</sup>	HCPV Oil [bbl] <sup>**</sup>
Totals	4,376,396,221	4,376,396,221	158,713,777	50,273,260	8,954,049
A2 Carbonate	1,013,195,065	1,013,195,065	51,554,432	-	-
A2 Evaporite	752,151,400	752,151,400	20,316,288	-	-
A1 Carbonate	224,747,445	224,747,445	24,378,815	14,532,853	2,588,412
A1 Carb Flank	734,876,664	734,876,664	12,731,839	1,517,232	270,231
A1 Salt	116,188,990	116,188,990	1,073,433	-	-
Brown Niagaran*	854,387	854,387	52,103	-	-
Reef Core	677,223,927	677,223,927	25,767,092	20,836,283	3,711,100
Windward	171,473,779	171,473,779	5,991,079	4,645,114	827,330
Leeward	285,837,699	285,837,699	8,010,516	6,090,491	1,084,763
Gray Niagaran	-	-	-	-	-
A1 Carb Saddle	399,846,866	399,846,866	8,838,181	2,651,286	472,214

\* Brown Niagaran here is referring to the perimeter region that flanks the reef.

\*\* Volume of oil at reservoir (in situ) conditions. Formation Volume Factor (Bo) = 1.

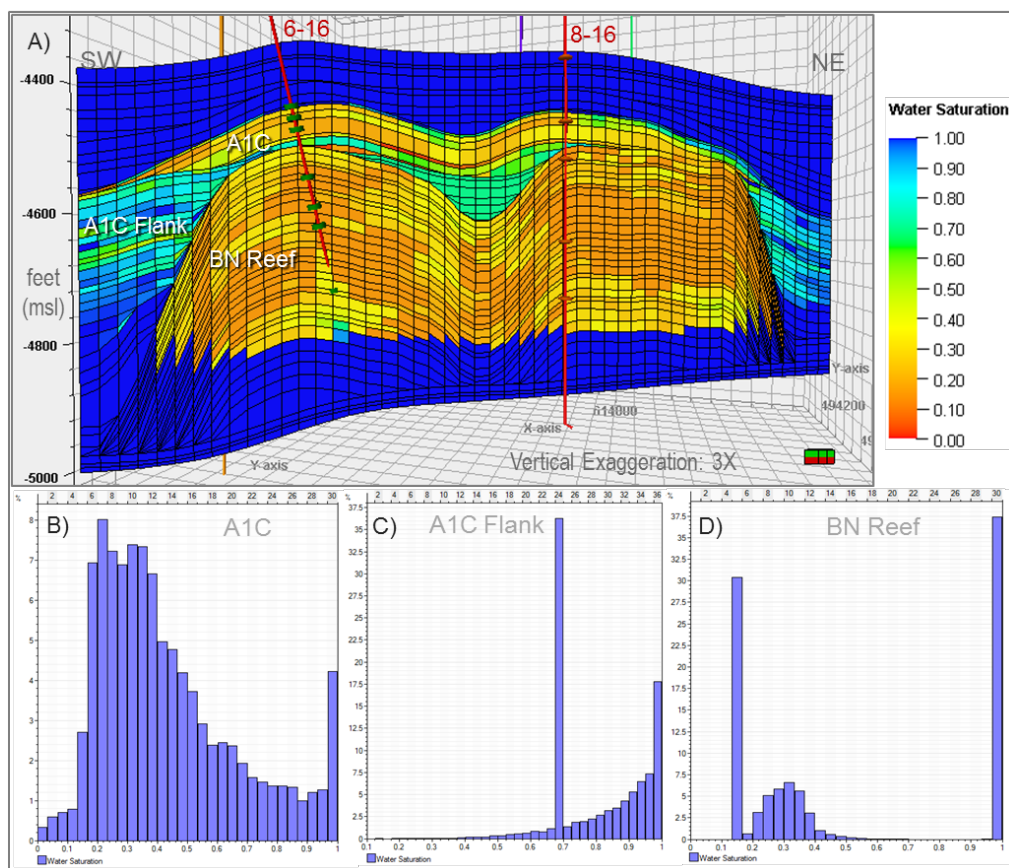


**Figure 4-39. Water saturation model with Brown Niagaran reef affected by seismic inversion.** A) Cross-section through the water saturation model. B) Water saturation histogram for the A1 Carbonate Crest. C) Water saturation histogram for the A1 Carb Flank that includes the saddle region. D) water saturation histogram for the Brown Niagaran reef consisting of the leeward, reef core, and windward lithofacies.

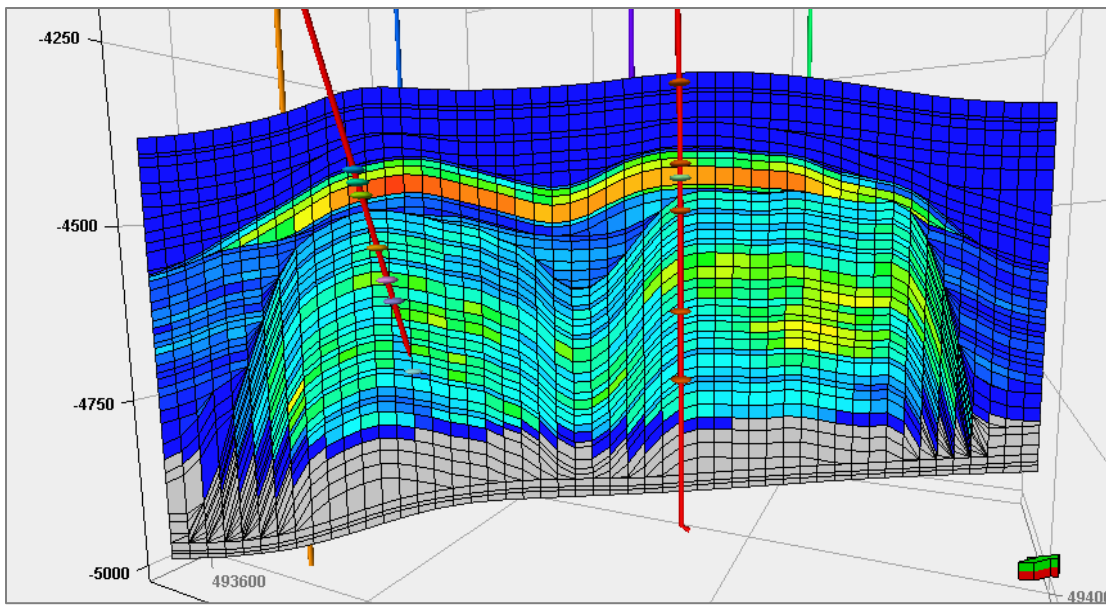


Figure 4-40. Cross-section through the new SEM of the alternative conceptualization, showing the computed HCPV on the upscaled, 79-layer grid.

Figure 4-40 summarizes the water saturation values for each SEM zone. As a result of this update, the Brown Niagaran reef's average water saturation changed from 0.49 to 0.52 and its standard deviation changed from 0.36 to 0.38.

#### 4.3.2.14 Property Modeling Summary (Based on Seismic Inversion)

The seismic inversion was used to update and condition property models and focused on the Brown Niagaran reef zone. Remaining model zones maintained their original properties. With this update, a higher porosity trend was noted within the Brown Niagaran and had a trend that dipped to the SW. This trend intercepted the 5-21 well where it corresponded to a high porosity streak seen in the porosity (NPHI) log response (Figure 4-36C).

Given the use of seismic inversion and resulting model changes, a summary is provided of property model averages in Table 4-14 and reflects the original and updated values for the Brown Niagaran reef zone. Cross-plots of these property models (updated vs original) are shown in Figure 4-41. Some observations are evident. As expected, the average porosity has not changed drastically (3.4 percent to 3 percent), and the presence of the higher permeability feature results in slightly higher average permeability (0.6md to 1.6md). Similarly, the average water saturation has not been altered significantly. However, the cross-plots comparing the seismic-derived porosity and permeability to the original properties provide additional information. They confirm that the spatial distribution of these properties has changed drastically — the points do not lie close to the  $y=x$  line. Both models (once history matched individually) may thus be taken to reasonably represent two *equi-probable* models representing the Chester 16, while acknowledging that the model that incorporates an additional layer of seismic information is likely to be the more *plausible* of the two.

**Table 4-14. Summary of computed average properties for the Brown Niagaran reef zone.**

Brown Niagaran	Average	Standard Deviation
	<b>Average SEM Porosity (decimal)</b>	<b>Standard Deviation (decimal)</b>
Original Model	0.034	0.032
Updated w/ Seismic Inversion	0.030	0.028
	<b>Average SEM Permeability (mD)*</b>	<b>Standard Deviation (mD)</b>
Original Model	0.649	10.813
Updated w/ Seismic Inversion	1.618	12.025
	<b>Average SEM Water Saturation (decimal)</b>	<b>Standard Deviation (decimal)</b>
Original Model	0.49	0.36
Updated w/ Seismic Inversion	0.52	0.38

\* Computed permeability averages are arithmetic averages, not harmonic averages.

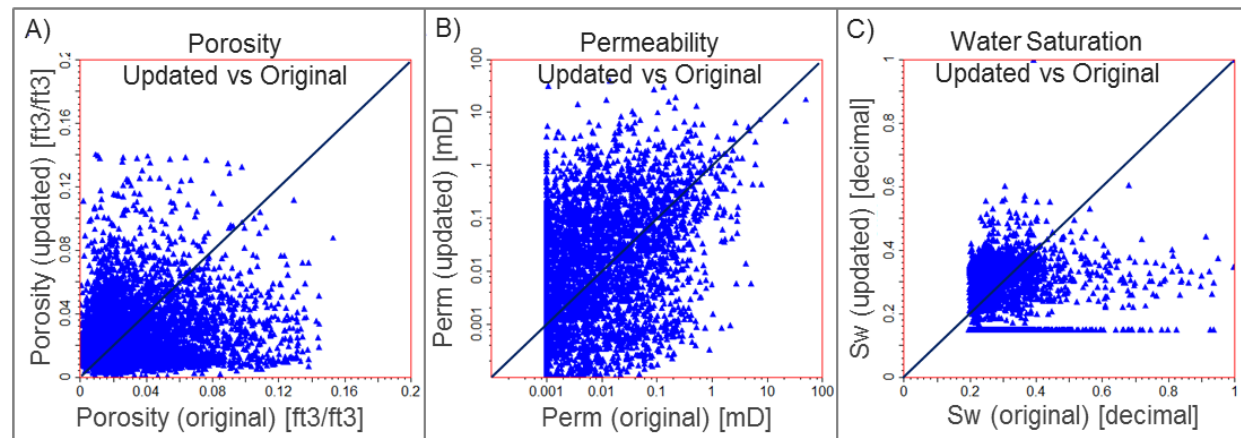


Figure 4-41. Cross-plots of Brown Niagaran model properties showing updated (with seismic inversion) versus original. A) Porosity models. B) Permeability models. C) Water saturation models.

#### 4.4 Dynamic Model

This section will discuss the essential details of the geocellular numerical model that was constructed to capture the complex fluid flow behaviors occurring in the Chester 16 hydrocarbon reservoir during CO<sub>2</sub> injection and hydrocarbon production activities. Numerical investigation of the operational scenarios of interest requires constructing a robust geological framework or static earth model (SEM) as the basis for a dynamic reservoir model for simulating fluid flow. The dynamic model is then initialized with a water saturation distribution and a pressure gradient. The initial set of geologic parameters assigned to this model are then adjusted via history matching to adequately replicate Chester 16's pressure and injection/production history. This includes data from both the primary and waterflooding phase, as well as the responses at the injection and monitoring wells recorded from the CO<sub>2</sub>-injection done to date. All simulations were done assuming black-oil and pseudo-miscibility of CO<sub>2</sub>.

## 4.4.1 Modeling Approach

### 4.4.1.1 Basic Numerical Features

All simulations were done in CMG's IMEX module, which assumes black-oil and pseudo-miscibility of CO<sub>2</sub>. Performing simulations with this module is a computationally efficient alternative to full blown compositional simulation (CMG-GEM), where the mass transport associated with each individual component of the reservoir fluid is calculated on the gridded domain. While such calculations are desirable considering the complex phase behavior associated with gas injection, such simulations require a laboratory-determined compositional breakdown of the Chester 16 reservoir fluid (unavailable), and an equation of state (EOS) calibrated to fluid interaction experiments and its measured black-oil properties. The black-oil option simplifies the numerical model by capturing the volumetric expansion of only oil, gas and water in each grid block and calculates the mobility of these fluid at a given pressure. Per the objectives of this project and the uncertainties inherent in the modeling, we are satisfied learning about the general movement or extent of the CO<sub>2</sub> plume, the average pressure response, associated oil production rates and gross CO<sub>2</sub>-storage capacity of Chester 16 with injection-production configuration. The data availability and computational-time constraints forced a trade-off where we chose general accuracy (pseudo-miscible mixing of CO<sub>2</sub> and oil via IMEX) over precision (fully compositional simulation via GEM) in this modeling effort.

Studies have shown that when the primary goal is to estimate cumulative fluid production, simplified-component models perform favorably to fully compositional reservoir simulation, (Islam and Sephernoori, 2013). Killough and Kossack (1987) for instance, (fifth Society of Petroleum Engineers' comparative solution project) performed a comprehensive comparative study (seven different cases spanning miscible, immiscible, and WAG-type scenarios) that determined that four-component miscible flood simulation estimated oil recoveries similar to an equivalent fully compositional reservoir simulation. The veracity of such simplified-component has also been tested in other CO<sub>2</sub> injection applications. Hassanzadeh et al. (2007) evaluated CO<sub>2</sub> injection into a saline aquifer, employing a black-oil simulation approach that reduced compositional information from a tuned EOS into an equivalent black-oil PVT data. This study concluded that utilizing such simplified models for CO<sub>2</sub> storage estimation purposes was beneficial in reducing simulation time without any significant loss of accuracy (as compared to a fully compositional model).

The pseudo-miscible CO<sub>2</sub> option in CMG-IMEX was invoked, in which CO<sub>2</sub> was introduced as a fourth component (a solvent) to the three-phase Black-Oil system (oil, gas and water). The miscibility between CO<sub>2</sub> and oil was modeled via an "omega" parameter where a zero value corresponded to complete immiscibility and unity represented complete mixing. The omega parameter was fixed at 0.7. This is different from a k-value specification, where the exact split of the CO<sub>2</sub> into the gas and oil phase at various pressures is specified. The density of the solvent at standard conditions was supplied with its formation volume factor and viscosity at various pressures (like a black-oil property). Note that while the miscibility of CO<sub>2</sub> with water can also be specified via an additional omega parameter, this dissolution effect has been ignored in the Chester 16.

### 4.4.1.2 Model Grid/Domain, Boundary and Initial Conditions

The Chester 16 reservoir model employed corner point gridding, with a total of 50 x 28 x 79 grid blocks (I x J x K) in a "shoe-box" type model (Figure 4-42). Each grid block is 25 m x 25 m (68.6 ft by 68.6 ft) with variable thickness. The thickness of each layer was determined separately during the upscaling phase. The model domain covers formations vertically from the A2 Carbonate to the top of the Gray Niagaran at the base (4,325 ft to 4,915 ft). Figure 4-42 shows the Chester 16 model and the location of the wells.

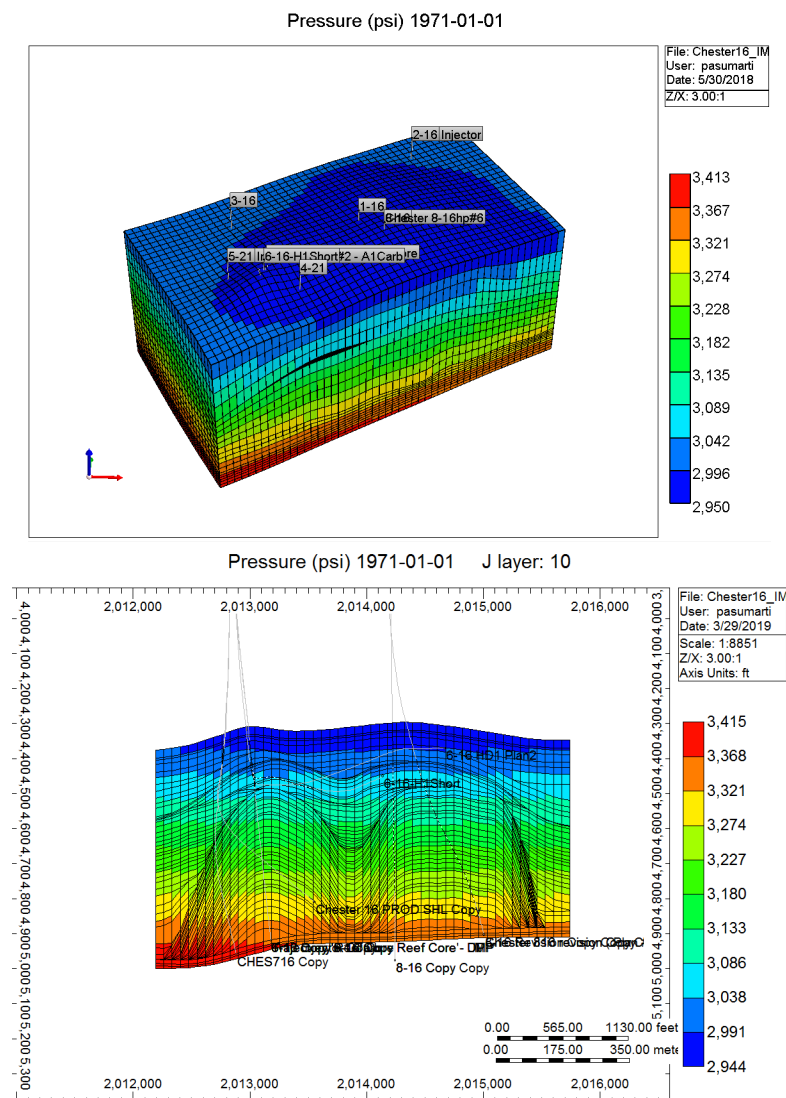


Figure 4-42. An aerial view of the reservoir model showing the gridding and location of all wells of the Chester 16 (top panel) and a cross-section through the model showing the initial pressure gradient (bottom panel).

The initial pressure in the reservoir was initialized with a gradient of 0.68 psi/ft (Figure 4-42). This brought the average initial pressure of the reservoir to the known discovery pressure of 3125 psi. Since there is no aquifer drive in the Chester 16, the number of water saturated layers below the OWC has been limited, and only 12 ft of the Gray Niagaran has been modeled. The Brown Niagaran and A1 Carbonate oil-bearing regions are both flanked by fully water saturated grid blocks. Because these grid blocks are very low permeability, however, the main point of hydraulic communication between the A1 Carbonate and the Brown Niagaran is at the structural highs of the two lobes of the Brown Niagaran. However, a tight “saddle” region and a permeability baffle at the base of the A1 throttles the pressure-equilibrium occurring between the two formations. The seal to the Chester 16 reservoir is the A2 Carbonate, which is also modeled as a very low permeability and fully water saturated layer. The Chester 16 model is bounded by no-flow boundaries on all four sides.

#### 4.4.1.3 Well Locations and Perforation Intervals

While well-location and well trajectory information is readily available (e.g., Figure 4-1), historical perforation data is uncertain. Though public records of well workovers and written correspondence regarding planned well activities that typically carry information on perforated intervals are available, this data is not available for every year of the well's life, nor has every well-workover activity been preserved. During the history matching process in numerical simulation, overlapping production layers or common production intervals tend to dictate the location of permeability modification to these intervals where flow is greatest. The production intervals for each well are described below. For each well in the numerical model, only the layers corresponding to these intervals have been opened for flow. The location of the original perforations in all wells is shown below in Figure 4-43.

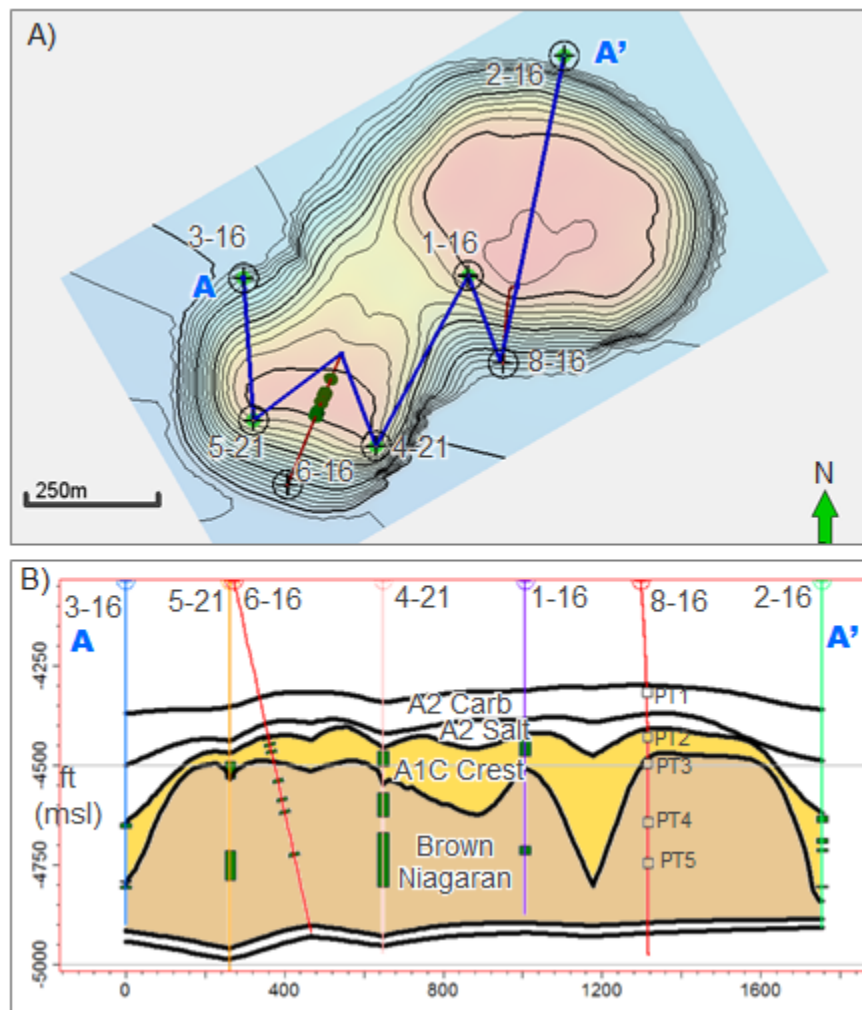


Figure 4-43. The location of the perforated intervals for all wells (bottom) with respect to the formation is shown via a customized cross-section through all wells (top).

The 1-16 well was originally perforated in the entire A1 carbonate (5,764' to 5,812' MD) and low in the Brown Niagaran (5,975' to 5,995' MD and 6,040' to 6,060' MD). It is thought that a couple of years of production later, around 1972/1973, the entire well was perforated to produce from throughout the Brown Niagaran (5764' to 6112' MD).

The 5-21 well produced exclusively from the bottom of the Brown Niagaran (6,039' to 6,114' MD). Very late in the life of the well in 1983, however, the A1 carbonate was also perforated in a bid to bolster oil production rates (5,815' to 5,857' MD). This was ultimately unsuccessful as the average reservoir pressure had fallen to around 500 psi by this time.

The 4-21 well originally produced from both the A1 carbonate (5,796' to 5,833' MD) and two intervals in the Brown Niagaran (5,900 to 5,959' MD and 6,001' to 6,137' MD). In 1977 however, the A1 carbonate perforations and those at the top of the Brown Niagaran were squeezed off, leaving the well to produce only from the bottom region of the Brown Niagaran. Very late in its life in 1983, the A1 carbonate and upper Brown Niagaran intervals were re-opened.

The 3-16 well is a flank well and produces from two intervals (5,972' to 5,982' MD and 6,116' to 6,120' MD) on the outer regions of the A1 Carbonate – the region flanking the A1 Carbonate “crest” is thought to be highly stratified with thin fractured oil-bearing intervals – and one thin zone at the top of outer reaches of the Brown Niagaran (6,128' to 6,136' MD).

The 2-16 well is also a flank well that produces from the outer regions of the A1 Carbonate. This region is slightly more prolific relative to the 3-16 well, and four intervals have been perforated (5,970' to 5,985' MD, 6,025' to 6,038' MD and 6,053' to 6,059' MD and 6,145' to 6,150' MD).

The general strategy in exploiting the Chester 16 appears to have been to produce from deep inside the Brown Niagaran, rather than the A1 carbonate. This may also have been because of the presence of the gas cap that invariably formed due to the reservoir pressure being allowed to fall well below bubble point pressure.

The 6-16 injection well is perforated at three locations in the A1 Carbonate Formation (5,892', 5,914' and 5,937' MD) and four locations in the Brown Niagaran Formation (6,033', 6,094', 6,135' and 6,274' ft MD). Each perforated zone is 10 ft. thick. The Chester #8-16 monitoring well is not perforated, but has gauges set at four depths (5,865' MD in A1 Carbonate, and three in the Brown Niagaran Formation at 5,932', 6,079', and 6,182' MD). Figure 4-17 displays the locations of the perforations and gauges in these two wells.

#### 4.4.1.3.1 Injection/Production Constraints

Annual oil production data for each well is available, although detailed bottomhole pressure associated with this annual production is not. Sales gas production data is available, from which produced gas was deduced by means of a scalar multiplier (to approximate the quantity of gas bled off or used for on-site facilities). The bottomhole pressure that is available is mainly from the 1-16 and 4-21 wells (through the middle of the reef) and has been used as a proxy for the average pressure decline in the entire Chester 16. Chester 16 began producing at a reservoir pressure of around 3,125 psi and was depleted down to around 500 psi after primary production. Waterflooding in the Chester 16 was not known to have been very effective for reservoir pressure management and the best available estimate for abandonment pressure at the end of the secondary production period does not vary too widely from the pressure at the end of the primary production period. While the individual water injection rates for the 5-21 and 2-16 wells are available, water production data is limited and only estimates of incremental water production (on an annual basis) are available. From the period of CO<sub>2</sub> injection began, however, pressure and volumetric data is readily available.

Simulations of the primary and secondary phases have been conducted assuming an oil rate constraint for each producing well (and a water injection rate for the injector wells), with the goal to match field-wide gas production and overall pressure decline. If the geologic description has been updated correctly during this phase, the simulator's prediction of the pressure increases at various depths in the reservoir with CO<sub>2</sub>

injection should align closely with that recorded at the monitoring gauges of the 8-16 well. The CO<sub>2</sub> injection was simulated with an injection rate constraint. An explicit fracture pressure limitation was not imposed via a bottomhole pressure constraint, due to low formation pressures and re-pressurization only to 1,300 psi.

#### 4.4.2 Model Inputs

This section described the key inputs involved in constructing the model. These are primarily (1) the assumptions used in building the relative permeability curves for oil-water and liquid-gas mobility and (2) the black-oil PVT properties used to describe the volumes and viscosity of oil and gas as a function of pressure.

##### 4.4.2.1.1 Rock Properties

Direct measurements of relative permeability measurements were unavailable. As a result, gas-liquid relative permeability curves were assumed via smooth exponent-type correlations, and oil-water relative permeability curves were scaled directly from those used to obtain a history match for Dover-33. The Dover-33 model's history match was used as a starting point since both reservoirs are considered to have similar levels of diagenesis and dolomitization. In numerical simulation, it is effective permeability (a product of absolute permeability of the cell and the relative permeability to a fluid phase) that ultimately controls fluid flow. As a result, changes to the relative permeability curves were limited as far as possible in this study, for simplicity. The endpoint of the relative permeability to gas was adjusted only slightly between very narrow bandwidths (0.1 to 0.2) where necessary, to adjust the mobility of gas to increase or decrease gas production output in the simulation. The maximum relative permeability to water was fixed at 0.75. 3-phase gas-oil-water relative permeability was interpolated using both these curves through internal correlations in CMG (Stone II model as modified by Aziz and Settari). Figure 4-44 and Figure 4-45 present a sample (base case) of the relative permeability curves used in the model.

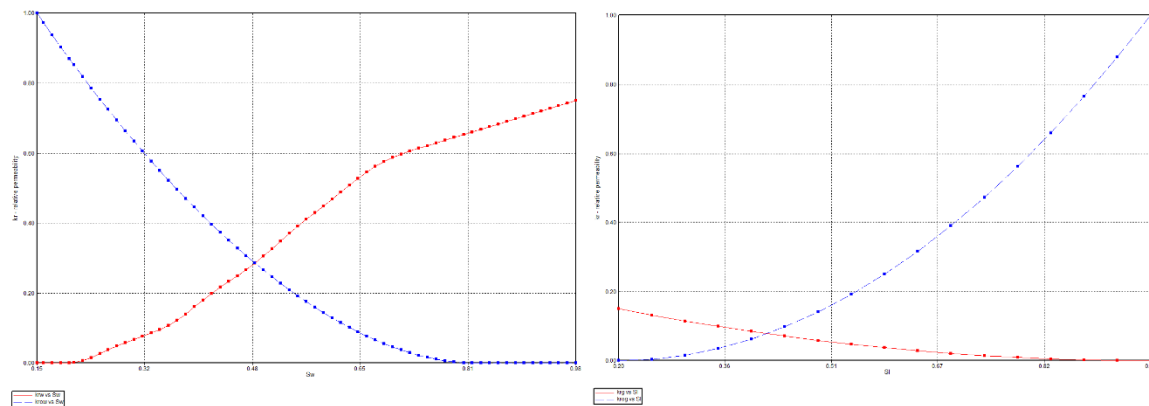


Figure 4-44. Simple relative permeability curves (oil-water on the left, and liquid-gas on the right) were used in the model.

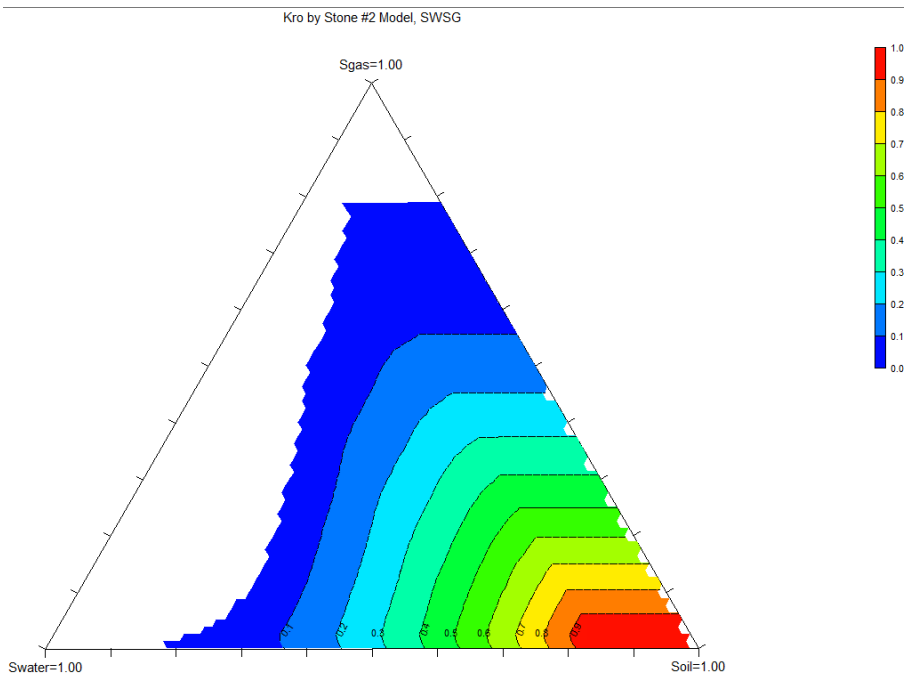


Figure 4-45. Ternary diagram displaying the oil relative permeability for 3-phase flow, as used in the model. The end points represent 100% saturations of water, oil and gas. Stone's second model as modified by Aziz and Settari was used to generate this diagram.

#### 4.4.2.1.2 Fluid Properties

Laboratory measured fluid compositional data was unavailable. As a result, industry-standard correlations were used to generate black-oil properties for the simulation. A similar approach was also successfully employed in a material balance analysis that was performed earlier in the life of the Chester 16 to estimate its OOIP. The black-oil fluid property correlations (Standing correlations) are recommended by McCain (1991) and the Society of Petroleum Engineers (SPE) monograph on Phase Behavior by Whitson and Brule (2000). These correlations require bubble point, the initial producing gas-oil ratio, reservoir temperature, and oil/gas density as inputs. The inflection point in observed field-wide pressure decline data from initial production to the end of the primary production period suggested a bubble point pressure of the fluid to be around 1,800 psi (Figure 4-46). The average initial producing GOR of the field was known to be around 650 scf/stb. This information, together with stock tank oil density (51.2 lb/ft<sup>3</sup>) and gas-gravity (0.83) and the temperature of the field (~100°F), were similar used as inputs to generate black-oil properties (formation volume factors of oil and gas, solution GOR, oil and gas viscosity) as a function of pressure in the IMEX model (Figure 4-47 to Figure 4-50). CMG-IMEX's pseudo-miscible CO<sub>2</sub> option – a less computationally intensive alternative to full blown compositional simulation – is enough where the objectives are limited mainly to monitoring pressure changes due to solvent injection and tracking the movement and extent of the CO<sub>2</sub> plume. CO<sub>2</sub> is assumed to be insoluble with formation water but assigned an Omega (mixing) parameter of 0.7 with oil, as was the case in the history match obtained for Dover-33. This omega parameter has been set to 0.7 at the miscibility pressure of 1,300 psi and above, and at 0 at sub-miscible pressures.

## Chester 16 Field BHP vs. Cumulative Oil

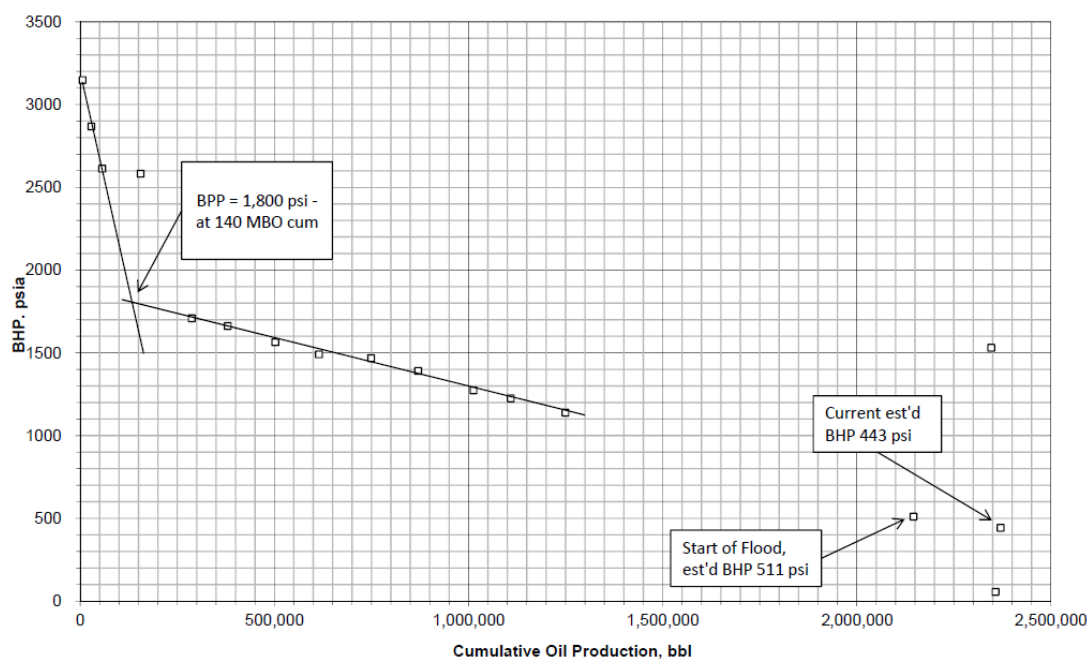


Figure 4-46. Inflection point in pressure decline in the Chester 16 was around 1800 psi.

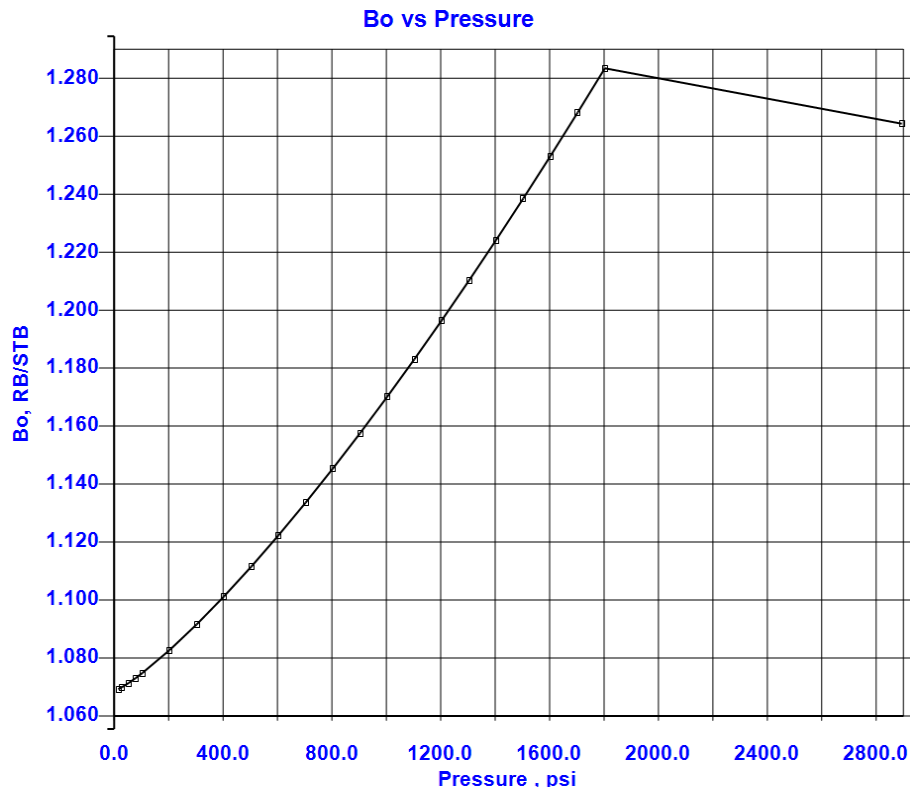


Figure 4-47. Oil Formation Volume Factor of the Chester 16 oil.

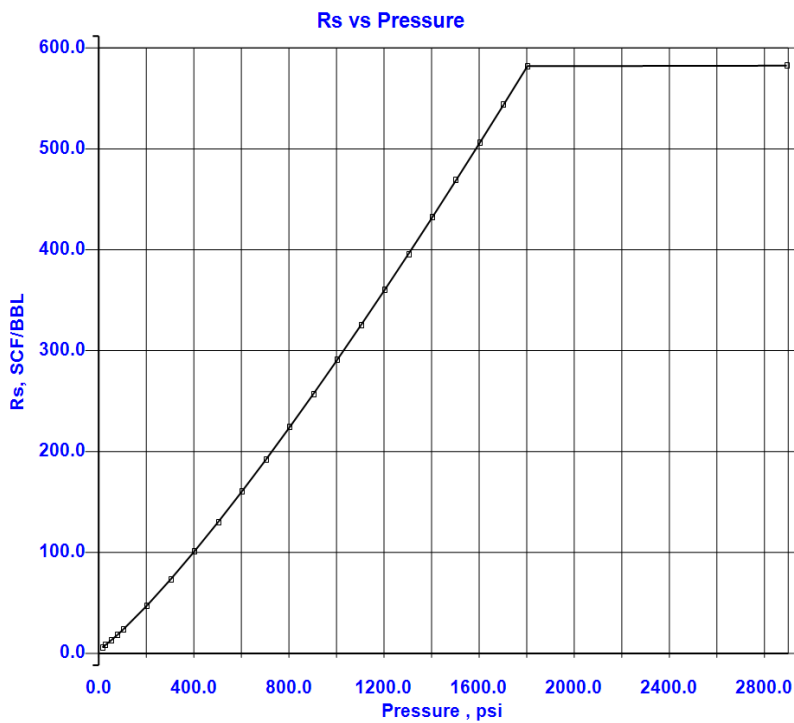


Figure 4-48. Solution GOR of the Chester 16 oil.

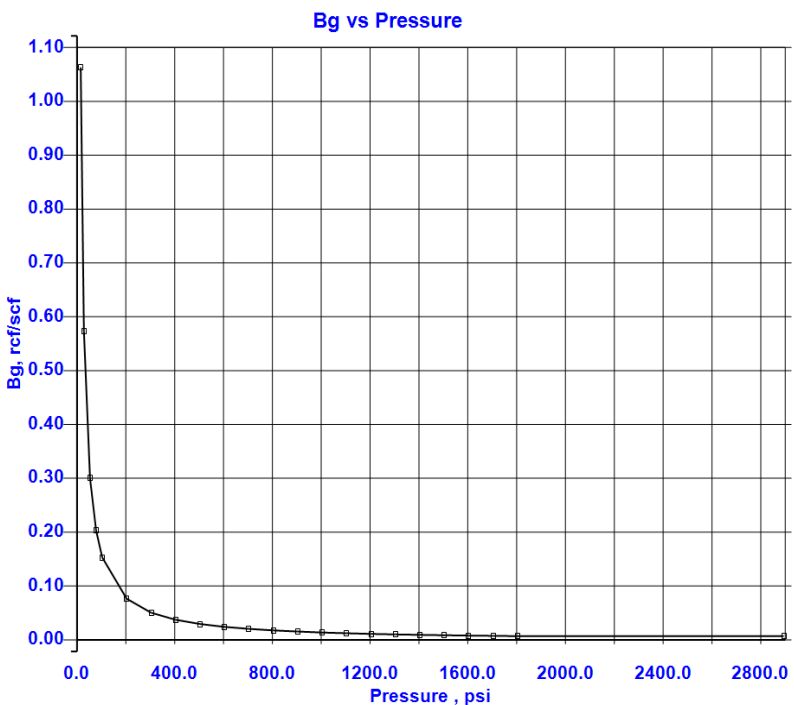


Figure 4-49. Gas formation volume factor of the Chester 16 oil.

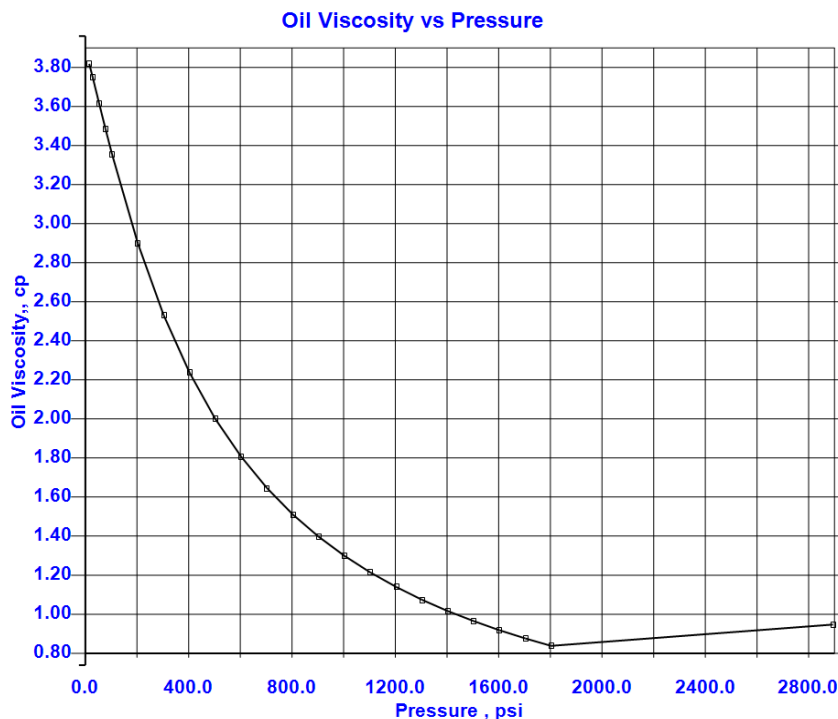


Figure 4-50. Oil viscosity of the Chester 16 oil.

#### 4.4.3 Primary Production History Matching Process

History matching of the Chester 16 reservoir model was a highly iterative process assessing model sensitivity to individual parameters via numerous forward simulations testing various parameter combinations in trial-and-error. The details of individual trial-and-error, iterative simulations, are beyond the scope of this report. A description of the changes incorporated in the last iteration of the model (leading to final history match) is meaningful and will thus be included.

The objectives (performance indicators) of the history match were to:

- (1) honor all individual well oil production rates via the oil constraints,
- (2) honor individual water injection and CO<sub>2</sub> injection rates,
- (3) reproduce the pressure decline history recorded from the primary production period and at abandonment after waterflooding,
- (4) reproduce the pressure deflections recorded at the various depths (gauges) of the 8-16 monitoring well during CO<sub>2</sub> injection through the 6-16 injection well.

Meeting objectives (1) to (3) involved revising the permeability field through the various layers. While (4) and (5) should generally be performance measures that serve as a demonstration of how accurately the permeability field in the Chester 16 has been represented, significant uncertainty exists as to the allocation of the CO<sub>2</sub> injection rates between A1 Carbonate and the Brown Niagaran due to a malfunctioning seal inside the 6-16 well. This prevented isolated injection into only one specific formation (injection periods 4 and 5), a finding consistent with DTS data. Furthermore, no production logging tools were employed to record the flow rates going through the individual perforations (or zones) over the many injection periods. As a result, meeting objective (4) required an estimation of the CO<sub>2</sub> injection volumetric split between the A1 and the Brown Niagaran that could reproduce the appropriate pressure deflections

at various depths. Note that matching 6-16 bottomhole pressures while only estimating rates split between the two formations and perforations is impractical. In addition, since regional permeability multipliers are employed in obtaining the history match (and characterizing the Chester 16 in a more general sense), matching the 8-16 pressures was given more credence to be consistent. This implies that a match to 6-16 injection bottomhole pressures is likely attributable to a near-well bore skin effect. Table 4-15 summarizes the various types of data the history matching process integrated into the reservoir model.

**Table 4-15. The various sources of data the model has integrated.**

Type and Source of Data	Nature of Data Integration
Injection / Production Volumes	Quantitative
Pressure history	Quantitative
Perforation history	Quantitative
Porosity, Permeability from core and well logs	Quantitative
Porosity, Permeability from Seismic Data	Quantitative
Pressure Transient Data from 8-16 well	Quantitative
8-16 Monitoring well pressure data	Qualitative
DTS information	Qualitative

#### 4.4.3.1 Preliminary Run Results

To understand the extent of modification required to calibrate the model, the Chester 16 model was run “as-is” with porosity and permeability as distributed from the SEM for the primary production phase. While the expectation with such runs is that simulated total hydrocarbon production is close to the actual field quantity – and therefore suggestive of the direction of minor revisions to the permeability distribution around individual wells – this was unfortunately not the case for the Chester 16. Figure 4-51 shows that the oil constraint was fundamentally not met for entire field for the primary production with the “as-is” model. This was reflected in the gas production as well (Figure 4-52). It was noted that the flank wells (accounting for around 10 percent of the total production) were essentially non-productive in these simulations. Numerous forward simulations that tested the sensitivity of the model’s hydrocarbon production to the following parameters were unsuccessful in meeting the oil production constraint:

1. the permeability of individual regions (applying regional permeability multipliers of up to 100x to the A1 carbonate, saddle region, and the hypothesized depositional lithofacies regions of leeward, windward and reef core within the Brown Niagaran);
2. lower end points of the relative permeability curves to gas and water (since gas and water production was seen to occur at the expense of oil production);
3. the vertical permeability to horizontal permeability ratio (increased vertical permeability leading to higher overall permeability);
4. spatial continuity of higher porosity regions in the Brown Niagaran (manually connecting grid blocks containing higher porosities specifically in layers wells were perforated through, to produce more spatially contiguous regions).

Figure 4-51 and Figure 4-52 also feature four such unsuccessful runs (labelled “...custom10”, to “...custom13”), where each run captures some permutation of the above listed parameters.

Considering there is virtually no uncertainty regarding well-level oil production, this posed a serious challenge to the calibration process. This suggests that the overall effective permeability of the reservoir is likely much higher than suggested by the SEM. The effective permeability of any given grid block in the

numerical model is a function of the fluid saturations, relative permeability to the fluids and the absolute permeability. However, considering the high degree of confidence in the initial water saturation distribution and the moderate assumptions behind the relative permeability curves – end point oil relative permeability has been set to the maximum of unity, gas relative permeability has been set to a low value of 0.2 (gas mobility generally competes with oil mobility), and water relative permeability end point has been set to a moderate 0.5 – an overly-conservative permeability field is likely culpable for the inability to match oil production constraints. While the permeability of the field overall is likely greater than in the SEM, the Brown Niagaran's permeability field appears to be aggressively underpredicted by the SEM workflow. This is because the three main oil producers, the 1-16, 4-21, and 5-21 wells that account for 90 percent of the oil production, collectively produce from the lower Brown Niagaran toward the latter period of primary production from the Chester 16. This was based on the available information on perforation history of the individual wells.

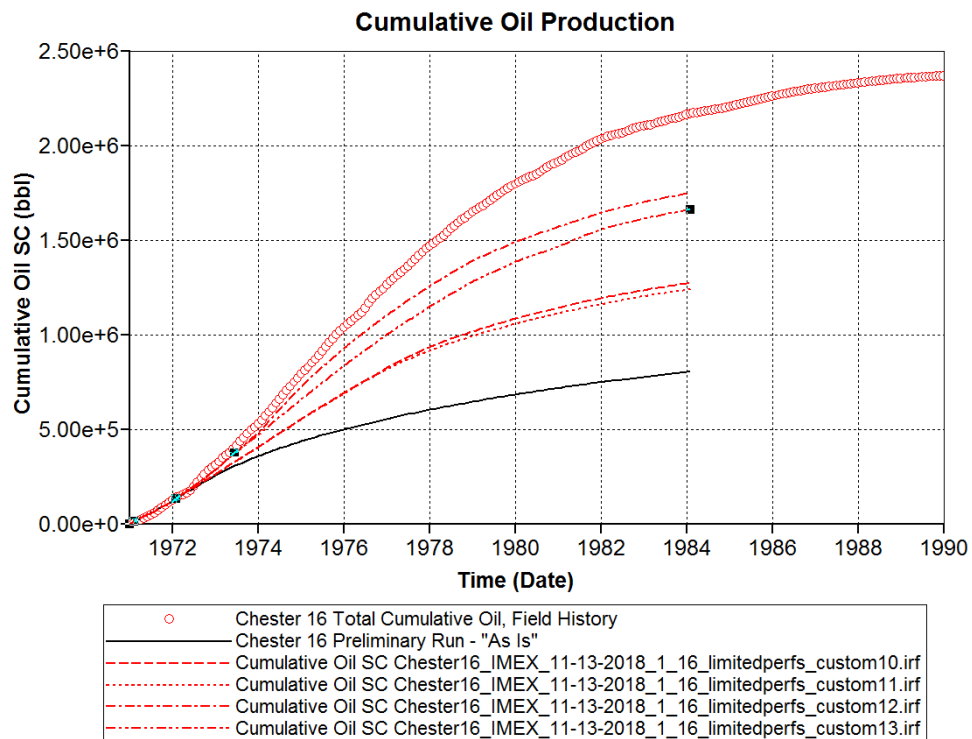


Figure 4-51. Oil production from the preliminary runs does not match.

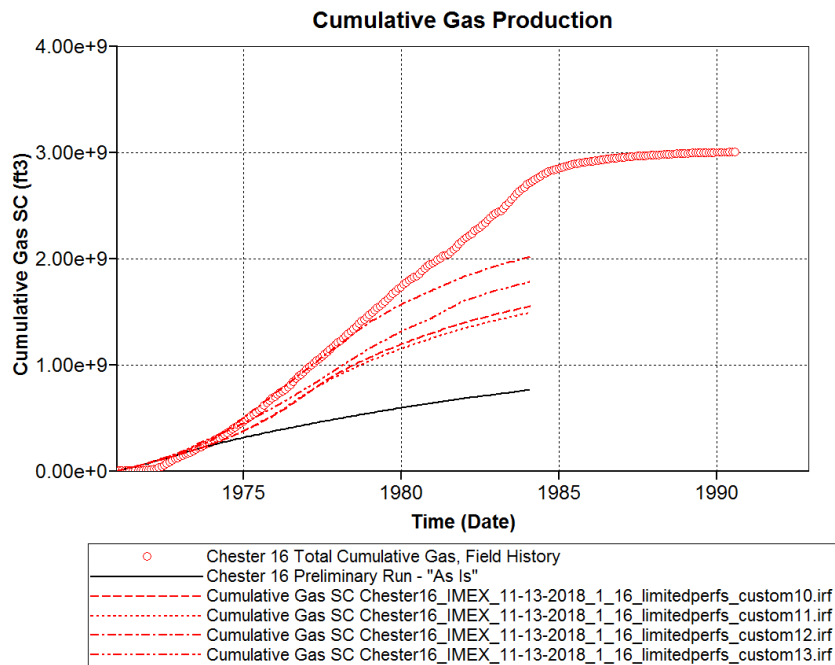


Figure 4-52. Gas production from the preliminary run does not match.

#### 4.4.3.2 Primary and Secondary Recovery Phases

The porosity distribution from the SEM workflow is considered to be reliable since it integrated core and log measurements alongside some assessment of uncertainty – the porosity property was populated in 3D using the GRFS option with a statistical quantification of distribution of data between upper and lower bounds. Note that for the Brown Niagaran, this process was designed to amalgamate all data without differentiating between the depositional lithofacies (leeward, windward and reef core). Since it was reasonable to assume that porosity and permeability were generally positively correlated, permeability was co-kriged with porosity, using the latter as the base variable. As a result, the initial permeability distribution in the SEM, although likely (and demonstrably) underpredicted, still reasonably approximates geo-bodies or contiguous spatial regions that reflect permeability groups in the reservoir – “sub-facies” for all practical purposes. The choices of the permeability values define the lower and upper bounds of such groups and the number of such groups are generally subjective. For the purposes of history matching the Chester 16 model, creating “sub-facies” that represent rock regions having permeability within an order of magnitude (e.g.: 0.1 md to 1 md, or 1 md to 10md.) was opted as it was sensible, minimized the number of permeability groups, and created sufficiently large contiguous groups. A permeability modification was then applied to each “sub-facies” as part of the history matching process.

Table 4-16 summarizes the modifications affected on the SEM, showing that this methodology leads to identifying a total of 17 regions of permeability modification/enhancement in the Chester 16 model. Three permeability groups were identified in the A1 carbonate from the SEM, generally representing permeability within two orders of magnitude. The Brown Niagaran on the other hand, is a generally more heterogeneous rock and thus had more permeability groups representing a much wider range (four orders of magnitude). There was also thought to be considerable vertical heterogeneity. Well testing data also pointed toward a thin but contrastingly low permeability region at the base of the A1 Carbonate (a baffle), in between the saddle region and the A1 carbonate. This layer was assigned a low permeability of 0.01 md. Finally, the well-test also suggested that the saddle region itself had a very low overall

permeability of 0.001 md. All other rock layers – the Gray Niagaran and all the outermost flank layers to the Brown Niagaran — retained the very low permeabilities assumed in the original SEM.

**Table 4-16. Shows the various permeability groups or “sub-facies,” and the permeability bounds used to identify these regions within the Chester 16 model. The permeability multipliers or the permeability to each group is included.**

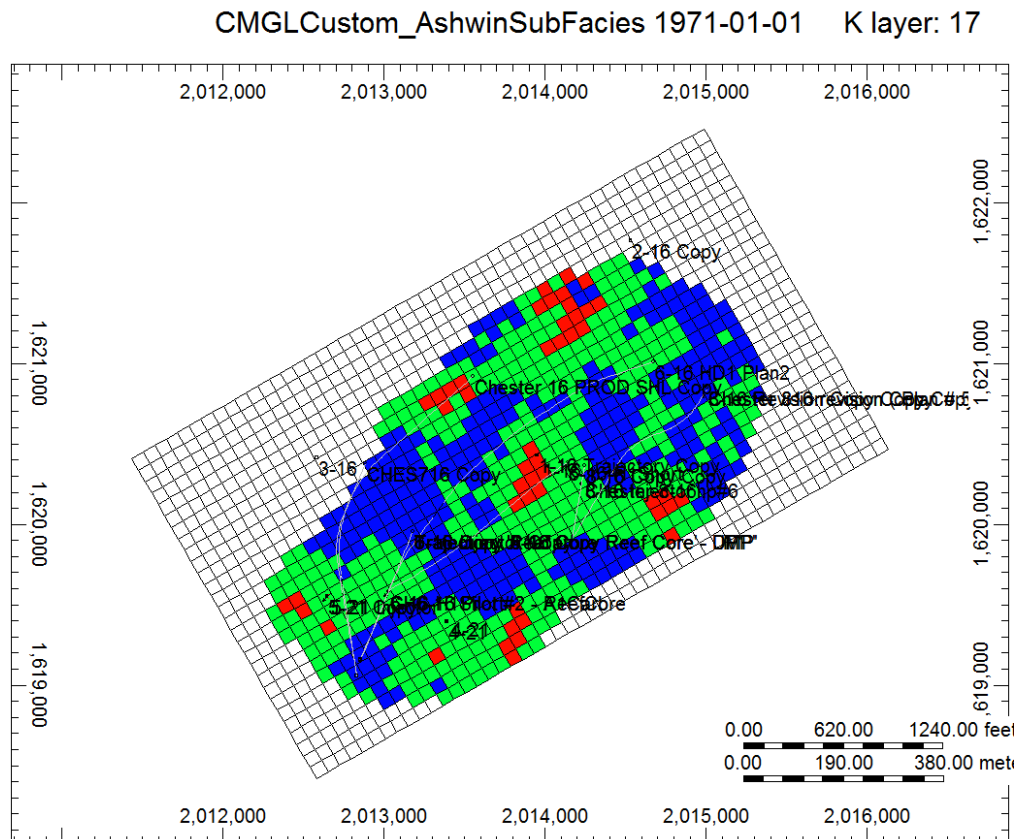
Location	Permeability Group	Lower Bound (md)	Upper Bound (md)	Multiplier (or assigned uniform value in md)
A1 Carbonate	1	As per SEM	1 md	(1)
A1 Carbonate	2	1 md	10 md	4x
A1 Carbonate	3	10	As per SEM	2x
A1 Carbonate Flank (perforated, low porosity)	4	N/A	N/A	(1 md)
A1 Carbonate Flank (perforated, high porosity)	5	N/A	N/A	(3 or 7 md)
Base of A1 Carbonate	6	N/A	N/A	(0.01 md)
Saddle Region	7	N/A	N/A	(0.001 md)
Upper Brown Niagaran (3-16 well)	8	N/A	N/A	40
Upper Brown Niagaran	9	As per SEM	0.01 md	(0.15 md)
Upper Brown Niagaran	10	0.01 md	0.1 md	75x
Upper Brown Niagaran	11	0.1 md	1 md	50x
Upper Brown Niagaran	12	1 md	As per SEM	3x
Middle Brown Niagaran	13	N/A	N/A	(40 md)
Lower Brown Niagaran	14	As per SEM	0.01 md	(0.05 md)
Lower Brown Niagaran	15	0.01 md	0.1 md	50x
Lower Brown Niagaran	16	0.1 md	1 md	30x
Lower Brown Niagaran	17	1 md	As per SEM	2x

A uniform permeability high perm streak was introduced to the middle of the Brown Niagaran after repeated attempts to meet oil production constraints with a model that retained the heterogeneity in this region were unsuccessful. While the porosity distribution in those layers was retained, the permeability heterogeneity in these layers was removed in favor of a uniform and layer-wide homogeneous permeability of 40mD. This model feature is likely to be a key driving force behind the quality of the history match.

Additionally, some gridblocks were manually assigned a permeability value. This reflects information from drill cuttings that suggests that the flank regions are highly vertically stratified with permeability stringers. Such “permeability zones” were selectively perforated in the flank wells of 2-16 and 3-16, as per records. Flank layers with these perforations were assigned a base permeability of 1 md in the model but retained the original SEM permeability in non-perforated layers. Further, within such perforated layers, grid blocks with porosities higher than 3.5 percent were assigned an even higher permeability, between 3 or 7 md. The 3-16 flank well was perforated in the corner of the “saddle” region between A1 and the Brown Niagaran, as well as at the top corner flank region of the Brown Niagaran. Selected grid blocks around

the 3-16 well were manually assigned a higher permeability in order to enable the well to meet its oil production constraints in the simulation.

Figure 4-53 color codes the distribution of the three sub-facies in the middle of the A1 Carbonate, with red being the highest permeability group and the blue being the lowest permeability region. Similarly, Figure 4-54 and Figure 4-55 show the distribution of the four sub-facies in the Upper and Lower Brown Niagaran, in a representative layer. Note that the Brown Niagaran, and especially the Lower Brown Niagaran, is predominantly the lowest permeability group. The patchy nature of the higher permeability groups may reflect the randomness of its diagenetic history. Figure 4-56 and Figure 4-57 show manual permeability modifications applied to the thin (1-3 ft) flank regions from which the 2-16 and 3-16 wells produce. Figure 4-56 shows that the permeability around the 3-16 well – representing a thin region at the very top of the Brown Niagaran in contact with the A1 Carbonate Flank – has been enhanced to 40 mD. Figure 4-57 shows another thin layer in the A1 Carbonate Flank, in which both the 2-16 and 3-16 are perforated, where permeability was manually assigned 1mD if the porosity is low, and between 3 or 7 mD if the porosity is high.



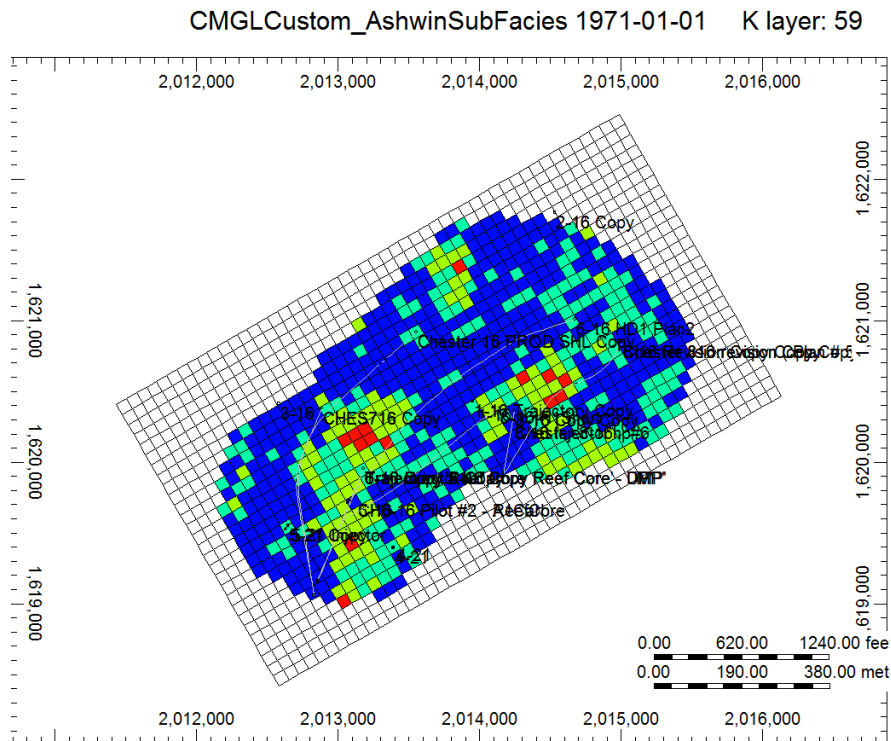


Figure 4-54. The distribution of the four sub-facies in the Upper Brown Niagaran, shown as blue (lowest permeability), light green, dark green and red (highest permeability).

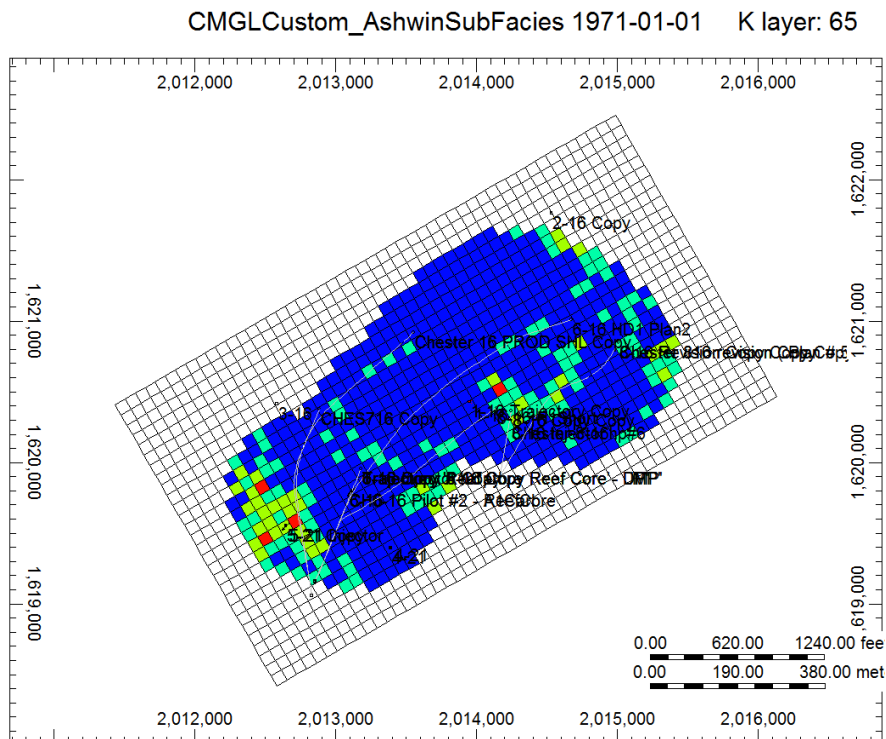


Figure 4-55. The four facies of the lower Brown Niagaran, shown in blue (lowest permeability), light green, dark green and red (highest permeability).

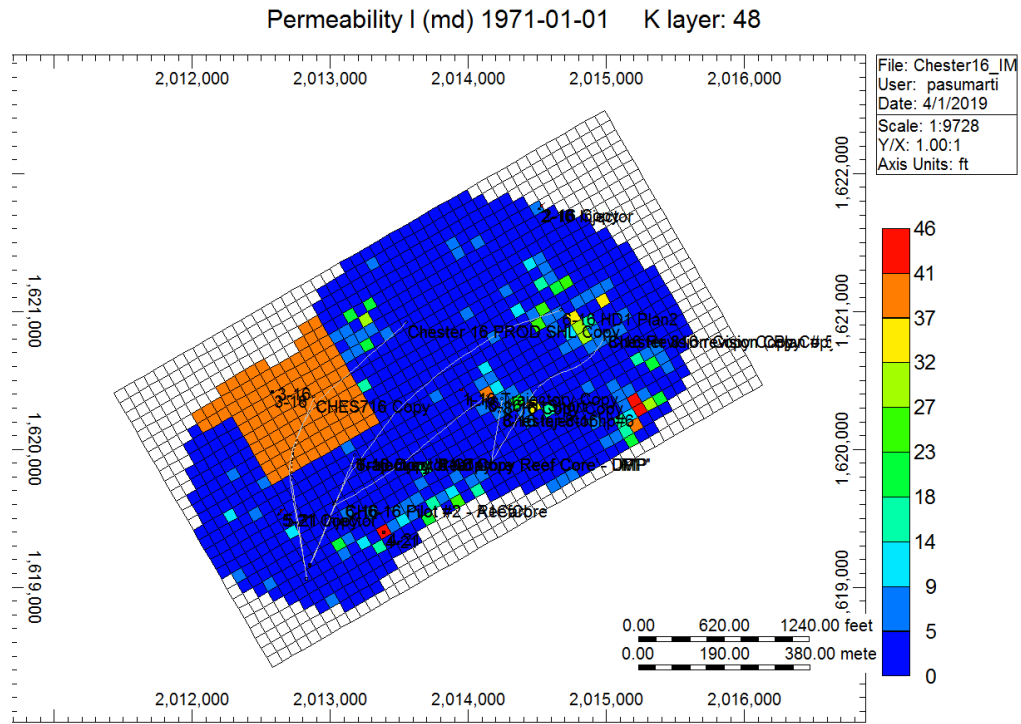


Figure 4-56. Manual assignment of a 40md permeability around the 3-16 well in the Upper Brown Niagaran.

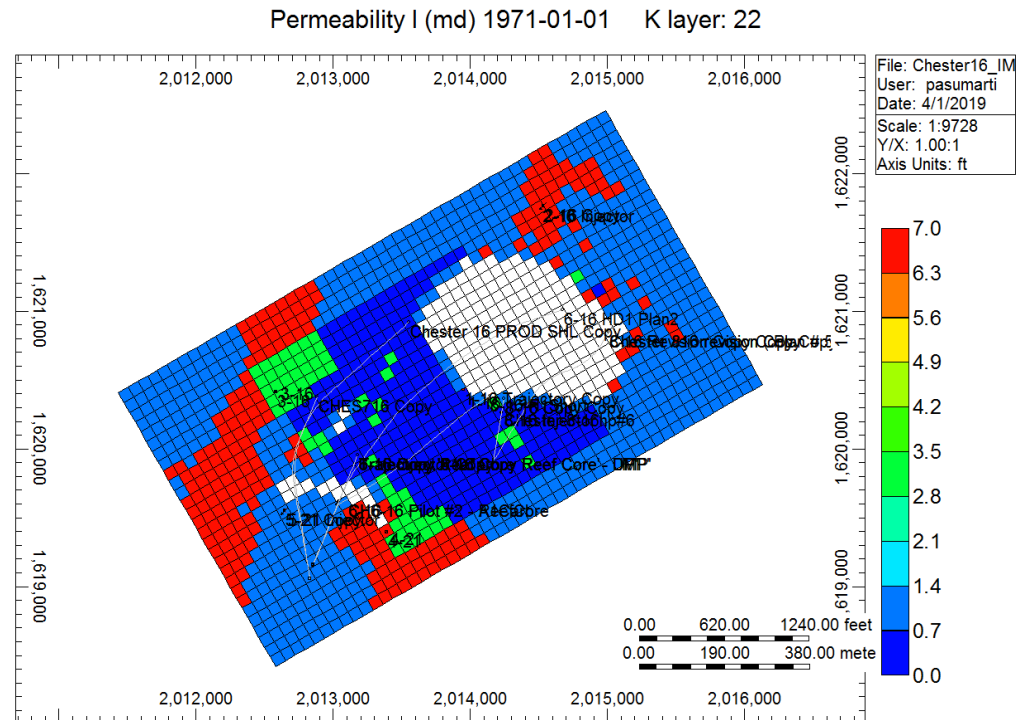


Figure 4-57. Some flank layers, such as this, have been manually assigned permeability values. The light blue, green and red regions are 1 md, 3 md and 7 md respectively. The higher permeabilities reflect regions of higher porosity. The inner most dark blue region is the Saddle region, with a very low permeability (0.001 md).

Figure 4-58 presents a representative cross-section through the Chester 16 showing how the permeability field after history matching in the model spans several orders of magnitude. More importantly, the figure highlights the 40 md high permeability zone in the middle of an otherwise low permeability Brown Niagaran. This permeability streak, composed of five layers and approximately 50 ft thick, is above the OWC. While several alternative permeability field modifications that avoided creating a homogeneous permeability zone were attempted, none of the forward simulations with this model produced a satisfactory history match. Attempts included (1) various combinations of permeability multipliers to the "sub-facies" in these layers (creating differing levels of heterogeneity and permeability contrast) and (2) introducing discontinuities to the permeability streak from left to right. This result reflects that all three of 1-16, 4-21 and 5-21 wells (that account for 90 percent of total cumulative oil production) have been perforated to produce exclusively from these depths. Specifically, records indicate that the 5-21 produces only from the Brown Niagaran for majority of its life, and all the upper perforations of the 1-16/4-21 wells were eventually plugged during the 1970s, leaving only the lower ones open. This may imply that previous owners were attempting to exploit this predominant geologic feature.

Figure 4-58 also presents other important facets of the final history matched Chester 16 model. It shows the 0.01 mD permeability baffle (light blue) separating the A1 Carbonate and Brown Niagaran. The A1 Carbonate is relative homogeneous with an average of around 12 md, although there are patches of very high permeability. The Brown Niagaran permeability ranges over four orders of magnitude, rendering the average permeability of the Brown Niagaran not as meaningful a parameter. Figure 4-59 contrasts with Figure 4-58, showing the permeability field in the Chester 16 before history matching, over the same scales. The history matching process has (1) lowered the overall heterogeneity in the entire model, (2) consistently increased permeability in the entire model by at least one order of magnitude, and (3) introduced a horizontal permeability streak in the Brown Niagaran that is surrounded by a low background permeability. Figure 4-60 presents histograms of the permeability distributions in the A1 Carbonate (top) and the Brown Niagaran (bottom) before and after history matching. It shows that the heterogeneity needed to be reduced significantly and permeability had to be scaled upward.

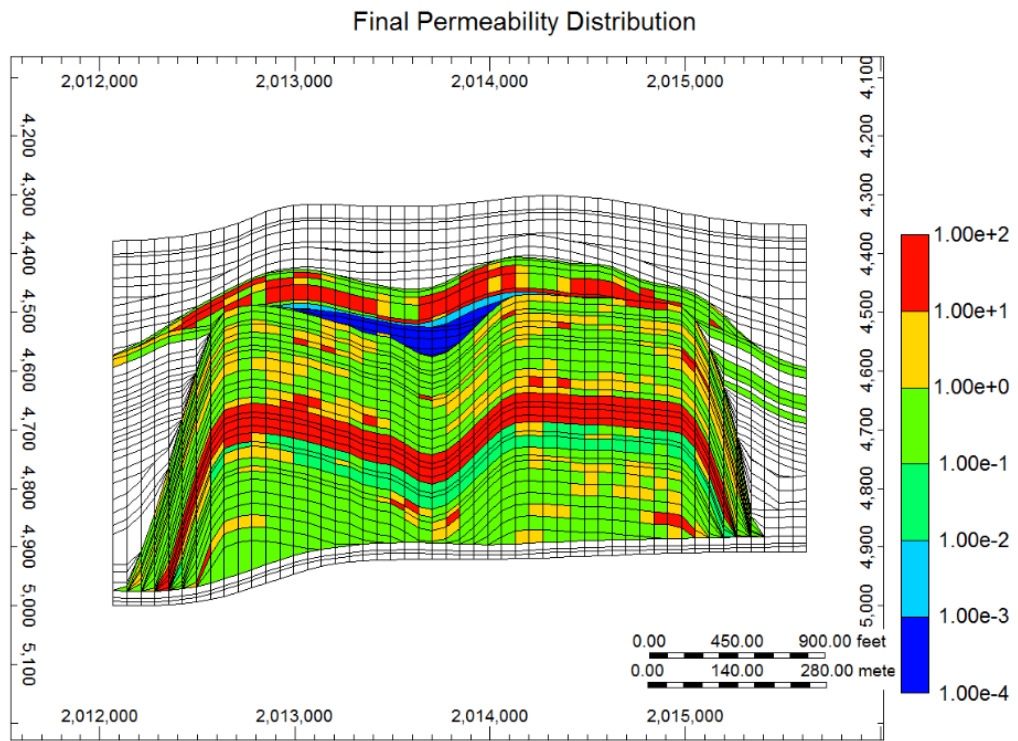


Figure 4-58. The higher permeability streak in the middle of the Brown Niagaran. The base of the A1 is a permeability baffle and has been assigned a low permeability of 0.01 md.

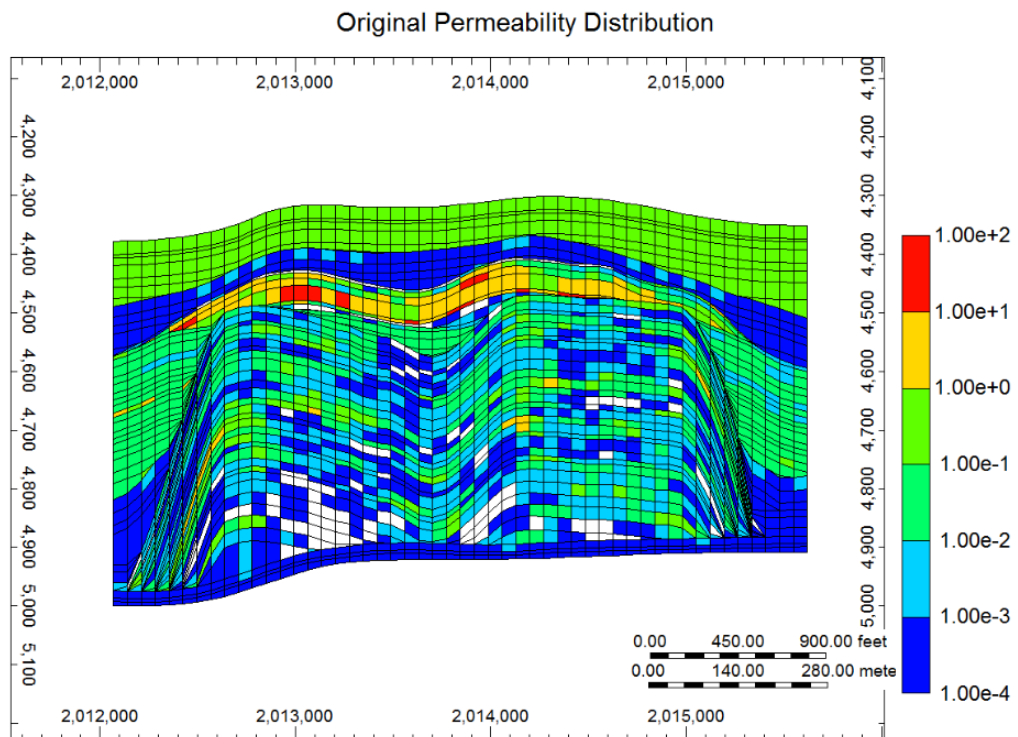


Figure 4-59. Original permeability field in the Chester 16 before history matching.

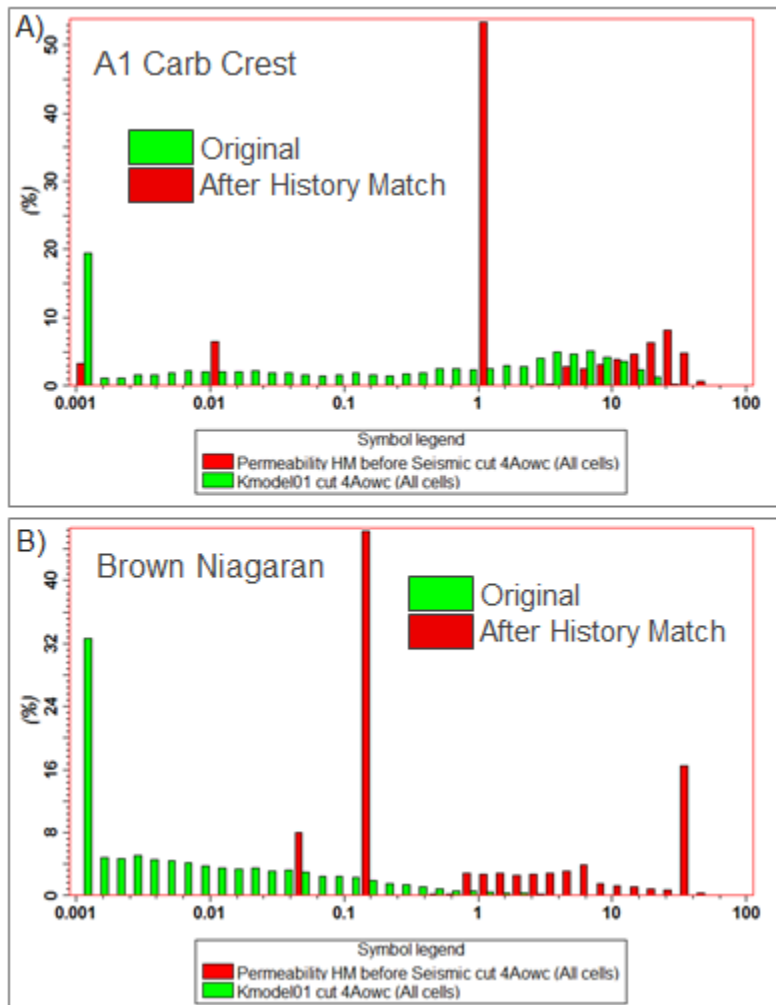


Figure 4-60. Permeability had to be scaled upward and the heterogeneity reduced significantly in order to obtain a history match.

#### 4.4.4 EOR/CO<sub>2</sub> Injection History Matching Process

Due to low reservoir pressures at abandonment, it is desirable to re-pressurize the reservoir to close to the MMP of the oil prior to EOR by injecting CO<sub>2</sub>. CO<sub>2</sub> fill-up in the Chester 16 has been ongoing since January of 2017 through the 6-16 CO<sub>2</sub> injection well, which has open perforations in both the A1 Carbonate and the Brown Niagaran. Two years of injection data (Jan 2017 to Dec 2019) was used to calibrate the reservoir model. The data used is briefly discussed below.

The 6-16 CO<sub>2</sub> injection well is perforated at three locations in the A1 Carbonate Formation and four locations in the Brown Niagaran Formation. The 6-16 well was completed with a plug positioned at the contact between the two formations, and a sliding sleeve system enables injection to be targeted/isolated into either formation separately. However, this system is believed to have been faulty, leading to improper isolation between the two formations. This causes uncertainty about injection rate allocation between the two formations. The unperforated 8-16 well, located approximately 1,200 ft away from the injector well, serves as the observation well for the injection. Both wells produce continuous measurements as they are equipped with memory gauges that measure pressure (at a given depths) and fiber optic cables that provide DTS across the length of the well. The 6-16 well generally produced bottomhole pressure

measurements from the bottom of the well (deep Brown Niagaran), unless injection was targeted into the A1 Carbonate only, when an additional measurement at the bottom of the A1 Carbonate was possible. The 8-16 well's pressure measurements from four depths were relevant to the history match. These gauge measurements are numbered (1) the bottom of the Brown Niagaran, (2) the middle of the Brown Niagaran, (3) the top of the Brown Niagaran and (4) the middle of the A1 Carbonate. Since the injected CO<sub>2</sub> is expected to be at a cooler temperature than the formation, the DTS produces a temperature profile that can indicate the presence of CO<sub>2</sub>.

Figure 4-61 presents the pressure/temperature/rate data gathered from the 6-16 well. The main graphic shows a waterfall plot or a depth vs time plot with the data points color coded to represent temperature. It illustrates the vertical temperature profile recorded at the 6-16 well through all injections occurring from 2017 to 2018, with the lighter regions taken to indicate cooling stemming from the presence of CO<sub>2</sub>. The formation tops are imposed as horizontal lines, and the locations of the well perforations have been marked as notches on the left axis. The green line shows the total volumetric rate, with a label for the intended formation target of the injection. Note also that the gaps in between injection periods provide time for the formation to warm back toward original formation temperature, although the presence of CO<sub>2</sub> serves to dampen the speed at which the rock regains its former (warmer) temperature. The blue line tracks the bottomhole pressure at the bottom of the A1 carbonate, while the cyan line tracks that at the bottom of the Brown Niagaran.

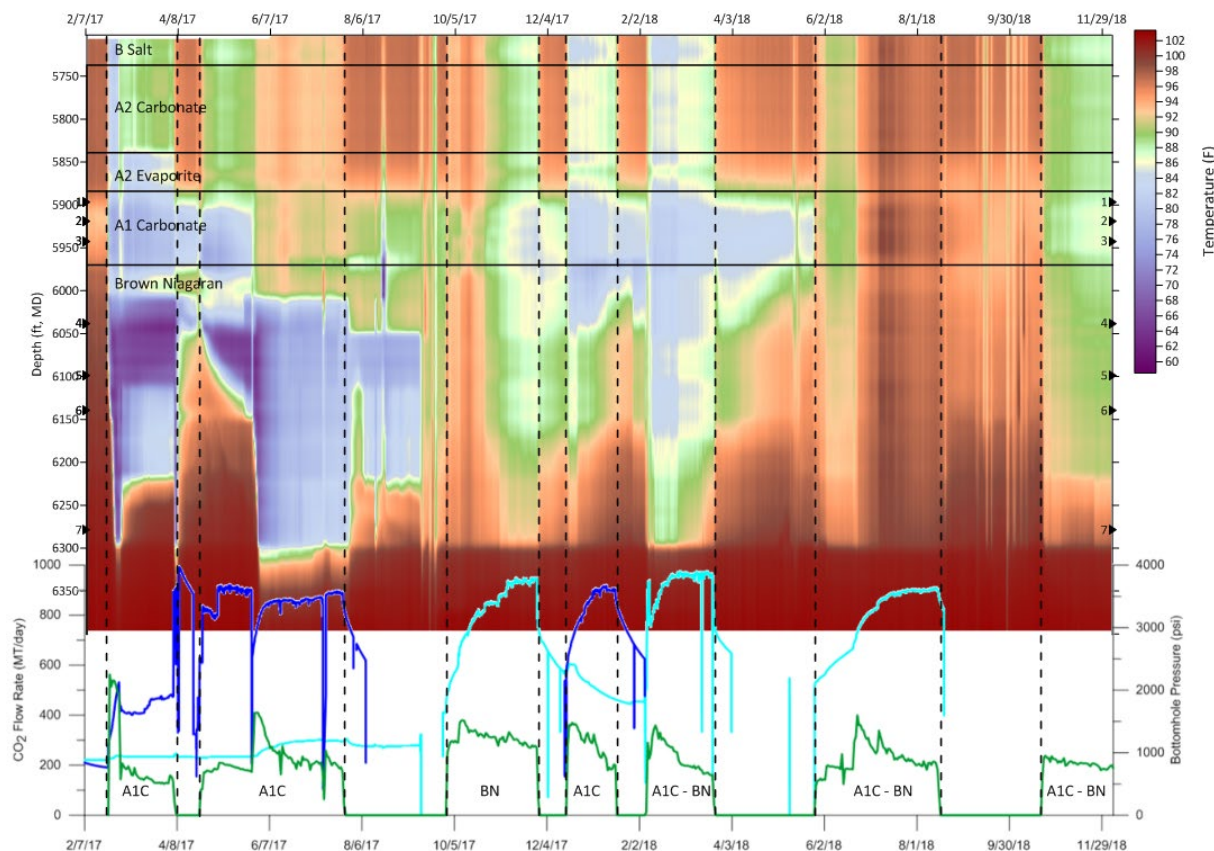


Figure 4-61. The temperature response at the 6-16 injector well through the seven main injection periods from 2017 through 2018.

The first injection period (first blue inflection period in Figure 4-61), where injection was intended to be isolated into the A1 Carbonate only, in fact shows significant cooling in the Brown Niagaran as well, although the short waiting period immediately after shows that the cooling was concentrated near the top perforation. The last two injection periods appear to be anomalous, possibly due to injecting warmer CO<sub>2</sub> in the first place. A mild cooling effect in the A1 carbonate is still discernable.

Figure 4-62 zooms into the temperature profile produced at the 6-16 well, representing the period when injection was attempted exclusively into the Brown Niagaran, and for a while afterward. During this injection, strong temperature deflections are in fact registered in the A1 Carbonate for over half the injection period. After injection has stopped, the region around the lowest perforation warms back toward its original temperature, in contrast to the upper regions of the well. Aside from a strong indication of the presence CO<sub>2</sub>, this qualitatively suggests that much of the CO<sub>2</sub> may have gone into the A1 Carbonate instead.

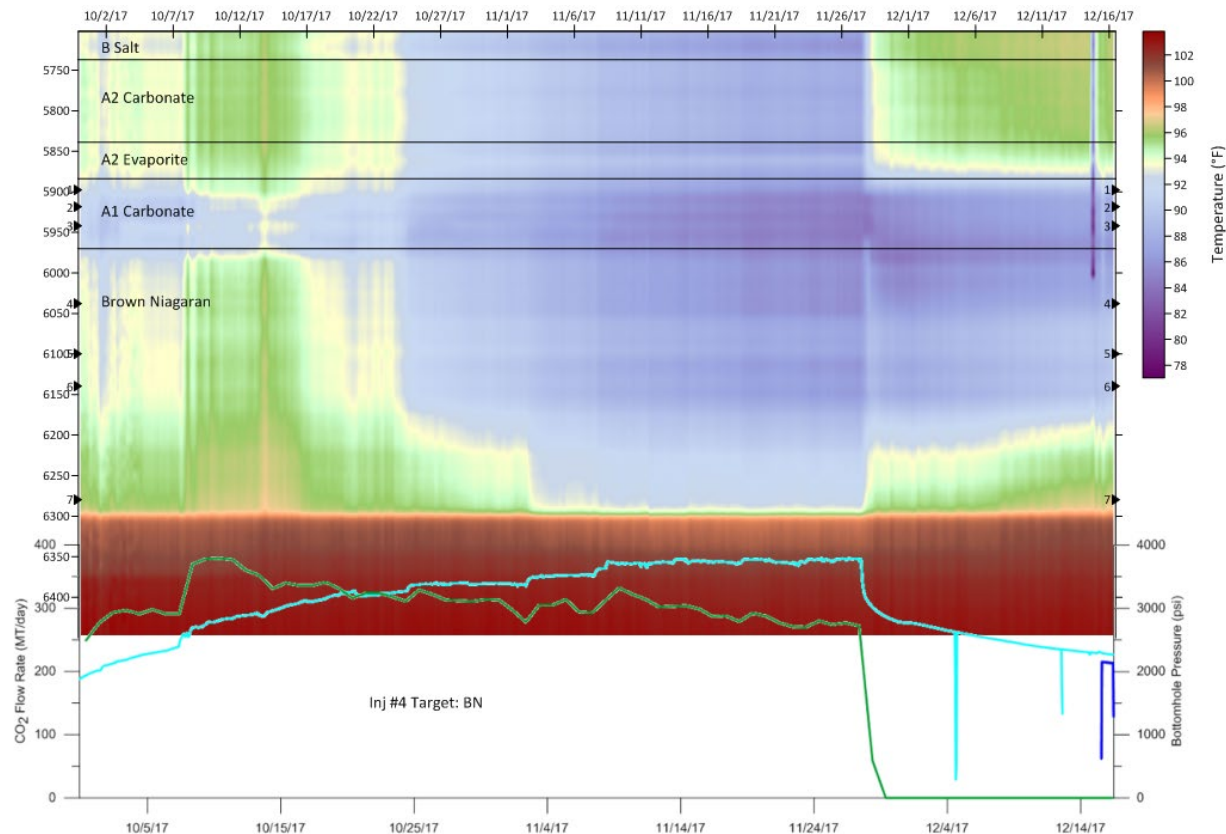


Figure 4-62. A closer look at the injection and warm back period at the 6-16 well for injection period 4.

Figure 4-63 shows the pressure response recorded at the four depths (gauges) at the 8-16 well from 2017 through 2018. The red line tracks the overall CO<sub>2</sub> injection rate into Chester 16 during this period. The pressure response is not felt at the monitoring well until around June/July of 2017. Until then, pressure is directly proportional to depth as expected. However, upon the pressure pulse reaching the 8-16 well, the A1 carbonate – green line – experiences a pressure increase far sharper than the Brown Niagaran. This effect in fact appears to dominate that of general hydrostatic equilibration, such that the A1 Carbonate attains (and remains at) a higher pressure than the Brown Niagaran despite being much shallower. This effect is less pronounced in the Brown Niagaran, as pressures at the three depths appear

to rise in sync and their lines (orange, beige and black for successively shallower depths) do not converge or cross.

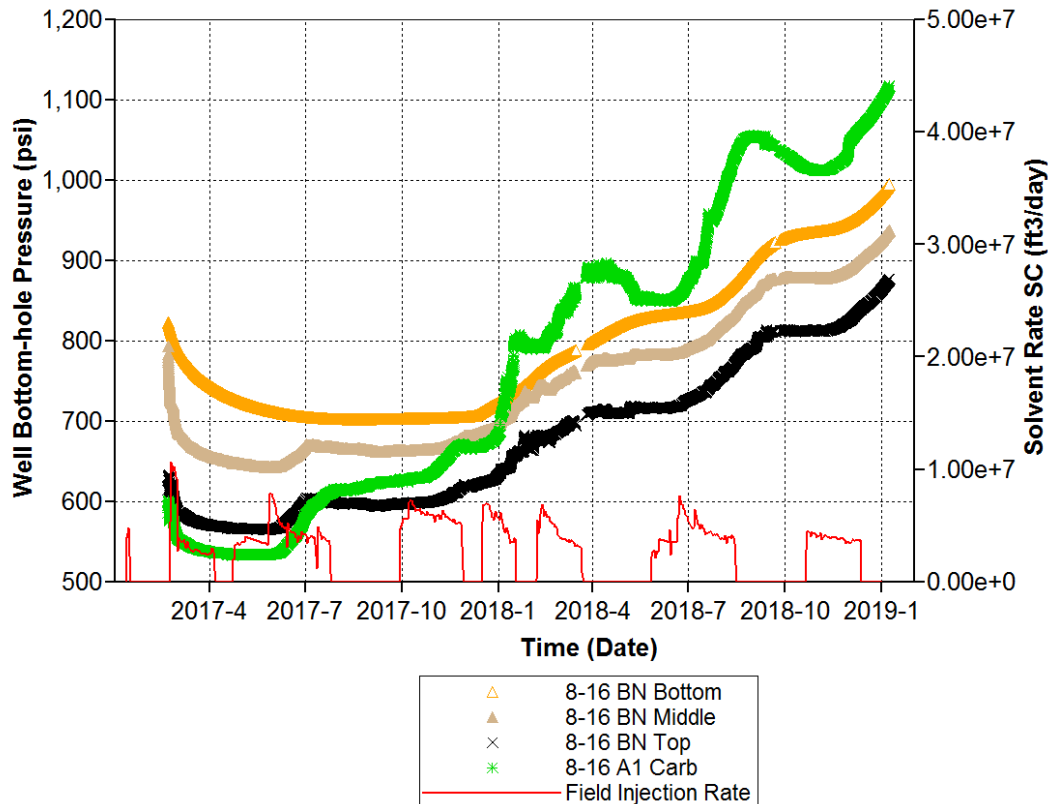


Figure 4-63. Gauge pressure responses of the 8-16 well to the 7 seven injection periods.

Figure 4-64 presents the temperature profile at the 8-16 well in 2018. Like the 6-16 well, the formation tops are imposed as horizontal lines, and the green line presents the total volumetric rate, with a label for the intended formation target of the injection. The dotted line tracks the total cumulative injection into the Chester 16. The cooling streak within the A1 Carbonate provides additional important information. First, as expected, the saturation front carrying cooler CO<sub>2</sub> arrived around April 2018, after the pressure front (June 2017). Temperature deflections suggest that the CO<sub>2</sub> has been contained to within the Chester 17. More interestingly however, despite injection into the Brown Niagaran in 2017 (either through targeted injection or via faulty well isolation) and sustained injection into both A1 Carbonate and Brown Niagaran afterward, only 8-16 well did not detect any temperature fluctuation in the Brown Niagaran at all. In fact, the cooling effect grew stronger and wider within the A1 Carbonate during this time.

Several inferences were drawn based on this data. Firstly, (1) the distance of the 8-16 well from the 6-16 injector well (~1200 ft) and (2) the length of time that passed before the response at the monitoring well was recorded (~9 months), proves that the cooling effect of the CO<sub>2</sub> is a dominant, long-lived reservoir effect and that CO<sub>2</sub> has strong thermal insulation properties. This also suggests that that the temperature deflections can be used as proxies for the volume of CO<sub>2</sub> injected. Figure 4-62 for instance, would thus suggest that a negligible amount of CO<sub>2</sub> entered the formation via the deepest perforation. Second, the observations that (1) the A1 Carbonate is unusually pressurized and (2) that the temperature deflections are far more pronounced in the A1 carbonate – as seen in the post-injection periods in the 6-16 (Figure 4-61) and the 8-16 wells (Figure 4-64) – indicate that majority of the CO<sub>2</sub> was injected into the A1 Carbonate. This is reasonable deduction considering that (1) the generally higher permeability (and lower

heterogeneity) of the A1 Carbonate leads to better injectivity, and that (2) more CO<sub>2</sub> in the Brown Niagaran would have resulted in a cooling signature detected in the 8-16 well, due to the high permeability streak. This data also suggests a strong barrier-like impact of the permeability baffle separating the A1 Carbonate from the Brown Niagaran that dampens the hydrostatic pressure equilibration.

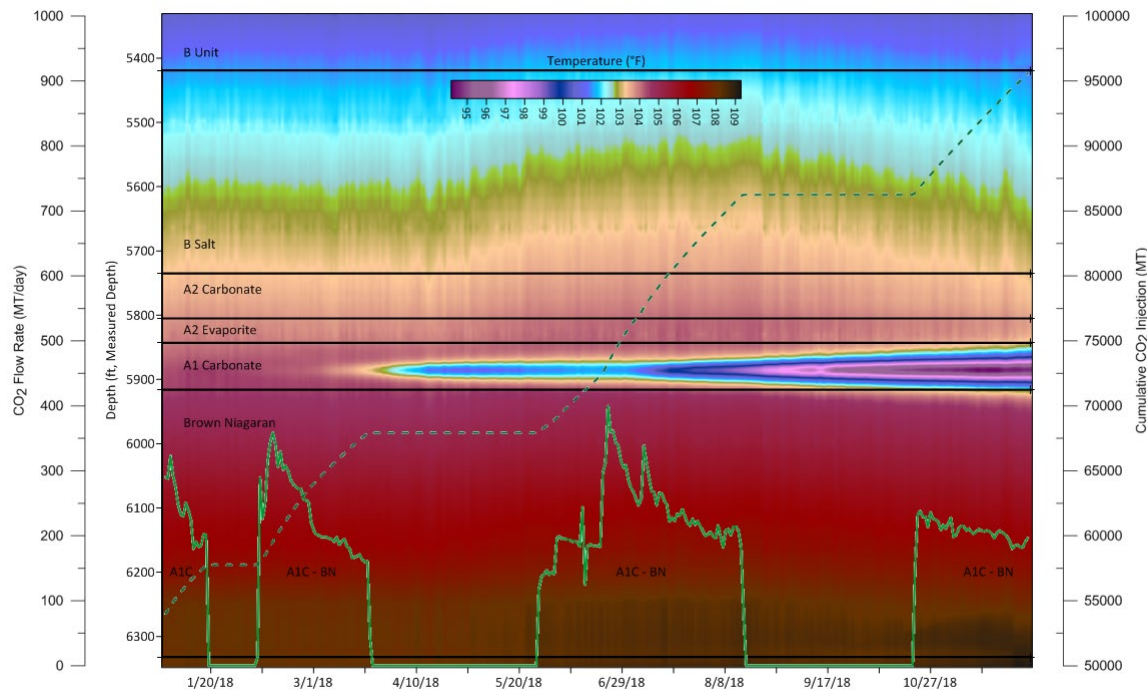


Figure 4-64. The temperature profile recorded at the 8-16 well. Data from the 2018, or the second year of injection is shown.

The CO<sub>2</sub> injection rate allotted to each formation (and thus each perforation) was therefore the main tuning parameter to match the pressure responses (via trial-and-error) at the various depths of the 8-16 well and qualitatively match the CO<sub>2</sub> saturation front. The matches to the pressures at the 8-16 well were treated as the primary history match performance metric since the pressure pulse from the 6-16 would have needed to travel through more than half the pore volume of the Chester 16 before reaching the 8-16. Figure 4-65 shows the injection volume allocated to each formation for each injection period in the final history matched model. In line with the implications previously discussed, a vast majority of the CO<sub>2</sub> was allotted to the A1 Carbonate. Even within the Brown Niagaran, most of it was allotted to its two upper perforations.

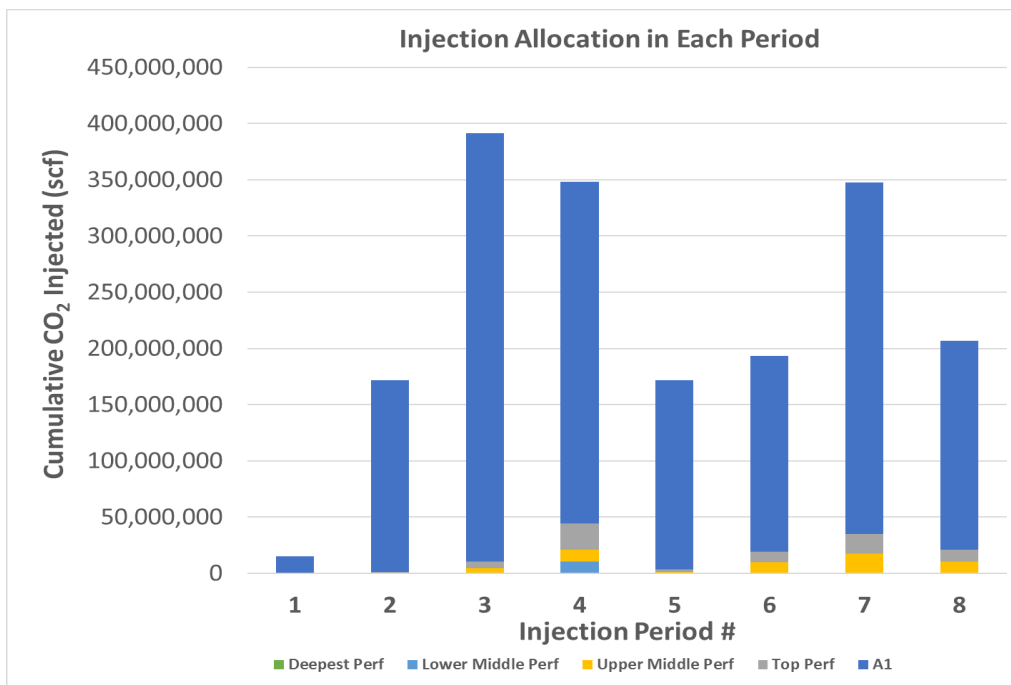


Figure 4-65. The allocation of injection volumes to each perforation of the 6-16 well for all eight injection periods.

#### 4.4.5 History Matching Results

##### 4.4.5.1 History Match for Primary and Secondary Recovery Phases

Figure 4-66 shows that the history matched model adequately captures the average reservoir pressure decline as recorded in the Chester 16. Continuous pressure decline data was unavailable. This data, however, which was obtained historically from the 1-16 well located in middle of the entire formation, was utilized in an independent material balance analysis that was used to the estimate the OOIP of the Chester 16. Only three data points were available for the waterflooding period. Only the endpoint was retained for the history match, as it was the most realistic data point. The model correctly predicts a post-waterflood, abandonment pressure of around 500 psi.

Figure 4-67 shows that with updated permeability field, the model was able to meet the oil production constraints for all five wells to cumulative produce the requisite 2.4 MMSTB of oil. Figure 4-68 shows that the model's prediction of the gas production from the Chester 16 captures both the global trend in gas production, as well as the overall cumulative produced volume (3 BCF). Water production data for the life of the field was unavailable. Although incremental water production data from after the waterflood was available, it is still a source of uncertainty. Figure 4-69, however, shows that the model overpredicts the water production from this period considerably. Figure 4-70 shows how lowering the water relative permeability end point to force the model to produce less water sacrifices the model's ability to match oil production constraints, producing 50 MSTB of oil less. Consequently, the match to the average reservoir pressure decline is lost (Figure 4-71). This observation suggests either a limitation of this model in overproducing water to keep in mind when using it for forecasting purposes or that there is significant uncertainty in the recorded water production data. The reality is likely a combination of both.

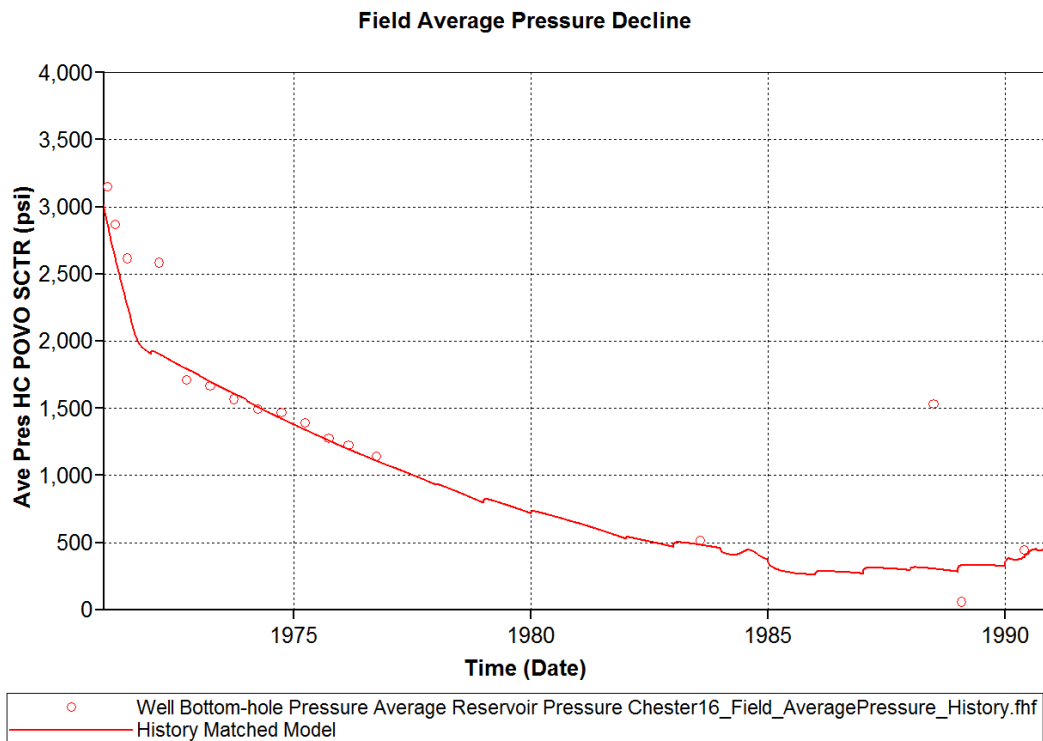


Figure 4-66. History Match to the average pressure decline during the primary and secondary phase.

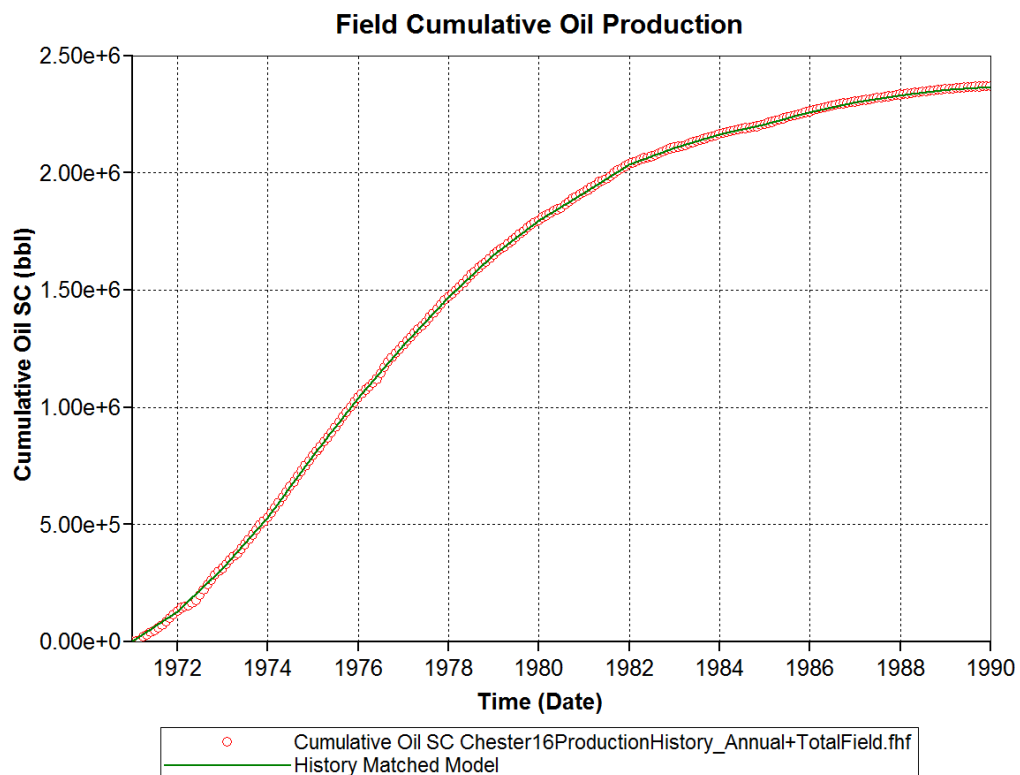


Figure 4-67. History matched model produces the cumulative volume of oil as expected.

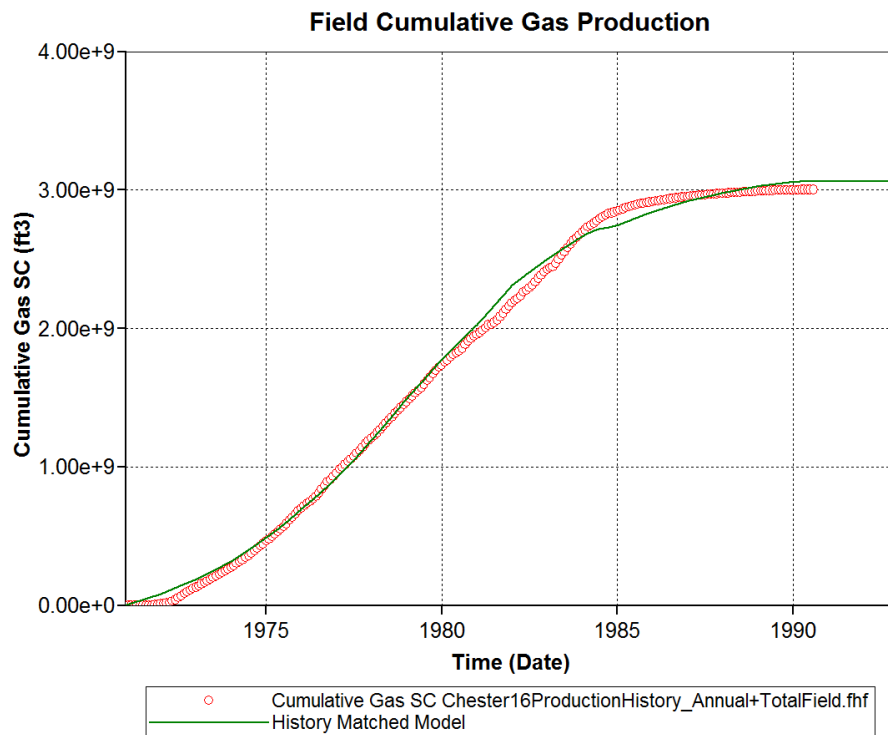


Figure 4-68. The cumulative gas production of the history matched model vs field data

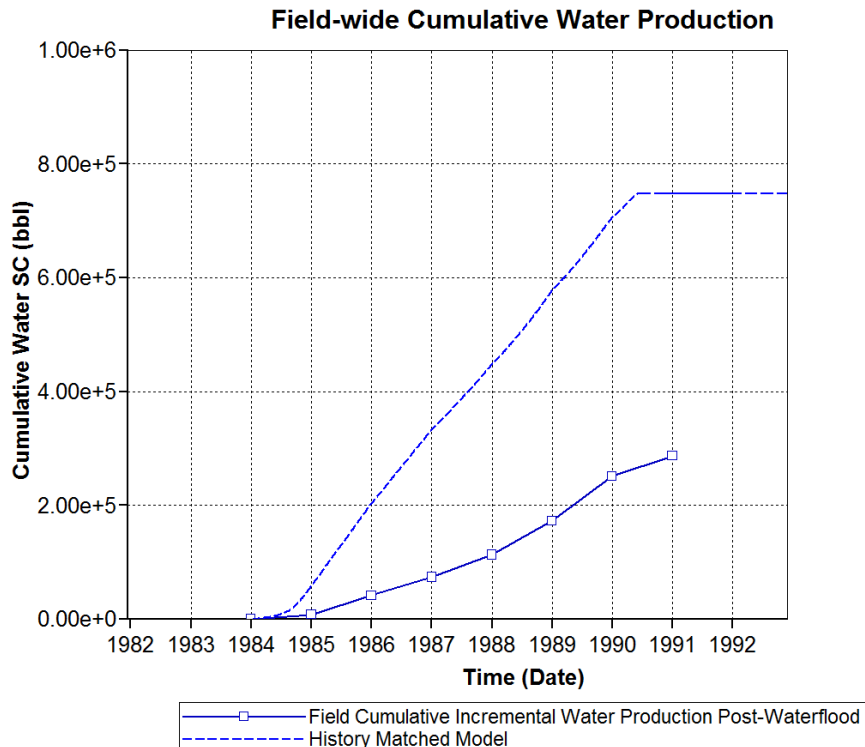


Figure 4-69. The cumulative water production of the history matched model vs field data

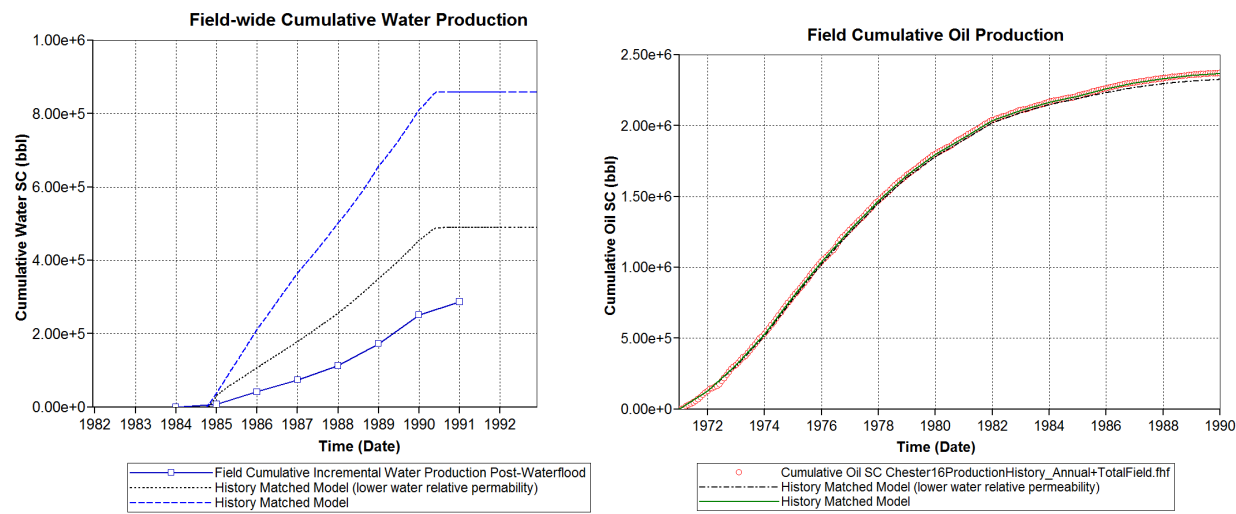


Figure 4-70. Lowering the relative permeability to water in the history matched model results in less water production from the waterflooding phase (left). However, this occurs at the expense of oil production (right).

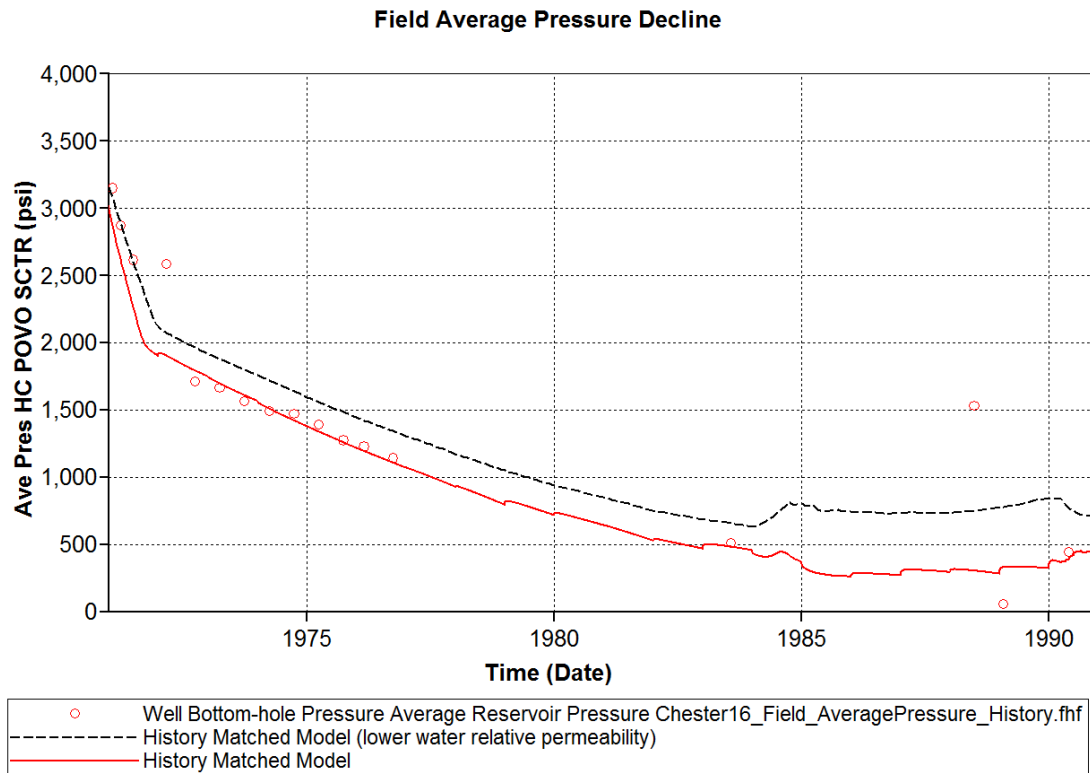


Figure 4-71. Lowered water production leads to a loss of the history match to the average reservoir pressure decline.

#### 4.4.5.2 CO<sub>2</sub> Fill-up Phase

The quality of the match during the CO<sub>2</sub> fill-up phase is an indication of the reliability of the permeability field and the CO<sub>2</sub> injection rates allocated to the individual formations (and perforations). The match to the bottomhole pressure data at various depths in the location of the 8-16 well is the primary performance indicator, while that to the temperature deflections (indicating saturation front arrival) is only a secondary parameter treated only qualitatively. Matching all three of the arrival times of the pressure/saturation pulse, the increase in pressure and the final reservoir pressure at the end of two years of injection is a very challenging task, amplified further considering the uncertainty in the quantity of CO<sub>2</sub> injected into the various layers. Of these three, the final end point reservoir pressure (which directly affects oil flow rates) and CO<sub>2</sub> pressure front arrival time were given priority, in that order. Several different rate allocations were attempted in trial-and-error, due to the non-uniqueness of the history matching problem. Figure 4-72 to Figure 4-76 present the results of the injection allocation scheme across the eight injection periods, as described in Figure 4-65.

Figure 4-72 shows that the match to the pressure in the middle of the A1 Carbonate at the 8-16 well is good. The black line represents the data from the field, while the dotted line represents simulation data. The blue line tracks the total injection rate for reference. The initial pressure prior to CO<sub>2</sub> injection has been matched nearly exactly. The model also captures the timing of the first arrival of the pressure pulse from the injection closely. The end point pressure at the end of injection has also been matched nearly exactly. However, the transition from the initial condition to the final has not been replicated, and the pressure increase predicted by the model is much sharper.

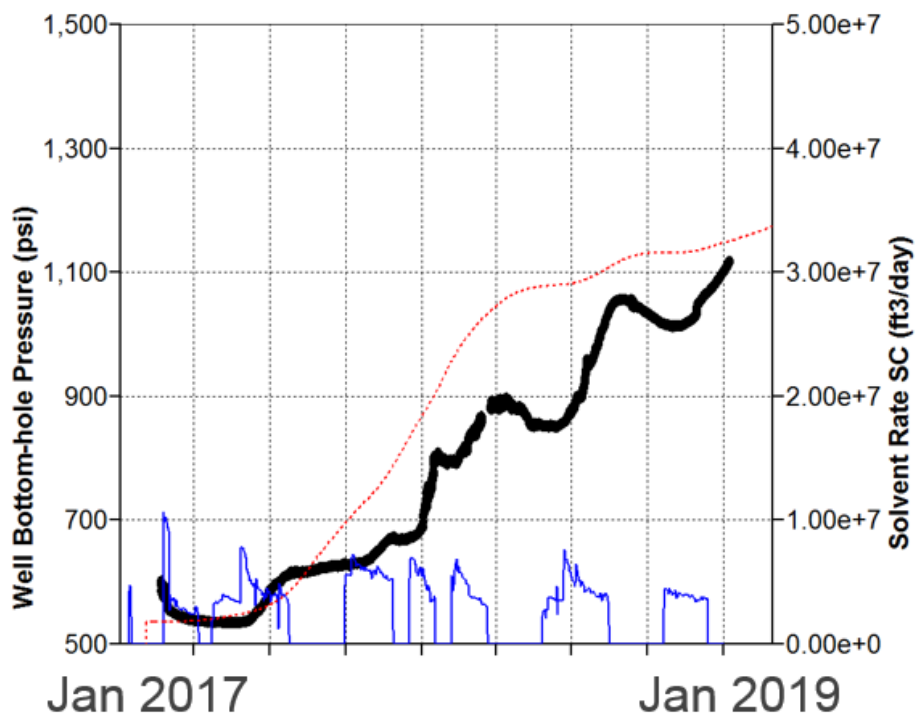


Figure 4-72. History match to the pressure response at the A1 carbonate, as measured at the 8-16 gauge.

Figure 4-73 to Figure 4-75 show the match to the pressure in the Brown Niagaran at the 8-16 well (the top, middle and bottom respectively). The pink line represents the data from the field, while the dotted line represents simulation data. The colored lines at the bottom track the total injection rate for reference. The initial pressure prior to CO<sub>2</sub> injection has been matched within 50 psi for the top and middle of the Brown Niagaran, although is about 100 psi off for the bottom of the Brown Niagaran. The end point pressure at the end of injection has also been matched closely for the top and bottom of the Brown Niagaran but is off by around 150 psi for the middle of the Brown Niagaran. However, the transition from the initial condition to the final has not been replicated, nor has the pressure pulse arrival time. Because (1) the Brown Niagaran is over 300 ft thick and highly heterogeneous and the A1 Carbonate is relatively thin homogeneous rock in comparison, and (2) the simulator employs a less rigorous pseudo-miscible black-oil model, the matches for the Brown Niagaran are not expected to be as good.

Figure 4-75 presents a cross-section through the Chester 16 model with the 8-16 well, showing the spatial distribution of CO<sub>2</sub> (yellow) in the reservoir. Two different dates are shown. Figure 4-76 shows that the model qualitatively corroborates the information shown in Figure 4-64, illustrating the (1) CO<sub>2</sub> front to have both reached the 8-16 well mainly in the A1 Carbonate and not as much in the Brown Niagaran (although the permeability streak demonstrates an impact) by the end of 2018 and arrived at the 8-16 well in the A1 Carbonate at a similar time (March 2018).

Overall, with the twin caveats that the model (1) overpredicts the pressurization from CO<sub>2</sub> injection between 100-150 psi in the Brown Niagaran and (2) offers more accurate pressure predictions over entire phases (such as the primary production phase or the CO<sub>2</sub> fillup phase) rather than the short-term (a solitary injection period), the history match to the primary, secondary and CO<sub>2</sub> fill-up cases is considered satisfactory.

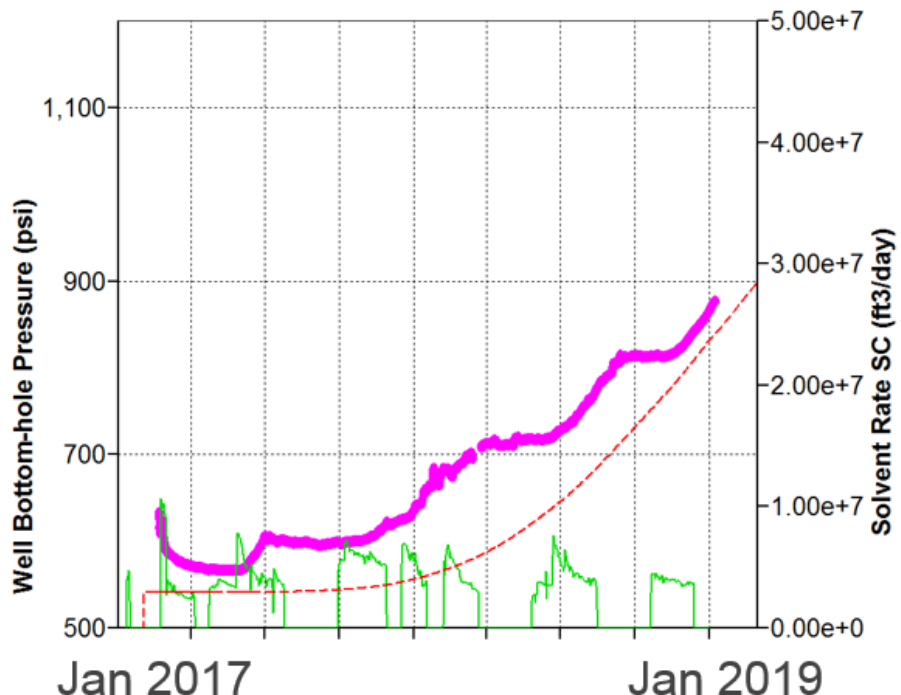


Figure 4-73. History match to the pressure response at the top of the Brown Niagaran, as measured at the 8-16 gauge.

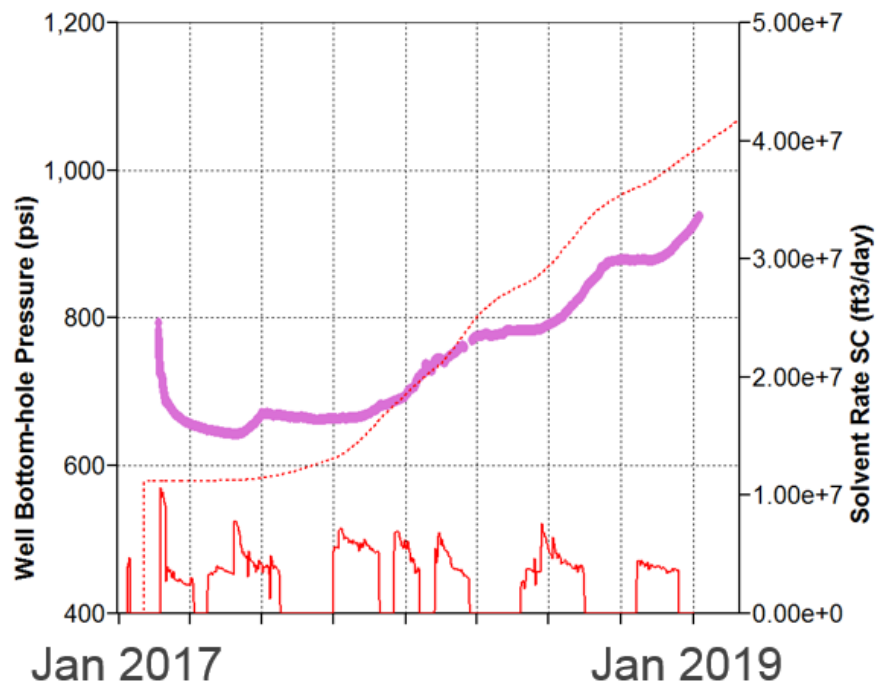


Figure 4-74. History match to the pressure response at middle of the Brown Niagaran, as measured at the 8-16 gauge.

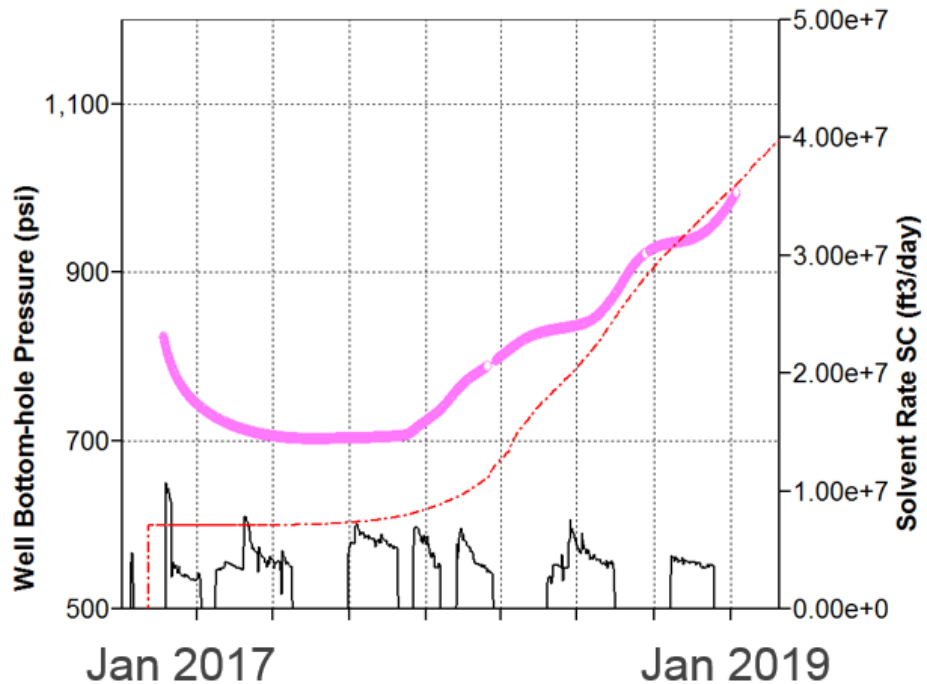


Figure 4-75. History match to the pressure response at the bottom of the Brown Niagaran, as measured at the 8-16 gauge.

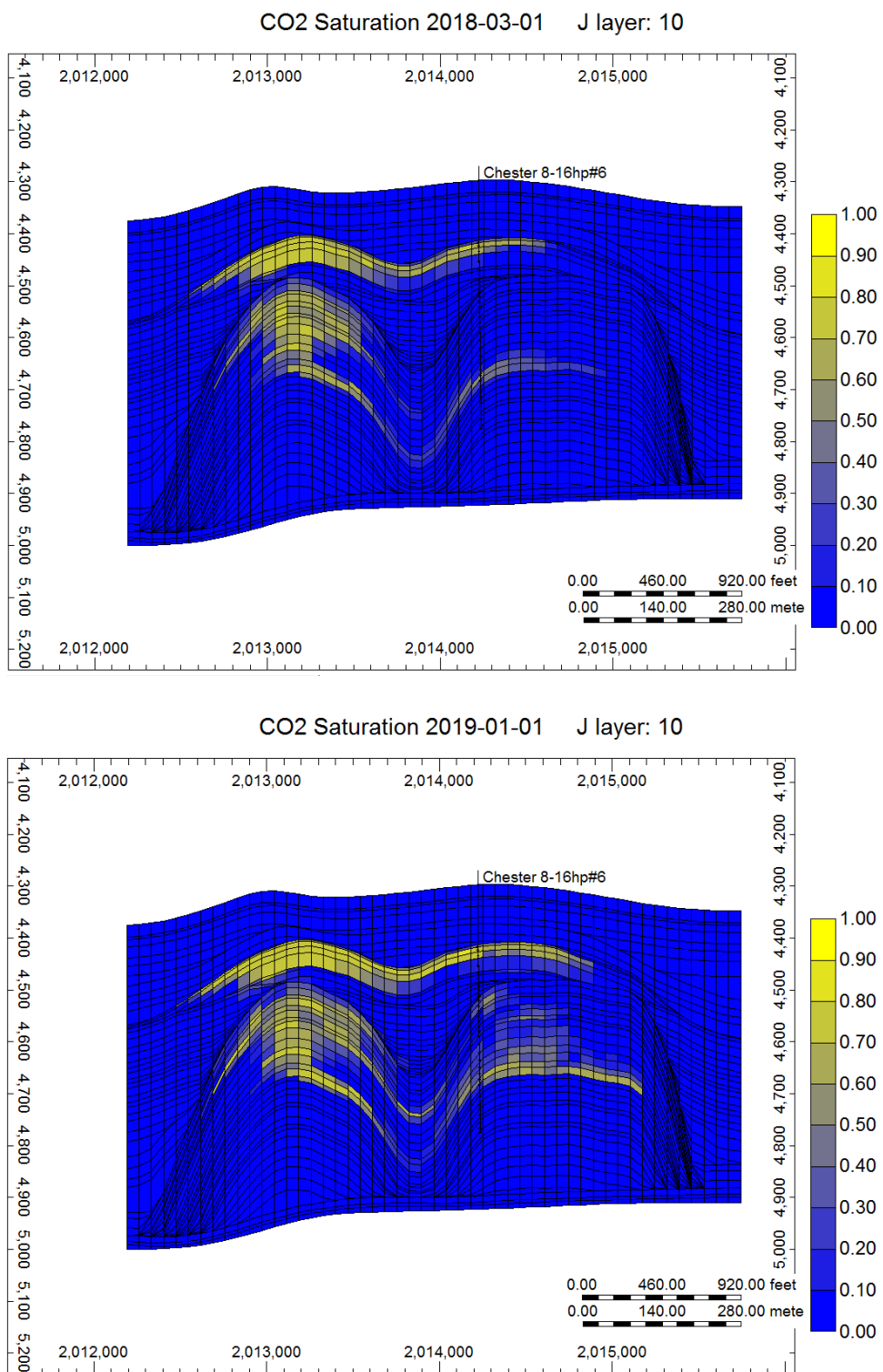


Figure 4-76. Shows the CO<sub>2</sub> saturation around the 8-16 monitoring well in April of 2018 (top) and the end of 2018 (bottom).

#### 4.4.5.3 Summary of Key Uncertainties

**Table 4-17. Key uncertainties in the data and its impact on the dynamic modeling.**

Key Uncertainty	Cause	Impact on Dynamic Model
Dynamic pressure data	<ul style="list-style-type: none"> <li>Well-wise bottomhole pressure decline data from oil production period is unavailable.</li> <li>Only limited field-scale pressure decline data is available. The data points from the waterflooding phase are unreliable; abandonment pressure is unknown.</li> </ul>	<ul style="list-style-type: none"> <li>Quality of history match judged more on producing correct field-scale cumulative volumes such that the average reservoir pressure decline is reasonable, rather than matching individual well production data.</li> <li>Desired end point pressure of the history match was preferentially set to be that recorded in the A1 carbonate before the first injection. This was because majority of the oil production, CO<sub>2</sub>-injection, and high-quality rock was judged to have been in this formation.</li> </ul>
Water production	<ul style="list-style-type: none"> <li>Well-wise water production data from all periods is unavailable.</li> <li>Only limited field-scale data is available. Total cumulative water production is unknown; total incremental water production after waterflooding is available.</li> </ul>	<ul style="list-style-type: none"> <li>Water production has been generally ignored as a primary history matching parameter, since water production data is not reliable. However, being close to produced volumes is desirable.</li> <li>Given that the water relative permeability curve end point has been fixed at 1, the maximum possible water production is assumed.</li> </ul>
Injection volume split-by-formation	<ul style="list-style-type: none"> <li>Leaky seal between the two formations inside the 6-16 well.</li> <li>No logging tool available to determine the exact quantity of the leak between the formations.</li> </ul>	<ul style="list-style-type: none"> <li>Injection throughout the period modeled was approximated to be varying in a simple step-wise manner such that the total cumulative volume injected was preserved. Varying rate due to the leak could not be captured.</li> <li>The split was estimated via a qualitative assessment from the DTS data.</li> <li>The quality of the history match during the injection phase was judged preferentially on monitoring response in the 8-16 well, rather than the injection bottomhole pressure in the 6-16 well.</li> </ul>

#### 4.4.6 History Matching with Alternative Conceptualization Using Seismic Data

As previously described, the horizontal permeability streak that was introduced in the Brown Niagaran was likely the predominant geologic feature that enabled the Chester 16 wells to meet their oil production constraints. Adding this feature, however, was unprecedented, as there was no direct evidence for an extensively enhanced (through fractures or dissolution enhanced porosity) zone from log, core, or well-test data. Yet, the failure to obtain even a satisfactory history match (to the primary production) via plain global permeability enhancement without adding this element, and the perforation/completion history of the main wells, along with the quality of the match with the permeability streak all lend indirect credence to its existence. Qualitative discussions regarding the geology of the Niagaran reefs suggest that since (1) the lithofacies categorization was not helpful in developing useful porosity-permeability relationships in the Brown Niagaran, and (2) the overall permeability of the Chester 16 had to be enhanced significantly to match field production data and (3) the wells sampled the Chester 16 ununiformly/sparsely, there was likely to have been significant regional diagenetic effects that were not integrated in the SEM. However,

even if such a strong permeability feature may be explained geologically via diagenesis, it was hypothesized to be patchier and dipping within the reef. In order to corroborate the existence of the permeability feature, a 3D seismic survey and a seismic inversion of the data was performed to yield an AI volume. The AI volume was then used to compute a porosity inversion. This seismic porosity inversion tied with the porosity well logs and featured a porosity trend internal to the reef in the Brown Niagaran. This is described and shown in the earlier section: Alternative Conceptualization (Seismic Inversion and Property Modeling).

The seismic survey led to revisiting the SEM to (1) check for the existence of the permeability streak and (2) repopulate the porosity, permeability and the water saturation distribution upon integrating trends gleaned from the 3D seismic property inversion (for rock property trends) exercise. The analysis proved a patchy but high permeability geologic feature extending from the deeper region of the southern pod to the upper region of the northern pod of the Chester 16. Note that the porosity, permeability, and the water saturation distribution was updated only in the Brown Niagaran and not the A1 Carbonate. These details are discussed in detail in Section 4.3.2.10 – 4.3.2.14.

A successful history match to this new model serves as an “alternative geologic conceptualization.” The process explained in Section 4.4.2 was re-applied to the new SEM. The 3D porosity from the previous version of the SEM, which integrated core and log data, was coupled with the seismic property 3D volume, via co-located co-kriging to produce a new porosity volume. Subsequently, the permeability was co-kriged to the new porosity distribution and the water saturation distribution regenerated to create a new SEM.

Figure 4-77 presents the porosity distribution in the new SEM. Note the Brown Niagaran retains its high variability, with an average of 4.4 percent but a maximum of around 14.8 percent. The A1 Carbonate in contrast, is relatively homogeneous with high porosity (13.4 percent). The SEM indicates that the northern pod has better porosity than the southern pod. Most importantly, a patchy but laterally extensive region of higher porosity in the middle of the Brown Niagaran is discernable.

## Porosity Distribution J layer: 16

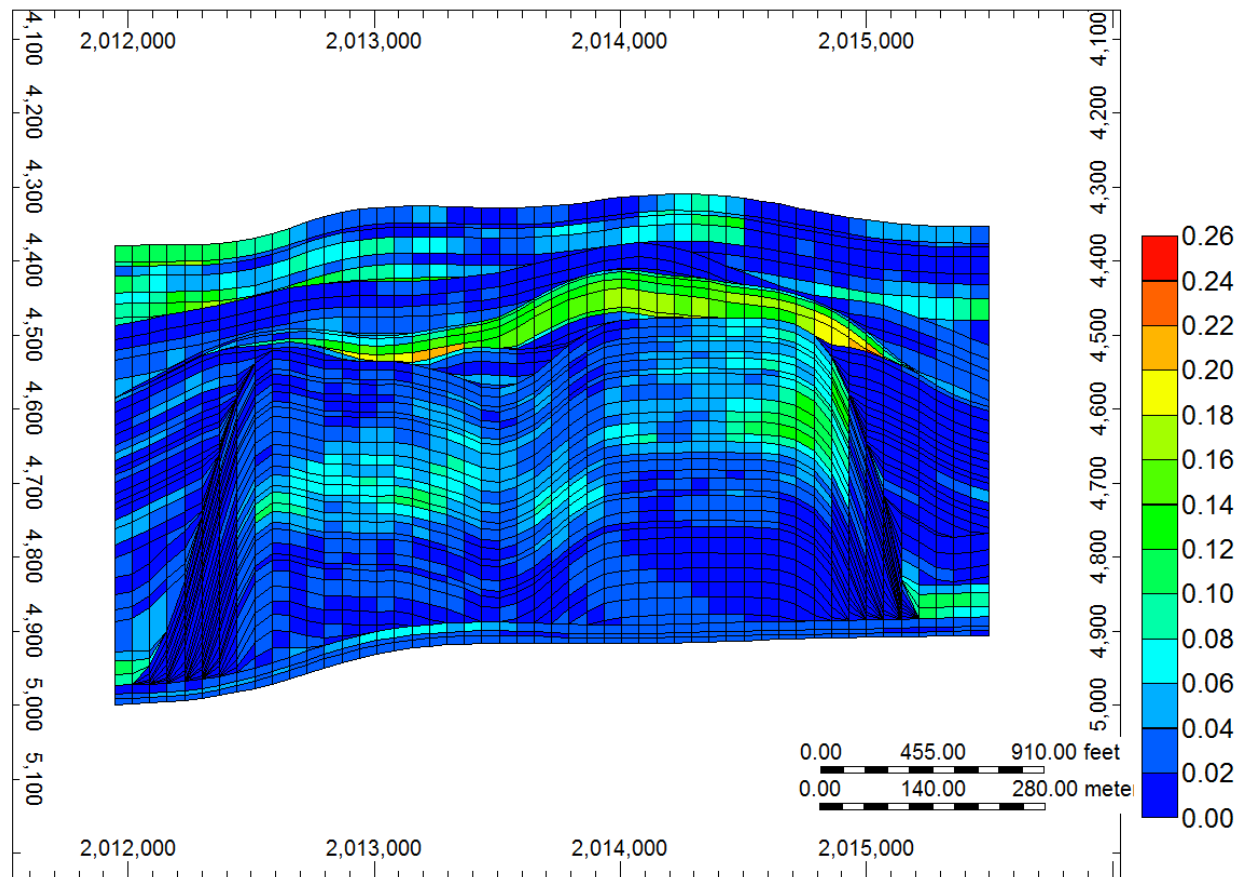


Figure 4-77. Cross-section of the Chester 16 showing its porosity distribution after integrating data from the seismic survey.

Figure 4-78 shows how the permeability field of the entire Brown Niagaran in the new SEM was scaled upward by a global multiplier of 300x in order to obtain a history match. The extreme values were truncated/modified such that the maximum permeability did not exceed 50 mD (the permeability of the high perm streak in the previous model was 40 mD), and the minimum permeability was at least 0.3 md (low permeability zones in the previous model ranged between 0.05 to 0.15 mD). Figure 4-78 is shown in a log-scale to demonstrate how higher permeabilities and lower heterogeneity was needed to obtain a history match. The right panel in Figure 4-78, compared with Figure 4-58, highlights the similar ranges of permeability (by design) and heterogeneity in both models, but more significantly, suggests that the permeability feature is generally much thicker than originally thought. Figure 4-80 shows two further cross-sections of the permeability field on a regular scale (from 0 to 50 mD), and highlights the patchy, angled nature of the permeability streak, surrounded by otherwise low background permeability rock. Figure 4-79 is a comparison of the distribution of the new permeability in the Brown Niagaran before and after history matching. This model thus offers an alternative to the “layer-cake” conceptualization of the previous model.

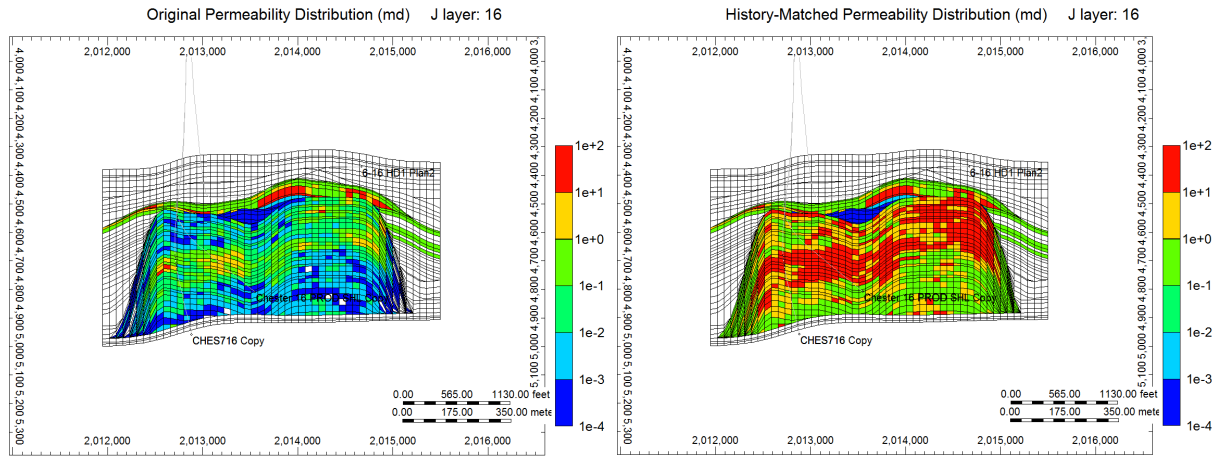


Figure 4-78. The permeability field in the new model has been scaled to obtain the history match.

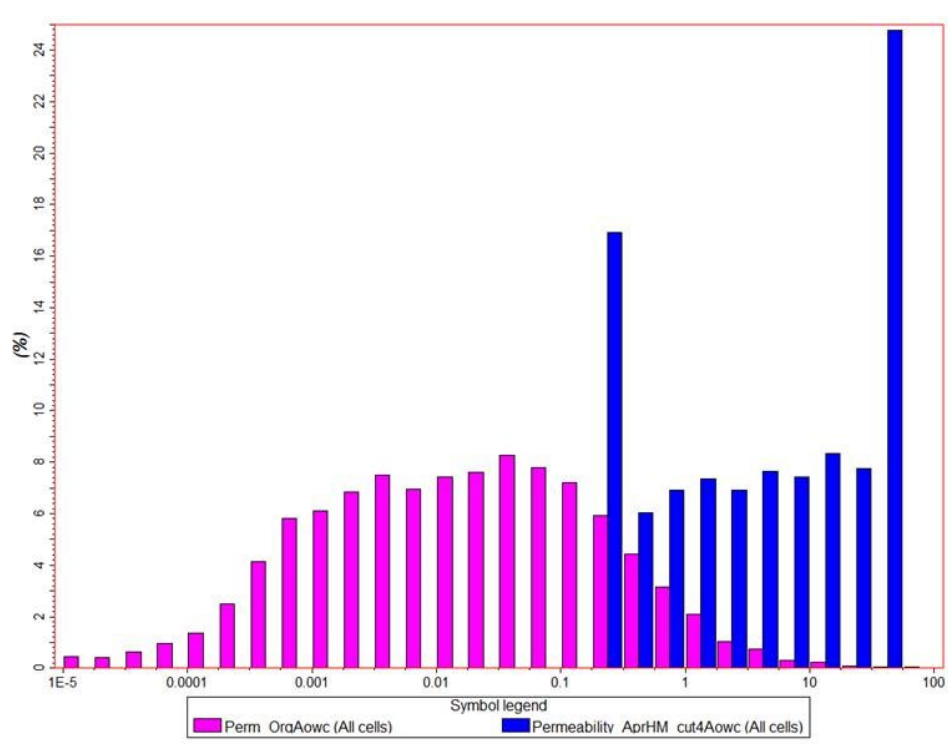


Figure 4-79. The permeability in the Brown Niagaran in the new model integrating seismic data also had to be modified similarly to the earlier model. The heterogeneity was reduced, and the model permeability was scaled upward.

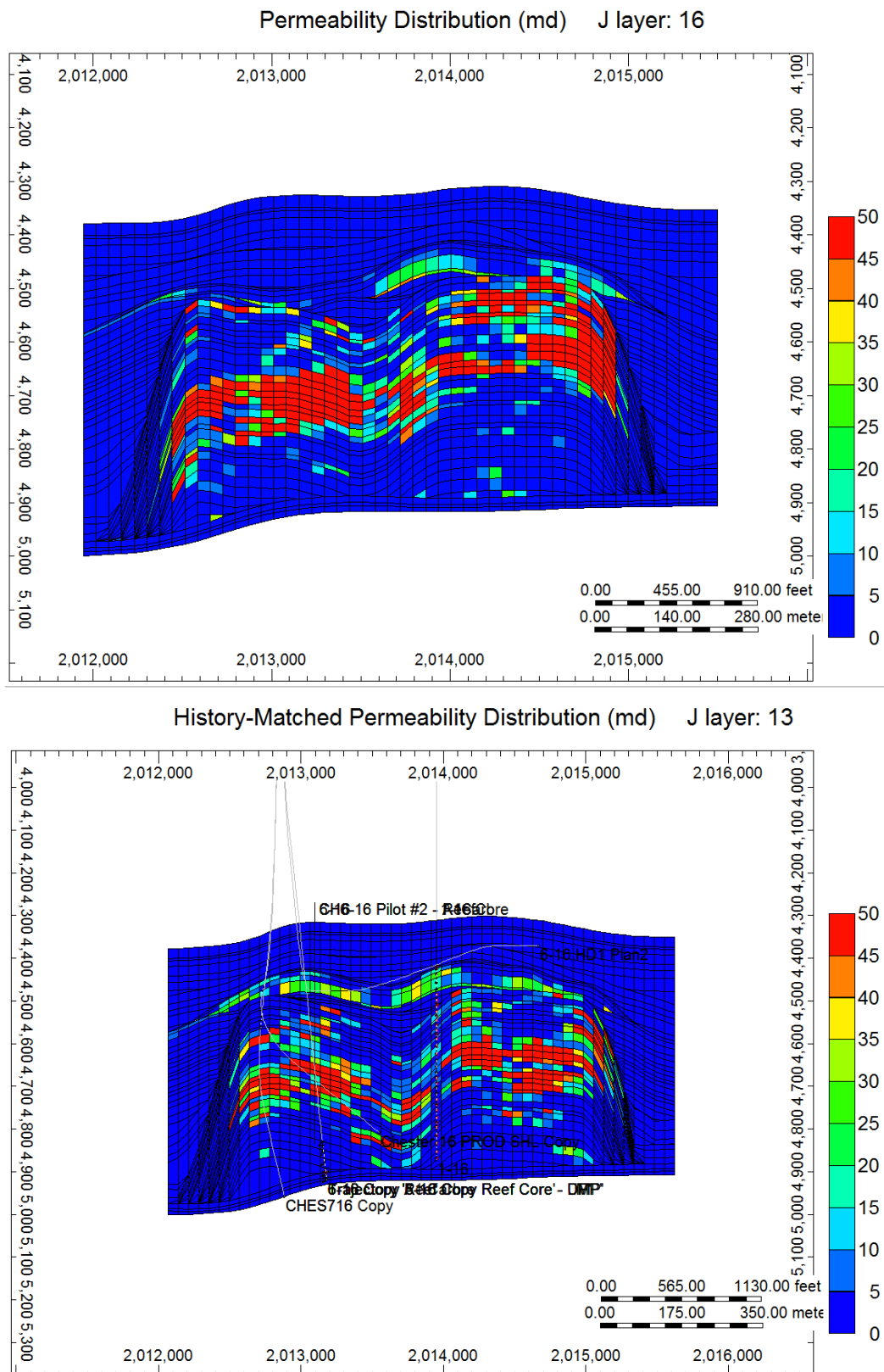


Figure 4-80. Two cross-sections of the permeability field in the new Chester 16 model after history matching.

Figure 4-81 shows the initial water saturation distribution in the new model. The OOIP of the new model was also approximately 7.0 MMSTB affirming its validity. Comparing the water saturation distribution with the previous model, shown in Figure 4-34, suggests that the northern pod contains more oil in the new model.

The CO<sub>2</sub>-injection rate allocations applied to the earlier “layer-cake” conceptualization were re-used in history matching this model.

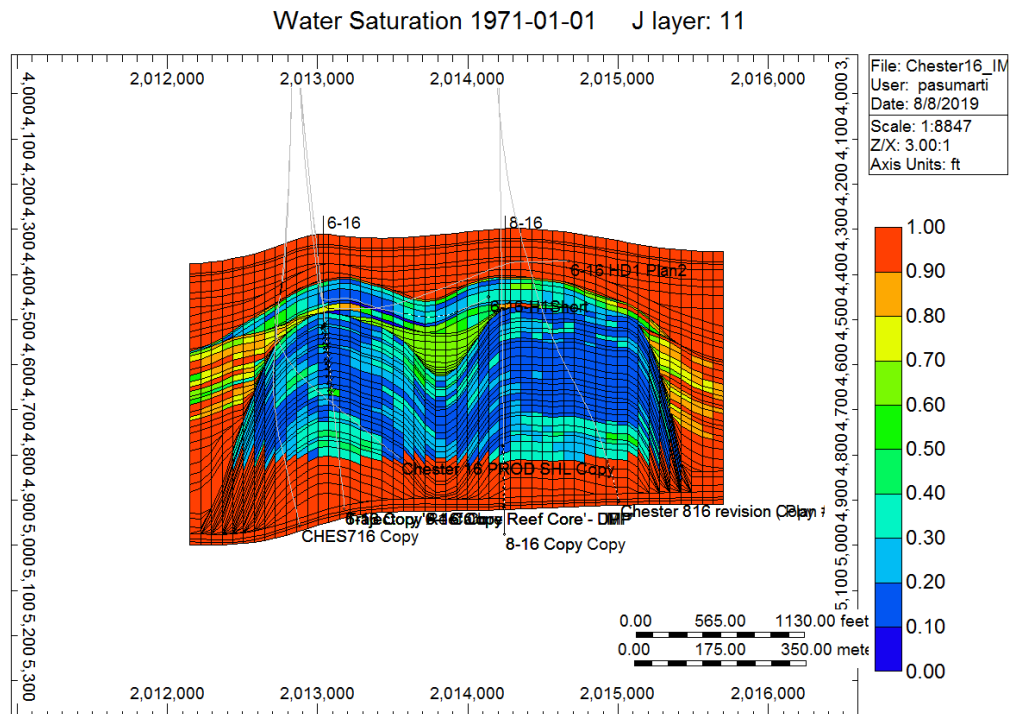


Figure 4-81. Cross-section showing the initial water saturation in the new model.

#### 4.4.7 Results of History Matching with Alternative Conceptualization

Figure 4-82 shows that the history matched model adequately captures the average reservoir pressure decline as recorded in the Chester 16. The model also correctly predicts a post-waterflood, abandonment pressure of around 500 psi. Figure 4-83 shows that with updated permeability field, the model was able to meet the oil production constraints for all five wells to cumulatively produce the requisite 2.4 MMSTB of oil. Figure 4-84 shows that the model’s prediction of the gas production from the Chester 16 captures both the global trend in gas production as well as the overall cumulative produced volume (3 BCF). Figure 4-85, however, shows that the new model produces much less water than the model with the “layer-cake” conceptualization, and approximates the field data (cumulative water production recorded from the onset of waterflooding) more closely. Although the cumulative water production data is still a source of uncertainty, that the model does not exceed the field data as significantly is viewed positively.

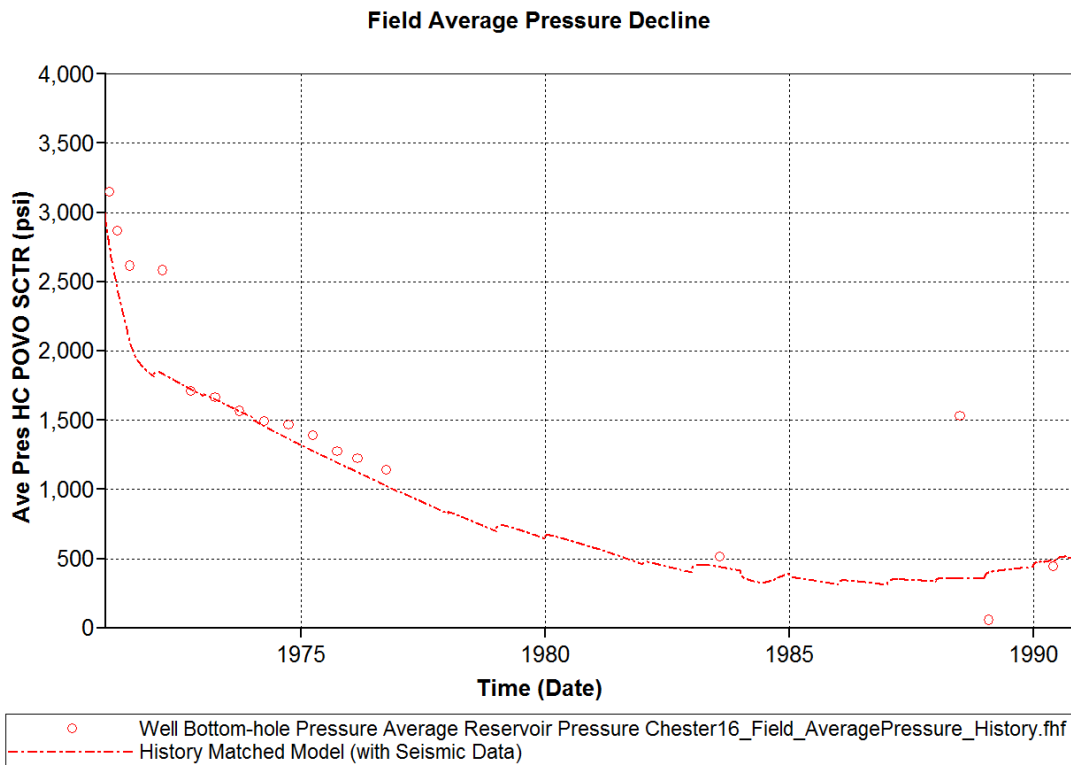


Figure 4-82. The average reservoir pressure decline in the alternative conceptualization.

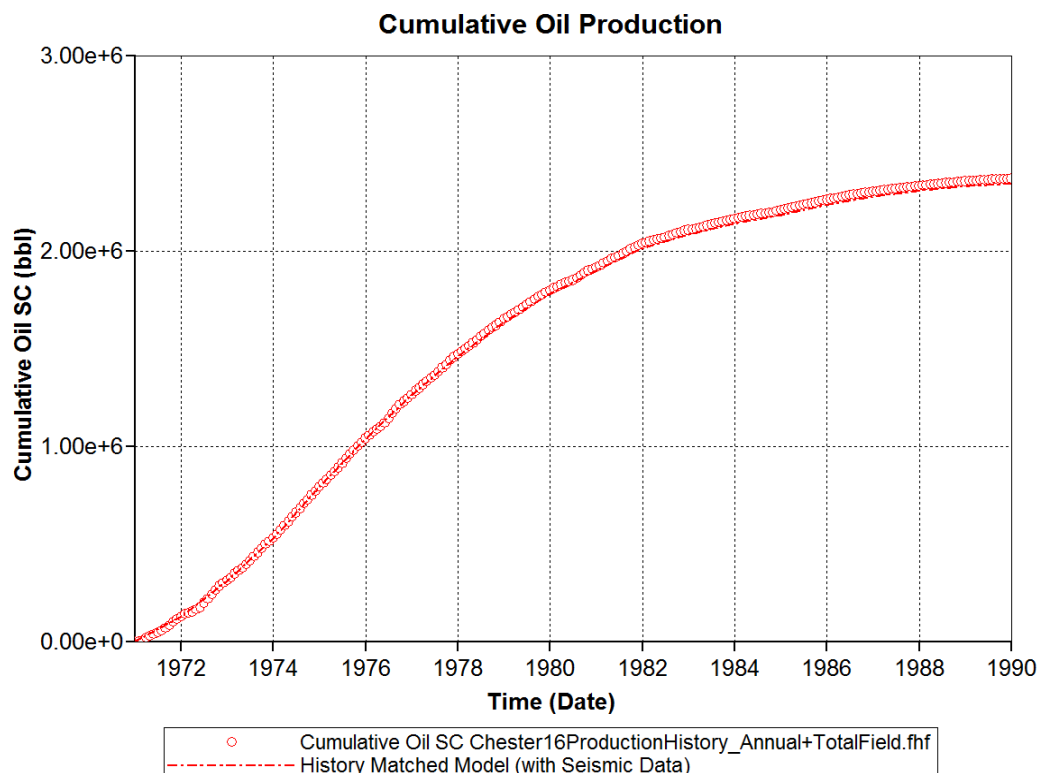


Figure 4-83. All the oil production constraints are met in the new model.

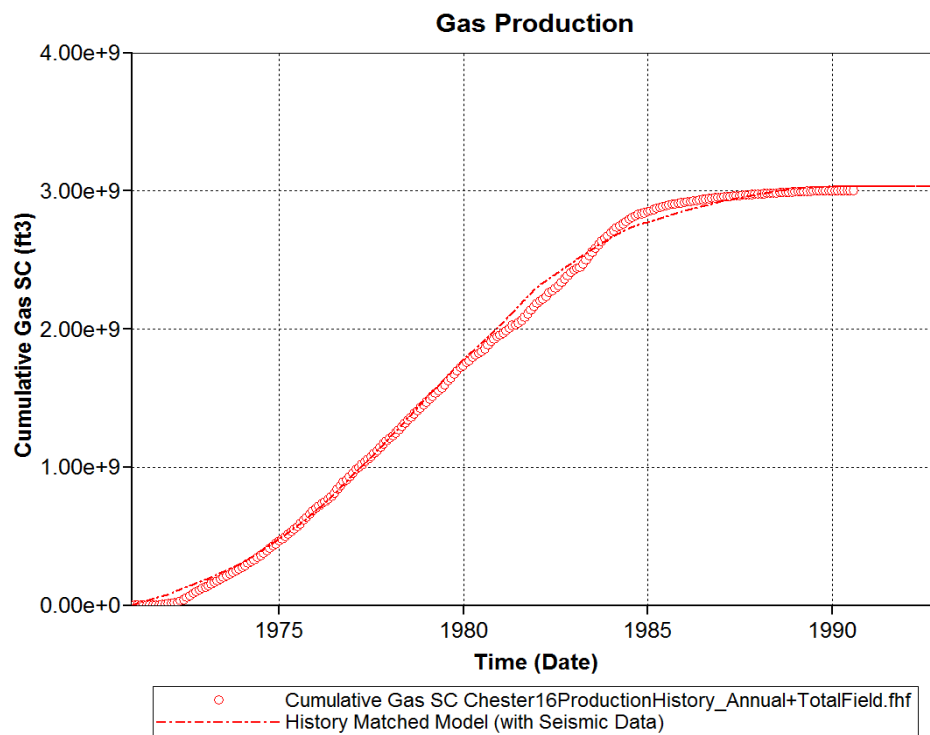


Figure 4-84. The gas production history match with the alternative conceptualization.

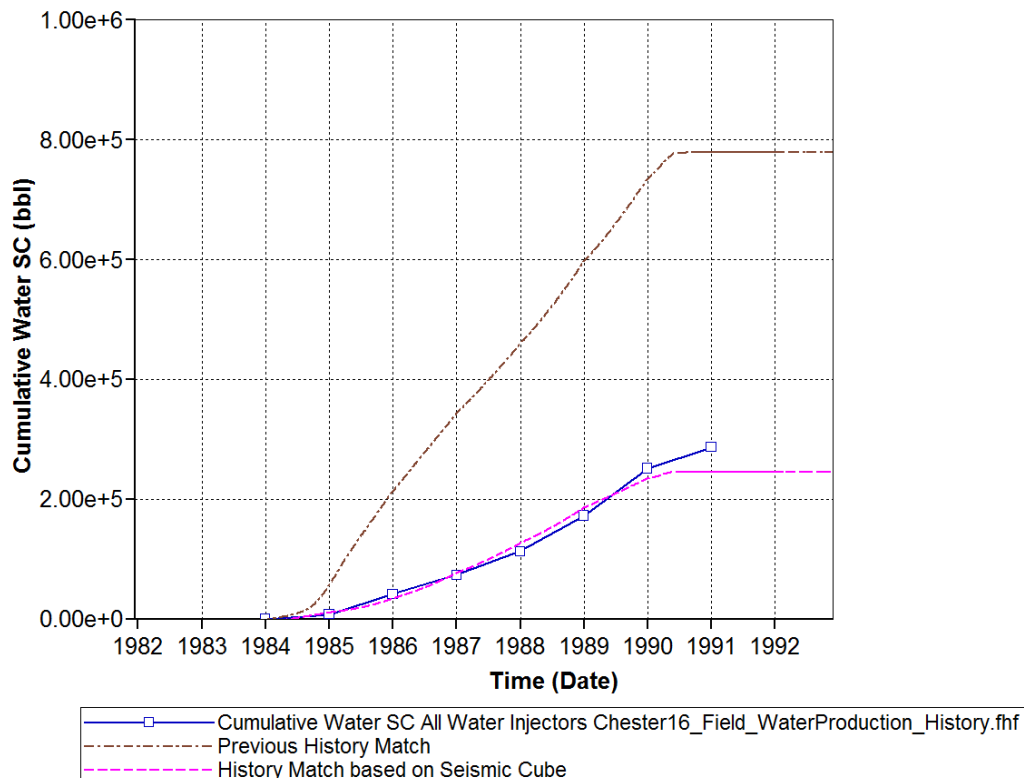


Figure 4-85. The cumulative water production from the waterflood is more closely matched in the new model.

Figure 4-86 shows that the match to the pressure in the middle of the A1 Carbonate is at the 8-16 well. The black line represents the data from the field, while the dotted line represents simulation data. The blue line tracks the total injection rate for reference. The initial pressure prior to CO<sub>2</sub> injection has been matched within 50 psi. The model also captures the timing of the first arrival of the pressure pulse from the injection closely. The end point pressure at the end of injection is higher than the field data by around 150 psi. As with the previous model, the transition from the initial condition to the final has not been replicated, and the pressure increase predicted by the model is much sharper.

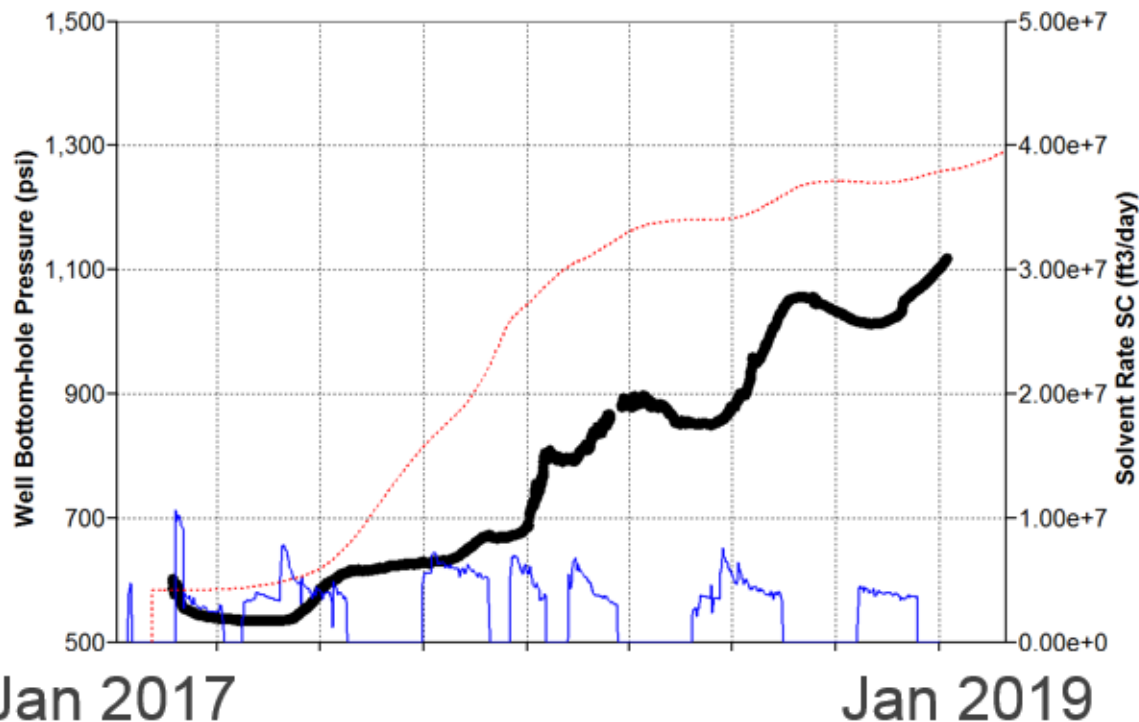


Figure 4-86. History match to the pressure response at the A1 carbonate, as measured at the 8-16 gauge, with the new model.

Figure 4-87 through Figure 4-89 show the matches to the pressure in the Brown Niagaran at the 8-16 well (the top, middle and bottom respectively). The pink line represents the data from the field, while the dotted line represents simulation data. The colored lines at the bottom tracks the total injection rate for reference. The initial pressure prior to CO<sub>2</sub> injection has been matched within 50 psi for the top and bottom of the Brown Niagaran, and nearly exactly for the middle of the Brown Niagaran. The end point pressure at the end of injection predicted by the new model is consistently around 150 psi higher. In addition, the transition from the initial condition to the final has not been replicated, nor has the pressure pulse arrival time.

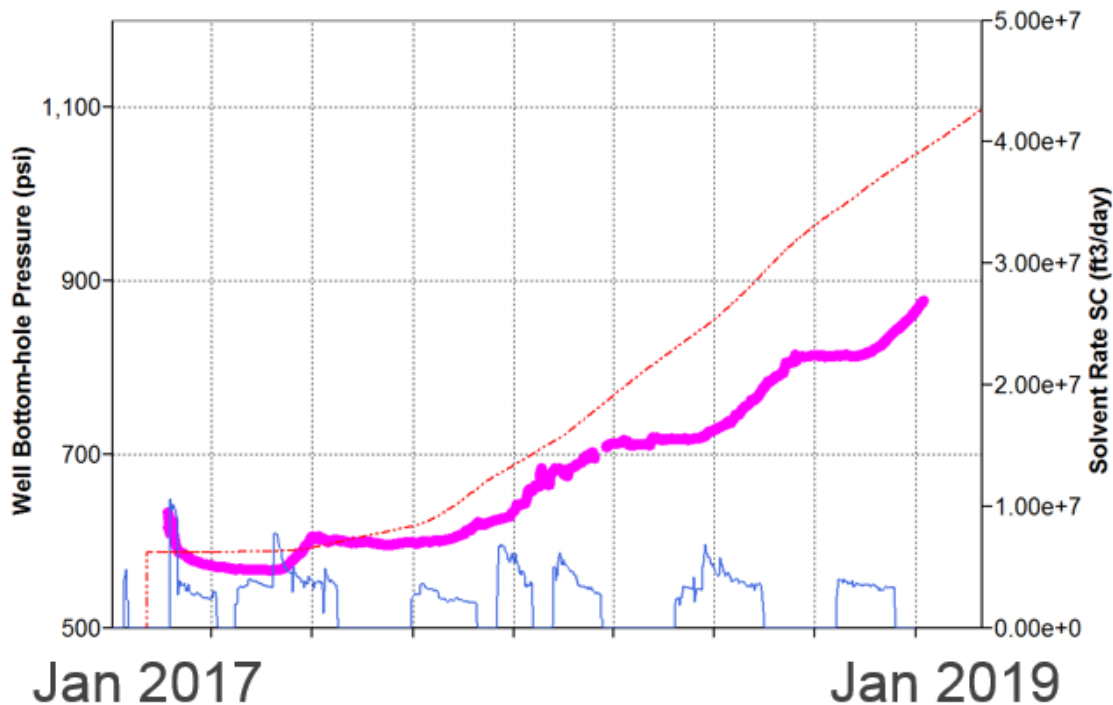


Figure 4-87. History match to the pressure response at the top of the Brown Niagaran, as measured at the 8-16 gauge, with the new model.

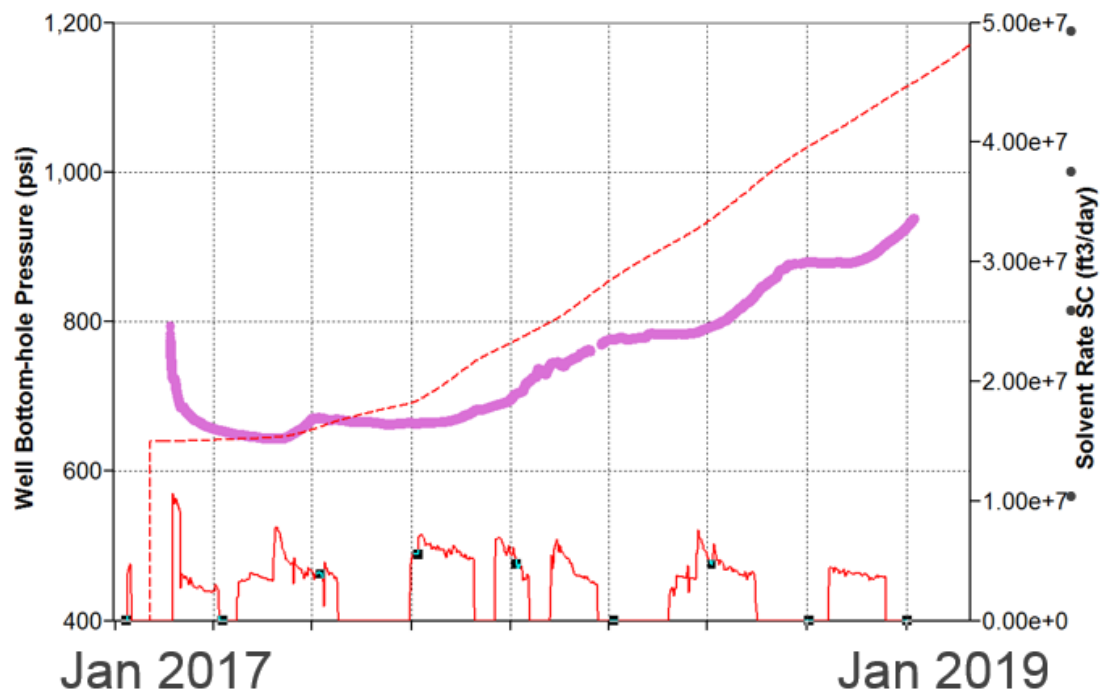


Figure 4-88. History match to the pressure response at the middle of the Brown Niagaran, as measured at the 8-16 gauge, with the new model.

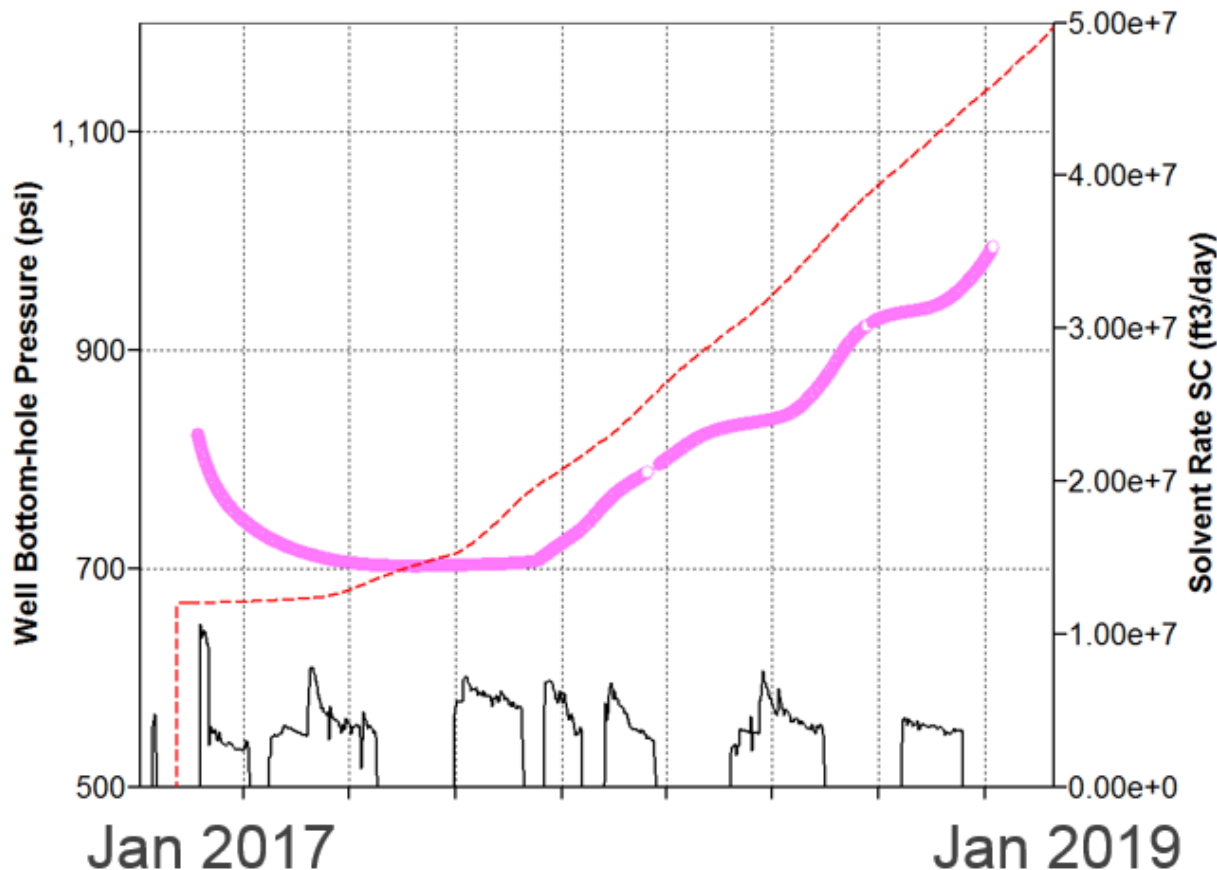


Figure 4-89. History match to the pressure response at the bottom of the Brown Niagaran, as measured at the 8-16 gauge, with the new model.

Although the permeability field in the new model represents a greater volume of information and may be viewed with a greater degree of confidence, this did not directly translate to a better history match to the CO<sub>2</sub> injection period. This may be related to the initial water saturation distribution. In the previous model, the overall water production from waterflooding was higher, and this greater volumetric withdrawal led to an underprediction of the initial vertical pressure gradient (before CO<sub>2</sub> injection) in the Brown Niagaran, as compared to field data. With the new model, its initial water saturation distribution (stemming from a different porosity-permeability distribution) resulted in more reasonable water production during the waterflood, and a closer match to the initial vertical pressure gradient. The nature of the pressure increase in Brown Niagaran subsequently also changed drastically. This reflects the fact that the water (and hydrocarbon) saturation distribution has a significant effect on how the pressure pulse from CO<sub>2</sub> injection propagates in the reservoir. As a result, compositional simulation (rather than pseudo-miscible black-oil) is warranted in order to better capture the intricacies of pressure behavior within the reservoir. Reusing the same CO<sub>2</sub> injection rate allocations to the perforations in the new model (as overall the volumetric allocation itself was deemed justifiable), instead of generating a new set of adjustments may have contributed to this phenomenon. In addition, instead of an angled high permeability geologic feature that rapidly transmits the pressure generally throughout the Brown Niagaran, a different conceptualization that retains more of the original heterogeneity using but employs a dual-porosity/dual-permeability feature may be better suited to capturing pressure propagation in the reservoir better.

With the twin caveats that the model overpredicts the pressures by around 150 psi throughout the model and is more suited to longer-term forecasts than short-term forecasts, it is still sufficiently calibrated to estimate oil and gas production rates from CO<sub>2</sub>-EOR (likely to be slightly optimistic) and more importantly, to evaluate reservoir management strategies. Overall, the history match to the primary, secondary, and CO<sub>2</sub> fill-up cases is considered satisfactory. This new model, which integrates log, core, and seismic data, was used as the basis to evaluate various CO<sub>2</sub>-EOR scenarios.

## 4.5 Forecasting Simulations

Both models described above are similar in terms of the primary driver of the history match, and the ranges of porosity-permeability throughout the model. With greater flexibility with time and computational resources, a preferred alternative would be to forecast production from multiple equi-probable models in order to ascribe a range of production outcomes from each strategy to design the most optimal exploitation method for the Chester 16. For this project, however, a deterministic analysis was more appropriate.

The match to the pressure increase from the injection period is not as strong as with the original “layer-cake” conceptualization; yet it is known that the alternative conceptualization has integrated a greater volume of data. Additionally, the more patchy and distributed nature of the permeability streak in the alternative conceptualization lends itself to greater geologic plausibility. Furthermore, the overprediction of the pressure response to CO<sub>2</sub> injection in alternative conceptualization is limited to around 250 psi, and this is understood to translate into more optimistic oil rate predictions (likewise for CO<sub>2</sub> storage). To determine the optimal exploitation strategy for the Chester 16, the decision was made to err on the side of geologic plausibility and account for the overprediction by the alternative conceptualization by using its forecasts to rank various strategies (instead of a hard estimate of future oil rates).

The model that integrated seismic data into an alternative conceptualization was thus used as the basis of all the projections discussed below.

### 4.5.1 CO<sub>2</sub>-EOR Scenarios

The second numerical model that integrated seismic data into the geologic property distributions is thought to reasonably capture the oil, gas and water flow behavior in the Chester 16. It is noted that while the model likely over-predicts the pressurization with CO<sub>2</sub> injection, the error is not egregious and is limited to around 250 psi. While this effect is expected to translate to systematically more optimistic oil rates from CO<sub>2</sub>-EOR forecasting simulations, these simulations can still be still effective in ranking oil production from various CO<sub>2</sub>-EOR injector producer configurations, especially over the long-term (more than five years).

Oil recovery from CO<sub>2</sub>-EOR was forecasted via 10 different injector producer configurations (scenarios). These scenarios are listed in Table 4-18.

**Table 4-18. The ten scenarios evaluated by the forecasting simulations.**

Scenario	CO <sub>2</sub> Injectors		Oil Producers	
	# of Injectors	Location and Target Formation	# of Producers	Location and Target Formation
1	1	Horizontal well along top 10ft, A1 only	2	North and south edges of reef; BN only
2	1	Vertical well through reef center, A1+BN	2	North and south edges of reef; A1+BN
3	1	Vertical well through reef center, A1 only	2	North and south edges of reef; BN only
4	2	North and south edges of reef; A1+BN	1	Vertical well through reef center, A1+BN
5	2	North and south edges of reef; A1 only	1	Vertical well through the reef center, BN only
6	1	Vertical well through reef center, A1 only	2	North and south edges of reef; A1 only
7	2	North and south edges of reef; A1 only	1	Vertical well through reef center, A1 only
8	1	South edge of reef, A1 only	2	North and south edges of reef; BN only
9 <sup>a</sup>	1	South edge of reef, A1 only	1	North edges of reef; BN only
10 <sup>b</sup>	1	Horizontal well along top 10ft, A1 only	2	North and south edges of reef; BN only

- a. Scenario 9 is nearly identical to Scenario 8, except that the production well in the southern pod is shut-in.
- b. Scenario 10 is identical to Scenario 1, except that the location of the production well in the northern pod is different.

These configurations were designed/studied with the intent of determining the optimal depletion strategy for the Chester 16. While 6-16, 8-16 and 1-16 are existing wells, 7-16, 8-16 Rev, and the horizontal well (Scenario 1 and 10) represent hypothetical wells that need drilling and completion. The 8-16 Rev is kicked off from the original 8-16 well directionally to target more of the center of the northern pod.

Scenario 1 represents a CO<sub>2</sub> injection through a horizontal well that generally spans the length of the spine of the reef at the top of the A1 Carbonate, accompanied by production in the Brown Niagaran through the 7-16 and 8-16 wells. This is a vertical flood. Scenario 2 represents CO<sub>2</sub> injection through a vertical well in the center of the reef (1-16) pushing oil outward toward the two producers, 6-16 and 8-16 Rev (a direction drilled from the 8-16 well), in a horizontal sweep of both A1 Carbonate and the Brown Niagaran. Scenario 3 represents injection only in the A1 Carbonate, and in the center of the reef, and producing in the Brown Niagaran through the 6-16 and 8-16 Rev wells. Scenario 4 is the inverted form of Scenario 2, with two outside injectors (6-16 and 8-16 Rev) pushing the oil inward toward the center of the reef (1-16 producer well), in a horizontal sweep. Similarly, Scenario 5 complements Scenario 3. While Scenario 3 consists of one injector sweeping oil toward two producers in a vertical flood, Scenario 3 consists of two outward injectors (6-16 and 8-16 Rev) in the A1 carbonate and pushing down oil for production from the center of the reef (1-16 well) in the Brown Niagaran. Scenarios 6 and 7 study the

impact of ignoring the Brown altogether and focus on producing only from the A1 Carbonate. Scenario 6 represents CO<sub>2</sub> injection in the center of the A1 Carbonate sweeping the oil outward toward the 6-16 and 8-16 Rev wells. Scenario 7 complements Scenario 6 by inverting the configuration. The 6-16 and 8-16 Rev wells sweep the oil toward the central producer (1-16 well). Scenario 8 explores the impact of simply continuing to inject in the present 6-16 well but only in the A1 Carbonate and producing from the 7-16 and 8-16 Rev well in the Brown Niagaran. Scenario 9 replicates Scenario 8 but without the 7-16 well, which targets the southern pod. Finally, Scenario 10 replicates Scenario 1 but with the 8-16 Rev well instead of the 8-16 well. Figure 4-90 to Figure 4-99 depict each scenario and the location of the wells.

The 10 scenarios collectively enable assessing the following questions:

- Is CO<sub>2</sub> injection through a horizontal well optimal?
- Which sweep (horizontal or vertical) is optimal for this field?
- Are two producers better than one?
- Where should the injectors/producers be placed?
- Should production be from both the A1 and Brown Niagaran or focused on one?

The forward simulation for each scenario followed the same constraints. All injectate was with a rate constraint that was capped at 6 MMSCFD (or 315 tons per day). This represents the maximum capacity of the surface facilities available in the field. Note also that where the injection was via two wells, each injector had a 3 MMSCFD constraint instead. More importantly, each injector well also included a monitor for the bottomhole pressure; the simulator throttled the injection rate whenever the bottomhole pressure rose beyond 4000 psi, which was the regulatory constraint for injection. The goal was to attain an average reservoir pressure of (at least) 1300 psi (MMP [minimum miscibility pressure]) in both the A1 Carbonate and the Brown Niagaran for optimal CO<sub>2</sub>-Oil mixing conditions. Note that if the simulation results show that the average reservoir pressure cannot be maintained at MMP, it means that the higher injection rates (or lower production rates) are required, rendering that strategy unviable. The voidage ratio was also maintained at 1 at reservoir conditions, meaning that total fluid rates of the injected and produced volumes were to be kept approximately equal for pressure maintenance. Note that all simulations included a fill-up period to Jan 2020 injecting around 5.5 BSCF before commencing EOR. Fill-up continued with the existing 6-16 injector well until May 2019, when the injectors of the proposed strategy took over and injected the remaining quantity evenly until January 2020. CO<sub>2</sub>-EOR will commence in Feb 2020 and continue for 15 years. The producer wells do not have any rate constraint and produce at the lowest bottomhole pressure possible.

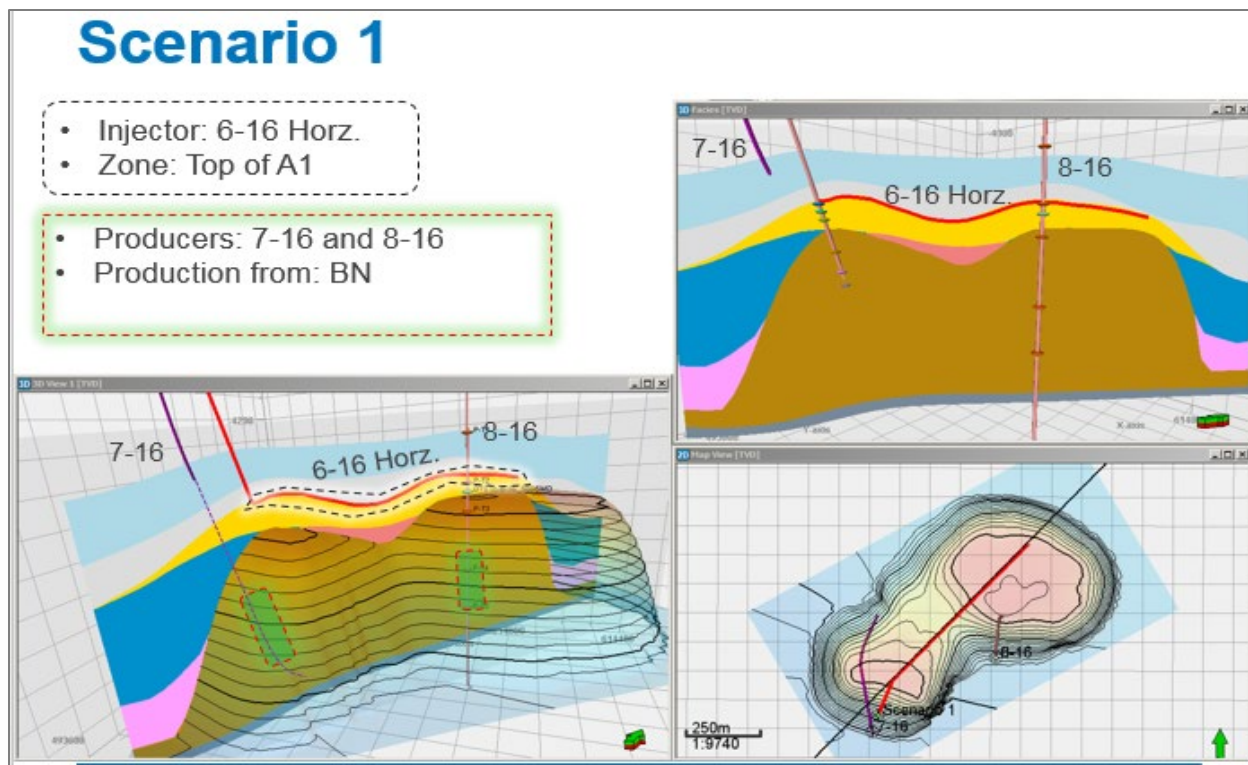


Figure 4-90. The injector producer configurations of Scenario 1 are shown via various cross-sections through the Chester 16.

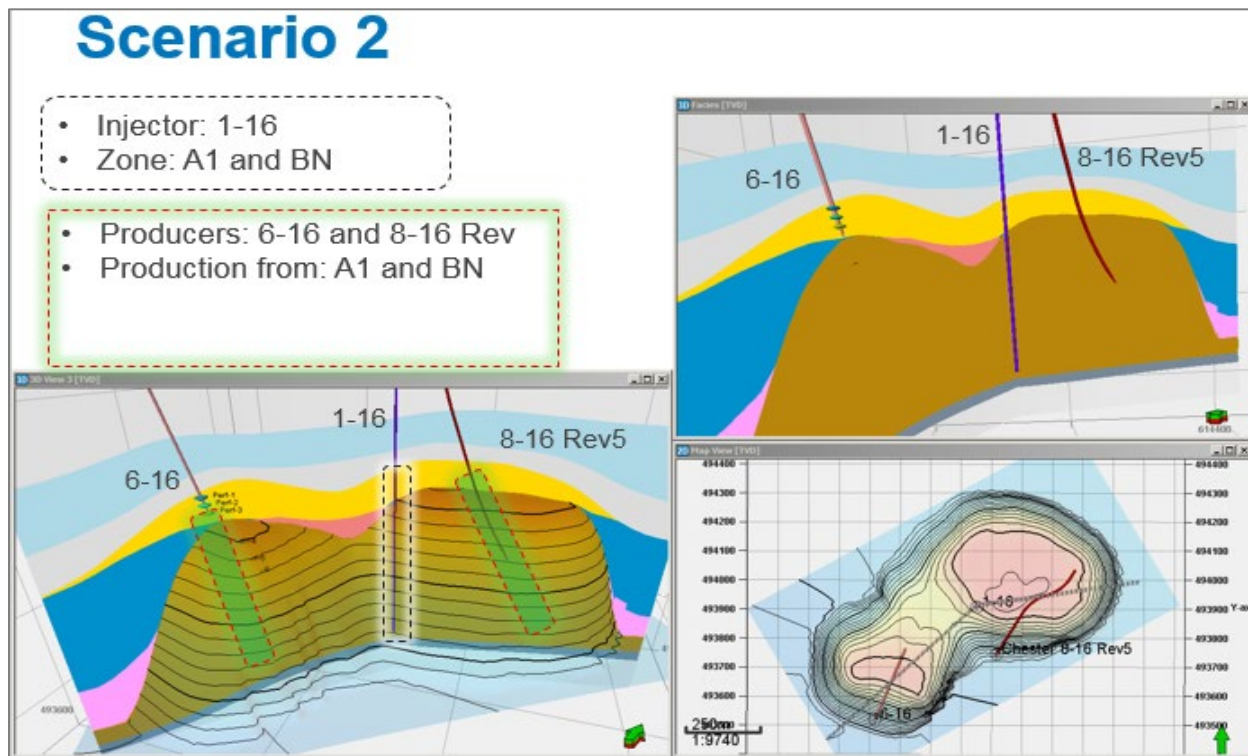


Figure 4-91. The injector producer configurations of Scenario 2 are shown via various cross-sections through the Chester 16.

## Scenario 3

- Injector: 1-16
- Zone: all of A1

- Producers: 6-16 and 8-16 Rev
- Production from: BN

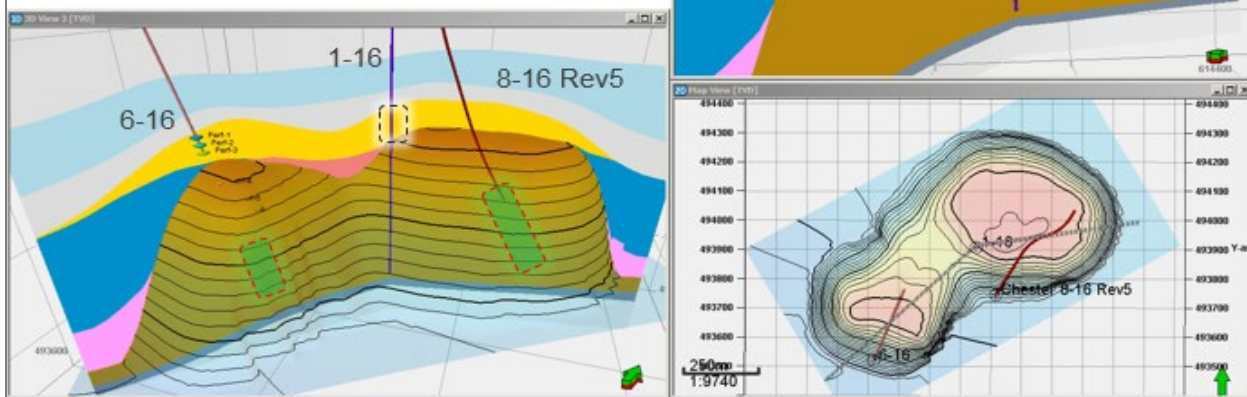


Figure 4-92. The injector producer configurations of Scenario 3 are shown via various cross-sections through the Chester 16.

## Scenario 4

- Injectors: 6-16 and 8-16 Rev
- Zone: A1 and BN

- Producers: 1-16
- Production from: A1 and BN

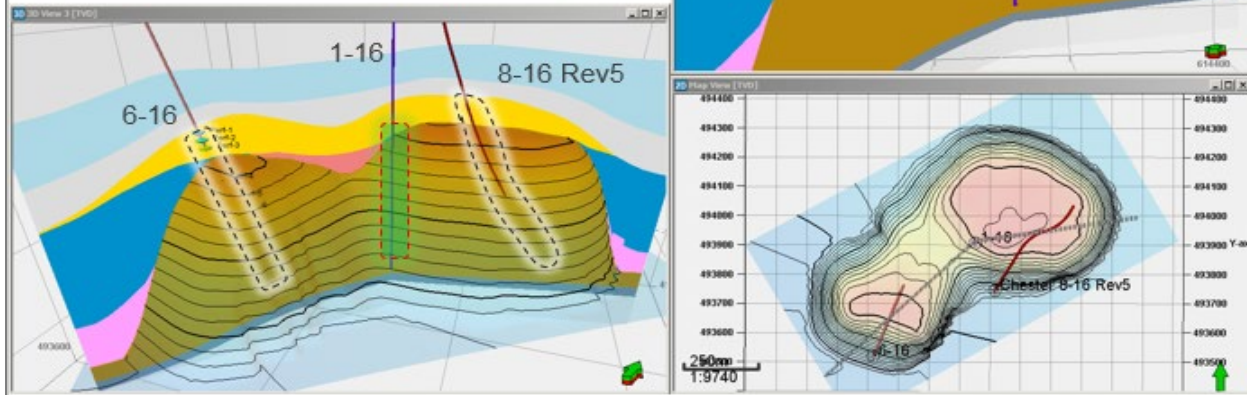


Figure 4-93. The injector producer configurations of Scenario 4 are shown via various cross-sections through the Chester 16.

## Scenario 5

- Injectors: 6-16 and 8-16 Rev
- Zone: All of A1

- Producers: 1-16
- Production from: Mid to low BN

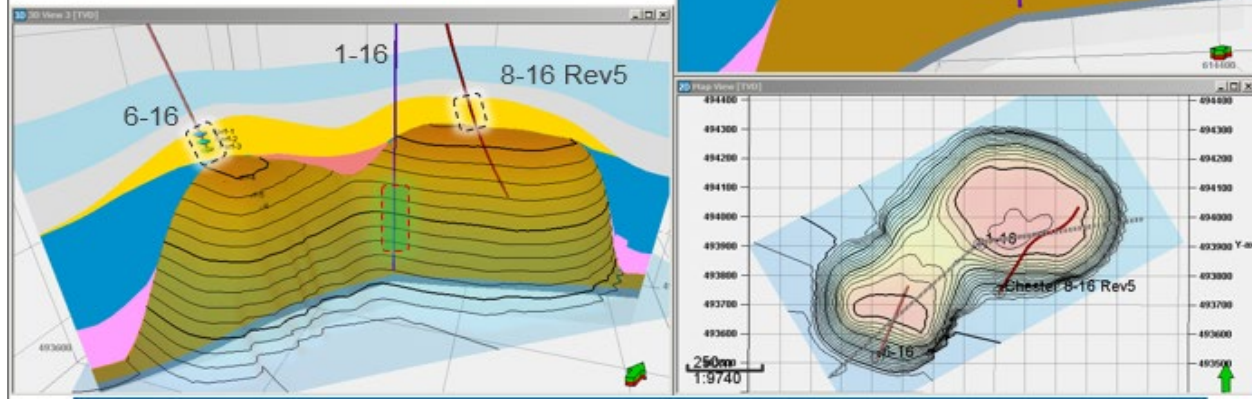


Figure 4-94. The injector producer configurations of Scenario 5 are shown via various cross-sections through the Chester 16.

## Scenario 6

- Injector: 1-16
- Zone: All of A1

- Producers: 6-16 and 8-16 Rev
- Production from: All of A1

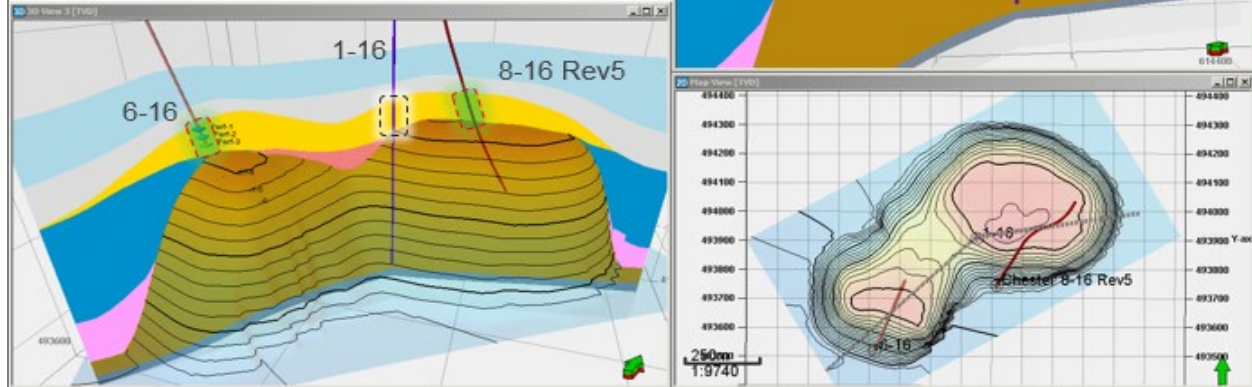


Figure 4-95. The injector producer configurations of Scenario 6 are shown via various cross-sections through the Chester 16.

## Scenario 7

- Injectors: 6-16 and 8-16 Rev
- Zone: All of A1

- Producers: 1-16
- Production from: All of A1

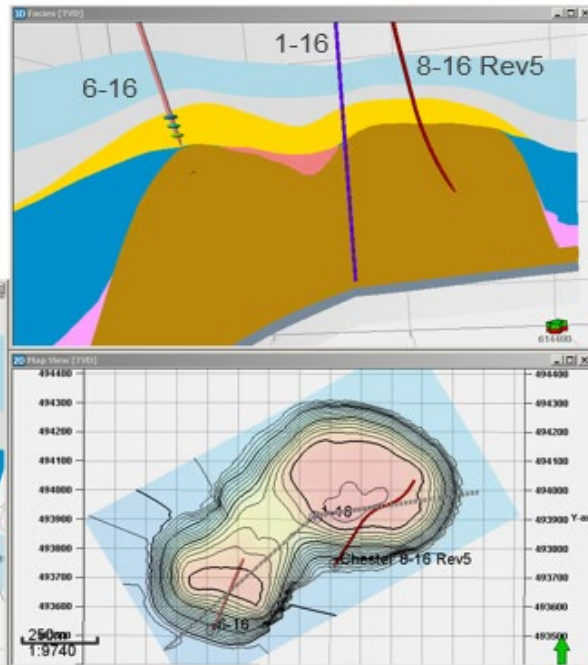


Figure 4-96. The injector producer configurations of Scenario 7 are shown via various cross-sections through the Chester 16.

## Scenario 8

- Injector: 6-16 "As Is" (no Horiz.)
- Zone: A1 Only

- Producers: 7-16 and 8-16 Rev
- Production from: BN

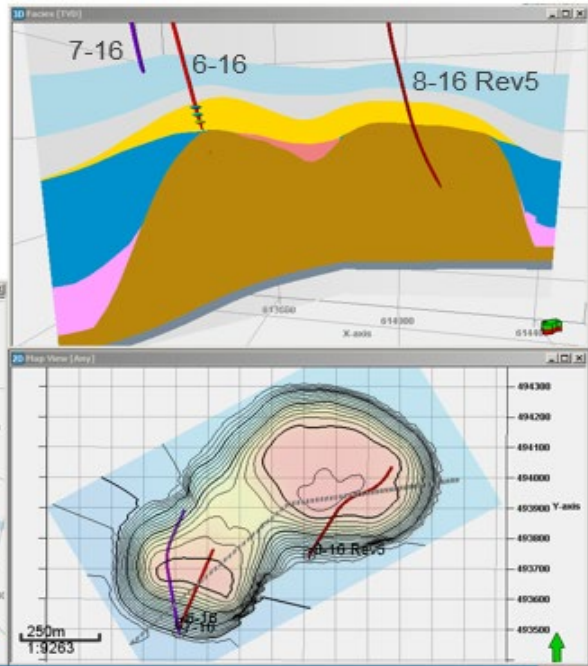


Figure 4-97. The injector producer configurations of Scenario 8 are shown via various cross-sections through the Chester 16.

## Scenario 9

*\*Like Scenario #8, but with only 8-16 rev producer.*

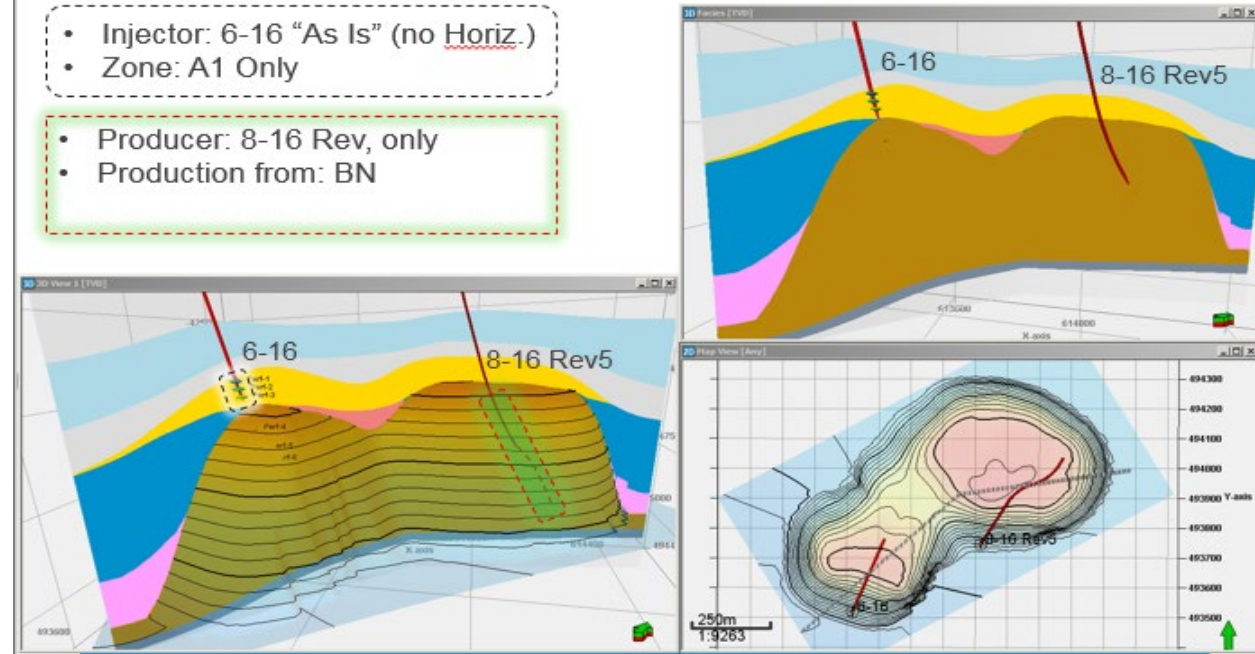


Figure 4-98. The injector producer configurations of Scenario 9 are shown via various cross-sections through the Chester 16.

## Scenario 10

*\*Like Scenario #1, but with 8-16 rev instead of 8-16.*

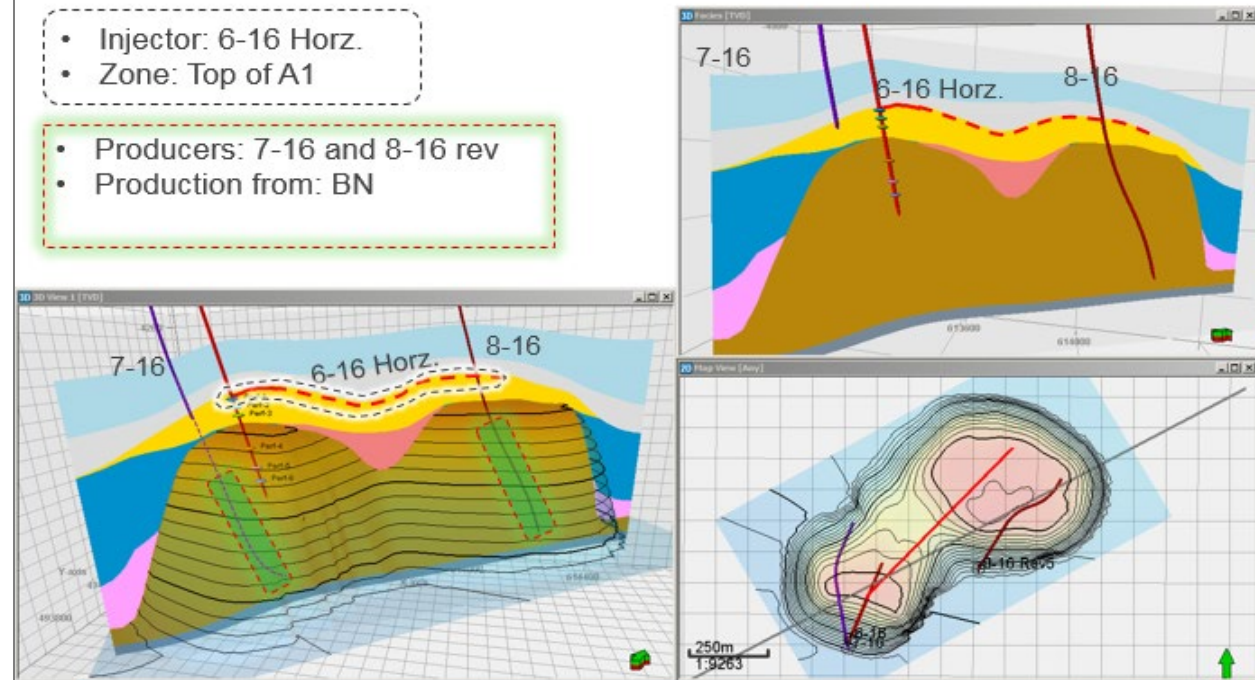


Figure 4-99. The injector producer configurations of Scenario 10 are shown via various cross-sections through the Chester 16.

#### 4.5.2 Results and Discussion

The key simulation outputs in ranking the various scenarios are as follows: cumulative incremental oil recovery, cumulative CO<sub>2</sub> injection required to produce this oil, the quantity of CO<sub>2</sub> permanently stored by the end of EOR, the producing gas-oil ratio (breakthrough), and the utilization factors (measure of efficiency). We note that because a single model has been used to forecast production (based on the 10 different scenarios above), this is a deterministic analysis, and is suitable for ranking the various scenarios. The optimal scenario for carbon capture and storage (CCS) purposes would be the scenario that injects and stores the most CO<sub>2</sub>. For CO<sub>2</sub>-EOR, the optimal scenario maximizes oil recovery, while minimizing CO<sub>2</sub> injected and stored. The optimal choice for CCUS can potentially be sub-optimal for CO<sub>2</sub>-EOR and finding an option that is suitable for both requires trade-offs affecting both oil recovery and CO<sub>2</sub> storage.

Figure 4-100 summarizes the first three metrics in the list described in the earlier paragraph, with each metric normalized to the highest quantity observed across all 10 scenarios. For instance, if the greatest volume CO<sub>2</sub> injection occurs via Scenario 1, the result for all other scenarios are expressed as a percentage of this number. Scenarios 3, 8, 9, and 10 stand out for producing the most oil while accompanied with the lowest levels of CO<sub>2</sub> injection required. From these, Scenario 9 ranks best in terms of needing the lowest amount of CO<sub>2</sub> injected, and yet storing the most CO<sub>2</sub>. Scenario 9 thus appears to be optimal for both CCUS and CO<sub>2</sub>-EOR from this ranking analysis, followed by Scenario 3. A more detailed discussion is provided below. Figure 4-101 is another summary figure that shows a scatterplot showing the incremental oil recovered (x-coordinate) vs. net CO<sub>2</sub> stored (y-coordinate) from each scenario. It confirms the condition of pareto optimality, i.e.: that there is no single scenario that stands out as maximizing both parameters simultaneously.

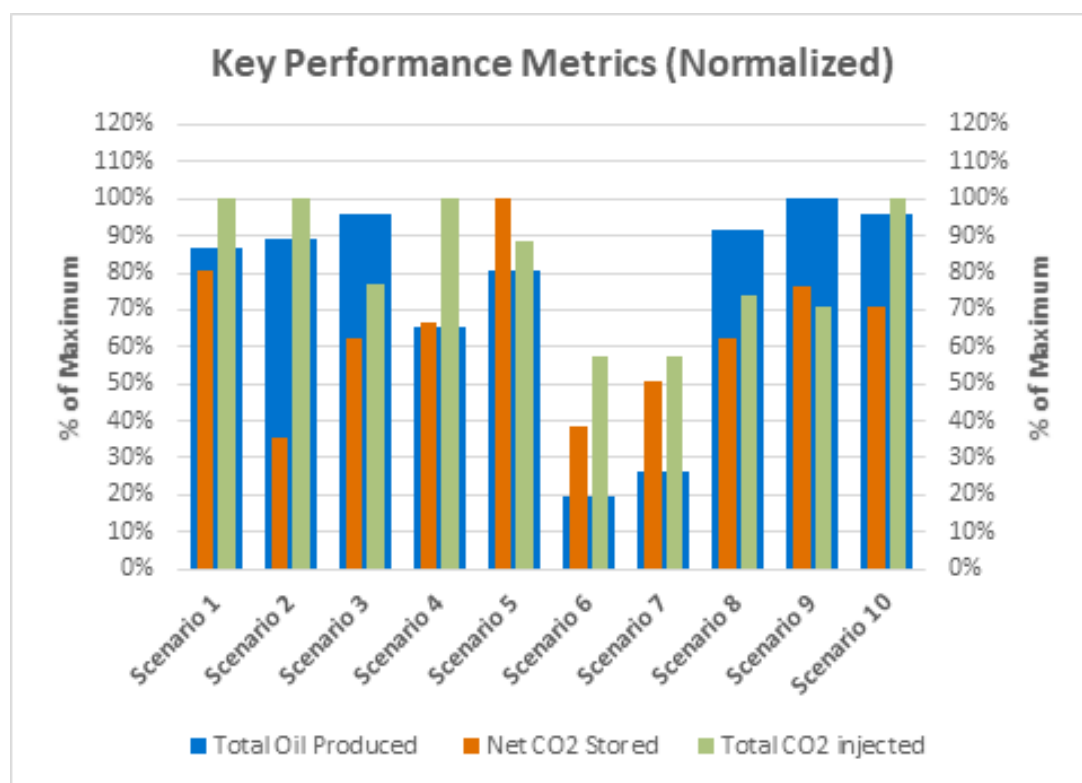


Figure 4-100. Comparison of all scenarios against each other in terms of oil recovery, CO<sub>2</sub> injection and CO<sub>2</sub> stored. Each performance metric is expressed as a percentage of the maximum observed across all 10 scenarios.

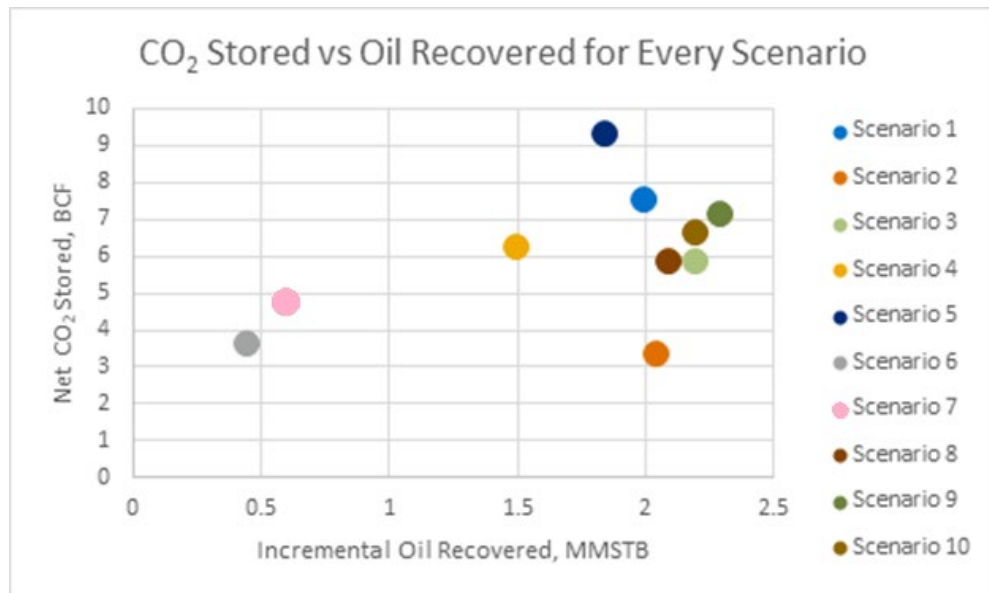


Figure 4-101. A scatterplot of cumulative oil recovered, and net CO<sub>2</sub> stored in each scenario.

Table 4-19 and Table 4-20 present a detailed summary quantifying the performance of each scenario. A few observations are made from these tables. Firstly, Scenarios 6 and 7 produce significantly lower volumes of oil from CO<sub>2</sub>-EOR over 15 years (less than 1 million STB) than the other scenarios (which produce at least 1.5 million STB), implying that the strategy of targeting only the A1 carbonate as the main source of oil production, regardless of the number/location of injectors, is not a viable strategy at all. Among the remaining configurations, Scenario 4 – which consists of two injectors horizontally sweeping the oil toward the central oil producer – is the poorest performer, producing only 1.5 MMSTB. Scenario 4 is complemented by Scenario 2 (a central CO<sub>2</sub> injector sweeping the oil horizontally outward toward the two producers), which produces significantly more oil (0.55 MMSTB more) for the same CO<sub>2</sub> injection rate. Note that Scenario 3 (vertical flood by injecting at a central zone in the A1, and producing from two wells in the Brown Niagaran), produces even more oil than Scenario 2 (2.2 MMSTB vs 2.05 MMSTB), despite having a lower injection rate (4.5 MMSCFD vs 6 MMSCFD). This is the best scenario (alongside Scenario 10). Scenario 5, which complements Scenario 3 as vertical flood with two injectors and one producer instead, in fact produces significantly less oil (2.2 MMSTB vs 1.85 MMSTB), despite injecting more CO<sub>2</sub> (4.5 MMSCFD vs 5.3 MMSCFD). Note that the horizontal well injection, Scenario 1, surprisingly, did not result in the greatest oil recovery.

**Table 4-19. Cumulative amount of oil produced with each injector producer configuration, after 15 years of EOR.**

Scenario	Total Oil Produced <sup>f</sup> (MMSTB)	Average CO <sub>2</sub> Injection Rate During EOR (MMSCFD)	Ultimate Recovery Factor (% of OOIP)
1	2.0	6	63.1%
2 <sup>a</sup>	2.05	6	63.6%
3 <sup>b</sup>	2.2	4.5	65.9%
4 <sup>a</sup>	1.5	6	55.6%
5 <sup>b</sup>	1.85	5.3	60.7%
6 <sup>c</sup>	0.45	3	40.6%
7 <sup>c</sup>	0.6	3	43.2%
8	2.1	4.2	64.5%
9 <sup>d</sup>	2.3	4.1	67.5%
10 <sup>e</sup>	2.2	6	65.9%

- a. Horizontal sweep scenario.
- b. Vertical sweep scenario.
- c. Target A1 Carbonate only.
- d. Scenario 9 is nearly identical to Scenario 8, except that the production well in the southern pod is shut-in.
- e. Scenario 10 is identical to Scenario 1, except that the location of the production well in the northern pod is different.
- f. Cumulative oil produced as a result of CO<sub>2</sub>-EOR.

**Table 4-20. Essential performance measures of each scenario relating to CO<sub>2</sub>, after 15 years of EOR.**

Scenario	Producing CO <sub>2</sub> -Oil GOR (SCF/STB)	Total CO <sub>2</sub> injected (BCF)	Total CO <sub>2</sub> produced (BCF)	Net CO <sub>2</sub> Purchased <sup>g</sup> (BCF)	Gross UF. <sup>h</sup> (SCF/BBL)	Net UF. <sup>i</sup> (SCF/STB)
1	36,000	38.3	30.8	7.5	17,000	3,800
2 <sup>a</sup>	60,000	38.3	35	3.3	15,000	1,700
3 <sup>b</sup>	36,000	29.5	23.7	5.8	10,500	2,700
4 <sup>a</sup>	36,000	38.3	32.1	6.2	23,000	4,000
5 <sup>b</sup>	25,000	33.8	24.5	9.3	16,500	5,000
6 <sup>c</sup>	45,000	21.9	18.3	3.6	47,500	7,900
7 <sup>c</sup>	45,000	21.9	17.2	4.7	32,000	7,500
8	33,000	28.4	22.6	5.8	10,500	2,800
9 <sup>c</sup>	28,000	27.2	20.1	7.1	12,000	3,000
10 <sup>d</sup>	50,000	38.3	31.7	6.6	14,000	3,000

- g. Equivalent to CO<sub>2</sub> stored during EOR.
- h. Cumulative CO<sub>2</sub> injected per barrel of incremental oil produced from CO<sub>2</sub>-EOR.
- i. Cumulative CO<sub>2</sub> stored per barrel of incremental oil produced from CO<sub>2</sub>-EOR.

The twin comparisons of Scenario 2 vs Scenario 4 (both targeting a horizontal sweep), and Scenario 3 vs Scenario 5 (both targeting a vertical flood), consistently demonstrate that having only one injector is much better than having two injectors. This also indicates that optimizing producer placement may be much more important than injector placement. Next, the twin comparisons of Scenario 2 vs Scenario 3 (both having one injector), and Scenario 4 vs Scenario 5 (both having two injectors), demonstrate that a vertical sweep is a better option than a horizontal flood, since more oil is produced with lower CO<sub>2</sub> injection rates. Exploring this same comparison based on the data in Table 4-20 shows that the vertical sweep scenarios are associated with a lower producing CO<sub>2</sub>-oil ratio at the producer wells than horizontal sweep scenarios. This is because of the strong permeability streak in the middle – while it raises the overall horizontal flow capacity (transmissibility) of the Brown Niagaran, it also leads to earlier breakthrough of the CO<sub>2</sub> at the producer wells. Comparing these scenarios in Table 4-20 also shows that while vertical flooding produces greater amount of oil, it also requires a greater cumulative volume of CO<sub>2</sub> injection. Vertical flooding is thus associated with a higher gross/net utilization factor, suggesting that Scenario 3 co-optimizes both CO<sub>2</sub> storage and oil recovery. The gross (and net) utilization factor tracks the cumulative quantity of CO<sub>2</sub> injected (stored) per barrel of oil produced.

Scenarios 8, 9, and 10 were built to explore the observations made by the previous two paragraphs further. If injector placement is secondary to producer placement and a vertical flood by injecting in the A1 Carbonate appears to be better than a horizontal flood, then avoiding the drilling/completion costs associated with changing the location of the injection currently – essentially continuing to inject via the current 6-16 well as-is, and injecting into only in the A1 Carbonate – and producing from the 7-16 and 8-16 Rev wells in the Brown Niagaran (Scenario 8), should be as effective as Scenario 3. Table 4-19 shows that Scenario 8 (2.1 MMSTB) does in indeed produce nearly as much Scenario 3 (2.2 MMSTB). Scenario 1 appears to underperform in general, with even the horizontal sweep of Scenario 2 producing marginally more oil. Scenario 10 shows that switching the location of the producer from 8-16 (Scenario 1) to 8-16 Rev has a very significant effect in increasing oil production, producing nearly 200 MSTB more of oil. This is linked to the fact that the northern pod has greater volume of untapped oil remaining after the primary and waterflooding activities, and that the 8-16 Rev as a directional well access the central region of the northern pod much better than the 8-16 well. Scenario 9 tests this hypothesis further by shutting in the 7-16 well in Scenario 8 and using the 8-16 Rev as the sole producer. Scenario 9 is the most optimal scenario producing the most amount of oil at 2.3 MMSTB. This is because avoiding production/depletion from the 7-16 well results in higher overall pressures in the Brown Niagaran. This drives greater a drawdown in the 8-16 Rev well. While Scenario 8 vs Scenario 9 suggests that having one optimally placed producer is better than two, it is generally safer to have two producer wells where one can be shut-in later and that the model may over-predict rates.

While Table 4-19 and Table 4-20 present simulation results gathered at the end of 15 years of CO<sub>2</sub>-EOR, Figure 4-102 to Figure 4-104 present the field-wide cumulative oil production, oil rates, and producing CO<sub>2</sub>-oil ratios for all the scenarios as a function of time. Figure 4-102 suggests that around 2 MMSTB may reasonably be extracted from Chester 16. Figure 4-102 also illustrates that Scenario 3 with a vertical well produces almost as much oil as Scenario 10 employing a horizontal well. Figure 4-103 suggests that field-wide oil rates of more than 1000 barrels per day may be expected initially, but also that rates will rapidly decline to less than 500 barrels per day within three to four years of CO<sub>2</sub>-EOR. Figure 4-104 confirms that vertical sweep scenarios have lower and less sharply increasing producing CO<sub>2</sub>-oil ratios with time. However, it also suggests that Scenario 10 with the 8-16 Rev well, despite being a vertical flood scenario, has CO<sub>2</sub>-oil ratio behavior similar to the horizontal sweep in Scenario 2. This is likely due to the proximity of the horizontal well to the 8-16 Rev well.

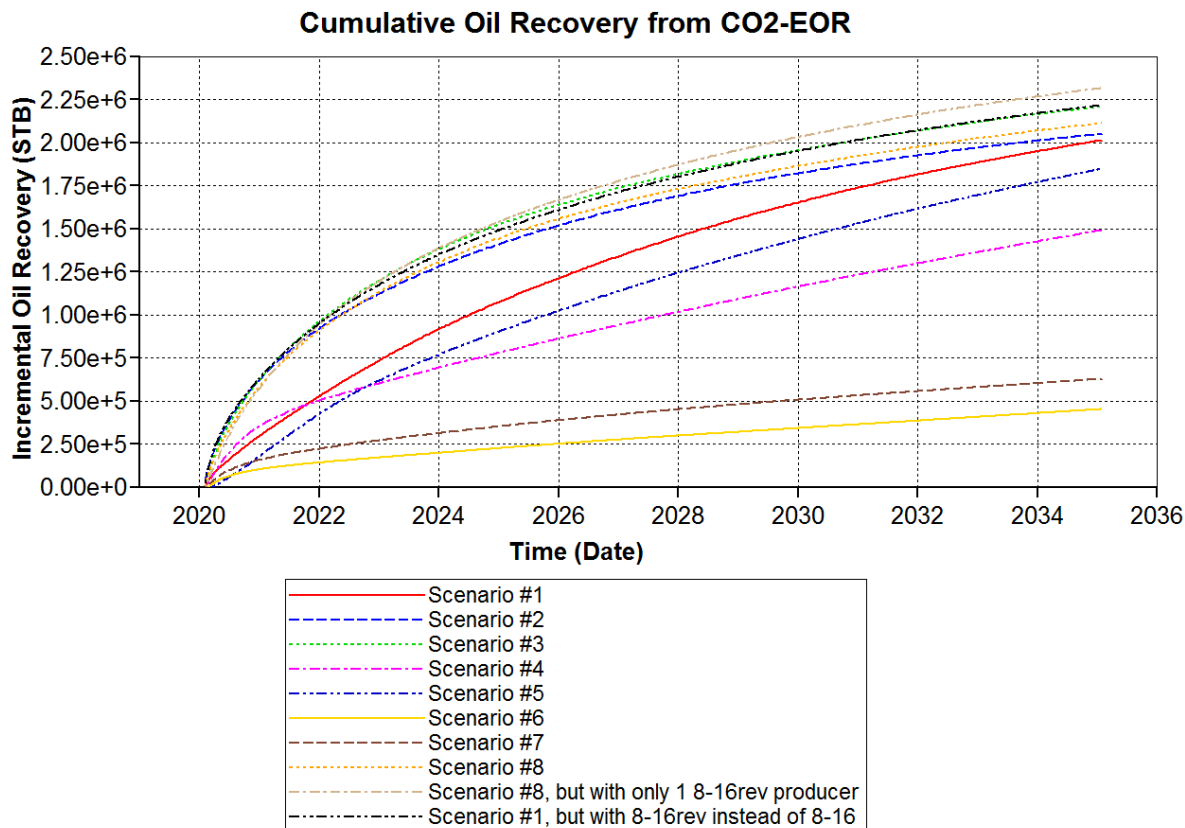


Figure 4-102. Cumulative oil recovery via CO<sub>2</sub>-EOR, from each scenario.

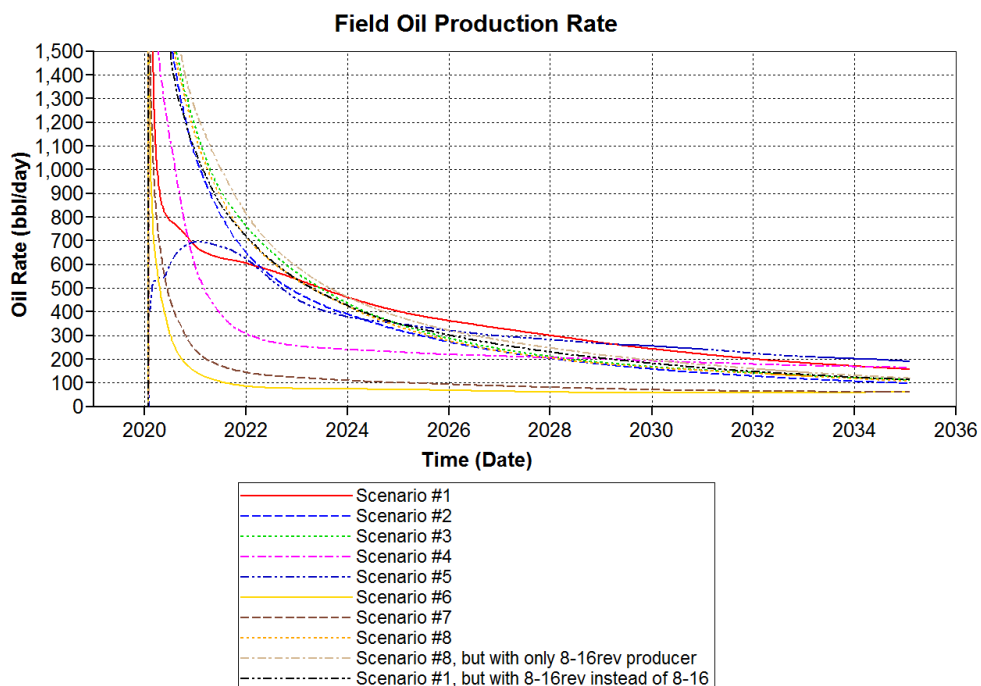


Figure 4-103. Total field oil production rate during CO<sub>2</sub>-EOR, from each scenario.

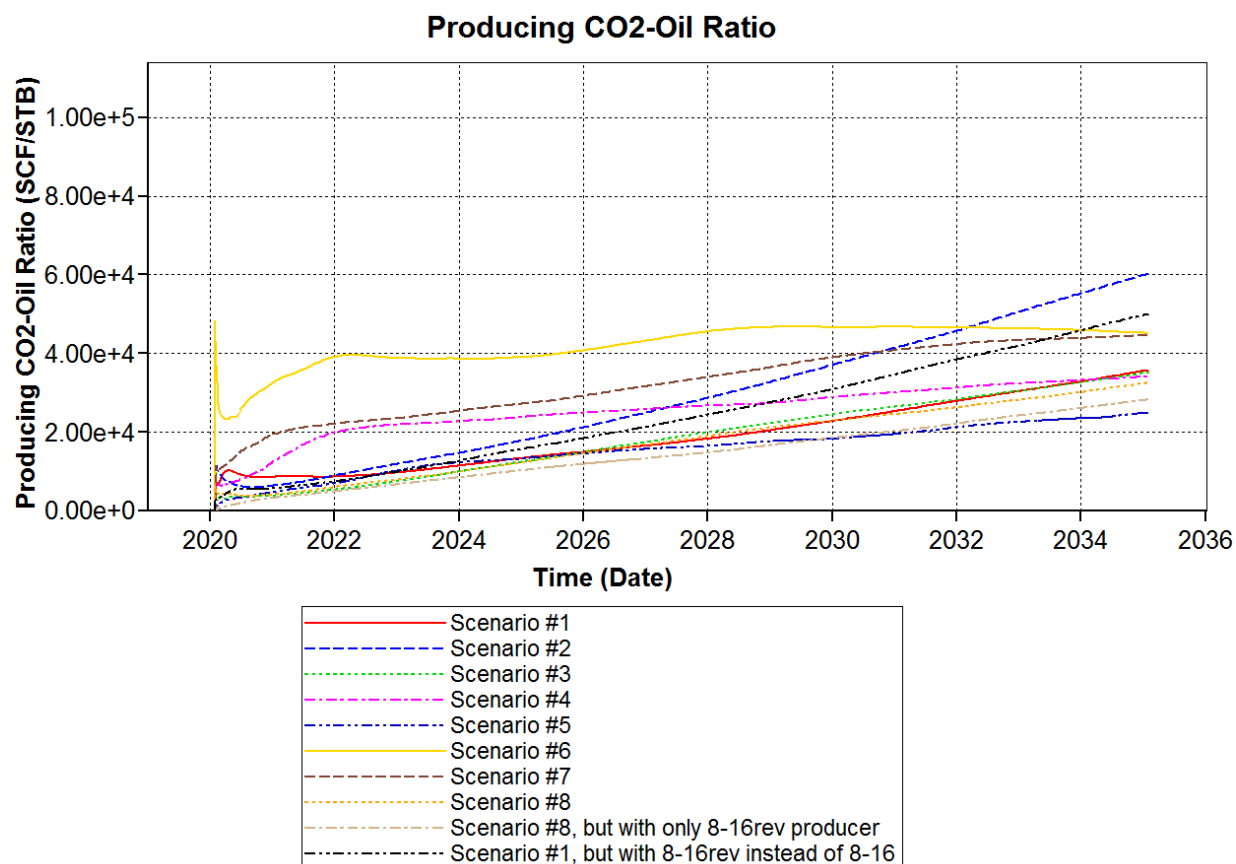


Figure 4-104. Producing CO<sub>2</sub>-oil ratio during CO<sub>2</sub>-EOR, from each scenario.

Overall, the optimal production concept may be summarized as “pressurize the A1 Carbonate, let pressure and eventually CO<sub>2</sub> bleed into the Brown Niagaran (dampening effect due to the baffle), and push the oil down toward the producers.” Employing a vertical sweep, CO<sub>2</sub> is more of a reservoir repressurizing agent in a gravity-stable downward sweep, than as a miscible solvent as typically employed in CO<sub>2</sub>-EOR. Note also that the relative homogeneity and generally high permeability of the A1 Carbonate relative to the Brown Niagaran, translates to significant confidence in the ability to inject the desired quantities into the target formation. Because injection will also not need any added isolation, injection rate allocations in future simulations will be straightforward. Note also that simulation results from the A1 Carbonate are also of greatest accuracy as compared to the Brown Niagaran.

Scenario 9 is co-optimal in terms of the highest oil production (2.3 MMSTB), lowest cumulative volume of CO<sub>2</sub> injected (27.2 BCF), and a high volume of CO<sub>2</sub> stored (7.1 BCF). Scenario 9 only requires drilling/completing the 8-16 Rev, and continuing injection from the 6-16 well. However, discussions with the asset operator highlighted that it is desirable to have multiple production wells to avoid the reliance on a single producer. Note also it is more economically desirable to minimize the quantity of CO<sub>2</sub> stored (purchased) during EOR. Finally, since (1) drilling/completing a horizontal well represents a significant capital investment, (2) Scenario 3 produces as much oil as the horizontal well scenario, and (3) the horizontal well runs the risk of inadvertently leading to high/earlier CO<sub>2</sub> breakthrough, Scenario 3 (2.2 MMSTB oil produced, 5.8 BCF CO<sub>2</sub> stored) is recommended as the most practical production and CO<sub>2</sub> storage strategy for the Chester 16. Detailed simulations results and cross-sections of this scenario are presented in Appendix B.

## 4.6 Conclusions

### Static Modeling

The SEM was successful at representing the geologic interpretations originating from the baseline characterization report and simulating key petrophysical properties in 3D space. The key findings are summarized below:

- The geologic framework was established and was consistent with formation tops and lithofacies interpretations. Petrel workflows were fully implemented wherever possible and ensure workflow documentation, traceability, and reproducibility.
- Property models showed good matches with original log data. The “permeability prediction” offered a more sophisticated method for developing permeability logs based on well porosity logs and core measured porosity and permeability. It started with fitting a power-law function between core porosity and permeability and then proceeds to characterize the variance of the permeability residuals. Essentially, the workflow captures some of the variability that basic poro-perm transforms generally miss.
- The best porosity and reservoir quality were in the upper A1 Carbonate overlying the reef structure with little to no porosity in the A1 Carbonate extending to the flanks.
- Salts and evaporites are strong geologic controls and were incorporated into the model and represent confining layers.
- Some porosity appears at the top of the Brown Niagaran, often occurs as horizontal streaks, and generally decreases toward the base. The intervals with high porosity mid-reef could be dolomitic streaks or fractured intervals.
- The water saturation property model incorporated the OWC and showed the lower portion of the reef as saturated. This SEM was used in the HCPV calculations which resulted in an estimated 9.2 million barrels of oil at reservoir (in situ) conditions. This estimate is consistent with the reported stock tank original oil-in-place (STOOIP) of 7.4 million STB.
- Advancements to the water saturation model was conducted during the DRM work, which implemented capillary pressure and the Leverett J-Function concept to develop water saturation above the OWC. This revised model was described in the DRM section.
- The SEM results show strong reservoir potential with intervals of moderate porosities and areas of low water saturation. This model can be updated and integrated with new data.
- Advancements in SEM upscaling used CONNECT UpGridTM, a Petrel plug-in, to optimize property upscaling by grouping adjacent layers together while trying to preserve flow units. Although no upscaling method is perfect, this application is an enhancement over arbitrarily changing a model’s layer count through the standard proportional layering method. The resulting upscaled 79-layer model consisted of 110,600 cells and was suitable for DRM work.
- The seismic inversion was used to update and condition property models and focused on the Brown Niagaran reef zone. Original properties from remaining model zones were maintained. With this update, a higher porosity trend was noted within the Brown Niagaran and had a trend that that dipped to the SW. This trend intercepted the 5-21 well where it corresponded to a high porosity streak seen in the porosity (NPHI) log response.

### History Matching

- Multiple lines of evidence suggest the possibility of an angular high permeability zone in the Brown Niagaran that is otherwise surrounded by low background permeability.
- Injecting into the more homogeneous, high permeability A1 Carbonate is likely a better option than running the risk of potential injectivity issues with the highly heterogeneous Brown Niagaran.
- Developing a dual-porosity, fully compositional model would be useful in developing more detailed process understanding of CO<sub>2</sub> transport and CO<sub>2</sub>-oil mixing in the reservoir.
- The challenges calibrating the model to pressure data from the CO<sub>2</sub> fill-up period likely translate to optimistic forecasts of oil recovery and CO<sub>2</sub> storage. The model is most suitable for ranking various injection strategies.
- Rock property trends derived from seismic data were highly effective in constraining the static model and earlier integration/application of such data may have shortened/simplified the history matching process.
- Operational conditions that resulted in unknown CO<sub>2</sub> injection rate allocations to the perforations introduced significant uncertainty to the model. This uncertainty, although somewhat mitigated by the semi-quantitative interpretation of the DTS data, retains a high degree of impact on the model, as exemplified by the mismatch of the predicted pressures at the 8-16 well to the recorded pressures.
- A more quantitative attempt at estimating CO<sub>2</sub> rate allocations (e.g. history matching the temperature profile recorded at the 8-16 well via non-isothermal compositional simulation) may improve the quality of the history match.

### Forecasting

- A gravity-stable vertical sweep, targeting CO<sub>2</sub> injection in the A1 Carbonate and production in the Brown Niagaran, is likely the most optimal development strategy.
- Chester 16 is more sensitive to optimal producer placement than injector placement.
- A producer penetrating the middle of the northern pod is beneficial since this region contains most of the unswept oil from the waterflood.
- Scenario 3, with a vertical injector, performs just as well as a horizontal injector in terms of oil production.
- While a horizontal well may enable reaching target fill-up quantity sooner or circumvent any potential injectivity problems, it may inadvertently cause earlier CO<sub>2</sub> breakthrough depending on the location and direction of the well with respect to the producers.
- Due to the difficulty in calibrating the model to the CO<sub>2</sub> fill-up period, up to 2.3 MMSTB of oil may be recovered from the Chester 16 and up to 9.3 BCF of CO<sub>2</sub> may be stored.
- There is merit in employing only a single producer (rather than two) in maximizing oil production from a reservoir pressure management perspective.

While Scenario 9 is preferable for co-optimizing oil recovery and CO<sub>2</sub> storage, Scenario 3 is likely to be a more practical approach providing similar results.



## 5.0 Dover-33 Geomechanics

### 5.1 Introduction

Understanding the geomechanical outcomes of CO<sub>2</sub> sequestration into geological formations is necessary since it affects CO<sub>2</sub> injectivity, reservoir mechanical integrity, and safety of the potential injection site (Akono et al., 2019; Bachu et al., 2007; Bradshaw et al., 2007; Fang, Khaksar, & Gibbons, 2012; Raziperchikolaee, Alvarado, & Yin, 2013). To ensure that the mechanical integrity of the reservoir-caprock system is maintained during injection, in situ stress changes caused by pore pressure changes (i.e., poroelastic effect of injection) should be investigated (Kaldi et al., 2011). Poroelastic effects of injection determine the final stress state in the reservoir as a precursor to evaluating tensile and shear failure potential (Fjar, Holt, Raaen, Risnes, & Horsrud, 2008; Rutqvist, Birkholzer, & Tsang, 2008). The final in situ stress also limits practical injectivity of the reservoirs (Anderson & Jahediesfanjani, 2019; Raziperchikolaee et al., 2013; Raziperchikolaee, Kelley, & Gupta, 2019). Ground surface uplift and induced seismicity, which could have a detrimental effect on the safety of the injection site and its surrounding area, also depends on the poroelastic effect of injection as well as stiffness of the reservoir and surrounding rocks (Cappa & Rutqvist, 2011b; Li & Laloui, 2016; Mazzoldi, Rinaldi, Borgia, & Rutqvist, 2012; Rinaldi, Vilarrasa, Rutqvist, & Cappa, 2015; Samsonov, Czarnogorska, & White, 2015).

Coupled hydromechanical modeling is typically used to evaluate the poroelastic effect of injection, as well as the resulting geomechanical outcomes, such as the potential for fracturing in reservoirs, analyzing slippage along faults, surface uplift, and associated seismicity (Ahmadinia, Shariati, Andersen, & Sadri, 2019; Le Gallo, 2016; Pereira, Roehl, Laquini, Oliveira, & Costa, 2014; Rinaldi & Rutqvist, 2013; Rutqvist, 2012; Rutqvist et al., 2008; Rutqvist, Vasco, & Myer, 2010; Rutqvist, Wu, Tsang, & Bodvarsson, 2002). Different numerical approaches including finite element method, finite difference method, discrete element method, and boundary element method have been used to address in situ stress changes and rock deformation (Nguyen, Hou, Bacon, & White, 2017; Raziperchikolaee, Alvarado, & Yin, 2014; Tenthorey et al., 2013; Tran, Nghiem, Shrivastava, & Kohse, 2010; Vidal-Gilbert, Nauroy, & Brosse, 2009; Yin, Dusseault, & Rothenburg, 2007). Combinations of different methods have also been developed to address the poroelastic response of injection. One commonly used tool is TOUGH-FLAC modeling, which is based on linking the finite-volume code for simulating multiphase fluid flow (TOUGH2) with the finite difference code for simulating geomechanics (FLAC). It has been extensively used to predict stress changes might activate the faults and induce seismicity (Jeanne et al., 2014; Rutqvist et al., 2016).

Numerical simulations generally require many grid blocks, since gridding of the surrounding rock to the surface as well as the reservoir is necessary. Also, a combination of multiple equations representing multiple components of fluids and elasticity of system should be solved either together (fully coupled) or iteratively (sequentially coupled) (Settari & Walters, 2001; Tran, Nghiem, & Buchanan, 2009; Tran et al., 2010). Solving several equations over many grid blocks numerically can be computationally expensive. Analytical methods are computationally cheaper, but are typically limited to single phase fluid flow under specific geomechanics scenarios such as uniaxial compression condition, homogeneity of the system, or plane strain/stress condition (Fjar et al., 2008; Soltanzadeh & Hawkes, 2009). The alternative method, presented in this report, is to only observe the response at a subset of independent values, and then fit a statistical response surface model to those points (Mishra & Datta-Gupta, 2017; Schuetter, Ganesh, & Mooney, 2014; Schuetter & Mishra, 2015). This section studies the poroelastic responses of a closed reservoir system and develops a response surface model predicting stress changes and surface uplift during CO<sub>2</sub> storage. A Niagaran carbonate reef system is used for modeling the base case as well as an additional 146 scenarios to develop the response surface. Hundreds of such carbonate reefs exist in the Michigan Basin. As a result, the simple predictive model provides an understanding of poroelastic effect

of injection in the whole system with varying reef parameters. Also investigated is the topic of uncertainty quantification associated with poroelastic responses of a closed reservoir system using Monte Carlo simulations. Finally, experimental and field test data are used to estimate stress changes and surface uplift due to injection into the reef (Dover-33) more accurately. Results of third part show that Biot's variability should be included in the poroelastic modeling of injection to accurately predict the geomechanical response of fluid injection. Using a constant stress independent Biot's Coefficient, which is the assumption in poroelastic modeling, leads to underestimating stress change and surface uplift due to injection.

## 5.2 System Description

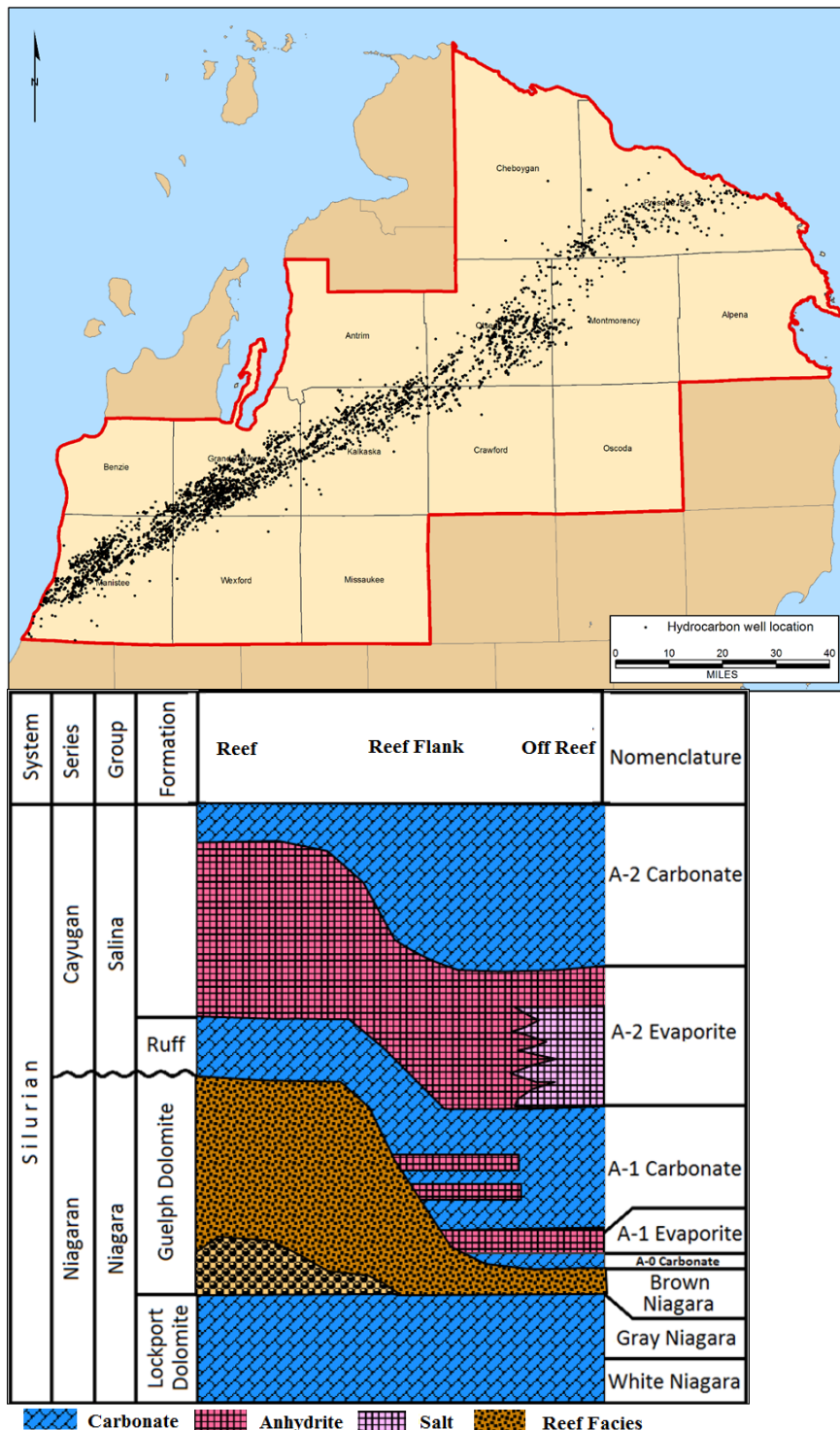


Figure 5-1. (A) Areal extend of pinnacle reefs in Northern Pinnacle Reef Trend of the Michigan Basin (B) Nomenclature and stratigraphy in Northern Pinnacle Reef Trend of the Michigan Basin.

A base case plus sensitivity scenarios were run to evaluate the poroelastic response of the closed reef with surrounding formations. CO<sub>2</sub> injection is the primary stress-inducing process that the modeling evaluates. In all model scenarios, a maximum bottomhole pressure (BHP) was specified. Four poroelastic responses were evaluated in this study including I-Stress (horizontal stress) Increment (IS), K-Stress (vertical stress) Increment (KS), Reservoir Vertical Displacement (RVD), and Surface Uplift (SU). The independent parameters include: (1) Reservoir Section Young's Modulus (E-Res), (2) Reservoir Section Poisson's Ratio (V-Res), (3) Caprock/surrounding Section Young's Modulus (E-CR), (4) Caprock/surrounding Section Poisson's Ratio (V-CR) (5) Reservoir Depth (Depth), (6) Reservoir Biot's Coefficient (Biot), (7) Pressure Increment in the injection well/ assigned block pressure at end of 30-year injection (BHP/ Block Pressure [BP]). For each synthetic case, simulations with seven different independent parameters representing high, medium, and low values of elastic parameters (E-Res, V-Res, E-Caprock, V-Caprock, Biot), Depth, and BHP/block pressure were run. Table 5-1 shows the distributions of independent parameters for the closed reservoir. In this work, 147 simulations were performed to develop the response surface. Box-Behnken design is mainly used to develop a proxy model for six parameters except for Biot's coefficients (total of 49 simulations) combined with full factorial for Biot coefficient.

**Table 5-1. Independent parameters distributions for the closed reservoir**

Input	Predictor Range
E-Res (psi)	(6000000, 10000000, 14000000)
V-Res	(0.21,0.25,0.3)
E-CR (psi)	(6000000, 10000000, 14000000)
V-CR	(0.21,0.25,0.3)
Depth (ft)	(3208,5308,8306)
Biot	(0.5,0.75,1)
BHP(psi)/ BP(psi)	(1200,3200,5200)/ (740, 2750, 4750)

### 5.3 Base Case Hydro-mechanical Response

The CMG-GEM® simulator (CMG-GEM, 2012) was used to conduct the modeling for this study. CMG-GEM® simulates CO<sub>2</sub> behavior in the subsurface by solving one equation for each component describing thermodynamic equilibrium between the gas phase and aqueous phase. Chemical reactions between CO<sub>2</sub> and other components in the system were not modeled. The model is isothermal. Henry's law was used to model CO<sub>2</sub> solubility into the brine. The geomechanics module within the CMG-GEM® code was used to simulate the poroelastic response during CO<sub>2</sub> injection periods. The geomechanics module uses a finite element grid to perform its calculations. Based on the value of pressure at every time-step, the geomechanics module computed stress and deformation in the system. An iterative feedback approach is used for coupling fluid flow and geomechanics (Tran et al., 2008; Tran et al., 2010; Tran, Settari, & Nghiem, 2004; Tran, Shrivastava, Nghiem, & Kohse, 2009).

The modeling analysis was conducted based on a carbonate reef located in northern Michigan, which is one of many Silurian-age pinnacle reefs in the Michigan basin. The reef underwent primary production and subsequently secondary recovery via CO<sub>2</sub>-EOR (Kelley et al., 2014). A rectangular prism shaped model was built for reservoir confined by the sideburden and overburden layers to represent the reef system and the surrounding rock. In this model, the reservoir facies, the Brown Niagaran formation, primarily consist of porous and permeable dolomite. The reservoirs are overlain by cyclic low permeability carbonate and evaporite formations as caprock. The thickness of the reservoir is 218 ft. The injection interval spans the 53 ft thickness in the middle of the reservoir. A single injection well is located at the center of the model grid. The CMG-GEM® Cartesian-coordinate grid for the fluid flow modeling divides

the reservoir-caprock sequence vertically into nine layers—seven reservoir layers and two caprock layers. A schematic of the CMG-GEM® Cartesian grid is shown in Figure 5-2. The CMG-GEM® geomechanics grid divides the reservoir-caprock sequence vertically into 25 layers — four reservoir layer and 21 caprock/surrounding/under-burden layers (Figure 5-2). Rock properties do not vary within the reservoir or surrounding rock but do vary from reservoir to surrounding rock. All models have a sealed outer model boundary. The model simulates a 30-year injection period to represent a commercial-scale CO<sub>2</sub> injection program. The injection rate is pressure-constrained at a maximum BHP of 3200 pounds per square inch (psi), compared to the initial pore pressure of 500 psi. The amount of CO<sub>2</sub> injected for the model is 39000 metric tons over the injection period for the base case. The mechanical properties of the reservoir were defined to the extent possible from laboratory core data and from results of analyses of sonic log data for the reference well and other close-by wells in the Northern Pinnacle Reef Trend of the Michigan Basin (S. Raziperchikolaee, 2018). The Young's modulus of the reservoir formation (Brown Niagaran) ranged from 6\*10<sup>6</sup> to 14 \*10<sup>6</sup> psi. A mean value of 10\*10<sup>6</sup> psi was used for the reservoir layers. The Poisson's ratio of the reservoir formation (Brown Niagaran) ranged from 0.2 to 0.32. A mean value of 0.25 was used for the reservoir layers in the fluid flow grid. Caprock/surrounding formations consist of cyclic carbonate and evaporite formations. For the base case, the same mechanical properties of the carbonate rock are used. The porosity of the reservoir formation (Brown Niagaran) ranged from 0.3 to 20 percent based on the porosity log data and core measurements. A mean value of 5 percent was used for reservoir layers in the fluid flow grid. Reservoir permeability ranges from 0.0001 mD in the low permeability zones to 900 mD in the vuggy zones. A constant value of 60 mD was used for reservoir layers in the fluid flow grid. The model uses a permeability of 0.00001 mD for the caprock formations. A base case relative gas-water permeability relationship was assumed for the reservoir and caprocks that is based on the Van Genuchten formulation (Van Genuchten, 1980). Model properties, geological, fluid flow, and geomechanical parameters, are summarized in Table 5-2.

Figure 5-4 also shows the CO<sub>2</sub> saturation in the reservoir grid after 30 years of CO<sub>2</sub> injection. CO<sub>2</sub> plume is located mainly near the injection well. Pressure increase, from 500 to 3200 psi, causes total stress increase in the reservoir. I-stress increases from 3021 to 4698 psi, and K-stress increases from 5777 psi to 6059 psi in the center of the reservoir. Vertical displacement at the top of the reservoir is 0.045 ft and surface displacement after 30 years of CO<sub>2</sub> injection is 0.0089 ft (Figure 5-5 and Figure 5-6).

**Table 5-2. Model parameters for the base case.**

Model	Parameter
Reservoir top (ft)	5,387
Thickness reservoir (ft)	218 (7 grids in z direction)
Model grid	3D square
Number of grids	21*21*9
Number of grids in grid refinement zone	7*7*9
Model areal dimensions (ft)	2500*2500
Outer boundary condition	Sealed
Property variability, vertical	Varies by layer
Property variability, horizontal	Homogeneous
Porosity caprock	0.01
Porosity reservoir	0.05
Permeability caprock (mD)	0.0001
Permeability reservoir (mD)	60
Relative permeability	Van Genuchten function with the exponent of 0.457
Injection time (years)	30

Model	Parameter
Pore pressure (psi)	500
Number of geomechanics model cells	25*25*25
Geomechanics model areal dimensions (ft)	12500 * 12500
Geomechanics model Overburden Thickness (ft)	5387 (15 grids in z direction)
Geomechanics model Reservoir Thickness (ft)	218 (4 grids in z direction)
Geomechanics model Underburden Thickness (ft)	3000 (6 grids in z direction)
Reservoir in situ stress gradient: Shmin, Shmax, Sv (psi/ft)	0.65, 0.8, 1
Wellbore constraint: Constant pressure (psi)	BHP constraint (3200 psi)
Temperature of injected CO <sub>2</sub> ; ambient reservoir (°C)	50, 50 (non-isothermal base case)

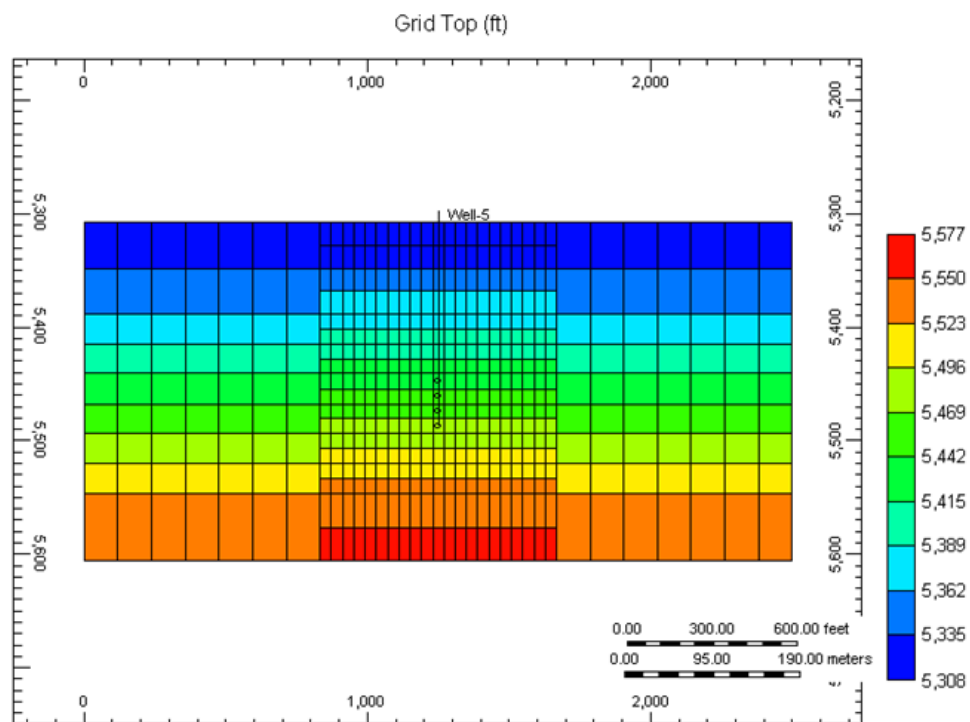


Figure 5-2. Reservoir cross-section

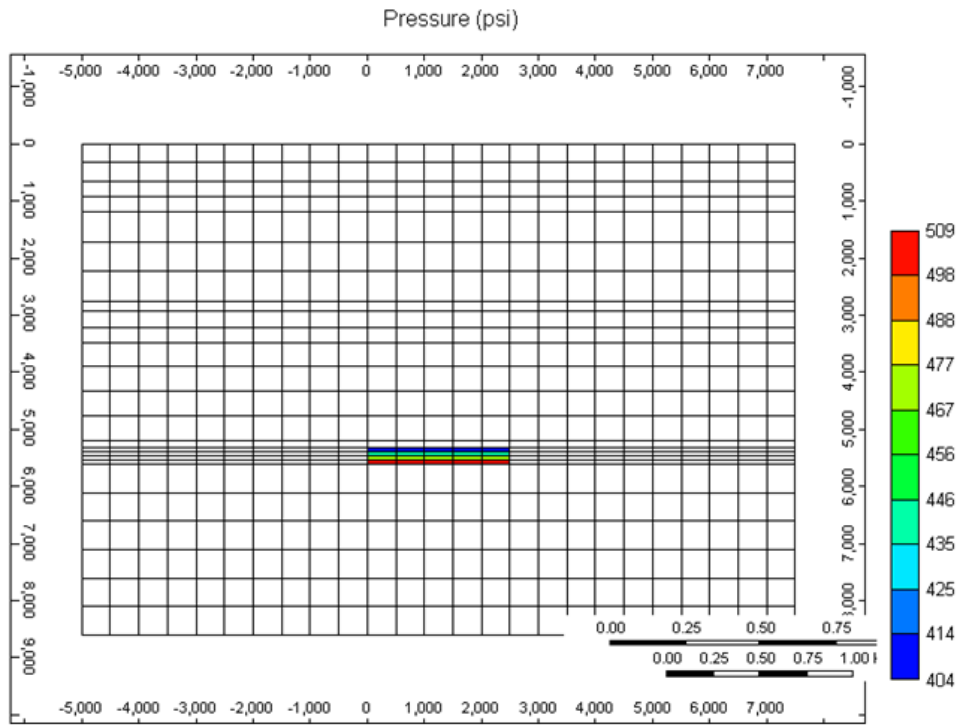


Figure 5-3. Geomechanics cross-section with reservoir in the middle

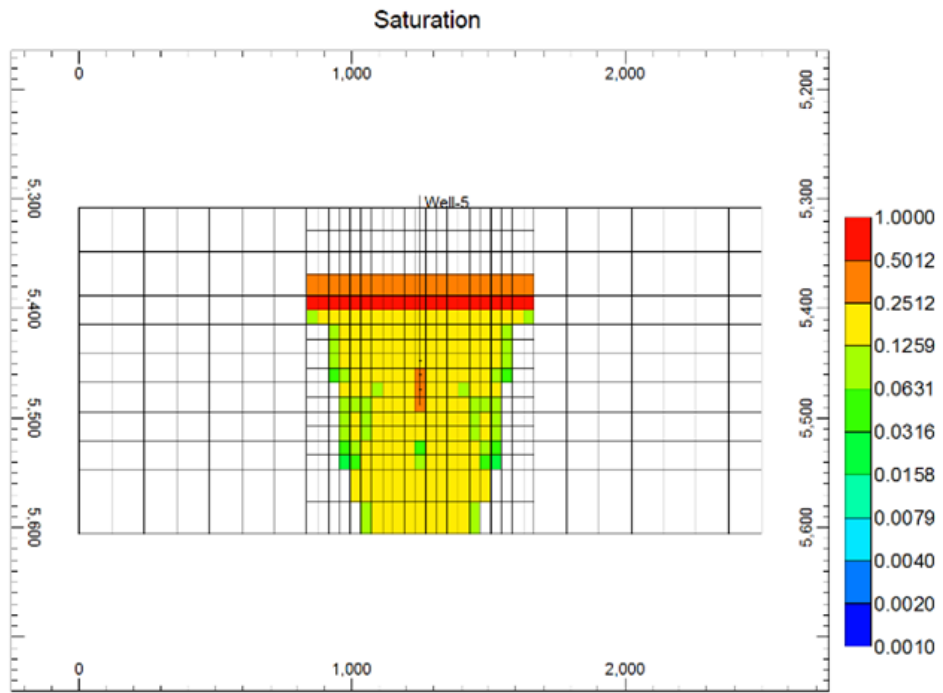


Figure 5-4. CO<sub>2</sub> saturation in the Reservoir cross-section at the end of 30 years injection period

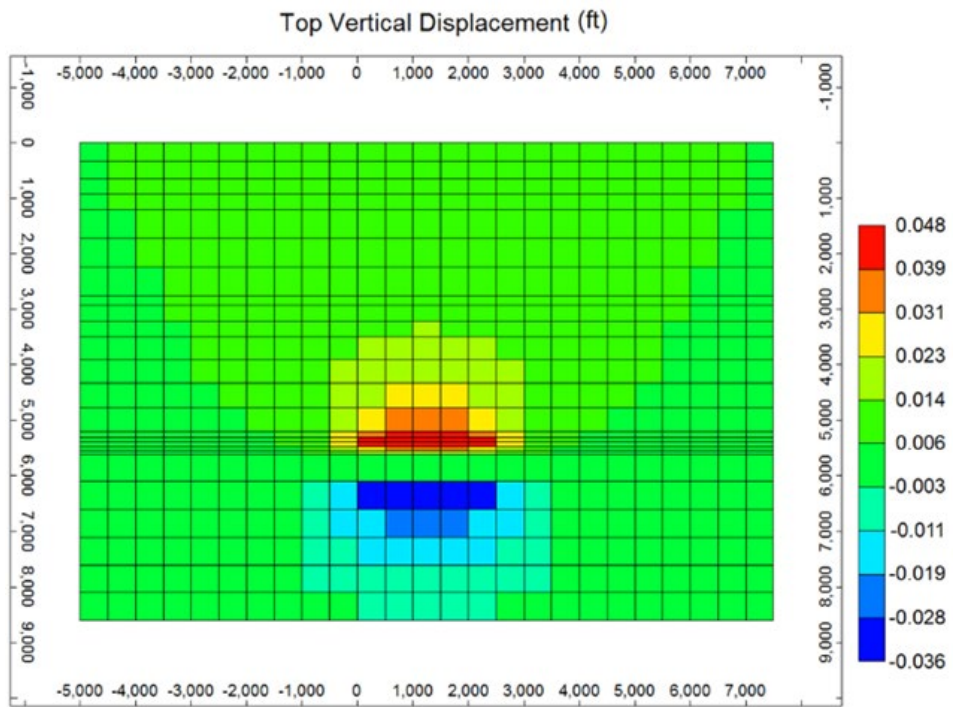


Figure 5-5. Vertical displacement in the geomechanics cross-section

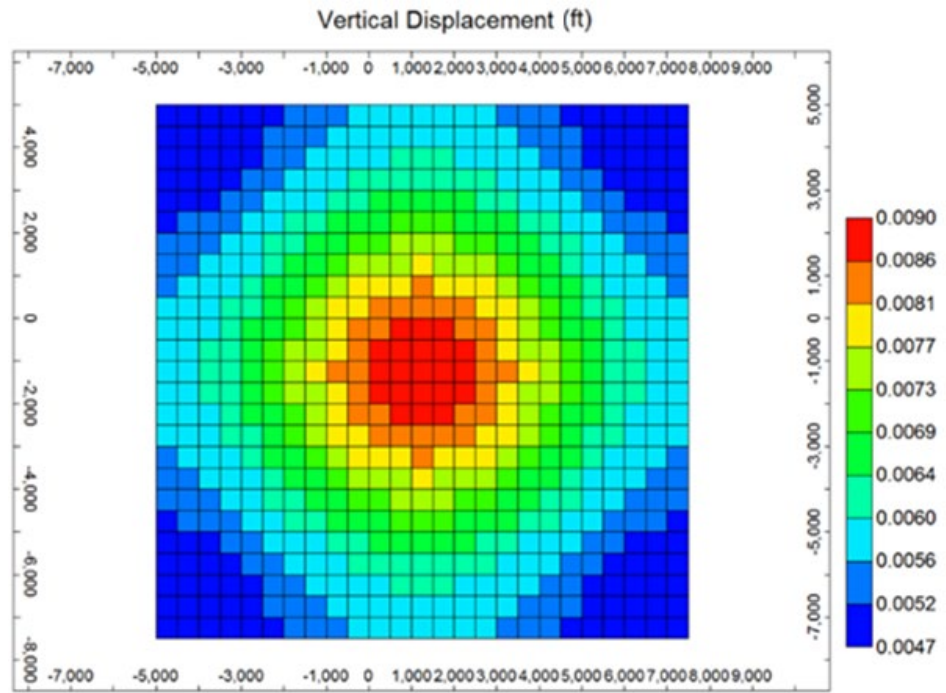


Figure 5-6. Surface uplift map in the geomechanics module

## 5.4 Response Surface Model Fit and Independent Validation Results

Different experimental designs can be used for variable screening or response surface optimization (Box & Behnken, 1960; Mishra & Datta-Gupta, 2017). The advantage of the Box-Behnken design is that only a limited combination of independent values will be selected for response surface model fit. As a result, a response surface model could be developed more quickly than full factorial design. The next step would be assigning the type of response surface model (e.g. linear and quadratic polynomial models, and Kriging models). Different response surface models have been used as proxies for uncertainty quantification studies relevant to oil and gas as well as CO<sub>2</sub> sequestration (Anbar, 2010; Ekeoma & Appah, 2009; Ghomian, Sepehrnoori, & Pope, 2010; Osterloh, 2008; Wriedt, Deo, Han, & Lepinski, 2014). In this study, a quadratic proxy model is used mainly for predicting poroelastic responses. The quadratic polynomial model is defined as a sum of all linear, quadratic, and pair-wise cross-product terms between predictors:

$$\hat{y} = b_0 + \sum_{i=1}^p b_i x_i + \sum_{i=1}^p \sum_{j>i} b_{ij} x_i x_j + \sum_{i=1}^p b_{ii} (x_i)^2$$

**Equation 5-1**

The coefficients (including constant, linear, interaction, and squared terms) are estimated so as to minimize the mean squared difference between the prediction vector and the true response vector.

Four poroelastic responses were recorded at the simulations representing a combination of low, medium, and high values of independent values using the experimental design. The first is I-direction stress increase in the center of the reservoir (reservoir grid # 11, 11, 6), the second is K-direction stress increase in the reservoir (reservoir grid # 11, 11, 6), the third is the vertical displacement of the reservoir top (reservoir grid # 11, 11, 1), and fourth is the surface displacement in the center of geomechanics grid (geomechanics grid # 13, 13, 1). For a given combination of input values, the response surface models were trained using the experimental design to make response predictions.

### 5.4.1 Reservoir Top Vertical Displacement

Cross plot of actual (i.e., based on numerical model) versus predicted (i.e. based on reduced order model) values using the response surface model is shown in Figure 5-5 for top reservoir displacement. Also, the residual plot shows no clear structure in Figure 5-5. The coefficients in the quadratic model (sorted based on coefficients in Equation 5-1: constant, linear, interaction, and squared terms) are mentioned in Table 5-3. Also, the statistical significance of each estimated coefficient in the response surface model was assessed (as shown in Table 5-3). The second column in Table 5-3 shows the coefficients in the full (with quadratic components) polynomial model. The third and fourth columns show the t-statistic and associated p-significance values. A threshold P-value, P-value<0.001, is set to test the significance of each parameter. Results for reservoir vertical displacements show that the retained input parameters are well-block pressure, reservoir and caprock Young's modulus as well as the interaction of the mentioned parameters with other parameters (i.e. Biot's coefficient, Reservoir, and reservoir Poisson's ratio). The model performance was measured using root mean squared error (RMSE) and pseudo-R<sup>2</sup> over the training data (Table 5-4). The high value of R<sup>2</sup> indicates most of the variability in top reservoir vertical displacement can be explained by the regression model. A smaller than threshold p-value means that selected parameters in the quadratic response surface have a significant effect on the response variable. Repeating the multiple regression with significant parameters leads to the following equation for the response surface:

$$\text{Resp-RVD} = b_0 + b_1 * \text{YM-Res} + b_2 * \text{YM-CR} + b_3 * \text{BP} + b_4 * \text{YM-Res} * \text{Biot} + b_5 * \text{YM-Res} * \text{BP} + b_6 * \text{PR-Res} * \text{BP} + b_7 * \text{YM-CR} * \text{BP} + b_8 * \text{PR-CR} * \text{BP} + b_9 * \text{Biot} * \text{BP} + b_{10} * \text{YM-Res}^2 + b_{11} * \text{YM-CR}^2$$

### Equation 5-2

The cross plot of actual versus predicted value using the reduced response surface model is shown in Figure 5-7 and Figure 5-8. The regression summary, the analysis of variance and the test of significance table for the revised response surface model are shown in Table 5-4 and Table 5-5. The small p-value indicates that the model adequately explains the response. Figure 5-9 shows the response surface plot for various combination of block pressure, caprock Young's modulus, and reservoir Young's modulus. We can see that as pressure increases, reservoir displacement increases. By increasing caprock or reservoir Youngs' modulus, top reservoir vertical displacement decreases.

**Table 5-3. Coefficient of quadratic polynomials and test of significance results for reservoir displacement (note: black color shows the excluded and red color shows the included terms).**

	Coefficient Definition	Coefficient Value	t-Stat	P-Value	Std Error
1	Constant	0.028636141	0.775915301	0.43944908	0.036906
2	YM-Res	-2.55E-09	-2.666648021	8.81E-03	9.58E-10
3	PR-Res	0.050151382	0.373940452	0.70916194	0.134116
4	YM-CR	-7.75E-09	-7.569573321	1.18E-11	1.02E-09
5	PR-CR	0.023997334	0.179116624	0.85817267	0.133976
6	Depth	-2.44E-06	-1.653562353	1.01E-01	1.48E-06
7	Biot	3.79E-02	3.041972501	0.00293349	1.25E-02
8	BP	3.68E-05	20.2508172	4.53E-39	1.82E-06
9	YM-Res*PR-Res	3.01E-09	1.433348269	0.15456906	2.10E-09
10	YM-Res*YM-CR	1.70E-17	0.717984717	4.74E-01	2.37E-17
11	YM-Res*PR-CR	-3.65E-10	-0.245451112	0.8065604	1.49E-09
12	YM-Res*Depth	1.98E-14	0.538543003	0.59128059	3.68E-14
13	YM-Res*Biot	-2.64E-09	-9.848842443	7.99E-17	2.68E-10
14	YM-Res*BP	-6.57E-13	-13.88066851	5.21E-26	4.73E-14
15	PR-Res*YM-CR	6.79E-10	0.323840149	7.47E-01	2.10E-09
16	PR-Res*PR-CR	1.32E-03	0.007118146	0.99433337	1.86E-01
17	PR-Res*Depth	2.50E-07	0.107892417	0.91427581	2.32E-06
18	PR-Res*Biot	-0.044160323	-1.859369022	0.06562306	0.02375
19	PR-Res*BP	-1.50E-05	-3.574849395	5.20E-04	4.19E-06
20	YM-CR*PR-CR	5.57E-09	2.657736592	0.0090279	2.10E-09
21	YM-CR*Depth	2.79E-14	0.757682308	0.45024673	3.68E-14
22	YM-CR*Biot	1.12E-10	0.417031753	0.67746061	2.68E-10
23	YM-CR*BP	-1.06E-12	-31.72825381	1.72E-57	3.35E-14
24	PR-CR*Depth	1.02E-06	0.312135959	0.75552278	3.26E-06
25	PR-CR*Biot	0.000198902	0.008374776	0.99333301	0.02375
26	PR-CR*BP	-1.80E-05	-4.306688132	3.59E-05	4.19E-06

	Coefficient Definition	Coefficient Value	t-Stat	P-Value	Std Error
27	Depth*Biot	-2.06E-07	-0.49362188	0.62254854	4.17E-07
28	Depth*BP	-2.41E-10	-3.284675324	0.00136647	7.35E-11
29	Biot*BP	8.37E-06	15.63876741	7.89E-30	5.35E-07
30	YM-Res^2	1.78E-16	6.105972706	1.54E-08	2.92E-17
31	PR-Res^2	-0.09628107	-0.411681845	0.68136649	0.233873
32	YM-CR^2	2.87E-16	9.835157051	8.59E-17	2.92E-17
33	PR-CR^2	-0.15273629	-0.653104971	0.5150391	0.233862
34	Depth^2	1.73E-10	2.328373994	2.17E-02	7.44E-11
35	Biot^2	7.12E-05	0.0136904	0.98910156	0.005198
36	BP^2	-6.81E-11	-0.584621286	0.5599888	1.16E-10

**Table 5-4. Regression summary for full and reduced order polynomial model.**

	Mean Square Error	R <sup>2</sup>	Adjusted R <sup>2</sup>	Sum of Squares Error	Sum of Squared Regression	F	P-value
Displacement (Full)	3.45E-06	0.996069	0.994830123	3.83E-04	0.096998	8.04E+02	2.20E-118
Displacement (Reduced)	7.79E-06	0.9892	0.988320122	1.05E-03	0.096329	1.12E+03	6.69E-127

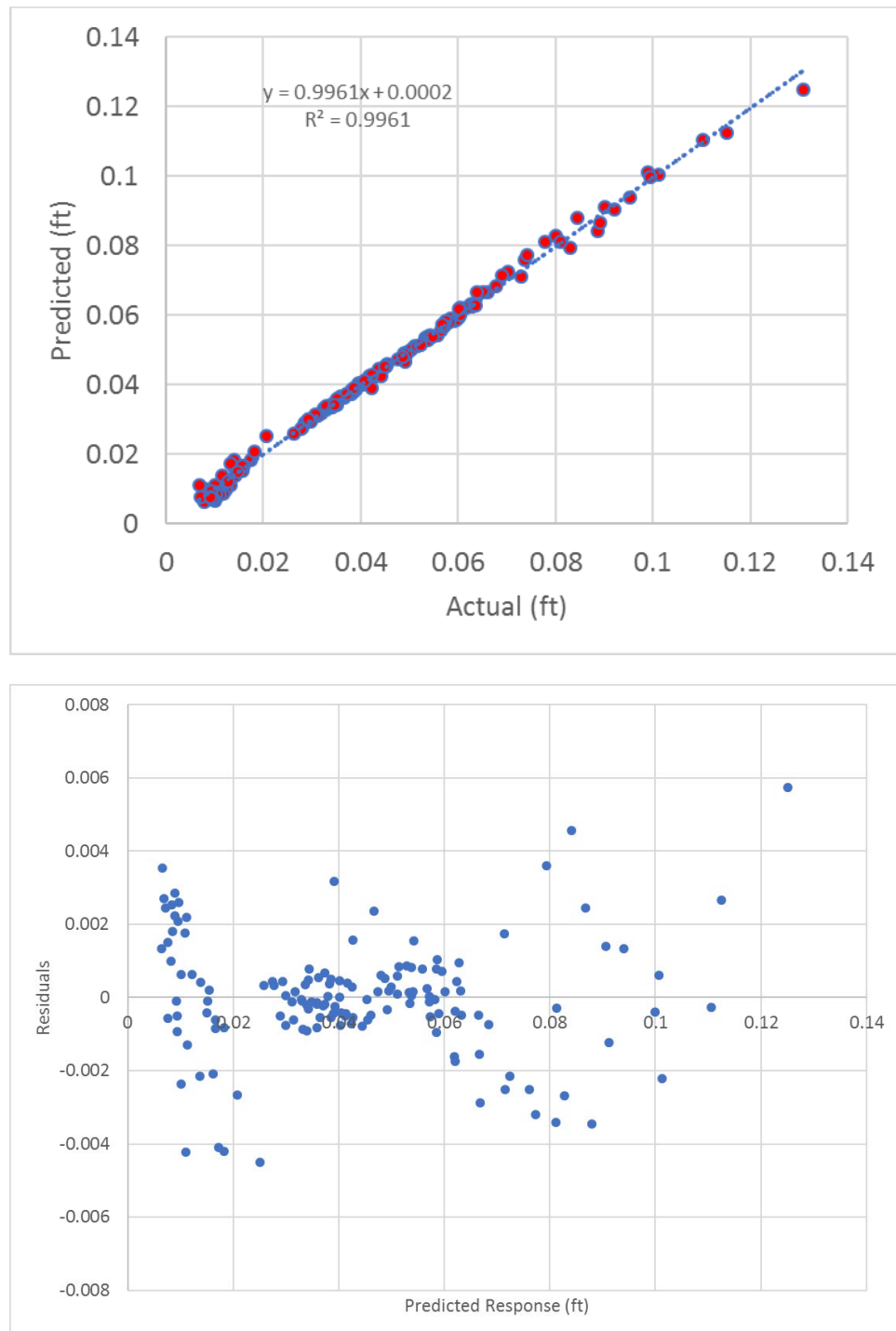


Figure 5-7. (A) Actual (i.e., based on numerical model) versus predicted (i.e. based on reduced order model) reservoir displacement for quadratic model (B) Diagnostic plot for residual: residual versus predicted.

**Table 5-5. Coefficient of reduced order polynomial and test of significance results for reservoir displacement.**

Coefficient	Coefficient Value	t-Stat	P-Value	Std Error
1	0.043218	7.93683	7.11E-13	0.005445
2	-2.94E-09	-4.40456	2.14E-05	6.67E-10
3	-5.44E-09	-8.68582	1.09E-14	6.26E-10
4	2.92E-05	24.13357	8.18E-51	1.21E-06
5	-4.09E-10	-1.56824	0.119167	2.61E-10
6	-6.57E-13	-9.23461	4.83E-16	7.11E-14
7	-0.0152727	-1.82053	0.070893	0.008389
8	-1.06E-12	-21.1093	1.34E-44	5.03E-14
9	-1.69E-05	-6.88431	1.99E-10	2.45E-06
10	1.08E-05	14.78515	5.14E-30	7.31E-07
11	1.61E-16	5.320973	4.18E-07	3.03E-17
12	2.71E-16	8.946741	2.50E-15	3.03E-17

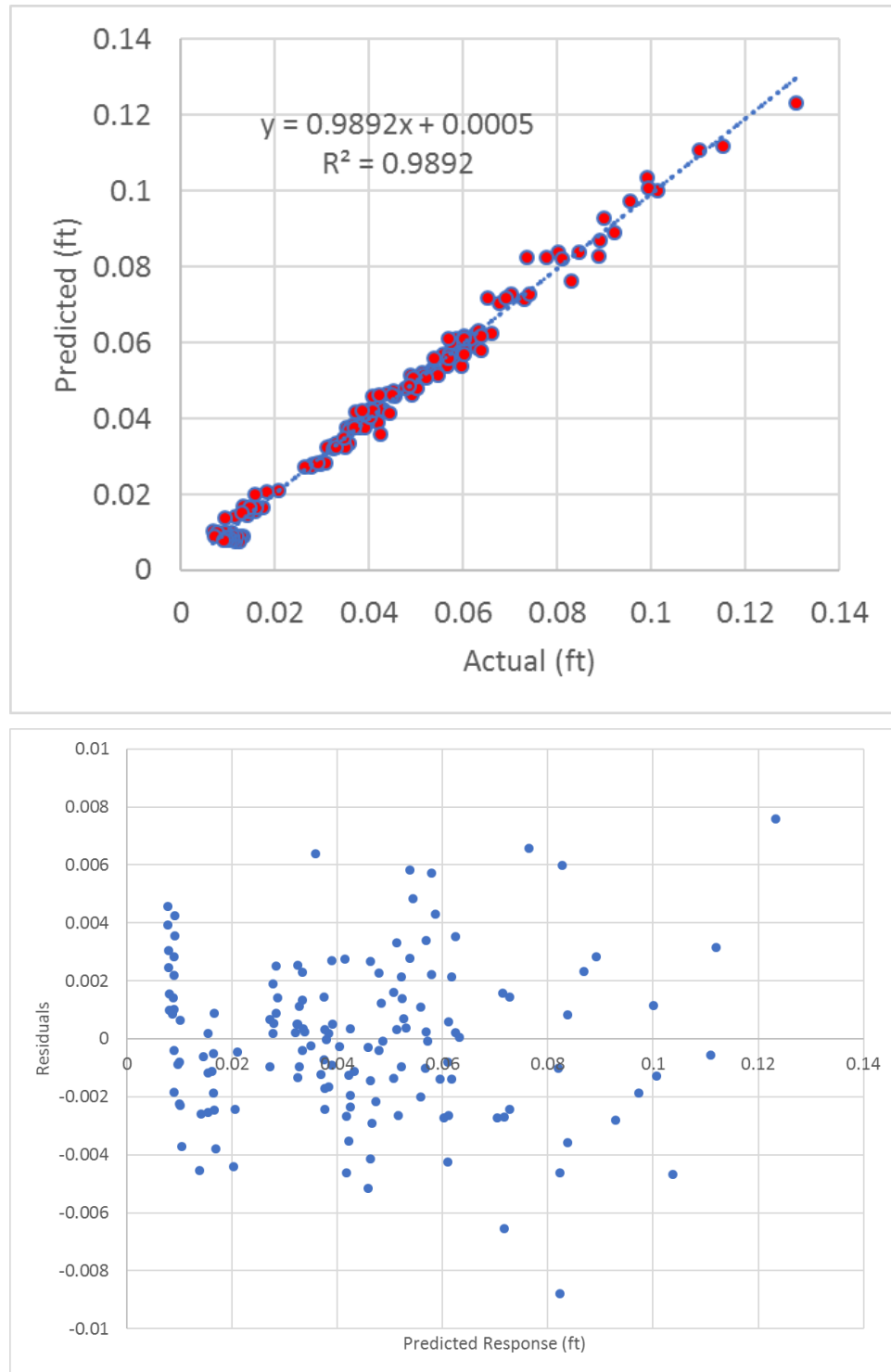


Figure 5-8. (A) Actual (i.e., based on numerical model) versus predicted (i.e. based on reduced order model) reservoir displacement for reduced order model (B) Diagnostic plot for residual: residual versus predicted.

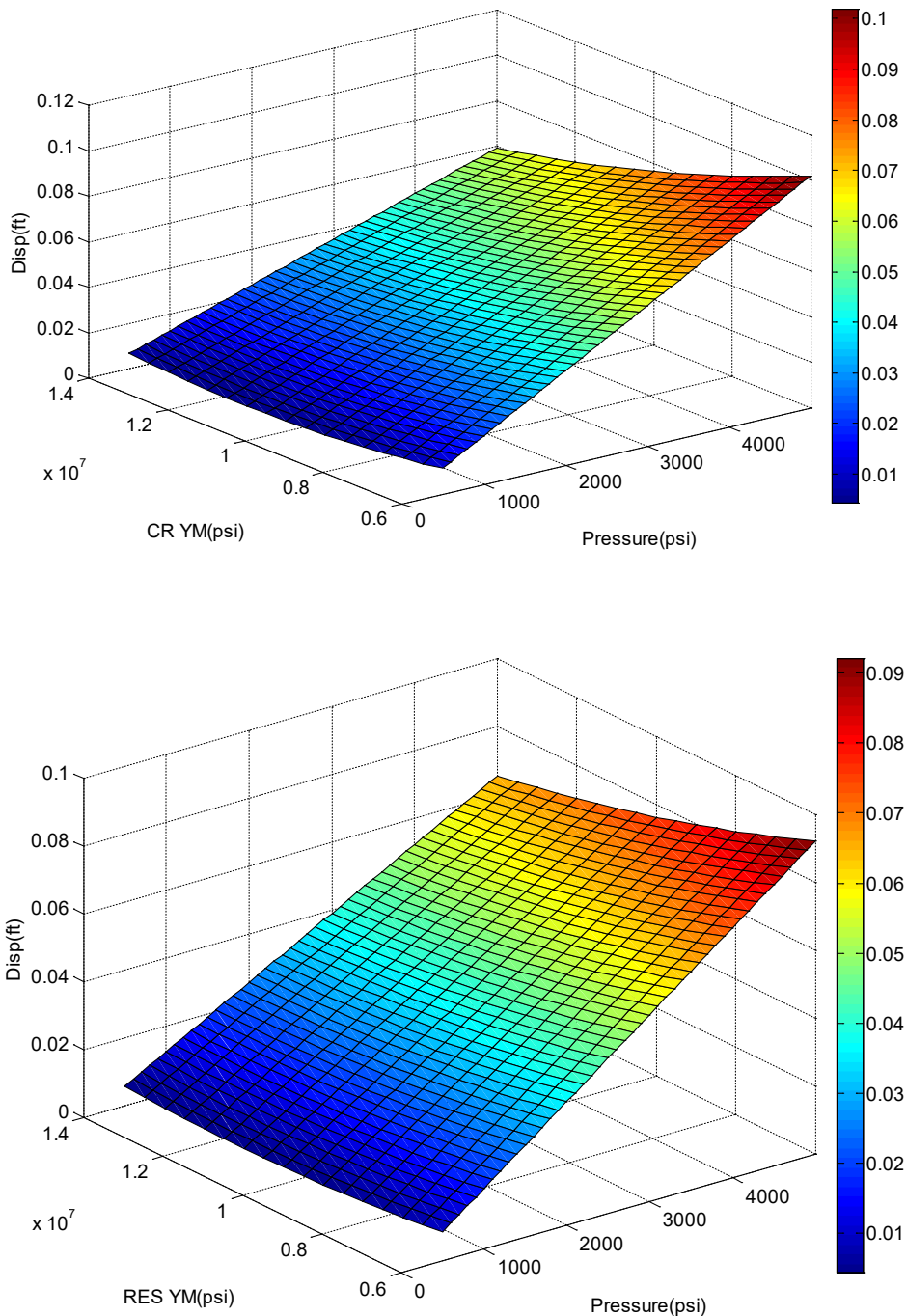


Figure 5-9. Reservoir Displacement Response Surface based on reduced order model.

### 5.4.2 Surface Uplift Prediction

The same procedure described for reservoir top displacement was applied to develop a full (including quadratic components) and a reduced order proxy model for the surface uplift prediction. Results for surface uplift show that the included input parameters are caprock Young's modulus, reservoir depth, and block pressure, as well as the interaction of the mentioned parameters with other parameters (reservoir Young's Modulus, caprock Poisson's ratio, and Biot's coefficient). Repeating the multiple regression with significant parameters leads to the following equation for the response surface:

$$\text{Resp-SU} = b0 + b1*YM-CR + b2*Depth + b3*BP + b4*YM-res*Depth + b5*YM-Res*Biot + b6*YM-Res*BP + b7*YM-CR*Depth + b8*YM-CR*BP + b9*PR-CR*Depth + b10*PR-CR*BP + b11*Depth*Biot + b12*Depth*BP + b13*Biot*BP + b14*YM-CR^2 + b15*Depth^2$$

#### Equation 5-3

The cross plot of actual values versus predicted values using the reduced order response surface model is shown in Figure 5-10. The regression summary, the analysis of variance and the test of significance table for the revised response surface model are shown in Table 5-6 and Table 5-7. Figure 5-11 shows the response surface plot for various combination of reservoir block pressure, reservoir Young's modulus, and reservoir depth. When pressure increases, surface uplift increases. Decreasing depth and Young's modulus cause surface uplift increase.

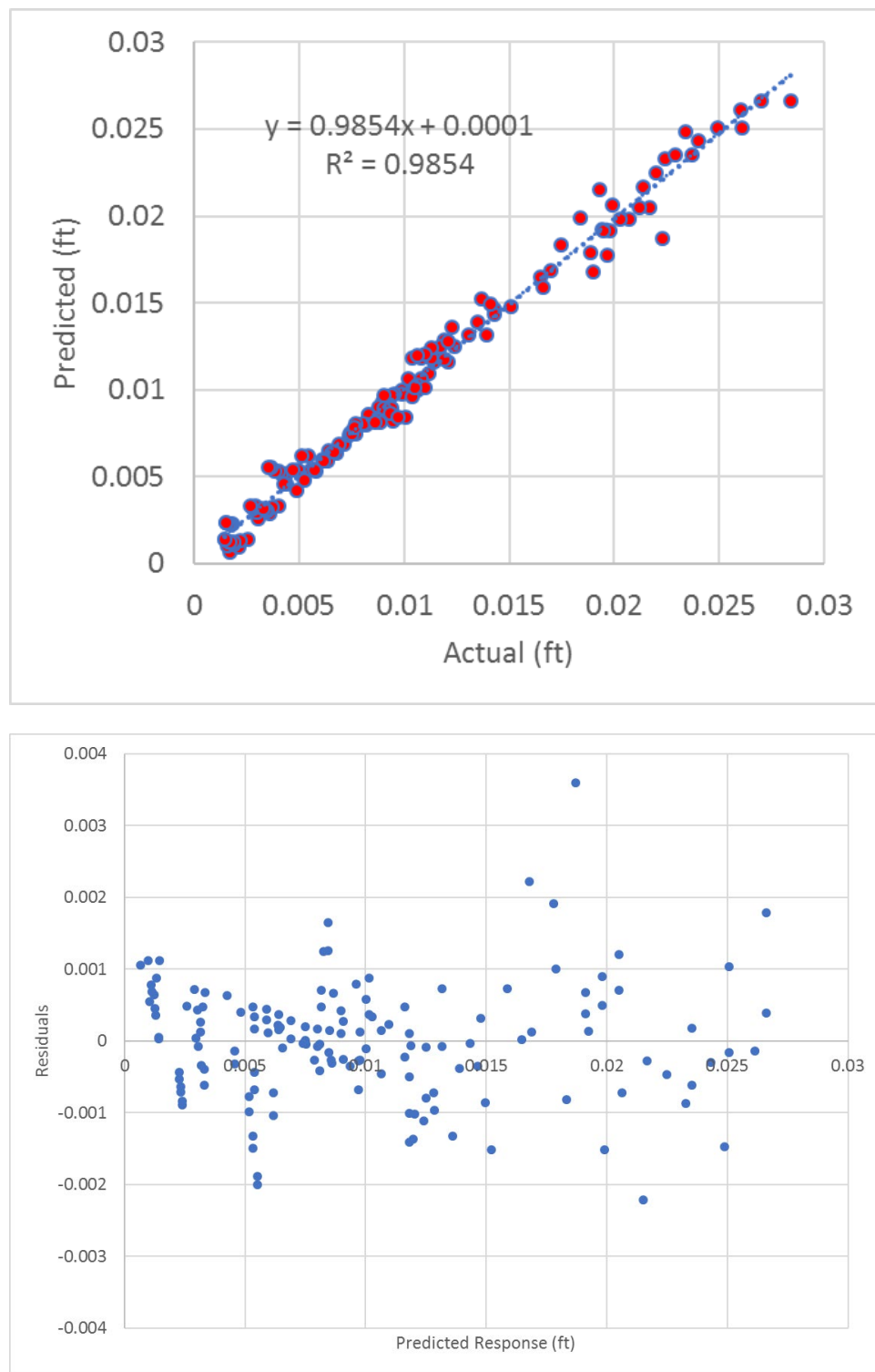


Figure 5-10. (A) Actual (i.e., based on numerical model) versus predicted (i.e. based on reduced order model) surface uplift for reduced order model (B) Diagnostic plot for residual: residual versus predicted.

**Table 5-6. Regression summary for full and reduced order polynomial model.**

	Mean Square Error	R <sup>2</sup>	Adjusted R <sup>2</sup>	Sum of Squares Error	Sum of Squared Regression	F	P-value
Surface Displacement (Full)	4.90E-07	0.991939	0.989397	5.44E-05	0.006694	3.90E+02	4.23E-101
Surface Displacement (Reduced order)	7.52E-07	0.985411	0.98374	9.85E-05	0.00665	5.90E+02	2.47E-112

**Table 5-7. Coefficient of reduced order polynomial and test of significance results for surface uplift.**

Coefficient	Coefficient Value	t-Stat	P-Value	Std Error
1	0.027547	14.74212	1.33E-29	0.001869
2	-1.72E-09	-7.97137	6.76E-13	2.16E-10
3	-7.34E-06	-16.1723	5.14E-33	4.54E-07
4	1.18E-05	21.19666	3.62E-44	5.58E-07
5	4.68E-14	3.828723	0.000199	1.22E-14
6	-2.33E-10	-2.98286	3.41E-03	7.81E-11
7	-1.48E-13	-7.53904	6.97E-12	1.97E-14
8	9.14E-14	5.318103	4.40E-07	1.72E-14
9	-2.42E-13	-15.4724	2.34E-31	1.56E-14
10	1.69E-06	1.93277	0.055422	8.73E-07
11	-9.74E-06	-5.86982	3.38E-08	1.66E-06
12	9.87E-08	0.672042	0.50274	1.47E-07
13	-5.84E-10	-17.0233	5.33E-35	3.43E-11
14	1.73E-06	7.610272	4.76E-12	2.27E-07
15	5.88E-17	6.257463	5.15E-09	9.40E-18
16	4.60E-10	19.13754	9.20E-40	2.41E-11

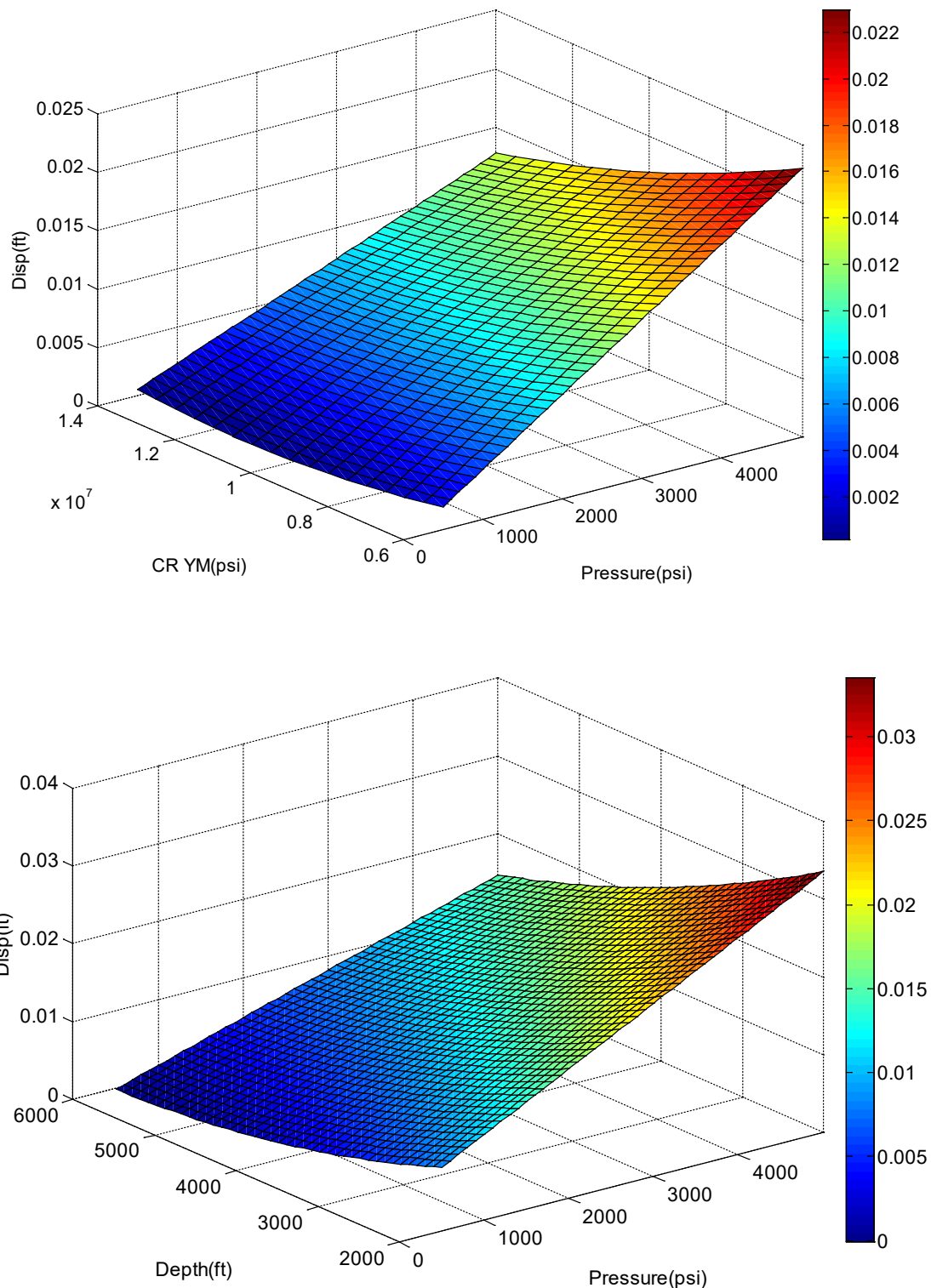


Figure 5-11. Surface uplift response surface based on reduced order model.

### 5.4.3 I-stress (Horizontal Stress) Increment Prediction

The same procedure described earlier for reservoir top displacement was applied to develop a full and a reduced order proxy model for the I-stress increment. Results for I-direction stress show that the included input parameters are well-block pressure, Biot's Coefficient and Poisson's Ratio, and caprock Young's modulus as well as their interaction with other parameters (reservoir Young's modulus and reservoir Poisson's ratio). Repeating the multiple regression with significant parameters leads to the following equation for the response surface:

$$\text{Resp-IS} = b_0 + b_1 * \text{PR-Res} + b_2 * \text{Biot} + b_3 * \text{Bp} + b_4 * \text{YM-Res} * \text{YM-CR} + b_5 * \text{YM-Res} * \text{Biot} + b_6 * \text{YM-Res} * \text{BP} + b_7 * \text{PR-Res} * \text{Biot} + b_8 * \text{PR-Res} * \text{BP} + b_9 * \text{YM-CR} * \text{Biot} + b_{10} * \text{YM-CR} * \text{BP} + b_{11} * \text{Biot} * \text{BP} + b_{12} * \text{YM-CR}^2$$

#### Equation 5-4

The cross plot of actual values versus predicted values using the reduced order response surface model is shown in Figure 5-12. The regression summary, the analysis of variance and the test of significance table for the revised response surface model are shown in Table 5-8 and Table 5-9. Figure 5-13 shows the response surface plot for various combination of block pressure and reservoir Poisson's ratio. As expected, as pressure increases, I-direction stress increment increases. Increasing reservoir Poisson's ratio causes a decrease in I-direction stress increment.

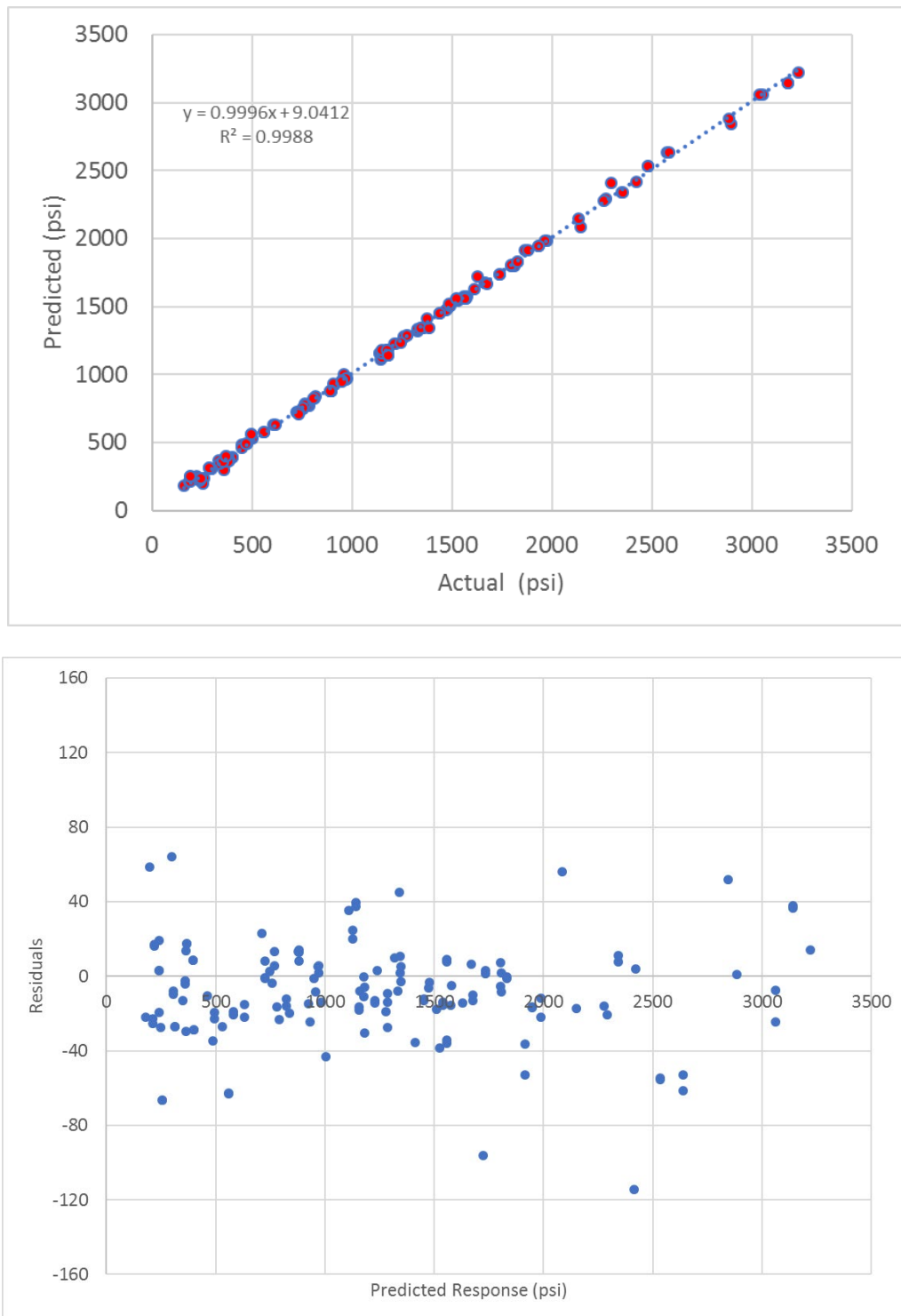


Figure 5-12. (A) Actual (i.e., based on numerical model) versus predicted (i.e. based on reduced order model) I-stress increase for reduced order model (B) Diagnostic plot for residual: residual versus predicted

**Table 5-8. Regression summary for full and reduced order polynomial model.**

	Mean Square Error	R <sup>2</sup>	Adjusted R <sup>2</sup>	Sum of Squares Error	Sum of Squared Regression	F	P-value
I-Stress (Full)	5.24E+02	0.999296	0.999073	5.81E+04	8.25E+07	4.50E+03	8.44E-160
I-Stress (Reduced order)	8.52E+02	0.998627	0.998492	1.13E+05	8.26E+07	7.45E+03	1.92E-183

**Table 5-9. Coefficient of reduced order polynomial and test of significance results for I-stress increase.**

Coefficient	Coefficient Value	t-Stat	P-Value	Std Error
1	-805.2992336	-8.80936016	5.97E-15	91.41404
2	3412.525265	9.981151248	7.46E-18	341.897
3	1.19E+03	10.56068618	2.62E-19	1.13E+02
4	0.244740083	10.91150333	3.42E-20	0.02243
5	1.84E-12	7.037566617	9.38E-11	2.62E-13
6	-2.79E-05	-7.635911447	3.90E-12	3.65E-06
7	2127307.401	2.590447163	0.010653884	821212.4
8	-4635.447345	-12.41331044	5.62E-24	373.4256
9	-1.204918074	-18.30058743	3.81E-38	0.06584
10	2.34E-05	6.116145002	1.00E-08	3.83E-06
11	1.04E-08	19.9559785	8.03E-42	5.23E-10
12	0.633661423	73.83256561	8.08E-110	0.008582
13	-1.85E-12	-9.94822719	9.02E-18	1.86E-13

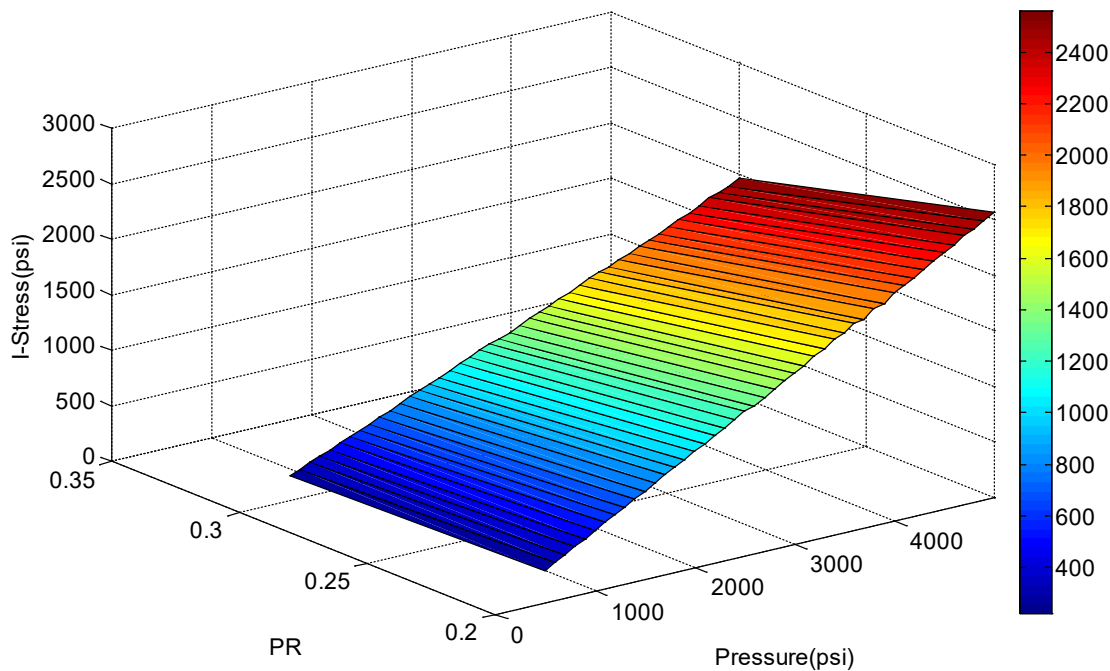


Figure 5-13. I-stress increase response surface based on reduced order model

#### 5.4.4 K-stress (Vertical Stress) Increment Prediction

The same procedure described earlier for reservoir top displacement was applied to develop a full and a reduced order proxy model for the I-stress increment. Results for I-direction stress show that the included input parameters is mainly well-block pressure, reservoir Young's Modulus, and the interaction of other parameters including caprock Young's modulus, reservoir and caprock Poisson's Ratio, Biot's coefficient. Repeating the multiple regression with significant parameters leads to the following equation for the response surface:

$$\text{Resp-KS} = b_0 + b_1 * \text{BP} + b_2 * \text{YM-Res} * \text{YM-CR} + b_3 * \text{YM-Res} * \text{Biot} + b_4 * \text{YM-Res} * \text{BP} + b_5 * \text{PR-Res} * \text{Biot} + b_6 * \text{PR-Res} * \text{BP} + b_7 * \text{YM-CR} * \text{Biot} + b_8 * \text{YM-CR} * \text{BP} + b_9 * \text{PR-CR} * \text{BP} + b_{10} * \text{Biot} * \text{BP} + b_{11} * \text{YM-Res}^2 + b_{12} * \text{BP}^2$$

#### Equation 5-5

The cross plot of actual values versus predicted values using the reduced order response surface model is shown in Figure 5-14. The regression summary, the analysis of variance and the test of significance table for the revised response surface model are shown in Table 5-10 and Table 5-11. Figure 5-15 shows the response surface plot for various combination of block pressure and caprock Young's modulus. As expected, as pressure increases, K-direction stress increment increases. Increasing caprock Young's modulus also causes increase in K-direction stress increment.

**Table 5-10. Regression summary for full and reduced order polynomial model.**

	Mean Square Error	R <sup>2</sup>	Adjusted R <sup>2</sup>	Sum of Squares Error	Sum of Squared Regression	F	P-value
K-Stress (Full)	77.26330648	0.997389	0.996566	8.58E+03	3.28E+06	1.21E+03	3.11E-128
K-Stress (Reduced Order)	1.07E+02	0.995642	0.995251	1.43E+04	3.27E+06	2.55E+03	9.35E-152

**Table 5-11. Coefficient of reduced order polynomial and test of significance results for K-stress increase.**

Coefficient	Coefficient Value	t-Stat	P-Value	Std Error
1	8.739554559	0.989845239	3.24E-01	8.829213
2	0.087948306	13.29110895	3.10E-26	0.006617
3	-7.54E-13	-9.498050496	1.13E-16	7.94E-14
4	-1.04E-05	-8.991825117	2.03E-15	1.16E-06
5	-4.09E-09	-16.07334331	4.64E-33	2.54E-10
6	-43.86309214	-0.783638372	0.434635255	55.97364
7	-0.066648516	-4.212722845	4.60E-05	0.015821
8	9.32E-06	9.228808388	5.27E-16	1.01E-06
9	4.30E-09	24.26434337	7.00E-51	1.77E-10
10	-0.147748003	-16.29977304	1.34E-33	0.009064
11	0.060029231	21.04417217	2.62E-44	0.002853
12	8.06E-13	12.27465047	1.12E-23	6.57E-14
13	2.80E-06	6.464974049	1.74E-09	4.33E-07

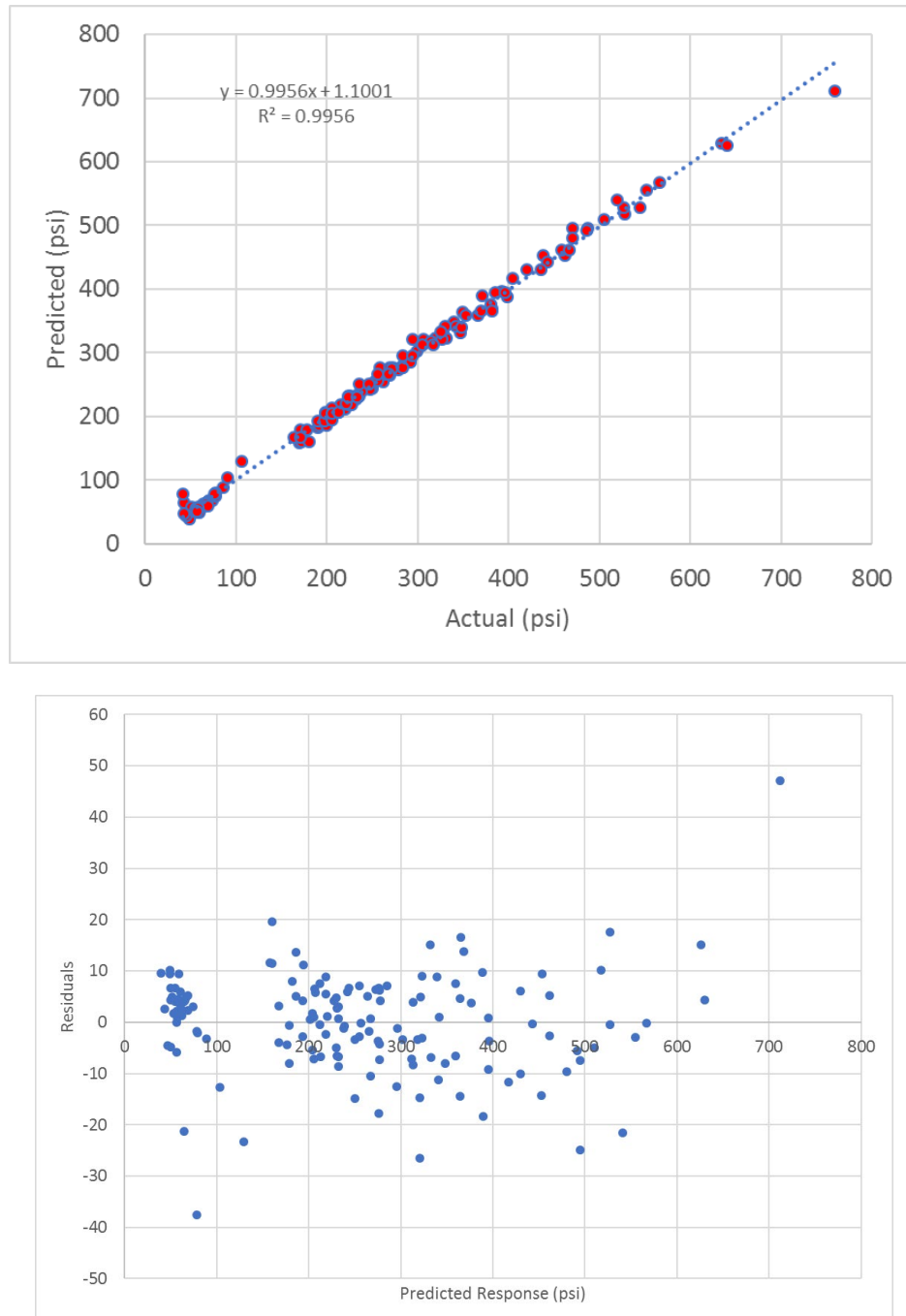


Figure 5-14. (A) Actual (i.e., based on numerical model) versus predicted (i.e. based on reduced order model) reservoir displacement for reduced order model (B) Diagnostic plot for residual: residual versus predicted

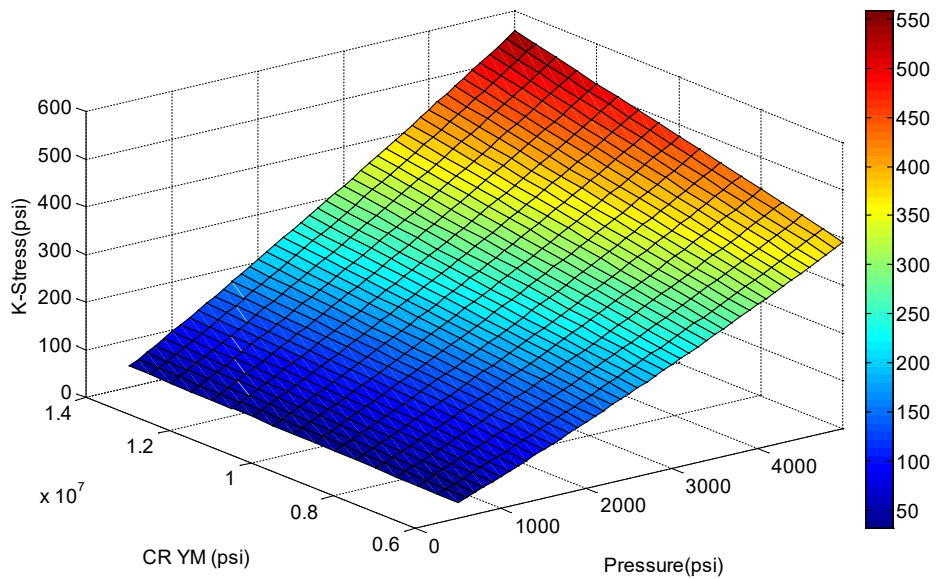


Figure 5-15. K-stress increase response surface based on reduced order model

## 5.5 Validation of Results

We estimate the accuracy of each response surface model by conducting numerical simulation on new test data that were not involved in training the model. The response surface model is then used to produce predictions of the response at those test locations, and an error estimate can capture the quality of the fit. The independent test designs are shown in Table 5-12. The results of the validation study for two cases, evaluating the closeness of predicted and simulated responses using relative error of prediction, are shown in Table 5-13.

Table 5-12. Predictor values for the validation simulations.

Case	YM-RES(psi)	PR-RES	YM-CR(psi)	PR-CR	Depth (psi)	Biot	BP (psi)
1	12000000	0.22	8000000	0.28	5308	1	1742.363525
2	8000000	0.28	12000000	0.22	4308	1	3747.813721
3	12000000	0.22	8000000	0.28	5308	0.75	1742.478149
4	12000000	0.22	8000000	0.28	5308	0.5	1743.648682

**Table 5-13. Simulation and model response prediction.**

Case #	I-Stress Increase (psi)	K-Stress Increase (psi)	Displacement (ft)	Surface (ft)
Simulation 1	1059.14	143.8174	0.030048	0.005826
Predicted 1	1060.2	135.4165	0.029668	0.005681
Relative Error 1 (Fraction)	0.001	0.0584	0.0126	0.0249
Simulation 2	2244.906	460.5015	0.06335	0.0157
Predicted 2	2256.075	477.1494	0.064865	0.0168
Relative Error 2 (Fraction)	0.005	0.036	0.0239	0.074
Simulation 3	777.2039	127.8857	0.027119	0.005523
Predicted 3	780.2004	124.3428	0.02703	0.005497
Relative Error 3 (Fraction)	0.0039	0.0277	0.0033	0.0047
Simulation 4	495.9072	111.2744	0.024218	0.00522
Predicted 4	500.2004	113.326	0.024405	0.005317
Relative Error 4 (Fraction)	0.0087	0.0184	0.0077	0.0186

## 5.6 Discussion

### 5.6.1 Importance of the Input Parameters

Equations 5-2 through 5-7 show that the interaction of input parameters to make each response model is complex (by including several terms) and non-linear. As a result, it is not straightforward to understand the importance of each input parameter on the responses by simply analyzing the derived regression-based equations (especially because of the difference in units). Such interactions are also unique for each response. To evaluate the importance of each parameter, we used  $R^2$  loss method for variable importance in regression models. This involves comparing the  $R^2$  of a full model (with all input parameters) with the  $R^2$  for the model that excludes the input parameter of interest. Higher difference between the  $R^2$  of the full model and  $R^2$  of excluded parameter shows the greatest influence of that parameter. Table 5-14 shows the  $R^2$  loss for each response. Results for surface uplift show that the most influential inputs are pressure, depth, and caprock Young's modulus. Results for reservoir displacement show that the most important inputs are pressure and caprock Young's modulus. Results for I-stress increase show that the most important inputs are pressure and Biot's coefficient. Results for K-stress increase show that the most important inputs are pressure and caprock Young's modulus.

**Table 5-14. Variable importance results of all responses in terms of  $R^2$  loss (red color shows high  $R^2$  loss).**

Input	Surface uplift (ft)	Vertical displacement (ft)	I-stress increase (psi)	K-stress increase (psi)
E-Res (psi)	0.041	0.066	0.019	0.067
V-Res	0.011	0.006	0.039	0.007
E-CR (psi)	0.151	0.176	0.029	0.087
V-CR	0.021	0.006	0.009	0.017
Depth (ft)	0.331	0.006	0.009	0.007
Biot	0.021	0.066	0.349	0.077
BHP(psi)/ BP(psi)	0.761	0.976	0.909	0.947

### 5.6.2 Optimization of Input Parameters Using Monte Carlo Simulation

A Monte Carlo-type uncertainty analysis was performed to assess the effect of the distribution of uncertain input parameters using probability distribution functions on the poroelastic responses. In fact, by applying Monte Carlo simulations we can estimate the expected mean of each response over a range of input parameters. This application also illustrated the computational efficiency achieved by using the developed response surface models. Poroelastic response of injecting can be estimated only in few seconds using the response surface model. Such estimation using coupled numerical simulation can take hours. Using response surface models, we were able to perform 10000 simulations in less than a minute. For the Monte Carlo simulation experiments, we created data sets based on what we predict the effects of different input parameters by modeling uncertainty. First, a probability distribution was assigned for each input parameters. For Young's modulus (mean of  $10 * 10^6$  psi and sigma of  $2 * 10^6$ ) and Poisson's ratio (mean of 0.25 and sigma of 0.02) a normal distribution was assigned since the mechanical properties typically show similar normal distribution behavior (Raziperchikolaee, Kelley, & Gupta, 2018). For depth, a uniform distribution was used from 3500 ft to 7500 ft. Biot's coefficient of 0.75 and pressure increase of 3000 psi was assumed. Then, 10000 random samples were generated using the assigned distribution functions. Figure 5-16 shows the probability distribution for input parameters. The relationships developed in previous sections were used to estimate the poroelastic responses (reservoir displacement, surface uplift, I-stress increase, and K-stress increase) for each randomly generated sample point. As a result, the distributions were also estimated for the poroelastic responses (Figure 5-17 and Figure 5-18). The mean of I-stress increase is 1343 psi and its standard deviation is 111. The mean of K-stress increase is 270 psi and its standard deviation is 35. The mean of reservoir displacement is 0.0461 ft and its standard deviation is 0.0077. The mean of surface uplift is 0.0099 ft and its standard deviation is 0.003.

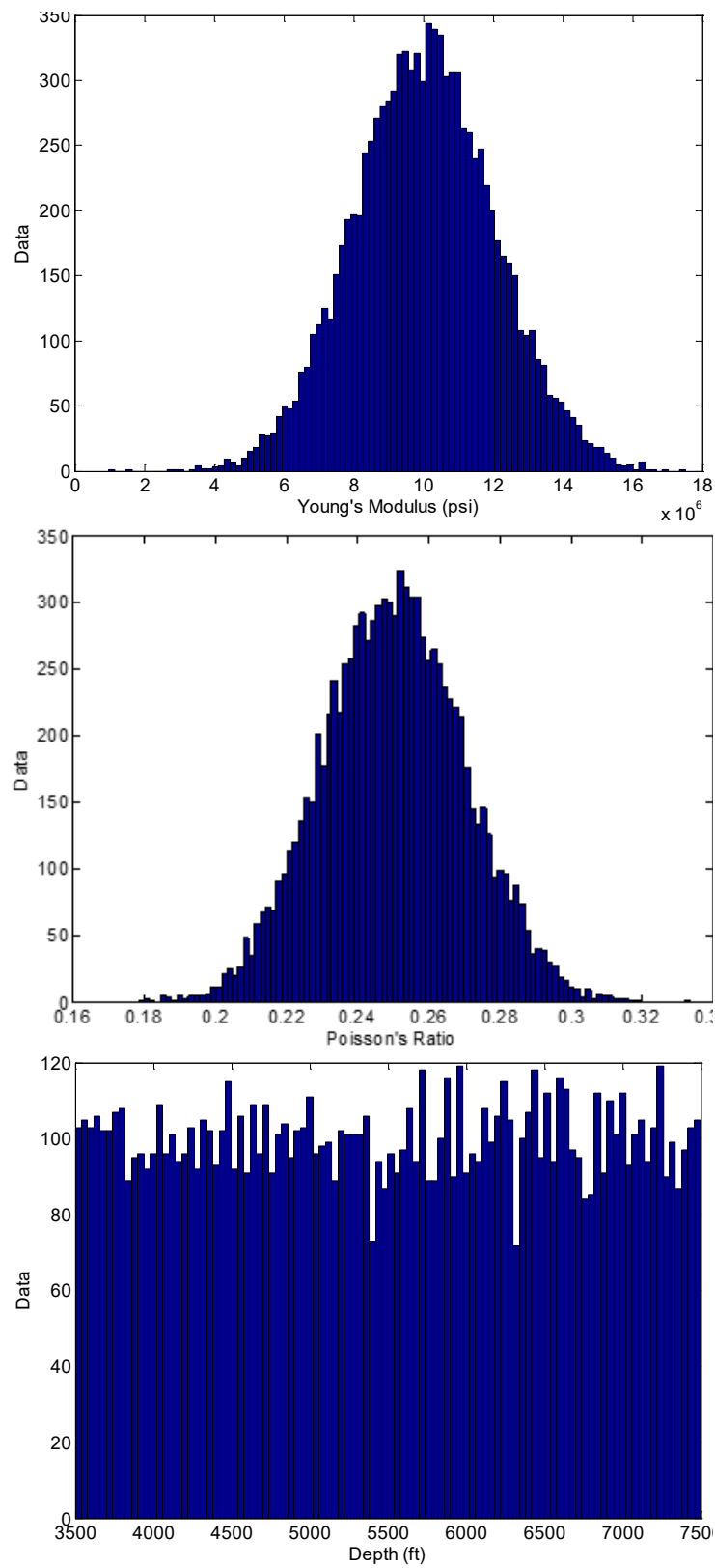


Figure 5-16. Input Parameters Distribution: (A) Young's modulus (B) Poisson's ratio (C) Depth

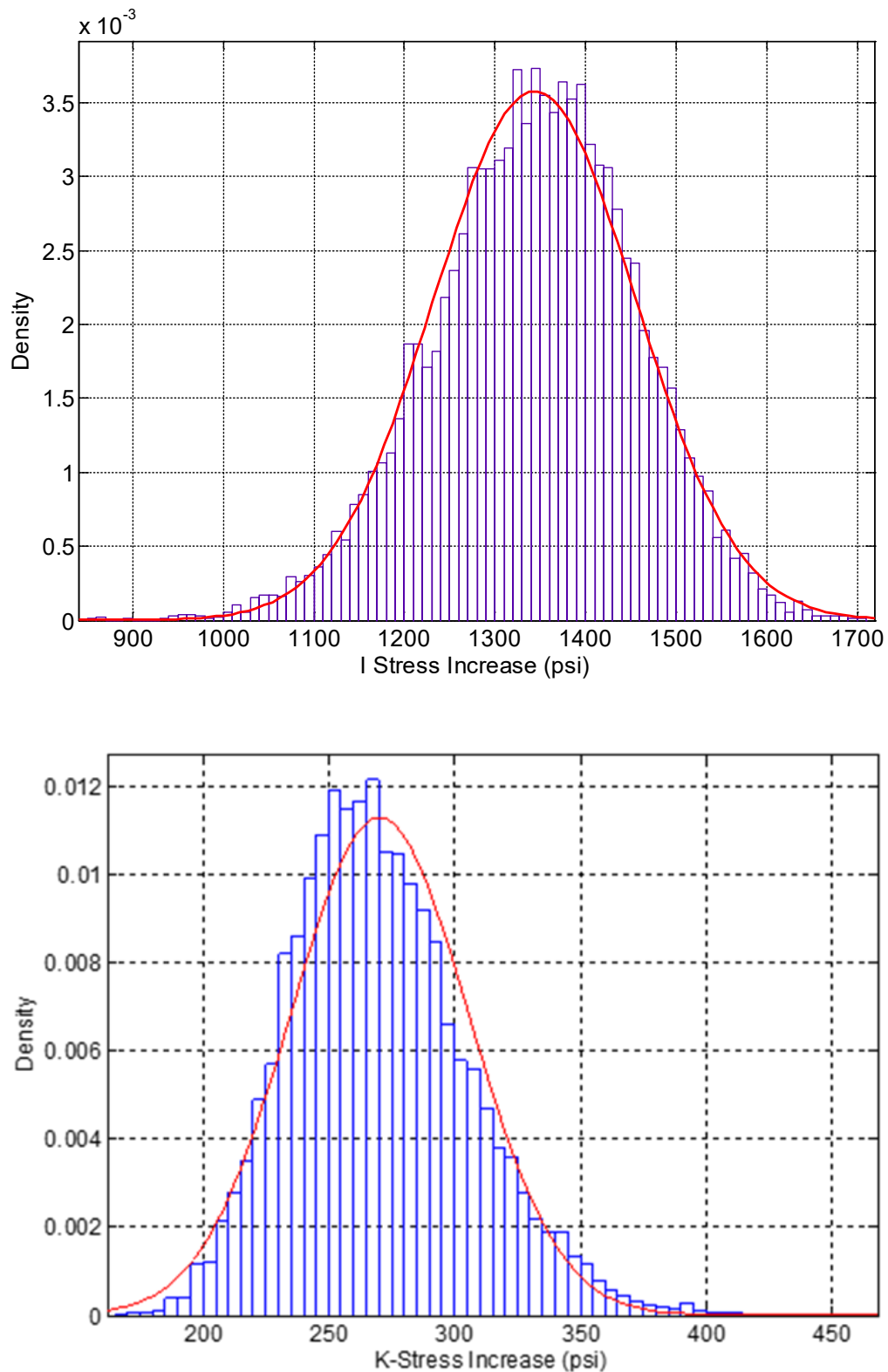


Figure 5-17. Poroelastic response distribution: (A) I-stress distribution (B) K-stress distribution

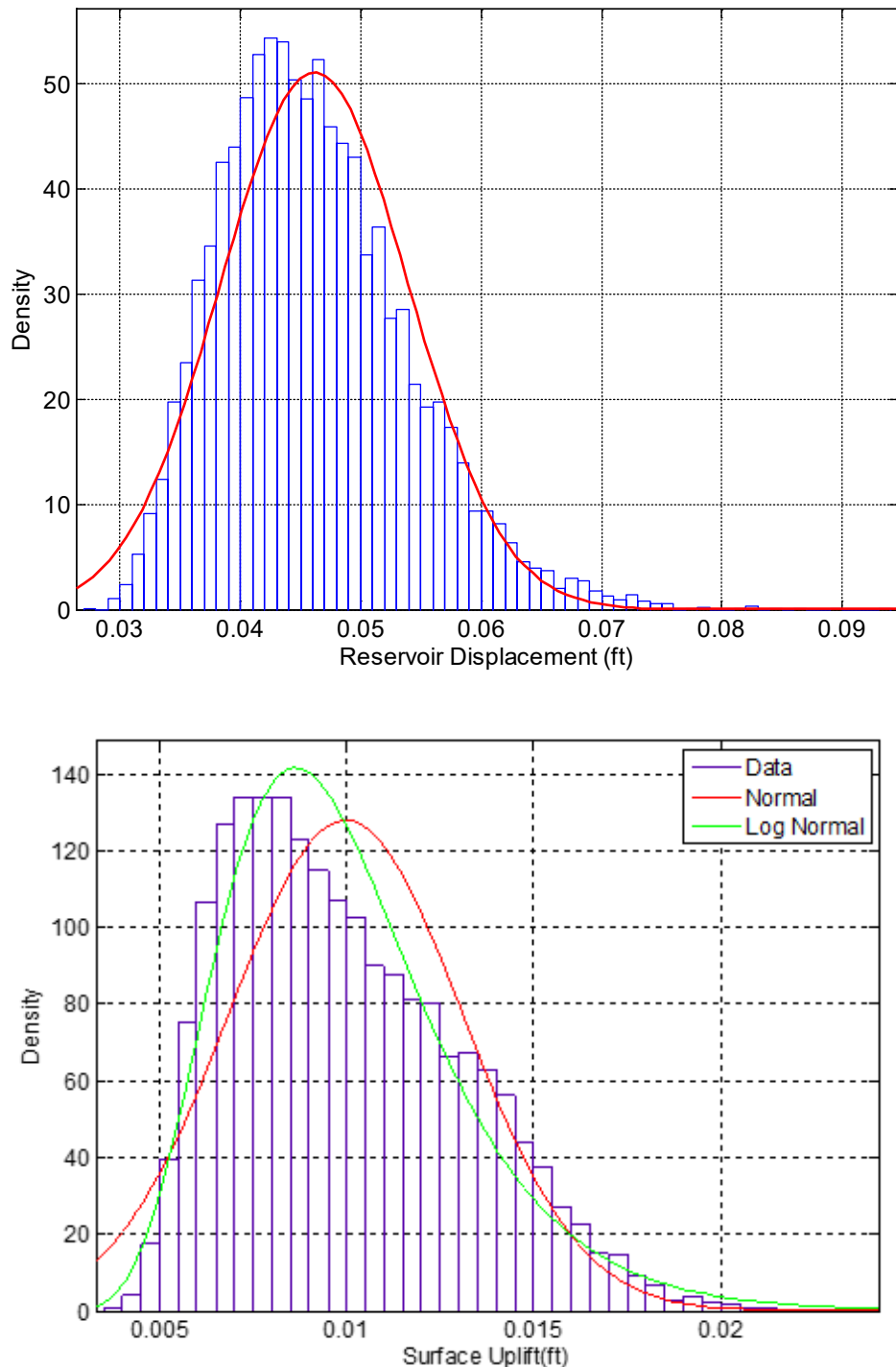


Figure 5-18. Poroelastic response distribution: (A) I-stress distribution (B) K-stress distribution (C) vertical displacement distribution (D) Surface uplift distribution

## 5.7 Estimating Poroelastic Response of Injection using Experimental and Field Data

Different geomechanical models (analytical poroelastic solutions) (Rudnicki, 1986) and numerical coupled models (Vidal-Gilbert et al., 2010) have been introduced to address geomechanical risks. In all of them, mechanical properties of the modeled formations, especially the reservoir, is an essential input data need when modeling geomechanical processes. These parameters vary as a function of formation types (rock types) as well as geological structures (e.g., faults and fractures). However, they are typically assumed to be constant during injection process. Biot's Coefficient, as one of the main input mechanical parameters, is not only assumed to be constant during injection, but also typically assumed to be equal to 1.0 regardless of rock/structure type (Rutqvist, Birkholzer, Cappa, & Tsang, 2007; Vilarrasa, Bolster, Olivella, & Carrera, 2010). A constant stress-independent Biot's Coefficient is typically used to estimate poroelastic response of injection such as surface uplift (Rinaldi & Rutqvist, 2013), predict reservoir stress path (Li & Laloui, 2016; Rutqvist et al., 2007; Vidal-Gilbert et al., 2010; Vilarrasa et al., 2010), and model fault activation and induced seismicity (Cappa & Rutqvist, 2011a, 2012; Jha & Juanes, 2014; Mazzoldi et al., 2012; van Wees et al., 2019). Bulk and grain compressibility of a carbonate (dolomite) Silurian–aged Brown Niagaran Formation is measured in a series of laboratory experiments to estimate Biot's Coefficient, using an indirect measurement method, under various values of confining stress (ranging from 700 psi to 5800 psi) and two values of pore pressure (500 psi and 3200 psi). A regression-based stress dependent Biot's Coefficient model (using laboratory experiments performed for a carbonate sample) is then used to include the stress dependency of Biot's Coefficient in the applied analytical and numerical model. Due to fluid injection, stress and pore pressure is changed in the reservoir in each time-step. At each time-step of injection, Biot's coefficient is updated using regression-based model and imported into the poroelastic model to recalculate effective stress. Analytical poroelastic and numerical geomechanical modeling were then performed under (1) a constant stress-independent Biot's Coefficient scenario (2) effective stress dependent scenarios using experimental measurement. Field test data (e.g., well log data and mini-frac tests) were also used to support modeling of poroelastic response.

### 5.7.1 Experimental Description

The core sample used for the Biot's measurement experiment is from a carbonate reef reservoir in the Northern Pinnacle Reef Trend of the Michigan Basin (Dover-33 reef). The carbonate reefs are considered valuable CO<sub>2</sub> storage sites due to their numerous existences in the Michigan basin and around the world. Approximately 800 such reefs have been mapped and drilled in the Northern Pinnacle Reef Trend of the Michigan Basin (Kelley et al., 2014). Niagaran reefs are significant hydrocarbon reservoirs in the Michigan Basin. Such reefs have typically undergone primary production and, in some cases, secondary recovery. CO<sub>2</sub> has been injected into a small number of reefs that have the potential capacity for supporting CO<sub>2</sub> sequestration (Kelley et al., 2014). The reservoir rocks include various proportions of dolomite and limestone; some reefs are completely dolomitized, while others are essentially all limestone. The Brown Niagaran, as the main reef facies, is overlain and encased by cyclic carbonate and evaporite sequences of the Salina Group (Kelley et al., 2014). A Brown Niagaran dolomitic core sample of 1 inch in diameter and 2.7 inch length was acquired at the depth of 5552 ft from one of the carbonate reefs to investigate the relation between confining pressure, pore pressure, and rock volumetric deformation. The porosity of the core was measured to be 11.58 percent. Triaxial rock testing system, controlling confining pressure axial load and pore pressure independently, was used in order to measure grain and bulk compressibility of the carbonate sample. Biot's Coefficient ( $\alpha$ ) is defined as the ratio of the volume of the fluid change divided by the change in bulk volume under the constraint that pore pressure remains constant (Wang, 2017). It appears in the equation of effective stress,  $\sigma' = \sigma - \alpha P$  and defines stress distribution across the solid skeleton ( $\sigma'$ ) and the pore fluid (P) (Nur & Byerlee, 1971). Biot's Coefficient can be estimated directly by

measuring pore volume change and volumetric strain (Al-Tahini, Abousleiman, & Brumley, 2005; Blöcher, Reinsch, Hassanzadegan, Milsch, & Zimmermann, 2014). It can also be computed using an indirect measurement method as (Biot & Willis, 1957):

$$\alpha = 1 - \left( \frac{C_g}{C_b} \right)$$

### Equation 5-6

where  $C_b$  represents the drained bulk compressibility of framework measured during hydrostatic compression test on a jacketed specimen, and  $C_g$  is the solid grains compressibility determined from a hydrostatic compression test on an unjacketed specimen. The method is called indirect method for measuring Biot's Coefficient because it is determined indirectly from the measurements of  $C_g$  and  $C_b$  (the coefficient may be called indirect measured Biot's coefficient (Al-Tahini et al., 2005) or effective pressure coefficient (Müller & Sahay, 2016)). The difference between Biot's Coefficient measured using the indirect and the direct method may be due to measurement error of pore volume (Blöcher et al., 2014) or inhomogeneity in the sample, such as microcracks (Müller & Sahay, 2016). However, the Biot's coefficient measurements using indirect or direct measurement methods show a similar trend in terms of stress dependency (Blöcher et al., 2014). The decrease of Biot's Coefficient by increasing effective stress in sandstone core samples has been investigated in several studies (Al-Tahini et al., 2005; Blöcher et al., 2014; Klimentos, Harouaka, Mtawaa, & Saner, 1998; Nur & Byerlee, 1971; Siggins & Dewhurst, 2003). In this work, we measured the stress dependency of Biot's Coefficient in a carbonate rock using indirect measurement method. The main objective of this study is to investigate the effect of Biot's coefficient stress dependency on poro-elastic response of injection. Bulk compressibility is measured at two different pore pressure of 500 psi and 3200 psi. The confining stress (equal radial and axial pressure) was increased from 700 psi to 3190 psi for the lower pore pressure scenario (500 psi), and from 3400 psi to the pressure of 5890 psi for the higher pore pressure scenario (3200 psi) both at the rate of 45 psi/min. Figure 5-19 displays the evolution of volumetric strain by increasing confining stress while performing experiments. The bulk compressibility is then calculated using the derivatives of confining stress – volumetric strain curve ( $C_b = \frac{\Delta \epsilon_v}{\Delta P_c}$ ) for every 15 time-step ( $\sim 115$  psi stress increase). The values of drained bulk compressibility and constant measured grain compressibility of  $2.6 \times 10^{-7}$  (1/psi) were used to calculate Biot's Coefficient. Figure 5-19 also shows how Biot's Coefficient changes as a function of confining stresses at two different pore pressure values. Experiment results reveal that Biot's Coefficient is a strong function of effective stress. Biot's Coefficient decreases with increasing confining stress. The value of Biot's Coefficient varies from 0.9 to 0.65 for the lower range of confining stress and pore pressure, and from 0.8 to 0.55 for the higher range higher confining stress and pore pressure (Figure 5-19). The relationship between effective stress and Biot's Coefficient (color coded by pore pressure) is also shown in Figure 5-20. Overall, Biot's Coefficient decreases by increasing effective stress linearly. A linear regression between Biot's Coefficient and effective stress was employed to quantify Biot's Changes as a function of effective stress (Figure 5-20).

In addition, a multi-variate linear regression was used to estimate Biot's Coefficient as a function of pore pressures and confining stress:

$$\alpha = 0.9133 - 9.148E - 5 * \sigma + 6.28E - 5 * P$$

### Equation 5-7

The cross plot of actual (i.e., measured) versus predicted (i.e. multivariate model) values is shown in Figure 5-20. The model performance was measured using R<sup>2</sup> over the training data. The high value of R<sup>2</sup> (0.98) indicates most of the variability in Biot's Coefficient can be explained by the regression model.

Associated p-values determines significance of each input parameter. A small p-value observed for each parameter ( $P(\sigma) = 3.15\text{E-}19$   $P(P) = 2.27\text{E-}14$ ) means that each parameter in the model has a significant effect on the response variable.

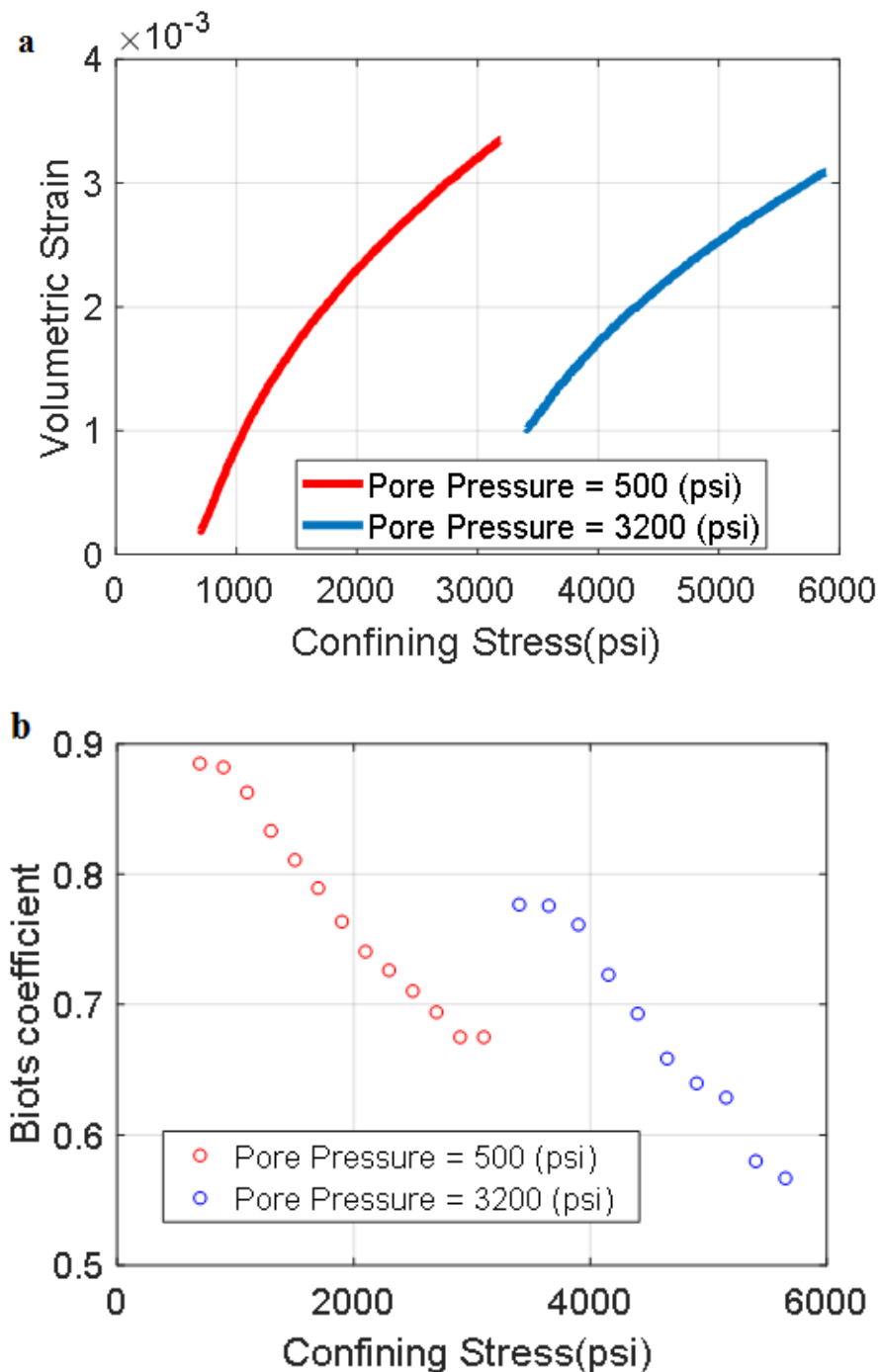


Figure 5-19. (a) plot of volumetric strain versus confining stress, (b) Biot's Coefficient versus confining stress

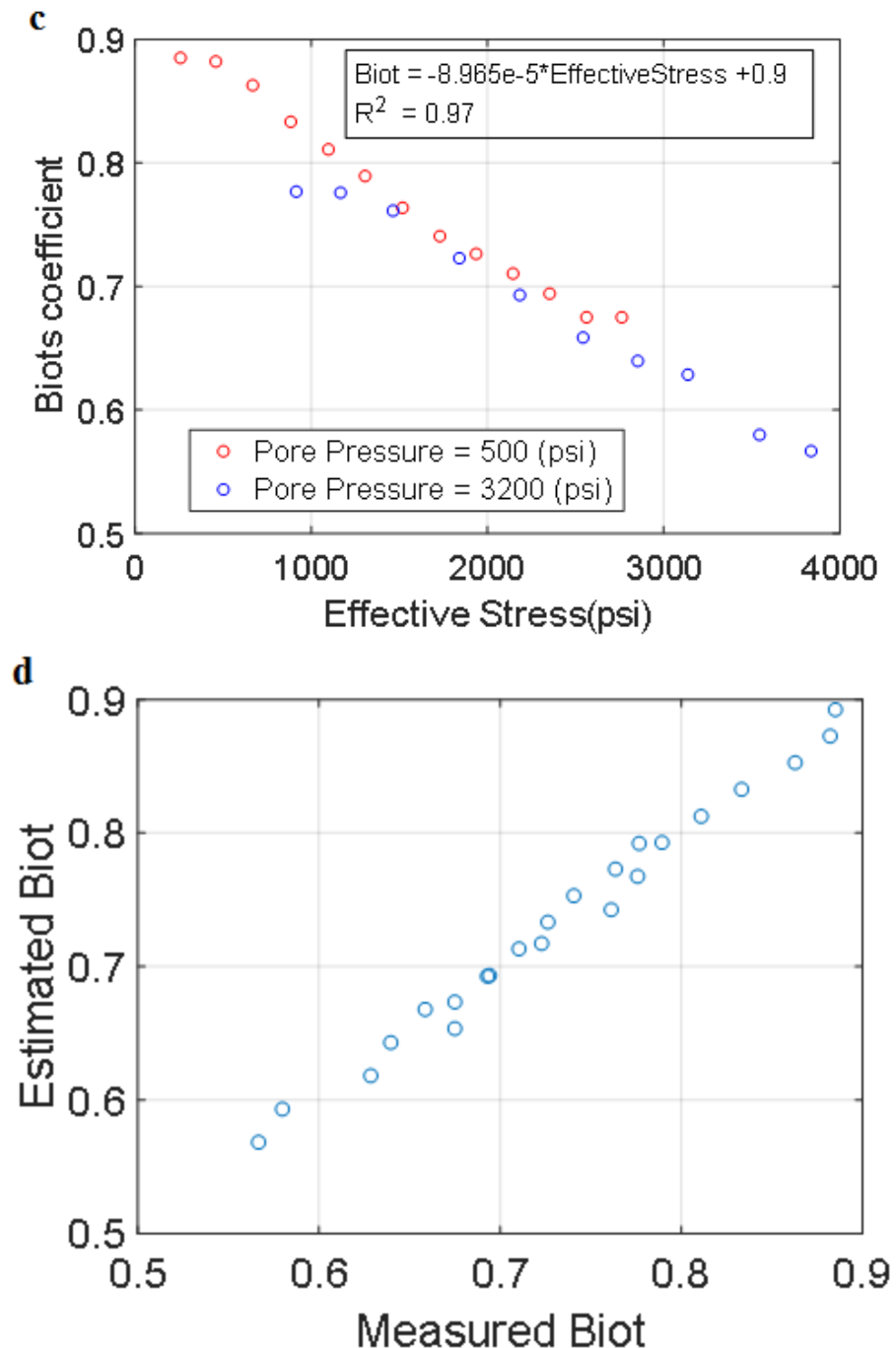


Figure 5-20. (c) Biot's Coefficient versus effective stress ( $\alpha = -8.965e-5\sigma' + 0.9$ ) (d) Predicted and measured Biot's Coefficient using multi-variate linear regression,  $R^2$  of 0.98.

### 5.7.2 Poroelastic Analytical Solution Results

Additional field and experimental data were acquired to investigate the effect of Biot's stress dependency on poroelastic response of injection. In situ stress data measured for deep formations shows that stress regime could be normal and/or strike-slip with minimum horizontal stress (Shmin) ranging from 0.62 to 0.83 psi/ft (Haimson, 1978). In addition, results of mini-frac tests, performed in an adjacent depleted reef in Michigan basin, are used to provide stress data for the modeling (S Raziperchikolaee et al., 2019). The pore pressure of depleted reef was 528 psi before performing the mini-frac test. Four injection and shut-in cycles were performed as part of mini-frac test for Brown Niagaran formation. The mini-frac tests achieved formation breakdown, fracture re-opening, and fracture propagations. The final fracture closure pressure for the Brown Niagaran test was estimated to be 1799 psi, which corresponds to a fracture gradient of 0.31 psi/ft. Shmin was changed formation by formation in carbonate sequence from 1799 at depth of 5967 ft (0.31 psi/ft), to 3084 psi at depth of 5765 ft (0.53 psi/ft).

An analysis of minimum horizontal stress increase during the injection process, due to the poro-elastic effect of injection, is then investigated using a constant and stress dependent Biot's Coefficient.

Estimation of Shmin is necessary to avoid tensile fracturing of the target reservoir during CO<sub>2</sub> injection. As a result, this work mainly focuses on studying changes of Shmin. While numerical simulations could be computationally expensive, analytical solutions could be used to predict stress changes quickly. The change in Shmin caused by changing pore pressure can be approximated by using different techniques (e.g., uniaxial compaction assumption, theory of strain nuclei, theory of inclusion, or theory of inhomogeneity (Fjar et al., 2008)). The Rudnicki model (Rudnicki, 1986) is used to study changes of Shmin in this work. In this model, the reservoir is assumed to be a spheroid inclusion in an infinite solid medium. By assuming the same elastic parameters in the reservoir and surrounding rock, the Shmin changes can be calculated using inclusion theory as:

$$\frac{\Delta\sigma}{\Delta P} = \alpha \frac{1-2v}{1-v} \left[ 1 - \frac{e}{2\sqrt{(1-e^2)^3}} (\arccos(e) - e\sqrt{1-e^2}) \right]$$

**Equation 5-8**

Where e is the reservoir aspect ratio (thickness to diameter ratio), and u is Poisson's ratio. The aspect ratio of the reservoir is calculated using the vertical axis of 280 ft and the horizontal axis of 2500 ft (~ 0.11). The reservoir pore pressure of 528 psi, to represent depleted reservoir, is used to estimate Shmin at higher pore pressures. Three initial Shmin values of 1799 psi based on measured mini-frac test results in Brown Niagaran, 3084 psi in another carbonate formation (A2-carbonate) in the sequence, and one additional higher Shmin of 5000 psi were used as an input to the model. Experimental measurement of Poisson ratio from laboratory triaxial test experiments (0.26) was used as an additional input parameter.

For the scenario with a constant Biot's Coefficient, Biot's Coefficient is estimated using initial Shmin and pore pressure of the reservoir by employing Equation 5-7. This would be 0.77 for the case with Shmin of 1700 psi, 0.65 for the case with Shmin of 3084 psi, and 0.48 for the case with Shmin of 5000 psi. Pore pressure step of 100 psi is assigned to increase reservoir pressure from 500 psi (initial reservoir pore pressure) to 10000 psi. Then, the Shmin increase was estimated at each pore pressure using Equation 5-8.

For the scenario with Biot's coefficient stress dependency, the changes in Shmin is estimated at each pore pressure step by employing Equation 5-8. Then, Equation 5-7 was used to update Biot's coefficient. Figure 5-21 shows the total and effective stress change by assuming constant versus stress dependent Biot's Coefficient for three different initial Shmin. All input parameters used to calculate stress changes

are summarized in Table 5-15. Figure 5-21 shows the magnitude of Shmin increase due to pore pressure rise (poroelastic effect of injection) is greater for the case of the stress dependent Biot's Coefficient. Effective Shmin stress changes would also be higher in comparison to the constant Biot's Coefficient scenarios. The observed trends can be explained by studying Biot's Coefficient evolution due to effective stress change. Figure 5-22 shows the Biot's coefficient changes at three scenarios with different initial Shmin. By increasing pore pressure, effective stress decreases. As a result, Biot's Coefficient increases. Increasing Biot's Coefficient leads to a higher stress change compared to the case with a constant Biot's Coefficient. The difference between constant and stress dependent Biot's coefficient response is greater in the scenario with the higher initial Shmin because the range of Biot's Coefficient increase is larger (0.18 at 5000 psi) than the two other scenarios (0.14 at 3084 psi, and 0.1 at 1799 psi). Figure 5-21 also shows that the stress change due to fluid injection depends on the initial Shmin in the reservoir. Higher initial Shmin in the reservoir could lead to a higher stress increase. Conversely, by assuming a constant Biot's Coefficient, stress changes would be independent of initial Shmin.

Geertsma model (Geertsma, 1973), is used to estimate surface uplift due to fluid injection. In this model, the uplift resulting from the expansion of a small sphere is calculated. Then, total uplift is estimated by adding the influence of many such spheres. Analytical solutions for a disk-shaped reservoir which give a surface uplift estimation at the center of a disk shape reservoir is:

$$U_z = 2C_m h \alpha \Delta P (1 - \nu) \left( 1 - \frac{D}{\sqrt{D^2 + R^2}} \right)$$

**Equation 5-9**

where  $U_z$  is surface uplift,  $C_m$  is uniaxial compressibility,  $h$  is reservoir thickness,  $D$  is reservoir depth and  $R$  is reservoir radius. The Geertsma model is limited to the case where there is no contrast in elastic properties between the reservoir and the surroundings. Parameters used to calculate surface uplift in Equation 5-9 are summarized in Table 5-15. Figure 5-22 shows the calculated surface uplift by assuming constant versus stress dependent Biot's Coefficient. Figure 5-22 shows surface uplift due to fluid injection would be larger by considering stress dependency of Biot's Coefficient. Because Biot's Coefficient increases as a function of pore pressure, greater surface uplift is estimated using a stress dependent Biot's Coefficient in comparison to the cases with a constant Biot's Coefficient at initial Shmin and pore pressure.

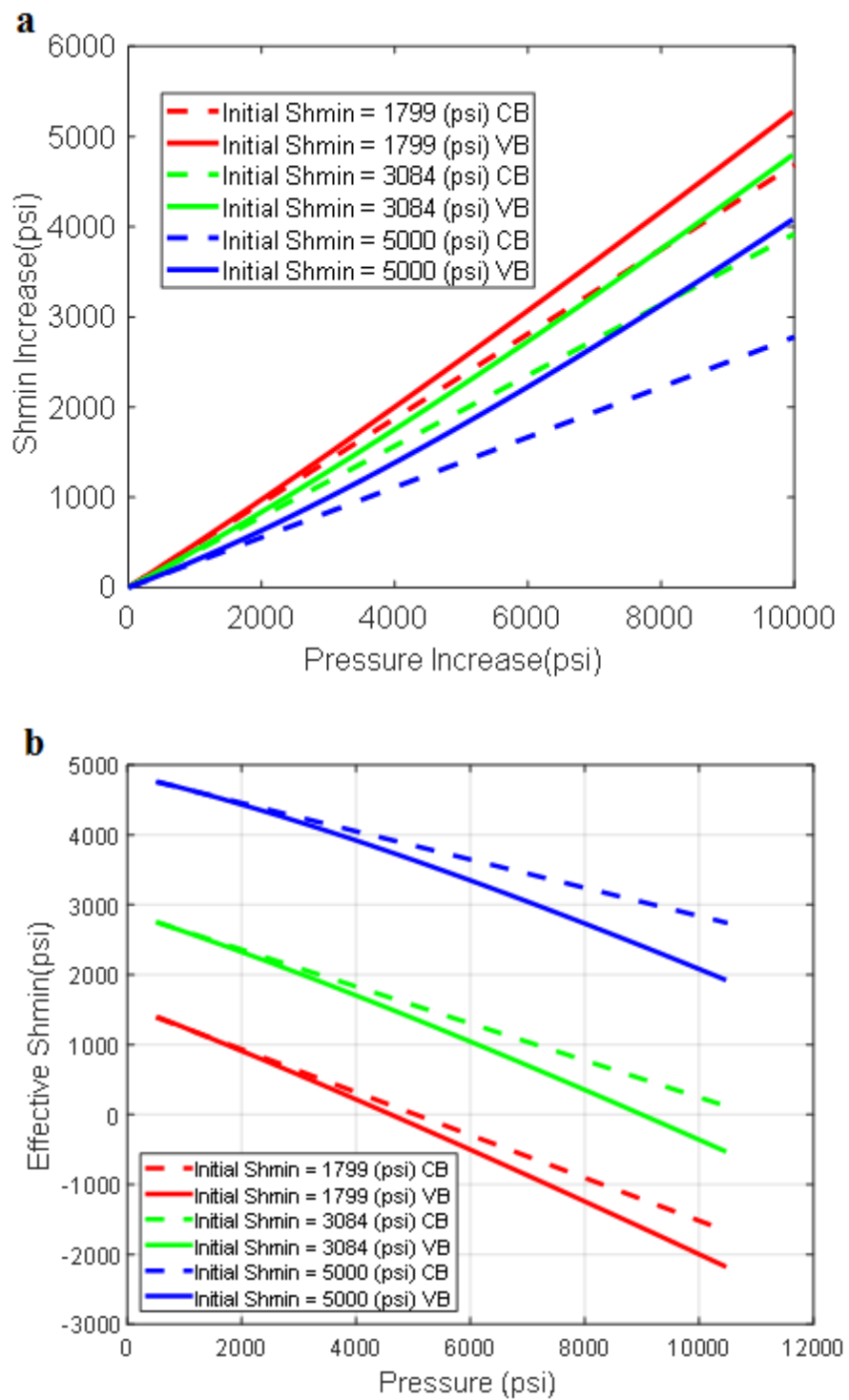


Figure 5-21. (a) total stress increase versus pore pressure increase (b) effective stress decrease by pore pressure increase

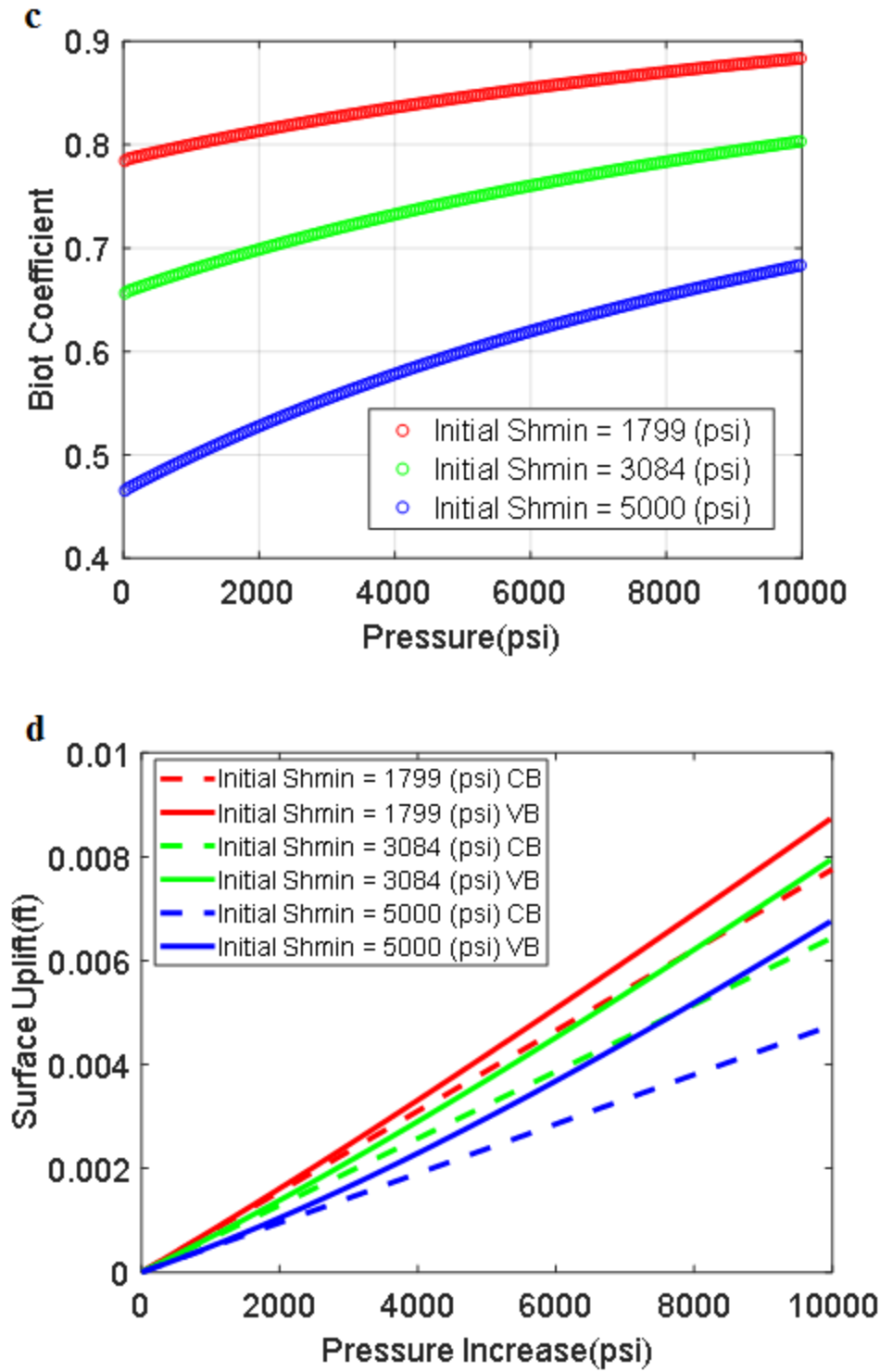


Figure 5-22. (c) trend of Biot's Coefficient as a function of pore pressure (d) surface uplift as a function of pore pressure increase.

### 5.7.3 Numerical Modeling Results of Multiphase Flow (CO<sub>2</sub> Injection)

Assumptions used to develop analytical models (e.g., constant elastic properties, single phase flow) limit its application to the simple general scenarios. Two-phase flow coupled with the geomechanics numerical simulation was used to assess poro-elastic response of CO<sub>2</sub> injection. A rectangular prism shape model for the reservoir (depleted reef) confined by the sideburden and overburden layers was built to represent the reef system and the surrounding rock. Different mechanical parameters were used for the reservoir and surrounding rock (which is mainly composed of salt formations). The reservoir is assumed to be saturated with water initially (at depleted state). Then, CO<sub>2</sub> is injected to the depleted reef using a single injection well in the center of the reservoir. A two-phase flow model is used to model CO<sub>2</sub> injection. An iterative feedback approach is used for coupling fluid flow and geomechanics modules in the model (Tran, Nghiem, et al., 2009). Model parameters are summarized in Table 5-15. The pore pressure increases up to 8000 psi compared to the initial pore pressure of 528 psi in the numerical model. The simulation was performed for a Shmin of 3084 psi by considering (1) constant Biot's Coefficients of 0.65 during injection and (2) a stress dependent Biot's Coefficient using the Equation 5-7. A pore pressure increase from 500 to 8500 psi causes Shmin to increase to 3915 psi using the stress dependent Biot's Coefficient compared to 3274 psi using the constant Biot's coefficient. Effective Shmin decreases to 556 psi using the stress dependent Biot's Coefficient, and 915 psi using the constant Biot's Coefficient (Figure 5-23). Surface displacement would be 0.0056 ft using stress dependent Biot's Coefficient and 0.0047 ft using constant Biot's Coefficient (Figure 5-24). A key observation is that both the analytical and numerical models predict larger changes in Shmin and uplift using a stress dependent Biot's Coefficient. Figure 5-25 shows Shmin increases would be higher by considering stress dependency of Biot's Coefficient. In addition, surface uplift due to fluid injection would be larger by considering stress dependency of Biot's Coefficient. By increasing pore pressure, effective stress decreases and Biot's Coefficient increases. This leads to larger Shmin changes when using the stress dependent Biot's Coefficient.

**Table 5-15. Parameters to build the analytical model and geomechanical - multiphase flow model.**

Analytical Models Parameters	
Reservoir thickness	280 ft
Reservoir diameter	2500 ft
Reservoir aspect ratio	0.11
Reservoir Poisson ratio	0.26
Reservoir Young's modulus	8.5e6 psi
is uniaxial compressibility	9.6e-8 1/psi
Reservoir depth	5500 ft
Initial Shmin scenarios	1799, 3084, 5000 psi
Initial reservoir pressure	528 psi
Reservoir pore pressure increase	Up to 10000 psi
Initial Biot's Coefficient	0.77, 0.65, 0.48
Numerical Simulation Parameters	
Reservoir top	5,500 ft
Thickness reservoir	280 ft
Model grid	3D square
Number of grids	31*31*12

Numerical Simulation Parameters	
Model dimensions	2500*2500*280 ft
Property variability, vertical	Varies by layer
Property variability, horizontal	Homogeneous
Porosity reservoir	0.05
Permeability reservoir	50 mD
Relative permeability	Van Genuchten function with the exponent of 0.457
Injection time	1 year
Pore pressure	500 psi
Wellbore constraint: pressure	100, 2500, 4500, 6500, 8500 psi
Reservoir Poisson's Ratio	0.26
Caprock Poisson's Ratio	0.25
Reservoir Young's modulus	8.5e6 psi
Caprock Young's modulus	8.2e6 psi
Biot's Coefficient	0.6563 in constant scenario, Variant by pressure and stress in dynamic scenario

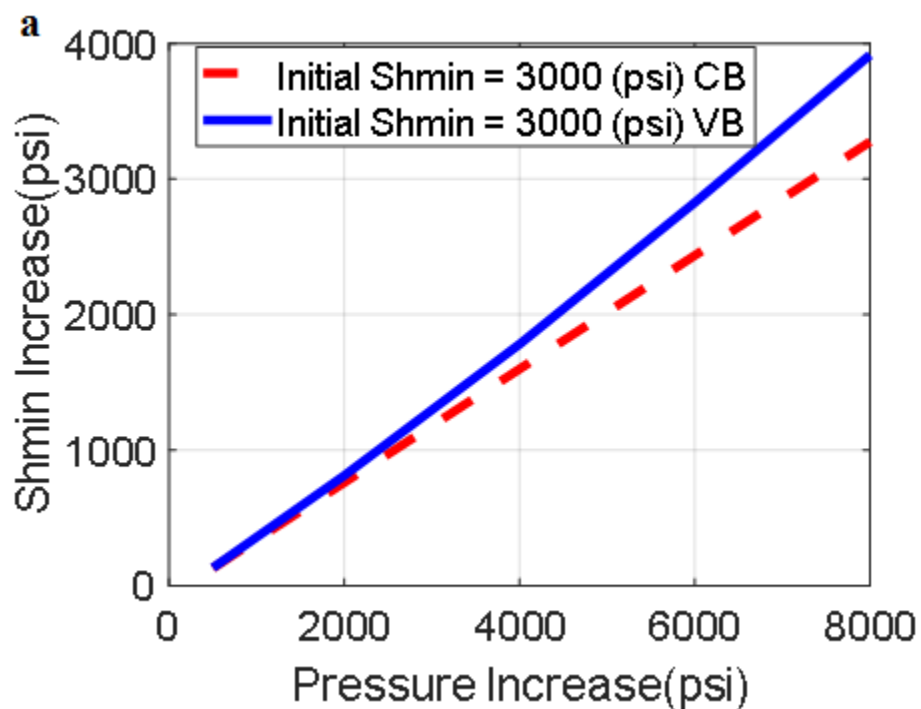


Figure 5-23. Total stress increase versus pore pressure increase

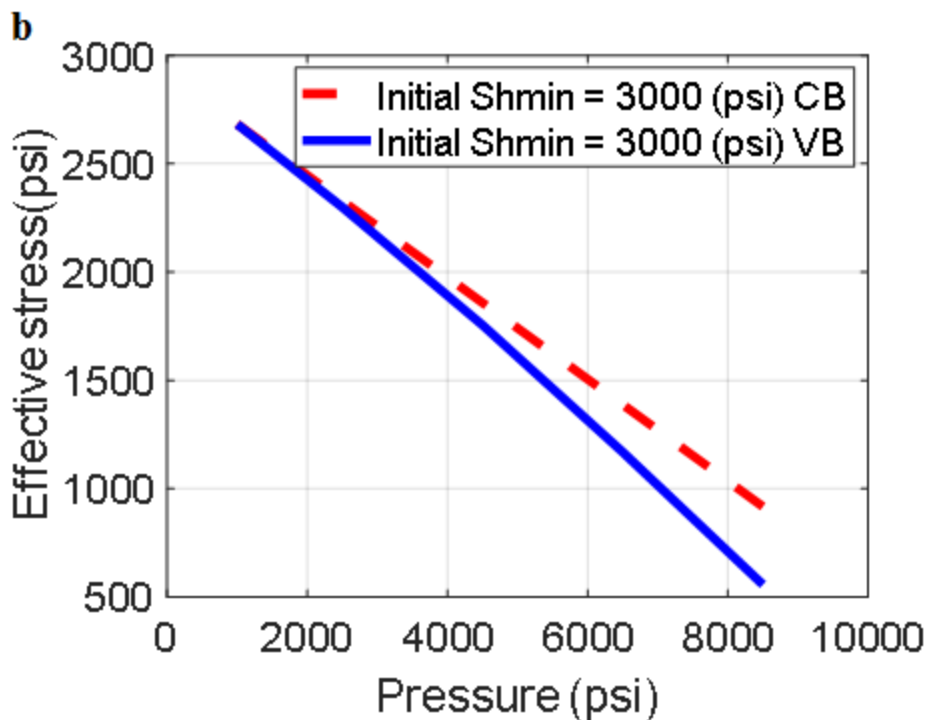


Figure 5-24. Effective stress decrease by pore pressure increase

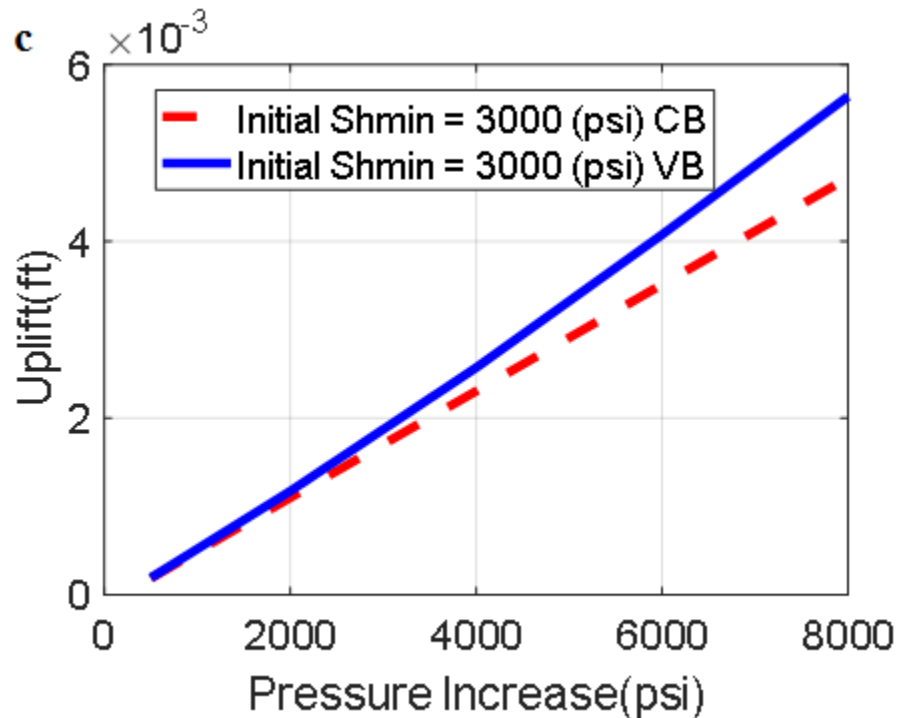


Figure 5-25. Uplift as a function of pore pressure increase.

## 5.8 Summary & Conclusions

A statistical reduced order modeling approach was used to predict stress changes and earth surface displacement during CO<sub>2</sub> Sequestration into a closed reservoir – as opposed to numerical or analytical modeling. The focus of this work was stress changes inside the reservoir (not stress changes in overburden or underburden), the displacement at the of the reservoir, and earth surface uplift. The independent parameters to evaluate poroelastic responses include Young's modulus and Poisson's ratio of the reservoir and surrounding rock as well as pressure increase by CO<sub>2</sub> injection, and Biot's coefficient. The results of the study provide a quick tool to evaluate mechanical response of caprock-reservoir systems during CO<sub>2</sub> injection by evaluating stress changes and reservoir and earth surface displacement. We determined the significance of the different independent parameters on each poroelastic response (i.e., vertical stress changes, horizontal stress changes, reservoir vertical displacement, surface uplift). We conclude that each reservoir type has different control parameters for each performance metric. The pressure increase is the main parameter that controls stress increase, reservoir displacement, and surface uplift. While the reservoir depth is a significant parameter to predict surface uplift, Biot's coefficient is the main parameter to evaluate horizontal stress increase. The predictive models developed in this work provide a simpler tool to evaluate the mechanical performance of CO<sub>2</sub> storage in the closed system not only in the Michigan basin but also for other reefs with similar characteristics. The response surface methodology and Monte Carlo simulations were utilized to maximize the information gained from each uncertainty analysis. Using the simple statistical based mechanical model, the screening process to select the best site for CO<sub>2</sub> sequestration, in terms of mechanical integrity, could be more efficient.

Grain and bulk compressibility of a carbonate (dolomite) reservoir was measured and used to model Biot's Coefficient stress dependency. The experimental program simulated different scenarios for Biot's measurement (using indirect Biot's Coefficient measurement) via changing both the confining stress and the pore pressure. The experimental results for stress dependency of Biot's Coefficient for carbonate reservoirs was then used to predict poroelastic response of injection. A stress-independent constant Biot's Coefficient has typically been used to estimate poroelastic response of injection such as surface uplift modeling, reservoir stress path prediction, and fault activation. Analytical and numerical models were then used to estimate the poroelastic response of injection by considering Biot's Coefficient dependency to the effective stress. The modeling results demonstrate how the assumption of a constant Biot's Coefficient affect geomechanical responses of the subsurface injection. Modeling results show that using a constant Biot's Coefficient would be inaccurate since effective stress changes cause Biot's Coefficient increase.



## 6.0 References

Ahmadinia, M., Shariatiipour, S. M., Andersen, O., & Sadri, M. (2019). Benchmarking of vertically integrated models for the study of the impact of caprock morphology on CO<sub>2</sub> migration. *International Journal of Greenhouse Gas Control*, 90, 102802.

Akono, A. T., Druhan, J. L., Dávila, G., Tsotsis, T., Jessen, K., Fuchs, S., . . . Tkach, M. K. (2019). A review of geochemical–mechanical impacts in geological carbon storage reservoirs. *Greenhouse Gases: Science and Technology*, 9(3), 474-504.

Al-Tahini, A. M., Abousleiman, Y. N., & Brumley, J. L. (2005). *Acoustic and quasistatic laboratory measurement and calibration of the pore pressure prediction coefficient in the poroelastic theory*. Paper presented at the SPE Annual Technical Conference and Exhibition.

Anbar, S. (2010). *Development of a predictive model for carbon dioxide sequestration in deep saline carbonate aquifers*. Paper presented at the SPE Annual Technical Conference and Exhibition.

Anderson, S. T., & Jahediesfanjani, H. (2019). Estimating the pressure-limited dynamic capacity and costs of basin-scale CO<sub>2</sub> storage in a saline formation. *International Journal of Greenhouse Gas Control*, 88, 156-167.

André, L., Audigane, P., Azaroual, M., Menjouz, A. (2007). Numerical modeling of fluid–rock chemical interactions at the supercritical CO<sub>2</sub>–liquid interface during CO<sub>2</sub> injection into a carbonate reservoir, the Dogger aquifer (Paris Basin, France), *Energy Convers. Manage.*, 48, pp. 1782-1797

Audigane, P. , Gaus, I. , Czernichowski-Lauriol, I., Pruess, K., Xu, T.F. (2007). Two-dimensional reactive transport modeling of CO<sub>2</sub> injection in a saline Aquifer at the Sleipner site, North Sea, *Am. J. Sci.*, 307, pp. 974-1008

Aziz, K., Ramesh, A., & Woo, P. (1987). Fourth SPE comparative solution project: comparison of steam injection simulators. *Journal of Petroleum Technology*, 39(12), 1,576-571,584.

Bachu, S., Bonijoly, D., Bradshaw, J., Burruss, R., Holloway, S., Christensen, N. P., & Mathiassen, O. M. (2007). CO<sub>2</sub> storage capacity estimation: Methodology and gaps. *International Journal of Greenhouse Gas Control*, 1(4), 430-443.

Bachu, S., Gunter, W. D., and Perkins, E.H. (1994). Aquifer disposal of CO<sub>2</sub>: hydrodynamic and mineral trapping, *Energy Convers. Mgmt.*, v. 35, p. 269-279.

Bilhartz, H., Charlson, G., Stalkup, F., & Miller, C. (1978). A Method for Projecting Full-Scale Performance of CO<sub>2</sub> Flooding in the Willard Unit. Paper presented at the SPE Symposium on Improved Methods of Oil Recovery.

Biot, M., & Willis, D. (1957). The elastic coeff cients of the theory of consolidation. *J. appl. Mech*, 24, 594-601.

Blöcher, G., Reinsch, T., Hassanzadegan, A., Milsch, H., & Zimmermann, G. (2014). Direct and indirect laboratory measurements of poroelastic properties of two consolidated sandstones. *International Journal of Rock Mechanics and Mining Sciences*, 67, 191-201.

Box, G. E., & Behnken, D. (1960). Some new three level designs for the study of quantitative variables. *Technometrics*, 2(4), 455-475.

Bradshaw, J., Bachu, S., Bonijoly, D., Burruss, R., Holloway, S., Christensen, N. P., & Mathiassen, O. M. (2007). CO<sub>2</sub> storage capacity estimation: issues and development of standards. *International Journal of Greenhouse Gas Control*, 1(1), 62-68.

Cappa, F., & Rutqvist, J. (2011a). Impact of CO<sub>2</sub> geological sequestration on the nucleation of earthquakes. *Geophysical Research Letters*, 38(17).

Cappa, F., & Rutqvist, J. (2011b). Modeling of coupled deformation and permeability evolution during fault reactivation induced by deep underground injection of CO<sub>2</sub>. *International Journal of Greenhouse Gas Control*, 5(2), 336-346.

Cappa, F., & Rutqvist, J. (2012). Seismic rupture and ground accelerations induced by CO<sub>2</sub> injection in the shallow crust. *Geophysical Journal International*, 190(3), 1784-1789.

Catacosinos, P., Harrison III, W., Reynolds, R., WestJohn, D., & Wollensack, M. (2000). Stratigraphic Nomenclature for Michigan: Michigan Department of Environmental Quality, Geological Survey Division, 1 sheet.

CMG, I. (2017). Advanced Oil/gas reservoir simulator version 2017 user's guide. Calgary, Alberta, Canada: Computer Modelling Group LTD.

CMG-GEM. (2012). *Advance compositional and GHG reservoir simulator user's guide*. Calgary, Alberta.

Coniglio, M., Frizzell, R., & Pratt, B. R. (2004). Reef-capping laminites in the Upper Silurian carbonate-to-evaporite transition, Michigan Basin, south-western Ontario. *Sedimentology*, 51(3), 653-668.

Dalkhaa, C., Shevalier, M., Nightingale, M., Mayer, B. (2013). 2-D reactive transport modeling of the fate of CO<sub>2</sub> injected into a saline aquifer in the Wabamun Lake Area, Alberta, Canada, *Applied Geochemistry*, 38, pp. 10-23

Delany, J.M. and Lundein, S.R. (1990). *The LLNL Thermo-chemical Database*, Lawrence Livermore National Laboratory Report UCRL-21658.

Ekeoma, E., & Appah, D. (2009). *Latin hypercube sampling (lhs) for gas reserves*. Paper presented at the Nigeria Annual International Conference and Exhibition.

Fang, Z., Khaksar, A., & Gibbons, K. (2012). Geomechanical risk assessments for CO<sub>2</sub> sequestration in depleted hydrocarbon sandstone reservoirs. *SPE Drilling & Completion*, 27(03), 368-382.

Fjar, E., Holt, R. M., Raaen, A., Risnes, R., & Horsrud, P. (2008). *Petroleum related rock mechanics* (Vol. 53): Elsevier.

Gaus, I., Azaroual, M., Czernichowski-Lauriol, I. (2005). Reactive transport modelling of the impact of CO<sub>2</sub> injection on the clayey cap rock at Sleipner (North Sea), *Chem. Geol.*, 217, pp. 319-337

Geertsma, J. (1973). Land subsidence above compacting oil and gas reservoirs. *Journal of Petroleum Technology*, 25(06), 734-744.

Ghomian, Y., Sepehrnoori, K., & Pope, G. A. (2010). *Efficient investigation of uncertainties in flood design parameters for coupled CO<sub>2</sub> sequestration and enhanced oil recovery*. Paper presented at the SPE International Conference on CO<sub>2</sub> Capture, Storage, and Utilization.

Grammer, G. M., Barnes, D. A., Harrison III, W. B., Sandomierski, A. E., & Mannes, R. G. (2009). Practical synergies for increasing domestic oil production and geological sequestration of anthropogenic CO<sub>2</sub>: An example from the Michigan Basin.

Haagsma, A., Conner, A., Cotter, Z., Grove, B., Main, J., Scharenberg, M., Larsen, G., Raziperchikolaei, S., McCarren, H., Goodman, W., Sullivan, C., and Gupta, N. (2020). Geologic Characterization for CO<sub>2</sub> Storage with Enhanced Oil Recovery in Northern Michigan. MRCSP topical report prepared for DOE-NETL project DE-FC26-05NT42589, Battelle Memorial Institute, Columbus, OH.

Haagsma, A., Kelley, M., Conner, A., Cotter, Z., and Gupta, N. (2017). Task 5: Baseline Geologic Characterization Report. MRCSP topical report prepared for DOE-NETL project DE-FC26-05NT42589, Battelle Memorial Institute, Columbus, OH

Haagsma, A., Rine, M., Sullivan, C., Conner, A., Kelley, M., Modroo, A., Gupta, N. (2017). Static Earth Modeling of Diverse Michigan Niagara Reefs and the Implications for CO<sub>2</sub> Storage. *Energy Procedia*, 114, 3353-3363.

Haimson, B. C. (1978). Crustal stress in the Michigan Basin. *Journal of Geophysical Research: Solid Earth*, 83(B12), 5857-5863.

Hitchon, B. (1996). Aquifer disposal of carbon dioxide: hydrodynamic and mineral trapping—proof of concept. Geoscience Publishing Ltd, Sherwood Park, AB, Canada (165 p., ISBN 0-9680844-0-0)

Jeanne, P., Rutqvist, J., Dobson, P. F., Walters, M., Hartline, C., & Garcia, J. (2014). The impacts of mechanical stress transfers caused by hydromechanical and thermal processes on fault stability during hydraulic stimulation in a deep geothermal reservoir. *International Journal of Rock Mechanics and Mining Sciences*, 72, 149-163.

Jha, B., & Juanes, R. (2014). Coupled multiphase flow and poromechanics: A computational model of pore pressure effects on fault slip and earthquake triggering. *Water Resources Research*, 50(5), 3776-3808.

Kaldi, J., Daniel, R., Tenthorey, E., Michael, K., Schacht, U., Nicol, A., . . . Backe, G. (2011). Caprock systems for CO<sub>2</sub> geological storage. *IAEGHG Rep*, 1, 149.

Kelley, M., Abbaszadeh, M., Mishra, S., Mawalkar, S., Place, M., Gupta, N., & Pardini, R. (2014). Reservoir characterization from pressure monitoring during CO<sub>2</sub> injection into a depleted pinnacle reef—MRCSP commercial-scale CCS demonstration project. *Energy Procedia*, 63, 4937-4964.

Kestin, J. , Khalifa, H.E., Correia, R.J. (1981). Tables of the dynamic and kinematic viscosity of aqueous NaCl solutions in the temperature range 20–150 °C and the pressure range 0.1–35 MPa, *Journal of Physical and Chemical Reference Data*, 10, pp. 71-88.

Kharaka, Y.K., Gunter, W.D., Aggarwal, P.K., Perkins, E., and Debraal, J.D. (1989). *SOLMINEQ.88: A Computer Program for Geochemical Modeling of Water-Rock Reactions*, U.S. Geological Survey Water-Resources Investigations Report 88-4227, Menlo Park, California.

Killough, J., & Kossack, C. (1987). Fifth comparative solution project: evaluation of miscible flood simulators. Paper presented at the SPE Symposium on Reservoir Simulation.

Klimentos, T., Harouaka, A., Mtawaa, B., & Saner, S. (1998). Experimental determination of the Biot elastic constant: Applications in formation evaluation (sonic porosity, rock strength, earth stresses, and sanding predictions). *SPE Reservoir Evaluation & Engineering*, 1(01), 57-63.

Le Gallo, Y. (2016). Hydro-mechanical influence of sub-seismic blind faults on integrity of CO<sub>2</sub> geological storage in deep saline aquifer. *International Journal of Greenhouse Gas Control*, 51, 148-164.

Li, C., & Laloui, L. (2016). Coupled multiphase thermo-hydro-mechanical analysis of supercritical CO<sub>2</sub> injection: Benchmark for the In Salah surface uplift problem. *International Journal of Greenhouse Gas Control*, 51, 394-408.

Mazzoldi, A., Rinaldi, A. P., Borgia, A., & Rutqvist, J. (2012). Induced seismicity within geological carbon sequestration projects: maximum earthquake magnitude and leakage potential from undetected faults. *International Journal of Greenhouse Gas Control*, 10, 434-442.

Miller, J. , Sullivan, C., Larsen, G., Kelley, M., Rike, W., Gerst, J., Gupta, N., Paul, D., Pardini, R., and Modroo.A. (2014). Alternative conceptual geologic models for CO<sub>2</sub> injection in a Niagaran pinnacle reef oil field, Northern Michigan, USA. *Energy Procedia*, 63, 3685-3701.Mishra, S., Ravi Ganesh, P., Kelley, M., Gupta, N. (2017). Analyzing the Performance of Closed Reservoirs Following CO<sub>2</sub> Injection in CCUS Projects. *Energy Procedia*, 114, 3465-3475.

Mishra, S., & Datta-Gupta, A. (2017). *Applied Statistical Modeling and Data Analytics: A Practical Guide for the Petroleum Geosciences*: Elsevier.

Müller, T. M., & Sahay, P. N. (2016). Biot coefficient is distinct from effective pressure coefficient. *Geophysics*, 81(4), L27-L33.

Ngheim, L., Shrivastava, V., Tran, D., Kohse, B., Hassam, M., Yang, C. (2009). Simulation of CO<sub>2</sub> storage in saline aquifers, SPE- 125848, Presented at the 2009 SPE/ EAGE Reservoir Characterization and Simulation Conference, Abu Dhabi, UAE, 19-21 October.

Nguyen, B. N., Hou, Z., Bacon, D. H., & White, M. D. (2017). A multiscale hydro-geochemical-mechanical approach to analyze faulted CO<sub>2</sub> reservoirs. *Greenhouse Gases: Science and Technology*, 7(1), 106-127.

Nur, A., & Byerlee, J. D. (1971). An exact effective stress law for elastic deformation of rock with fluids. *Journal of geophysical research*, 76(26), 6414-6419.

Ortoleva, P. J., Dove, P., and Richter, F. (1998). Geochemical perspectives on CO<sub>2</sub> sequestration, Manuscript prepared for U. S. Department of Energy Workshop on "Terrestrial Sequestration of CO<sub>2</sub> - An Assessment of Research Needs," Gaithersburg, MD, May 10 - 12.

Osterloh, W. T. (2008). *Use of multiple-response optimization to assist reservoir simulation probabilistic forecasting and history matching*. Paper presented at the SPE Annual Technical Conference and Exhibition.

Peng, D.Y., and Robinson, D.B. (1976). A New Two-Constant Equation of State. *Industrial and Engineering Chemistry: Fundamentals*, 15:59-64. doi:10.1021/i160057a011

Pereira, F. L., Roehl, D., Laquini, J. P., Oliveira, M. F. F., & Costa, A. M. (2014). Fault reactivation case study for probabilistic assessment of carbon dioxide sequestration. *International Journal of Rock Mechanics and Mining Sciences*, 71, 310-319.

Place, M., Hawkins, J., Grove, B., Keister, L., Sheets, J., Welch, S., Cole, D., and Gupta, N. (2020). Geochemical Changes in Response to CO<sub>2</sub> Injection in a CO<sub>2</sub> EOR Complex in Northern Michigan, MRCSP topical report prepared for DOE-NETL project DE-FC26-05NT42589, Battelle Memorial Institute, Columbus, OH

Huh, J. M. S. (1974). GEOLOGY AND DIAGENESIS OF THE NIAGARAN PINNACLE REEFS IN THE NORTHERN SHELF OF THE MICHIGAN BASIN.

Raziperchikolaee, S., Alvarado, V., & Yin, S. (2013). Effect of hydraulic fracturing on long-term storage of CO<sub>2</sub> in stimulated saline aquifers. *Applied energy*, 102, 1091-1104.

Raziperchikolaee, S., Alvarado, V., & Yin, S. (2014). Microscale modeling of fluid flow-geomechanics-seismicity: Relationship between permeability and seismic source response in deformed rock joints. *Journal of Geophysical Research: Solid Earth*, 119(9), 6958-6975.

Raziperchikolaee, S., Kelley, M., & Gupta, N. (2018). Geomechanical characterization of a caprock-reservoir system in the Northern Appalachian Basin: Estimating spatial variation of in situ stress magnitude and orientation. *Interpretation*, 6(3), T759-T781.

Raziperchikolaee, S., Kelley, M., & Gupta, N. (2019). A screening framework study to evaluate CO<sub>2</sub> storage performance in single and stacked caprock-reservoir systems of the Northern Appalachian Basin. *Greenhouse Gases: Science and Technology*, 9(3), 582-605.

Raziperchikolaee, S., Kelley, M., Moronkeji, D., Xu, H., Guillermo, B., & Pardini, R. (2019). *Advanced Formation Testing Using a Wireline-Deployed Formation Testing Tool to Characterize In situ Stress Parameters in a Depleted Niagaran Pinnacle Reef Carbonate Reservoir*. Paper presented at the 53rd US Rock Mechanics/Geomechanics Symposium.

Raziperchikolaee, S., M. K., W. Garnes. (2018). *Regional Geomechanical characterization of Northern Pinnacle Reef Trend of the Michigan Basin*. Retrieved from

Reid, R.C., Prausnitz, J. M., Sherwood, T.K. (1977). *The Properties of Gases and Liquids*, 3rd Ed. McGraw-Hill, New York.

Riley, R., Harper, J., Harrison III, W., Barnes, D., Nuttall, B., Avary, K. L., . . . Harris, D. (2010). Evaluation of CO<sub>2</sub>-Enhanced Oil Recovery and Sequestration Opportunities in Oil and Gas Fields in the MRCSP Region MRCSP Phase II Topical Report October 2005 October 2010. DOE Cooperative Agreement No. DOE Cooperative Agreement No.

Rinaldi, A. P., & Rutqvist, J. (2013). Modeling of deep fracture zone opening and transient ground surface uplift at KB-502 CO<sub>2</sub> injection well, In Salah, Algeria. *International Journal of Greenhouse Gas Control*, 12, 155-167.

Rinaldi, A. P., Vilarrasa, V., Rutqvist, J., & Cappa, F. (2015). Fault reactivation during CO<sub>2</sub> sequestration: Effects of well orientation on seismicity and leakage. *Greenhouse Gases: Science and Technology*, 5(5), 645-656.

Rine, M., Barnes, D., & Harrison, W. B. (2015) *Petrophysical and Stratigraphic Characterization of Michigan Silurian Reefs*. Paper presented at the 44<sup>th</sup> Annual Eastern Section Meeting.

Rowe, A.M. and Chou, J.C.S. (1970). Pressure–volume–temperature-concentration relation of aqueous sodium chloride solutions, *Journal of Chemical & Engineering Data*, 15, pp. 61-66

Rudnicki, J. W. (1986). Fluid mass sources and point forces in linear elastic diffusive solids. *Mechanics of Materials*, 5(4), 383-393.

Rutqvist, J. (2012). The geomechanics of CO<sub>2</sub> storage in deep sedimentary formations. *Geotechnical and Geological Engineering*, 30(3), 525-551.

Rutqvist, J., Birkholzer, J., Cappa, F., & Tsang, C.-F. (2007). Estimating maximum sustainable injection pressure during geological sequestration of CO<sub>2</sub> using coupled fluid flow and geomechanical fault-slip analysis. *Energy Conversion and Management*, 48(6), 1798-1807.

Rutqvist, J., Birkholzer, J., & Tsang, C.-F. (2008). Coupled reservoir–geomechanical analysis of the potential for tensile and shear failure associated with CO<sub>2</sub> injection in multilayered reservoir–caprock systems. *International Journal of Rock Mechanics and Mining Sciences*, 45(2), 132-143.

Rutqvist, J., Rinaldi, A. P., Cappa, F., Jeanne, P., Mazzoldi, A., Urpi, L., Vilarrasa, V. (2016). Fault activation and induced seismicity in geological carbon storage—Lessons learned from recent modeling studies. *Journal of Rock Mechanics and Geotechnical Engineering*, 8(6), 789-804.

Rutqvist, J., Vasco, D. W., & Myer, L. (2010). Coupled reservoir-geomechanical analysis of CO<sub>2</sub> injection and ground deformations at In Salah, Algeria. *International Journal of Greenhouse Gas Control*, 4(2), 225-230.

Rutqvist, J., Wu, Y.-S., Tsang, C.-F., & Bodvarsson, G. (2002). A modeling approach for analysis of coupled multiphase fluid flow, heat transfer, and deformation in fractured porous rock. *International Journal of Rock Mechanics and Mining Sciences*, 39(4), 429-442.

Samsonov, S., Czarnogorska, M., & White, D. (2015). Satellite interferometry for high-precision detection of ground deformation at a carbon dioxide storage site. *International Journal of Greenhouse Gas Control*, 42, 188-199.

Schuetter, J., Ganesh, P. R., & Mooney, D. (2014). Building statistical proxy models for CO<sub>2</sub> geologic sequestration. *Energy Procedia*, 63, 3702-3714.

Schuetter, J., & Mishra, S. (2015). *Experimental Design or Monte Carlo Simulation? Strategies for Building Robust Surrogate Models*. Paper presented at the SPE Annual Technical Conference and Exhibition.

Settari, A., & Walters, D. A. (2001). Advances in coupled geomechanical and reservoir modeling with applications to reservoir compaction. *Spe Journal*, 6(03), 334-342.

Siggins, A. F., & Dewhurst, D. N. (2003). Saturation, pore pressure and effective stress from sandstone acoustic properties. *Geophysical Research Letters*, 30(2).

Soltanzadeh, H., & Hawkes, C. D. (2009). Induced poroelastic and thermoelastic stress changes within reservoirs during fluid injection and production. *Porous Media: Heat and Mass Transfer, Transport and Mechanics*, 27.

Tenthorey, E., Vidal-Gilbert, S., Backé, G., Puspitasari, R., Pallikathekathil, Z. J., Maney, B., & Dewhurst, D. (2013). Modelling the geomechanics of gas storage: A case study from the Iona gas field, Australia. *International Journal of Greenhouse Gas Control*, 13, 138-148.

Thibeau, S. and Nghiem, L.X. (2007). A modeling study of the role of selected minerals in enhancing CO<sub>2</sub> mineralization during CO<sub>2</sub> aquifer storage, SPE-109739, Presented at the 2007 SPE Annual Technical Conference and Exhibition, Anaheim, CA, USA, 11-14 November.

Tran, D., Nghiem, L., & Buchanan, L. (2009). *Aspects of coupling between petroleum reservoir flow and geomechanics*. Paper presented at the 43rd US Rock Mechanics Symposium & 4th US-Canada Rock Mechanics Symposium.

Tran, D., Nghiem, L., Buchanan, L., Geilikman, M., Leshchyshyn, T., Hannan, S., & Wong, S. W. (2008). *Modelling Thermal Geomechanical Effects on Simulation Porosity*. Paper presented at the The 42nd US Rock Mechanics Symposium (USRMS).

Tran, D., Nghiem, L., Shrivastava, V., & Kohse, B. (2010). *Study of geomechanical effects in deep aquifer CO<sub>2</sub> storage*. Paper presented at the 44th US Rock Mechanics Symposium and 5th US-Canada Rock Mechanics Symposium.

Tran, D., Settari, A., & Nghiem, L. (2004). New iterative coupling between a reservoir simulator and a geomechanics module. *Spe Journal*, 9(03), 362-369.

Tran, D., Shrivastava, V. K., Nghiem, L. X., & Kohse, B. F. (2009). *Geomechanical risk mitigation for CO<sub>2</sub> sequestration in saline aquifers*. Paper presented at the SPE Annual Technical Conference and Exhibition.

Van Genuchten, M. T. (1980). A closed-form equation for predicting the hydraulic conductivity of unsaturated soils 1. *Soil science society of America journal*, 44(5), 892-898.

van Wees, J.-D., Pluymakers, M., Osinga, S., Fokker, P., Van Thienen-Visser, K., Orlic, B., . . . Candela, T. (2019). 3-D mechanical analysis of complex reservoirs: a novel mesh-free approach. *Geophysical Journal International*, 219(2), 1118-1130.

Vidal-Gilbert, S., Nauroy, J.-F., & Brosse, E. (2009). 3D geomechanical modelling for CO<sub>2</sub> geologic storage in the Dogger carbonates of the Paris Basin. *International Journal of Greenhouse Gas Control*, 3(3), 288-299.

Vidal-Gilbert, S., Tenthorey, E., Dewhurst, D., Ennis-King, J., Van Ruth, P., & Hillis, R. (2010). Geomechanical analysis of the Naylor Field, Otway Basin, Australia: Implications for CO<sub>2</sub> injection and storage. *International Journal of Greenhouse Gas Control*, 4(5), 827-839.

Vilarrasa, V., Bolster, D., Olivella, S., & Carrera, J. (2010). Coupled hydromechanical modeling of CO<sub>2</sub> sequestration in deep saline aquifers. *International Journal of Greenhouse Gas Control*, 4(6), 910-919.

Wang, H. F. (2017). *Theory of linear poroelasticity with applications to geomechanics and hydrogeology*: Princeton University Press.

Welch, S.A., Sheets, J.M., Place, M.C., Saltzman, M.R., Edwards, C.T., Gupta, N., Cole, D.R. (2019). Assessing geochemical reactions during CO<sub>2</sub> injection into an oil-bearing reef in the northern Michigan basin, *Applied Geochemistry*, 100, pp. 380-392.

Wriedt, J., Deo, M., Han, W. S., & Lepinski, J. (2014). A methodology for quantifying risk and likelihood of failure for carbon dioxide injection into deep saline reservoirs. *International Journal of Greenhouse Gas Control*, 20, 196-211.

Xu, T., Apps, J. A. and Pruess, K. (2004). Numerical simulation of CO<sub>2</sub> disposal by mineral trapping in deep aquifers, *Applied Geochemistry*, 19, pp. 917-936.

Yin, S., Dusseault, M. B., & Rothenburg, L. (2007). Coupled multiphase poroelastic analysis of reservoir depletion including surrounding strata. *International Journal of Rock Mechanics and Mining Sciences*, 44(5), 758-766.

Youngren, G. K. C., Gary S. (1980). History Match Analysis of the Little Creek CO<sub>2</sub> Pilot Test. *Journal of Petroleum Technology*, 32(11), 2,042-042,052.

# **Appendix A Chester 16 Well-wise Oil and Gas Production History**

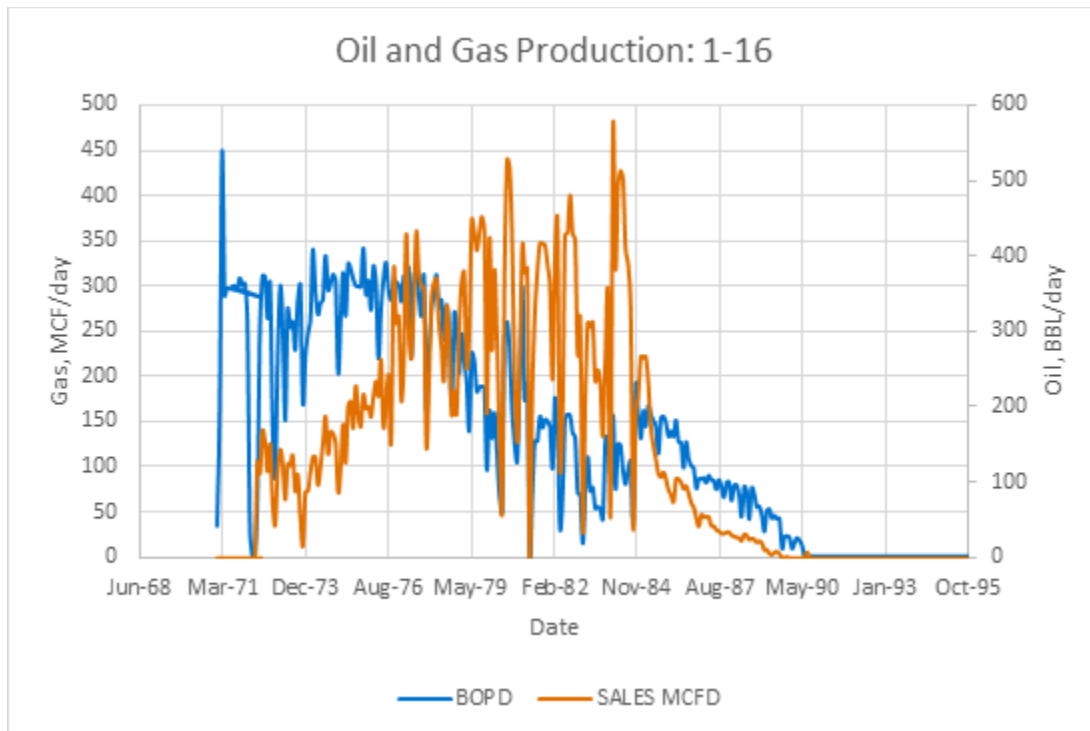


Figure A-1. Production history of the 1-16 well

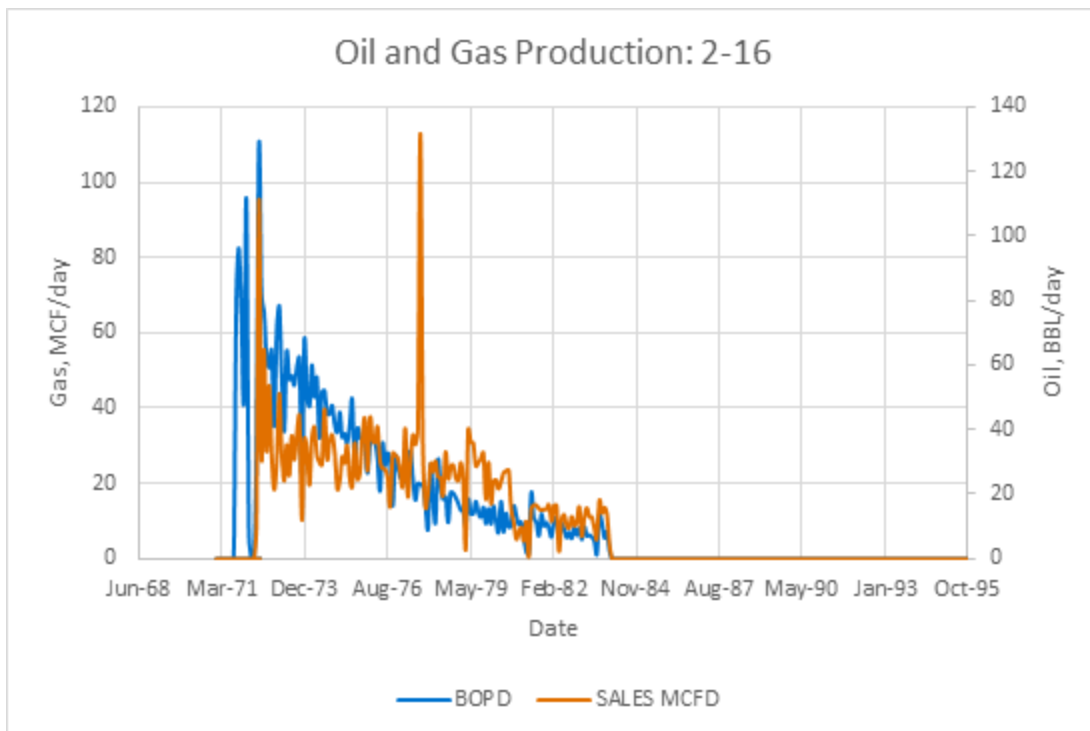


Figure A-2. Production history of the 2-16 well.

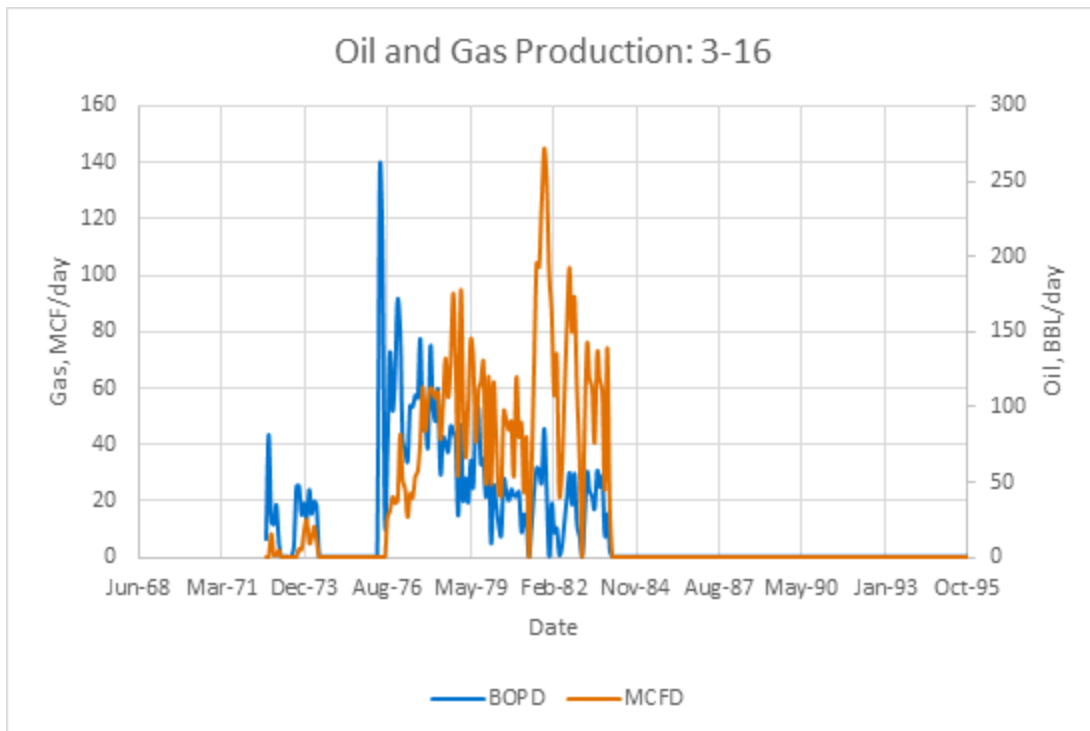


Figure A-3. Production history of the 3-16 well

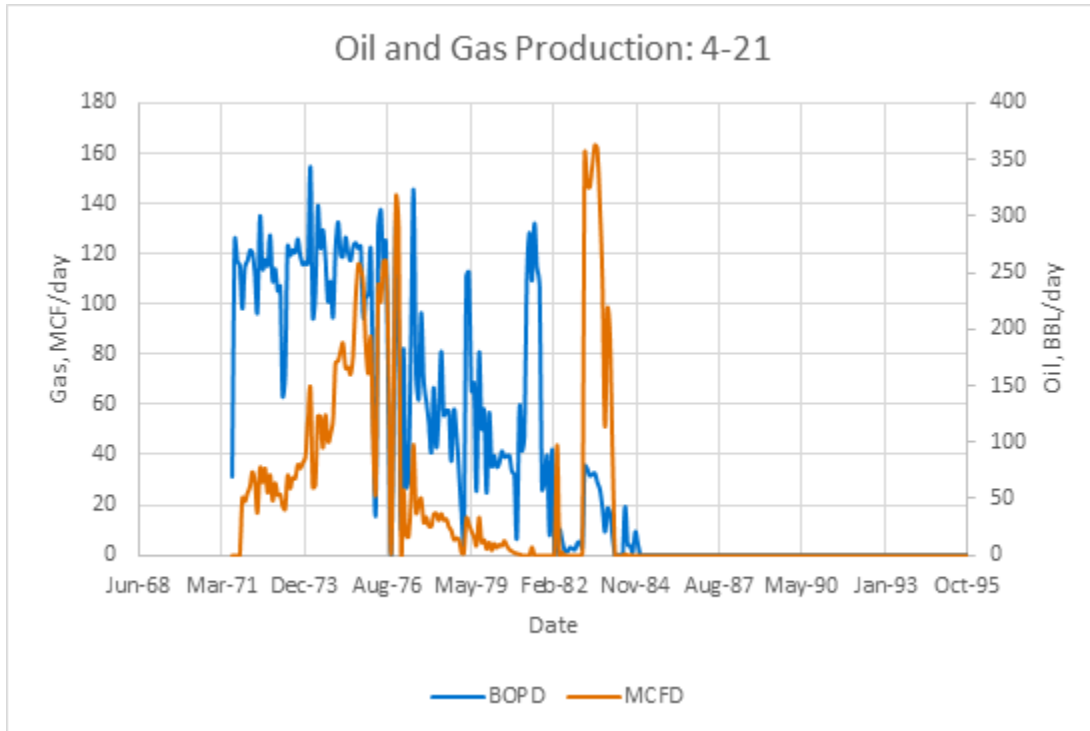


Figure A-4. Production history of the 4-21 well.

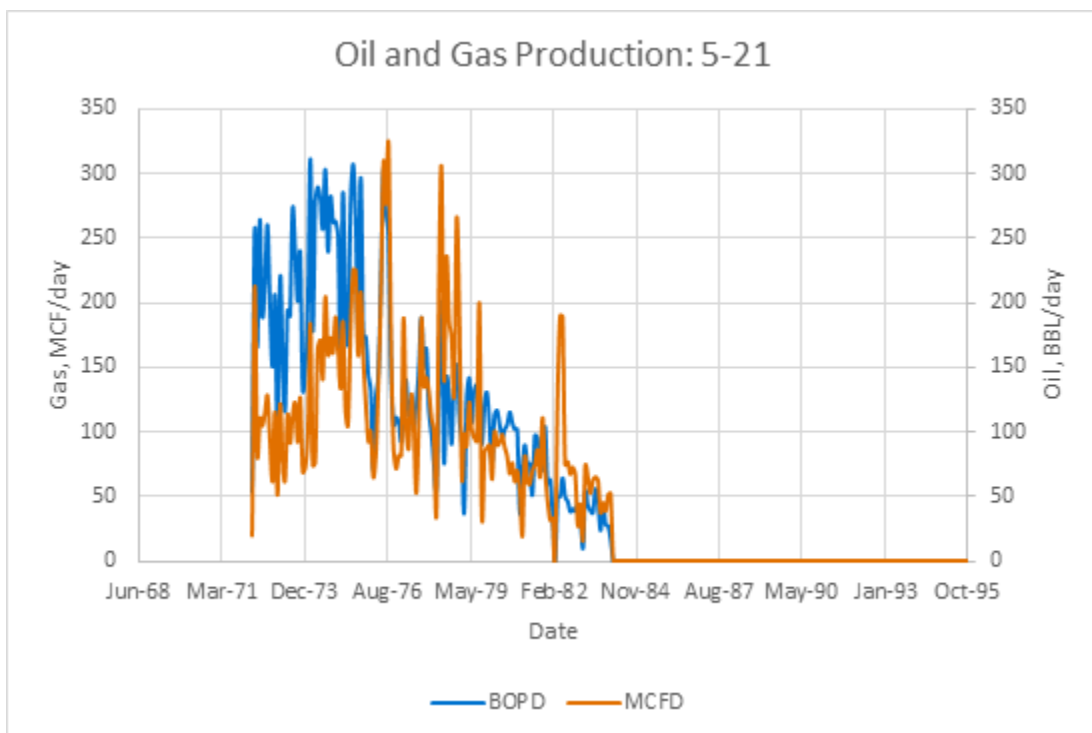


Figure A-5. Production history of the 5-21 well

BALTIMORE

It can be done

# **Appendix B Chester 16 Scenario**

## **3 Simulation Results**

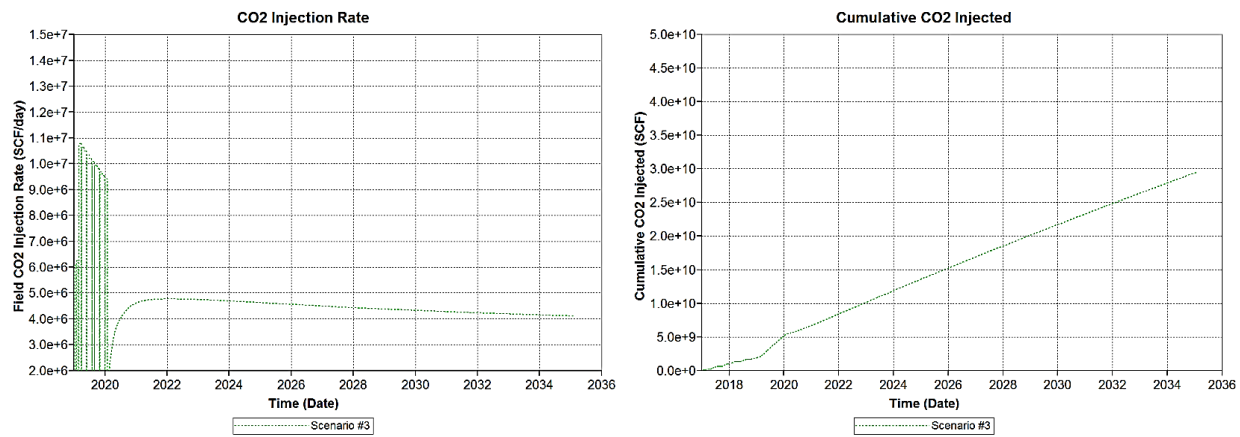


Figure B-1.  $\text{CO}_2$  injection rate (left) and the cumulative  $\text{CO}_2$  injected (right).

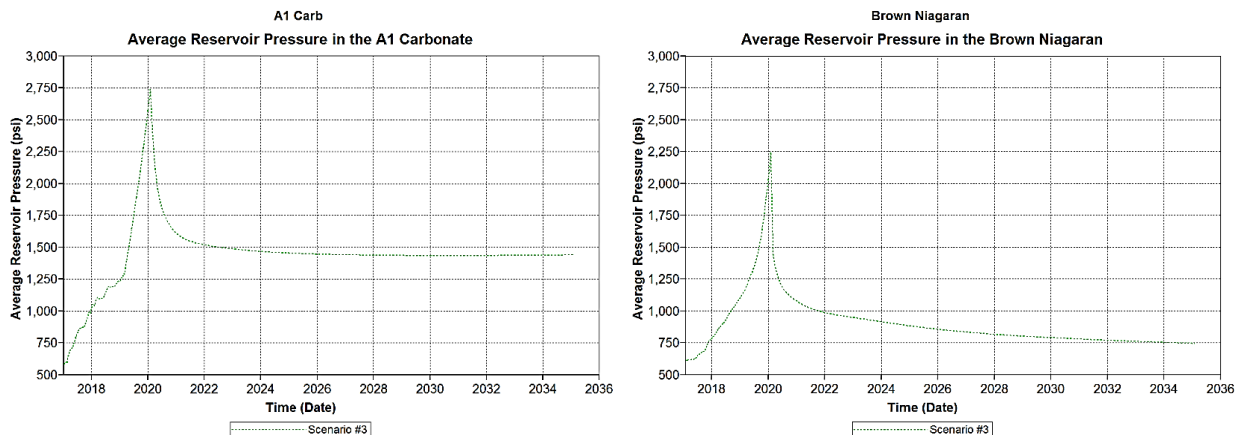


Figure B-2. Average reservoir pressure in the A1 Carbonate (top) and the Brown Niagaran (bottom) during  $\text{CO}_2$ -EOR

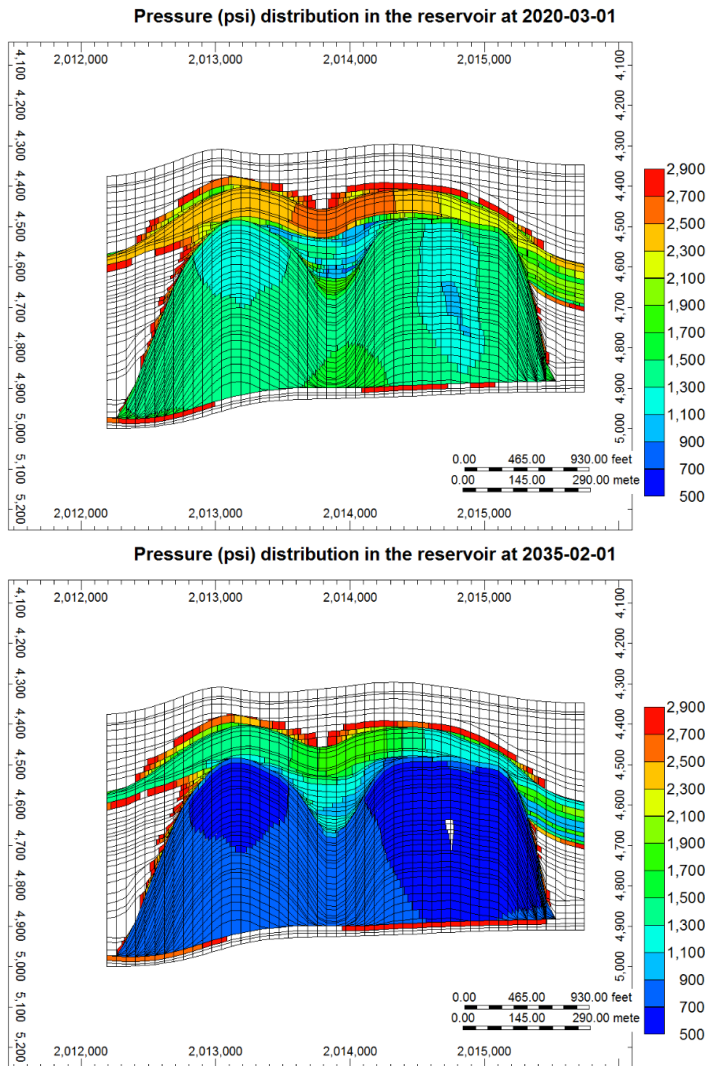


Figure B-3. Pressure distribution in the reservoir at the end of fill-up (top) and at the end of EOR (bottom)

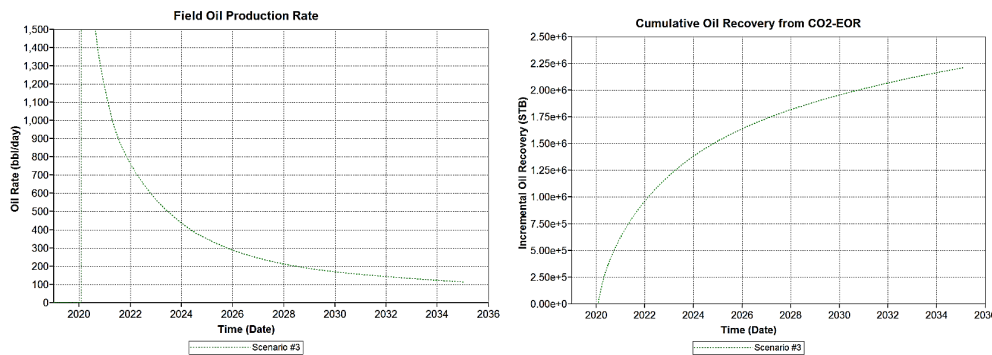


Figure B-4. Field oil rate (top) and Cumulative oil production (bottom)

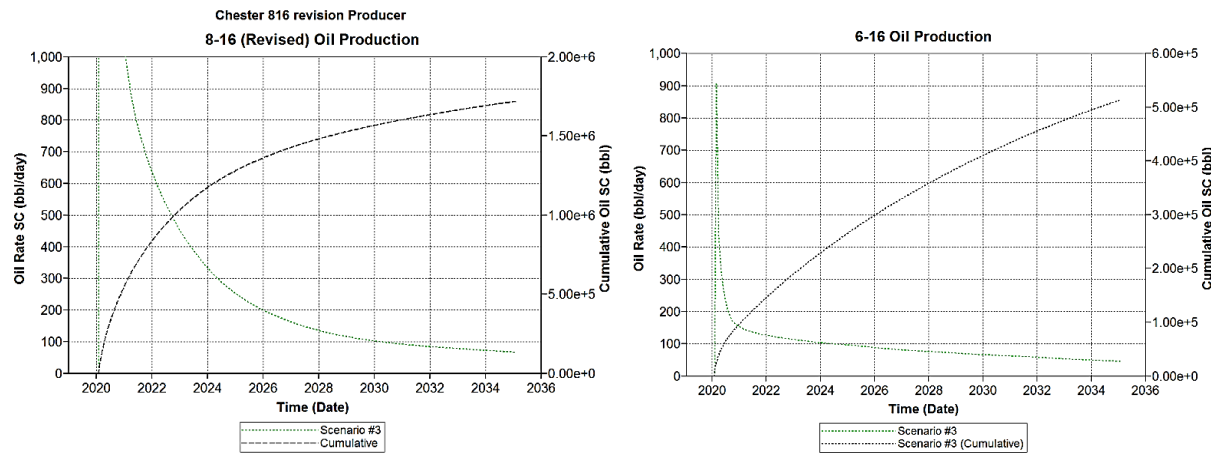


Figure B-5. Oil production contributions of individual producers. 8-16 Rev is shown on top and 6-16 is shown at the bottom.

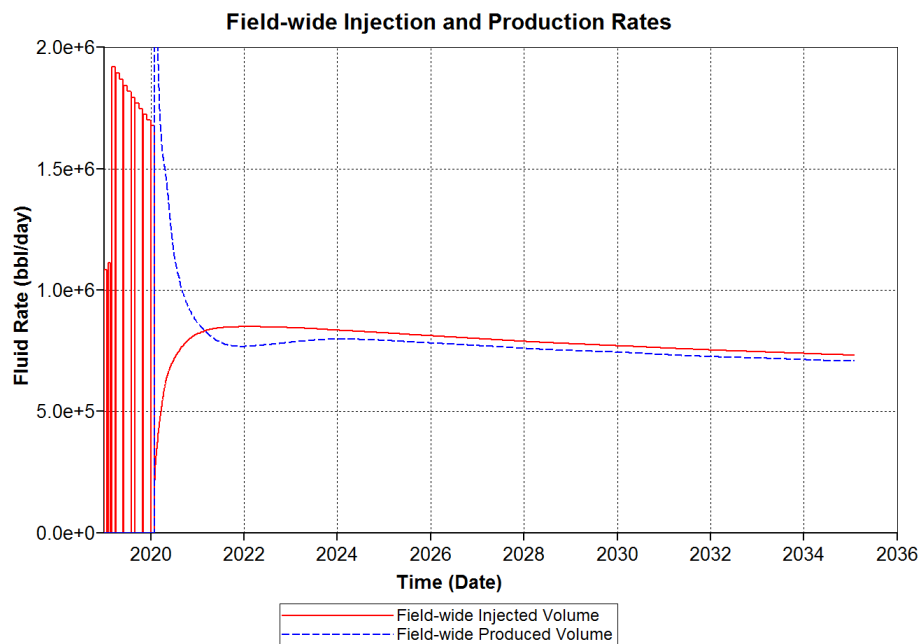


Figure B-6. The bottomhole voidage replacement rate is kept as close to unity as possible for the duration of EOR

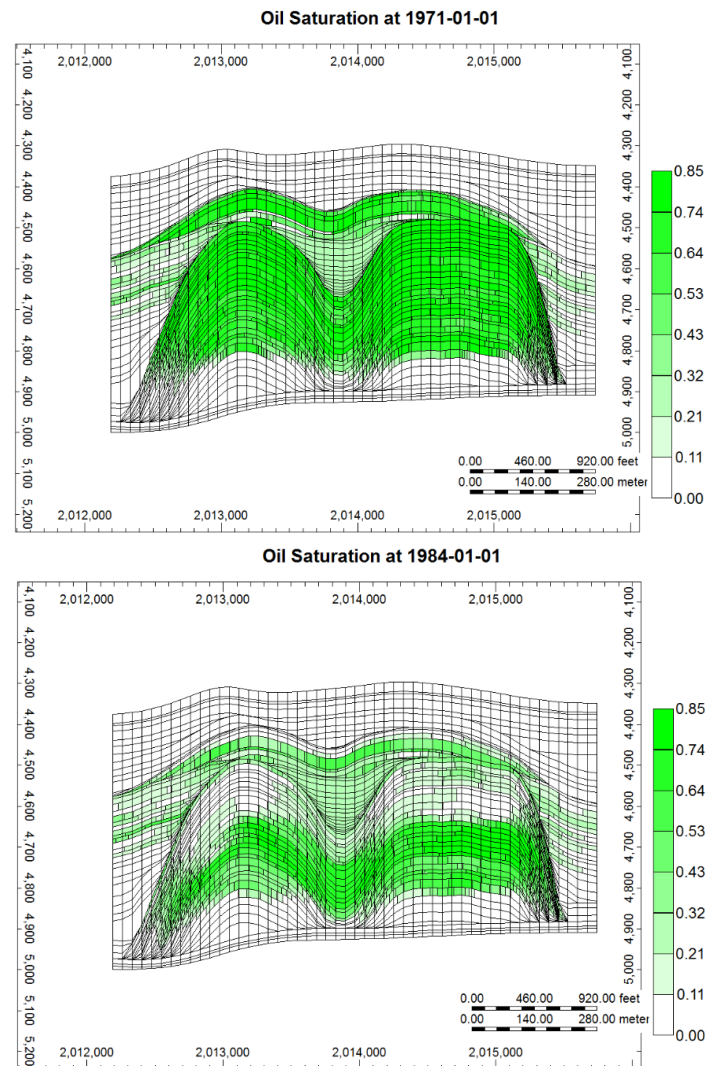
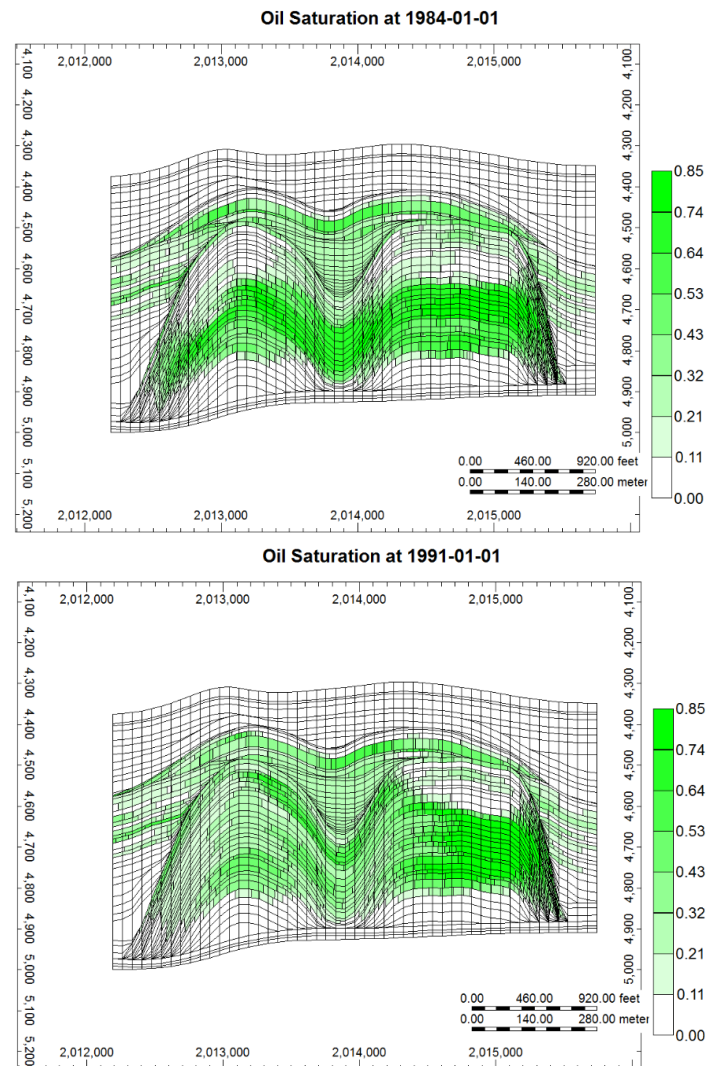


Figure B-7. Oil saturation distribution initially (left) and after primary depletion (right)



*Figure B-8. Oil saturation at the end of primary depletion (right) and at the end of waterflooding (right)*

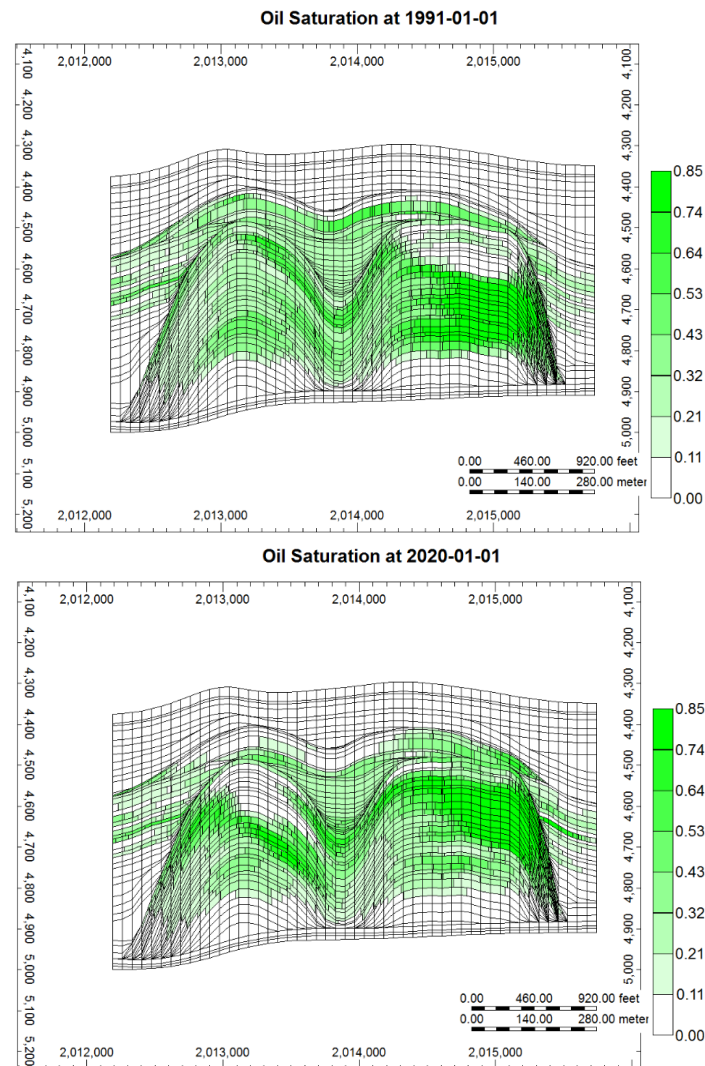
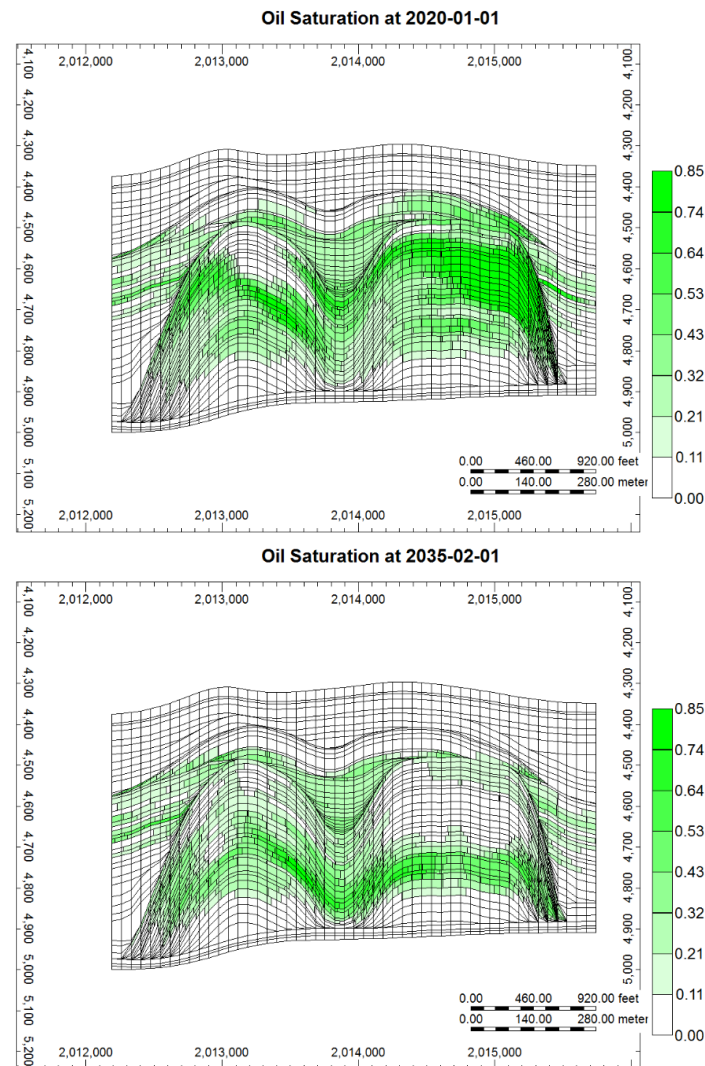


Figure B-9. Oil Saturation at the end of waterflooding (left) and at the end of the fillup period (right)



*Figure B-10. Oil saturation at the end of fill-up (left) to the end of EOR (right)*

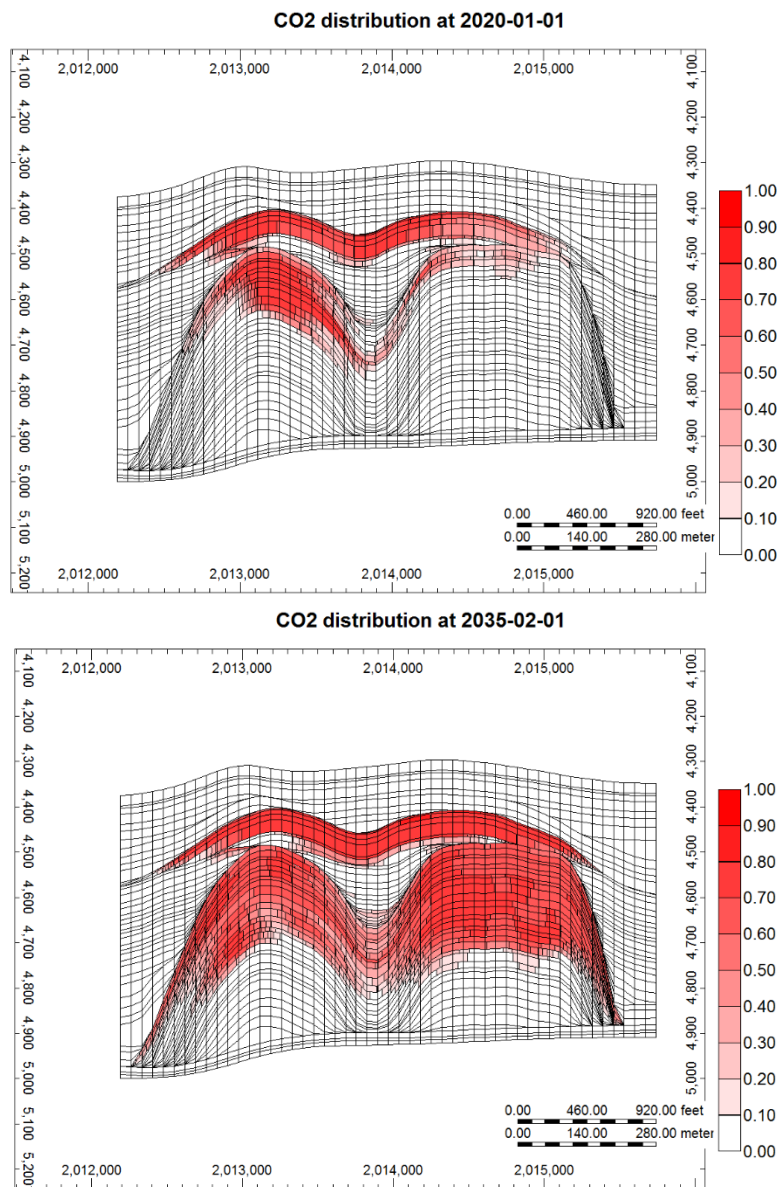


Figure B-11. CO<sub>2</sub> saturation from the end of the fill-up period (left) to the end of CO<sub>2</sub>-EOR (right)

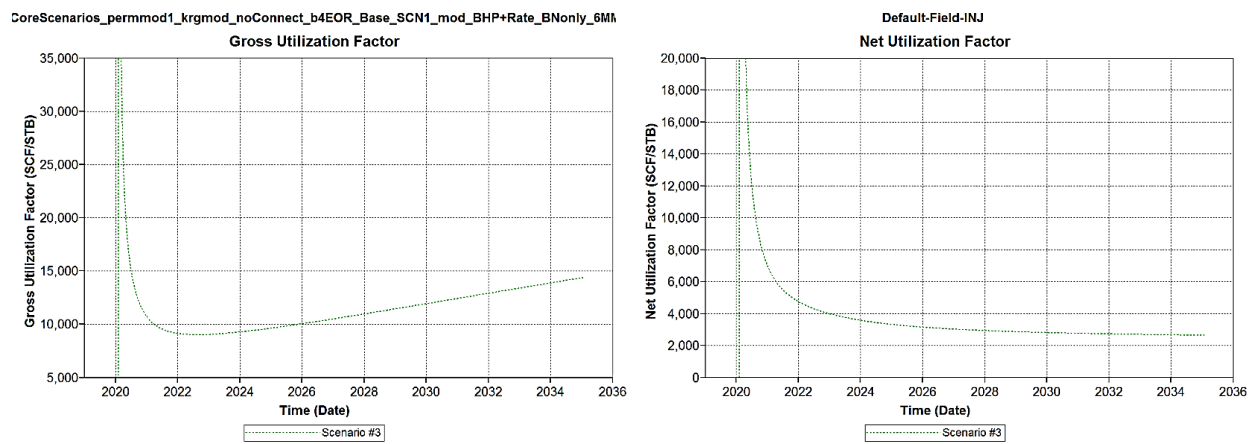


Figure B-12. Gross (left) and Net (right) utilization factors.

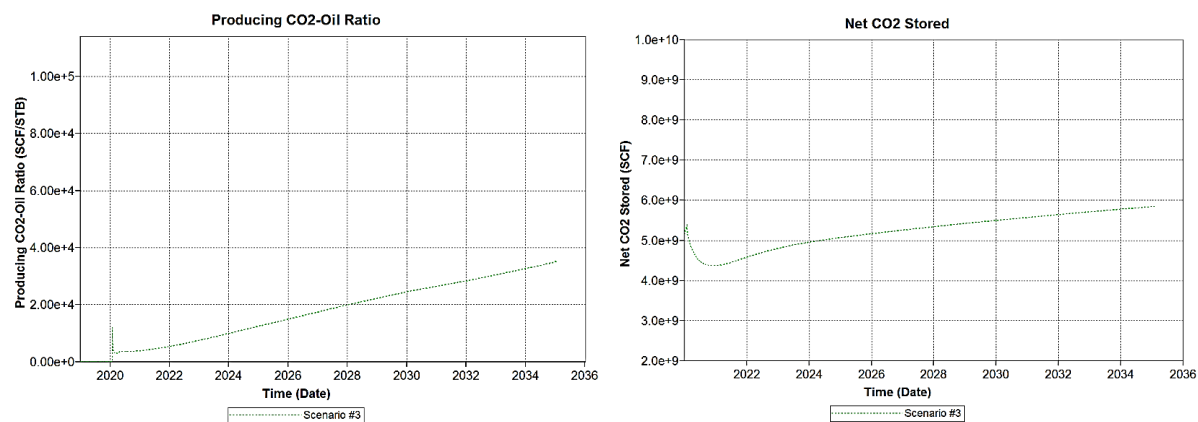


Figure B-13. Producing CO<sub>2</sub>-oil ratio (left) and the total CO<sub>2</sub> stored during EOR (right)

# **Appendix C Understanding Reservoir Mechanism Using History Matching: Dover 33 Field Carbon Dioxide EOR**

## **Understanding Reservoir Mechanism Using History Matching: Dover 33 Field Carbon Dioxide EOR**

Authors: Hye Young Jung<sup>1</sup> and Akhil Datta-Gupta<sup>1</sup>

<sup>1</sup> Department of Petroleum Engineering, Texas A&M University, College Station, Texas, USA

### **Abstract**

CO<sub>2</sub> injection in hydrocarbon reservoirs contributes to not only improvement in oil recovery but also climate changes by reducing the amount of CO<sub>2</sub> in the atmosphere. Even though CO<sub>2</sub> injection has been considered as one of the most effective EOR methods in the conventional reservoir, applying it to unconventional resources still remains uncertain in various aspects. In addition, subsurface systems can be understood by learning from the reservoir response through a history matching process, which involves the integration of observed data into a prior geologic model. In the development of Dover 33 field, which is located in the Northern Michigan, there have been mainly three production periods: primary depletion, CO<sub>2</sub> EOR and CO<sub>2</sub> injection only period for storage purposes. Previous efforts of manual history matching process achieved a reasonable match quality until a certain point of the CO<sub>2</sub> injection period. However, a steeper pressure buildup near the end of CO<sub>2</sub> injection period is not being captured successfully. The major issue in the CO<sub>2</sub> injection only period is that a sharp increasing trend of bottomhole pressure takes place even with the reduced injection rate. This indicates that changing reservoir properties and adjusting relative permeability curves in the previous production periods were not sufficient to identify the reservoir mechanism that is involved in the pressure rise during the CO<sub>2</sub> only injection period. In this paper, we develop the workflow of a multi-stage model calibration by incorporating fluid model adjustment as well as reservoir model calibration using Genetic Algorithm. First, parameters of the Equations of State (EOS) will be calibrated with available experimental data.

Then, several sets of EOS models will be carried over to the history matching process for primary depletion where reservoir properties including permeability multiplier, pore volume multiplier and relative permeability will be changed to match the observed data such as oil and gas production, and bottomhole pressure. Once the process of history matching is successfully finished for primary depletion, further adjustment will continue for CO<sub>2</sub> EOR period and CO<sub>2</sub> injection only period with the reduced ranges from the primary depletion period.

## 1. Introduction

Dover 33 field is one of the oil-bearing pinnacle reefs in Northern Michigan. It is a small reservoir with approximately 3 MM STB original oil in place. It has been developed since 1975 starting from primary depletion followed by an enhanced oil recovery (EOR) using carbon dioxide. After the EOR, there is a CO<sub>2</sub> injection only period without producers for storage purposes. Previous studies focused on the investigation of CO<sub>2</sub> EOR and associated storage issues by updating a reservoir model manually to match the history data for primary depletion and CO<sub>2</sub> EOR period respectively. They also have used different geologic conceptual model realizations from homogeneous to heterogeneous models. Various realizations were able to achieve reasonable match during primary depletion and CO<sub>2</sub> EOR period but not during CO<sub>2</sub> injection only period where the pressure build up is steeper even with a decreasing injection rate. In addition, the way of adjusting parameters during manual history matching is more or less local where box-type areas are specified, especially near the wells.

Therefore, the objective of this project is to perform an assisted history matching for primary depletion as well as CO<sub>2</sub> EOR, rather than a manual history matching. Once acceptable history matched models are obtained, they are used to predict the behavior of pressure response during CO<sub>2</sub> injection only period. In case that prediction of bottomhole pressure of an injector does not

follow the observed data, an additional history matching incorporating CO<sub>2</sub> injection only period will be performed to investigate and understand the behavior of pressure response.

In this paper, we present a hierarchical workflow of the model calibration to understand the reservoir mechanism of the Dover 33 field. Prior to a reservoir model calibration, the EOS model is calibrated using a population-based approach to obtain several sets of updated EOS models, which lead to improved fluid characterization and reduces uncertainty in various phases of productions. Then, a hierarchical history matching using Genetic Algorithm is conducted including three stages of model calibrations in sequence (1st stage history matching for primary depletion period, 2nd stage history matching for CO<sub>2</sub> EOR period and 3<sup>rd</sup> stage history matching for CO<sub>2</sub> injection only period).

## 2. Methodology

This section describes the simulation methodology for the hierarchical model calibration using a population-based approach, which includes a fluid model calibration as well as a reservoir model calibration as shown in Figure C-1.

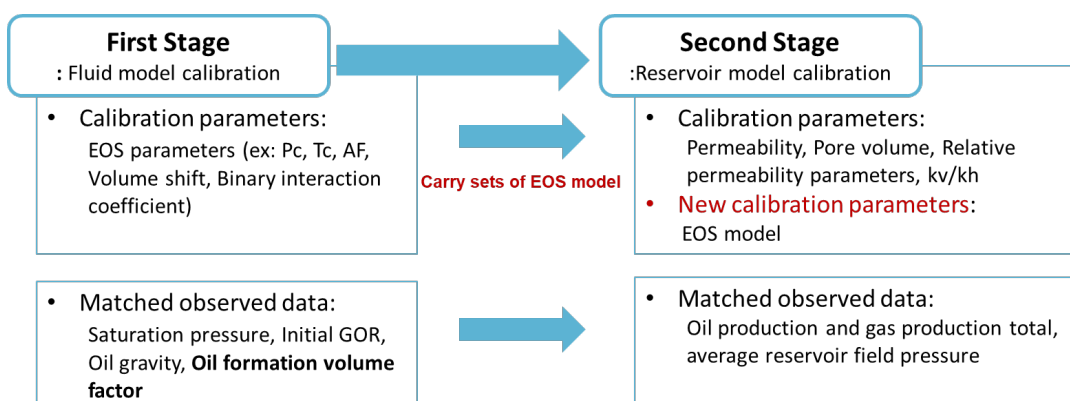


**Figure C-1. Flowchart of hierarchical model calibration**

### ***EOS Model Calibration Using Genetic Algorithm***

Equations of State (EOS), which predicts multi-phase behavior of fluids and volumetric properties, is considered as one of the calibration parameters during the history matching process because current fluid model has some level of uncertainty. This is because reservoir fluid samples are not collected at the beginning of primary production. Then, the composition of reservoir fluids is characterized based on the fluid samples from the end of primary depletion by adding the lighter components to match the available experimental data, which are bubble point pressure, initial oil gravity and initial GOR. However, there are several limitations to directly change parameters of an EOS model during the reservoir model calibration. First, the number of parameters in EOS model is considerable since each component in a fluid model has several associated parameters, such as critical properties (critical pressure and critical temperature), binary interaction coefficient, volume shift and acentric factor. If those parameters are incorporated in the history matching process using Genetic Algorithm, the population for each generation is required to increase proportionally to explore the parameter space, which might cause severe computational inefficiency. Second, a set of parameters are randomly selected for each model during the Genetic Algorithm, which is typically not an issue for most of parameters. However, arbitrarily selected parameters in an EOS model are able to generate non-monotonicity, especially for critical pressure/temperature and acentric factor, which leads to unphysical phase behavior as shown in Figure C-2. Therefore, in order to avoid the complexity involved in EOS parameters, the fluid model calibration is performed separately prior to the reservoir model calibration to obtain several sets of EOS models. Then, we take those EOS models as one of the tuning parameters in primary depletion history matching.

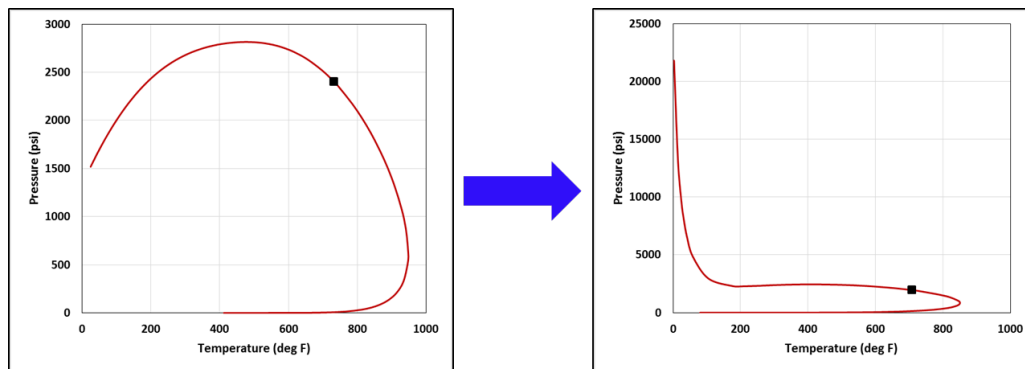


**Figure C-2. Examples of phase behavior: Physically correct (left) and physically incorrect (right)**

Furthermore, in order to achieve several fluid models efficiently, a population-based approach is used for the EOS model calibration. It is common to apply the regression method for most of fluid model calibration because this gradient-based approach shows faster convergence than stochastic methods. Even though it is computationally expensive to employ Genetic Algorithm, it is useful to search for several optimal solutions. Figure C-3 represents the workflow of the fluid model calibrations in detail. The Objective function during Genetic Algorithm is to minimize the misfit of experimental data and simulated responses, which is calculated as shown in Eqs. (1) and Eqs. (2).

$$f(x) = \sum_{i=1}^n r_i(x)^2 \quad (1)$$

$$r_i = \frac{e_i(x) - y_i}{y_i} \quad \& \quad x = [x_1, x_2, \dots, x_m] \quad (2)$$

Where  $e_i(x)$  represents Equations of state results,  $y_i$  is experimental data points and  $x$  is regression parameters.

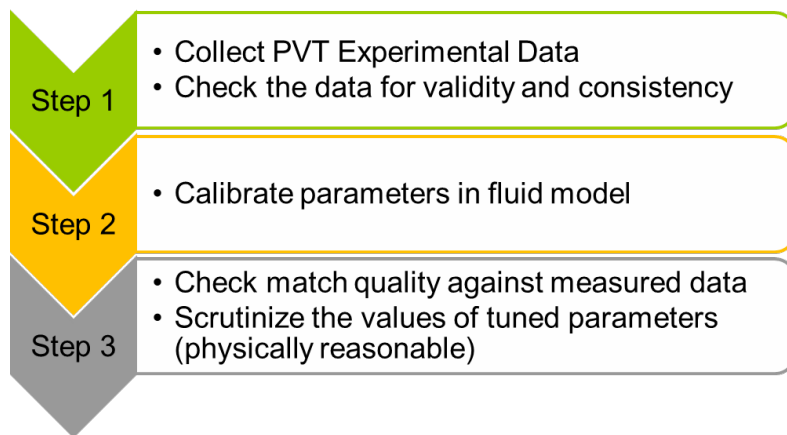


**Figure C-3. Workflow of fluid model calibration**

#### ***Hierarchical History Matching Using Genetic Algorithm***

Assisted history matching using multi-objective Genetic Algorithm has been performed for the Dover 33 field. As compared to a manual history matching process where parameters are selected by human subject each time and the quality of match is evaluated qualitatively by visualizing simulation responses, the GA-based automatic history matching provides a systematic and efficient way to evaluate possible sets of parameters. In addition, instead of using single-objective GA, which aggregates all objective functions into one scalar value, multi-objective GA is well suited to simultaneously consider multiple objective functions allowing for trade-off between them (Park et al (2015)). The methodology of the history matching is summarized in Table C-1.

**Table C-1 Summary of hierarchical history matching**

Method	Multi-objective Genetic Algorithm
Forward Simulation	Eclipse (e300: compositional simulator)
Simulation Constraint	Reservoir fluid volume production rate
Objective Function	Misfit of Well cumulative oil production, Well cumulative gas production and Average field pressure

History Matching Period	Hierarchical history matching 1st stage HM: Primary depletion 2nd stage HM: CO <sub>2</sub> EOR period 3rd stage HM: CO <sub>2</sub> injection only period
-------------------------	---

In this Dover 33 field, there are three different field development plans, which consist of primary depletion, CO<sub>2</sub> enhanced oil recovery and CO<sub>2</sub> injection only period (Figure C-4). Therefore, the history matching process includes these three phases in a hierarchical manner. In other words, all the initial parameters are varied to obtain the desired match during the primary depletion. Subsequently, a further tuning with reduced ranges from the previous history match will be conducted by incorporating the following production period and additional parameters added, if needed. Then, if updated models with the calibrated parameters from the first two stages of the history matching are not able to predict the behavior of pressure responses during the CO<sub>2</sub> injection only period (Figure C-5), which demonstrate a sharp increasing trend, an additional history match will be required.

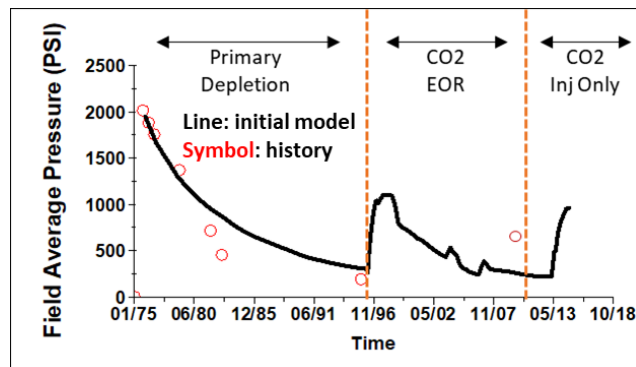
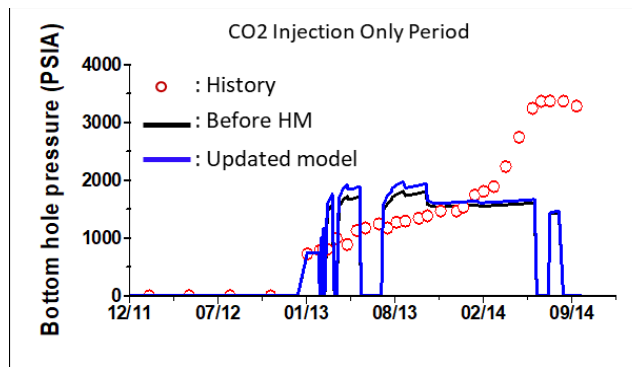
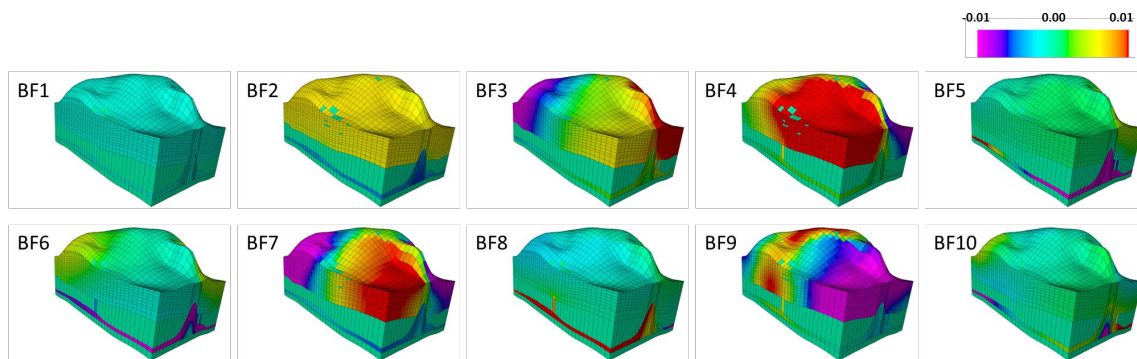


Figure C-4. Three production periods in the Dover 33 field



**Figure C-5. Comparison of the bottomhole pressure of the injector during CO<sub>2</sub> injection only period**

As for the adjustment of reservoir permeability during the GA, the parameterization using the Grid Connectivity-based Transform (GCT) has been performed instead of using a uniform multiplier that is applied to artificially cropped regions. A variety of parameterization methods has been widely used in the petroleum engineering where parameters are represented as a linear combination of basis functions. The GCT has been developed by only accounting for grid connectivity information which is independent of grid properties (Bhark et al. 2011). For the Dover 33 field, 10 basis functions have been generated (Figure C-6), which results in smooth changes in permeability field with a geological continuity using a small number of parameters.



**Figure C-6. Basis functions using Grid Connectivity-based Transform (GCT)**

### 3. EOS Model Calibration

In this section, we demonstrate the workflow of the fluid model calibration utilizing a population-based approach. Based on the oil formation volume factor and the initial gas-oil ratio, three different GA runs are evaluated in order to tune parameters in the EOS model.

#### *Initial EOS model*

For an initial case, reservoir fluids are characterized through the Equations of State model. Although original fluid samples were not taken in this field when primary depletion begins, analysis of the produced gas from the field has been obtained and performed periodically. Later, the first fluid sample was collected in order to prepare the enhanced oil recovery project. Based upon the fluid sample at the end of primary production and analyses of the produced gas, composition of the original fluids (Table C-2) are predicted to match some of fluid properties. In the Table C-2, components are listed as pseudo components which have been lumped from the original fluid components to prevent expensive computations that can be caused by detailed fluid description and the lumping has been performed by the field operator. The phase behavior of initial reservoir fluids is shown in Figure C-7 and associated volumetric properties for oil and gas phases are presented in Figure C-8. Since this fluid characterization was conducted with the limited data without the original fluid sample, there are still uncertainties inherent in an initial fluid characterization, which will be discussed in the following sections.

**Table C-2. Composition of the original fluid**

Component	ZI (%)
F1	40.912
F2	0.1019
F3	20.235
F4	17.389
F5	14.725
F6	2.7514
F7	3.8855

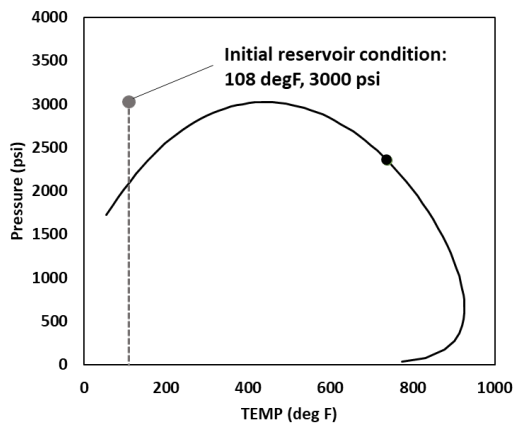


**Figure C-7. Phase behavior of the original fluid**

C-

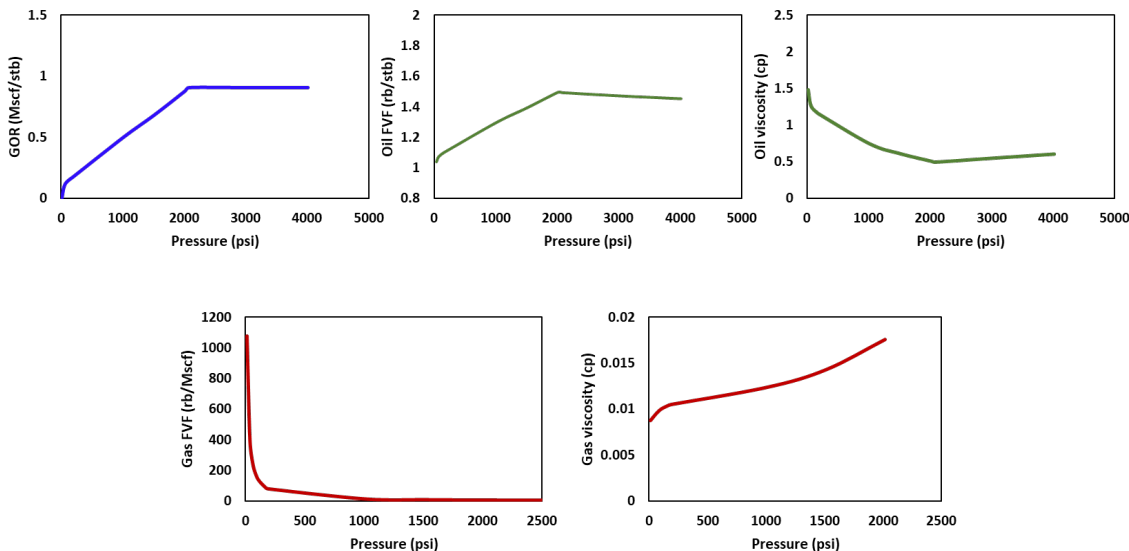


**Figure C-8. Volumetric properties of the original fluids**

#### ***Experimental Data to be Matched***

As explained before, there were limited experimental data for fluid properties due to the lack of original fluid samples. According to the operator, three properties are available in this study: initial oil gravity (43.6 API), initial producing gas-oil ratio (600-800 scf/stb) and approximated bubble point pressure (2017 psi) from the material balance calculation. Since the reservoir was indicated to be under-saturated, the initial producing gas-oil ratio should approximate the original solution gas-oil ratio. In addition to the available data for the fluid model calibration, the oil formation volume factor from the initial fluid model has been adjusted to represent different behaviors of oil with respect to pressure changes (Figure C-9). Typically, when checking and correcting fluid data, bubble point properties can be altered while the trend of properties can be preserved. Therefore, oil formation volume factor at the bubble point pressure has been changed with the same oil compressibility above the bubble point pressure. On the other hand, the gradient below the bubble

point pressure is different to see the effect of change of oil volume in the reservoir. In the following sections, all three data including the initial oil gravity, a producing gas-oil ratio and bubble point pressure are used with the different oil formation volume factor to perform the fluid model calibration respectively. As a result, multiple updated fluid models are obtained from each model calibration, which will be one of parameters for history matching during primary depletion.

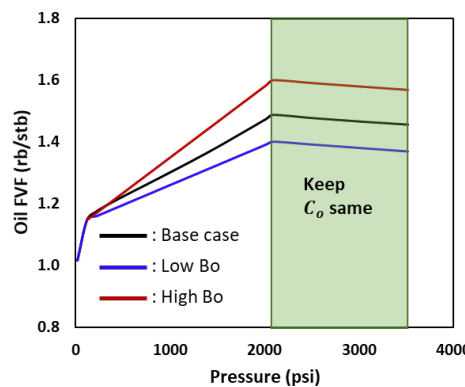


**Figure C-9. Three different oil formation volume factor cases**

#### ***Case 1: Low Oil Formation Volume Factor***

We first performed Genetic Algorithm for the low oil formation volume factor case in this section. Parameters of Equations of State are adjusted including critical properties, binary interaction coefficients, volume shift and acentric factor. As shown in Figure C-10, misfit between experimental data and simulated responses is reduced over the generation. After finishing the model calibration using Genetic Algorithm, four fluid models are selected as an input for reservoir model calibration in the next step. Figure C-11 and Table C-3 show the match quality for one of the selected models.

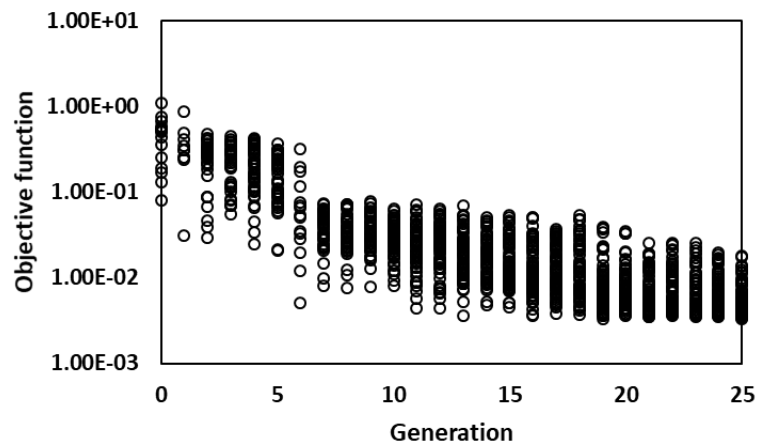


**Figure C-10. Results of Genetic Algorithm for Case 1**

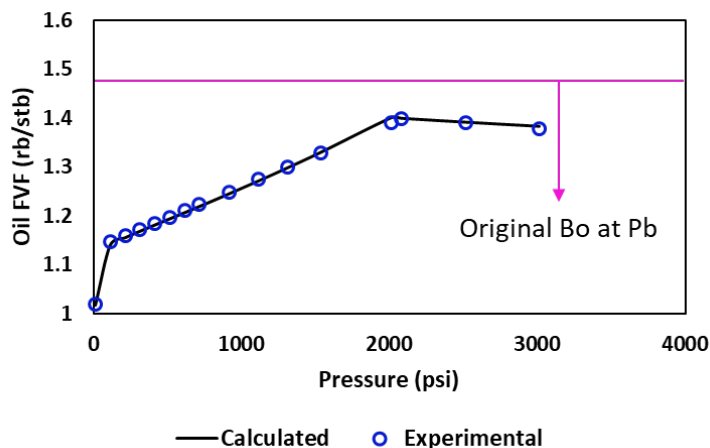


**Figure C-11. Oil formation volume factor of the history matched model for Case 1**

**Table C-3. Comparison of experimental data with the calculated values from the history matched model for Case 1**

	Experimental	Calculated
Bubble point pressure (psi)	2017	2015
Initial oil gravity (API)	43.6	43.998
Initial GOR (scf/stb)	700	698.46

**Case 2: High Oil Formation Volume Factor**

Similarly, the model calibration is performed by changing the parameters of the EOS model with high oil formation volume factor. As demonstrated in Figure C-12, objective function has been reduced as the generation goes. We also choose four updated models from this fluid model calibration and properties of one of chosen models are presented in Figure C-13 and Table C-4. It has been noticed that the reasonable match quality of the high oil formation volume factor is achieved even though it is not excellent as we have seen in the case of the low oil formation volume factor.

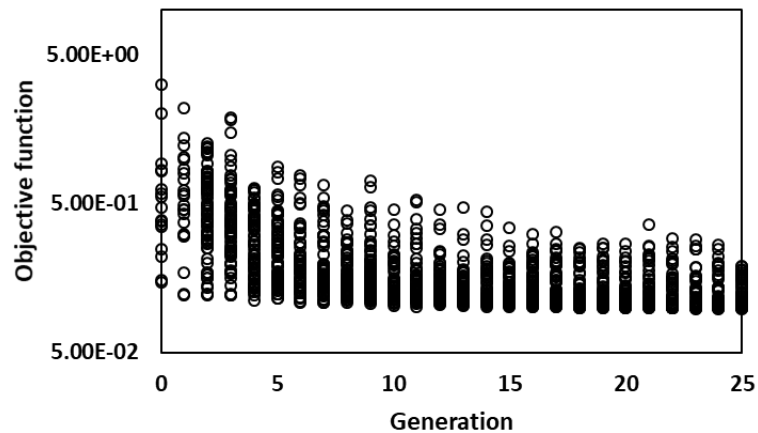


**Figure C-12. Results of Genetic Algorithm for Case 2**

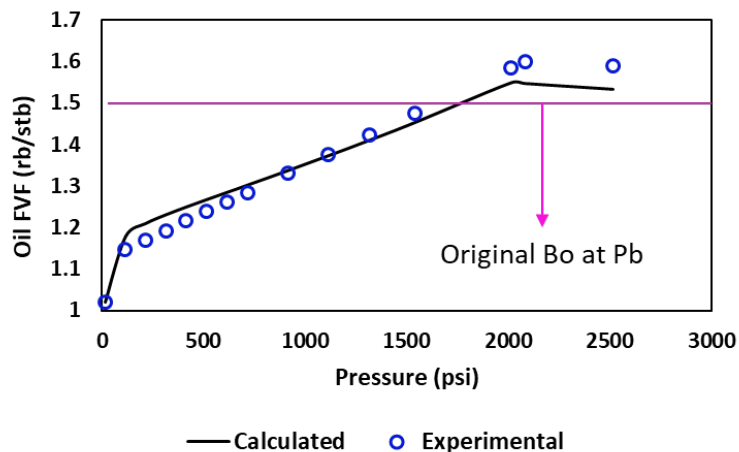


**Figure C-13. Oil formation volume factor of the history matched model for Case 2**

**Table C-4. Comparison of experimental data with the calculated values from the history matched model for Case 2.**

	Experimental	Calculated
Bubble point pressure (psi)	2017	2015
Initial oil gravity (API)	43.6	46.037
Initial GOR (scf/stb)	700	865.73

### ***Case 3: Low Oil Formation Volume Factor with Low Gas-Oil Ratio***

In addition to the first case where the fluid model calibration has been performed with the low oil formation volume factor, one more case has been studied with low gas-oil ratio. In the report provided by an operator, the initial gas-oil ratio has been observed between 600-800 scf/stb so that initial GOR has been setup as 700 scf/stb for the first two fluid model calibrations. However, in the observed data, the initial GOR that is available for the well during primary production is between 628 and 667 scf/stb which seems slightly lower than what we used. Therefore, another model calibration with the low oil formation volume factor as well as the low gas-oil ratio (600 scf/stb) has been conducted to obtain several updated fluid models. The progress of objective

functions and comparison of fluid properties for the selected model are presented in Figure C-14, Figure C-15 and Table C-5. As you can see, the obtained initial GOR from this GA runs is lower than the one from the Case 1 while achieving reasonable match quality for the other properties.

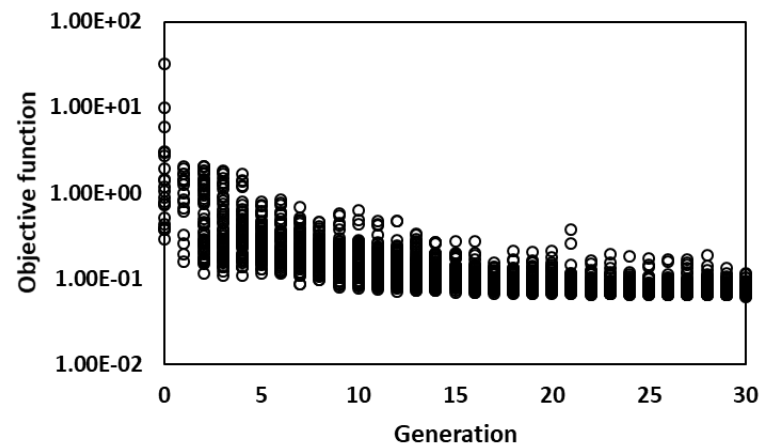


**Figure C-14. Results of Genetic Algorithm for Case 3**

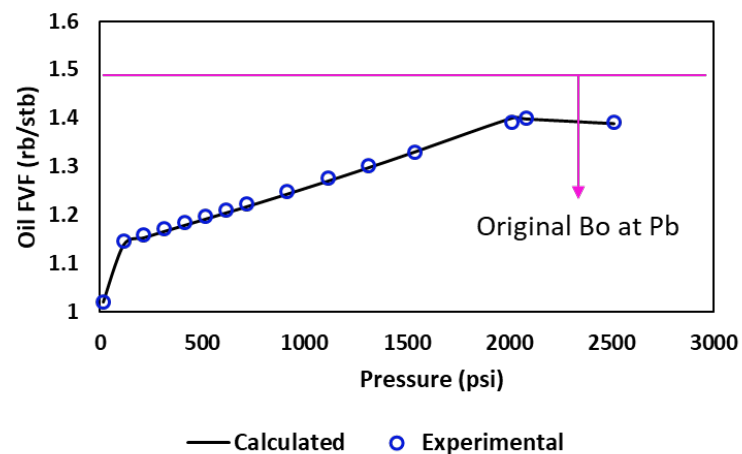


**Figure C-15. Oil formation volume factor of the history matched model for Case 3**

**Table C-5. Comparison of experimental data with the calculated values from the history matched model for Case 3**

	Experimental	Calculated
Bubble point pressure (psi)	2017	1999
Initial oil gravity (API)	43.6	46.2
Initial GOR (scf/stb)	600	663

#### 4. Reservoir Model Calibration

In this section, we present a hierarchical history matching that has been done in several stages that are associated with different production periods. Our focus is to show the applicability of multi-stages of history matching, narrowing down uncertainties of reservoir properties.

##### *Initial Model Setting*

We first present an initial model that is provided by the operator. The reservoir model is modeled using about 68,000 grid blocks and each grid cell is about 80 ft in x and y direction. The simulation model is a heterogeneous reservoir as shown in porosity and permeability distribution (Figure C-16) with an approximate dome shape. There is one vertical well in the center of the reservoir, which is an originally producer and will be converted to an injector during the enhanced oil recovery process. Figure C-17 also shows initial saturation and initial pressure distribution of the field. Due to the lack of information, water saturation below subsea level is set to one whereas the other area has water saturation of between 0.2 and 0.3, which is close to the critical water saturation. In addition, water saturation will not be included during the history matching process since the water production data is not reliable according to an operator. In this field case, three phase relative permeability curves are used as presented in Figure C-18. Although it is provided by the operator, we will use Corey type relative permeability curves in the following history matching process to adjust the relative permeability. Therefore, the overall shape of the relative permeability will be different from the current one. Lastly, pore volume of the reservoir as well as

fluid in place are listed in Table C-6. Because the operator is confident with the original volume of oil in place, we try to keep changes small in pore volume during the history matching process.

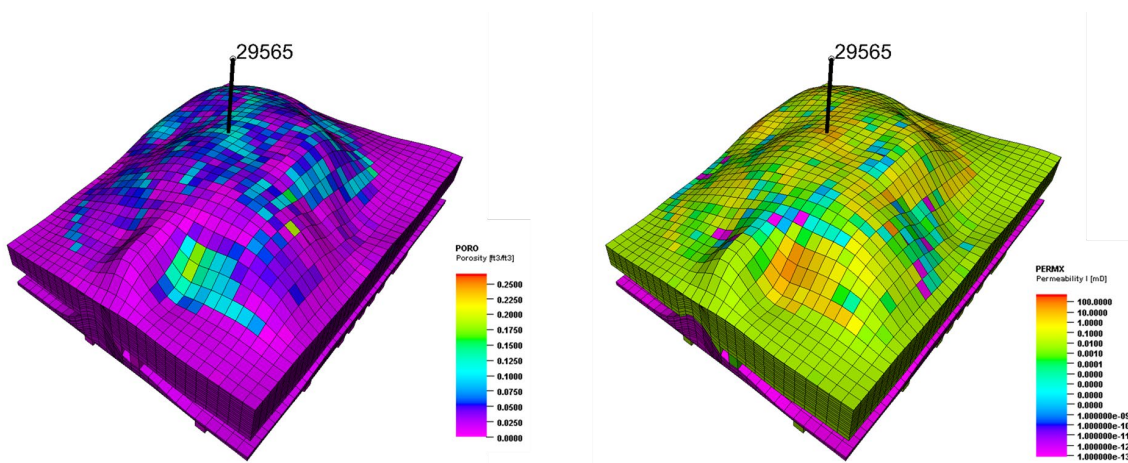


**Figure C-16. Reservoir properties: porosity (left) and permeability (right)**

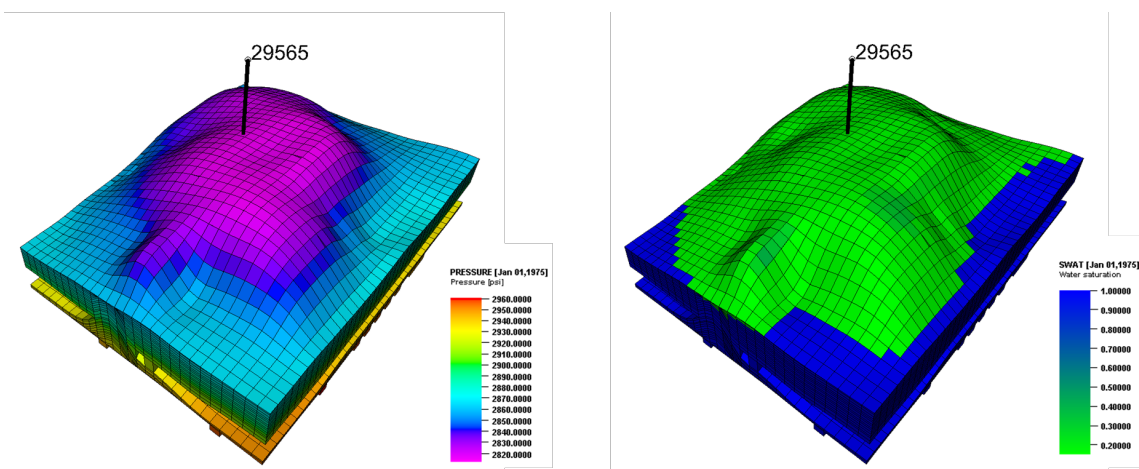


**Figure C-17. Initial pressure (left) and initial water saturation (right)**

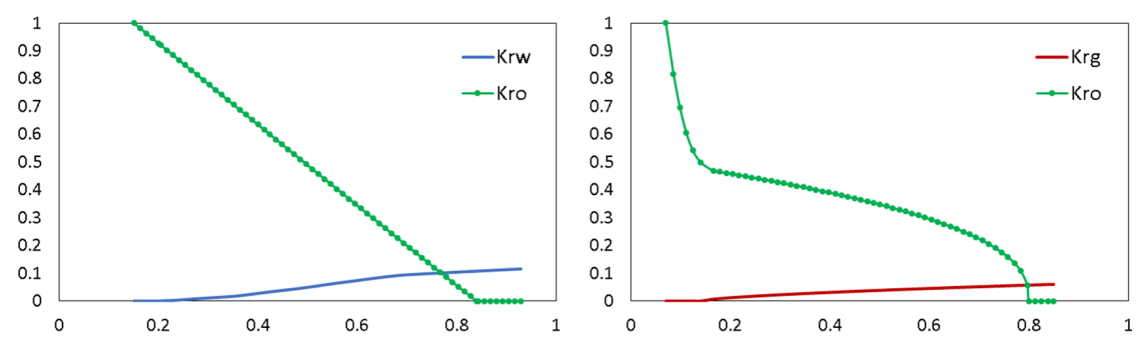


**Figure C-18. Three phase relative permeability curves provided by the operator**

**Table C-6. Pore volume and fluid in place of the reservoir**

	Finite Difference Simulation
Pore volume ( $MM\ res\ ft^3$ )	118.76
Reservoir volume of oil ( $MM\ STB$ )	3.28
Reservoir volume of water ( $MM\ STB$ )	16.41
Reservoir volume of gas ( $MM\ SCF$ )	3.13

### ***Sensitivity Analysis***

The list of parameters in Table C-7 is considered before history matching to evaluate the impact of each parameter. For this sensitivity study, permeability, pore volume and water saturation are varied using multipliers for the entire reservoir. The relative permeability is modeled using Corey correlation by specifying exponents and endpoints for each phase respectively. As a result, the tornado charts are plotted for the all objective function (oil production rate, gas production rate and average reservoir pressure) by perturbing each parameter from the given base value to low and high values respectively (Figure C-19). The range of parameters are determined based on experimental data and it is also discussed with an operator. The tornado chart shows that the effect of the endpoint for oil relative permeability is significant and reservoir permeability is also influential compared to the other parameters. On the other hand, rock compressibility is nearly

insensitive to the objective function. Therefore, the rock compressibility was removed from the list of parameters that will be used for history matching. By reducing the number of parameters, the population of each generation during Genetic Algorithm can be decreased accordingly, which can result in more efficient history matching with the fewer number of total simulation runs.

**Table C-7. List of parameters to be considered for history matching**

		Base	Low	High
Permeability multiplier		1	0.3	3
Pore volume multiplier		1	0.3	3
Initial water saturation multiplier		1	0.5	2
Rock compressibility (1/psi)		0.1e-6	0.1e-6	3.0e-5
kvkh		0.1	0.05	1.0
Relative permeability endpoint	kro	0.8	0.5	1.0
	krog	0.8	0.5	1.0
	krw	0.7	0.35	0.9
	krg	0.1	0.01	0.5
Relative permeability exponent	no	3	1	5
	nog	3	1	5
	nw	3	1	5
	ng	3	1	5

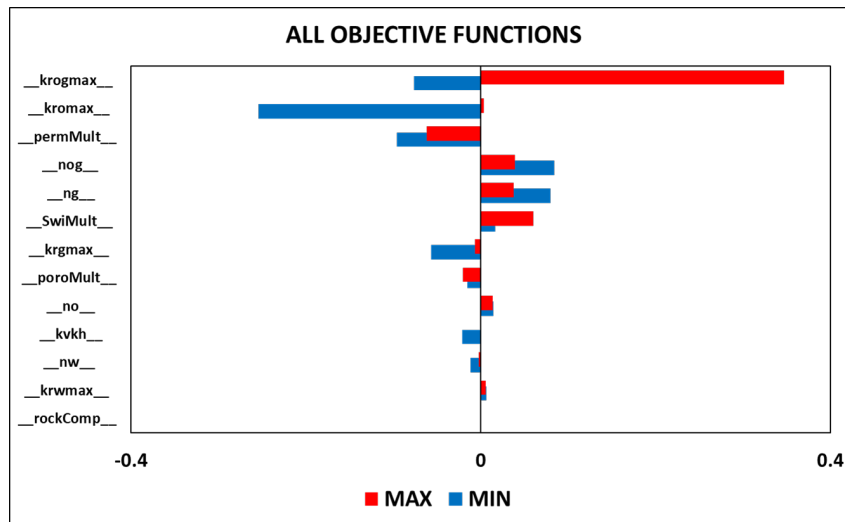
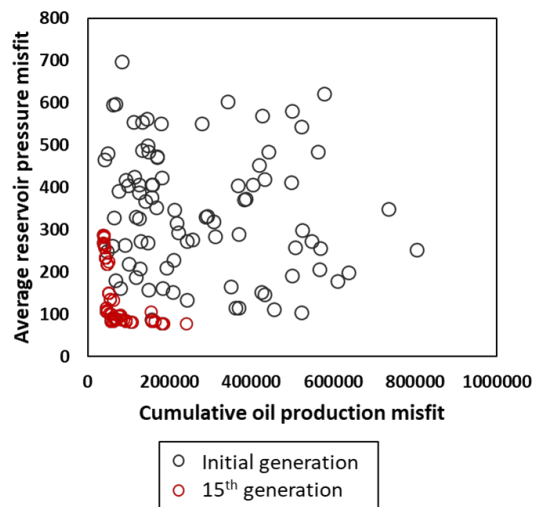


**Figure C-19. Tornado chart for all objective functions**

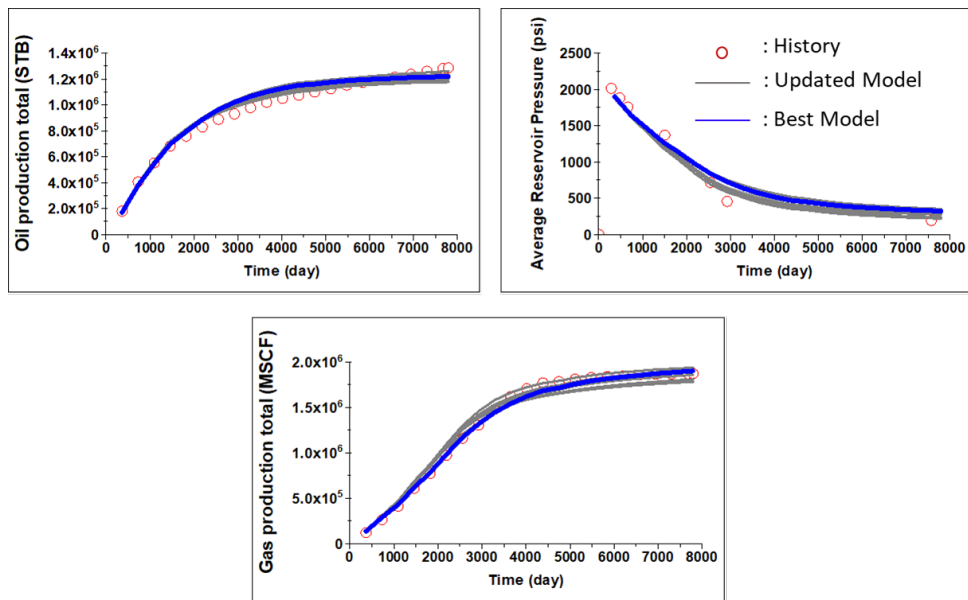
### Primary Depletion

Beginning with 1<sup>st</sup> stage of hierarchical history matching for the primary depletion period, Figure C-20 shows the performance of Multi-objective Genetic Algorithm. Compared to an initial generation, the misfit of average reservoir pressure as well as oil production rate for updated models after 15th generation has been reduced as it forms the Pareto front.

As a further comparison, several optimal solutions have been selected among population of the final generation and simulation responses are compared with the observed data in Figure C-21. The match quality of all objective functions is in an acceptable range for most of the updated models where the best model is represented as blue line.

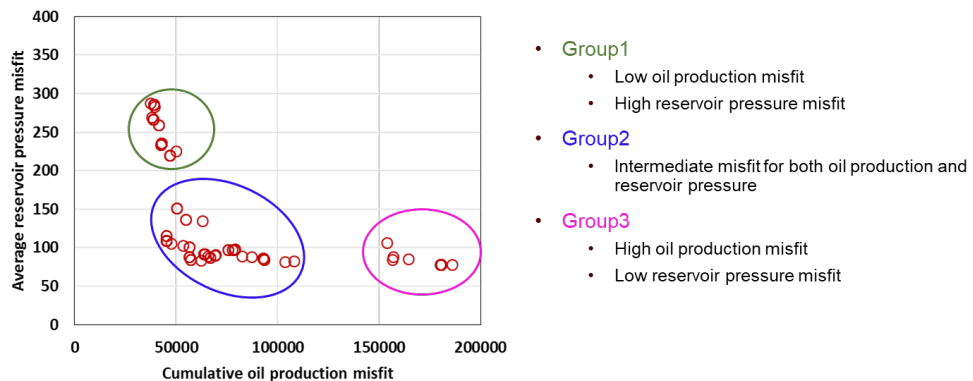


**Figure C-20. Performance of MOGA for primary depletion**

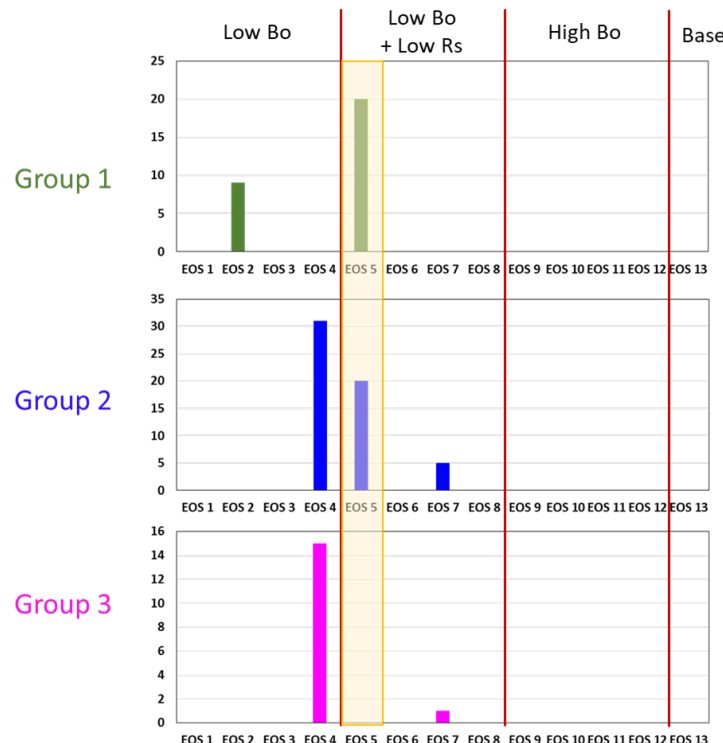


**Figure C-21. Comparison of simulation responses of the history matched model with the observed data for primary depletion**

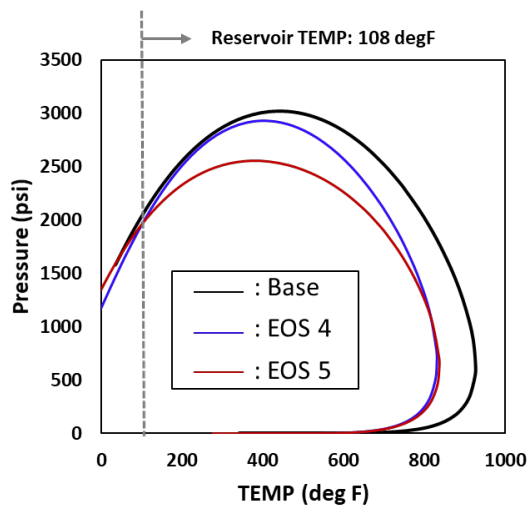
Depending on the influence of each objective function, optimal solutions can be divided into three groups as described in Figure C-22. Group 1 represents a good match with oil production while there is inconsistency in average reservoir pressure. In contrast, Group 3 has low average reservoir misfit whereas models cannot meet oil production as shown in observed data. Group 2 shows intermediate level of misfit for both objective functions including oil production and average reservoir pressure, which indicates optimal solutions in this history matching process. In this first stage of history matching, we adjusted not only reservoir properties but also EOS models that have been selected from the previous fluid model calibration. In Figure C-23, histograms of EOS models for each group respectively are demonstrated. It can be seen that EOS models from high oil formation volume factors are not included in the final generation. In addition, EOS model #4 and #5 are dominant in general but especially in Group 2. The comparison of phase behaviors of those two fluid models are also represented in Figure C-24.



**Figure C-22. Three different groups in optimal solutions depending on the importance of objective functions**

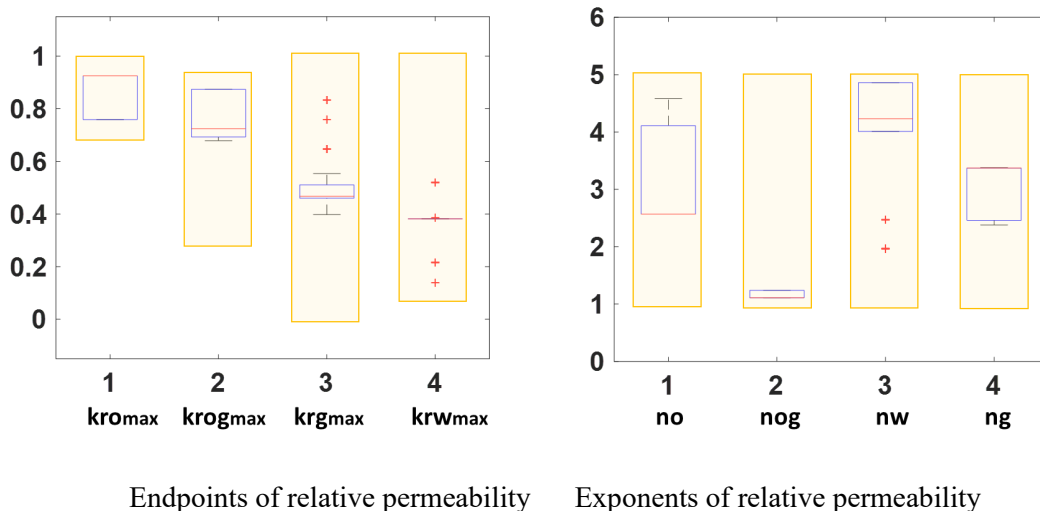


**Figure C-23. Histogram of EOS models for each group**

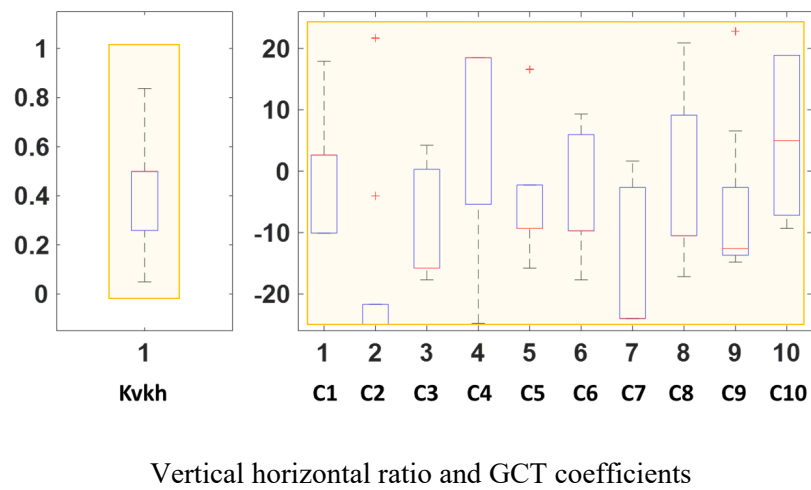


**Figure C-24. Comparison of phase behavior**

Moving on to the investigation of other calibrated parameters, Figure C-25 and Figure C-26 presents box plots of each parameter. In the box plot, yellow boxes represent the ranges that we specified in the beginning. It has been observed that endpoints of relative permeability for all phases have been reduced overall, where the endpoints for oil are converged to the higher value. The distribution of pore volume multipliers is narrowed down significantly where pore volume of region 1~4 decreases whereas pore volume of the rest of regions increases. On the other hand, there are still some level of uncertainties in the permeability multiplier, which we can continue to reduce in the next stages of history matching process where we further include more production periods.



**Figure C-25. Box plots of calibrated parameters for primary depletion for relative permeability**



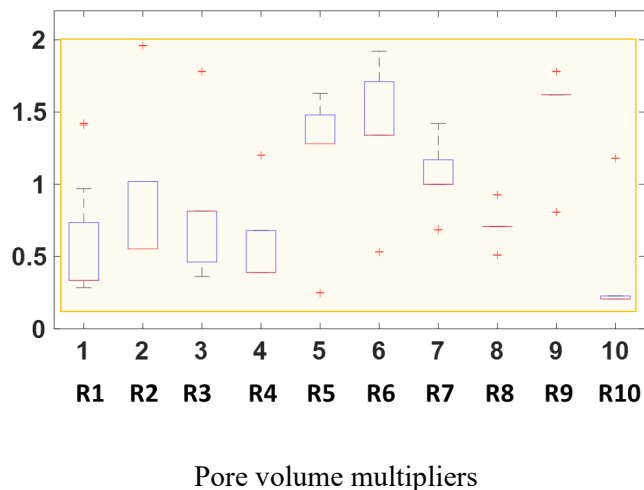


**Figure C-26. Box plots of calibrated parameters for primary depletion for permeability and pore volume**

In Figure C-27 we show the comparison of simulation responses with the observed data for the best match model including the water production. As explained before, due to the reliability issue of water production as well as the lack of water saturation distribution, water production was not considered as the objective functions. The relative permeability curves for the best case are presented as compared with the previous relative permeability curve provided by an operator (Figure C-28). It can be seen that oil and gas relative permeability increases in general whereas the ability for water to flow has been decreases.

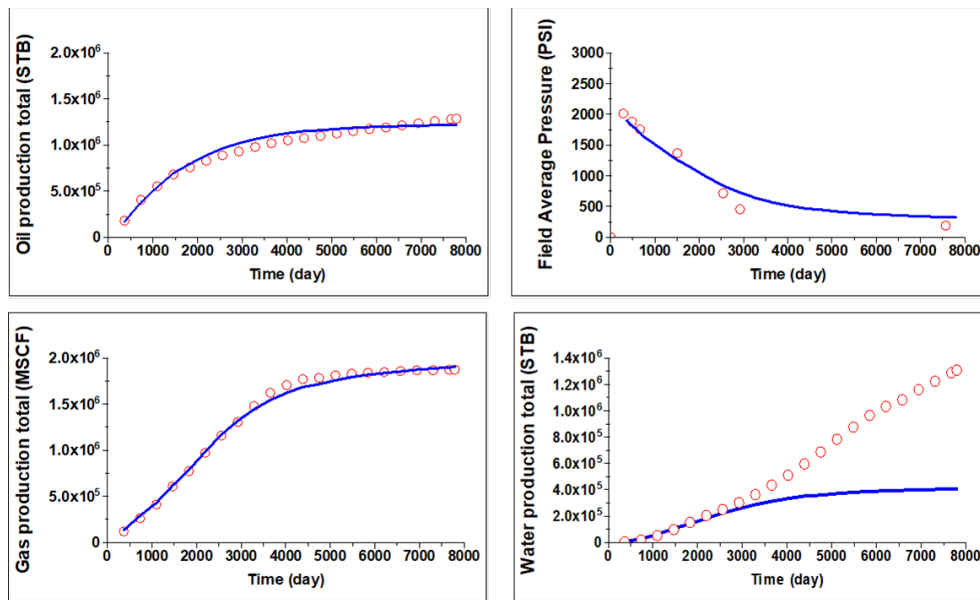


**Figure C-27. Comparison of simulation responses of the best updated model with the observed data**

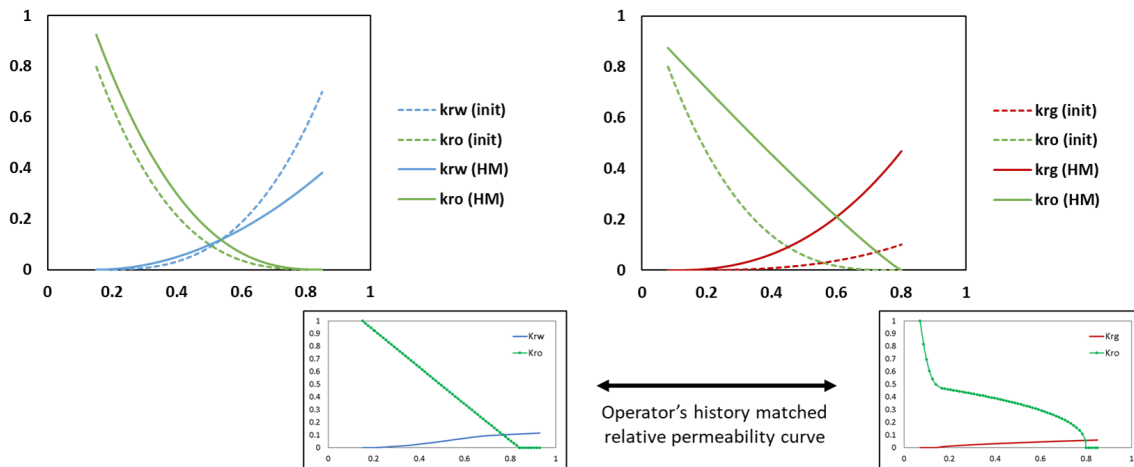


**Figure C-28. Comparison of relative permeability before and after history matching during primary depletion**

### ***Enhanced Oil Recovery***

In Dover 33 field, there was an enhanced oil recovery project utilizing carbon dioxide after 20 years of primary depletion. Although the history matching process for primary recovery is

performed successfully, the updated model is not able to match historical fluid production as shown in Figure C-29. Therefore, a further model calibration including the EOR period needs to be conducted with the reduced ranges of parameters, such as GCT coefficients for reservoir permeability and pore volume multipliers, which are used in the previous stage of history matching. However, we will apply different relative permeability curves for the EOR period as CO<sub>2</sub> is injected into the reservoir.

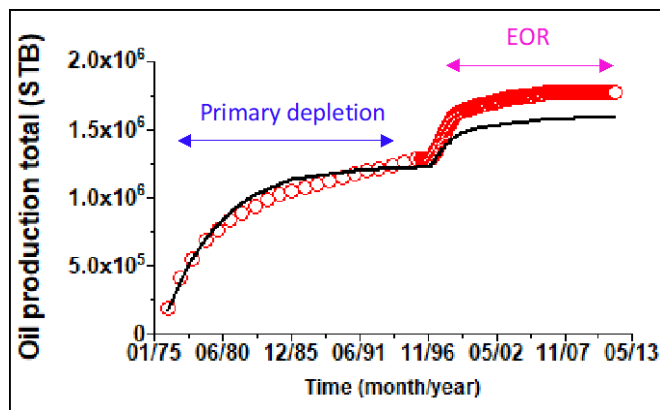


**Figure C-29. Comparison of cumulative oil production with the updated model from primary depletion**

Before performing history matching for the EOR period, the selected EOS model from the previous stage has been examined in terms of a phase behavior as well as physical properties of oil-CO<sub>2</sub> mixtures to see the impact of CO<sub>2</sub> injection. First, the comparison of phase behavior for three different CO<sub>2</sub> and oil mixtures with respect to different CO<sub>2</sub> mole fractions has been made (Figure C-30). Then, Minimum Miscibility Pressure (MMP) has been determined by a slimtube test at the pressure of around 1350 psi, which indicates that supercritical CO<sub>2</sub> is employed to displace the oil in the reservoir where the pressure is greater than 1350 psi and eventually to improve the oil recovery (Figure C-31). In addition, as CO<sub>2</sub> dissolves in oil, it has a substantial impact on the swelling of crude oil, which eventually leads to an increase in oil mobility as shown

in Figure C-32. The swelling factor is defined as a volume of mixture at a saturation pressure per a volume of the original fluid at its saturation pressure. Lastly, the density of oil-CO<sub>2</sub> mixtures for 50% CO<sub>2</sub> mole fraction is compared with that of original fluid (Figure C-33). It can be seen that the density of mixtures increases with the added CO<sub>2</sub>.

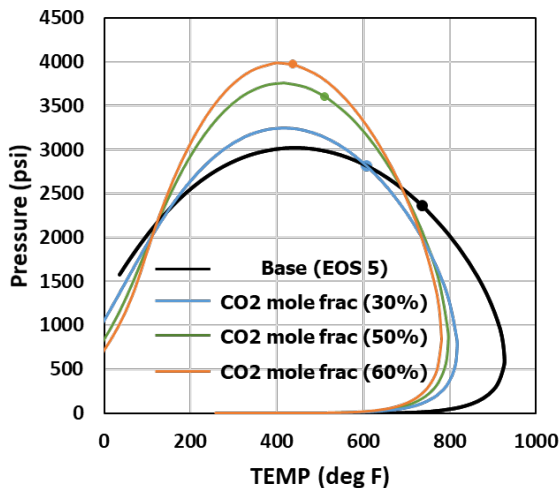


Figure C-30. Comparison of phase diagram for different oil and CO<sub>2</sub> mixtures

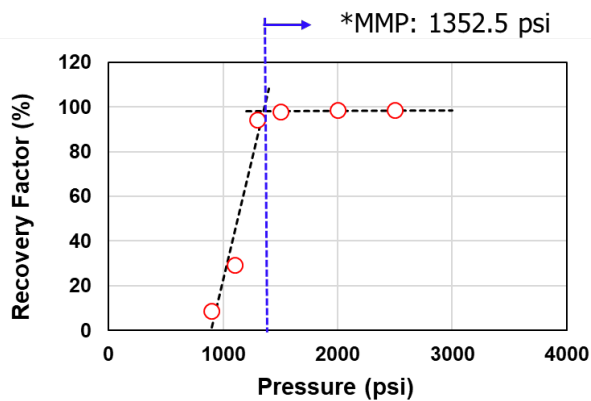
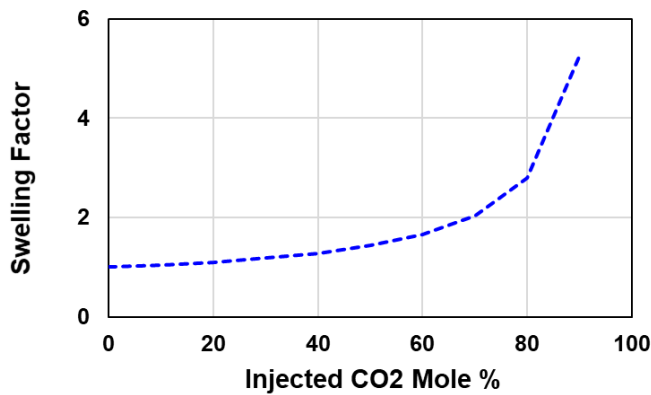
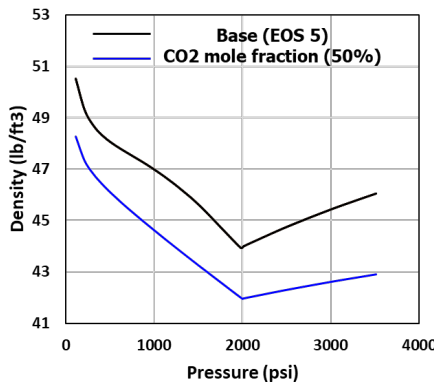


Figure C-31. Determination of Minimum Miscibility Pressure (MMP)



**Figure C-32 Swelling factor of EOS 5**



**Figure C-33. Density of original fluid compared with oil and CO<sub>2</sub> mixture (CO<sub>2</sub> mole fraction of 50%)**

For the second stage of history matching, we also consider three objective functions, which are the misfits of average reservoir pressure, cumulative oil production and cumulative gas production respectively. All objective functions are evaluated during the primary production and EOR period as well. We also continue to utilize Multi-objective Genetic Algorithm to effectively optimize all objective functions simultaneously. Figure C-34 shows the results of MOGA indicating the significant reduction of misfits after 17<sup>th</sup> generation. Solutions from the final generation are forming the Pareto front whereas models from an initial generation are scattered to cover all possible solutions in the beginning. In Figure C-35, the comparison of simulation responses against

the observed data is presented for one of the updated models from MOGA. It can be seen that they are showing a good agreement.

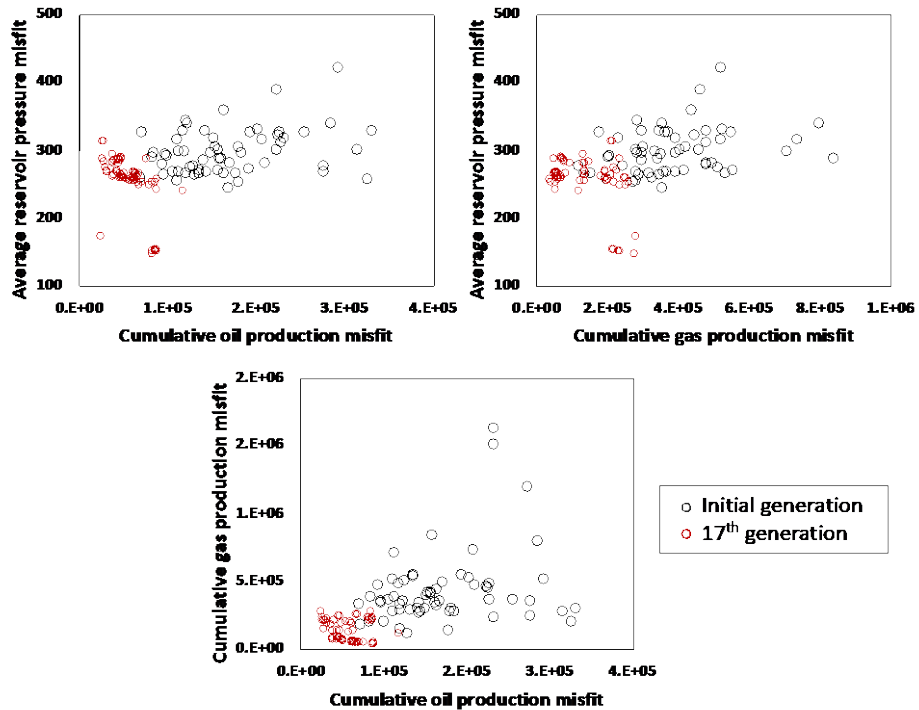


**Figure C-34. Performance of MOGA for CO<sub>2</sub> EOR period**

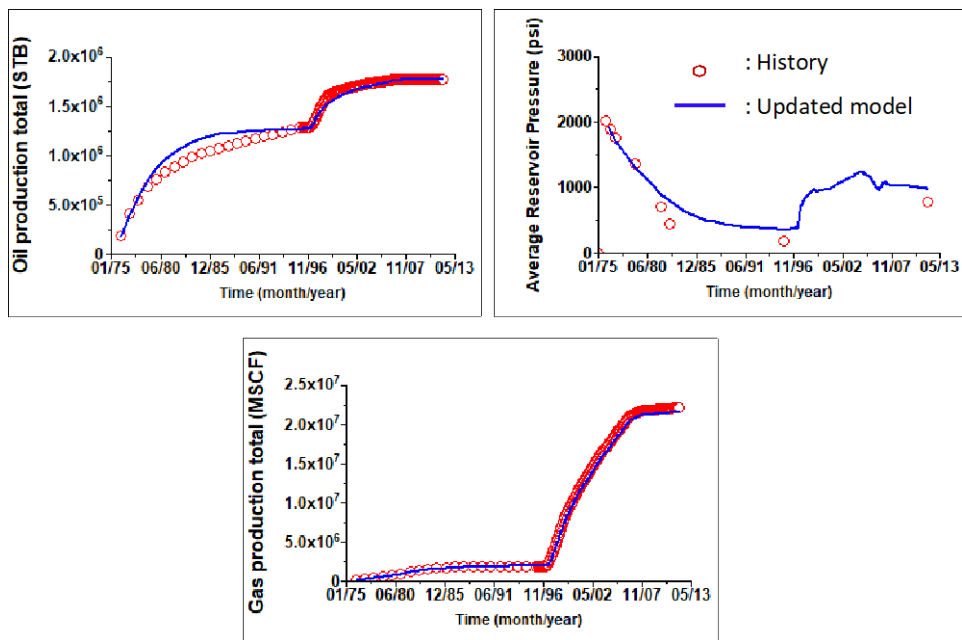


**Figure C-35. Comparison of simulation responses of the history matched model with the observed data for CO<sub>2</sub> EOR period**

As for the parameters that have been calibrated through the second stage of history matching, the distribution of each variables is now presented. First, most of endpoints and exponents of relative permeability for the EOR period are converged well except for the exponent of gas relative permeability (Figure C-36). Compared to the relative permeability curves for primary production (Figure C-37), gas-oil relative permeability curves are quite analogous whereas water-oil relative permeability curves are fairly different. In the water-oil relative permeability curve, it can be seen that oil relative permeability increases compared to the one for primary depletion due to the effect of CO<sub>2</sub> injection. In addition, it is noted that the shape of relative permeability curves seems to be more reasonable compared with operator's history matched ones. Then, the distributions of GCT coefficients and pore volume multipliers are shown in Figure C-38 and Figure C-39. The ranges of each parameter are further narrowed down during the second stage of history matching.

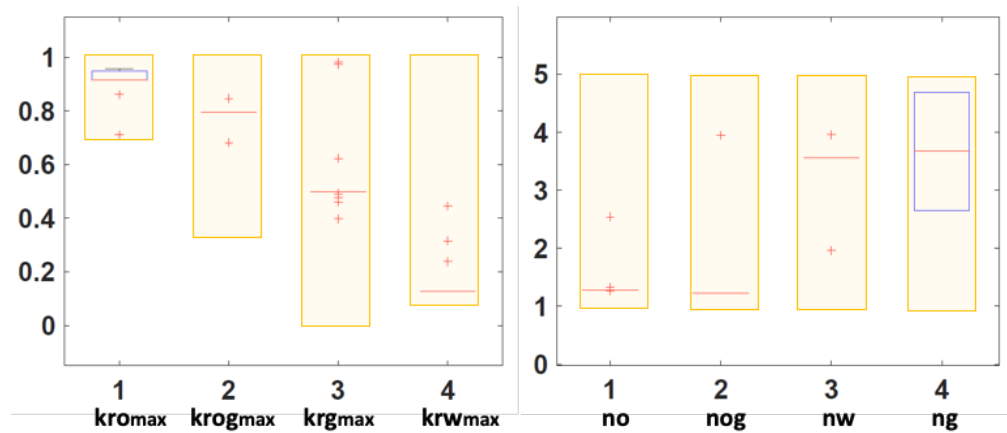


**Figure C-36. Box plots of parameters associated with relative permeability: endpoints (left) and exponents (right)**

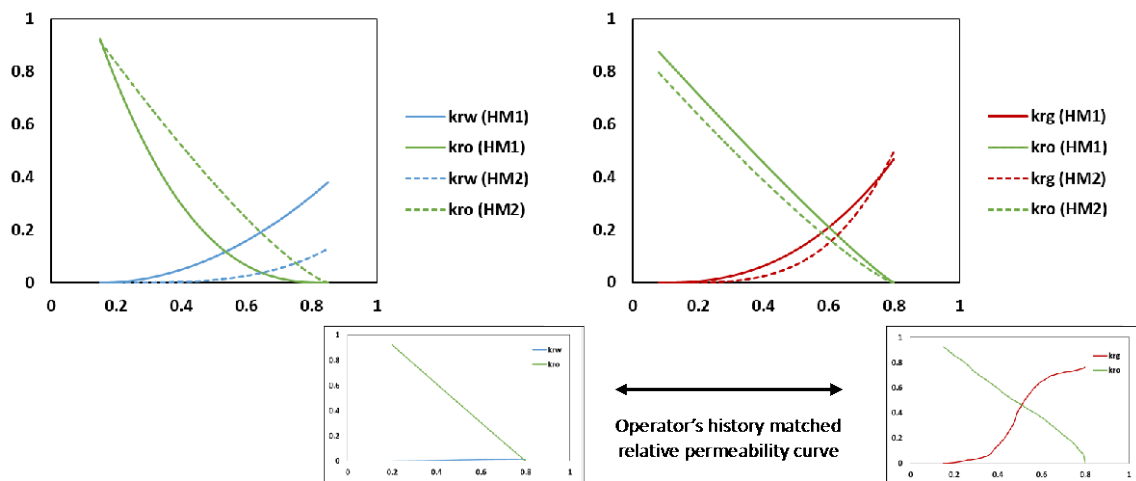


**Figure C-37. Comparison of relative permeability before and after history matching during CO<sub>2</sub> EOR period**

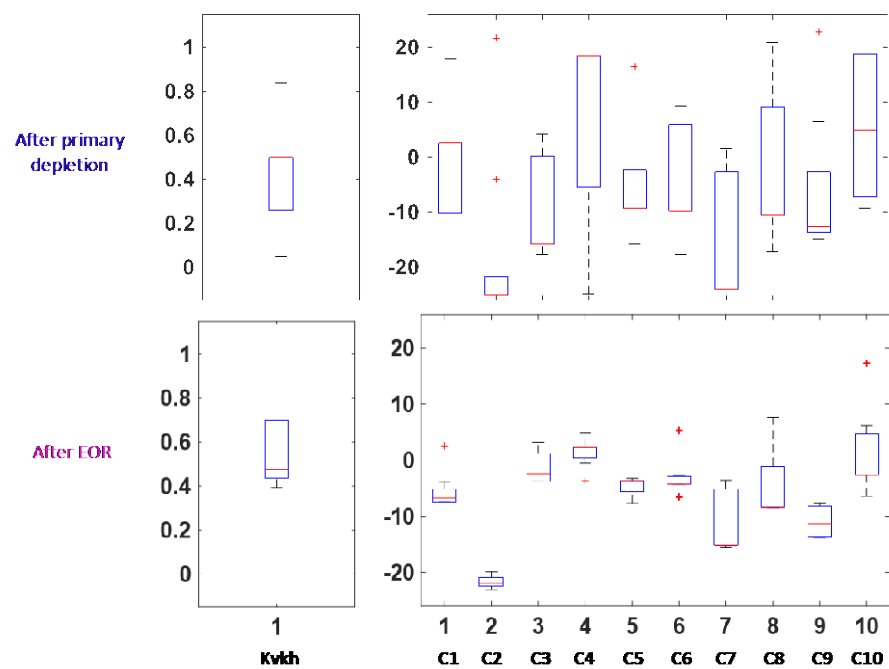


**Figure C-38. Comparison of distribution for parameters associated with permeability between after primary depletion and after EOR period**

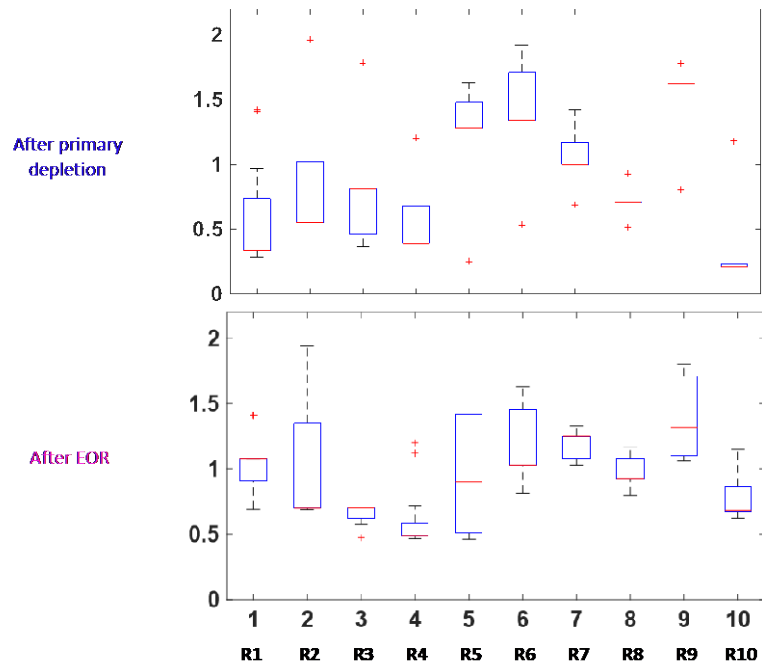


**Figure C-39. Comparison of distribution for pore volume multipliers between after primary depletion and after EOR period**

### ***CO<sub>2</sub> Injection Only Period***

After the primary production followed by the enhanced oil recovery using carbon dioxide, there is a CO<sub>2</sub> injection only period for the purpose of CO<sub>2</sub> sequestration. One of the history matched models from the first and second stage of model calibration process is used to simulate this period. However, when bottomhole pressure is predicted during CO<sub>2</sub> injection only period, the behavior of bottomhole pressure in an injector is not well matched with the measured data that shows the sharp increasing trend (Figure C-40). Moreover, a sudden increase in pressure response occurs with a reduced injection rate as shown in Figure C-41. Therefore, additional reservoir model calibrations are required to capture an abrupt rise of bottomhole pressure, which eventually includes entire production periods from primary depletion to CO<sub>2</sub> injection only period. In this stage, the range of parameters that is narrowed down from the previous history matching is carried over to preserve the previous matching quality.

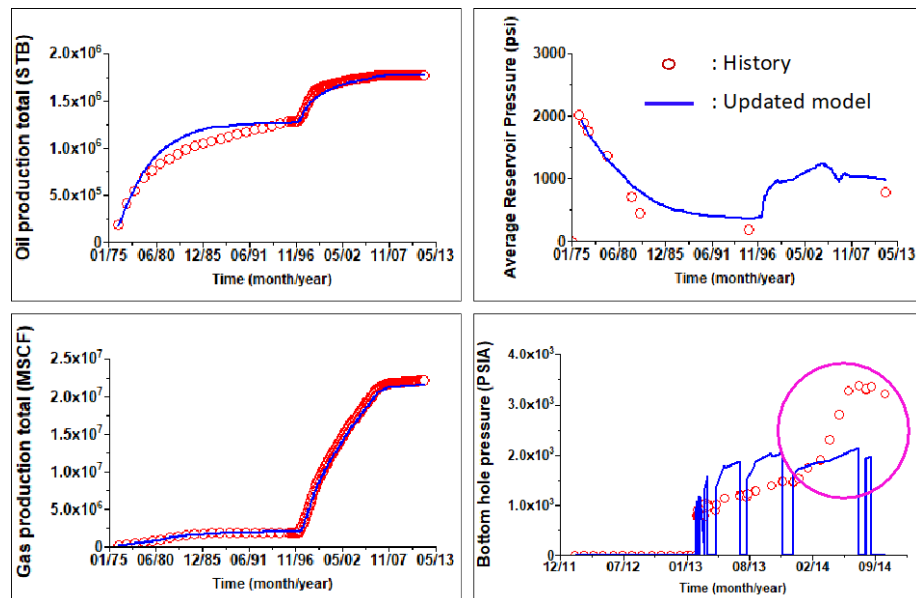


**Figure C-40. Comparison of simulation responses of the history matched model with the observed data (BHP: prediction)**

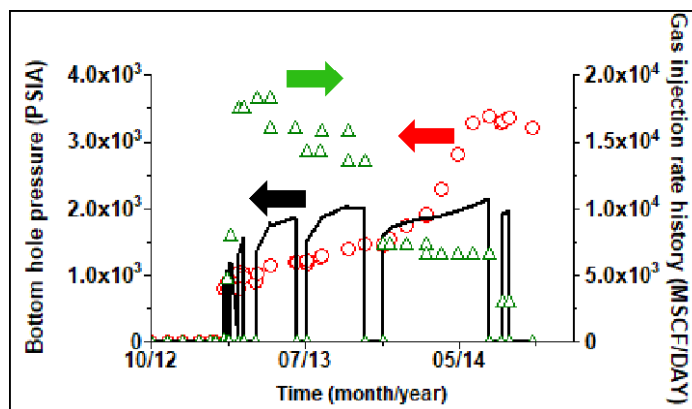


**Figure C-41. Difference in bottomhole pressure between simulation response and the measure data in comparison to the reduced gas injection rate**

As a result of a third stage of history matching using MOGA, objective functions are significantly reduced after several generations (Figure C-42). In this stage, three objective functions are the misfit of cumulative oil production, average reservoir pressure and bottomhole pressure of the injector. Even though the match quality of bottomhole pressure has been improved compared to the previous model (Figure C-43), the misfit of average reservoir pressure increases especially during the EOR period, which indicates that two objective functions are conflicting with each other.

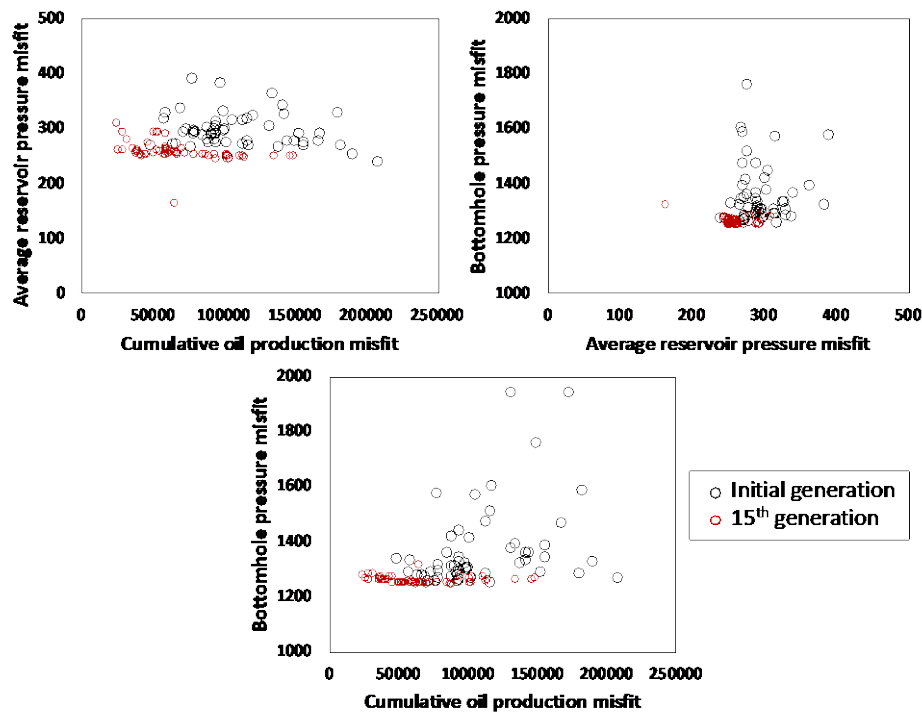


Figure C-42. Performance of MOGA for CO<sub>2</sub> injection only period

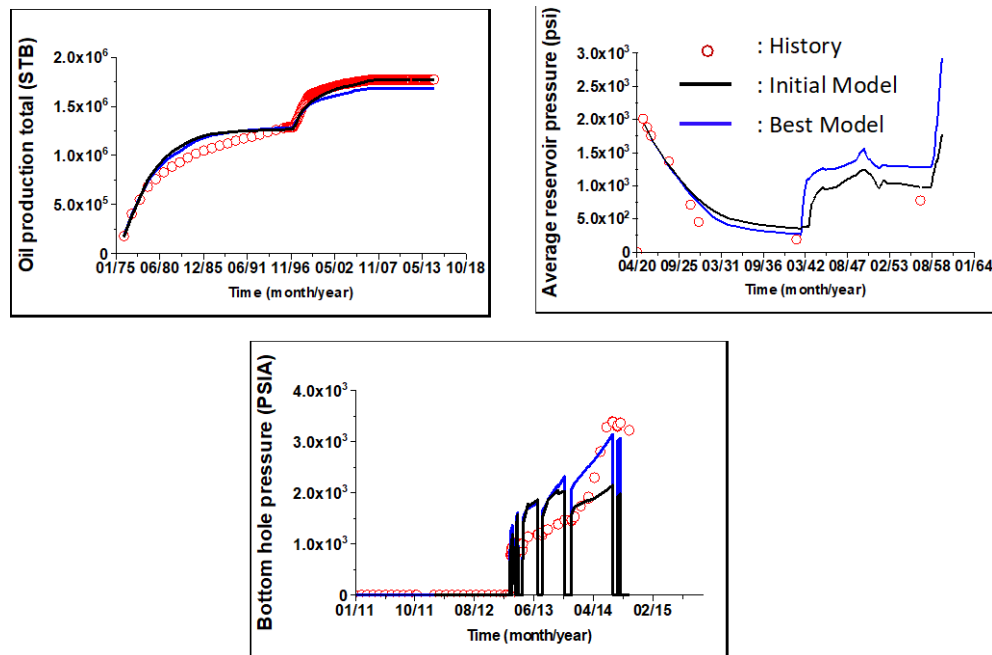
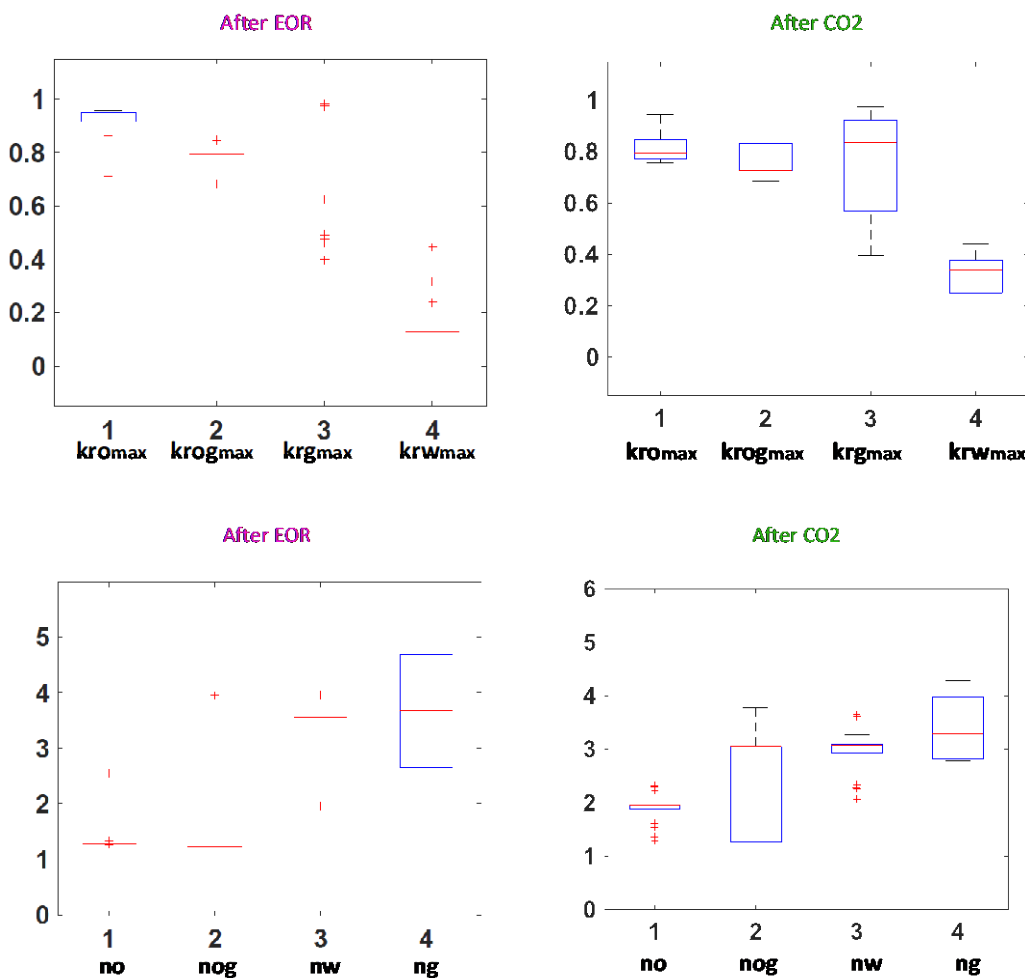
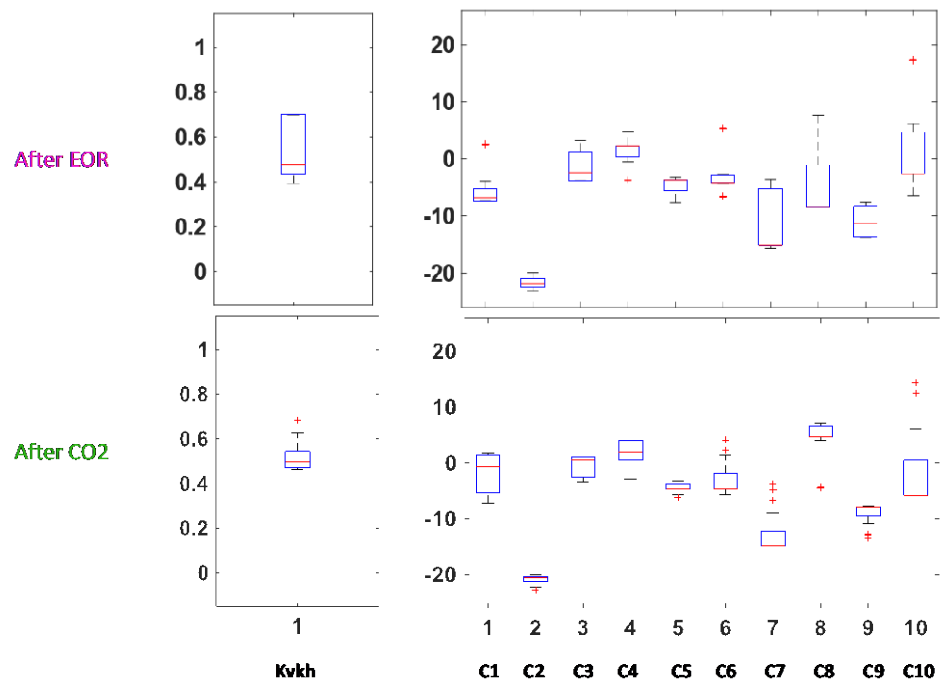


Figure C-43. Comparison of simulation responses of the history matched model with the observed data for CO<sub>2</sub> injection only period

In terms of parameters that have been calibrated through several stages of history matching, reservoir permeability and pore volume related parameters are even further narrowed down (Figure C-45 and Figure C-46) whereas exponents and endpoints of relative permeability are more widely distributed than the previous history matching (Figure C-44). This is because the range including outliers is provided to allow some level of flexibility. In addition, less convergence of these parameters represents difficulties in achieving the conflicted objective functions especially between average reservoir pressure and bottomhole pressure of the injector.



**Figure C-44. Comparison of distribution for parameters associated with relative permeability between after EOR period and after CO<sub>2</sub> injection only period: endpoints (top) and exponents (bottom)**



**Figure C-45. Comparison of distribution for parameters associated with permeability between after EOR period and after CO<sub>2</sub> injection only period**

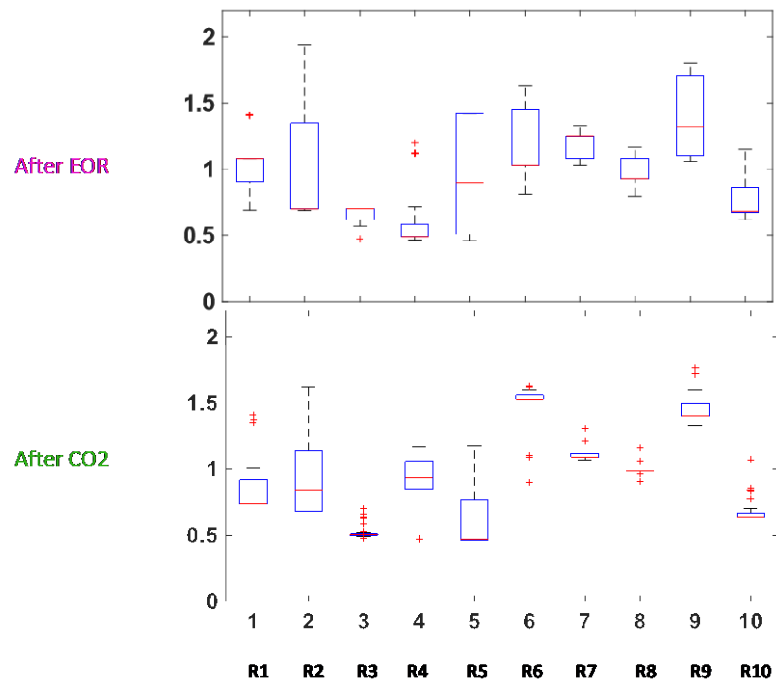


**Figure C-46. Comparison of distribution for pore volume multipliers between after EOR period and after CO<sub>2</sub> injection only period**

Although Multi-objective Genetic Algorithm has been used to solve multi-objectives problems in the previous history matching, it was not sufficient to minimize misfits of all objective functions simultaneously. Therefore, GA with a single objective function, which only focuses on the misfit of bottomhole pressure, has been performed to investigate parameters that makes difference (Figure C-47). As shown in Figure C-48, the simulated response of the updated model from GA is better matched with the observed data than the one from MOGA as well as the initial model.

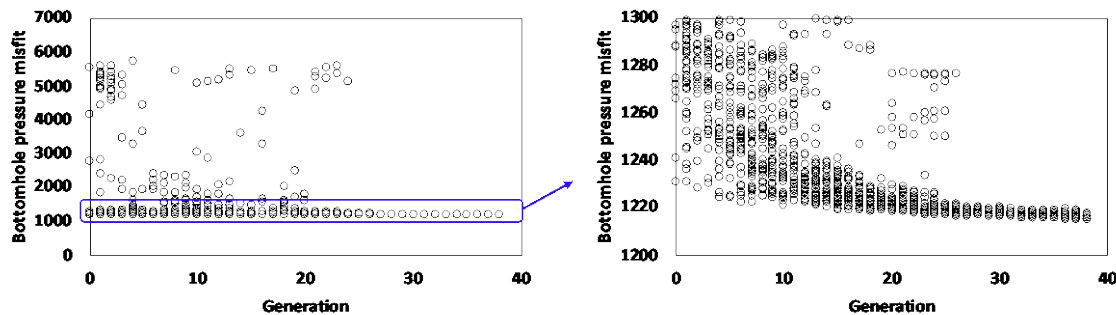


**Figure C-47. Results of Genetic Algorithm with a single objective function**

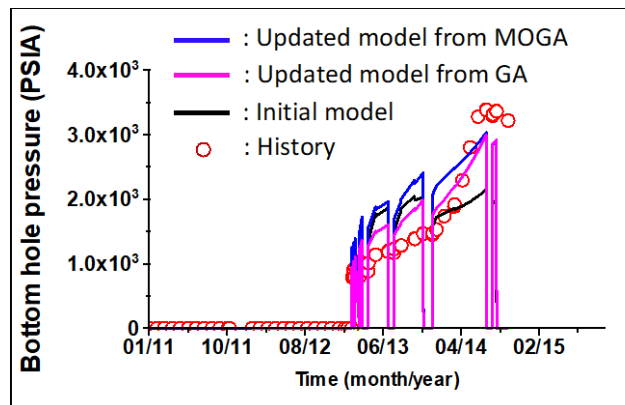


**Figure C-48. Comparison of bottomhole pressure between updated models and history data**

### Discussion

As a hierarchical history matching for all production periods is finished, the bottomhole pressure of two monitoring wells (Figure C-49) during CO<sub>2</sub> injection only period has been compared as a validation. Figure C-50 and Figure C-51 show that the simulated responses of the bottomhole pressure from the two last updated models (one from the Multi-objective GA and the other from the single GA) are well matched with the observed data, which indicates that history matchings have been performed successfully.

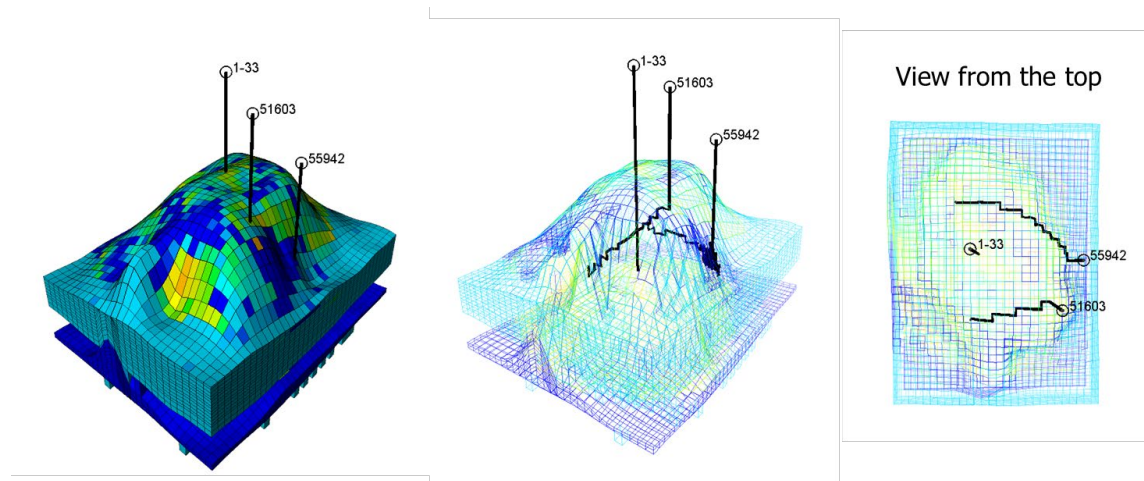


**Figure C-49. Location of monitoring wells**

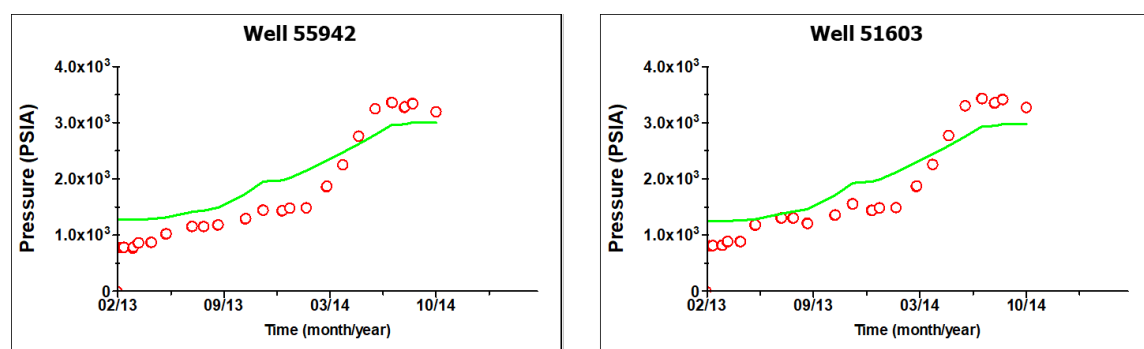


**Figure C-50. Comparison of the bottomhole pressure for two monitoring wells: the history matched model from MOGA**

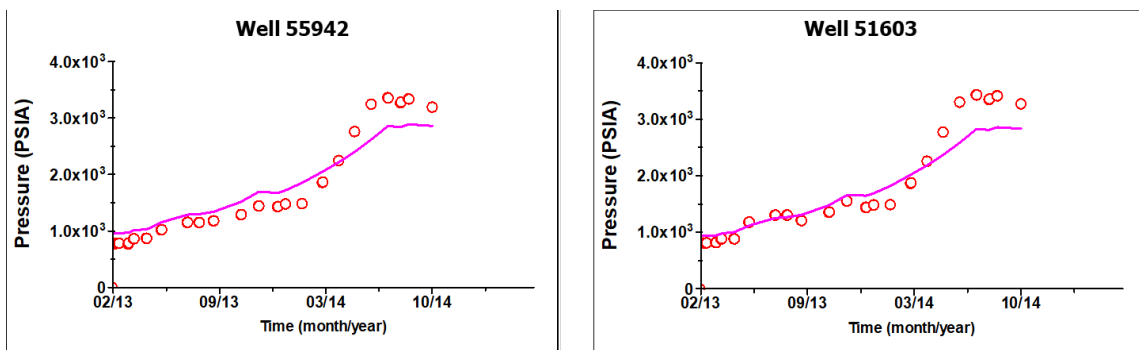


**Figure C-51. Comparison of the bottomhole pressure for two monitoring wells: the history matched model from GA**

It has been noticed that there is an apparent difference in pore volume multipliers especially for region 6 and region 8 (Figure C-52). In other words, pore volumes of regions around the injector has been reduced to achieve better bottomhole pressure match, which indicates the possibility of pore volume reduction during CO<sub>2</sub> injection. Also, as shown in the comparison of the histogram of pore volume for history matched models at every stage (Figure C-53), higher and lower part of pore volume in the last updated model (After CO<sub>2</sub> only) have been decreased to obtain a better match for bottomhole pressure whereas pore volume in the middle has been increased, compared to the previous history matched models.

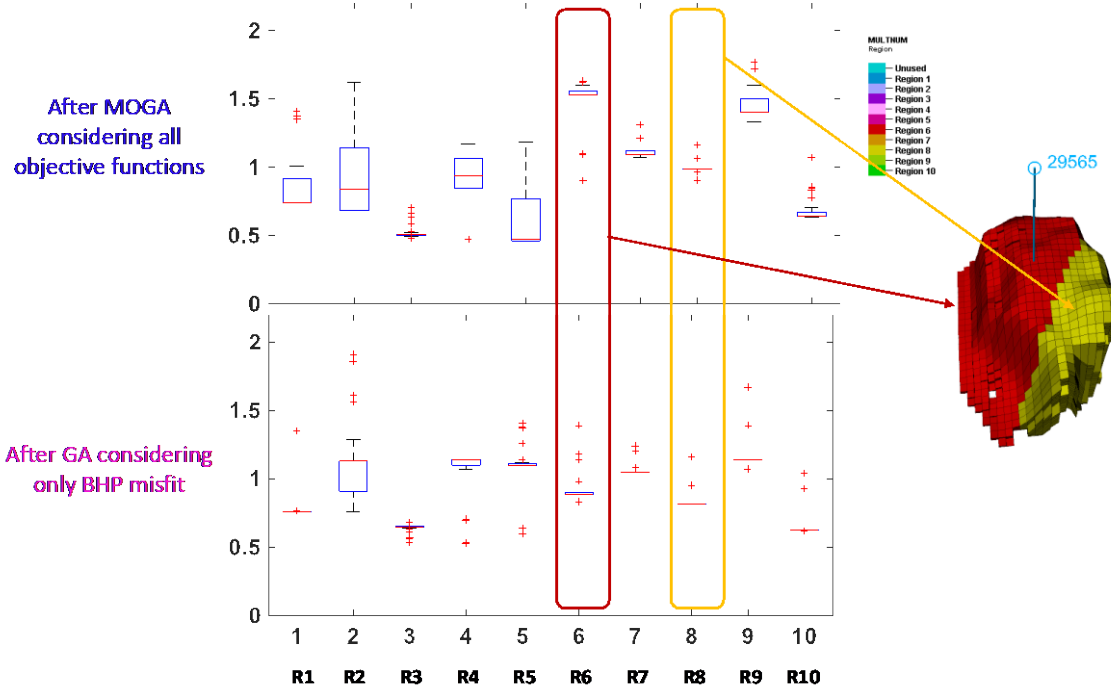


**Figure C-52. Comparison of distribution of pore volume multipliers between MOGA results and GA results**

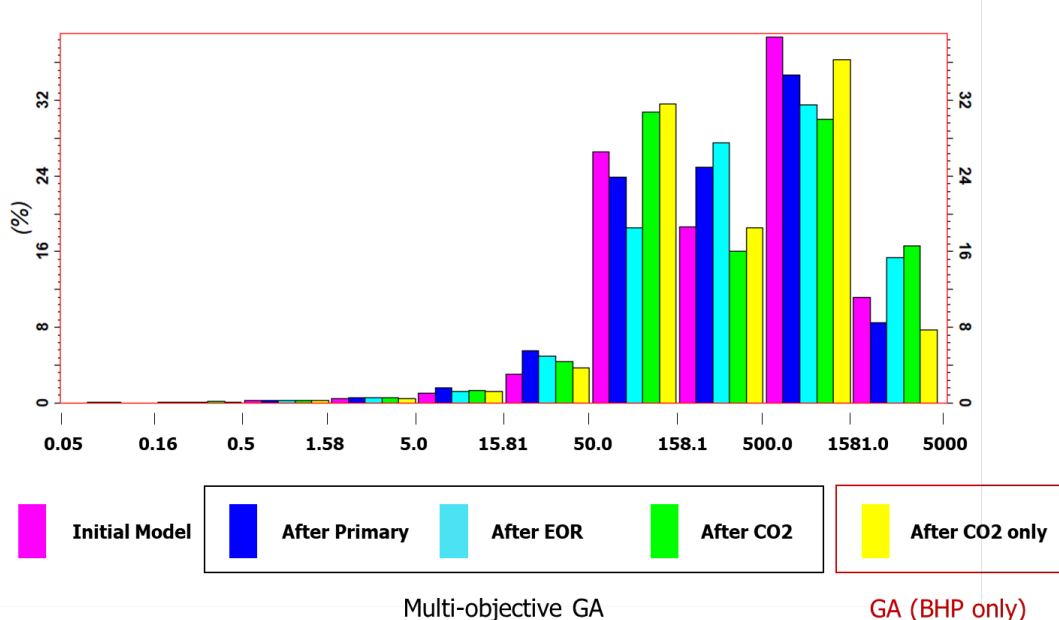


**Figure C-53. Comparison of the histograms of pore volume for the updated models**

In addition, the permeability distribution has been investigated among the history matched models. Compared to an initial model, overall permeability has been increased as several stages of history matching have been performed (Figure C-54). There has been an increase in the higher permeability while the lower part of permeability has been reduced. More specifically, the difference in the permeability between the history matching during EOR period and the history matching during CO<sub>2</sub> injection only period has been examined. As shown in Figure C-55 and Figure C-56, there has been an increase in permeability around regions between an injector and producer '51603' whereas permeability for the regions around producer '55942' has been decreased. For the last updated model from the single GA, an increase of permeability is more noticeable, compared with the updated model during CO<sub>2</sub> injection only period using the Multi-objective GA. Lastly, the permeability of the last updated model from the single GA is presented in the Figure C-57 and Figure C-58 with the certain threshold to see the characteristics of permeability distribution. As shown in Figure C-57, all three wells are connected with a higher permeability channel, whereas the lower permeability regions are located at the upper part of the reservoirs (Figure C-58), which might be the cause of the sharp increasing trend of the bottomhole pressure during the last stage of production period.

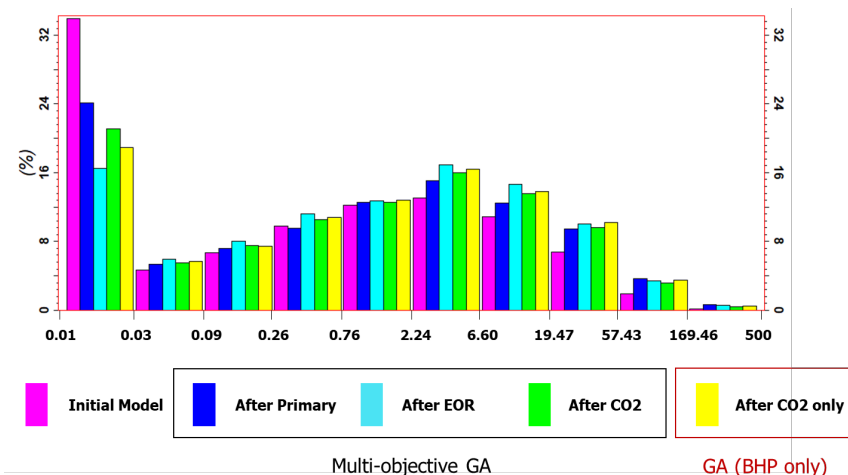


**Figure C-54. Comparison of the histograms of permeability for the updated models**

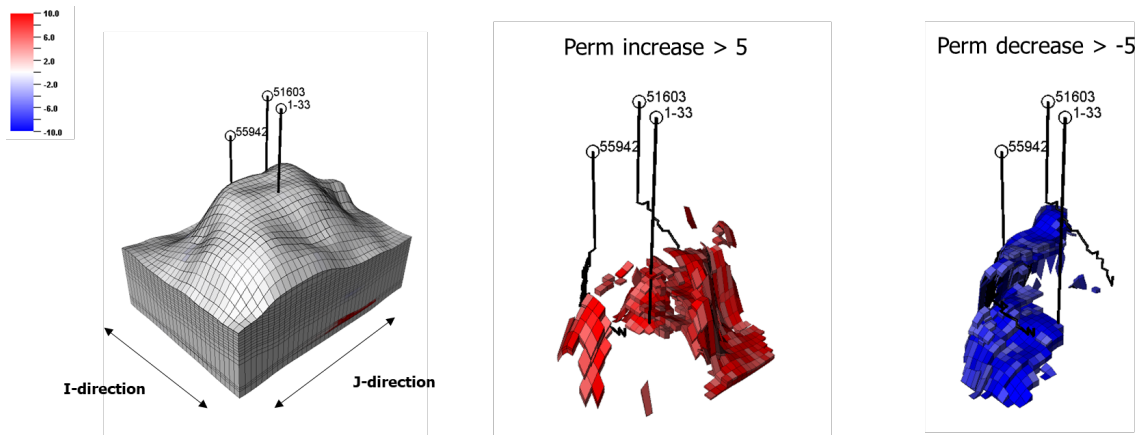


**Figure C-55. Difference in permeability (CO<sub>2</sub> injection only period (GA) and CO<sub>2</sub> EOR period)**

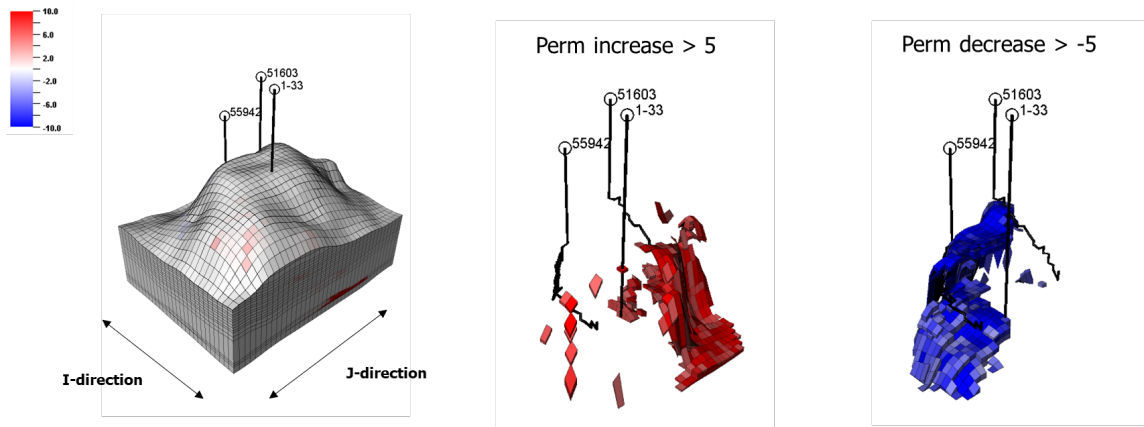


**Figure C-56. Difference in permeability (CO<sub>2</sub> injection only period (MOGA) and CO<sub>2</sub> EOR period)**

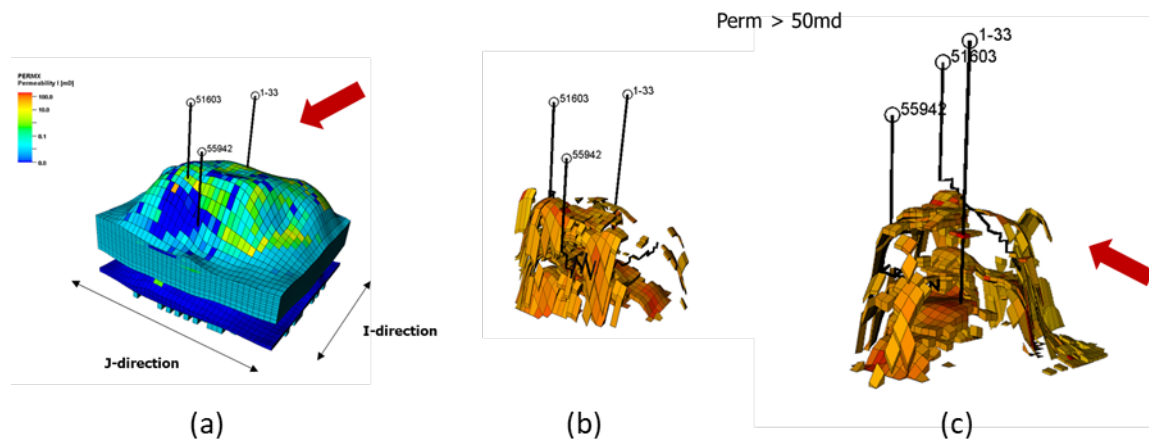


**Figure C-57. Permeability of CO<sub>2</sub> injection only period after GA: (a) permeability distribution (b) and (c) with the high threshold (Perm > 50md) from two different perspective**

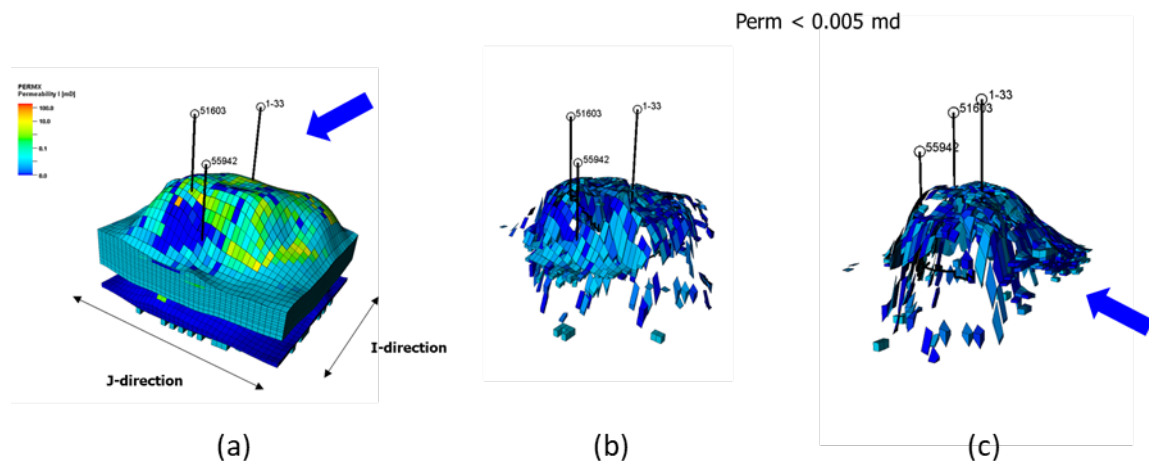


**Figure C-58. Permeability of CO<sub>2</sub> injection only period after GA: (a) permeability distribution (b) and (c) with the low threshold (Perm < 0.005md) from two different perspective**

## 5. Conclusions

In this paper, we proposed the workflow of a multi-stage model calibration that involves a fluid model adjustment and a reservoir model calibration in the Dover 33 field. Due to the lack of reliability in the initial fluid model provided by the operator, parameters in the EOS model have been changed using the Genetic Algorithm that leads to several updated models. Then, the sensitivity analysis has been performed to investigate the impact of parameters in history matching. With the results of the fluid model calibration and the sensitivity study, the history matching process has been divided into three stages based on its production period to calibrate reservoir parameters in a hierarchical manner. Following conclusions are obtained below:

The uncertainty in the original fluid model that has been determined with the limited number of experimental data has been reduced by conducting the fluid model calibration. In this model calibration, three different oil formation volume factors are assumed to obtain updated fluid models that have distinct characteristics.

As a result of incorporating an EOS model as one of the parameters in the reservoir model calibration during primary depletion, Multi-objective Genetic Algorithm proves to be an efficient in finding optimal solutions that show a good agreement for all objective functions respectively. While history matched models have been obtained, the uncertainty in parameters is also substantially reduced.

In the following history matching during the CO<sub>2</sub> EOR period as well as the CO<sub>2</sub> injection only period, parameters are further narrowed down with acceptable matching results. It has been noticed during the last stage of history matching that there are difficulties in finding optimal solutions for both oil productions and pressure responses. In comparison, the results of single objective Genetic Algorithm that only accounts for bottomhole pressure responses, possible pore volume reductions

during the CO<sub>2</sub> injection in regions around an injector has been indicated to capture the sharp increasing trend.

## REFERENCES

Bhark, Eric Whittet, Akhil Datta-Gupta, Behnam Jafarpour. (2011). History matching with a multiscale parameterization based on grid connectivity and adaptive to prior information. Proc., SPE Annual Technical Conference and Exhibition, Denver, Colorado, USA.

Park, H.-Y., Datta-Gupta, A., and King, M.J. (2015). Handling Conflicting Multiple Objectives Using Pareto-Based Evolutionary Algorithm During History Matching of Reservoir Performance. Journal of Petroleum Science and Engineering 125: 48-66.

